Interior of Philips' Lightbulb Factory, Hamilton, Scotland.

UNIVERSITY OF SOUTHAMPTON

FACULTY OF ENGINEERING AND APPLIED SCIENCE

INSTITUTE OF SOUND AND VIBRATION RESEARCH

AN INVESTIGATION OF THE FACTORS WHICH CONTROL NON-DIFFUSE SOUND FIELDS IN ROOMS

by

Neil Christie Baines

A thesis submitted for the
award of Doctor of Philosophy

March 1983

ACKNOWLEDGEMENTS

The author would like to thank the following for their help in the production of this epic -

- *Professor P.E. Doak*, for his patient supervision.

- *All the members of the joint ISVR - Cambridge University modelling project*, especially *Murray Hodgson* and *Raf Orlowski*, for their help and encouragement.

- *The 'inmates' of 15a University Crescent*, especially *Stuart Bolton* and *Steve ('Booky') Baxter*, for many helpful discussions, suggestions and racing tips.

- *TAC roofing manufacturers* for the supply of roofing materials.

- *S.E.R.C.* for keeping the 'wolf from the door' financially.

- *Hazel Paul* for her efficient typing.

- *All my friends, family* and *colleagues* who have put with me during this mammoth production.

CONTENTS

Page No.

CHAPTER 2 (continued)

Page No.

CHAPTER 3 (continued)

Page No.

CHAPTER 4 (continued)

Page No.

CHAPTER 5 (continued)

Page No.

CHAPTER 6 (continued)

Page No.

UNIVERSITY OF SOUTHAMPTON

ABSTRACT

FACULTY OF ENGINEERING AND APPLIED SCIENCE

INSTITUTE OF SOUND AND VIBRATION RESEARCH.

Doctor of Philosophy

AN INVESTIGATION OF THE FACTORS WHICH CONTROL NON-DIFFUSE SOUND FIELDS IN ROOMS

by Neil Christie Baines

When a sound field in a room is not diffuse, the assumptions of Sabine's theory are invalid. A fundamental investigation of the major factors controlling the acoustics of such 'non-Sabine' spaces, and their interactions, is described. The factors are scattering, absorption, and room shape.

Theoretical and experimental investigation of both single and multiple scattering phenomena shows that, in addition to'near field' effects, scattering affects the distribution of energy reflected from a surface and hence alters the effective mean free pathlength.

Analytic models are developed for the absorption characteristics of surfaces constructed from lightweight panels, since these enclose many non-Sabine spaces. Their absorption at low frequencies is shown to be due to the dissipation of vibration energy in the individual panels; hence the absorption characteristics depend strongly on the angle of sound incidence. It is shown that, although an angle-averaged absorption coefficient can be used for the prediction of proportionte rooms' acoustics, the actual angular variation can have a large effect on the reverberant decay in disproportionate spaces. Analysis of the angular distribution of incident energy on a wall demonstrated that it is the same for both proportionate and disproportionate rooms. An alternative weighting function to that of Paris is suggested for use in rectangular rooms with spherically spreading waves.

Finally, analytic models are developed to study the interaction of rough floor surfaces with absorbent ceilings under highly disproportionate conditions. The two factors are found to affect each other significantly (i.e. the magnitude of their effects are not independent). Comparison of the results with scale model measurements is sufficiently encouraging to recommend further development of the more accurate model formulated.

CHAPTER 1

INTRODUCTION

One of the main weapons at the disposal of the practical acoustician in his struggle against recalcitrant acoustics in enclosed spaces is the Sabine theory of room acoustics. Developed by W.C. Sabine [1.1] in the early part of this century, this theory covers the calculation of space and'short-time-averaged' acoustic energy densities for a given class of rooms. When a simple acoustic source operates in a 'Sabine-room' it is possible to evaluate not only the steady state sound level when the source operates continuously, but also the transient behaviour when the source is switched on or off.
Such calculations are now covered in most standard building acoustics texts (see for example References [1.2 and 1.3]). The only parameters required for the calculation of the rate of build-up or decay are the volume of the room and its ability to absorb sound. This latter factor was expressed by Sabine [1.1] as an equivalent area of open window. To compute absolute levels under either steady state or transient conditions the acoustic power of the source must also be specified. This extremely simple theory applies best to rooms which have typical dimensions (i.e., length, breadth, and height) which are all appreciably greater than the acoustic wavelength under consideration and which are of roughly the same magnitude as each other. The room should also possess relatively hard bounding surfaces so that the total acoustic absorption in the room is low. Under such conditions, as are found in reverberation chambers, the acoustic energy density is statistically approximately uniform over the majority of the room and the equations derived by Sabine perform adequately.

Unfortunately many classes of rooms and buildings common in modern architecture do not satisfy the Sabine requirements. This category of 'non-Sabine' spaces includes many environments encountered in everyday life, such as factories, open-plan offices, corridors, supermarkets, school halls, airport buildings, tunnels and even domestic living rooms. The lack of an approximately statistically uniform sound energy density throughout the enclosed volume in such cases can normally be attributed to the enclosure possessing one or more of the three following attributes.

(i) 'Disproportionality'. Where one dimension is much bigger or smaller than the other two, a room may be termed 'disproportionate'. In the limiting case of a single source in an infinitely long tunnel it is obvious that a statistically uniform sound energy distribution is impossible.

(ii) Non-Uniform Wall Absorptivity. In cases where there is a highly non-uniform distribution of wall absorption, or even a uniform distribution of high absorptivity, a statistically uniform sound energy density distribution will not exist. In non-Sabine spaces, since the energy distribution is non-uniform, it may well prove necessary to possess a knowledge of the variation of a surface's absorption characteristic with angle of sound incidence.

(iii) Non-Uniform Reflectivity. In many non-Sabine spaces there are objects present which cause sound waves that impinge upon them to be scattered and/or absorbed. Such scattering bodies may typically be distributed in one of two ways: the first class of distribution is termed'volume scattering' and covers cases where the objects are situated throughout the room's volume, as opposed to the second distribution where all the objects are located on one or more surfaces of the enclosure. This second category may be termed that of 'irregular surface scattering'. For the range of object sizes typically encountered in non-Sabine spaces it is unlikely that sound waves which impinge upon surfaces covered with such scatterers will be either uniformly scattered or perfectly reflected. In these cases a certain proportion of the incident energy will be specularly reflected whilst the remainder is either absorbed or scattered in some non-specular manner. The detailed behaviour is obviously a function of the ratio of scatterer size to acoustic wavelength, the density of the scatterer distribution, and the acoustical properties of both the scattering bodies and the enclosure surface on which they are situated. The presence of either type of scatterers may create non-Sabine conditions since both can contribute to inhibition of the even distribution of sound energy throughout the enclosed volume.

In rooms which possess one or more of the above features, to a significant extent, the assumptions of Sabine are not justified, so that the simple thoeretical models may well prove inadequate and some alternative prediction method(s) must be devised.

Factories are a major class of non-Sabine rooms, and are especially worthy of fundamental study since they often exhibit all three of the above features. For example, the factory illustrated in the frontispiece is approximately 120 m × 40 m × 10 m and is thus highly 'disproportionate'. The majority of its surface absorption is provided by the roof. Such an absorption distribution is obviously highly non-uniform. The absorption of the roof structure may also be expected to be a strong function of angle of incidence due to the lightweight panel construction employed. Finally the floor is covered by an array of machine lines of about 1.5 m height and 1 m breadth which will obviously scatter an incident sound wave to an extent determined by its frequency and angle of incidence. The particular factory illustrated was chosen to be scale-modelled by the SERC funded-joint ISVR-Cambridge acoustical modelling group [1.4], [1.5]. It is believed that this is the first time that an existing factory has been modelled in detail and the results of the model tests compared with those at full scale. Such an exercise is of fundamental importance before a modelling technique is used for predictive purposes. (In this connection it is worthwhile mentioning here that the absorption characteristics of scale model materials are often matched to those at full scale by reverberation chamber measurements (see for example, Reference [1.4] Section 1.4). Whilst this technique is undoubtedly adequate to provide absorption values for use in the modelling of Sabine spaces, it may well prove erroneous in non-Sabine spaces if the material to be modelled displays an absorption characteristic which varies strongly with angle of incidence, unless the absorption mechanism is reproduced at scale. No detailed investigation of such possible errors or the degree of accuracy required in modelling scatterers has apparently ever been performed previously).

Although theories have been developed to predict the acoustical behaviour of factories (these are discussed in the text), they generally contain *ad hoc* assumptions or even parameters to be chosen on a 'best fit' basis. It would therefore appear that an in-depth study of the factors which characterise non-Sabine spaces is required, to be performed in such a way as to permit the inclusion of their behaviour in prediction schemes for the acoustics of such spaces. The research programme described aims to satisfy these deficiencies. It progresses

from a fundamental consideration of the acoustical behaviour of the main individual parameters to a synthesis of the entire field within an enclosure. This approach permits the effects of the components to be studied one by one, and together, under typical non-Sabine conditions. As a consequence of this approach the initial chapters are relatively self-contained and all contain both literature review and conclusions sections. Specifically, the major aspects of scattering as related to non-Sabine spaces are covered in the next three chapters. The first two are concerned with single body free field scattering from both theoretical and experimental viewpoints, over the range of object size to wavelength ratios that are of most interest in room acoustics. The next chapter is devoted to multiple scattering with the emphasis on 'rough surface' models. A model is developed in the fifth chapter to describe the absorption characteristics of surfaces composed of either single or double layer arrays of panels. This class of surface is typical of a whole range of constructions used in modern buildings, such as walls of glazing or lightweight roofing structures and is a previously poorly documented area. The work is unified in the final chapters by the study of the effects of aspect ratio, and non-uniform absorption distribution and characteristics on both steady state levels and reverberant decay rates under typical non-Sabine conditions. Finally, the effect on steady state levels in highly disproportionate spaces of the interaction between hard surfaces that do not reflect sound in a totally specular manner, and surfaces which are smooth but partially absorbent is investigated. These aims are achieved both by use of analytic models and selected scale model tests.

Thus this work is a complete investigation, as thorough as possible, of the major factors which influence the acoustics of non-Sabine spaces, and their possible interactions under such conditions. The objective is not to provide a thoroughly validated universal prediction method for such spaces, but rather to understand the behaviour of the factors present which influence the sound field, and investigate their combined interactions. This is performed in an original manner, and presented in such a way as to permit the future development of more accurate prediction techniques for specific non-Sabine cases. The scale

modelling of such spaces will also be assisted by the results of this work since it indicates the degree of accuracy necessary in the modelling of some of the major features of non-Sabine spaces. Hence the work satisfies many of the demands of acousticians faced with the practical problem of estimating the acoustics of non-Sabine spaces.

CHAPTER 1 : REFERENCES

1.1 W.C. SABINE, 1900. The American Architect and Engineering Record, 3-42. Reverberation. (Reprinted in, R.B. Lindsay (Ed) Acoustics : Historical and Philosophical Development.418-457. Stroudsburg, Pennsylvania : Dowden Hutchinson and Ross, Inc.).

1.2 A.D. PIERCE, 1981. Acoustics : An Introduction to its Physical Principles and Applications. New York : McGraw-Hill.

1.3 H. KUTTRUFF, 1973. Room Acoustics. London : Applied Science Publishers.

1.4 R.J. ORLOWSKI, M.R. HODGSON, N.C. BAINES and M.F.E. BARRON, 1980. ISVR Memorandum. No.603. Progress Report on Acoustic Modelling of Factories.

1.5 R.J. ORLOWSKI, M.R.HODGSON, N.C. BAINES, and M.F.E. BARRON, 1981. ISVR Memorandum No. 614. Final Report on Acoustic Modelling of Factories and Auditoria.

CHAPTER 2

A THEORETICAL CONSIDERATION OF ACOUSTICAL SCATTERING BY SINGLE BODIES UNDER FREE FIELD CONDITIONS

2.1 Introduction

From the discussion of Chapter 1, it is apparent that the scattering of sound waves by one or more objects within a room can be a major factor in the creation of non-Sabine conditions. Although there may often be many objects present in the room (in which case multiple scattering may be important), it is nevertheless essential to grasp the fundamentals of single body scattering, prior to progression to these rather more complicated situations. For these reasons, the vast literature on the mathematical description of scattering and diffraction of sound by single free field objects has been studied, and a review follows. This review is not exhaustive; the aim is rather to cover the main mathematical approaches currently in use in this area. The review section ends with a discussion of the relative merits and applicability of the various analytic methods to the case in hand. The subsequent requirements for further theoretical and experimental research are then outlined. Analytic investigation of some theoretical models completes this chapter. The aim of this investigation is to study both the models' applicability to the problem under consideration, and the intrinsic physical nature of the solutions. The experimental programme of work is described in the next chapter.

2.2 An Overview of the Analytic Methods Used for Single Body Free Field Scattering Problems

2.2.1 The requirements of a mathematical solution to freefield scattering problems

Acoustic scattering occurs when a sound field impinges upon a body immersed in the medium through which the sound propagates. Due to the presence of the body a secondary, or scattered field is produced.

The total field can be represented as the sum of incident and scattered components. Any mathematical solution of this problem must be subject to a series of conditions. These conditions may be stated as follows (further details are contained in References [2.1, 2.2 and 2.3]).

(i) The total field must everywhere satisfy the wave equation
(ii) The total field must satisfy the boundary conditions (taken here as acoustic impedance) at the surface of the scatterer.
(iii) The scattered field must satisfy a radiation condition at infinity: that is, at large distances from the scatterer, the scattered field should appear to originate from the object and produce waves which propagate away from it.
(iv) The scattered field must everywhere remain finite. (except possibly at mathematically sharp edges - see (v) below).
(v) The field must satisfy an edge condition, such that no sound is generated at sharp edges (see Reference [2.2]).

The required conditions for the solution have now been stated. It remains to investigate methods of calculating solutions which satisfy these requirements for given bodies and incident fields. In the next section two exact approaches to the problem, are considered, and in the following section high and low frequency approximations are considered. Both of these sections are concerned with the techniques involved rather than investigation of specific cases. Certain single body free field scattering problems are studied in the concluding sections of this chapter.

2.2.2 *Exact solution techniques*

Two main classes of approach are covered. They are as follows.

i) Series Solution Approach

For certain simple cases it is possible to express both the field scattered by the object (which has a form similar to that for the object acting as a radiator) and the incident wave as infinite series eigenfunction expansions. This is normally only possible for co-ordinate

systems in which the wave equation is separable. It then only remains to apply the boundary conditions at the scatterer's surface. Equating individual terms in the series for the scattered and incident fields (possible because of the orthogonality of the eigenfunctions) then provides values for the unknown weighting coefficient in each term of the scattered series expansion. This technique will be employed to study the case of a rigid sphere in section 2.3.

ii) Integral Equation Approach:

It is well known that any solution of the wave equation inside a closed volume can be represented in terms of an integral of the field and its normal derivative on the enclosing surface, on the assumption that the corresponding Green functions exist and can be found. This is considered in References [2.1, 2.4 and 2.5]. The enclosing surface can normally be split into two parts, one around the scatterer, the other at infinity (as is shown in Reference [2.6]). The latter gives a zero contribution, which leaves an integral in terms of the unknown surface values on the scatterer. The boundary condition at the scatterer's surface and the incident field there are known however. The field at a point on the scatterer can also be constructed in terms of an integral of the field over all points on the surface. Insertion of this integral expression into the boundary condition results in an integral equation for the surface field at any point. The solution of this equation can then be used in the earlier expression for the scattered field at any point off the surface.

Both of these exact solution methods have drawbacks in practice. The eigenfunction approach has two drawbacks. First, it works effectively only for co-ordinate systems in which the wave equation is separable, and for bodies which are suitable (see Reference [2.7] for the complete range of cases where this type of solution is possible). Secondly, it involves the summation of an eigenfunction series which may contain functions which are difficult to compute, and also the summation may be exceedingly slow to converge at large ka values (where k is the acoustic wavenumber, and a is a typical object dimension e.g. the radius of a sphere). The integral equation approach is also only exactly solvable in relatively few cases. However it does provide the basis for many numerical or approximate techniques,

some of which are covered in the next section. The advantage of these exact solutions is that they do provide "absolute calibration" of any approximate analytical or experimental method used. It is partly for this reason that the series solution for the case of the rigid sphere is used later in this chapter. Exact solutions also permit the physics of a situation to be investigated: this is why the infinite half plane case is similarly studied.

2.2.3 *High and low frequency scattering approximations*

This section contains details of some of the major approximation techniques used in the prediction of single body scattering. One of the most important is the Kirchhoff method. This is broadly similar to the integral equation approach, except that instead of solving an integral equation in order to obtain the surface field it is normally approximated by values related to the incident field there. It too suffers from some drawbacks since the predictions for the field off the surface are inconsistent as the field point approaches the scatterer surface (see Reference [2.1] Section 4). This is because specification of both the pressure and the velocity distribution at the scatterer is strictly impermissible. Improved versions in terms of either velocity or pressure distributions have been formulated. These are termed Rayleigh-Kirchhoff equations. For predictions off the surface, for ka values greater than about 5, this technique has been shown to work very well (see for example References [2.3 and 2.8]). It is also possible to reduce the surface integral to a line integral around the object's edge. This approach has been applied by Embleton [2.10] to the practical problem of noise barrier performance prediction in the presence of the ground. Skudzryk [2.9] further showed that for cases where this line integral is over a closed curve there are two types of region where the major contribution to the integral occurs. One region occurs where the source to receiver distance via the edge is a maximum, and the other is where this distance is a minimum. This latter criterion has been used by Keller [2.11] as the basis of an extensive theory called 'Geometric diffraction'.

This theory is most useful in connection with ray acoustics (see Reference [2.12] for a good description of ray acoustics). It states that any incident ray which strikes the edge of a scatterer generates diffracted rays. The initial value of a scattered ray is obtained by multiplying the field on the incident ray by a diffraction coefficient. This coefficient may be obtained for a particular type of edge either by solution of a canonical problem or from experimental results, and is determined by the local conditions at the point of diffraction (i.e. the directions of incidence and diffraction, the wavelength, and the geometric and physical properties of the media at the point of diffraction). Although this technique is essentially a high frequency approximation it has been shown to give good agreement with experiment provided that the diffracting edge is greater than about three wavelengths, as is shown in Reference [2.13]. Ray diffraction methods are common in barrier attenuation calculations, Reference [2.14] gives details of such techniques. Pierce [2.15] has extended the theory to thick barriers, and Kawai [2.16] has employed Pierce's approach to cover diffraction by objects such as pillars. Other frequently used barrier prediction methods are based on the Fresnel number, which is twice the ratio of the extra pathlength in going from source to receiver via the barrier edge, as opposed to directly, to wavelength (see Reference [2.17] for further details).

All of the above methods are only applicable at high frequencies. There are no specialised techniques as such for low frequency scattering calculations, but it is often adequate to take only the initial terms in an expansion in these cases. This allows it to be shown (see Reference [2.12]), that for any shape of body, at low frequencies (i.e. small ka) , the scattered wave is composed entirely of point monopole and dipole terms. For a rigid body these terms are of the same magnitude in the far field. The monopole term can be attributed (as is shown by Lighthill [2.18]), to the difference between the compressibility of the scatterer and that of the fluid it has displaced, whilst the dipole term is due to the change in mass. Low frequency approximations are often referred to as Rayleigh scattering due to his contributions to the understanding of the behaviour at low ka (see for example Reference [2.19]).

2.2.4 *Analysis of the implications of the literature review for this research programme*

It is immediately apparent that none of the techniques outlined is directly applicable to practical scattering predictions in non-Sabine spaces. The solutions described are either exact, in which case they are of limited applicability and are difficult to calculate, or they are only approximate solutions, which are valid for either high or low frequency regimes. In the normal range of room acoustics predictions, the ratio of scatterer size to wavelength can typically vary from less than unity to much greater than it. The use of one approximation for all frequencies or scatterers may not therefore be justified. Furthermore, in a practical situation, the acoustic sources will undoubtedly be of a broadband nature, and may be distributed throughout the room. The scatterers may be similarly distributed and may quite possible be of complicated or irregular shapes. Whether the receiver position is in a particular scatterer's near or far field will also vary from one situation to another. The usefulness of a given approximation is therefore not evident *a priori* unless the nature of the scattering process and the approximations made are fully understood.

In the literature there is a complete lack of results presented in a manner which is pertinent to a study of non-Sabine room acoustics. Where diagrams of the distribution of the scattered field exist (as in References [2.5, 2.9 and 2.12]), they are often only plots of its modulus. This provides no indication of the behaviour of the steady state overall level at any point. The other well documented index of an object's scattering ability is it's scattering cross-section (see References [2.5 and 2.12]. This denotes the ratio of the total power scattered to that incident, and thus there is no indication of the angular distribution of the scattered energy. An adequate scattering theory for inclusion in room acoustics models would appear to require an assessment of both the power scattered and its directional distribution, and possibly its phase relative to the incident field.

The experimental and theoretical investigations described in the remainder of this and the next chapter are designed to at least partially

fill the gaps evident in the literature. The experimental procedure involves measurement of the distribution of total sound pressure level around various objects, at distances which are comparable to object size for both pure tone and bandlimited white noise incident sound fields. The theoretical programme begins with a study of the exact solution to the problem of scattering by a rigid sphere. This is used to provide an indication of the absolute accuracy of the experimental method. The remaining cases examined were selected to investigate the applicability of some high frequency models and to study the physics of the scattering processes involved.

2.3 The Series Solution to Scattering by a Rigid Sphere:

2.3.1 The exact series solution:

The exact mathematical solution to the problem of the scattering of sound by a sphere has been known for a long time (see e.g., Reference [2.19]). It is now included in many standard texts (e.g. References [2.5 and 2.9]). In order to introduce notation and facilitate comprehension of the decomposition performed in the next section, the solution's derivation will be sketched out below.

For the geometry of Figure 2.1 and an assumed time factor $e^{i\omega t}$, the pressure at a general receiver point at a distance R' from the source may be written as

$$\frac{e^{ikR'}}{kR'} = -i \sum_{n=0}^{\infty} (2n+1) P_n(\cos\theta) h_n^{(2)}(kr_o) j_n(kr) \qquad (2.1)$$

where $R' = \sqrt{r^2+r_o^2-2rr_o\cos\theta}$, P_n is a Legendre function of order n, and h_n and j_n are spherical Hankel and Bessel functions respectively. Due to the presence of the sphere there must be a scattered outgoing pressure wave of the general form

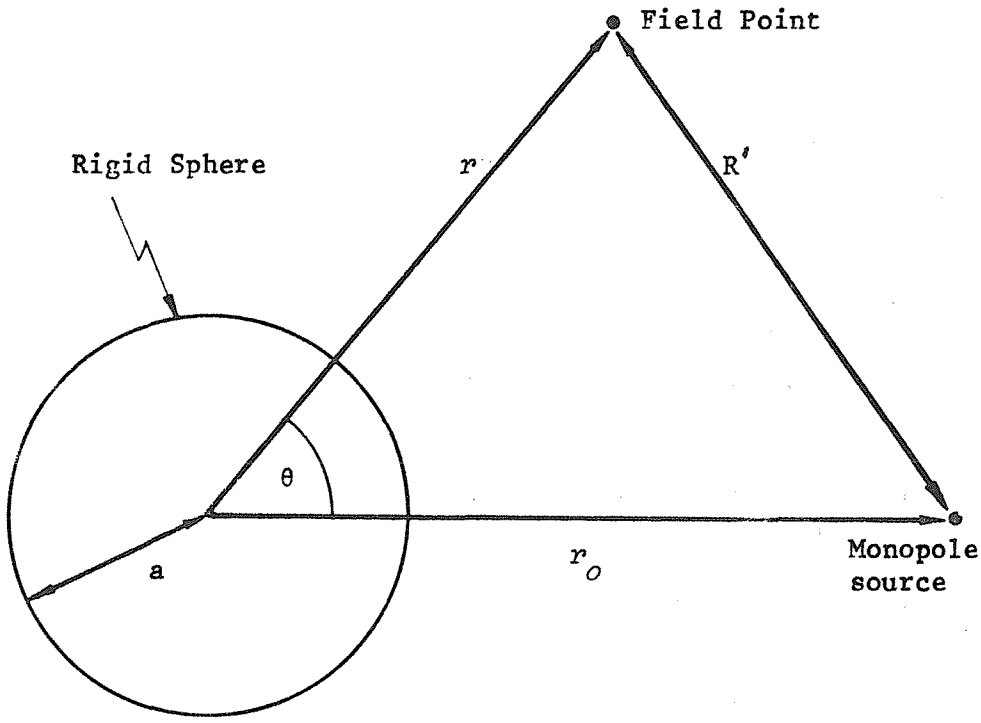

Figure 2.1 The geometry used for the derivation of the series solution for scattering by a rigid sphere.

$$P_s(\underline{r}) = i \sum_{n=0}^{\infty} (2n+1) P_n(\cos\theta) h_n^{(2)}(kr_o) \sigma_n h_n^{(2)}(kr) \qquad (2.2)$$

where σ_n is an unknown weighting factor, to be determined by the boundary conditions at the sphere's surface. For the case of a rigid sphere, the total normal velocity at the surface must be zero. Thus σ_n can be shown to equal $j_n'(ka)/h_n^{(2)\prime}(ka)$. This gives the following expression for the total pressure at $\underline{r}$:

$$P(\underline{r}) = P_i(\underline{r}) + P_s(\underline{r}) = i \sum_{n=0}^{\infty} (2n+1) P_n(\cos\theta) h_n^{(2)}(kr_o) \left\{ \frac{j_n'(ka)}{h_n^{(2)\prime}(ka)} h_n^{(2)}(kr) - j_n(kr) \right\} \qquad (2.3)$$

Numerical values of this expression were computed on the Univesity's ICL2970 computer by using standard recursion relations (as given in Reference [2.20]) for the various functions. The results are presented normalised by the incident pressure at the field point. The series was truncated at the stage when the magnitude of two successive terms fell below some specified limit. Alteration of this value from 10^{-12} to 10^{-15} produced no changes in the results to five decimal places of a decibel (relative to the incident value), which suggests that an adequate number of terms in the series has been taken. (This point was also verified by the check on the scattered power described in the next section). For the results displayed the 10^{-12} criterion was used. Some results of the computations are shown for surface points in Figure 2.2, and for receiver positions off the surface in Figure 2.3.

The computed results show that for points on the surface, even at relatively high frequencies, the shadow may be far from absolute, there being a diffraction pattern evident. The surface sound pressure level in the 'bright region' is 6 dB greater than the incident value, which implies that the behaviour in this area is governed by 'perfect reflection'. Figure 2.3 shows that this 'perfect reflection' behaviour is less easily observed for points off the surface, although a similar diffraction pattern can still be seen in the 'shadow zone'. The results of Figure 2.3 will also permit the accuracy of the next chapter's experimental technique to be investigated.

2.3.2 Decomposition of the series solution:-

Since equation (2.3) is an exact solution to scattering by a rigid sphere, it can now be used to investigate the accuracy of approximate methods. Dissection of the complete series into component parts may also show which terms are responsible for the various observed effects described in Section 2.3.1.

The decomposition chosen is based on the fact that at high frequencies the scattered pressure terms at the sphere's surface asymptote to minus ρc times the incident field's radial velocity there.

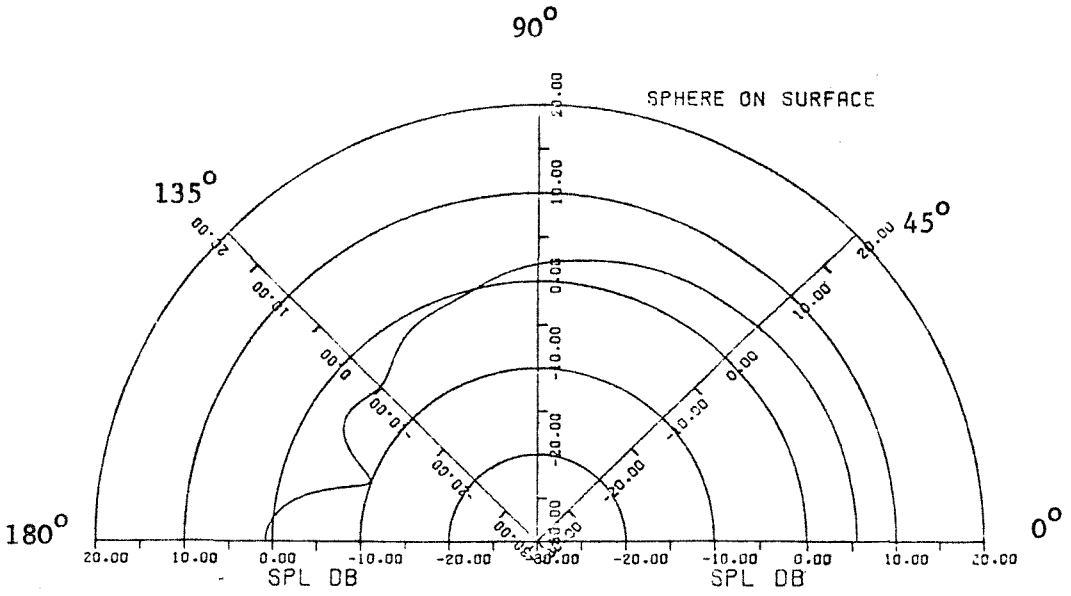

Figure 2.2(a) ka = 5.96; kr_o = 140.44.

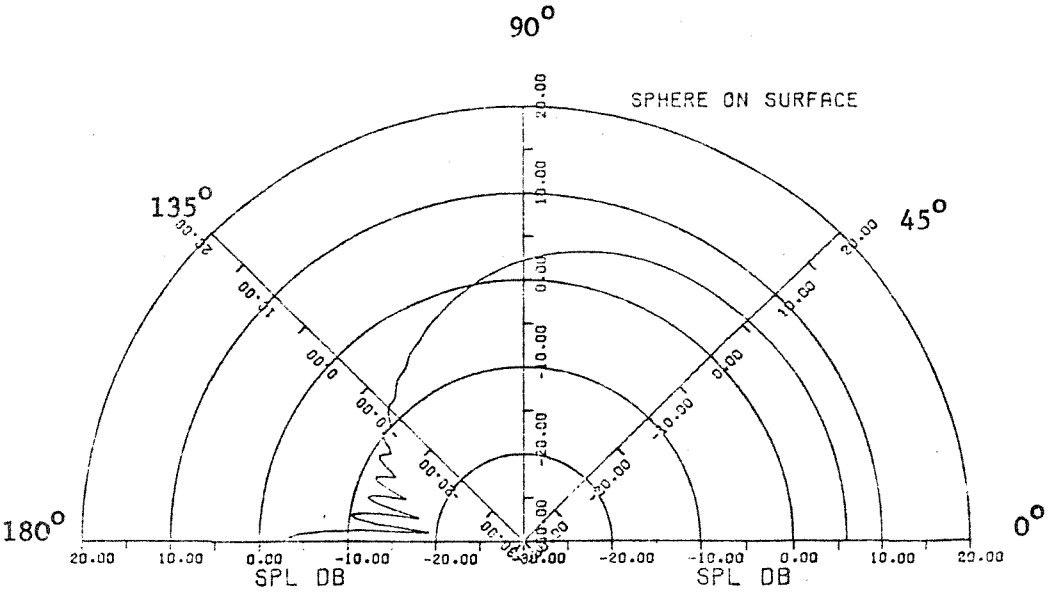

Figure 2.2(b) ka = 23.84; kr_o = 561.84

Figure 2.2. Calculated values for the overall SPL (relative to that incident) on the surface of a rigid sphere. Parameter values as indicated.

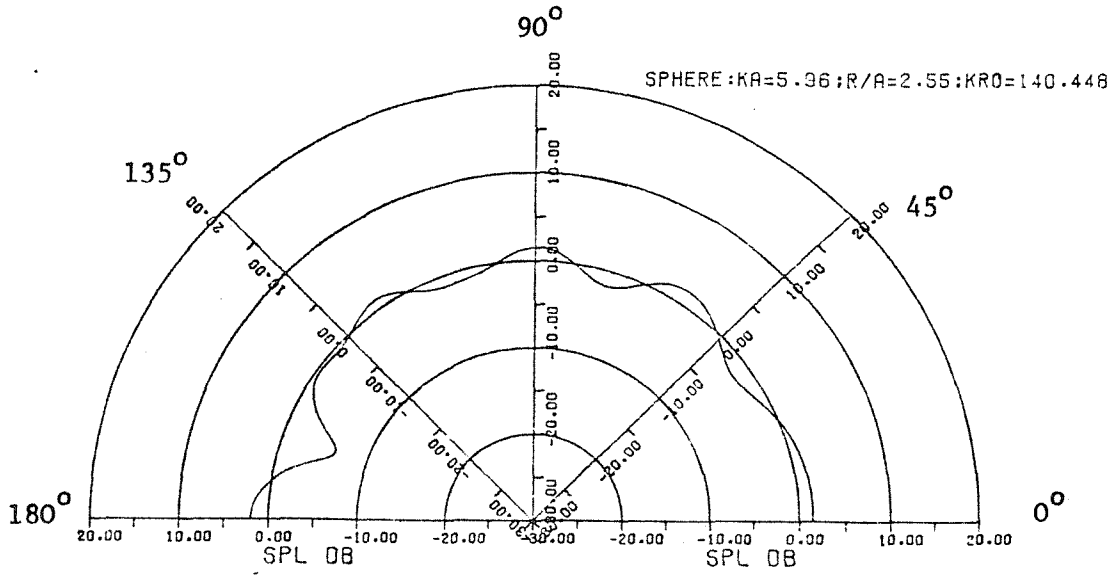

Figure 2.3(a) ka = 5.96; r/a = 2.55; kr_o = 140.448

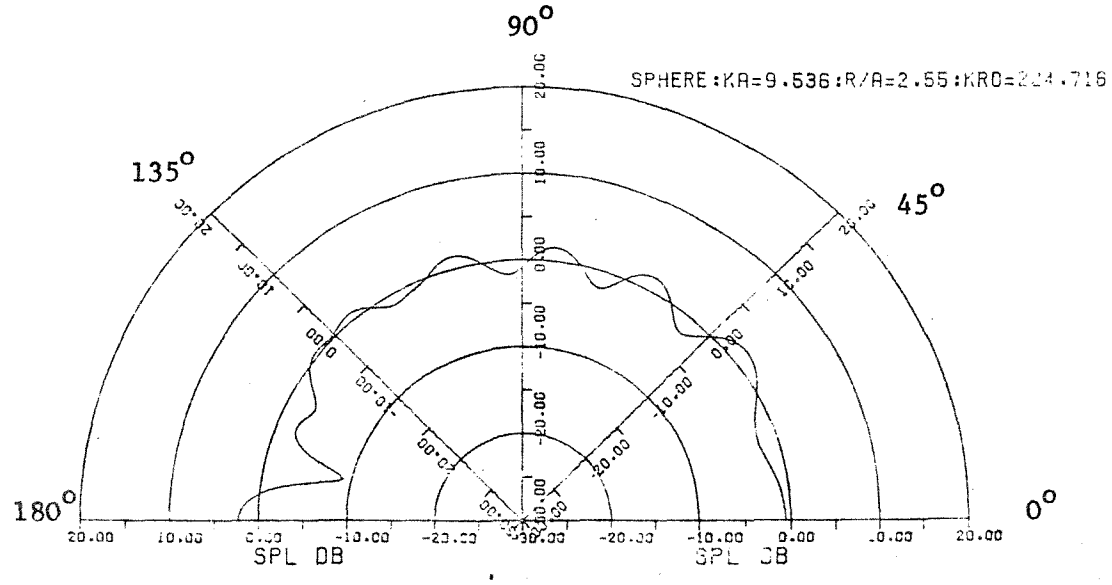

Figure 2.3(b) ka = 9.536; r/a = 2.55; kr_o = 224.716

Figure 2.3. Computed values for the overall SPL (relative to that incident) for points off the surface of a rigid sphere irradiated by a spherical source. Parameter values as indicated.

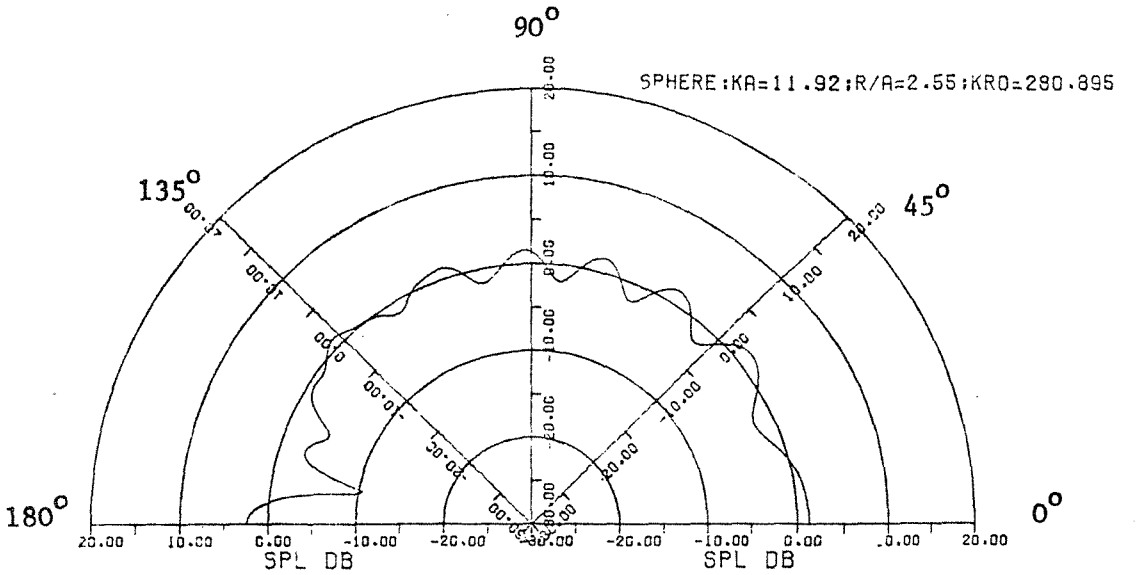

Figure 2.3(c) ka = 11.92; r/a = 2.55; kr_o = 280.895

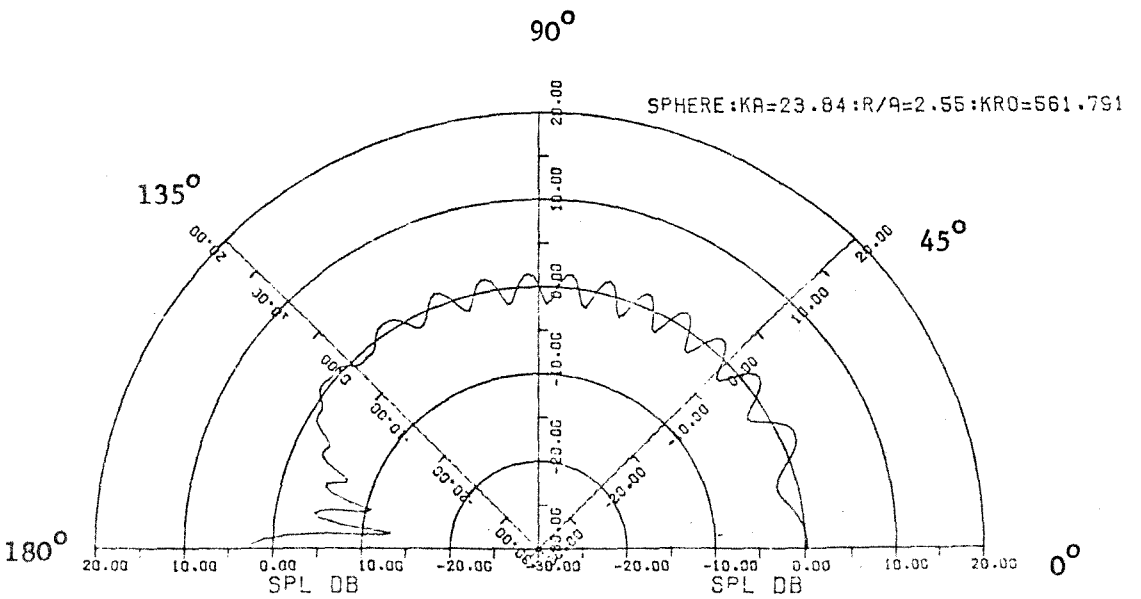

Figure 2.3(d) ka = 23.84; r/a = 2.55; kr_o = 561.791

Figure 2.3. (cont'd).

This decomposition is described in Appendix A, and results in the following expression for the scattered pressure:

$$P_s(\underline{r}) = P_R(\underline{r}) + P_D(\underline{r})$$

where P_R represents the 'high frequency', or reflected, approximation, and is given by

$$P_R(\underline{r}) = - \sum_{n=0}^{\infty} (2n+1) P_n(\cos\theta) \frac{j_n'(ka)}{h_n^{(2)}(ka)} h_n^{(2)}(kr) \quad . \qquad (2.4)$$

and P_D consists of the 'low frequency' terms required to complete the total scattered field, that is,

$$P_D(\underline{r}) = \sum_{n=0}^{\infty} (-i)^n (2n+1) P_n(\cos\theta) j_n'(ka) \left[\frac{1}{h_n^{(2)'}(ka)} + \frac{1}{h_n^{(2)}(ka)} \right] h_n^{(2)}(kr) \qquad (2.5)$$

The value of the time-averaged radial intensity at any point $\underline{r}$ can be written in terms of all the component parts as follows:

$$J(\underline{r}) = \frac{1}{2} \mathrm{Re}\left\{ (P_I + P_R + P_D)(V_{Ir}^* + V_{Rr}^* + V_{Dr}^*) \right\}$$

However computation of each term requires calculation of the product of two infinite series at every field point. It is more informative to use the orthogonal properties of the functions in the series to facilitate calculation of the total power scattered by each term (as described in Appendix A). This reduces the calculation to one 'infinite' series for the power scattered by each component PV^* product.

Figure 2.4 shows the results of such calculations. It is immediately apparent that the sums 'add up', since as there are no sources within the enclosed volume the net power flow should be zero.

ka	W_{RR}	W_{RI}	W_{RD}	$W_{IR}=-W_{ID}$	W_{DD}	W_{DI}	W_{DR}
1	0.1816	-0.3333	0.1517	-0.1704	0.1369	0.2529	-0.3898
2	0.2363	-0.3333	0.0.971	-0.0965	0.0912	0.1380	-0.2291
3	0.2476	-0.3333	0.0857	-0.0678	0.0698	0.7496	-0.1447
4	0.2511	-0.3333	0.0822	-0.0525	0.0594	0.0351	-0.0945
5	0.2524	-0.3333	0.0809	-0.0429	0.0541	0.7493	-0.0616
10	0.2528	-0.3333	0.0805	-0.0227	0.0492	-0.0590	0.0097
20	0.2517	-0.3333	0.0816	-0.0119	0.0538	-0.1010	0.0472
30	0.2512	-0.3333	0.0822	-0.0081	0.0578	-0.1175	0.0597
40	0.2509	-0.3333	0.0825	-0.0061	0.0608	-0.1266	0.0658
50	0.2507	-0.3333	0.0826	-0.0049	0.0630	-0.1325	0.0695
100	0.2503	-0.3333	0.0830	-0.0025	0.0690	-0.1456	0.0766
	$W_{RR} + W_{RI} + W_{RD} = 0$				$W_{DD} + W_{DI} + W_{DR} = 0$		

Figure 2.4 Decomposition of the power scattered by a sphere into high and low frequency terms.

$$W_{AB} = \frac{1}{2} \mathrm{Re} \int (p_A \cdot V^*_{Br}) dS / 2\pi a^2 A^2 / \rho c \ .$$

This occurs here since each set of terms containing either P_R or P_D individually adds up to zero, and the terms involving the product of the incident pressue with V^*_{Rr} and V^*_{Dr} are equal and opposite.

It should be noted that the 'W_{RR}' term (i.e. the integral of the product of P_R with V^*_{Rr}) accounts for all the geometrically incident power at all but the very lowest ka values. This suggests investigation of how adequately P_I and P_R can approximate the total pressure field (i.e., P_I+P_S). Figure 2.5 shows the results of such computations for ka equal to 4 , for field points on and off the surface.

From the surface pressure results of Figure 2.5(a) it is immediately obvious that the asymptotic solution is an inadequate approximation to the exact result in the shadow region (note the magnitude of the scale). In the far field, as is shown in Figure 2.5(b), the agreement is much better although the approximate solution again fails in the geometric shadow zone (between about 165 and 180 degrees). Even in this region however, the discrepancy is not so great as in the first case, presumably because the contribution of the scattered field to the overall level becomes less the further away the field point is from the scatterer.

The decomposition performed demonstrates that the shadow zone detail is provided by the 'low frequency' terms, which could be termed the 'diffracted field'. Also, although the 'high frequency' terms can account for all the geometrically incident power even at low ka values, their behaviour only approaches that of the complete solution for high ka values and in the scattered far field.

In order to investigate whether similar behaviour holds true for 'thin' objects, in the next section an approximate model for diffraction by a disc is investigated. This model is again a high frequency approximation.

2.4 *Models for Scattering by Thin Rigid Objects, Specifically Applied to the Case of a Disc.*

In this section, a model will be developed to describe scattering by thin, acoustically hard objects. 'Thin' here is used to imply that there is no change in the incident pressure, P_I, between the front and back faces. An integral formulation will be derived for the far field scattered pressure in terms of an assumed known scatterer surface pressure distribution. Two different surface pressure distributions will then be examined; one is based upon the high frequency (geometric acoustics) limit, the other on published exact surface pressure results. This will allow the effects of inaccurate assumptions about the scatterer's surface pressure on far field predictions to be investigated.

Figure 2.5. Comparison of the total fields predicted by the exact and high frequency series solutions for scattering by a rigid sphere.

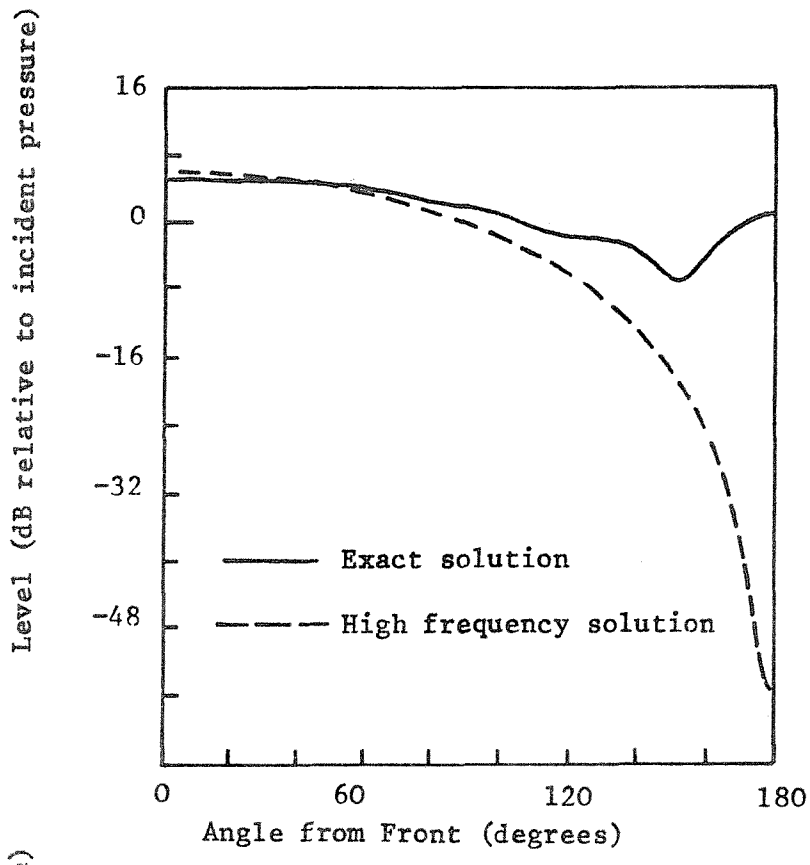

Figure 2.5(a)

ka = 4
r/a = 1
kr_o = 555

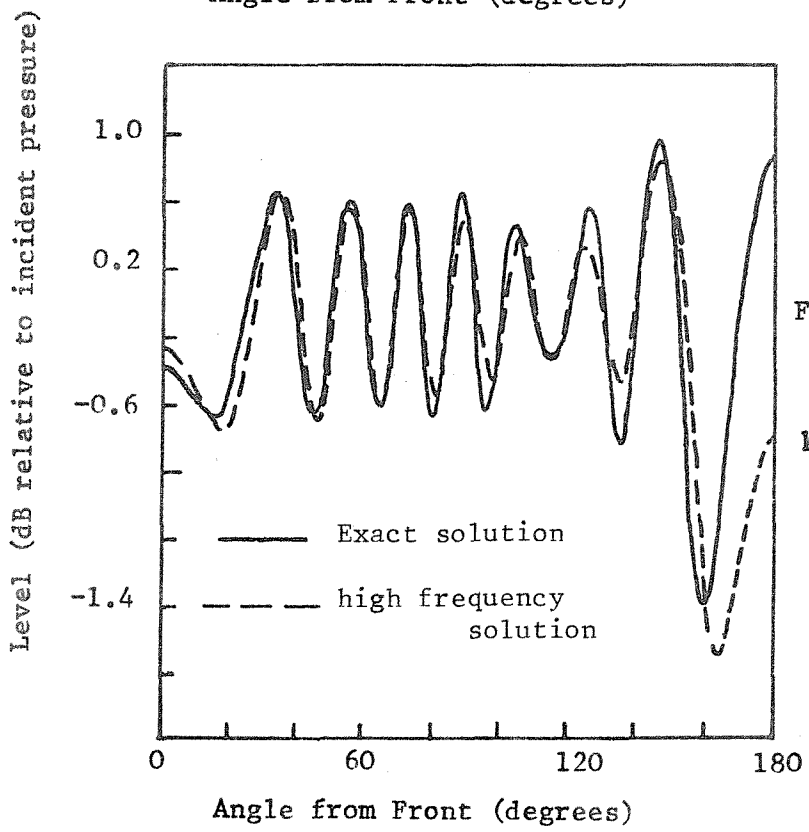

Figure 2.5(b)

ka = 4
r/a = 6.25
kr_o = 555

2.4.1 *A Green function formulation of scattering by thin hard objects of arbitrary cross-section*

It can be shown that the scattered pressure at any point in an infinite fluid medium can be represented as an integral of the surface pressure and its normal derivative over a surface just enclosing the scattering object (this is considered in Reference [2.6]). This surface integral may be arbitrarily split in two, one part for the 'bright' region, the other for the 'shadow' region. A general expression for the scattered pressure at a field point $\underline{r}$ may now be written as,

$$P_s(\underline{r}) = \int_{S_+} \left\{ P_+(\underline{r}') \frac{\partial G_\infty}{\partial n} (|\underline{r}-\underline{r}'|) - G_\infty(|\underline{r}-\underline{r}'|) \frac{\partial P_+}{\partial n}(\underline{r}') \right\} dS_+$$

$$+ \int_{S_-} \left\{ P_-(\underline{r}') \frac{\partial G_\infty}{\partial n} (|\underline{r}-\underline{r}'|) - G_\infty(|\underline{r}-\underline{r}'|) \frac{\partial P_-}{\partial n}(\underline{r}') \right\} dS_+ \qquad (2.5)$$

where P is the total surface pressure at a surface point $\underline{r}'$, G_∞ is the free field Green function $\partial/\partial n$ is the outward normal gradient to the scatterer at $\underline{r}'$, and the '+' and '-' subscripts represent 'bright' and 'shadow' zone values respectively.

Now, for an acoustically hard object the pressure gradient terms will be zero at the scatterer's surface. Furthermore, for a general thin object (of the geometry shown in Figure 2.6) since the total normal pressure gradient is zero, the following expressions hold true. At the front surface, $\partial P_I/\partial n = (\partial P_I/\partial z)_{z=0} = ikP_o = -\partial P_s^+/\partial n$, whilst at the rear surface, $\partial P_I/\partial n = -(\partial P_I/\partial z)_{z=0} = -ikP_o = -\partial P_s/\partial n$. Therefore the normal scattered pressure gradients are equal in magnitude but opposite in sign on the two sides of the scatterer. Hence the scattered pressure at the scatterer must be an odd function across the body. This was mentioned by Leitner [2.8].

The argument of the free field function can be written as

$$|\underline{r}-\underline{r}'| = \left((x-x')^2 + (y-y')^2 + (z-z')^2\right)^{\frac{1}{2}}, \qquad (2.6)$$

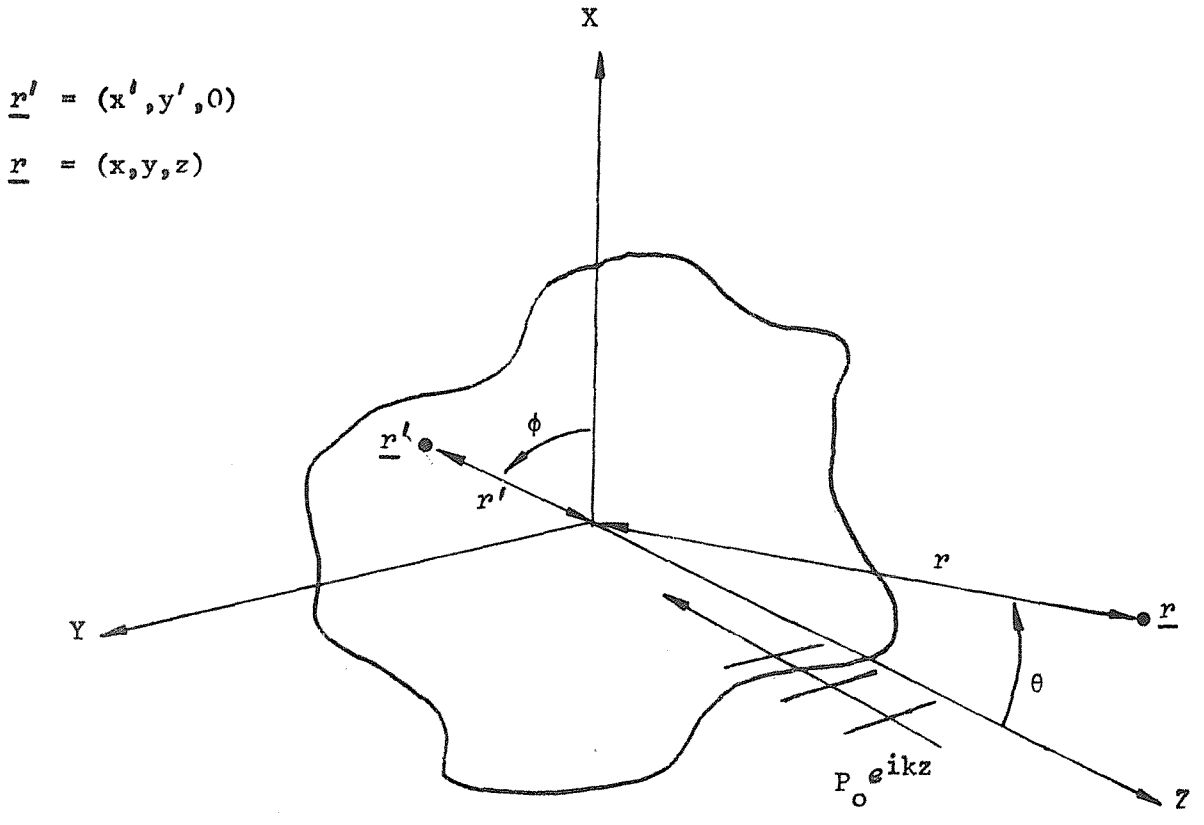

Figure 2.6 The geometry considered in section 2.4. The thin scatterer is entirely in the x-y plane. An $e^{i\omega t}$ time factor is assumed.

from which it can be seen that the normal derivative of the Green function on the front surface can be expressed in terms of z as

$$\frac{\partial G_\infty}{\partial n}(|\underline{r}-\underline{r}'|) = \frac{\partial G_\infty}{\partial z'}(|\underline{r}-\underline{r}'|) = -\frac{\partial G_\infty}{\partial z}(|\underline{r}-\underline{r}'|) \quad ,$$

and on the back surface as

$$\frac{\partial G_\infty}{\partial n}(|\underline{r}-\underline{r}'|) = -\frac{\partial G_\infty}{\partial z'}(|\underline{r}-\underline{r}'|) = \frac{\partial G_\infty}{\partial z}(|\underline{r}-\underline{r}'|) \quad .$$

In view of these expressions, equation (2.5) can now be rewritten, without loss of generality, as

$$P_s(\underline{r}) = -\int_A 2P_s(\underline{r}') \frac{\partial G_\infty}{\partial z}(|\underline{r}-\underline{r}'|)dA \quad . \tag{2.7}$$

where $P_s(\underline{r}')$ is the scattered surface pressure at a point $\underline{r}'$ on the bright side of the object, and the integral is now only over the cross-section.

2.4.2 *The application of far field conditions*

In the far field, that is for $\underline{r} >> \underline{r}'$, it is possible to simplify the form of the Green function used. This is because, under such conditions, equation (2.6) becomes, for $z' = 0$,

$$|\underline{r}-\underline{r}'| \simeq |\underline{r}|(1-xx'/|\underline{r}|-yy'/|\underline{r}|) \tag{2.8}$$

For the case of a disc with the co-ordinate system origin at its centre and a receiver in the x-z plane, equation (2.8) reduces to the form in polar co-ordinates,

$$|\underline{r}-\underline{r}'| \simeq r(1 - \frac{r'}{r}\cos\phi\sin\theta) \tag{2.9}$$

Use of this form in the three-dimensional free field Green function therefore gives

$$G_\infty(|\underline{r}-\underline{r}'|) = \frac{e^{-ik|\underline{r}-\underline{r}'|}}{4\pi|\underline{r}-\underline{r}'|} \simeq \frac{e^{-ikr(1-\frac{r'}{r}\cos\phi\sin\theta)}}{4\pi r} \quad . \tag{2.10}$$

Substitution of this form for the Green function into equation (2.7) yields the following expression for the far field scattered pressure from a disc of radius a :

$$P_s(\underline{r}) = -\frac{\partial}{\partial z}\left\{\frac{e^{-ikr}}{4\pi r}\int_0^a\int_0^{2\pi} 2P_s(\underline{r}')e^{ikr'\cos\phi\sin\theta}r'dr'd\phi\right\} \tag{2.11}$$

It now only remains to specify the distribution of the scattered pressure field on the scatterer, for the scattered pressure to be defined at any point in the far field. In the following sections, two cases will be studied. In the first case a high frequency (geometrical acoustics) pressure distribution is used. This will then be compared with the second case, where published exact surface pressure results are used.

2.4.3 *A high-frequency model for the far-field scattering of sound by a thin rigid disc.*

At high frequencies it may be assumed that the limit of geometric acoustics is ultimately reached. In that case the total surface pressure is twice that incident on the front surface, and zero on the back face. This implies that the scattered surface pressure is equal to the incident pressure on the bright side, and minus that value in the shadow zone. Under such circumstances, equation (2.7) becomes:

$$P_s(\underline{r}) = -\int_0^a \int_0^{2\pi} 2P_o \frac{\partial}{\partial z}\left(\frac{e^{-ik|\underline{r}-\underline{r}'|}}{4\pi|\underline{r}-\underline{r}'|}\right) r'dr'd\phi \quad . \qquad (2.12)$$

This reduces to the following form in the far field:

$$P_s(\underline{r}) \simeq -2P_o \frac{\partial}{\partial z}\left\{\frac{e^{-ikr}}{4\pi r}\int_0^a \int_0^{2\pi} e^{ikr'\cos\phi\sin\theta} r'dr'd\theta\right\}$$

$$= -P_o a^2 \frac{\partial}{\partial z}\left\{\frac{e^{-ikr}}{r}\ \frac{J_1(ka\sin\theta)}{ka\sin\theta}\right\} \qquad (2.13)$$

Since $\frac{\partial}{\partial z} = \frac{\partial}{\partial r}\cdot\frac{\partial r}{\partial z} + \frac{\partial}{\partial \sin\theta}\frac{\partial \sin\theta}{\partial z}$, the last member of equation (2.13) can be expanded to give

$$P_s(\underline{r}) = -P_o\left\{-\left(\frac{a}{r}+ika\right)e^{-ikr}\frac{a}{r}\frac{J_1(kasin\theta)}{kasin\theta}\cos\theta - e^{ikr}(ka)^2\frac{a^2}{r^2}\frac{J_2(kasin\theta)}{(ka\ sin\theta)^2}\cos\theta\right\}$$

In the far field, terms in $(\frac{a}{r})^2$ may be neglected to leave,

$$P_s(\underline{r}) \simeq ika^2 P_o \frac{e^{-ikr}}{r}\frac{J_1(kasin\theta)}{kasin\theta}\cdot\cos\theta \qquad (2.14)$$

It should be noted that equation (2.12) expresses the field scattered by a thin rigid object in terms of a uniform dipole layer. This model has resulted in a far field scattered pressure that can be seen to consist of an outgoing wave from the origin with a directionality factor $(J_1(kasin\theta)/kasin\theta)\cos\theta$, and a strength proportional to ka^2P_o . The $\cos\theta$ in the directionality term indicates that there is no 'sideways scattering'. The strength of the scattering is directly proportional to incident frequency and the area of the disc.

2.4.4 A model for far field scattering of sound by a thin rigid disc with an arbitrary axisymmetric surface pressure distribution.

In the previous section an approximate expression for the pressure scattered by a thin rigid disc was derived for far field conditions by use of a uniform surface pressure distribution. This model contains an unrealistic discontinuity in the surface pressure at the disc edges where the pressure changes from being twice the incident value on the front to zero on the back surface. To investigate the effect of this assumption on the far field behaviour, a model is developed in this section where any axisymmetric surface pressure distribution may be employed. This is possible since any totally symmetric surface pressure distribution can be represented as a sum of Bessel functions,

$$P_+(\underline{r}')-P_-(\underline{r}') = 2\sum_{n=1}^{\infty}\underline{C}_n J_o(\kappa_n\frac{r'}{a}) \quad . \qquad (2.15)$$

where the $\underline{C}_n$ are complex weights to be determined by a Fourier-Bessel

decomposition of the derived surface pressure distribution, (see References [2.21 and 2.22] for a description of this technique) and the κ_n are chosen such that $J_o(\kappa_n) = 0$.

Insertion of equation (2.15) into equation (2.11) yields

$$P_s(\underline{r}) \simeq -2 \frac{\partial}{\partial z} \frac{e^{-ikr}}{4\pi r} \sum_{n=1}^{\infty} \underline{C}_n \int_0^a \int_0^{2\pi} J_o(\kappa_n \frac{r'}{a}) e^{ikr'\cos\phi\sin\theta} r'dr'd\phi$$

The integration can be performed to give:

$$P_s(\underline{r}) \simeq -\frac{\partial}{\partial z} \frac{e^{-ikr}}{r} \sum_{n=1}^{\infty} \underline{C}_n \frac{\kappa_n a^2}{\left(\kappa_n^2 - (ka\sin\theta)^2\right)} J_o(ka\sin\theta) J_1(\kappa_n) \quad . \quad (2.16)$$

Since $\frac{\partial}{\partial z} = \frac{\partial}{\partial r} \cdot \frac{\partial r}{\partial z} + \frac{\partial}{\partial \sin\theta} \cdot \frac{\partial \sin\theta}{\partial z}$, equation (2.16) may be rewritten as

$$P_s(\underline{r}) \simeq \sum_{n=1}^{\infty} \underline{C}_n \frac{e^{-ikr}}{r} \frac{a \kappa_n}{\left(\kappa_n^2 - (ka\sin\theta)^2\right)} J_o(ka\sin\theta) J_1(\kappa_n) \cdot$$

$$\cdot \cos\theta \left\{ (ika + \frac{a}{r}) - \frac{a}{r} \left(\frac{J_1(ka\sin\theta)}{(\sin\theta)^2} - \frac{2(ka)^2}{\left(\kappa_n^2 (ka\sin\theta)^2\right)} \right) \right\} \quad (2.17)$$

Since a far field approximation is desired, terms in $\left(\frac{a}{r}\right)^2$ may be neglected. This results in the following expression for the far field scattered pressure:

$$P_s \simeq ika^2 \sum_{n=1}^{\infty} \underline{C}_n \frac{e^{-ikr}}{r} \frac{\kappa_n}{\left(\kappa_n^2 - (ka\sin\theta)^2\right)} J_o(ka\sin\theta) \cos\theta J_1(\kappa_n) \quad . \quad (2.18)$$

The physical interpretation of equation (2.18) is that in the far field, the scattered pressure can be represented as a series of directional sources situated at the origin. Each component source possesses its own directivity factor $J_o(ka\sin\theta) / \left(\kappa_n^2 - (ka\sin\theta)^2\right) \cos\theta$. Here, as in equation (2.14) the $\cos\theta$ term indicates that there is no far field 'sideways scattering', and when κ_n equals $ka\sin\theta$, the directivity

factor stays bounded and tends to $(J_1(\kappa_n)/2\kappa_n)\cos\theta$. The strength of each component source is determined by the term $ka^2\underline{C}_n\kappa_n J_1(\kappa_n)$. The $\underline{C}_n$ terms supply both phase and magnitude information relative to the incident wave, and are calculated by Fourier-Bessel decomposition of the surface pressure distribution. This distribution may either be assumed, calculated or measured.

2.4.5 *A comparison of the calculated far field pressures scattered by a thin rigid disc when two different surface pressure distributions are assumed.*

In this section the results of computations of far field scattered sound pressure levels based on equations (2.14) and (2.18) are presented. The $\underline{C}_n$ coefficients used in equation (2.18) in this case were derived from exact solution results as presented by Leitner [2.8] (see Appendix B for details of the computation of the $\underline{C}_n$ terms). The surface pressure distribution used is shown in Figure 2.7. Twenty terms were calculated in the Fourier-Bessel series for ka values of 3,4 and 5. The values of the coefficients thus computed are shown in Figure 2.8.

It is now therefore possible to compare the results of what is essentially a Kirchhoff-type model, which has a surface pressure discontinuity at the edges, with those of an 'exact' solution. The results of such computations are shown in Figure 2.9 for a range of ka and r/a values.

It is immediately apparent that both models display the expected trends. This is evidenced by the 'diffraction type' behaviour in the shadow zone, where the central region is always a local maximum, whereas the bright region behaviour typifies reflection phenomena, the central region here being either a local maximum or a local minimum. The interesting point to notice however is that the agreement between the two approaches is comparatively good. This suggests that the far field scattered sound pressure levels due to a finite sized thin rigid object may be adequately represented by a single directional "point source", with a weighting factor(including the directivity) derived from modelling the surface field as a uniform dipole layer. Other

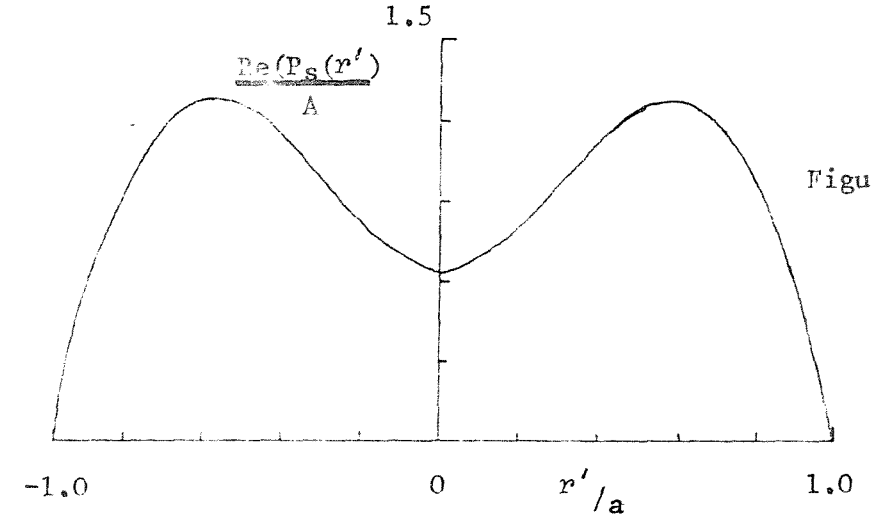

Figure 2.7(a)

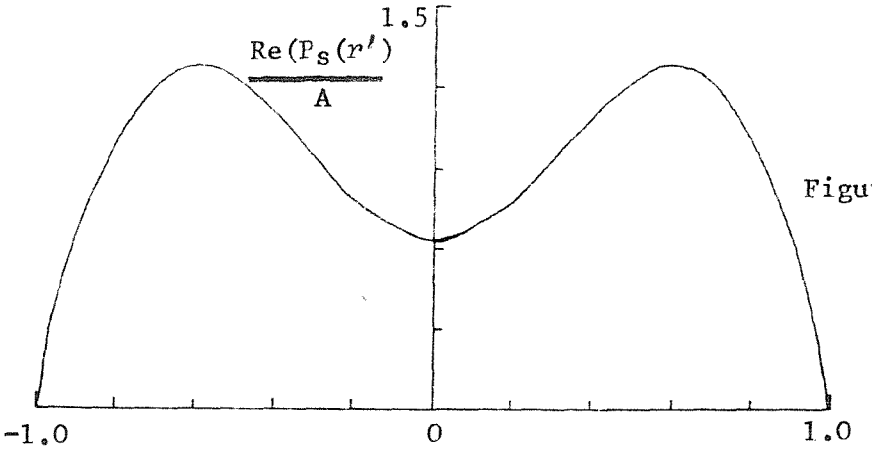

Figure 2.7(b)

Figure 2.7. The real part of the exact scattered surface pressure field for ka = 5. a) From Leitner's results (see Reference (2.8)); b) Generated by the summation (according tc equation (2.15) of the first twenty Fourier-Bessel coefficients, derived from Leitner's results.

r'/a	ka = 3		ka = 4		ka = 5	
	$Re(\psi_s)$	$Im(\psi_s)$	$Re(\psi_s)$	$Im(\psi_s)$	$Re(\psi_s)$	$Im(\psi_s)$
0	2.325	-0.065	1.965	0.85	0.63	1.58
0.1	2.28	-0.07	1.925	0.815	0.685	1.5
0.2	2.2	-0.1	1.83	0.68	0.78	1.225
0.3	2.055	-0.13	1.7	0.5	0.938	0.87
0.4	1.88	-0.175	1.52	0.275	1.1	0.42
0.5	1.64	-0.215	1.315	0.01	1.225	0
0.6	1.39	-0.27	1.09	-0.22	1.275	-0.5
0.7	1.08	-0.3	0.83	-0.42	1.2	-0.8
0.8	0.78	-0.28	0.56	-0.475	1.0	-0.84
0.9	0.45	-0.145	0.3	-0.385	0.65	-0.675
0.95	0.22	-0.08	0.13	-0.225	0.4	-0.49
1.0	0	0	0	0	0	0

The above date is taken from Leitner [2.8].

n	$\underline{C}_n = A_n + iB_n$					
	ka = 3		ka = 4		ka = 5	
	A_n	B_n	A_n	B_n	A_n	B_n
1	2.451	-0.326	1.974	0.072	1.684	0.074
2	-0.223	0.372	-0.062	1.058	-1.283	1.951
3	0.149	-0.161	0.050	-0.419	0.358	-0.686
4	-0.100	0.058	-0.015	0.209	-0.204	0.333
5	0.048	-0.001	0.018	-0.114	0.151	-0.156
6	-0.043	-0.011	-0.017	0.083	-0.113	0.173
7	0.065	0.010	0.017	-0.05	0.093	-0.206
8	-0.023	-0.004	0.007	0.046	-0.072	0.179
9	0.042	0.005	-0.014	-0.046	0.053	-0.105
10	0.032	0.002	0.02	0.015	-0.056	0.090
11	0.010	-0.015	-0.023	0.001	0.042	-0.116
12	0.007	0.011	0.020	-0.006	-0.040	0.078
13	-0.016	-0.008	-0.017	-0.001	0.028	-0.056
14	0.011	0.005	0.014	0.001	-0.022	0.046
15	-0.006	-0.003	-0.009	-0.001	0.016	-0.037
16	0.004	0.000	0.006	0.001	-0.012	0.027
17	-0.003	0.002	-0.004	-0.001	0.008	-0.018
18	0.001	-0.003	0.002	0.001	-0.005	0.011
19	-0.001	0.005	0.001	-0.001	0.003	-0.006
20	-0.000	-0.005	0.000	0.000	-0.001	0.002

Figure 2.8 Data for, and results of the Fourier-Bessel decomposition of the scattered surface pressure of the disc.

Figure 2.9(a)

ka = 4
kr = 24.8

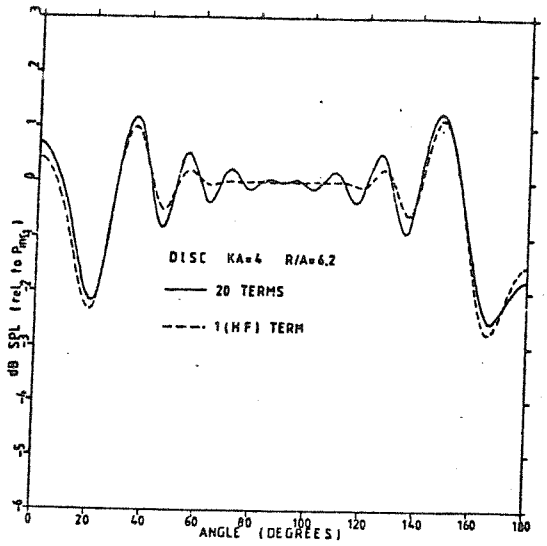

Figure 2.9(b)

ka = 4
kr = 18.6

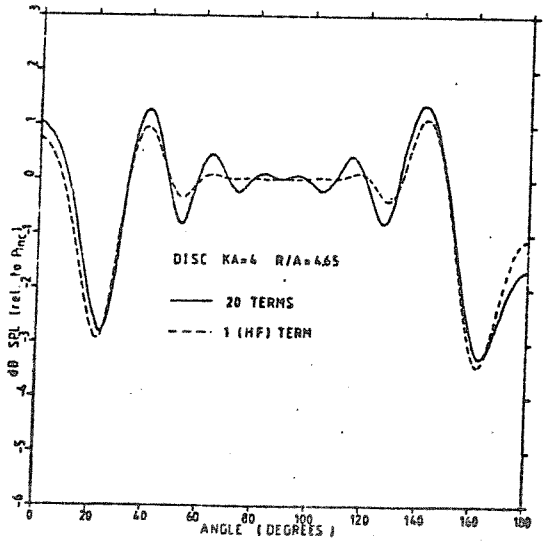

Figure 2.9(c)

ka = 5
kr = 27.15

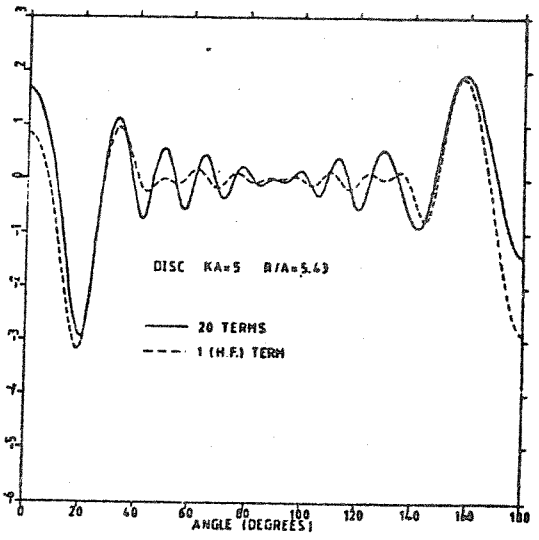

Figure 2.9. Comparison of the far-field levels predicted by the high frequency and 'exact' Green function formulations of scattering by a rigid disc.

N.B. In these plots 0^{o} is the centre of the shadow.

worthwhile observations include the fact that there is no real 'shadow' in the far field cases investigated, and that whereas the high frequency sphere model produced no shadow zone diffraction behaviour in the near field, the analogous approach here appears to produce such behaviour in the far field. However, in the latter case the "exact" method obviously cannot be expected to be as accurate as the exact sphere solution computations.

2.5 *An Investigation of Acoustic Intensity Flow Across Geometric Shadow Boundaries:*

It was observed in the last section that a model based on a geometric acoustics approximation for the surface pressure distribution on a rigid disc produced reasonable results in the far field for ka values of 3 or greater. In this section the accuracy of this type of model is studied for a situation representative of a totally different class of scattering geometries, namely the 'near field' of infinite scatterers.

The best documented thin infinite body diffraction solution is that for the infinite hard half-plane, due to Sommerfeld [2.24]. Many standard acoustics texts now cover this topic (e.g. References [2.5, 2.9 and 2.12]). The study of this particular scattering situation permits a single diffracting edge to be examined alone. This can be thought of as the limit of many very large objects' high frequency scattering behaviour in the near field of an edge. To gain a greater insight into the physics of the situation, intensity flow will be studied. The use of intensity is contrary to the normal practice of acoustical scattering literature, which generally is concerned with mean square pressure results. However, since intensity is a vector quantity it is more informative, as it indicates the actual direction of acoustical energy flow. In this case the flow across the geometric acoustics shadow and bright zone edges is studied, by use of both the exact solution and an approximate ('high frequency') model similar to that employed for the case of the rigid disc in Section 2.4.3. Comparison of the results of the two prediction methods will permit evaluation of the approximate model's accuracy under near field conditions. Furthermore, the use of intensity to characterise their behaviours

may indicate where the acoustic energy which enters the shadow zone originates. This may in turn reveal the possible casuses of any failure by the approximate model under these circumstances.

2.5.1 *The exact solution for diffraction by an infinite hard half-plane:*

The geometry to be considered is shown in Figure 2.10. It should be noted that there is an implicit time factor $e^{-i\omega t}$ in this section. This is contrary to that used elswhere in this research programme, but it agrees with Summerfeld's original derivation, and permits easy cross-referencing to the standard texts (e.g. References [2.5, 2.9 and 2.12]).

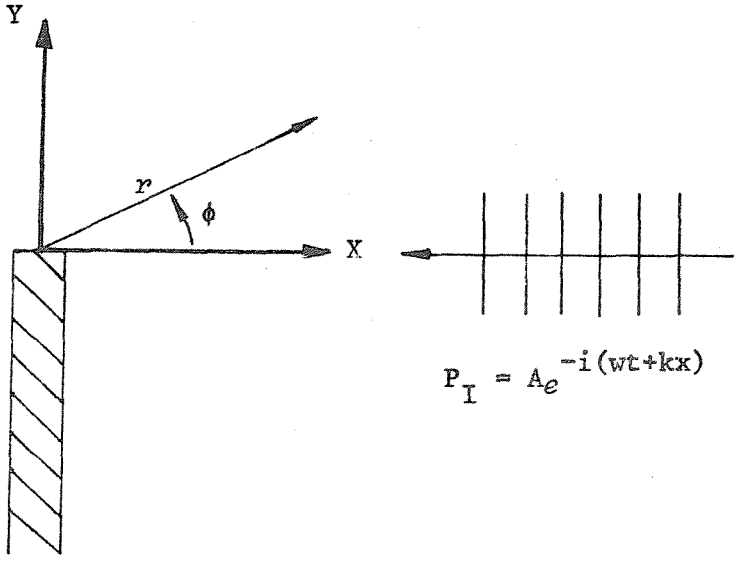

Figure 2.10: The geometry of the situation considered in the exact solution for diffraction by an infinite half-plane.

For the case of a screen with a normally incident plane wave, the exact solution for the pressure at a point (r,ϕ) is:

$$P(r,\phi) = A\left\{e^{-ikrcos\phi}E(\sqrt{2kr}\ cos\phi/2) + e^{+ikrcos\phi}E(-\sqrt{2kr}\ sin\phi/2)\right\} \qquad (2.19)$$

where

$$E(z) = (1/\sqrt{i\pi}) \int_{-\infty}^{z} e^{it^2} dt \ . \qquad (2.20)$$

In order to calculate intensity values, it is necessary to also formulate expressions for the velocity components at any field point. These can be obtained by use of the linearised momentum equation,

$$\frac{\partial \underline{u}(r,\phi)}{\partial t} = - \left(\frac{\underline{i}_r}{\rho} \frac{\partial P}{\partial r} + \frac{\underline{i}_\phi}{\rho r} \frac{\partial P}{\partial \phi} \right) \ , \qquad (2.21)$$

where $\underline{i}_r$ and $\underline{i}_\phi$ are the unit vectors in the radial and tangential directions respectively. Substitution of equation (2.19) into equation (2.21) results in the following forms for radial and tangential velocity components:

$$U_r(r,\phi) = \frac{A}{\rho C} \left\{ \cos\phi \left(e^{ikr\cos\phi} E(-S_1) - e^{-ikr\cos\phi} E(C_1) \right) + \right.$$

$$\left. + \frac{e^{i\pi/4}}{\sqrt{2\pi kr}} \left(e^{ikr\cos\phi + iS_1^2} \sin\phi/2 - e^{-ikr\cos\phi + iC_1^2} \cos\phi/2 \right) \right\} \qquad (2.22)$$

$$U_\phi(r,\phi) = \frac{A}{\rho C} \left\{ \sin\phi \left(e^{-ikr\cos\phi} E(C_1) - e^{ikr\cos\phi} E(-S_1) \right) + \right.$$

$$\left. + \frac{e^{i\pi/4}}{\sqrt{2\pi kr}} \left(\sin\phi/2 \ e^{-ikr\cos\phi + iC_1^2} + \cos\phi/2 \ e^{ikr\cos\phi + iS_1^2} \right) \right\} . \qquad (2.23)$$

Here

$$C_1 = \sqrt{2kr} \cos\phi/2 \ ,$$

and

$$S_1 = \sqrt{2kr} \sin\phi/2 \ .$$

The calculation of the time averaged intensity components at any point now simply requires the evaluation of one half of the real part of the product of the pressure with the velocity term's complex conjugate. Since it is only the tangential components at the geometrical shadow boundary which can give rise to intensity within the shadow region, this case (in conjunction with the behaviour at the similar bright region edge) will be studied analytically in what follows.

At the shadow boundary ($\phi = \pi$), equations (2.19) and (2.23) reduce to:

$$P(r,\pi) = A\left\{e^{ikr}/2 + e^{-ikr}\, E(-\sqrt{2kr})\right\} , \tag{2.24}$$

$$U_\phi(r,\pi) = A/\rho c\,(e^{i\pi/4+ikr}/\sqrt{2\pi kr}) , \tag{2.25}$$

whilst on the edge of the bright zone ($\phi = 0$), their forms are

$$P(r,0) = A\left\{e^{ikr}/2 + e^{-ikr}\, E(\sqrt{2kr})\right\} , \tag{2.26}$$

$$U_\phi(r,0) = A/\rho C(e^{i\pi/4+ikr}/\sqrt{2\pi kr}) . \tag{2.27}$$

Comparison of equations (2.27) and (2.25) indicates that the tangential velocity is symmetrical in these cases. However, the pressure field is not, and thus the intensities that cross the two boundaries are not equal. The intensity which travels into the shadow zone at a distance r from the tip of the half-plane can be formulated from equations (2.24) and (2.25) as

$$I_\phi(r,\pi) = A^2/2\rho c \cdot 1/\sqrt{2\pi kr} \cdot \mathrm{Re}\left\{e^{-i\pi/4}\left[\frac{1}{2} + e^{-2ikr}\, E(-\sqrt{2kr})\right]\right\}. \tag{2.28}$$

Similarly, the intensity which leaves the bright region can be found from equations (2.26) and (2.27):

$$I_\phi(r,0) = A^2/2\rho C \cdot 1/\sqrt{2\pi kr} \cdot \mathrm{Re}\left\{e^{-i\pi/4}\left[\frac{1}{2} + e^{-2ikr}\, E(\sqrt{2kr})\right]\right\}. \tag{2.29}$$

It is apparent that equations (2.28) and (2.29) display a marked similarity; this similarity becomes more obvious if the function $E(z)$ (see equation 2.20)) is reformed as

$$E(z) = \frac{1}{\sqrt{i\pi}} \left\{ \int_{-\infty}^{0} e^{it^2} dt + \int_{0}^{z} e^{it^2} dt \right\} = \frac{1}{2} + 1/\sqrt{i\pi}\left[C(z) + iS(z) \right] , \quad (2.30)$$

where

$$C(z) = \int_{0}^{z} \cos t^2 dt$$

and

$$S(z) = \int_{0}^{z} \sin t^2 dt .$$

It can now be seen that there are terms common to both equations (2.28) and (2.29), and terms of opposite sign.

The expression for the intensity component that has the same value in both cases is

$$I_{\phi common} = \frac{A^2}{2\rho c} \cdot \frac{1}{4\sqrt{\pi kr}} \cdot \left(1+\cos(2kr)-\sin(2kr)\right) . \quad (2.31)$$

The form of the intensity component that has opposite sign in the two cases is

$$I_{\phi oppos.} = \frac{A^2}{2\rho c} \cdot \frac{1}{4\sqrt{\pi kr}} \cdot \left\{ \cos(2kr) S(\sqrt{2kr}) - \sin(2kr) C(\sqrt{2kr}) \right\} . \quad (2.32)$$

The intensity component described by equation (2.31) has the same magnitude and sign in both cases under consideration. The $\cos(2kr)$ and $\sin(2kr)$ terms fluctuate about zero, and hence the 'average net intensity' is $\frac{A^2}{2\rho c} \cdot 4\sqrt{\frac{1}{\pi kr}}$. This value is always positive and therefore represents a flow out of the bright region, and similarly into the shadow zone. It is not possible to state categorically that the flow which leaves the bright region actually goes into the shadow, without following the intensity lines in detail.

Equation (2.32) similarly represents a flow out of both bright and shadow zones, although physically this may just be the component of the intensity flow leaving the bright region which doesn't arrive in the shadow.

The expressions for the acoustic power per unit length of the diffracting edge which enters or leaves the two zones can be found by integration of equations (2.31) and (2.32) with respect to r. This results in the following expression for the symmetrical component,

$$W_{same} = A^2/16\rho C \cdot \sqrt{r/\pi k} + \text{Fluctuating term}, \qquad (2.33)$$

from which it can be seen that although the intensity is infinite at $r = 0$, the power is not. Equation (2.33) also indicates that as r goes to infinity, power continues to cross the shadow boundary. The $I_{\phi oppos.}$ equation cannot easily be integrated to yield an expression for the power associated with this term. However its general form may be deduced, since both $S(\sqrt{2kr})$ and $C(\sqrt{2kr})$ tend to $\sqrt{\pi/8}$ for large values of argument. The $I_{\phi oppos.}$ term then becomes

$$I_{\phi oppos.} \xrightarrow[kr\to\infty]{} \frac{A^2}{2\rho c} \cdot \frac{1}{4\sqrt{\pi kr}} \cdot (\cos 2kr - \sin 2kr) \; . \qquad (2.34)$$

This equals the oscillatory terms in the $I_{\phi common}$ expression (equation (2.31)), and hence the fluctuations in the total intensity on the shadow edge will be cancelled in the far field, whilst those on the bright zone edge are twice the amplitude of those of equation (2.34). Since there is no constant term in the brackets of equation (2.34), $I_{\phi oppos.}$ can be clearly seen to oscilate about a zero mean and hence to represent a small net power flow anyway.

The various expressions for the radial and tangential intensity have been computed (by using the standard Fresnel integral approximations of equations 7.3.32 and 7.3.33 of Reference [2.20]), and the results are shown in Figure 2.11.

The behaviour of equations (2.31) and (2.32) is illustrated by Figure 2.12. Discussion of these graphs is left until Section 2.5.3, where a comparison with the results of the approximate model (to be developed in the next section) is made.

Figure 2.11(a) Shadow edge tangential intensity.

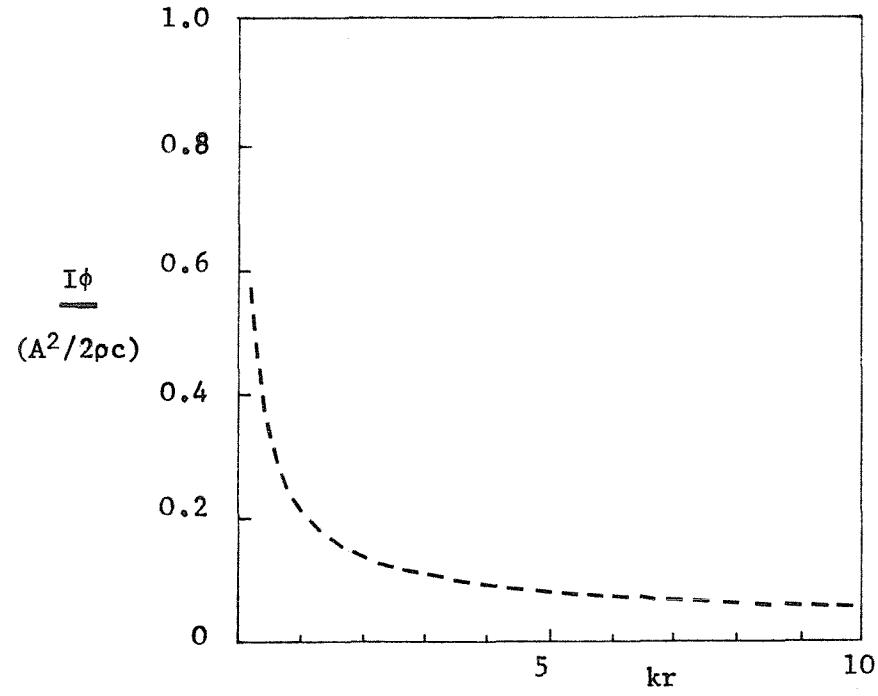

Figure 2.11(b) Bright edge tangential intensity.

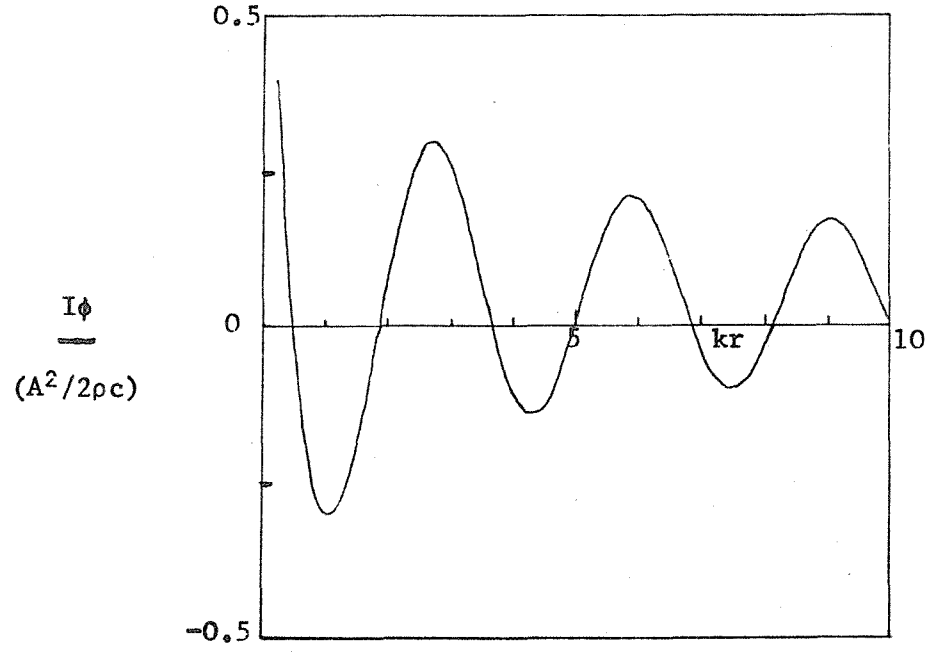

Figure 2.11. Intensity on the geometric shadow and bright boundaries' edges, as predicted by the exact solution for diffraction by a half-plane.

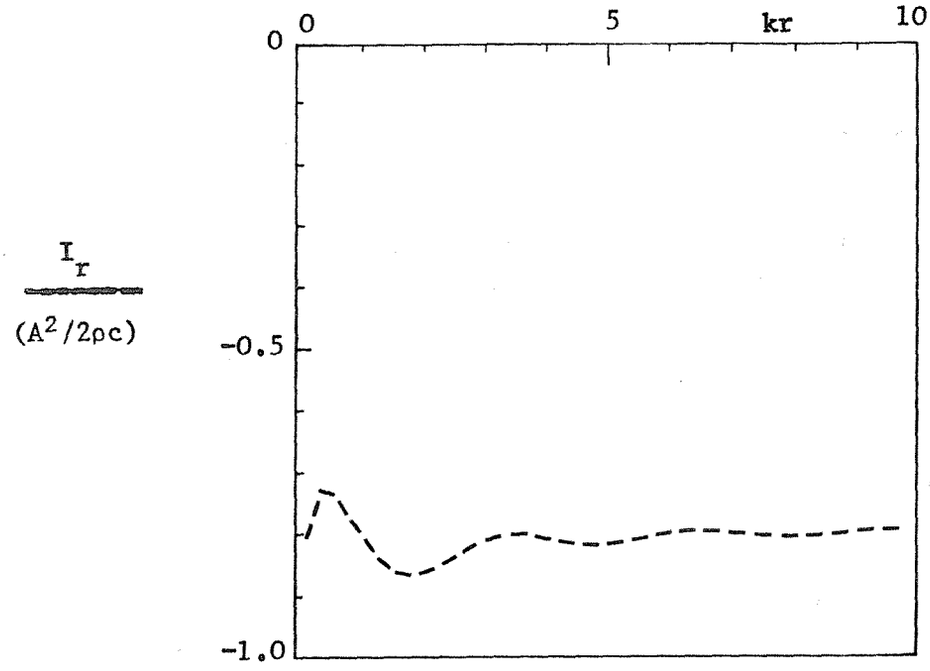

Figure 2.11(c) Bright edge radial intensity.

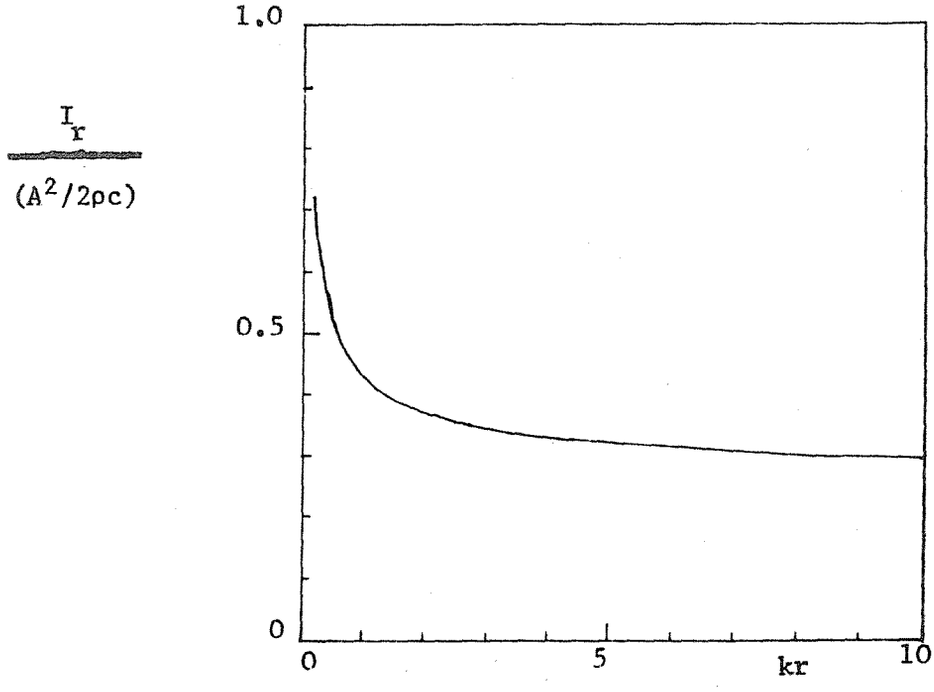

Figure 2.11(d) Shadow edge radial intensity.

Figure 2.12. $I_{\phi common}$ and $I_{\phi oppos}$ as functions of kr from the exact solution for diffraction by a half-plane (equation (2.31) and 2.32)).

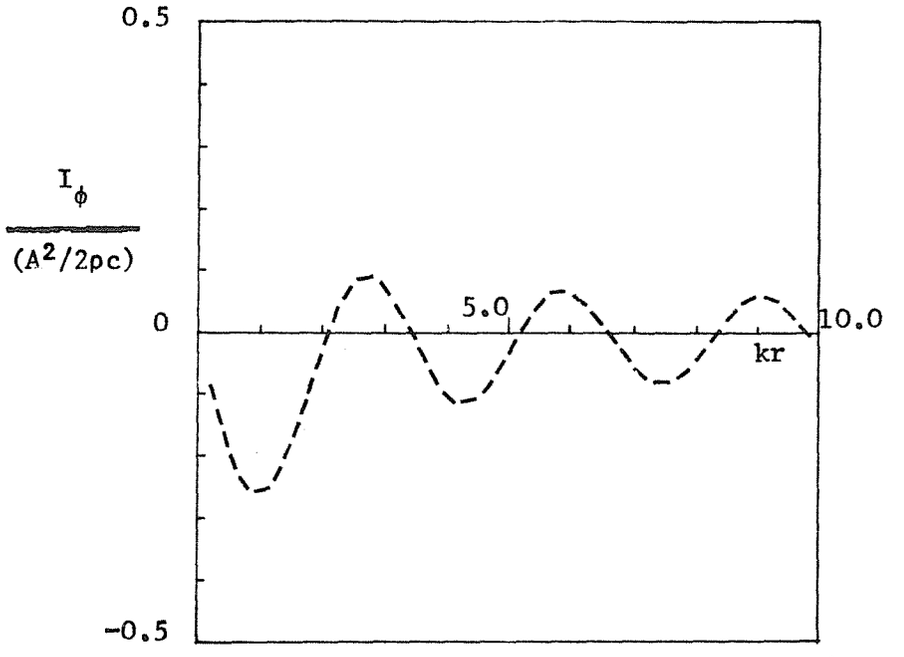

Figure 2.12(a) The tangential intensity component travelling in opposite directions on the edges of the geometric bright and shadow zones.

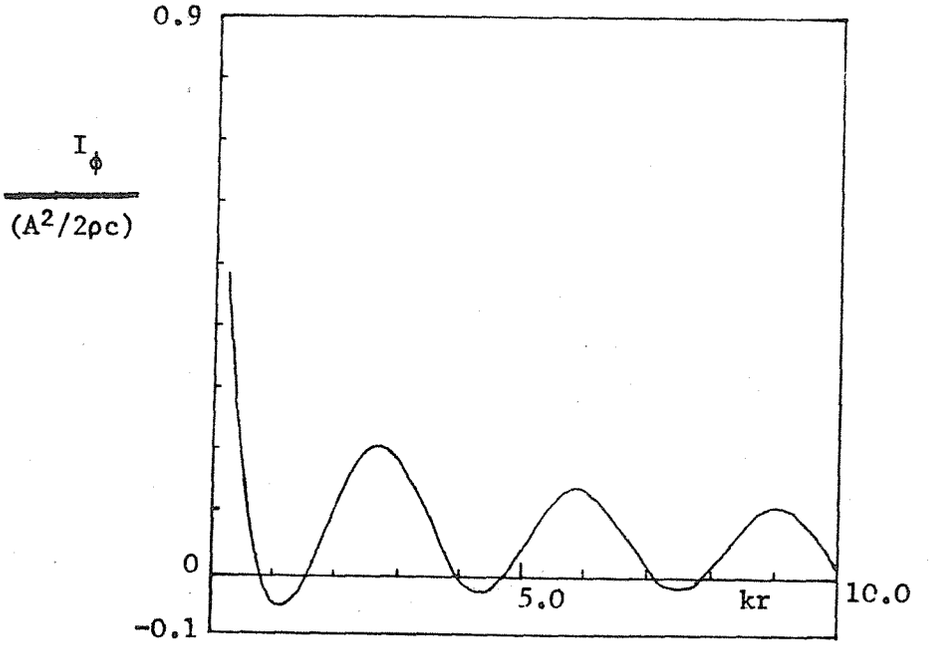

Figure 2.12(b) The tangential intensity component travelling in the same directions on the edges of the geometric bright and shadow zones.

2.5.2 *An approximate model for intensity flow around an infinite hard half-plane*

This section contains the details of an approximate model for diffraction by an infinite hard half plane, based on similar principles to those used for the case of a rigid disc in Section 2.4.3. The geometry to be considered in this section is shown in Figure 2.13. In the geometric acoustics (high frequency) limit, the total surface pressure on the front is assumed to be uniformly twice that incident, whilst on the back it is zero. This (by similar reasoning to that outlined in Section 2.4.3 for the case of a rigid disc) leads to a model for the half-plane as a uniform dipole distribution. This model will be used to study the tangential and radial intensity flow in a manner similar to that of the last section. Direct comparison of the results of the two models will enable the validity of the approximate model to be investigated in both the near and 'far' fields. (Obviously it is impossible to satisfy the far field requirement $r/a \gg 1$, as was necessary in Section 2.4.3, since here a is infinite).

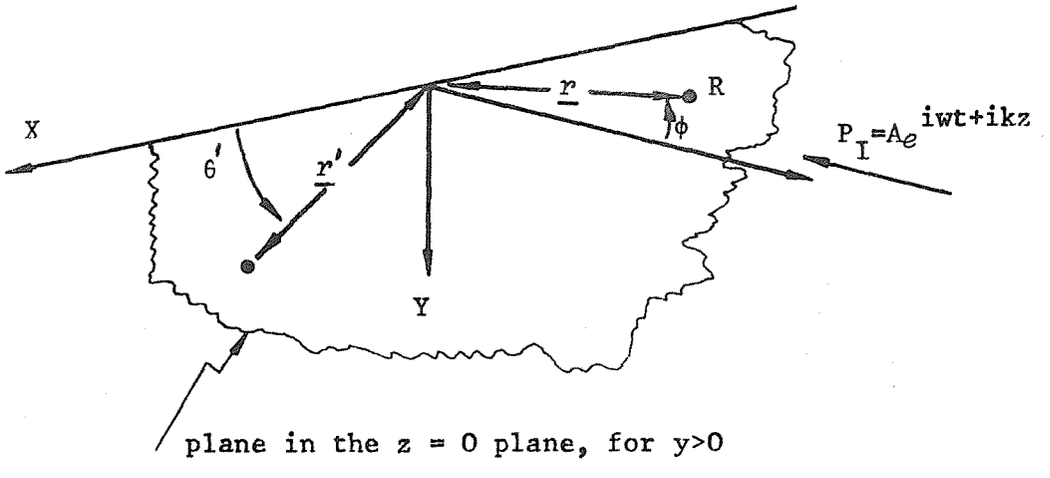

Figure 2.13 : Geometry for the approximate 1/2 plane diffraction problem.

This model assumes that the scattered wave can be represented by that due to a uniform dipole distribution in the x-y plane, for $Y > 0$. This allows the scattered pressure field's formulation in terms of an integral of the incremental dipoles' contributions.

$$P_s(\underline{r}) = \int_0^{\pi}\int_0^{\infty} \frac{b(1+ik|\underline{r}-\underline{r}'|)}{|\underline{r}-\underline{r}'|^2}\cos\psi e^{-ik|\underline{r}-\underline{r}'|} r'dr'd\theta' \qquad (2.35)$$

where ψ is the angle subtended by the receiver at $\underline{r}$ to the normal to the X-Y plane in the positive z direction, at $\underline{r}'$; and b is the incremental dipole strength. The value of b can be inferred to equal $A/2\pi$ from comparison with equation (2.11). For points on the z axis, equation 2.35 simplifies to:

$$P_s(0,0,z) = A/2 \int_0^{\infty} \frac{(1+ik\sqrt{z^2+r'^2})}{(z^2+r'^2)} \cdot \frac{z}{\sqrt{z^2+r'^2}} e^{-ik\sqrt{z^2+r'^2}} r'dr' \ .$$

Upon substitution of $t = k\sqrt{z^2+r'^2}$, this reduces to

$$P_s(0,0,z) = \frac{Akz}{2} \int_{k|z|}^{k\infty} \left(\frac{1+it}{t^2}\right) e^{-it}\, dt \ . \qquad (2.36)$$

Evaluation of the integral in equation (2.36) results in the following expression for the scattered pressure:

$$P_s(0,0,z) = \frac{Akz}{2} \left[\frac{e^{-it}}{t}\right]_{k\infty}^{k|z|} \qquad (2.37)$$

The assumption of some losses being present in the air, which is equivalent to k being a complex quantity with a small imaginary part , removes the contribution from the infinite integration limit. Thus the total pressure field for points on the edge of the geometrical bright region is

$$P(0,0,z) = P_I(0,0,z) + P_s(0,0,z) = A\left(e^{ikz} + \frac{e^{-ikz}}{2}\right) , \qquad (2.38)$$

whilst on the geometric shadow's edge

$$P(0,0,z) = A\,\frac{e^{ikz}}{2} \ . \qquad (2.39)$$

The results of this simple model indicate that the scattered pressure on these geometric boundaries is similar to half the incident field:

The scattered wave is out of phase behind the half-plane, and in phase (but travelling in the positive z-direction) in front.

In order to calculate the radial, and tangential intensity components along the boundaries, it is necessary to evaluate the relevant velocity components there. Application of the linearised momentum relation of equation (2.21) to equation (2.35) results in the following expression for the radial component of the scattered velocity,

$$U_{s_r}(0,0,z) = -\frac{A}{2i\omega\rho}\frac{\partial}{\partial t}\int_{k|z|}^{k\infty}\frac{(1+it)}{t^2}k^2 z\, e^{-it}dt\cdot\frac{k|z|}{t}$$

$$= \frac{A}{2i\omega\rho}z\left[\frac{k^3|z|}{t^3}(1+it)e^{-it}\right]_{k\infty}^{k|z|}, \qquad (2.40)$$

where $t = k\sqrt{z^2+r'^2}$. The modulus of z is used in these expressions to indicate that 'radial', rather than 'z-direction' velocity is being considered. This will facilitate comparison with the results of the exact solution. Substitution of the limits into equation (2.40) results in

$$U_{s_r}(0,0,z) = \frac{A}{2\rho c}\cdot\frac{z}{|z|}\left\{1+\frac{1}{ik|z|}\right\}e^{ik|z|}. \qquad (2.41)$$

To obtain the total radial velocity components the values obtained from equation (2.41) must be added to the incident field's radial velocity. The total radial velocities bear a plane wave relationship to the total pressure as z goes to infinity; thus any tangential velocity component must go to zero there. The fact that the velocity is singular at the edge of the half-plane in this model is due to the step change in the pressure field there.

It is more convenient to derive the tangential velocity component from a reformulation of the problem in two dimensions. This is possible since the solution will be independent of the receiver's x co-ordinate and the dipole model is equivalent to modelling the plane as an array of oscillating cylinders. The details of this derivation are contained in Appendix C, where it is shown that the tangential component of the

scattered velocity at the edges of both the shadow and bright zones is given by:

$$U_{\phi} = \frac{-A}{2\rho c} H_1^{(2)}(k|z|) \quad . \tag{2.42}$$

This scattered velocity is also the total tangential velocity, since the incident wave has no velocity normal to its direction of propagation. As required, this velocity tends to zero at infinity, but is again singular at the edge.

Equations (2.38) - (2.42) can now be used to calculate values of both radial and tangential intensity at the shadow and bright zone boundaries. The results of such computations are shown in Figure 2.14 superimposed upon the exact results. Discussion of these results and comparison with the results of the exact solution is contained in the next section.

2.5.3 *Comparison and discussion of the results of the exact and approximate half-plane diffraction models*

Examination of the equations of Sections 2.5.1 and 2.5.2 for the pressure and velocity components at the geometric shadow and bright zone boundaries reveals extremely close agreement between the two models for large kr values. This can be seen for the case of the pressure results (see equations 2.24 and 2.26) tend to

$$P(r,0) \sim A\left\{e^{ikr}/2 + e^{-ikr}\right\} \quad , \tag{2.43}$$

$$P(r,\pi) \sim A\left\{e^{ikr}/2\right\} \quad . \tag{2.44}$$

When it is remembered that there is an implicit $e^{-i\omega t}$ time factor in these results, they can be seen to agree exactly with those of the approximate model, as given by equations (2.38) and (2.39). Thus at distances which are many wavelengths away from the tip of the half plane, the dipole model will predict the pressure field on the geometric shadow and bright zone boundaries adequately accurately. The physical

Figure 2.14. Comparison of the geometric shadow and bright zone boundaries intensity flows predicted by the exact and approximate models for diffraction by a half-plane.

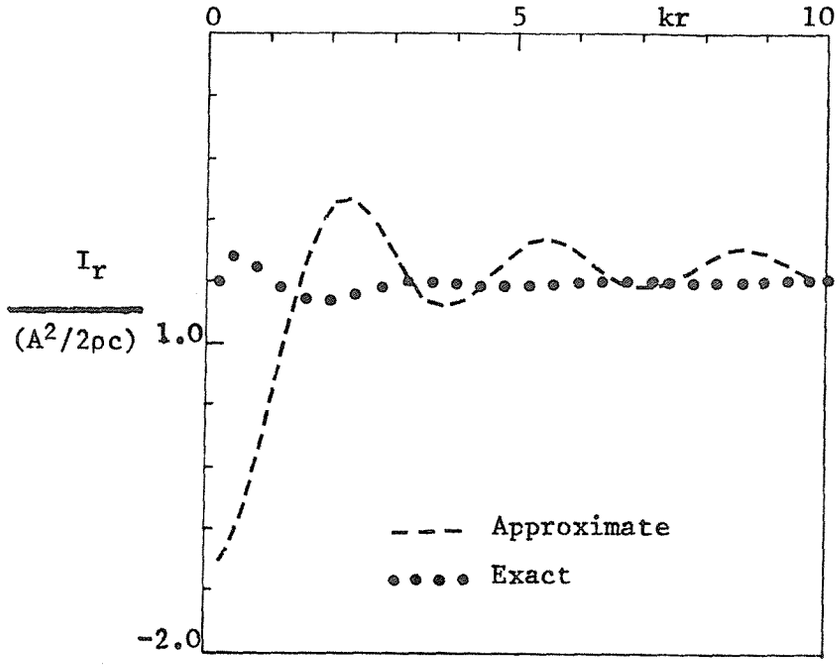

Figure 2.14(a) Bright edge radial intensities.

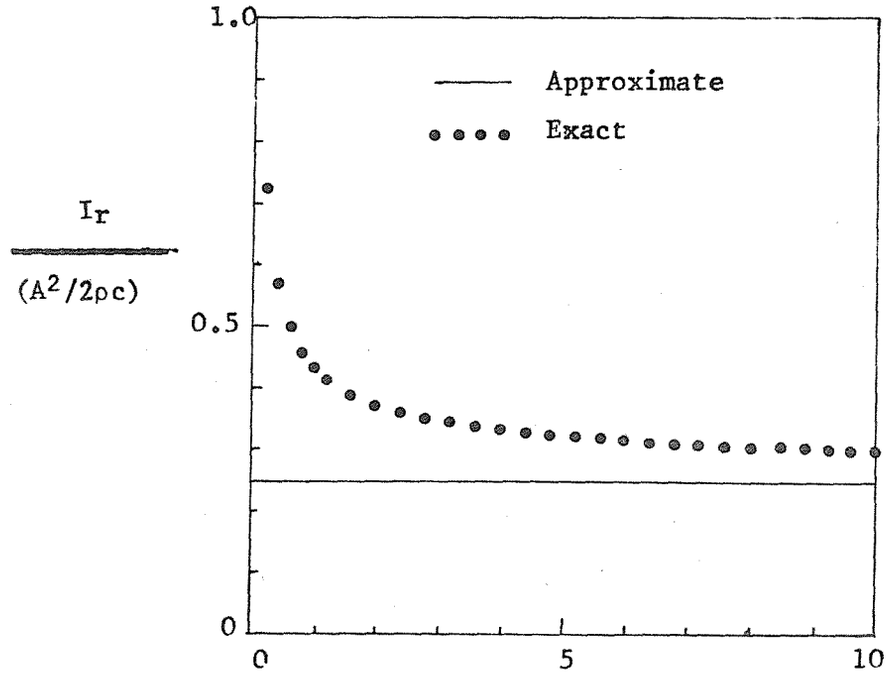

Figure 2.14(b) Shadow edge radial intensities.

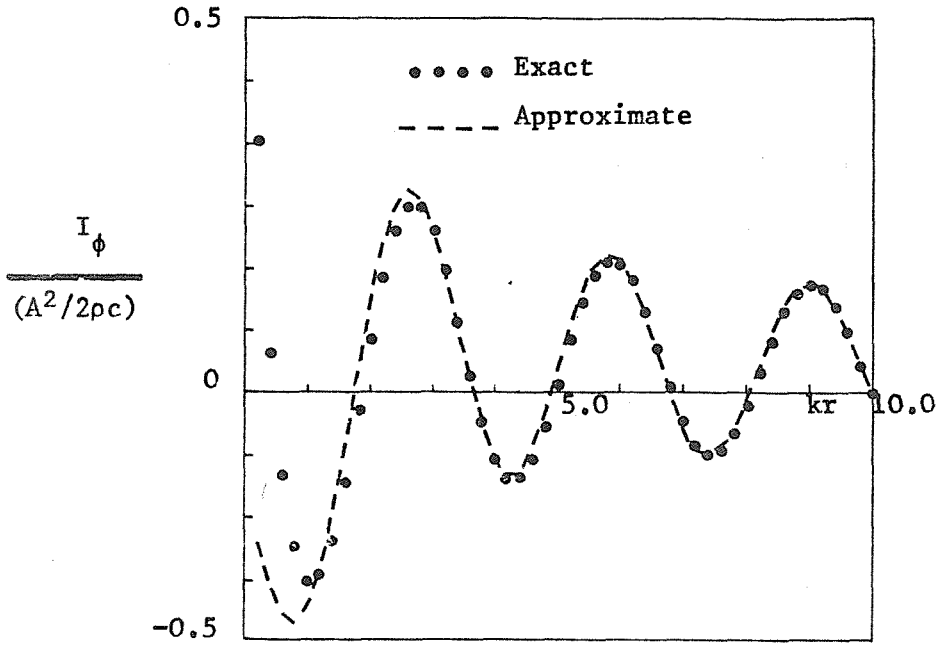

Figure 2.14(c) Bright edge tangential intensities.

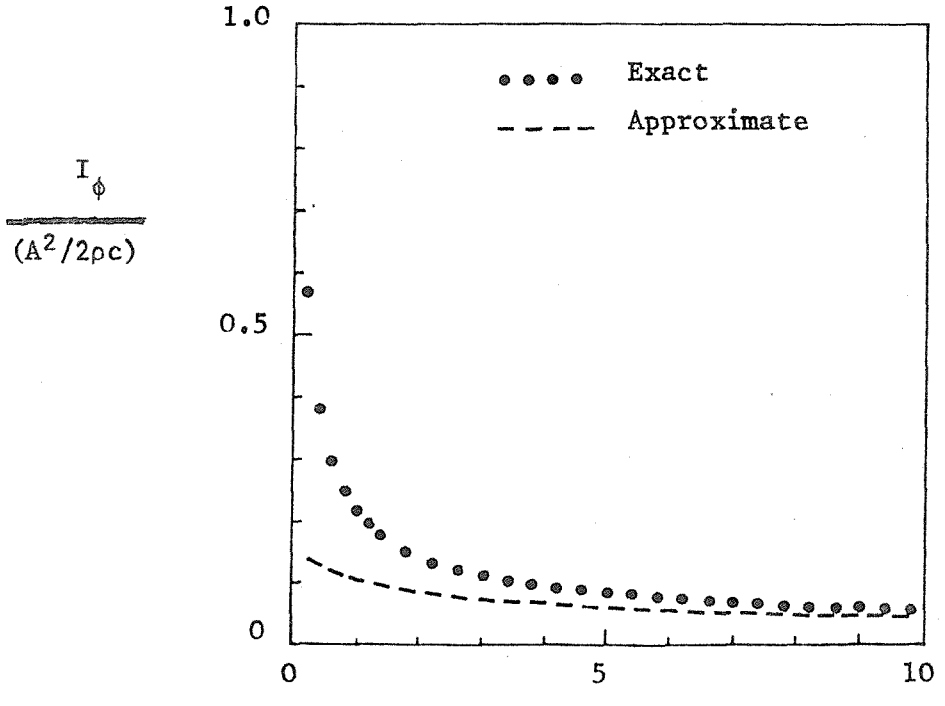

Figure 2.14(d) Shadow edge tangential intensities.

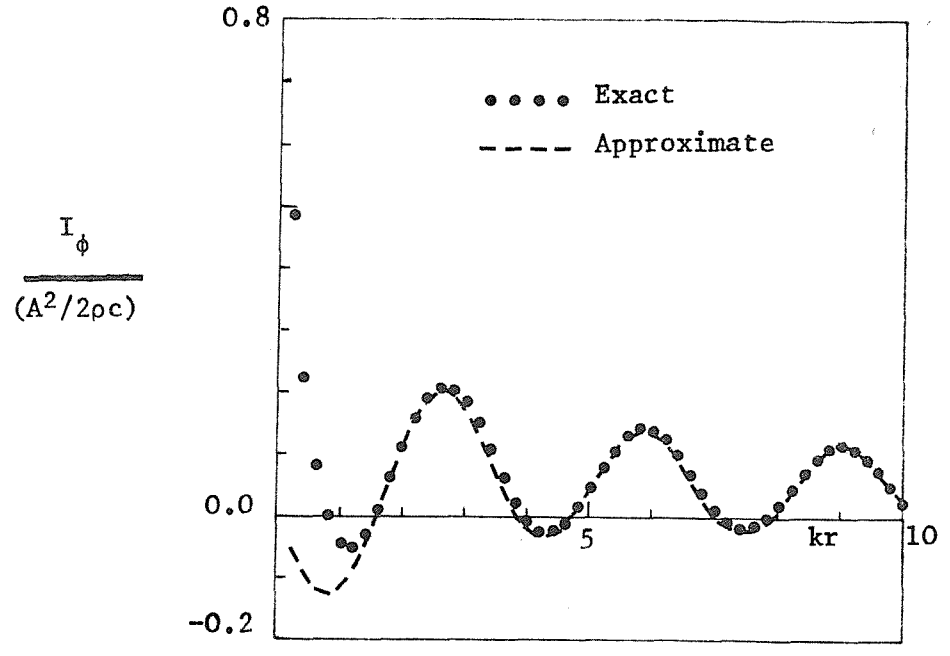

Figure 2.14(e) $I_{\phi same}$, (ie. the component of the tangential intensity flow that is in the same direction on the bright and shadow zone edges)

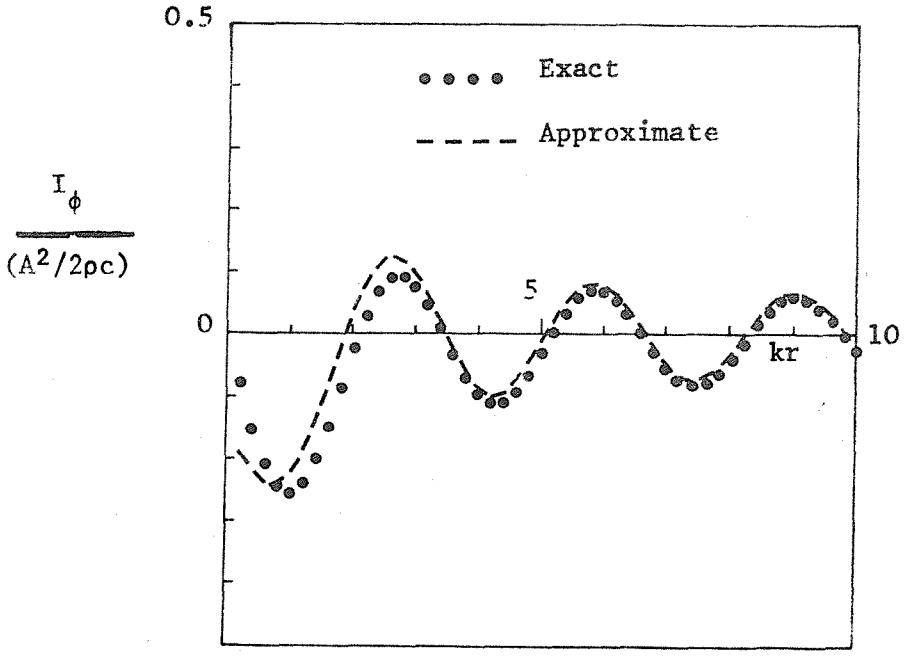

Figure 2.14(f) $I_{\phi oppos}$ (ie. the component of the tangential intensity flow that is in opposite directions on the geometric bright and shadow zone edges)

form of this total far field pressure on the shadow boundary is identical to half the incident pressure there, whilst on the edge of the bright zone, the scattered pressure is like half the incident component, but travelling in the opposite direction, thus creating a standing wave pattern. The scattered radial velocity component similarly possesses a plane wave relation to the scattered pressure in the far field for both models. Thus the far field 'radial' intensity on the shadow and bright zone geometric boundaries can be assumed to be well represented by the simple dipole model.

Substitution of the asymptotic form of the Hankel function for large $k|z|$ in the approximate model's expression for the shadow or bright zone boundary tangential velocity (i.e. equation (2.42)) yields

$$U_\phi \sim \frac{A}{\rho C} \frac{e^{i\omega t} e^{-i\pi/4 - ik|z|}}{\sqrt{2\pi k|z|}} \qquad (2.45)$$

Comparison of this with equations (2.25) and (2.27) reveals perfect agreement of the two models' tangential velocity predictions in the far field. (N.B. equations (2.25) and (2.27) have a suppressed $e^{-i\omega t}$ time factor).

Since all the component terms in the two models correspond in the far field, it can be surmised that for large kr the agreement in intensity flow across the shadow and bright zone boundaries predicted by both models will be extremely good. This is borne out by comparison of the results shown in Figure 2.14. The tangential intensities appear to generally agree more closely than the radial components. The most probable reason for the discrepancies at small kr is the unrealistic pressure discontinuity of the approximate model at the half plane's tip.

The physical behaviour of the exact solution's results indicates that the majority of the intensity which enters the shadow region does so at very small kr values. Far from the half-plane very little energy actually crosses the shadow boundary and a plane progressive wave of half the magnitude of that originally incident predominates. Examination of the plots of Figure 2.12 for the components of the exact solution's tangential intensity terms which cross the geometric boundaries

in the same or opposite directions, reveals that for very small kr the I_{same} component is much larger than the $I_{oppos.}$ term. The implication of this behaviour is that, for kr less than about 0.25, the majority of the intensity arriving in the shadow zone comes from the bright region. This might resemble a near field 'hydrodynamic intensity flow', although this obviously cannot be proved without detailed tracing of the intensity flow lines. It is quite possibly the poor representation of this behaviour by the approximate solution that accounts for its comparatively poor agreement with the exact solution for small kr values.

It is also apparent from Figure 2.12 that whilst both of the component intensity terms are oscillatory with kr the oscillations are about different overall trends - the mean of the I_{same} curve being obviously more positive than the $I_{oppos.}$ curve, which appears to fluctuate about an average value of zero.

It is unfortunately impossible to make any more definite statements about the physical behaviour of the solutions without tracing the intensity flow lines in much greater detail, for points off the geometric acoustics boundaries. The aims of this research programme do not warrant such investigations.

2.6 Discussion and Conclusions:

In each section of this chapter, an exact analytic solution to a scattering problem has been examined, and the results compared to those of an approximate solution for a similar geometry based on an assumed surface pressure distribution. The models used include finite-sized objects (flat and solid) and an infinite object. Where it has been possible to study the models' near field behaviour, the approximate solutions have proved rather inaccurate. However their far field accuracy has been seen to be surprisingly good, even at comparatively low ka. However under these conditions, the magnitudes of any bright or shadow zone effects observed are small.

The implications of the above points are that for well separated scatterers, and a receiver position that lies outside any particular scatterer's near field, a high frequency source distribution type model for each individual scatterer would predict the total field reasonably well. Under these circumstances, as was noted for the case of the disc, the scattered field from a finite object can be approximated by a directionally weighted point source in place of the object. This offers opportunities for the modelling of scatterers in reflecting environments, since the field could be modelled by the combined effects of the real scatterers and their images in the reflecting surfaces. More consideration is given to this type of problem in Chapter 4.

The other practical use of the results of this chapter will lie in the application of the exact solution results for scattering by a rigid sphere to 'calibrate' the experiments performed.

CHAPTER 2 : REFERENCES

2.1 C.J. BOUWKAMP, 1954 Reports on Progress in Physics, 17, 35-100. Diffraction Theory.

2.2 D.L. LANSING, C.H. LIU and T.D. NORUM. Applications of diffraction theory to aeroacoustics.

2.3 J.W.M. BAARS, 1964. Acustica, 14, 289-300. On the diffraction of sound waves by a circular disc.

2.4 B.B. BAKER and E.T. COPSON, 1950. The Mathematical theory of Huygens' Principle. Oxford : The Clarendon Press.

2.5 P.M. MORSE and K.U. INGARD, 1968. Theoretical Acoustics. New York : McGraw-Hill Book Company.

2.6 T. TERAI, 1980. J. Sound Vib. 69, 71-100. On calculations of sound fields around three dimensional objects by an integral equation method.

2.7 J.J. BOWMAN, T.B. SENIOR and P.L.E. USLENGHI, 1969. Electromagnetic and Acoustic Scattering from Simple Shapes. Amsterdam : North-Holland Publishing Company (Wiley Interscience).

2.8 A. LEITNER, 1949. J. Acoust. Soc. Amer. 21, 331-334. Diffraction of sound by a circular disk.

2.9 E. SKUDRZYK, 1971. The Foundations of Acoustics, Basic Mathematics and Basic Acoustics. Wien, New York : Springer-Verlag.

2.10 T.F.W. EMBLETON, 1980. J. Acoust. Soc. Amer. 67, 42-45. Line integral theory of barrier attenuation in the presence of the ground.

2.11 J.B. KELLER 1962. J. Opt. Soc. Amer. 52, 116-130. Geometrical theory of diffraction.

2.12 A.D. PIERCE, 1981. Acoustics : An Introduction to its Physical Principles and Applications. New York : McGraw-Hill Book Company.

2.13 J.B. KELLER, 1957. J. Appl. Phys. 28, 426-444. Diffraction by an aperture.

2.14 U.J. KURZE, 1974. J. Acoust. Soc. Amer. 55, 504-518. Noise reduction by barriers.

2.15 A.D. PIERCE, 1974. J. Acoust. Soc. Amer. 55, 941-955. Diffraction of sound around corners and over wide barriers.

2.16 T. KAWAI, 1981. J. Sound Vib. 79, 229-242. Sound diffraction by a many-sided barrier or pillar.

2.17 Z. MAEKAWA, 1968. Applied Acoustics, 1, 157-173. Noise Reduction by Screens.

2.18 J. LIGHTHILL, 1978. Waves in Fluids. Cambridge : Cambridge University Press.

2.19 J.W. STRUTT, BARON RAYLEIGH, 1896. The Theory of Sound. London : McMillan and Company Limited.

2.20 M. ABRAMOWITZ and I. STEGUN (Eds). 1970 Handbook of Mathematical Functions. New York : Dover Publications Inc.

2.21 P.M. MORSE and H. FESHBACH, 1953. Methods of Theoretical Physics. New York : McGraw-Hill Book Company Inc.

2.22 A. KUFNER and J. KADLEC, 1971. Fourier Series, London : Iliffe.

2.23 Data Analysis Centre Manual. 1978. I.S.V.R. University of Southampton.

2.24 A. SOMMERFELD, 1964. Optics. London : Academic Press.

APPENDIX A

Derivation of the Decomposition of the Series Solution for Scattering by a Rigid Sphere

The exact expression for the scattered pressure at the surface of a sphere, for the geometry of Figure 2.1, with an incident spherical wave of the form $e^{-ikR'}/kR'$ (as described in Section 2.3.1) may be written as

$$P_s(\underline{a}) = i \sum_{n=0}^{\infty} (2n+1) P_n(\cos\theta) h_n^{(2)}(kr_o) \frac{j_n'(ka)}{h_n^{(2)\prime}(ka)} h_n^{(2)}(ka) . \tag{A1}$$

The incident radial velocity at the same point has the form

$$V_{Ir}(\underline{a}) = \frac{-1}{i\omega\rho} \frac{\partial P_I(\underline{a})}{\partial r} = \frac{1}{\rho c} \sum_{n=0}^{\infty} (2n+1) P_n(\cos\theta) h_n^{(2)}(kr_o) j_n'(ka) . \tag{A2}$$

Now for $ka >> 1$, $h_n^{(2)\prime}(ka) \simeq -ih_n^{(2)}(ka)$. Therefore the high frequency limit of equation (A1) can be shown to equal minus the product of ρc with the incident radial velocity. This suggests the decomposition of equation (A1) into a high frequency behaviour term, and a term to account for the deviation from this limit at finite frequencies. This could be written as

$$\begin{aligned} P_s(\underline{a}) &= -\rho c V_{Ir}(\underline{a}) + P_{ex}(\underline{a}) \\ &\equiv P_R(\underline{a}) + P_D(\underline{a}) . \end{aligned} \tag{A3}$$

The expressions for the behaviour of these terms at points off the surface can be obtained by assuming that P_R and P_D have the following forms:

$$P_R(\underline{r}) = \sum_{n=0}^{\infty} (2n+1) P_n(\cos\theta) h_n^{(2)}(kr_o) \alpha_n h_n^{(2)}(kr) \qquad (A4)$$

$$P_D(\underline{r}) = \sum_{n=0}^{\infty} (2n+1) P_n(\cos\theta) h_n(kr_o) \beta_n h_n^{(2)}(kr) \qquad (A5)$$

The value of α_n in equation (A4) can be found from the identity $P_R = -\rho c V_{Ir}$ for field points on the sphere's surface. Substitution of equations (A2) and (A4) into this expression yields $\alpha_n = -j_n'(ka)/h_n^{(2)}(ka)$. Similarly substitution of equations (A1), (A4) and (A5) into the identity (A3) now gives:

$$\beta_n = \left[i j_n'(ka)/h_n^{(2)\prime}(ka) + j_n'(ka)/h_n^{(2)}(ka) \right] .$$

Thus for a general field point $\underline{r}$, equations (A4) and (A5) now assume the forms

$$P_R(\underline{r}) = - \sum_{n=0}^{\infty} (2n+1) P_n(\cos\theta) h_n^{(2)}(kr_o) \cdot \frac{j_n'(ka)}{h_n^{(2)}(ka)} \cdot h_n^{(2)}(kr) , \qquad (A6)$$

$$P_D(\underline{r}) = \sum_{n=0}^{\infty} (2n+1) P_n(\cos\theta) h_n^{(2)}(kr_o) j_n'(ka) \left[\frac{i}{h_n^{(2)\prime}(ka)} + \frac{1}{h_n^{(2)}(ka)} \right] h_n^{(2)}(kr) . \qquad (A7)$$

Investigation of the power scattered by each term in the decomposition

The total acoustic intensity at any point $\underline{r}$, can be written as the sum of the components in the decomposition described above,

$$J(\underline{r}) = \frac{1}{2} \mathrm{Re}\left\{ \left(P_I(\underline{r}) + P_R(\underline{r}) + P_D(\underline{r})\right) \left(V_{Ir}^*(\underline{r}) + V_{Rr}^*(\underline{r}) + V_{Dr}^*(\underline{r})\right) \right\} , \qquad (A8)$$

where the radial velocity terms can be obtained by use of the linearised momentum equation on expressions (A6) and (A7). However the calculation of intensity requires the computation of two 'infinite' series at every field point for each component term. It is easier, and more informative, to investigate the decomposition of the scattered power. The derivation

of a typical component term is as follows:

$$W_{AB} = \int_S \frac{1}{2} \mathrm{Re}(P_A V_{Br}^*) dS.$$

$$= \frac{1}{2} \mathrm{Re} \left\{ \int_S \sum_M A_m P_m(\cos\theta) \sum_N B_n^* P_n(\cos\theta) dS \right\} .$$

For the sphere $dS = 2\pi a^2 \sin\theta d\theta$ and the expression becomes

$$W_{AB} = \pi a^2 \mathrm{Re}\left\{ \sum_M A_m \sum_N B_n^* \int_0^\pi P_m(\cos\theta) P_n(\cos\theta) \sin\theta d\theta \right\} . \qquad (A9)$$

Due to the orthogonal properties of the Legendre functions over the range of integration, equation (A9) may now be written as

$$W_{AB} = 2\pi a^2 \mathrm{Re}\left\{ \sum_N A_n B_n^* / (2n+1) \right\} . \qquad (A10)$$

The expression has been computed for each cross-product of equation (A8), and the results are shown in Figure 2.4.

APPENDIX B

Details of the Fourier-Bessel Decomposition of the Surface Pressure on a Rigid Disc

It has been shown in section 2.4.1 that for a thin rigid disc, the scattered pressure is an odd function across the thickness of the disc. The difference between the front and back total surface pressures is therefore simply twice the value of the scattered component at that point on the front surface. For the case of normal incidence, the scattered pressure is only a function of the magnitude of $\underline{r}'$, and can hence be represented as a series of zero order Bessel functions. This technique is termed a Fourier-Bessel decomposition (see References [2.21, 2.22] for more details) and can be expressed as

$$P_+(\underline{r}') - P_-(\underline{r}') = 2P_{s+}(\underline{r}') = 2 \sum_{n=1}^{\infty} \underline{C}_n J_o(\kappa_n r'/a) , \qquad (B1)$$

where $J_o(\kappa_n) = 0$, and the $\underline{C}_n$ values are calculable from

$$\underline{C}_n = \frac{\int_0^a r' P_{s+}(r') J_o(\kappa_n r'/a) dr'}{\int_0^a r' J_o^2(\kappa_n r'/a) dr'} = \frac{\int_0^a r' P_{s+}(r') J_o(\kappa_n r'/a) dr'}{\frac{a^2}{2} J_1^2(\kappa_n)} \qquad (B2)$$

Leitner [2.8] graphically presented the results of exact calculations of the real and imaginary scattered velocity potential components on the surface of a thin rigid disc with a plane wave normally incident. Data was taken from Leitner's results at 25 points across the diameter of the disc for ka equal to 3,4 and 5. These values were then stored on the ISVR's DAC (Data Analysis Centre) computer and a standard analysis program 'RESAMP', (see Reference [2.23] for more details) used to resample the data to give 200 data points. Equation (B2)

was then evaluated : Simpson's rule was used to perform the integration and standard Bessel function generation procedures (as given in Reference [2.20]) adopted.

The first twenty terms in the series were computed in this manner, and the C_n values thus calculated are tabulated in Figure 2.8. As a check the C_n values were substituted back into equation (B1). The results were in almost perfect agreement with the original surface potential distribution of Leitner, as is shown by the example in Figure 2.7.

APPENDIX C

Derivation of the Tangential Velocity Component at the Geometric Acoustics Boundaries in the Dipole Half-Plane Model

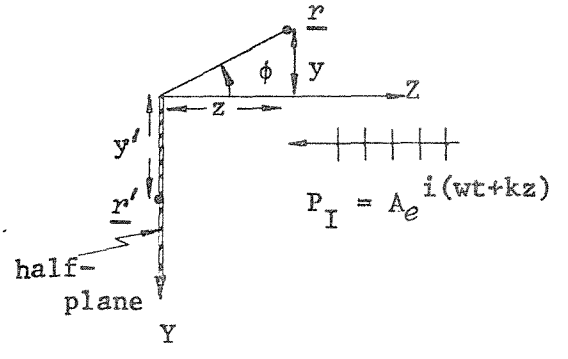

Figure C1 : The two-dimensional half-plane geometry used for the derivation of the tangential velocity at the geometric shadow and bright zone boundaries.

As was stated in Section 2.4.1, the scattered pressure due to any body can be represented as an integral over the object's surface. Thus for a receiver point, $\underline{r}$, and a surface point , $\underline{r}'$, the pressure scattered by any rigid object can be written:

$$P_s(\underline{r}) = \int_S P(\underline{r}') \frac{\partial G}{\partial n} (\underline{r}/\underline{r}') dS \ , \qquad (C1)$$

where G is the relevant Green function, S is the body's surface area, and $\partial/\partial n$ is the outward gradient normal to that surface at $\underline{r}'$. For the geometry of Figure C1 the two dimensional free-field Green function is $-\frac{i}{4} H_0^{(2)}\left(k\sqrt{(z-z')^2+(y-y')^2}\right)$. Thus on the front surface, $\partial G(\underline{r}/\underline{r}')/\partial n = \partial G(\underline{r}/\underline{r}')/\partial z' = -\partial G(\underline{r}/\underline{r}')/\partial z$, whilst on the rear surface $\partial G(\underline{r}/\underline{r}')/\partial n = \partial G(\underline{r}/\underline{r}')/\partial z$. Substitution of these relationships into equation (C1) results in the following form for the scattered pressure,

$$P_s(\underline{r}) = -\int_{S_+} P_+(\underline{r}') \frac{\partial G}{\partial z}(\underline{r}/\underline{r}')dS_+ + \int_{S_-} P_-(\underline{r}') \frac{\partial G}{\partial z}(\underline{r}/\underline{r}')\, dS_- , \qquad (C2)$$

where the + and - subscripts indicate integration over the front and back faces of the half plane respectively. It if is now assumed that the total bright side surface pressure is twice that incident, whilst that on the shadow side is zero, equation (C2) becomes:

$$P_s(\underline{r}) = \frac{2iA}{4}\int_0^\infty \frac{\partial}{\partial z} H_0^{(2)}\left(k\sqrt{z^2+(y-y')^2}\right)dy' .$$

$$= -\frac{iA}{2}\int_0^\infty \frac{kz}{\sqrt{z^2+(y-y')^2}} H_1^{(2)}\left(k\sqrt{z^2+(y-y')^2}\right)dy' . \qquad (C3)$$

Use of the linearised momentum equation for the particle velocity across the geometric shadow and bright zones' boundaries gives

$$\frac{\partial U_\phi}{\partial t}(0,0,z) = -\frac{1}{\rho r}\frac{\partial P}{\partial \phi}(0,0,z) = \pm\frac{1}{\rho}\frac{\partial P}{\partial y}(0,0,z) , \qquad (C4)$$

where the upper (positive) sign in the last member represents the bright zone's edge values, and the lower (negative) sign those of the shadow zone's boundary. Substitution of equation (C3) into equation (C4) yields

$$U_\phi = \mp \frac{A}{2\rho c} \frac{\partial}{\partial y} \int_0^\infty \frac{z}{\sqrt{z^2+(y-y')^2}} H_1^{(2)} \left(k\sqrt{z^2+(y-y')^2}\right) dy'$$

$$= \mp \frac{A}{2\rho c} \left[\frac{z}{\sqrt{z^2+(y-y')^2}} \cdot H_1^{(2)} \left(k\sqrt{z^2+(y-y')^2}\right) \right]_{k\infty}^{0}$$

$$= \mp \frac{A}{2\rho c} \frac{z}{|z|} H_1^{(2)} (k|z|)$$

$$= \frac{-A}{2\rho c} H_1^{(2)} (k|z|) \quad . \qquad \text{(C5)}$$

The last member of equation (C5) represents the total tangential velocity since the incident wave has no velocity component normal to its direction of travel. The velocity flow out of the bright zone can therefore be seen to be equal to that entering the shadow, as was found in the case of the exact solution in Section 2.5.1.

CHAPTER 3

EXPERIMENTAL INVESTIGATION OF SINGLE BODY FREE FIELD SCATTERING

3.1 Introduction

3.1.1 Background:

From the introduction to Chapter 2 it is immediately apparent that there are relatively few scattering problems that can be solved exactly by analytic methods. Even where such a solution is possible, its bare form may not be particularly physically informative, and often the complexity of the calculations required to compute the scattered field numerically renders the method virtually useless from a practical point of view. Approximate solutions are often not much better, since even when they are easily calculable or physically informative, their accuracy is questionable without recourse to some 'absolute calibration'. Furthermore these solutions are generally derived from either high or low frequency assyptotes of exact solutions, and hence must be used with extreme caution at intermediate frequencies, where the wavelength is of the same order of magnitude as the size of the scattering object. In many room acoustics situations, the range of wavelength to object size passes through this intermediate regime. In addition the everyday objects found in rooms seldom resemble the simple shapes, or even materials, that can easily be handled analytically. Moreover, practical building acoustics measurements are frequently performed with bandlimited white noise, and under such circumstances use of exact analytic solutions for prediction purposes proves almost impossible.

In view of the above points, the advantages of an experimental investigation into single body scattering are obvious, since it allows a variety of scattering objects to be investigated in the regime where the wavelength is the same order of magnitude as the object size, for either pure tone or bandlimited white noise incident fields. The scattering geometries chosen can either be those for which simple analytic solutions exist, or those for which analytic methods are inappropriate. It should be noted that the choice of a scattering situation for which a simple analytic solution exists, for the initial experimental method to be determined prior to progression to more complicated scattering cases.

Since this research programme is not concerned with one specific type of scatterer, the experiments performed have to be carefully chosen in order to allow generalisation of the effects observed. Where possible, the frequencies and geometries investigated should be typical of those found in room acoustics. The results should also be presented in the form most readily applicable to building acoustics. In this particular branch of acoustics it appears that the redistribution in angle of the incident energy is the prime concern. This is unlike some other areas of acoustics, such as sonar, where a simple scattering cross section (the ratio of scattered power, either total or in some specified direction, to that incident) will suffice. The difference in requirements is due to the fact that a room is an enclosed environment, and hence sound energy scattered by an object in a particular direction may undergo a series of wall reflections, or further scatterings, before arriving back at the receiver position; the energy scattered in different directions will obviously follow different paths and hence if prediction of the total level at a given point is to be made accurately, detailed knowledge of the scattering process would appear to be required.

In order to discover what experimental data was available a literature search was performed. This is described in the next section. It should be stressed that this review is primarily concerned with experiments which yield information on both the directional distribution and magnitude of the field scattered by single finite-sized rigid objects under free field conditions. For this reason a large number of papers on scattering cross-section (or 'target strength') measurements, barrier attenuation, and multiple (or 'rough surface') scattering properties are omitted.

3.1.2 *Literature review of experimental single body free field acoustical scattering results.*

The earliest experimental single body free field acoustical scattering investigations were concerned with the measurement of the total surface pressure on a scatterer. Sivian and O'Neil [3.1] appear to have been the first to report such measurements. They investigated the diffraction effects at the surfaces of rigid square and circular

plates, in the range $0.55 < ka < 16.5$. Most of their measurements were performed inside an 'absorbing box' with a probe microphone. The results are presented as the variation of total pressure amplitude with frequency at certain points for given angles of incidence. They found a 'bright spot' in the centre of the shadow side, and a marked variation of the total pressure amplitude in the centre of the 'bright side'. Both of these features were more pronounced for the disc than for the square plate. Muller, Black and Davis [3.2] extended the range of variables investigated by Sivian and O'Neil, and also extended the measurements to include cylinders and cubes. When the practical problems involved in making the measurements are considered (e.g. the probe microphone's finite size and 'end correction', and the problem of minimising the number of unwanted reflections) the results of these early investigations appear to be surprisingly good.

Wiener performed an extensive series of measurements of the distribution of total surface pressure on rigid objects in the range $0.4 < ka < 10$. The objects included spheres and cylinders [3.3], cones [3.4], and discs and square plates [3.5]. He obtained similar results to those or the earlier investigators, and noted a general similarity between the results of certain of the objects investigated (e.g., the finite length cylinder and sphere he used). His presentation of 'isopressure' contours for the surface pressure is much more informative and easily interpreted than the results of the earlier investigators.

Primakoff *et al.* [3.6] appear to be the first to report detailed measurements of total pressure for field points off the scatterer's surface. This was carried out for the case of circular discs in water with bandlimited noise, and a hydrophone mounted on a linear traverse which was positioned at various distances from the scatterer, on the opposite side to the source. They were primarily concerned with comparison of their experimental results with a line integral theory which they had developed. A bright spot was observed in the centre of the shadow region, surrounded by interference rings. There was good agreement between the theoretical position of the first minimum adjacent to the bright spot, and that observed experimentally. However the agreement between the predicted and measured values for the magnitude of the bright spot was poor; the authors suggest that this was due to difficulty in

the reproduction of the theoretical models boundary conditions in their tests.

Primakoff *et al.* differentiated between geometric and physical shadow behaviour, the latter being characterised by the presence of a bright spot in the centre of the shadow region, surrounded by periodic 'bright' and 'dark' rings, which they stated are bounded on their outer edge by a region of higher intensity (the 'annular ring'). They obtained an approximate expression for the behaviour in the region of the physical shadow boundary and demonstrated that it represents a level increase towards the shadow edge. They then estimated the distance, x , from the scatterer where the physical shadow ceases to exist by equating the position of the start of this level increase to that of the first minimum adjacent to the bright spot. This results in the expression $x \simeq 1.5(a^2/\lambda)$, which they found to agree reasonably well with their experimental results when the approximations in their theory are considered.

Most of the papers so far discussed are concerned with measurements of acoustical scattering properties in air. The next three papers (References [3.7, 3.8, 3.9]) are reports of scattering measurements made in water. They are only included since they are representative of major contributions to the understanding of scattering processes, and typical of a different type of experimental technique. It should be stressed however, that great care must be exercised in the interpretation or application of any results obtained in water to scattering situations in air. This is because in underwater scattering problems, the propagation medium has a density which can be comparable to that of the scatterer, which may thus behave as an elastic body and support the propagation of internal compressional and shear waves. Most scattering objects encountered in room acoustics can be assumed to be immovable, and to possess a rigid surface or some impedance boundary condition.

Faran [3.7] developed the theory for scattering by solid spheres and cylinders which can support compressional and shear waves, and performed a few experiments for comparison on 'infinitely long' cylinders.

He found that large changes in the distribution in angle can be observed around the frequencies of the normal modes of free vibration of the body in question. Barnard and McKinney [3.8] employed sound pulses to study far field scattering by solid and air-filled cylinders of different lengths over the range $0.33 \lesssim ka \lesssim 24.4$. The use of pulses allowed them to 'gate out' the scattered energy alone. They investigated the distribution of this scattered energy for various configurations. For cases where the sound was incident normal to the longitudinal axis of the cylinder and the microphone traversed an arc equidistant from the centres of the cylinder's parallel faces, they discovered that, whilst the 'target strength' was dependent upon the logarithm of the cylinder's length squared, the pattern of the distribution was similar in all cases for given pulse length. The behaviour in the bright region was also more susceptible to change with variation in pulse length than was that in the shadow zone. Use of shorter pulses to study the echo structure revealed the existence of a multiple reflection phenomenon. Barnard and McKinney postulated that this was direct experimental evidence of the existence of 'creeping waves'. These waves arise from the physical interpretation of using a Watson transformation to predict scattering from convex shaped bodies; they travel around the outside of the scatterer at a velocity less than the ambient sound propagation speed, whilst being attenuated by radiation processes in tangential directions. In principle, these waves can circumnavigate the scatterer many times; in practice the attenuation due to radiation rapidly reduces their effectiveness. Hampton and McKinney [3.9] performed similar experiments for solid spheres in water over the range $4.1 \lesssim ka \lesssim 57$. Numerous other researchers have subsequently investigated these creeping wave effects in water.

Harbold and Steinberg [3.10] experimentally demonstrated the existence of 'creeping waves' in air, for cases of rigid spheres and cylinders in the range $1 \lesssim ka \lesssim 100$. They used 10μS acoustic pulses which were generated by modulating an ionised air column in a small open ended quartz crystal, and then focussed into a horn. From the output of ¼ inch surface-mounted microphones they found pulses circumnavigating the scatterer, as distinct from the incident and reflected pulses. They discovered that the tone burst enters the shadow region at the free space sound speed, but that the velocity of

the pulse front then decreases to a constant level. The distance required to attain a constant front velocity was found to be dependent upon the width of the pulse's spectrum. They postulate that this is because the high frequency creeping wave components move into the shadow zone fastest, but are rapidly attenuated to leave only the dominant centre frequency components after a short distance into the shadow. These lower frequency components then travel at a constant speed and are attenuated less than the higher frequency components. The experimental results proved to be in excellent agreement with theoretical predictions.

Pulse tests are only really indicative of a scatterer's transient behaviour, except in cases where the length of the pulse when travelling in the propagation medium is much greater than the size of the scatterer. In such cases the 'gating out' of the scattered energy may prove impossible at all but points in the extreme far field, and an alternative method must be devised. A technique for the extraction of the scattered field from steady state tests has been described by Baars [3.11]. This method involves the measurement of the pressure field at a receiver point in the absence of the scatterer. The scatterer is then inserted and both the amplitude and phase of the resultant signal at the receiver compensated for the original incident field. By rotation of the scatterer and repetition of this sequence of events for a number of receiver points on an arc centred on the scatterer, it is possible to build up the directional distribution of the scattered field for all angles of incidence in the plane investigated. Baars performed this procedure for the case of a rigid disc for values of ka less than 10, and achieved good agreement to both exact and approximate theories which he considered.

In some other recent papers the results of particular theories are compared with experimental results. Worthy of mention in this context are papers by Terai [3.12], Kawai, Fujimoto and Itow [3.13] and Kawai [3.14], all of whom have presented the detailed distribution of the total pressure field amplitude around various objects (Terai around discs and plates of different compositions, Kawai *et al.* around a thin half-plane, and Kawai around 'pillar-shaped' objects).

3.1.3 The implications of the literature review for the experimental programme of research into single body scattering.

Once the decision has been taken to experimentally investigate the detailed distribution of the field around a scatterer, it is apparent from the literature that there are still a large number of choices to be made. For instance, quite apart from the choice of objects to be used, there remain the questions as to whether to choose measurement points on or off the surface, and whether to use a continuous, or a pulsed incident field. From the published literature it also appears that there are a number of areas that remain poorly documented. For example, there is a lack of a comprehensive range of tests on different scattering bodies under identical test conditions. This is particularly true for receiver locations that are neither on the scatterer's surface nor in the far field, but lie somewhere in-between. There also does not seem to exist a comparison of pure tone and bandlimited noise results for similar test conditions. Where the scattered field component is presented in the literature, there does not seem to be any indication of its relative phase, and thus the overall steady-state field cannot be computed without some assumption. Baars [3.11] assumed that in the far field for the case of a rigid disc, the scattered and incident fields are in quadrature, which by comparison with the form of the exact solution he showed to be very nearly correct for the situations considered.

For application to practical building acoustics problems, the most useful measurements would represent the magnitude of the total sound pressure level variations around a scatterer for ka values and scatterer to receiver distances typical of real situations. The presentation of these results for, say, 1/3 octave bandlimited white noise, would give an indication of the maximum shielding or reinforcement effects likely in such circumstances. Examination of the observed diffraction pattern features for a carefully chosen range of objects might then enable generalisations to be made which could be used to extend the experimental findings to predict the behaviour of other scattering configurations. The additional performance of a few selected pure tone tests would allow comparison with exact theoretical predictions (where applicable) and also demonstrate the effect of using bandlimited noise. From measurements of relative phase, carried out in

conjunction with these single frequency steady state tests, it may also prove possible to gain some insight into the scattered component alone; total mean square pressure level results alone are generally of little use in this context since they represent the time-averaged value of the sum of the incident and scattered pressures squared.

The apparatus used and the experiments performed are described in detail in the next section.

3.2 The Experimental Programme Details:

3.2.1 The experimental apparatus

The main experiments, described in this section were designed to study the variation of the total field for receiver positions on a closed circular arc centred on a scatterer which is being irradiated with sound. These measurements were made with and without the scatterer present, so that the effect of the scatterer could be separated out from that of unwanted reflections. In order to avoid such reflections, the experiments were performed inside anechoic chambers. The majority were in the ISVR's large anechoic chamber which has internal dimensions when empty 9.15 m square by 7.32 m high, with 0.91 m long wedges on all surfaces. (See Reference [3.15] for a full description of its acoustical performance). Some measurements were performed in the semi-anechoic chamber in the ISVR's teaching laboratory. This measures 2.7 m high × 2.4 m × 2.5 m when empty, and has 0.3 m deep wedges on all surfaces. Only bandlimited noise tests were performed in the smaller chamber. Comparison of identical tests between the two chambers indicated good agreement (this is discussed further in the results section). In order to minimise any unwanted reflection or diffraction effects due to the scatterer's suspension mechanism, the objects were initially hung from the roof of the anechoic chamber by use of one or more thin nylon lines. However, it was then extremely difficult to define the position of the scatterer relative to the source and receiver locations since the object was very prone to movement. For this reason the rig shown in Figure 3.1 was constructed. This permitted the scattering configuration to be defined with much greater accuracy, and produced highly repeatable

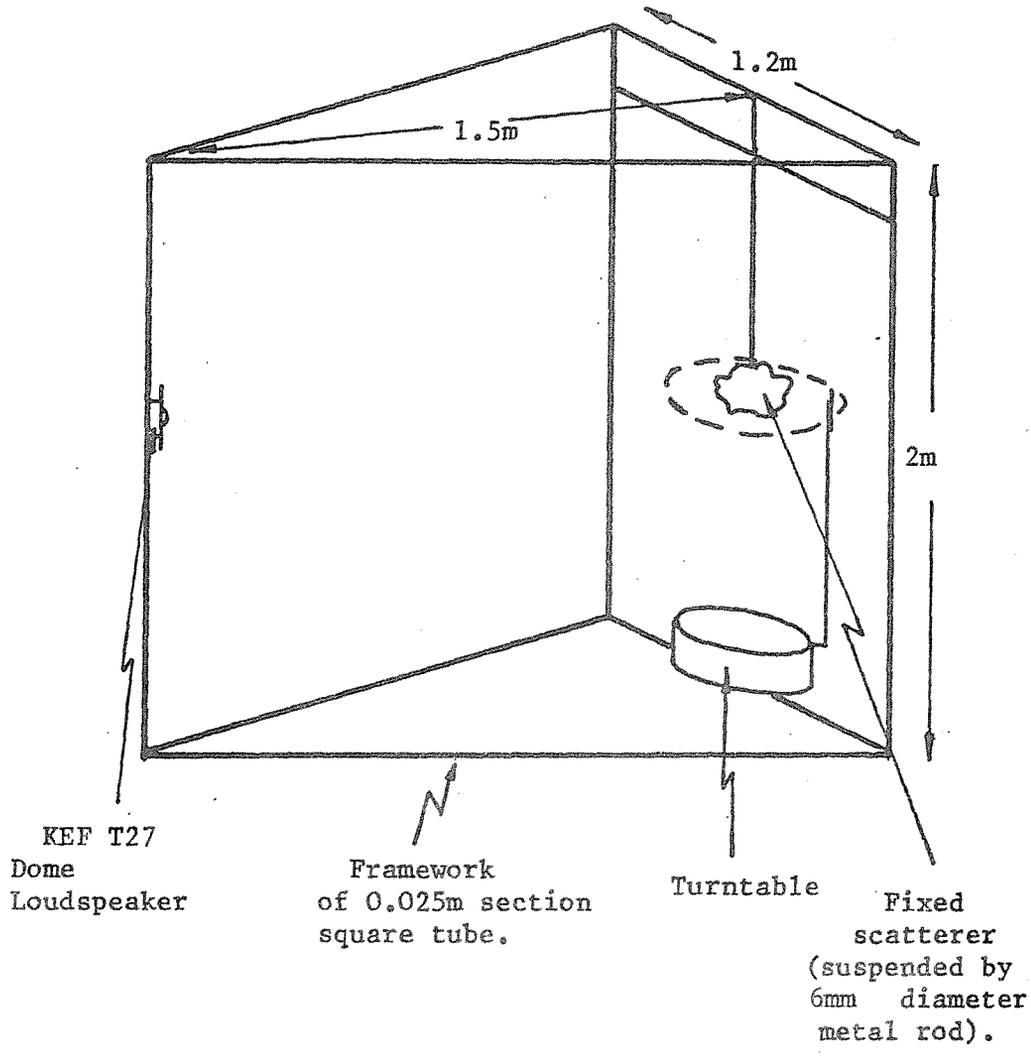

Figure 3.1 Sketch of the rig used for the experimental investigation of single body free field scattering.

Notes: i) All the experimental plots cover a 50dB range.
ii) On the experimental plots, $\theta=0^{o}$ is where the microphone is directly in between the source and scatterer, $\theta=180^{o}$ is where the microphone is on the opposite side of the scatterer to the source.

results. Obviously, the metal framework causes some interference, particularly when the microphone traverse passes close to the vertical supports and at higher frequencies. For this reason the framework was 'lagged' with 0.045 m thick foam rubber, and measurements performed both with and without the scatterer.

In order to initially investigate a finite-sized scatterer for which exact results can also be computed analytically, it was decided to examine first the case of a rigid sphere. With the time and funds available for apparatus construction , and the size of the rooms in which the experiments were to be performed, it was decided to use a 0.129 m diameter shot putt. To obtain a value of ka equal to π , (at which frequency the wavelength of sound equals the sphere's diameter) therefore requires a source that operates down to about 2.6 kHz. Ideally the loudspeaker chosen should have 'point source' characteristics over a wide frequency range; this implies a small cone, and minimal rearwards radiation (to avoid dipole radiation characteristics). Investigation of the drive units commercially available indicated that a dome 'tweeter' should best meet these requirements. The unit chosen was a KEF T27. This has a solid metal back with a 20 mm Melinex dome which gives a nominal frequency range of 1 kHz to 40 kHz that is essentially flat from 3 kHz to 20 kHz, but should not be used much below 3 kHz without a cut-off filter, due to the loudspeaker's fundamental resonance at about 1.2 kHz.

A diagrammatic representation of the electronic equipment arrangement used in the experiments is shown in Figure 3.2.

3.2.2 The experimental procedure:

After the scatterer to be investigated had been hung from the rig (generally so that its centre was directly over that of the turntable), the loudspeaker was positioned so that the middle of the cone was at the same height as the centre of the scatterer's vertical axis. The microphone was then adjusted so that it was pointing vertically (so that incident and scattered pressure fields are approximately equally weighted by the microphone's directivity at higher frequencies), and its diaphragm was at the required height (normally in the same plane

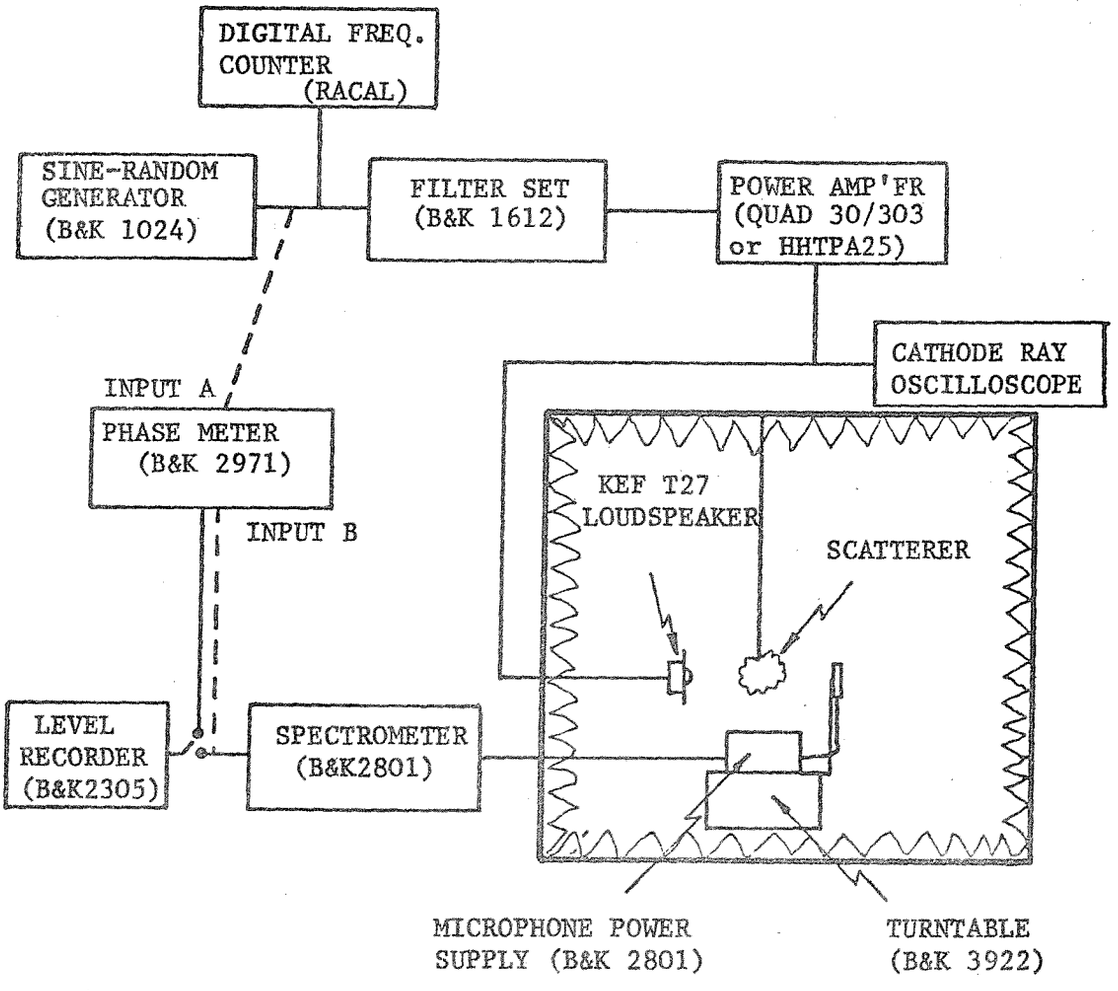

Figure 3.2 Schematic diagram of the electronic equipment used. (N.B. Phasemeter only connected when pure tone used, and then the phasemeter's output was fed directly into the level recorder.

as the centres of both loudspeaker and scatterer). The radius of the microphone traverse was then adjusted to the required value, by alteration of the length of the boom attached to the turntable. The microphone was then positioned to lie exactly in between the source and the scatterer, and the anechoic chamber's door closed.

The loudspeaker was then activated from outside the chamber, the turntable started and the sound pressure level, or relative phase value recorded over a complete 360^{o} arc in a horizontal plane. The chamber door was then opened, the scatterer removed, and the process repeated.

For sound pressure level measurements a calibrator (B&K Type 4230) was used before measurements commenced, so that, if necessary, the levels could be interpreted in terms of dB *re* 2×10^{-5} Nm^{-2}.

For phase measurements the plot paper was calibrated from 0 to 360 degrees upon each occasion before the experiments started. During the experiments the phase of the microphone output was recorded relative to that of the electrical signal leaving the signal generator.

3.2.3 The range of variables investigated:

The range of possible experimental variables' combinations is vast. The various parameter headings and the range covered in each case is discussed below. The actual combinations used are indicated in Figure 3.3.

The range of objects:

Listed below is the range of objects used as scatterers and their construction. It should be noted that once the shot putt had been chosen, it was necessary to make the other scatterers of comparable size, so that any 'family resemblances' might be observed. The objects had holes tapped in the centres of their 'sides', so that they could be suspended about any major axis of symmetry (i.e. the sphere and discs had one suspension point, the rectangle two etc.). Thus, for the

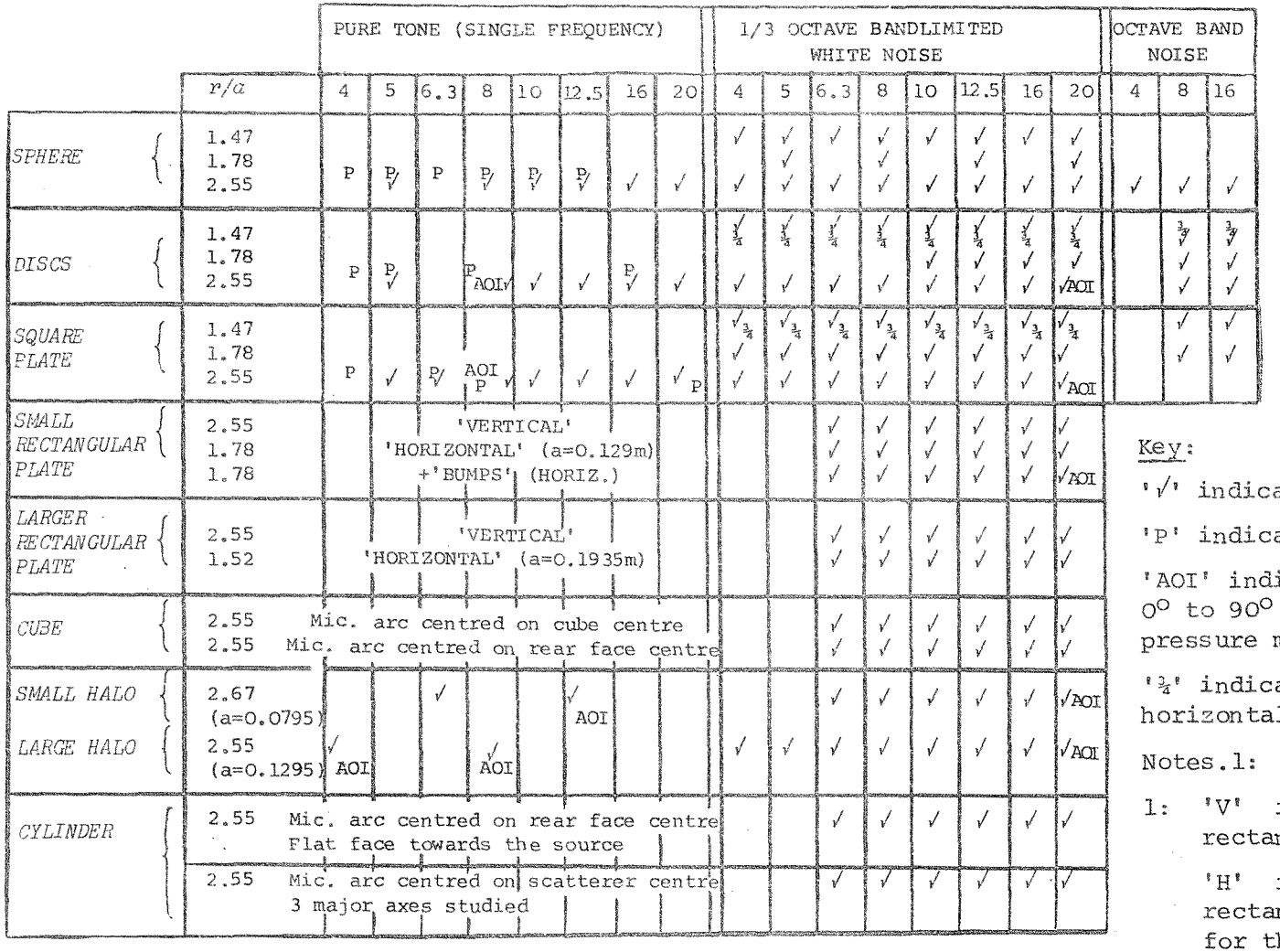

Figure 3.3 : Table showing Parameter Combinations Investigated.

Key:

'√' indicates r.m.s. pressure measured.

'P' indicates that phase was measured

'AOI' indicates that angles of incidence from 0^{o} to 90^{o} in 15^{o} steps were used for f.m.s. pressure measurements.

'¾' indicates the microphone traverse was in a horizontal plane mid-way between.

Notes.1:

1: 'V' indicates that the long-sides of the rectangle was vertical, (thus a=0.0645 m)

'H' indicates that the long-sides of the rectangle were horizontal (thus a=0.129 m for the small rectangular plate and a=0.1935 m for the large rectangular plate).

2: The pure tone frequencies for the small halo were 6.5 kHz and 13 kHz (in order to give the correct ka values).

rectangular plates, 'vertical' is used to represent configurations where their longer edges are vertical, and 'horizontal' cases where they are horizontal.

Object	*Size*	*Material*
1. Sphere (Shot Putt)	0.129m diameter	Solid Steel
2. Disc 1 (thin)	0.129m diameter, 0.0095m thick	Duralumin Alloy
3. Disc 2 (thick)	0.129m diameter, 0.0191m thick	Duralumin Alloy
4. Square Plate	0.129m × 0.129m × 0.0095m	Duralumin Alloy
5. Small Rectangular Plate	0.129m × 0.258m × 0.0095m	Duralumin Alloy
6. Large Rectangular Plate	0.129m × 0.387m × 0.0095m	Duralumin Alloy
7. Cube	0.129m × 0.129m × 0.129m	Varnished Wood
8. Cylinder	0.129m diameter; 0.129m long	Varnished Wood
9. Small 'halo' on sphere	The 'haloes' are rings designed to to fit around the sphere on a plane passing through its centroid. They are both fabricated from 0.0095m thick plate.	Duralumin Alloy
10. Large 'halo' on sphere	Outside diameters: Small halo 0.159m Large halo 0.259m	Duralumin Alloy
11. "Lumps" on Small Rectangular Plate.	11 Plasticene Lumps (0.02m high × 0.03m × 0.03m) distributed over the front surface of the plate.	Plasticene on Duralumin Alloy

The range of frequencies and signal bandwidths:

The range of frequencies investigated covers from 2 kHz to 20 kHz. However, initial experiments revealed little diffraction behaviour at frequencies below 4 kHz, and thus this is the lowest frequency reported in the results section. The majority of the tests were performed with 1/3 octave bandlimited white noise. However, single frequency sound was used in some experiments, and octave band limited white noise in others.

The range of angles of incidence:

The majority of tests were performed with the sound arriving normal to the surface of the scatterer closest to the source. This geometry will be termed zero degrees (0°) angle of incidence. The design of the experimental rig permits the variation of this angle from 0° to 90° in units of 15°.

The range of microphone traverse conditions:

For most tests the plane of the microphone traverse was the same as that in which the centres of both loudspeaker and scatterer were located. In this configuration, the range of the ratio r/a (the ratio of microphone traverse arc radius to scatterer 'radius') was from 1.47 to 2.55. In addition, for some scatterers, at the smallest r/a ratio, measurements were made with the plane of the microphone traverse mid-way between the centre and the uppermost point of the scatterer.

3.3 Discussion of the Experimental Single Body Free Field Scattering Results:

3.3.1 Consideration of the experimental accuracy:

Before any discussion of the features exhibited by the experimental results can be commenced, their accuracy must be determined. There are a number of factors that govern the possible magnitude of the errors. The factors discussed below are those remaining after it is assumed that the plots shown are adequate representations of the microphone's electrical output (i.e., there is no detailed discussion of possible inaccuracies in the electronic equipment, since it was all laboratory standard, well maintained and calibrated). The aim of the discussion which follows is to ascertain how accurately the microphone's output represents the physical pressure field which it was desired to measure.

Since the plots are intended to represent free field scattering behaviour it is essential to decide initially whether all the experiments were performed under approximately uniform conditions, and whether these conditions were anechoic (i.e., free field). The uniformity of the measurement conditions is easily proven, since there were only two test sites, and a number of identical experimental configurations were investigated in both of the rooms employed. Comparison of the results from similar tests (as shown in Figure 3.4) indicates that the results obtained in the two cases were identical to within ± 1.5 dB. These results imply that the smaller, semi-anechoic chamber is almost as good as the larger anechoic chamber for the type of 1/3 octave bandlimited white noise measurements performed. The degree to which the conditions in the larger chamber approximate to free field must therefore be considered next.

Jackson [3.15] presented results of the maximum possible deviations from spherical spreading in this chamber, for frequencies up to 15 kHz, and source to receiver distances up to 3m. This deviation is within ± 1.1 dB for frequencies between 200 Hz and 10 kHz, and within ± 1.8 dB for frequencies between 10 kHz and 15 kHz. The insertion of the experimental rig into the chamber will obviously alter these figures. However, since all measurements were made with and without the scatterer present, it is possible to estimate the variability of the incident field alone under experimental conditions. From the results (see for example Figures 3.5 and 3.6) the maximum deviation of a single frequency incident field appears to be ± 2 dB. This was estimated by measuring the deviation of the pressure maxima and minima from a smooth line drawn through the experimental trace. The value obtained also includes any effects due to the non-uniformity of the loudspeaker's radiation pattern.

The next possible source of error is the degree of certainty with which the position of the microphone diaphragm can be specified. There are two aspects to this problem: the first concerns the accuracy with which the microphone is situated relative to the scatterer (and hence also the source). This includes the accuracy with which both the height and radius of the microphone traverse can be set. The microphone traverse radius has to be adjusted to the desired magnitude,

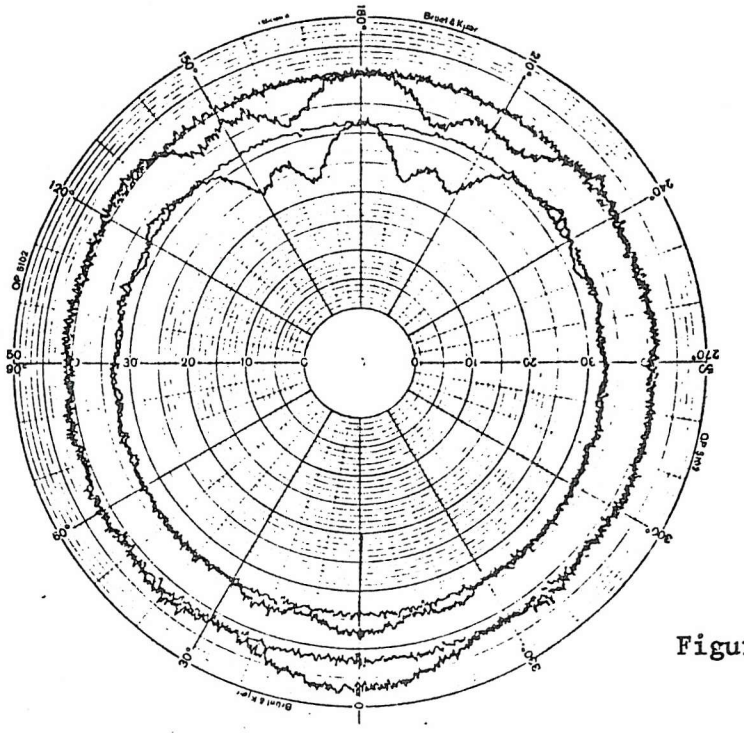

Figure 3.4(a)

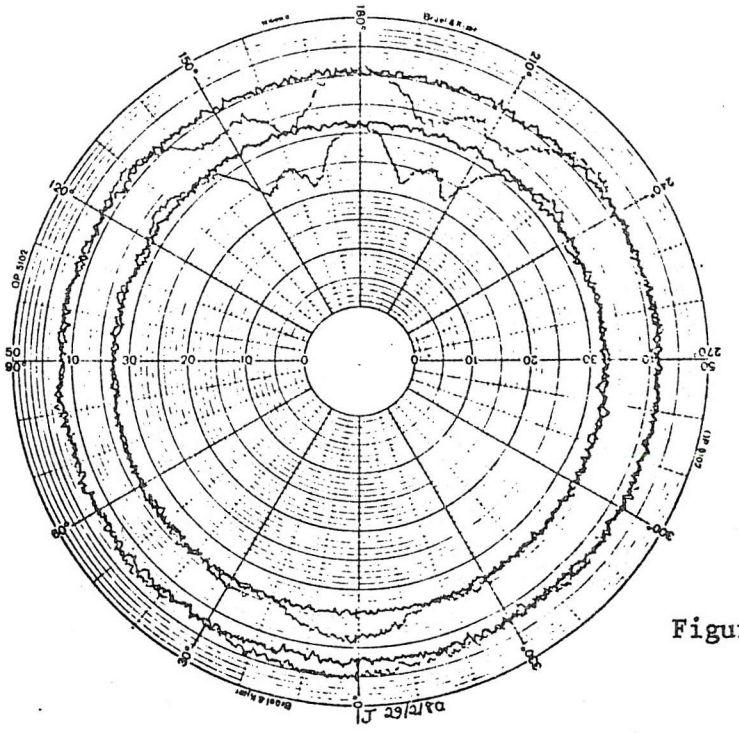

Figure 3.4(b)

Figure 3.4 Comparison of the results from the small and large anechoic chambers, for the square plate with 6.3 and 8kHz 1/3 octaves bandlimited white noise, microphone traverse radius = 0.1645m
a) Small (teaching laboratory) chamber,
b) Large (Rayleigh building) chamber.

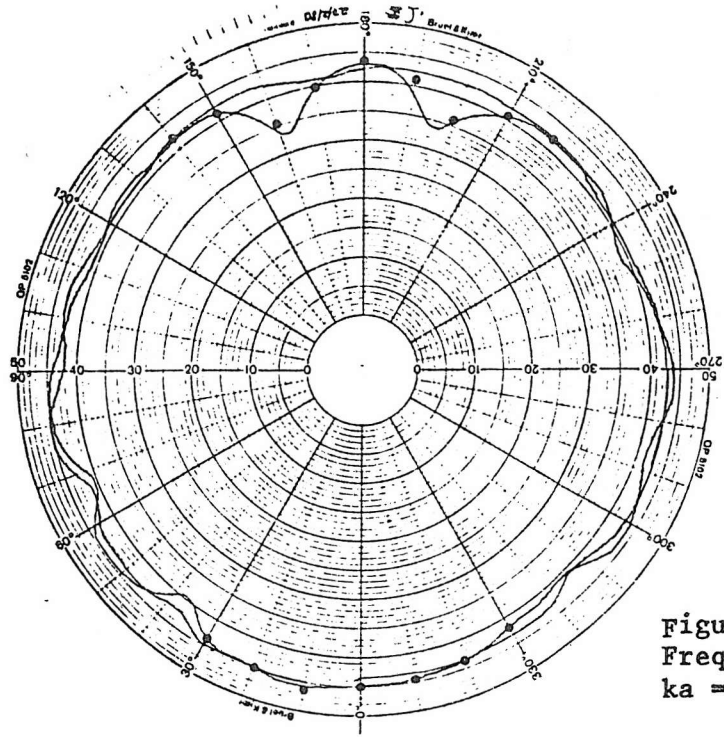

Figure 3.5(a)
Frequency = 5kHz
ka = 5.96

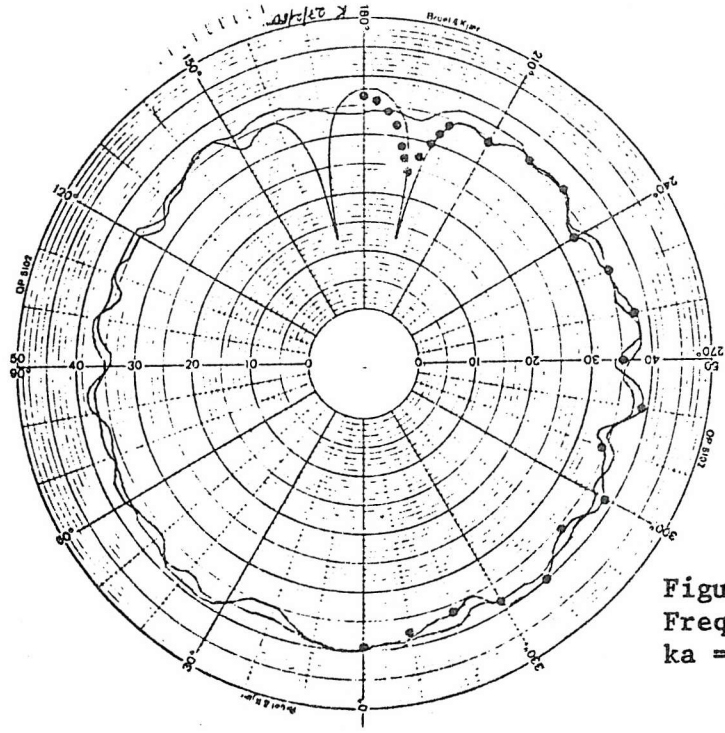

Figure 3.5(b)
Frequency = 8kHz
ka = 9.54

Figure 3.5 Comparison of the experimental and theoretical results for the distribution of single frequency overall SPL with/without the sphere. Microphone traverse radius = 0.1645m (r/a = 2.55) Frequencies as indicated. The black spots indicate the computed values for the total level.

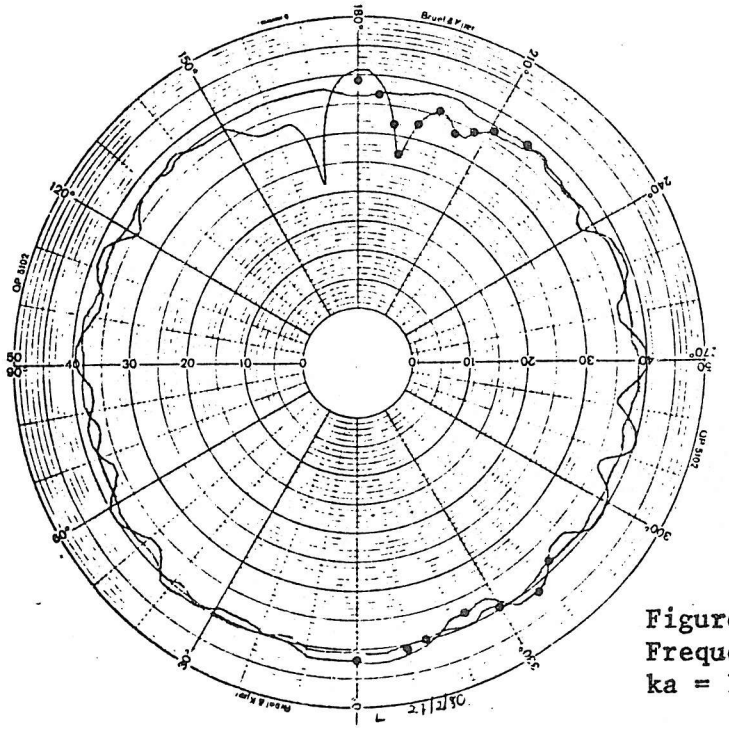

Figure 3.5(c)
Frequency = 10kHz
ka = 11.92

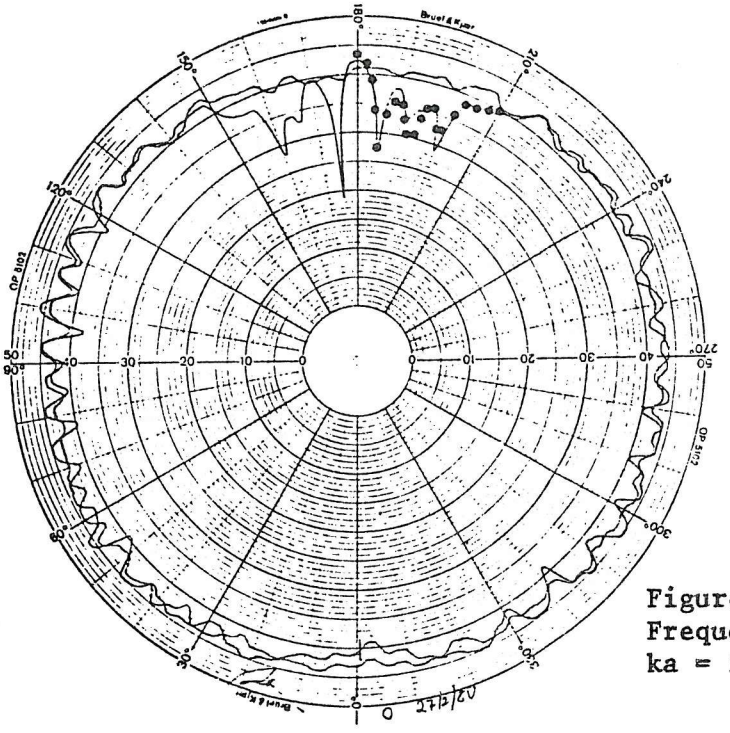

Figure 3.5(d)
Frequency = 20kHz
ka = 23.84

Figure 3.5 Continued.

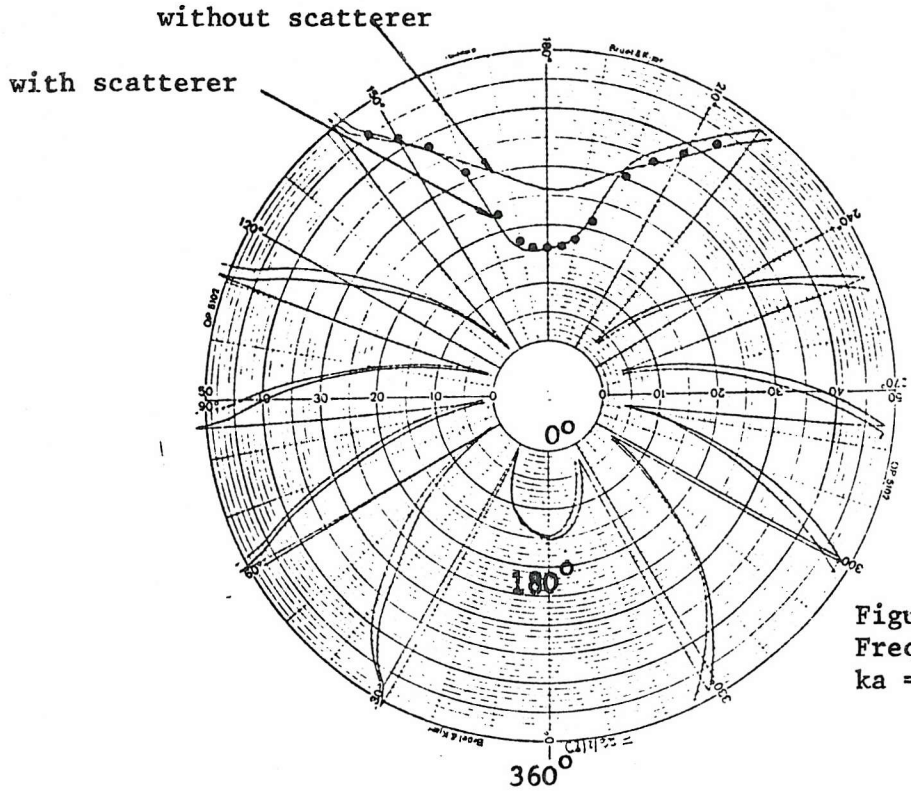

Figure 3.5(e)
Frequency = 5kHz
ka = 5.96

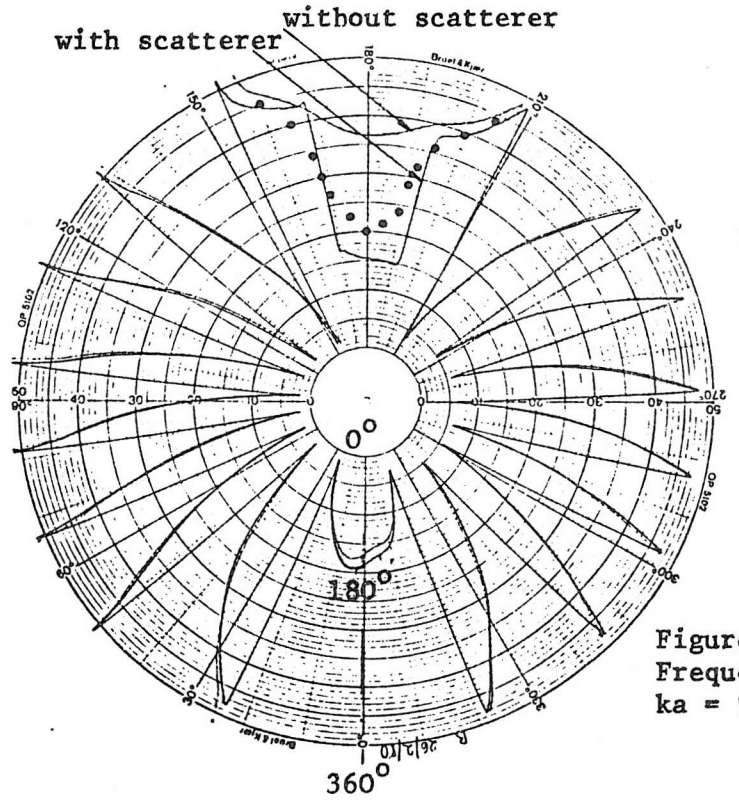

Figure 3.5(f)
Frequency = 8kHz
ka = 9.54

Figure 3.5(e) and (f) Plots of the experimental phase measurements with and without the sphere, and theoretical values with sphere. Microphone traverse radius = 0.1645m (r/a = 2.55). Frequencies as indicated.

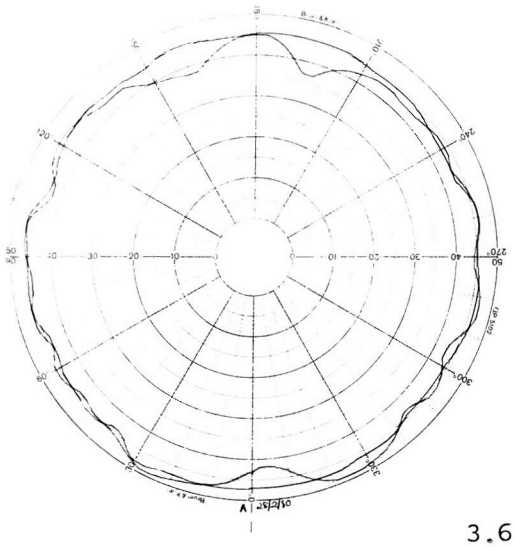

3.6(a)

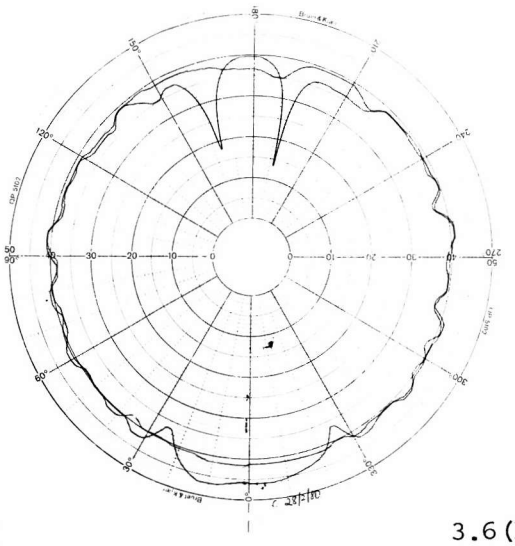

3.6(b)

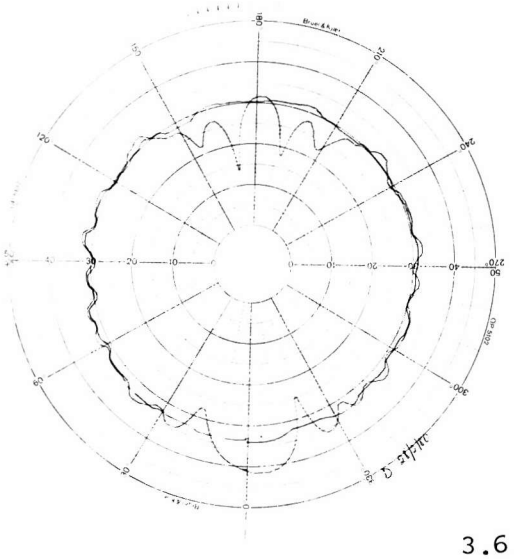

3.6(c)

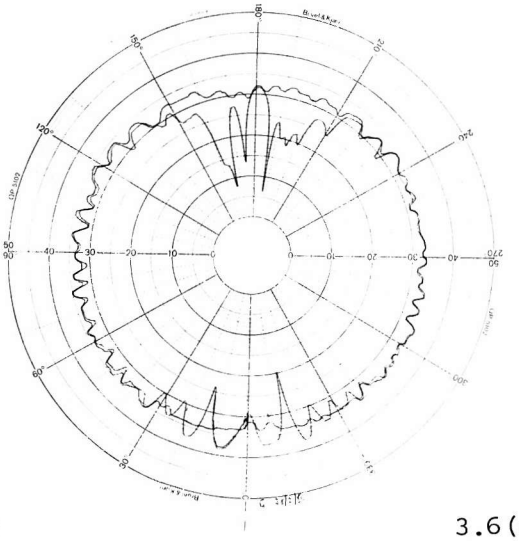

3.6(d)

Figure 3.6 Single frequency sound pressure level results for the disc (with and without the scatterer present). Microphone traverse radius = 0.1645 m (r/a = 2.55).

(a) 5 kHz (ka = 5.96)
(b) 8 kHz (ka = 9.54)
(c) 10 kHz (ka = 11.92)
(d) 20 kHz (ka = 23.84)

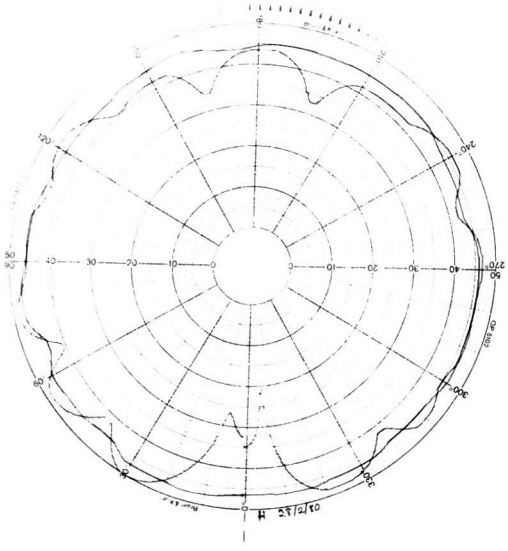

3.6(e)

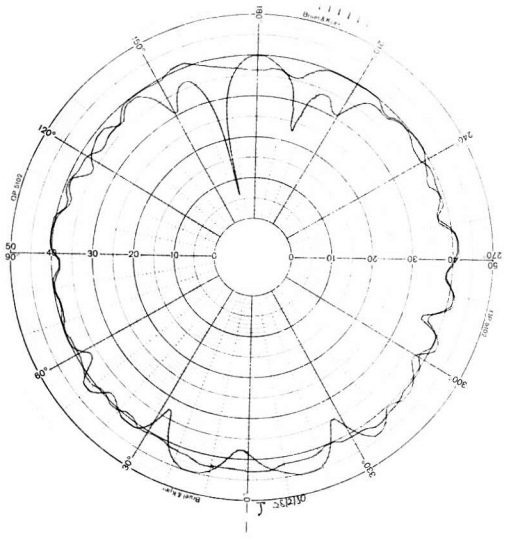

3.6(f)

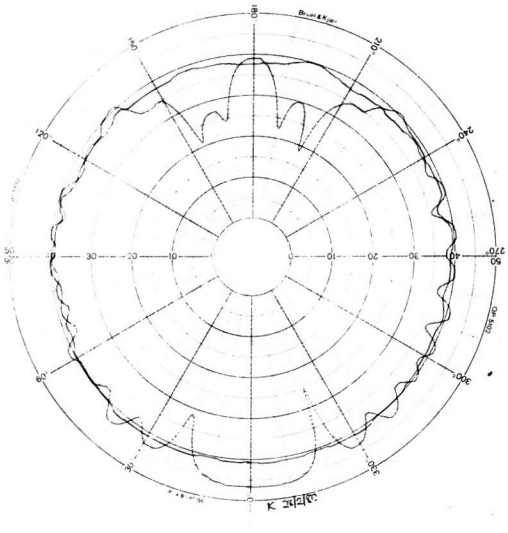

3.6(g)

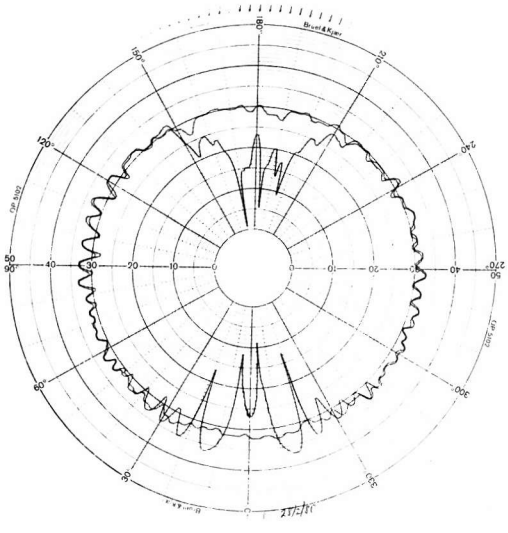

3.6(h)

Figure 3.6 (cont'd.) Single frequency sound pressure level results for the square plate (with and without the scatterer present). Microphone traverse radius = 0.1645 m (r/a = 2.55)

(e) 5 kHz (ka = 5.96)
(f) 8 kHz (ka = 9.54)
(g) 10 kHz (ka = 11.92)
(h) 20 kHz (ka = 23.84)

and also accurately centred on the chosen point. It is estimated that all these measurements were achieved to within an accuracy of ± 2.5 mm. Obviously any errors made in the positioning of the microphone will be most significant at higher frequencies. The other aspect of microphone positioning which can lead to errors is caused by failure to correctly align the start of the traverse with the zero degrees mark on the plot paper. This results in a slight shift of all the results in angle, which can easily be detected. Inspection of the results presented indicates that this error is insignificant in most cases. Where it does occur, provided the results were more or less symmetrical about some line, close in angle to the 0°-180° line on the plot paper, it is assumed that this is the true 0° position.

Another source of possible error is the directional sensitivity of the microphone at higher frequencies due to its own diffraction effects. For the microphone traverse arc most used in this programme of 0.1645 m with a 0.0645 m radius sphere or disc, the maximum vertical angle subtended by the scatterer at the microphone diaphragm is ± 21 degrees, either side of grazing incidence (90°). The manufacturer's literature indicates that with the microphone used, for 10 kHz plane waves arriving within ± 30° of grazing, the levels will be within ± 2 dB of that due to a similar plane wave at 90°; whilst at 20 kHz the levels will be within ± 4 dB of that due to grazing incidence plane waves. It is not clear what relationship there is between the diffracted waves measured and the planes waves of the manufacturer's data, but it can be stated that possible errors due to microphone directivity will be largest at high frequencies, for receiver points closer to the scatterer. Use of a ¼ inch microphone would have lessened the magnitude of these possible errors; however, such microphones are 10 to 15 dB less sensitive than those used, and since the shadow region levels fall on occasion in the lower part of the 40 to 50 dB sound pressure level range, it was thought that this might prove unacceptable under some experimental conditions.

The combined effects of all the errors discussed, and any possible inaccuracies due to the electronic equipment used, can be determined from direct comparison of experimental results with a

computed exact analytic solution. Since the solution to scattering by a rigid sphere has been computed (as described in Chapter 2), this case was chosen for the comparison and the results are shown in Figure 3.5 (where the computed phase values plotted have been obtained by subtraction of the difference between the computed total and incident phase values from the incident phase value measured experimentally). It can be seen from these results that the computed and measured mean square pressure are within 3 dB of each other, except in the region of some shadow region minima, across the range of frequencies investigated. The phase plots (which are only compared in the shadow region) appear to be accurate to within 15^{o} for the 5 KHz results (see Figure 3.5(e)) and about 70^{o} for the 8 KHz results (see Figure 3.5(f)). Although the latter trace is harder to compare due to the large jump at around 168^{o}, and the fact that the experimental plot is very slightly mis-aligned (i.e. the axis of symmetry appears to be about the 1^{o} - 181^{o} line). Of course, this use of the computed solution to check the experimental results, assumes the former is accurate. However, for the reasons discussed in Chapter 2, it is felt to be completely adequate for the current purposes.

All of the accuracy comparisons above are for the case of the rigid sphere. It was in order to ensure its rigidity that a shot putt was chosen. It is possible however, that although the diffraction pattern measured around the other scatterers is that which actually exists there, the objects are not behaving in a rigid manner, but may be vibrating. In order to check this point, two discs were constructed of the same material (duralumin alloy) and diameter (0.129 m) but different thicknesses (0.0095 m and 0.0191 m). This should ensure that their vibrational characteristics are sufficiently different to produce radically different results if vibration is important. Although there were differences in the pure tone results (these could be due to the different diffraction effects in the two cases), when 1/3 octave bandlimited white noise was used the agreement was almost perfect. For this reason only the thin disc results are actually reported. Further indication that scatterer vibration is not significant can be obtained from inspection of the results for the small rectangular plate, with and without plasticene bumps on it (Figure 3.10(d) and (m)).

Since the application of plasticene to the surface would drastically change the plate's damping, the fact that the results with and without plasticene are virtually identical in the shadow region substantiates the argument that plate vibration is insignificant.

After full consideration of the possible error sources, it actually appears however that the sound pressure levels measured may be expected to lie within about 3 dB of the 'correct' values. This is based on comparison of single frequency experimental and theoretical results. It may be expected that the 1/3 octave averaged results might exhibit a lower error, since the incident field is less variable. No direct check of this has been performed however. The accuracy of the experiments having been determined, the detailed discussion of the experimental results follows.

3.3.2 *The effect of frequency on the single frequency mean square pressure results:*

Examination of the results for the case of the rigid sphere (see Figure 3.5) reveals that in the ka and r/a range investigated, there is little 'shadow' behind the scatterer. However a distinct diffraction pattern is visible. This pattern has a 'bright'spot (or Poisson spot) in the centre of the region (i.e. 180°) which can be of greater magnitude than the incident sound pressure level. With increased frequency, the angular width of this spot decreases, further maxima and minima become evident to either side of the main peak, and the shadow depth marginally increases. This behaviour is repeated in the results for the disc and square plate (see Figure 3.6), which are markedly similar to those for the sphere in the shadow region, but display a much more pronounced interference pattern on the 'bright' side of the scatterer. For these thin objects on axis (i.e. 0°) the pressure may be greater or less than that incident.

For all the objects described so far, the angular spread in the shadow region, where the total mean square pressure is less than that incident (not counting the bright spot), is greater than would be indicated by geometric acoustics.(For the plots shown the half-angle width of the geometric acoustics shadow would be 25.49°).

3.3.3 *The variation of the phase of the pressure field around the scatterers:*

Over the majority of the microphone traverse, there is little difference between the total and incident fields' phase values. The main differences for the case of the sphere (see Figure 3.5(e) and (f)) lie in the shadow region where large phase changes can occur (see Figure 3.5(f)). It also appears that for the larger ka values investigated, where the region around the Poisson spot is well developed, rapid 180^{o} phase changes are evident in the phase of the total field at pressure minima. Thus the pressure in two adjacent lobes of a shadow zone diffraction pattern can be seen to be out of phase with each other (which is similar to the behaviour of any high order radiation pattern).

The behaviour of the phase measurements for the disc and square plate (see Figure 3.7) are again generally similar to those for the sphere in the shadow region, but may be substantially different on the central axis of the bright region (i.e. 0^{o}). Here, in the case of flat objects, much larger changes in phase can occur when the scatterer is put in position. From these results, reflection phenomena would appear to dominate the bright zone behaviour under the conditions investigated. Although in principle it is possible to evaluate the scattered field component alone from tests such as these (as performed by Baars [3.11]), it would either require the construction of electronic compensation equipment, or manipulation of the data acquired (most probably on a computer). It was not felt that the aims of this investigation justified the development of such techniques.

3.3.4 *The effect of the use of bandlimited white noise*

The results obtained by use of 1/3 octave bandlimited white noise are shown in Figure 3.8 for the sphere and disc for four frequency bands in each case: namely, the two adjacent 1/3 octave bands at opposite extremes of the frequency range covered. From comparison with the single frequency results of Figures 3.5 and 3.6 it will be seen that a large

amount of the incident field's variability has been removed, although the major trends with frequency observed in section 3.3.2 still persist. It will also be noticed that the region of marked sound pressure level fluctuation to the front of the scatterer is removed, to be replaced by one of overall slight level increase for flat scatterers, and that 'sideways scattering' appears minimal. However, perhaps more interesting is the behaviour in the shadow region, where the trend of the maxima and minima is much as for the single frequency results, but the magnitude of the fluctuations is reduced, thus obscuring any small perturbations. It is however still possible for the peak level in the Poisson spot to equal the incident field level.

The results obtained by use of octave bandlimited white noise are shown in Figure 3.9 for the case of the sphere. Here the observable detail is reduced further still, although the Poisson spot remains visible in the centre of the shadow region.

It is again evident from these results that for the ka and r/a range illustrated the phase change involved with the majority of the features seen when a scatterer is placed in a pure tone field must be reasonably small, with the exception of the behaviour in the vicinity of the Poisson spot. This is in agreement with the observations of Section 3.3.3. It is also interesting to note that, after 1/3 octave averaging, the behavours in the shadow regions of the sphere and disc under the conditions discussed here are almost identical. The behaviours in the bright region are however quite dissimilar. Further discussion on the extent of similarities between the scattering behaviours of the various objects examined is contained in the next section. It was decided that, for practical purposes, the 1/3 octave results yielded the most informative data, since they preserve the major trends but remove any small fluctuations and are more representative of practical requirements. The remainder of the discussion sections is therefore concentrated on results obtained with the use of such signals.

3.3.5 The variation of the pressure distribution around a scatterer with object shape.

The distribution in angle of 1/3 octave averaged sound pressure level around the other objects investigated is shown in Figure 3.10

(a) Disc (b) Square Plate

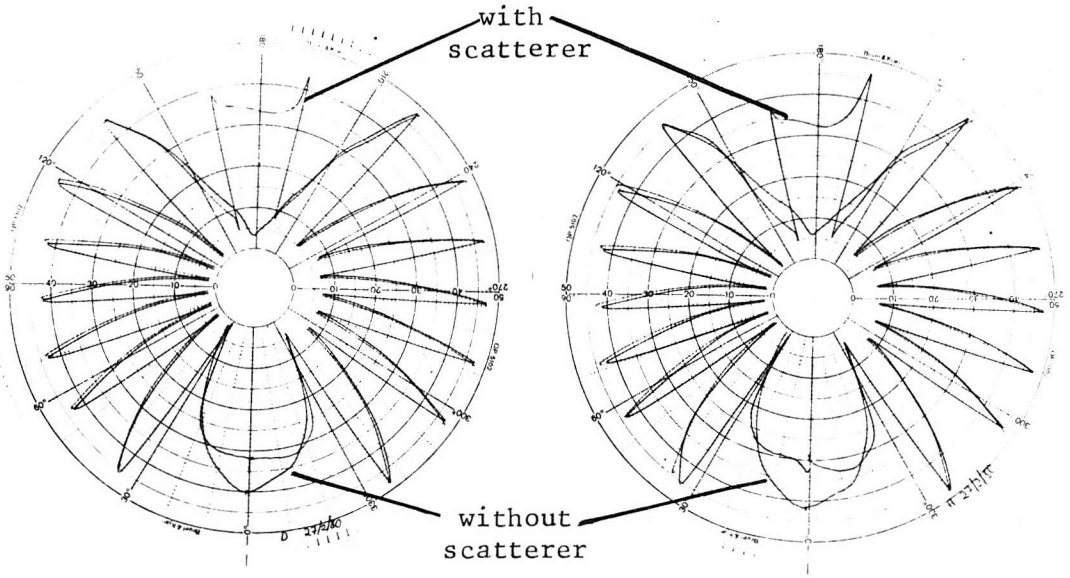

3.7(a) 3.7(b)

Figure 3.7 8 kHz Single frequency phase plots (ka = 9.54). Microphone traverse radius = 0.1645 m (r/a = 2.55).

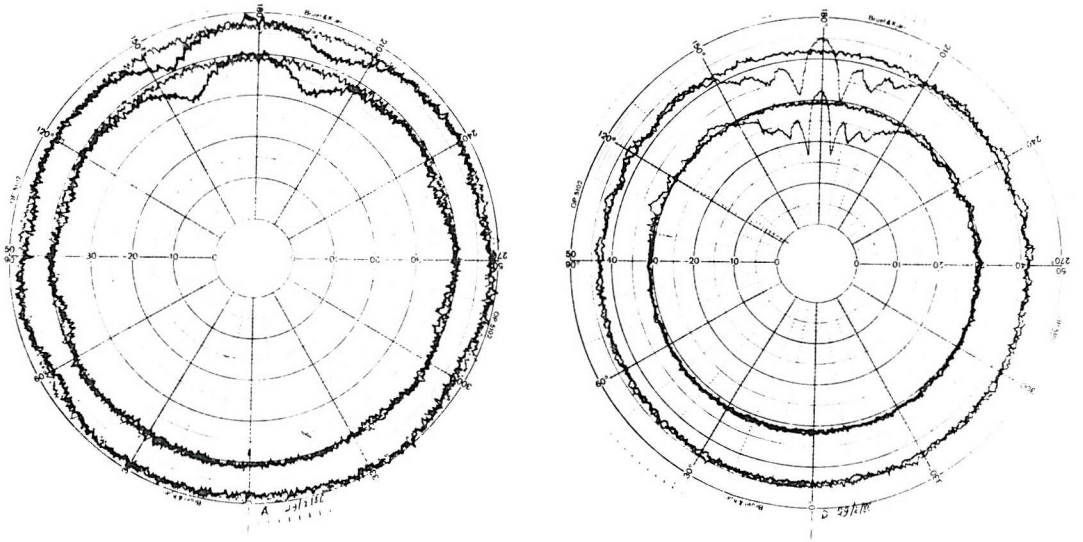

3.8(a) 3.8(b)

Figure 3.8 Sphere : $\frac{1}{3}$ octave bandlimited white noise sound pressure level results. Microphone traverse radius = 0.1645 m (r/a = 2.55).

N.B. There are two sets of traces per Figure, each set containing results both with and without the scatterer.

(a) Outer traces : 4 kHz (ka = 4.77); Inner traces : 5 kHz (ka = 5.96).

(b) Outer traces :16 kHz (ka = 19.07); Inner traces : 20 kHz (ka = 23.84).

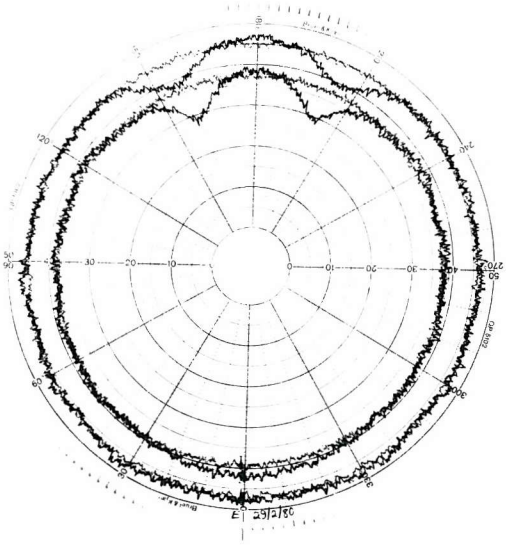

3.8(c)

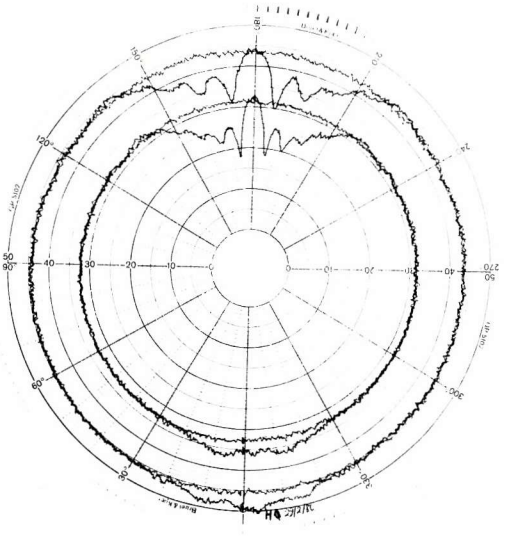

3.8(d)

Figure 3.8 (cont'd). Disc : 1/3 octave sound pressure level results.
Microphone traverse radius = 0.1645 m (r/a = 2.55).

(c) Outer trace : 4 kHz (ka = 4.77); Inner trace : 5kHz (ka = 5.96).
(d) Outer trace : 16 kHz (ka = 19.07); Inner trace : 20 kHz (ka = 23.84).

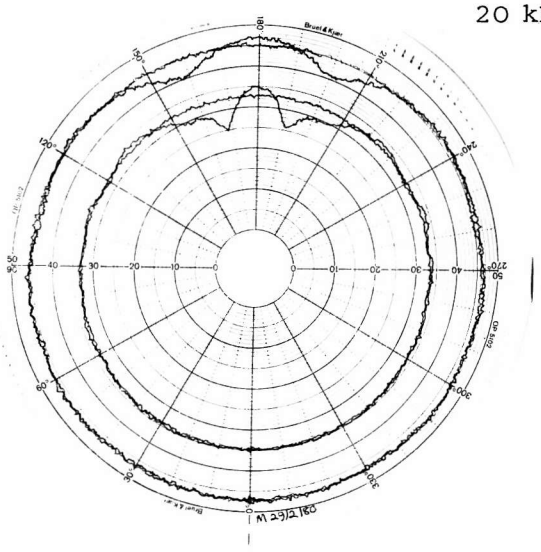

3.9(a)

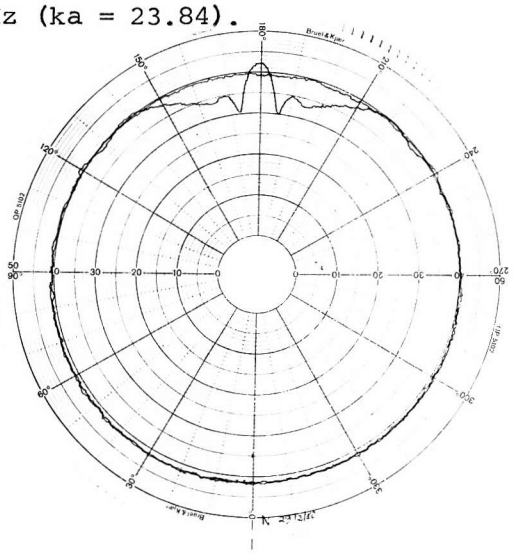

3.9(b)

Figure 3.9 Sphere : Octave sound pressure level results.
Microphone traverse radius = 0.1645 m (r/a = 2.55).
(a) Outer trace : 4 kHz (ka = 4.77); Inner trace : 8 kHz (ka = 9.54).
(b) 16 kHz (ka = 19.07).

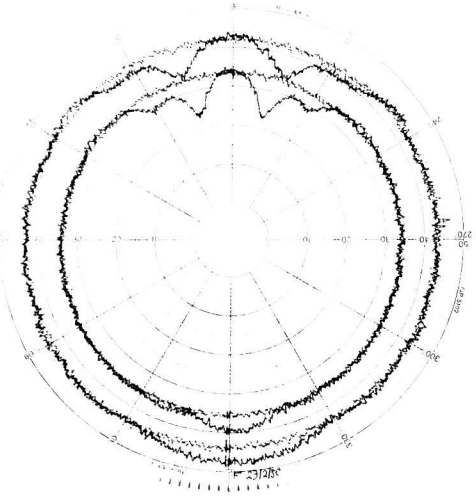

3.10(a)
Disc

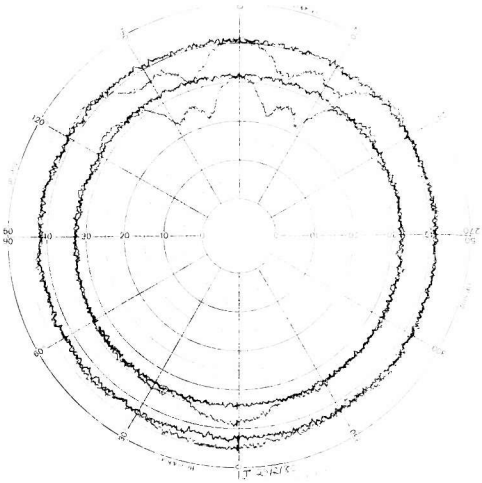

3.10(b)
Square Plate

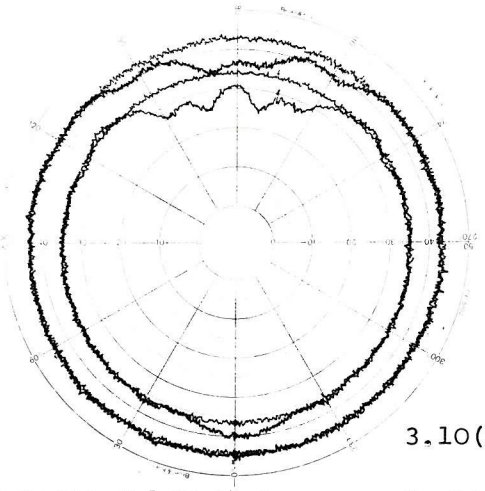

3.10(c)

Smaller rectangular plate 'vertical' (i.e. the longer edges are vertical).

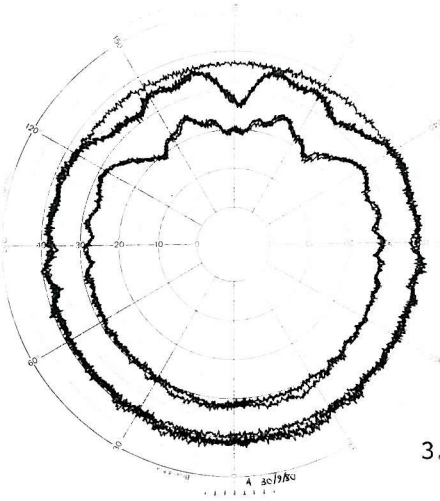

3.10(d)

Smaller rectangular plate with plasticene lumps on the front surface. Longer plate edges are horizontal. Microphone traverse radius 0.229 m.

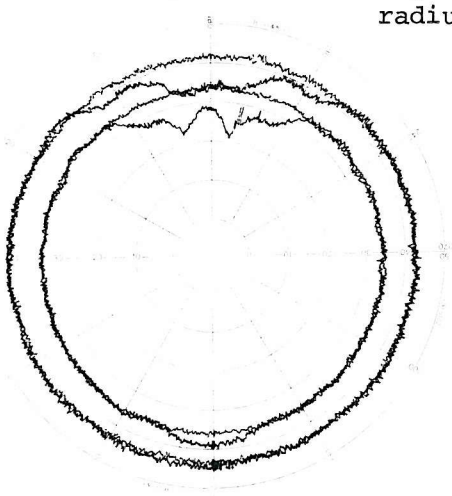

3.10(e)

Larger rectangular plate 'vertical'

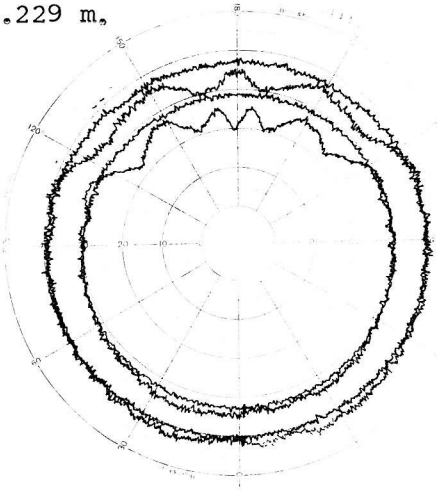

3.10(f)

Larger rectangular plate 'horizontal'. Microphone traverse radius = 0.2935 m.

Figure 3.10 Comparison of 1/3 Octave SPL results for the various objects. Unless otherwise stated, microphone traverse radius 0.1645 m (r/a = 2.55) and centre frequencies are 6.3 kHz (outer trace) and 8 kHz (inner trace).

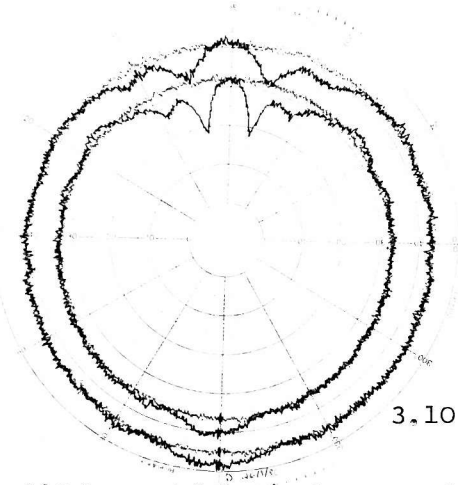

3.10(g)

Larger 'Haloed'Sphere 4 kHz (outer trace) and 5 kHz (inner trace) 1/3 octave bands, microphone traverse radius = 0.3295 m.

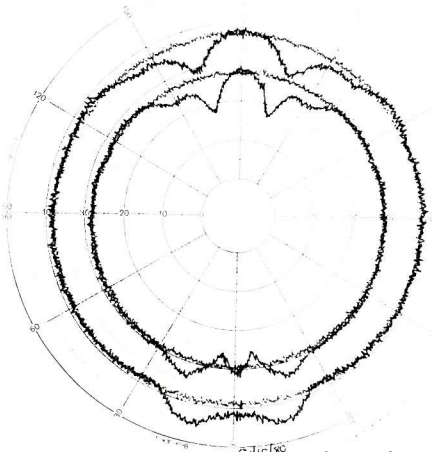

3.10(h)

Cylinder (suspended with its flat faces vertical, and normal to the incident sound, the microphone traverse centred on its rear face).

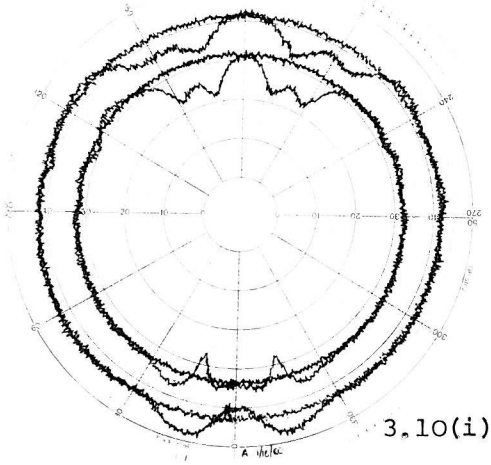

3.10(i)

Cube (flat face normal to incident sound, microphone traverse centred on its rear face).

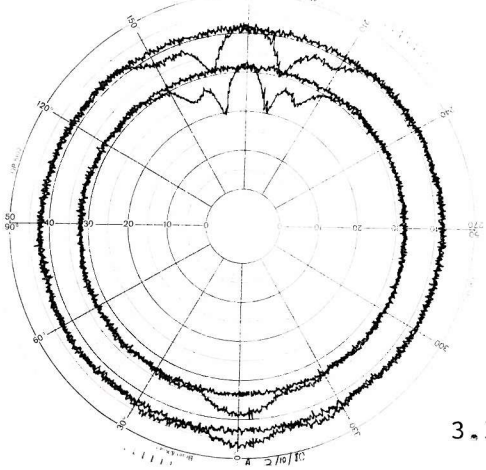

3.10(j)

Cylinder (flat face normal to incident sound, microphone traverse centred on its rear face).

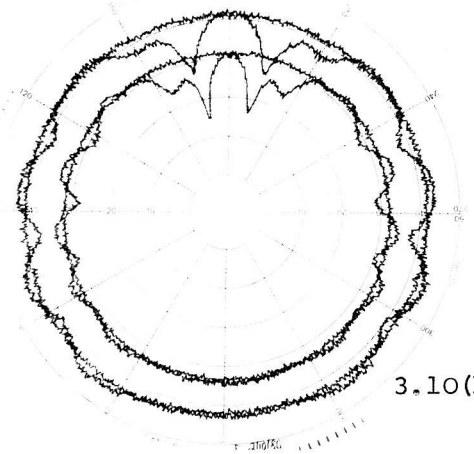

3.10(k)

Cylinder (flat faces horizontal microphone traverse centred on object's centroid).

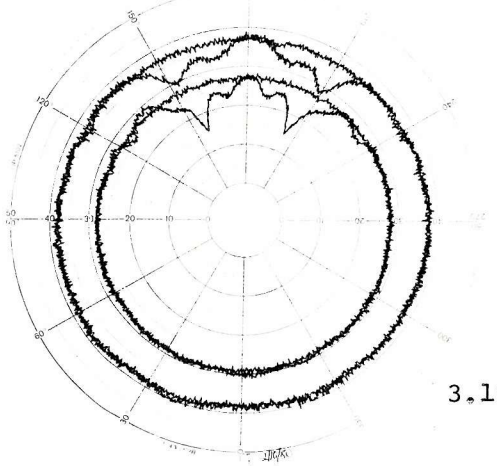

3.10(l)

Cylinder (flat faces vertical, sound normally incident on curved face, microphone traverse centred on object's centroid).

Figure 3.10 (Cont'd).

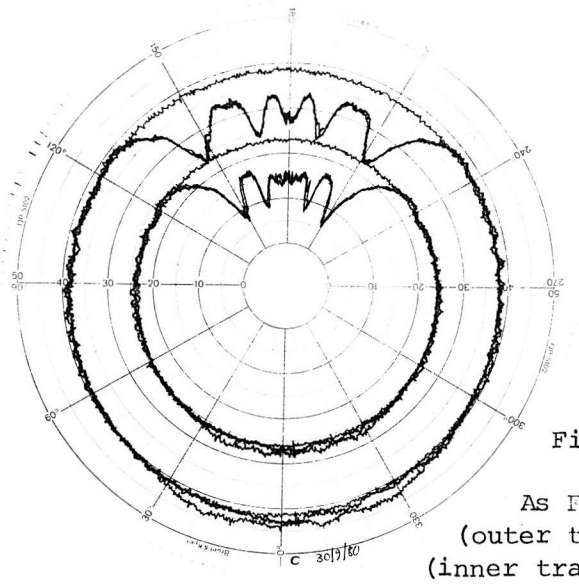

Figure 3.10(m)

As Figure 3.10d), but 16 kHz (outer trace) and 20 kHz (inner trace) 1/3 octave bands.

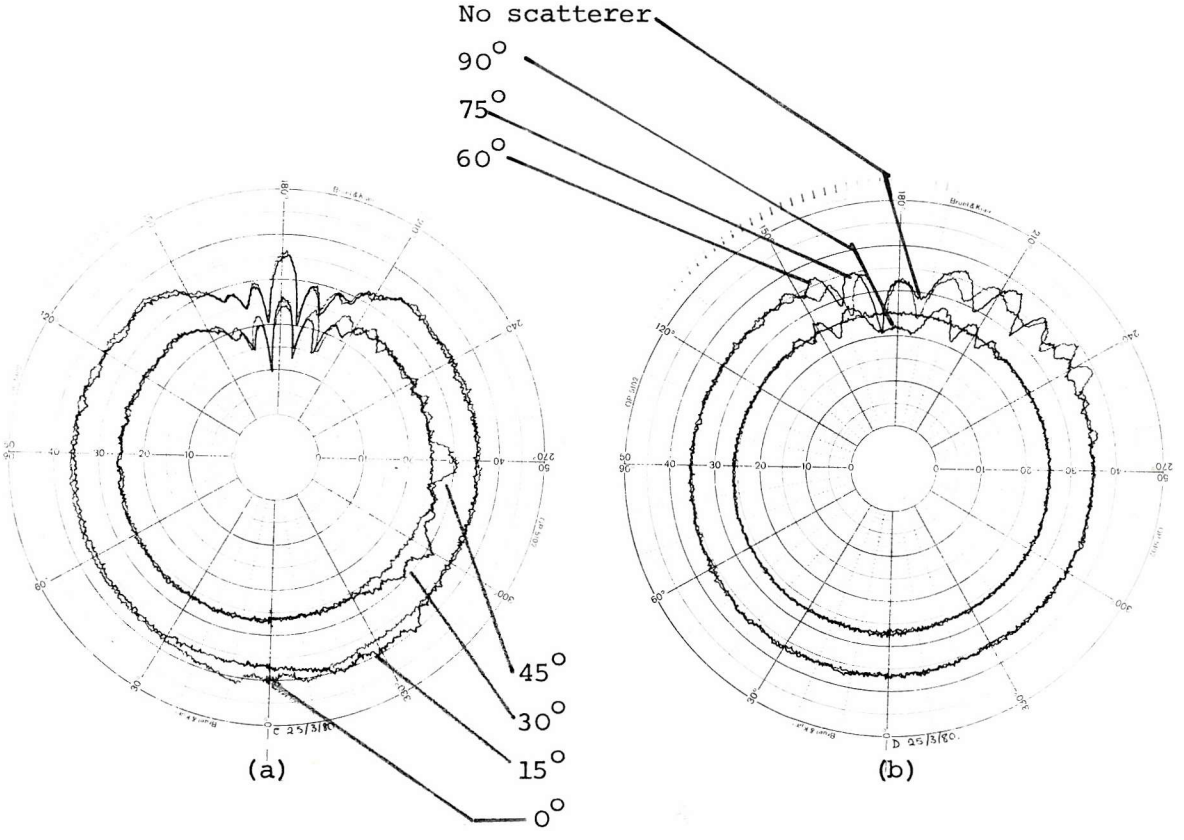

Figure 3.11 Square Plate : The effect of angle of sound incidence on the 20 kHz 1/3 octave band sound pressure level distribution (0° = Normal incidence). Microphone traverse radius = 0.1645 m (r/a = 2.55).

(a) Angles of Incidence : 0°, 15°, 30°, and 45°.

(b) Angles of Incidence : 60°, 75°, 90° (and trace without scatterer).

for ka values representative of the centre of the range of frequencies employed. (The ka value is based on the centre frequency of the 1/3 octave band used). The results for the disc are included for comparison, since it was observed in the previous section how these resembled those of the sphere at both ends of the spectrum examined. It will immediately be apparent that there is a certain 'family likeness' between some of the results of Figure 3.10, and that parts of certain plots are (to well within the experimental accuracy) identical with the same angular range of a different object's plot. For example, comparison of the shadow region of the disc with that of the cylinder with a flat face normal to the incident sound, and the microphone traverse arc centred on its rear face (see Figure 3.10(a) and (h)) , reveals an agreement to within 1.5 dB at all points in the shadow region. Similar agreement (this time to within 1 dB for ka = 9.54) can also be seen between the shadow zone behaviour of the square plate and the cube with the microphone traverse arc centred on its rear face (see Figures 3.10(b) and (i)). For the same ka value of 9.54 the agreement between the shadow behaviours of the disc and the large 'halo' on the sphere (see Figures 3.10(a) and (g)) can also be seen to be within about 2 dB of each other, since the ka and r/a values were matched and the effect of the bandwidth of the noise also appears to scale.

The shadow zone behaviour under these conditions might therefore appear to be determined by the silhouette of the scattering object as seen by the source. Examination of the results for the cylinder in the three orientations used with the microphone traverse arc centred on its centroid (see Figures 3.10(j), (k) and (l)) shows, however, that the silhouette is not the only important factor. This is evident since the three sets of results are somewhat different, yet the three configurations show more or less the same silhouette to an incident plane wave. The shadow zone behaviour for the case where the flat faces are horizontal (Figure 3.10(j)) is very similar to the situation where they are normal to the incident sound (Figure 3.10(k)), with the former geometry displaying greater levels of destructive interference in this region. However, the shadow behaviour is totally different for the third orientation, where the flat faces are vertical and the sound is normally incident on the curved side (Figure 3.10(l)), although the Poisson spot is still about the same level. It appears from these results that although the silhouette is important

in the determination of the shadow zone behaviour, consideration must be given as to where the 'diffracting edges' actually are in space, although comparison of the sphere and disc results indicates that the type of diffracting edge does not alter the pattern seen, only the magnitude of the levels. Even this difference in magnitude is only generally of the order of 2 dB.

The three cylinder results also suggest that it is the scatterer's front surface contour that determines the bright zone behaviour, since only the configuration with a flat surface normal to the incident sound produced any marked increase in the overall level there. Indeed, for the case where the flat faces are horizontal the level in front (near 0°) is actually lower than that incident, and there is evidence of substantial 'sideways scattering', visible as maxima and minima even after 1/3 octave averaging. The presence of 'creeping waves' circumnavigating the cylinder is suggested by these results for this configuration.

Comparison of the results for the disc and square plate suggests that the magnitude of the interference pattern for 'thin' objects of comparable length and breadth (x and y dimensions) is determined by their degree of symmetry. That is to say that since all the diffracted components that arrive at the centre of the disc's shadow will have travelled identical distances from the disc's perimeter, they can be assumed to produce a greater pressure than for the case of the square plate where they will not. These experimental results are in agreement with the theoretical predictions of Carlson and Hunt [3.16] and Morse and Feshbach [3.17]. The latter authors showed that in the limit of $ka >> 1$, the scattered wave is independent of the shape of the scattering surface, but is determined by the shadow line. Carlson and Hunt used this idea, and considered the numerical evaluation of a line integral, based on a Kirchhoff approximate formulation for the scattering of normally incident sound by regular polygonal plates. They demonstrated that decreased plate symmetry results in a smaller Poisson spot, but that its half-angle is almost independent of the number of sides to the polygon. Examination of the results presented here suggests that these ideas are applicable down in the region $ka \simeq \pi$.

In this experimental investigation, the range of thin objects is however extended to objects which do not have comparable dimensions along their major axes. In the cases examined, the shadow zone diffraction patterns are markedly different to those in the situations already discussed in this section. This is evident from comparison of Figures 3.10(b),(c) and (e) which show respectively the results for the square plate, and the small and large rectangular plates with their longer sides vertical. For the two rectangles, although their behaviour is similar and a periodicity can be seen in their shadow zones which is attributable to the smaller dimension, their behaviour is very different to that for the square plate. Traversal of the microphone around the scatterer in the other plane results in a completely different type of pattern (see Figure 3.10(d) for the small rectangular plate $r/a = 1.775$, and Figure 3.10(f) for the larger rectangular plate $r/a = 1.517$, where a in both cases is half the plate's dimension in the plane of the microphone traverse). The lack of a pronounced Poisson spot on these traces is thought to represent accurately the physical behaviour, as although the larger microphone traverse arcs may increase the positional uncertainty, repeated experiments produced similar results. The 'vertical' plate tests may also have increased error due to the large vertical angle subtended by the scatterer's edges at the microphone diaphragm; however these results are included to provide a complete picture of the experiments performed, and since the results shown in Figures 3.10(c) and (e) are similar. It can therefore be assumed that the shadow zone patterns observed are a direct consequence of the fact that the range of distances travelled by diffracting wavelets from the plate's edge will be much greater for the case of a rectangular plate than for a square one. Thus they will not all arrive in the centre of the shadow zone with the same phase. The range of phases with which these waves reach the receiver will obviously be related to the range of distances they travel and their frequency. This behaviour can also be seen for the square plate and disc results: These are virtually identical in the low frequency 1/3 octave bands used but in the higher frequency bands the square plate's Poisson spot is much lower in level (e.g. about 5 dB lower at $ka = 23.84$).

It is further assumed that for an infinitely long 'rectangular plate' the contributions from adjacent areas of the edges which give rise

to wavelets that arrive at a shadow zone receiver point out of phase with each other, will tend to cancel out. Ultimately this process of cancellation leaves only an area on the edge, which lies on a direct 'line of flight' from source to receiver via the plate's edge, to contribute. The length of this zone is from the point where the source to receiver distance via the edge is a minimum to those points where the wave has to travel a quarter of a wavelength more in going from source to receiver. This process is well understood in optics (see, for example, Reference [3.18]) where the wavelength is often much smaller than object size, and is termed Fresnel diffraction. Obviously here the objects are unlikely to appear infinite to the pressure waves, and thus complicated interference patterns can arise which could possibly be interpreted in terms of uncancelled Fresnel zones.

Thus for any simple, regularly shaped body, it is apparent that for normally incident sound even after 1/3 octave averaging, there still remains some distinct shadow detail in the ka and r/a range investigated. However except for objects where the central region of the shadow zone is approximately equidistant from all points on the scatterer's silhouette, it appears that a distinct Poisson spot will not necessarily be evident, and where it is its magnitude will often be much less than the incident field's value. 'Sideways scattering' only appears to remain to any extent after 1/3 octave averaging for the case of the cylinder with its flat faces horizontal, and the sound incident normal to the curved surface whilst the receiver traversed an arc equidistant from that surface. Appreciable backscattering is only noticeable where the object has a major flat surface normal to the incident sound field.

The effect of disturbing a flat surface was briefly studied by the application of very roughly hemispherical lumps of plasticene about 0.02m high by 0.015m radius to the front flat surfaces of the disc and smaller rectangular plate. The results are shown in Figures 3.10(d) and (m) for the rectangular plate for two sets of 1/3 octave band frequencies. For the lower frequencies the change in the bright region was hardly noticeable, as the effect of adding the lumps to the plate was to lower the level by about 1 dB and increase the fluctuations near 90° and 270°.

At the higher frequencies investigated (16 KHz and 20 kHz 1/3 octaves), the reduction in the bright region increased to give up to a 3 dB drop in the level when the plasticene was added. There also appear to be slight increases in the levels between 60^{O} to 90^{O}, and 270^{O} to 300^{O}.

The plasticene is undoubtedly more acoustically absorbent than the metal plate, but it appears that the reduction in the level must be at least partly due to the redistribution of sound by the 'lumps' since the level outside of the normal bright zone increases. This demonstrates how easily the coherent reflection from a hard flat scatterer can be broken up by protruberances which are comparatively small, whilst the diffraction pattern behind the scatterer is unchanged. These results appear to be further proof that the shadow zone behaviour in the regime investigated is largely an 'edge effect'. Scattering by rough surfaces and multiple scattering configurations are considered from a theoretical point of view in the next chapter.

It must be stressed that the discussion of this section is only for 1/3 octave measurements in the ka range 4.76 to 23.84, where k is based on the centre frequency of the band, and a is the typical object dimension in the plane of the microphone traverse, and for r/a values of about 2.55. The effect of variation of the r/a parameter is discussed in section 3.3.7.

3.3.6 The effect of variation of angle of incidence

The variation of the angular distribution of sound pressure level around the square plate as the angle of incidence goes from 0^{O} (where sound arrives normal to the flat surface) to 90^{O} (where sound arrives at grazing incidence) is shown in Figure 3.11 in 15^{O} steps. In the bright region the area of pressure reinforcement moves through twice the angle through which the plate has been turned. Thus on the plot for 15^{O} angle of incidence, there is a net pressure increase over an arc centred around 30^{O} on the resultant plot. The area over which this increase occurs diminishes with increased angle of incidence, although the magnitude of the reinforcement at the centre of this pressure increase actually appears to increase with angle. This behaviour is only readily

discernible up to an angle of incidence of 45°; beyond this point the fluctuations attributable to the front surface seem to interfere with those associated with the 'shadow' region.

In the shadow region, as the angle of incidence is increased, the magnitude of the Poisson spot decreases and the interference pattern becomes asymmetric. These changes can be explained by the increase in the range of distances travelled by the 'secondary wavelets' in going from the plate's perimeter to the centre of the shadow region as the angle of incidence is increased. This is in general agreement with the discussion of Fresnel diffraction in the previous section. It should be noted that as the angle of incidence increases, the average depth of shadow decreases, whilst the angle to either side of 180° over which significant level fluctuations extend increases. It is also interesting to observe how large the fluctuations around the 'shadow zone' are for an angle of incidence of 90°, especially when it is considered the plate is only 0.0095 m thick. It must be stressed of course that the only frequency band investigated was the 20 kHz 1/3 octave, and this discussion is based solely on such experiments.

3.3.7 The effect of receiver traverse location variation:

The 6.3 kHz and 8 kHz 1/3 octave band results for the case of the square plate with microphone traverse radii of 0.0945 m and 0.1145 m are shown in Figures 3.12(a) and 3.12(b) respectively, for a height of traverse equal to that of the scatterer's centroid. Also shown in Figure 3.12(c) are similar results for the small traverse radius when its height is midway between the centre and top of the plate. These results should be compared with those of Figure 3.10(b) for the square plate, which were performed under similar conditions to those of Figures 3.12(a) and (b), except the microphone traverse radius is 0.1645 m in this case.

Comparison of Figures 3.12(a), 3.12(b) and 3.10(b) shows that there is a general increase in the magnitude of the sound pressure level difference between results with and without the scatterer, as the traverse radius is decreased. Distinct maxima and minima also become apparent to either side of the region of pressure reinforcement. In some cases

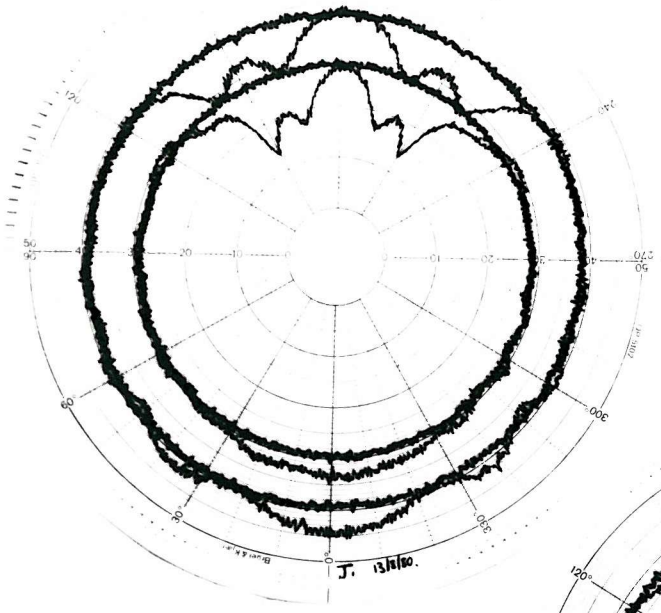

3.12(a)

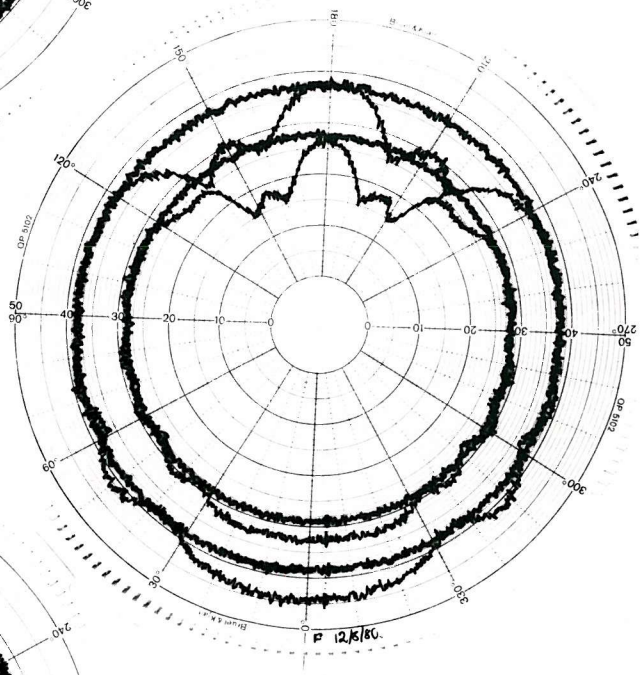

3.12(b)

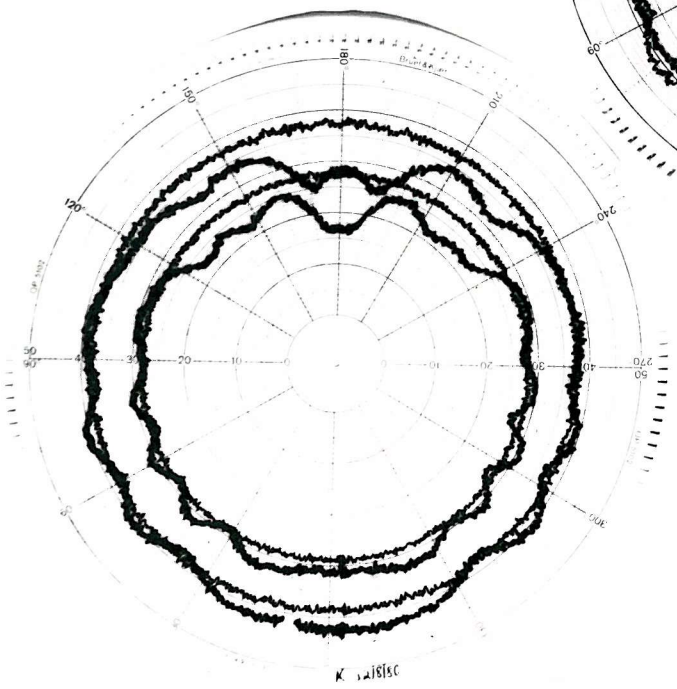

3.12(c)

Figure 3.12. Square plate : The effect of microphone traverse location on the 6.3 kHz (outer trace) and 8 kHz (inner trace) 1/3 octave sound pressure level results.

(a) Microphone traverse radius = 0.1145 m (r/a = 1.775)

(b) Microphone traverse radius = 0.0945 m (r/a = 1.465).

(c) As for Figure 3.10(b) but microphone traverse in the horizontal plane midway between the centre and top of the scatterer.

this 'ripple' seems to extend into the normal area of level increase. This can lead to a reduction in the pressure increase on axis (i.e. 0^{o}) as the traverse radius is decreased. This effect becomes more appreciable at the higher frequencies investigated. This decrease was less apparent in the results for the sphere but was broadly similar for disc and square plate results. This behaviour therefore appears to be a real feature of the measurements, specific to the bright region of flat-faced scatterers for small r/a values. Since it has been noted that the level in front of most of the scatterers under the conditions investigated is governed by reflection phenomena, it is plausible that the level variation observed in the bright region at small r/a values is due to the existence of pronounced interference effects even after 1/3 octave averaging. A theoretical approach to the problem of reflection of 1/3 octave bandlimited white noise from an infinite surface is developed in Appendix D . Some results of such computations for the source-receiver geometries used are shown in Figure 3.12(d), compared to the relevant experimental measurements. It will be seen that the trends observed are in general adequately predicted by the model, although the absolute levels predicted are sometimes somewhat different to those measured experimentally. However, when the inaccuracies of the model as a representation of the physical situation are considered (see Appendix D), it appears that a simple reflection model does indicate the frequency of the SPL fluctuations and the magnitude of variations likely. Thus the level in front of the flat scatterers can be seen to remain dominated by reflection phenomena even at the smaller r/a values. However due to the finite bandwidth signal used, under these conditions interference may be observed, and energy addition calculations will not be sufficient to estimate the effects observed.

In the shadow region the effect of decreasing the microphone traverse radius is to decrease the SPL in the first minimum adjacent to the Poisson spot, but apparently to leave the Poisson spot essentially unaltered, although slightly broader in angle. Over the major part of the frequency range investigated, the behaviour in the shadow region was broady similar to previous tests. At the higher frequencies employed however, the square plate's shadow behaviour was different to that for the sphere and disc. In the square plate's case the diffraction pattern was considerably altered in the vicinity of the Poisson spot, whereas for the other two objects the pattern remained similar but further

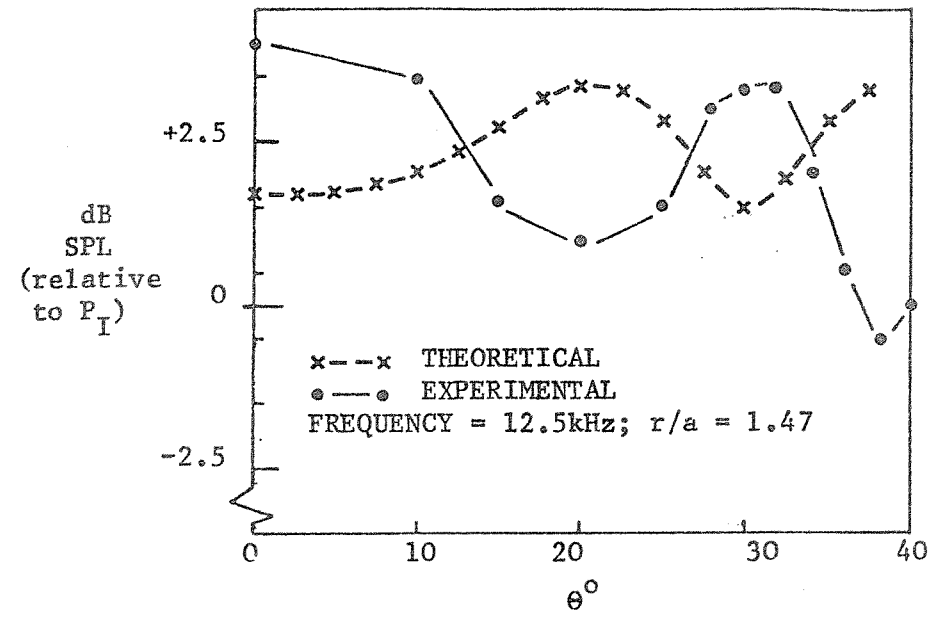

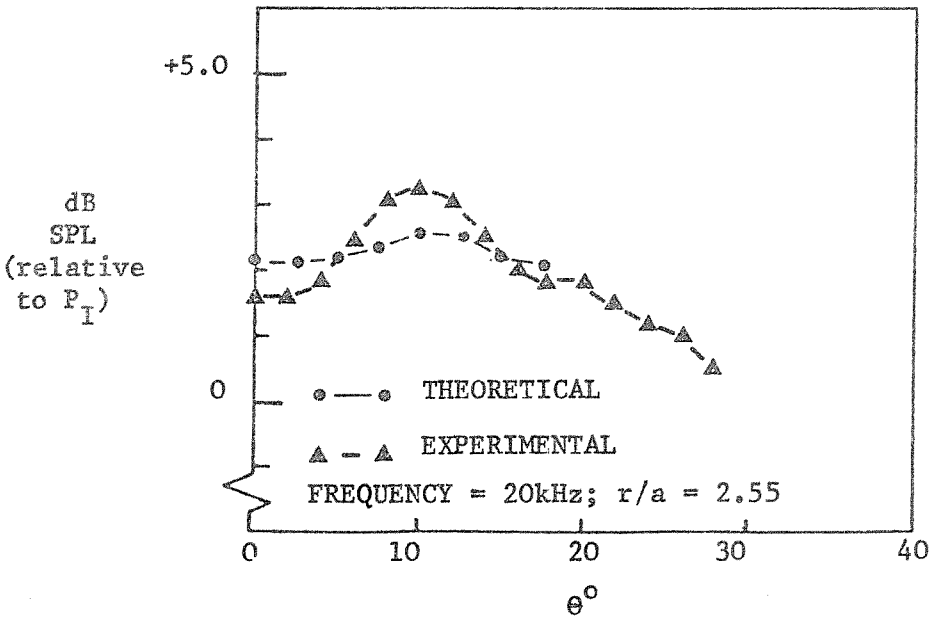

Figure 3.12(d) Comparison of experimentally measured 1/3 octave band SPL in the bright region in front of the disc with those predicted by the reflection model of Appendix D.

regular minima and maxima became visible towards the edge of the shadow zone. It is assumed that this difference in the two types of behaviour observed is due to the fact that the range of distances travelled by the diffracting wavelets from the scatterer's edge to any receiver point (other than on axis for the sphere and disc) increases with decreased traverse radius. In the case of the square plate, the distances travelled by all the wavelets are not equal even on axis. Thus further increases in the range of these distances will obviously alter the pattern seen and this will be accentuated at higher frequencies, where the range of phases with which the diffracting waves arrive will be greatest. It should be noted that any directional effects of the microphone will be greatest at high frequencies. Thus, since more of the square plate's diffracting edge subtends a larger angle at the microphone diaphragm than do those of the sphere and disc, the square plate's diffraction pattern may be assumed more prone to error.

The other obvious effect of decreasing the traverse radius is to increase the angular width of the shadow zone. The angle at which the total pressure equals that incident is still greater than that predicted by geometrical acoustics.

The effect of alteration of the traverse height is to reduce the level at 180° even in some cases to the extent of removing the central Poisson spot completely. It is proposed that this is again due to the pathlength (and hence phase) differences of all the waves diffracted from the edge into the shadow zone region. Use of octave bandlimited white noise under conditions where the microphone traverse height was mid-way between the scatterer's centre and top resulted in a 'smooth' behaviour in the shadow zone. The maximum shadow depth under these circumstances in the 8 kHz octave was however only 7 dB, for a microphone traverse radius of 0.0945 m.

3.3.8 Discussion of further experiments possible:

Obviously the range of further experiments possible is only limited by the number of different objects that it is desired to investigate. However, all of the major classes of simple, acoustically hard, finite sized scattering objects were studied in this reseach programme.

This range included solid and planar objects; those with similar characteristic dimensions and those with different ones;scatterers with flat or curved surfaces; and objects with a 'rough' surface. These studies were performed over a range of angles of sound incidence. It would also be possible to extend the ranges of ka or r/a used, but this would necessitate new transducers and/or a different rig. It should also be noted that for low ka values there is less evidence of scattering, whilst at high ka observable trends were developing in the cases investigated. To work at higher ka values, either larger objects or higher frequencies can be used: The former alternative would require the construction of a new experimental rig, since this would result in the microphone passing closer to the framework of the current rig, with subsequent decreased accuracy. The option of increasing the frequency would require the development of a new source and microphone. The microphone would have to be much smaller (less than 1/8 inch diameter), and at least as sensitive as that used in this research programme, unless a new more powerful source were to be employed. Such a microphone would also ideally be used for any measurements performed at small r/a values in order to minimise diffraction effects under these conditions. The use of such a microphone might have also increased the measurement accuracy of some of the configurations examined in this research programme. However there did not appear to be such units readily commercially available, and the current research objectives did not warrant the time-consuming development of such a transducer.

Thus, although other experiments are undoubtedly possible, since the aims of this research programme were essentially to investigate the scattering behaviour of simple objects under situations typical of those found in room acoustics, the range and accuracy of the experiments performed is thought adequate to compare and contrast these behaviours. The results obtained permit the major trends displayed to be noted, and their implications for practical room acoustics to be discussed. More detailed conclusions would require further experiments which,as outlined above, would almost inevitably necessitate the use of different equipment, both to permit extension of the range of variables covered, and to increase the experimental accuracy.

3.4 Conclusions:

This chapter has presented the results of a series of measurements of the overall sound pressure level around a selection of scattering bodies. Although a large literature on acoustical scattering exists, there are a number of reasons why this programme of tests was necessary. For example, the majority of the tests in this chapter are for the total SPL level in a 1/3 octave band; this is undoubtedly more useful for practical purposes than the normal single frequency results, which are often also presented solely in terms of the scattered component. Furthermore, the measurements reported here are concentrated in the region where the wavelength is the same order of magnitude in size as the object's typical dimension, and the receiver positions are at distances from the scatterer comparable to its size. The tests also cover a carefully chosen range of objects: This allows both similarities and differences to be observed in the diffraction pattern, which in turn permits both generalised statements to be made about the scattering behaviour in the regime investigated, and for the parameters and physical processes which govern the effects seen to be deduced. Since there did not appear to be any published reports which cover all these points under similar conditions, the results of this series of tests are highly instructive. Their degree of accuracy is indicated by the agreement of the theoretical and experimental results for the case of single frequency scattering by a rigid sphere.

The main conclusions derived from the experimental programme are in the two sections below:

i) Shadow zone behaviour

The shadow zone behaviour is largely determined by the silhouette of the scatterer as 'seen' by the incident waveform. The position of the scatterer's perimeter in space affects the degree of detail seen in the shadow zone, and this detail was little changed by the use of 1/3 octave bandlimited white noise as opposed to single frequency sound. The effects observed in the shadow for this 1/3 octave noise were not sensitive to changes from sharp to curved edges (cf. sphere and disc results). Where objects possessed dimensions of comparable length in orthogonal directions normal to the incident wavefront a bright spot

(or 'Poisson spot') existed in the centre of the shadow region. This had comparable magnitude to the incident SPL in some cases, even after 1/3 octave averaging. For objects with a larger range of distances from the scatterer's perimeter to the central shadow zone region (e.g., rectangular plates, or plane objects at large angles to the incident wavefront) the shadow behaviour is much less regular. All of the above features of the shadow region can be qualitatively explained by the presence of diffracting wavelets from the scatterer's edge (after Huygens). However, it is probably of greater practical significance that for less regular objects, or greater bandwidth averaging, there will be little shadow detail. Under these conditions the shadow depth appears to be determined by the smallest 'ka' of the object in question. For these cases, over the ka and r/a ranges investigated, the depth of shadow is comparatively small. Since these ranges were specifically chosen to be broadly representative of room acoustics configurations, the importance of this fact is that it implies there will be little evidence of a shadow once a few reflecting surfaces are placed in the object's vicinity. Thus other than for extreme near field or large ka values, any shadow zone due to the presence of scatterers in rooms will be extremely small, or localised, when only a few scatterers are present in a large room. For these reasons multiple scattering is considered in the next chapter, so that the combined effects of large numbers of scatterers can be investigated.

ii) The bright region behaviour:

The general magnitude of the pressure increase observed in the bright region to the front of the scatterers is not large (normally a maximum of 6 dB near the scatterer's surface), although it should be noted that only convex or plane objects were used. The features observed in this region are governed by the object's front surface contour, from which it can be surmised that reflection phenomena govern the bright zone behaviour. This is borne out by the change that results from 1/3 octave averaging, when a large amount of the bright region's variability is removed. For small r/a values however, interference effects are visible even when 1/3 octave bandlimited white noise is used. The coherence of these reflections can be much reduced by the introduction of surface roughness, especially when the size of this roughness is greater than the wavelength in use. It can

therefore be surmised that, apart from cases where the scatterer has a plane surface which is much larger in size than the typical wavelength, and/or the receiver is in its immediate vicinity, the practical effects of a single scatterer on the levels in a large room will be minimal. Little can be inferred from the experimental results concerning the behaviour of configurations of scatterers where multiple scattering may occur. It is these situations which are most likely to have a pronounced effect on the overall acoustical behaviour of a large room, and for this reason, methods of predicting the behaviour of such groups of scatterers are studied in the next chapter. The experimental results of this chapter however will still be useful in estimation of any single body order of magnitude scattering effects.

CHAPTER 3 : REFERENCES

3.1 L.J. SIVIAN and H.T. O'NEIL, 1932 J. Acoust. Soc. Amer. 3,483-510. On sound diffraction caused by a rigid circular plate, square plate and semi-infinite screen.

3.2 G.G. MULLER, R. BLACK and T.E. DAVIS, 1938 J. Acoust. Soc. Amer. 10, 3-13. The diffraction produced by cylindrical and cubical obstacles, and circular and square plates.

3.3 F.M. WIENER, 1947 J. Acoust. Soc. Amer. 19, 444-451. Sound diffraction by rigid spheres and circular cyclinders.

3.4 F.M. WIENER, 1948 J. Acoust. Soc. Amer. 20, 367-369. Notes on sound diffraction by rigid circular cones.

3.5 F.M. WIENER, 1949 J. Acoust. Soc. Amer. 21, 334-347. Diffraction of sound by rigid discs and rigid square plates.

3.6 H. PRIMAKOFF, M.J. KLEIN, J.B. KELLER and E.L. CARTENSTEIN, 1947 J. Acoust. Soc. Amer. 19, 132-142. Diffraction of sound around a circular disc.

3.7 J.J. FARAN, 1951 J. Acoust. Soc. Amer. 23, 405-418. Sound scattering by solid cylinders and spheres.

3.8 G.R. BARNARD and C.M. McKINNEY,1961 J. Acoust. Soc. Amer. 33, 226-238. Scattering of acoustic energy by solid and air-filled cylinders in water.

3.9 L.D. HAMPTON and C.M. McKINNEY, 1961 J. Acoust. Soc. Amer. 33, 664-673. Experimental study of the scattering of acoustic energy from solid metal spheres in water.

3.10 M.L. HARBOLD and B.N. STEINBERG, 1969 J. Acoust. Soc. Amer. 45, 592-603, Direct experimental verification of creeping waves.

3.11 J.W.M. BAARS, 1964 Acustica 14, 289-296. On the diffraction of sound waves by a circular disc.

3.12 T. TERAI, 1980 J. Sound Vib. 69, 71-100. On calculation of sound fields around three-dimensional objects by an integral equation method.

3.13 T. KAWAI, K. FUJIMOTO and T. ITOW, 1977 Acustica 38, 313-323. Noise propagation around a thin half-plane.

3.14 T. KAWAI, 1981 J. Sound Vib. 79, 229-242. Sound diffraction by a many-sided barrier or pillar.

3.15 P. JACKSON, 1970 M.Sc. Thesis, Southampton. The design, construction and calibration of free-field rooms.

3.16 M. CARLSON and J.T. HUNT, 1974 J. Acoust. Soc. Amer. 55, 964-967. Effect of geometrical symmetry on acoustic scattering into the shadow region.

3.17 P.M. MORSE and H. FESHBACH, 1953 Methods of Theoretical Physics. New York : McGraw-Hill Book Company Inc. (see Part II, p.1551-1553).

3.18 F.A. JENKINS and H.S. WHITE, 1976 Fundamentals of Optics. Tokyo : McGraw-Hill Kogakusha Ltd.

APPENDIX D

THE REFLECTION OF BANDLIMITED WHITE NOISE FROM AN INFINITE HARD PLANE

For the geometry of Figure D1, the total mean square pressure at the receiver point, P , may be written as:

$$\overline{p^2} = \frac{1}{T}\int_{-T/2}^{T/2} (P_I+P_R)^2 \, dt \ , \qquad (D1)$$

where P_I is the incident pressure field, and P_R its reflection in the hard plane. This is equivalent to the square of the sum of the contributions due to the real source S , and its image, S' , in the reflecting surface. Under certain conditions expression (D1) approximates to $(P_I^2+P_R^2)$ and it is sufficient to merely sum the energy contributions of the real and imaginary sources at the receiver. The occasions when this approximation is adequate are determined by the bandwidth of the noise source and the geometry of the source, wall and reciever configuration. In all other cases the $2P_IP_R$ cross-term must be considered. This is an interference term and may be either positive or negative.

If equation (D1) is rewritten in terms of the time histories of the real source and its image, it becomes

$$\overline{p^2} = \frac{1}{T}\int_{-T/2}^{T/2}\left\{\left(\frac{A(t)}{r_1}\right)^2 + \left(\frac{A(t-\tau)}{r_2}\right)^2 + \frac{2}{r_1r_2}\cdot A(t)\,A(t-\tau)\right\} dt \ , \qquad (D2)$$

where τ equals $(r_2-r_1)/c$ and A(t) is the source strength at time t , which is at a time r_1/c before the time it arrives at the receiver. The first two terms of equation (D2) are energy addition terms, whilst the last term is the interference term which can be seen to have the form of an autocorrelation function,

$$R(\tau) = \underset{T\to\infty}{\text{Lim}}\ \frac{1}{T}\int_{-T/2}^{T/2} A(t)\ A(t-\tau)\ dt \ .$$

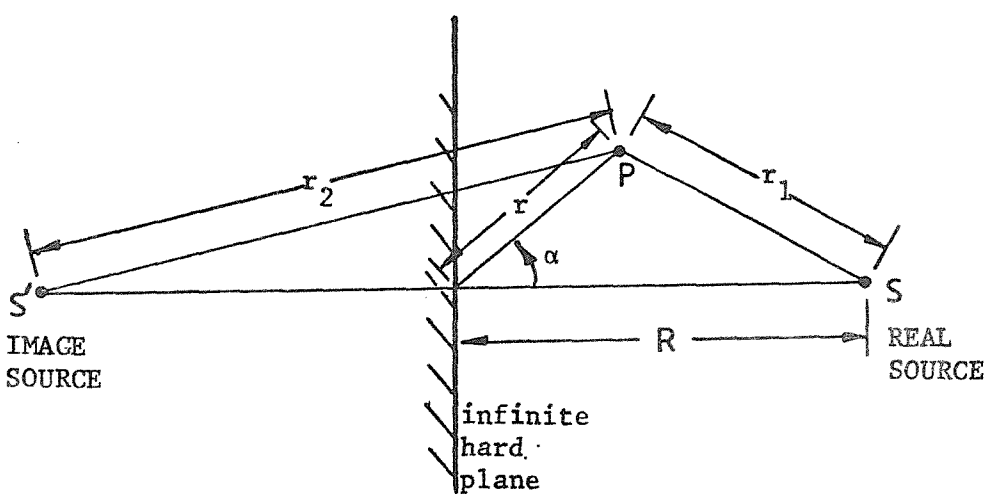

Figure D1 The geometry considered in the bandlimited noise reflection model of Appendix D.

It is the strength of this term which decides whether energy addition calculations are adequate. For a bandlimited white noise source $R(\tau)$ can be written (see Reference [D1])

$$R(\tau) = A^2 \cos(\omega_c \tau)\ \sin(b_w \tau/2)/(b_w \tau) \qquad (D3)$$

where ω_c and b_w are the centre frequency and bandwidth of the noise signal (in rad/s) respectively. It is thus clear that the magnitude of the interference term is controlled by the $1/(b_w \tau)$ term. Increasing either the signal bandwidth or the time lag between the arrival of the real and imaginary sources contributions therefore reduces the level of interference observed.

For the geometry of Figure D1 the time delay τ can be shown to approximate to $2r\cos\alpha/c$ for $R>>r$. For 1/3 octave bandlimited white noise the signal bandwidth is 23% of the centre frequency. Thus for a 1/3 octave bandlimited white noise source under the geometry of Figure D1, the interference term (equation (D3)) may be rewritten as

$$R(\tau) = A^2\ \cos(2kr\ \cos\alpha)\ \sin(0.23\ kr\cos\alpha)/(0.46\ kr\cos\alpha)\ , \qquad (D4)$$

from which it can be seen that this interference term is the product of two fluctuating components which possess different cycle periods. The cosine term has a characteristic frequency of 8.7 times that for the sine term for variations in τ.

If the likely reflections from the plane-fronted scatterers used in the experimental programme are considered, it would seem that under some conditions (i.e., small kr, large ka) the objects may appear 'infinite'. Under these circumstances a certain degree of SPL fluctation may be observed in the bright region. Over the arc of the microphone traverse where a reflection model might work, the frequency of these fluctations will be governed by the $\cos(2kr\cos\alpha)$ term of equation (D4). The overall level of the SPL deviations from those predicted by energy addition will be governed by the $\sin(0.23\ kr\cos\alpha)/(0.46\ kr\ \cos\alpha)$ term, since this varies much more slowly over the traverse arc where a reflection model might be expected to work (i.e. small α).

Calculations have been performed for some of the experimental geometries, and the results are shown in Figure 3.12(d). The mean square levels due to the real and imaginary source terms are assumed to be constant over the arc for which the calculations' results are shown. Their values were obtained from the experimental incident field's SPL values in the region of 0° and 180°. The cross-product magnitude was similarly estimated. This approximation will obviously introduce a degree of inaccuracy into the results, but they should still indicate whether the reflection model produces the correct behaviour. At the higher frequencies used, the agreement between the theoretical and experimental values can be expected to be poor, although the magnitude and general behaviour of the trends should be reproduced. This is because the finite size of the microphone causes a degree of spatial averaging to occur. This fact becomes evident when it is appreciated that the change in r required for the phase of the $\cos(2kr\cos\alpha)$ term to change by 360° at 20 kHz for points on axis (i.e. 0°) is 0.0085 m (in which distance the sine component changes by only 40°). Thus the microphone's output is very hard to predict for a specific r value, especially since the level would appear to be very sensitive to any errors made in mis-setting the radius of the traverse arc. However, although the change of SPL with r may be rapid on axis, the variation with angle is much slower for small α : For 20 kHz and $r = 0.0945$ m, it can be seen that α must go from 0° to 25° for a complete cycle of the cosine term, and this equates to a microphone travel of about 0.04m Thus although the microphone will present a spatially averaged value, it should 'track' the variations of SPL with angle in the bright region. This means that poor agreement may exist between the theoretical and experimental magnitudes, but the variation in angle should be reproduced (e.g. the angular spacings of maxima and minima).

When all the above factors are considered, it appears that the reflection model does reproduce the observed experimental trends adequately well. This indicates that the main acoustical feature of the bright zone is one of reflection. However, for small r/a and large ka values interference effects exist, even with bandlimited noise signals. The only way to be able to predict these effects would be to use a much smaller (but hence generally less sensitive) microphone.

APPENDIX D : REFERENCES

D.1 D.E. NEWLAND, 1975 An Introduction to Random Vibration and Spectral Analysis, London : Longman. See Chapter 5.

CHAPTER 4

THE APPLICABILITY OF VARIOUS SCATTERING MODELS TO ACOUSTICAL PREDICTIONS IN ENCLOSED SPACES

4.1 Examination of the Analytic Models Available:

4.1.1 Introduction:

Single body free field acoustical scattering has already been covered from theoretical and experimental viewpoints in Chapters 2 and 3 respectively. This chapter is a description and assessment of the various analytic methods currently available for the evaluation of scattering effects when more than one scatterer is present. This includes, in particular, the case of one (or more) scatterer(s) in the presence of highly acoustically reflective surfaces, which will indicate how the effects due to individual scatterers seen in Chapters 2 and 3, are altered in ensemble situations or when placed in rooms.

There appear to be three basic ways of formulating the scattering problems discussed above. The first is to postulate the form for the acoustic field incident upon the scatterer when it is in a room in terms of a superposition of plane waves. The use of the free field formulation of the object's scattering behaviour in response to an individual plane wave then permits its behaviour in the assumed acoustical environment to be built up. The second method of modelling the scatterers is as a distribution throughout space. This will be termed 'volume scattering', and is primarily used in situations where the objects are distributed throughout the enclosed volume, and the walls are highly reflective. The last model is to represent the scatterers as perturbations of a flat surface. This will be termed 'rough surface scattering', and is particularly applicable to the many cases where the objects in a room are situated on the floor, and their height is only a relatively small fraction of the total room height. For all of these three types of model both exact and approximate formulations of the problems will be considered.

Prior to explicit consideration of these three models in the following sections, two general points about these more complicated scattering situations will be considered. The first is the possibility of 'imaging' scatterers, which is a basic feature of many of the models to be discussed. For a scatterer above an acoustically hard reflecting surface, illuminated by an incident field ψ_i , as shown in Figure 4.1(a), the boundary condition at the plane's surface $(x = 0)$ is zero normal velocity. This condition can be met by the system shown in Figure 4.1(b), where the hard plane has been removed and been replaced by an image incident field, ψ_i' , and scatterer. This produces the correct total field which satisfies the wave equation and boundary conditions for $x \geq 0$. This technique can obviously be extended to model the presence of scatterers in rooms with perfectly reflecting walls. In such cases, a lattice of image cells, each of which contains image source(s) and scatterer(s), will be created. Where the walls do not reflect perfectly, the model will not be exact, its error increasing with wall absorptivity until for highly absorbent surfaces it is better to remove all the images due to that particular surface.

The other point worthy of consideration at this stage is that of multiple scattering. This is a feature of real situations where the field incident upon a given scatterer is the sum of the direct field from the source and that scattered by all the other objects. This latter component will in turn be affected by the field scattered by the body originally under consideration; thus a recursion relationship is built up in terms of orders of scattering. In many approximate models this pehnomenon is not considered,and instead a single scattering approximation is adopted (i.e. the field scattered by an object is just that due to the directly incident field). Whilst this assumption may prove perfectly adequate under some circumstances, there may well be occasions where an observed physical phenomenon is not represented by this simple model.

Further consideration will be given to both the above topics at appropriate stages in the next three sections.

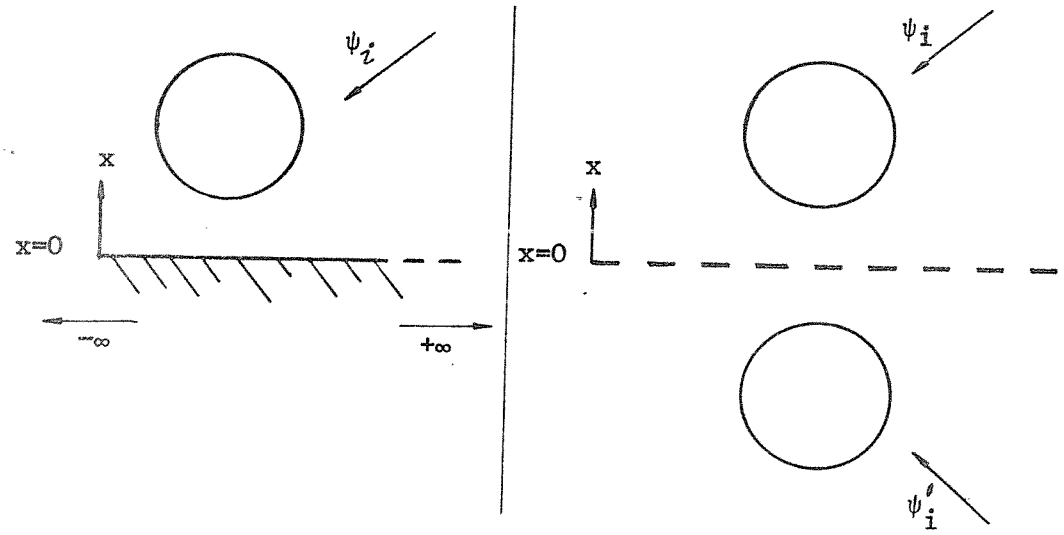

Figure 4.1(a)

Figure 4.1(b)

Figure 4.1 The Geometry Applicable to Considerations Concerning the Imaging of Scatterers.

4.1.2 Diffuse field scattering:

The models covered in this section are generally applicable to a room acoustics situation in which the field at any point where the scatterer is to be situated in the room can be specified in terms of component plane waves. For cases where this is possible, the method essentially consists of the superposition of the field scattered by the object in response to each component wave, in order to evaluate the total field at some desired point. Such calculations are generally feasible for diffuse field conditions. In such situations, the field can be considered to be composed of equal intensity plane waves, which arrive from all directions with a random phase relationship to each other. This is the only case widely treated in the published literature (see for example References [4.1, 4.2, 4.3, 4.4]). Before specific consideration of these papers, it should be noted that there is a further assumption inherent in this method: namely, that the presence of the scattering object does not alter the field at the point in question. This implies a restriction to small objects, placed well away from the boundaries of the reverberant room under study.

Cook and Chrzanowski [4.1] and [4.2], were apparently the first to consider this type of approach. They used exact formulations of the scattering behaviour of cylinders [4.1] and spheres [4.2], with a uniform normal impedance boundary, to estimate their diffuse field absorption coefficients. They were thus able to take into account diffraction effects, and the fact that sound would be incident over a solid angle of 4π rather than 2π, as would be the case for absorbent placed on a wall surface.

Waterhouse [4.3] studied diffraction effects for points on and off the surface of various objects under diffuse field conditions. He presented results in terms of total sound pressure level based on exact solutions for diffraction by rigid spheres and cylinders, and also for a point at the tip of a rigid wedge as a function of wedge angle. It is interesting to note that his results for the case of a rigid sphere at $ka = 3$, indicate that the level around the object is within $\pm$ 1 dB of the asymptotic limit for the region beyond $\lambda/6$ away from the surface. This suggests that diffraction effects due to a single body in a statistically diffuse field at low ka are of a very localised nature, as was hypothesised from the results of Chapters 2 and 3.

Baars [4.4] proposed the concept of a'random scattering cross-section'to characterise the ability of a body to scatter sound under statistically diffuse sound field conditions. He defined this quantity as the amount of power scattered by an obstacle, divided by that striking it when incident plane waves are equally distributed over all angles of incidence. Baars evaluated this parameter for the case of a rigid circular disc, by use of a Kirchhoff approximation. and numerical integration techniques. His results suggest that below a ka value of 2 the scattering effect of the disc was minimal under such conditions.

The methods described in this section can be seen to be limited by practical considerations to the investigation of scattering or absorption effects under statistically diffuse conditions. Under such circumstances it is however often possible to use the exact formulations of single body free field scattering, subject to the assumption that the presence of the scatterer does not significantly alter the structure of the incident acoustic field (i.e., there is no explicit consideration of multiple scattering). Thus although it would be possible to incorporate the results of Chapter 2 in this type of model, it is of little direct practical use for the study of 'non-Sabine' spaces.

4.1.3 Volume scattering

In this section, the problem of predicting volume scattering effects is discussed : this covers situations where the scatterers are distributed right across the vertical cross-section of a room, or where the height of a scatterer situated on the floor is comparable to the room height. Initially a generalised, but exact, formulation will be given, various approximate methods will then be considered and their regions of applicability studied. The formulation of the general problem used here, owes much to Twersky [4.5].

For any combination of N scatterers, with an incident field ψ_i , the wave that would be scattered by an object S on its own will be written ${}^{S}\psi^{1}$, (where the superscript letter indicates the particular object under consideration and the number, the 'order' of the scattering

process) such that $\psi_i + {}^{S}\psi^1 = \Psi^1$. Here Ψ^1 is a solution of the wave equation, which satisfies the boundary conditions at the surface of S and which has a scattered component which fulfils the required radiation condition at infinity. Thus a single scattering approximation for the total field , Ψ , can be written as

$$\Psi = \psi_i + \sum_{S=0}^{N} {}^{S}\psi^1 \quad .$$

Next, in response to all the first order scattered fields due to the other objects (which will be written $\Sigma'_{S'} {}^{S'}\psi^1$, where the dashes indicate that the summation is over all the objects apart from S itself), the scatterer S will produce a second order scattered field ${}^{S}\psi^2$, such that

$$\psi^2 = \Sigma'_{S'} {}^{S'}\psi^1 + {}^{S}\psi^1 \quad .$$

This again satisfies the wave equation and the relevant radiation and boundary conditions in the coordinate frame of scatterer S . Extrapolation of this process to any order of scattering allows the total field, Ψ, at any point due to the presence of all N scatterers to be written as

$$\Psi = \psi_i + \sum_{S=0}^{N} \sum_{m=1}^{\infty} {}^{S}\psi^m \quad . \qquad (4.1)$$

At the surface of any particular object the field is simply $\sum_{m=1}^{\infty} \psi^m$. Now, since all the individual $\psi^m (m=1,2,\ldots\infty)$ satisfy the required boundary and radiation conditions, so will their sum. Equation (4.1) therefore represents an exact solution to any multiple scattering problem. However for practical purposes, some simplifying assumptions would appear necessary, since for any hard-walled room acoustics situation there will be an infinite number of both sources and scatterers. The use of exact scattering solutions for the evaluation of such problems would therefore appear to necessitate the treatment of some simplified arrangement. The complexity of an exact solution can be seen from inspection of the problem of scattering from a

distribution of parallel cylinders with a plane wave incident (as considered in Reference [4.5]). In such a case, the form of the m^{th}-order wave scattered by object S can be assumed to be:

$$ {}^{S}\psi^{m} = \sum_{n=-\infty}^{\infty} {}^{S}A_{n}^{m} \, H_{n}^{(2)}(kr_{s}) e^{in\theta_{S}} \quad , $$

where $H_{n}^{(2)}$ is an n^{th} order Hankel function of the second kind (to satisfy the radiation condition with an implicit time factor $e^{i\omega t}$), r_S is the cylinder's radius, and θ_S the angle of observation in the cylinder's coordinate frame. The ${}^{S}A_{n}^{m}$ coefficients must be determined from application of the boundary conditions. Thus ${}^{S}A_{n}^{1}$ is obtained for a rigid boundary condition from the expression, $\partial/\partial n(\psi_i + {}^{S}\psi^{1})\Big|_{r_S=a_S} = 0$, and hence the general form of ${}^{S}A_{n}^{p}$ from $\partial/\partial n(\Sigma'_{S'} {}^{S'}\psi^{(p-1)} + {}^{S}\psi^{p})\Big|_{r_s=a_s} = 0$. However to evaluate the field at any point still in theory involves three nested summations, two of them infinite.

It can be seen therefore that a single scattering approximation is very appealing since it brings the evaluation of such problems within easy reach. The validity of such an approximation can be determined from the ratio $|{}^{S}\psi^{2}/{}^{S}\psi^{1}|$, since it can be shown (see Reference [4.5]), that if $|{}^{S}\psi^{2}| << |{}^{S}\psi^{1}|$, then $|{}^{S}\psi^{3}| << |{}^{S}\psi^{2}|$ etc., Physically, the single scattering assumption implies that the objects are so far apart that their excitation can be considered as due to the incident field alone, and/or the field scattered by each body has no coherence with that scattered by the other scatterers. Under such circumstances the scattered energy is directly proportional to the density of the distribution of the scatterers. The adoption of a single scattering model is often termed the Born approximation. If small ka values are considered the Rayleigh approximation may be used (where only the first terms in a series expansion of any exact solution are required). This much simplified case is treated in some text books (see for example Reference [4.6]), but is more suited as a model for the scattering of sound by suspensions of particles in air, such as water droplets in a fog.

Other possible methods to reduce the complexity of the problem involve consideration of either random or regularly spaced arrays of identical objects. These cases have been studied by Twersky [4.7,4.8], and results of typical calculations have been presented by Embleton [4.9] for a random array of cylinders as a function of surface impedance.

As an alternative to the often unmanageable exact wave equation based methods, it is possible to use a statistically based approach in which one utilises the concepts of random walk theory. In this model a source is assumed to emit sound particles, or 'phonons'. These set off in random directions in a propagation medium which contains some (assumed statistically known) distribution of scatterers. Upon collision with a scatterer, the phonon may go off in any direction. The probability of any particular direction is determined by a probability function which characterises the scatterer's behaviour. In order to evaluate the probability that a phonon has arrived at a particular point, $\underline{R}$, after k scatterings at a certain time, t, the probility that the phonon has reached a point $\underline{R}$ after k scatterings, $(P_k(\underline{R}))$, must be multiplied by the probability that the phonon will have undergone k scatterings in the time t, $(P_k(t))$. The total energy at a point $\underline{R}$ at a time t due to an impulse at $t = 0$ can then be found from summing this probability product over an infinite number of collisions. This gives,

$$E(\underline{R},t) = \sum_{k=0}^{\infty} P_k(\underline{R}) P_k(t) dV \ , \qquad (4.3)$$

The form of $P_k(\underline{R})$ has been discussed by Chandrasekhar [4.10] for the generalised problem of random flights. This was applied to the case of reverberation in media containing randomly-distributed scattering objects by Kuttruff [4.11], who assumed that the scatterers are independent of one another and that the same mean free pathlength distribution $\omega(r)$ holds throughout the medium. This allows the probability that a phonon has reached $\underline{R}$ after k scattering processes to be written as

$$P_k(\underline{R}) = \tfrac{1}{8}\pi^3 \int e^{i\underline{R}.\underline{S}} |P(\underline{S})|^K d\underline{S} \quad , \tag{4.4}$$

where $P(\underline{S})$ is the Fourier-transform of $\omega(\underline{r})$. The scatterers are then assumed to scatter equally in all directions (isotropically), with a scattering cross-section Q, which is generally taken as being equal to the object's cross-sectional area as 'seen' by a phonon. The further assumption that the mean free path, r, follows an exponential distribution (obtained from the postulate that there is an equal chance of meeting a scatterer at any point on a phonon's path) allows the respective forms of the probability of k scatterings in a time t, and the mean-free pathlength distribution, to be written as

$$P_t(k) = e^{-\nu t}(\nu t)^k/k! \quad , \tag{4.5}$$

and

$$\omega(\underline{r})d\underline{r} = (nQ/4\pi r^2)e^{-nQr}d\underline{r} \quad , \tag{4.6}$$

where n is the density of the scatterers' distribution, and ν is the mean scattering 'frequency' (nQ). Evaluation of $\omega(\underline{r})$ in equation (4.6) and subsequent substitution into equation (4.4) permits equations (4.4) and (4.5) to be combined in the form of equation (4.3). In the limit of $nQct >> 1$ (i.e., the total time elapsed is much greater than the time between individual scatterings), the resultant integral can be solved to give

$$E(\underline{R},t) \simeq (3nQ/4\pi ct)^{3/2} e^{-(3nQ/4ct)R^2} \quad . \tag{4.7}$$

Kuttruff observed that this is the solution to a form of the diffusion equation in three-dimensions. Kuttruff [4.11] used this approach to study reverberation behaviour in woods, and reverberation chambers with diffusing elements. In a subsequent paper [4.12], he used a diffusion theory-based approach to study the effect of scatterer density in a reverberation chamber with one highly absorbent wall. In these same papers, Kuttruff also used computer-based 'Monte-Carlo' methods to study these Poisson-distributions of isotropic scatterers in rooms. He obtained good agreement between the two methods.

Jovicic [4.13] employed the form of equation (4.7) to evaluate the far field steady state scattered level for a source between two parallel planes, by integration over all possible times of arrival for phonons which have had more than one collision. In order to estimate the total energy at a point, he performed a similar analysis for the arrival of the unscattered sound energy which he then added to the scattered components. He found that adding scatterers increases sound pressure levels close to a source, and reduces them further away.

Lindqvist [4.14] used a broadly similar formulation of the problem of multiple scattering, but did not "accept Kuttruff's compounding of the distance and time dependencies as if they were independent". She proposed instead that the probability of a phonon being within a certain distance , r , of the source at time t is the sum over all orders of scattering of the product of the probability that k scatterings will have occurred by t , with the conditional probability that the phonon is within r at t , given that k scatterings have taken place. By introduction of a new variable $\underline{U}_k$, which is the position of a phonon after k scatterings, normalised by its total travelled pathlength, the conditional probability is removed. The second term in the original product then be comes the probability that $|\underline{U}_{k+1}| \leq r/ct$. The probability distribution for $\underline{U}_k$ is then derived, to result in an expression for the scattered energy density at r at time t , in an infinitely large room, in terms of a sum over all orders of scattering from one to infinity. The unscattered sound energy is considered separately, and the two components added. In order to account for the presence of partially absorbent walls, the scattered energy is multiplied by an approximate factor derived from modification of the Poisson probability distribution of the free paths, whilst the unscattered components are calculated by use of appropriately attenuated image sources.

Lindqvist's work still contains the isotropic scattering assumption and a Poisson distribution for the scatterers. However, a correction is suggested to account for the finite size of the objects in real life, since they may overlap in the assumed Poisson distribution. This is modelled by a change in the effective scattering cross-section Q, which also alters the frequency of scattering term , ν . Concerning

the isotropic scattering assumption, Lindqvist stated that at high frequencies "one half of the scattered energy as observed at large distances is fairly uniformly distributed over all directions and the other half is propagated in the forwards direction", and thus assumed that the distribution of scattered energy from a machine will be omnidirectional, with the value of Q chosen as equal to half that of the free field plane wave value.

A similar isotropic scattering assumption is made in the statistically based two-dimensional scattering model used by Bullen [4.15] to study urban noise propagation. However, Bullen acknowledged that this is an approximation and studied the effect this assumption has on his expression for the intensity at a point due to phonons which have undergone a single order of scattering. He found that there is only a slight change in the results when the isotropic scatterers are replaced by randomly orientated finite size planar scatterers that reflect sound specularly, the effect being to further increase sound levels close to the source, and reduce them more at greater distances. He argued that the consequences of this change of scatterers for the second (and subsequent) order(s) of scattering will be smaller, since the phonons then do not arise from a single source and can be travelling in any direction.

Another particle-, or ray-acoustics-based method for the evaluation of diffraction effects in rooms is to use geometric diffraction theory in a ray-tracing computer program. In such a model, the rays which can get from source to receiver in a given number of reflections from the surfaces of the room are traced exactly, and their energies summed at the receiver. The inclusion of scatterers is essentially performed by establishing which rays collide with objects in the room; the ray path is then re-routed via the objects' edges and diffraction coefficients applied to the energy contribution due to these rays. Finally, some 'diffuse' energy term is normally added to the level which is calculated from the sum of these exactly-traced rays. Such models have been used by Bschorr [4.16] and by Hurst and Mitchell [4.17]. This type of approach has also led to several studies of the simpler problem of the prediction of a noise barrier's performance when it is placed between two reflecting planes (see, for example References [4.18, 4.19, 4.20]). This situation typifies the conditions found in large

industrial workspaces where the end and side walls may be a long way from a location where it is desired to reduce the sound pressure level due to a particular noise source by the interposition of a barrier. Under such conditions the steady state levels are generally controlled by the floor and ceiling reflections. A two-dimensional image model, as shown in Figure 4.2, is therefore an adequate representation of the situation for practical purposes.

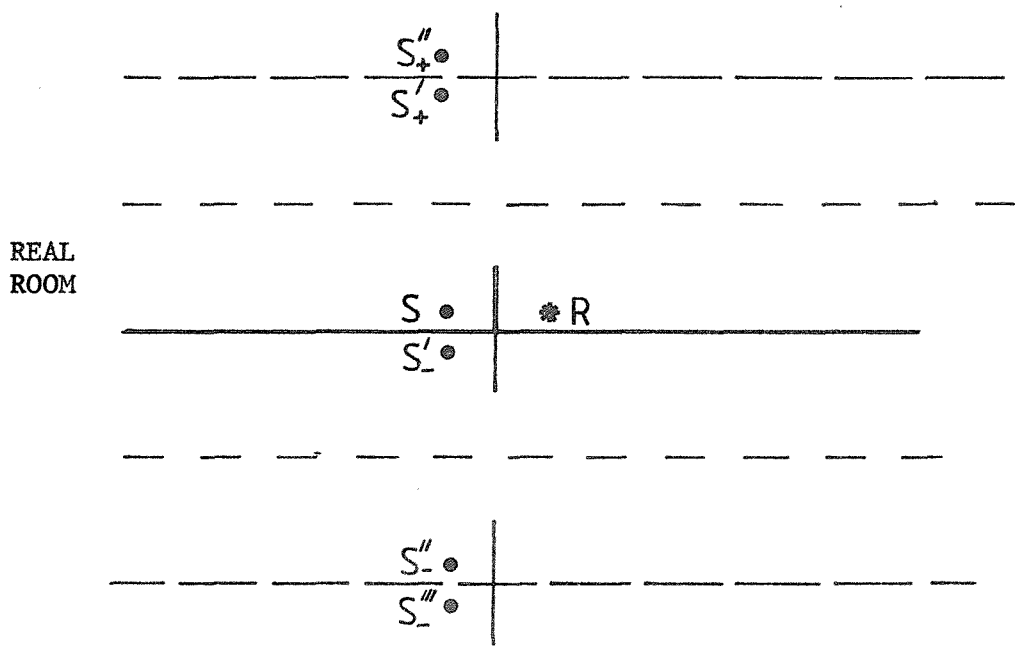

Figure 4.2 : Geometry for the estimation of a noise barrier's effectiveness in a large, flat room.

In this model, the energy contributions from the real source and its images in the ceiling and floor are summed at the receiver position for some given number of image orders. For any source to receiver paths that intersect either the real barrier or one of its images the route must be retraced via the top and bottom of the strip in image space (which is twice the height of the real barrier). The additional attenuation of sound along any of these ray paths can then be found from barrier noise reduction prediction methods, or from geometric diffraction theory. When there are many small barriers present it may be more appropriate to model them as a 'rough surface' and use one of the models of the next section.

4.1.4 Rough surface scattering:

In this section models will be considered which are applicable to situations where the scattering bodies are all attached to one or more of a room's boundary surfaces. A further limitation on the geometry is that the objects should not extend out a significant proportion of the room's dimension in the direction in which they protrude. Thus this type of model is normally applicable to a distribution of many objects on the floor of a large room, but could equally well apply to the modelling of such features as saw-tooth roof structures. There exists a vast literature on rough surface scattering, since this type of model is often used in underwater acoustics and in electromagnetic wave propagation studies. However, the particular approximations applicable in these two areas may not be valid in the regime of interest here. This section will therefore cover the main methods of modelling these surfaces, their main features, and hence their applicability to certain types of situation.

There is obviously a requirement for some criterion to gauge when a surface becomes appreciably 'rough'. The normal measure used is that due to Rayleigh; namely, that a surface can be considered rough when the phase of a wave reflected from the uppermost point of the surface is $\pi/2$ different from that reflected from the lowest point. This, although it can be used as an indicator, is an almost arbitrary measure and values of $\pi/4$ and $\pi/8$ have been alternatively suggested.

In the extreme of a completely rough surface it is well known that the cosine or Lambert's law applies (see for example Reference [4.21], Section IV.1). This states that the intensity I observed at a distance r from a perfectly rough surface and at an angle θ to the normal, equals $I_o \cos\theta dS/\pi r^2$, where dS is the element of surface area at which the reflection occurs and I_o is the normal component of the incident intensity there. Joyce demonstrated (see Reference [4.22], Appendix A) that the assumption of omnidirectional scattering inherent in some published work is incorrect, since it contravenes the laws of thermodynamics, and that a cosine reflection law must be used for totally diffuse reflections. This reflection feature has been included in a number of different types of models for

rooms with diffusely reflecting walls. The form of Lambert's law indicates that each element of the wall surface can be considered as a secondary sound source, since the spherical divergence factor, $1/\pi r^2$, includes the distance r from the wall to the receiver, rather than the distance from the image source to the receiver as in the case of specular reflection. This model is therefore ideally suited to incorporation in room acoustics models via integration of these contributions over the room's boundary surfaces. The behaviour of sound in enclosures with diffusely reflecting boundaries has been formulated by means of integral equations by Kuttruff [4.21, Section V.1] for an arbitrary room shape, but with particular emphasis on the particular case where the normal incident intensity component is uniform over all the boundary surfaces; this is shown to produce a completely diffuse field. Similar techniques have been used by Carroll and Chien [4.23] to study reverberant sound decay in a spherical enclosure with diffusely reflecting boundaries, and by Carroll and Miles [4.24] to investigate steady-state sound in a similar enclosure. An alternative technique for the inclusion of diffusely reflecting boundaries in a room acoustics prediction method is to model the reflection process as a Markov chain, or a series of random walks. This approach has been used in computer based models by Gerlach [4.25, Chapter 9] and by Kruzins and Fricke [4.26].

Joyce [4.27] considered the effect of altering the surface roughness for the case of a spherical enclosure, from completely rough to completely smooth, by use of a surface reflection model that contains a combination of both specular and totally diffuse terms. Chien and Carroll [4.28] studied the case of a sound source over a rough absorbent plane, where the energy reflected is split into similar specular and diffuse components. For the case of a fully diffuse reflection, they demonstrated that it is possible to represent the sound energy density of the scattered field due to a source of power W above a plane of reflectivity μ as due to an image of the real source in the plane with an apparent power output of μW and a directional weighting of $2\cos\theta$, where θ is the angle subtended by the incident sound to the normal to the surface at the point of specular reflection. For a partly diffuse reflection, they therefore split the energy reflected between

that due to a conventional image source and that due to this directional diffuse term source. They observed that this is only an approximation, since it is based on energy principles (i.e., there are no interference effects included) and since in their model they assumed the surface to be a flat one which can reflect sound in a partly or wholly diffuse manner; thus shadowing effect are also neglected. Furthermore, because the image principle for random reflection involves reflections from the entire plane, it is unlike specular reflection which is controlled entirely by contributions from the area close to the point of specular reflection, and so rough surfaces of finite extent may be significantly mis-modelled by this technique. Kuttruff, in his book on room acoustics, suggested that such a decomposition of reflection phenomena should be useful room acoustics models (see Reference [4.21], Chapters 4 and 5). Davies [4.29] has also applied such a reflection law model to the predication of sound levels in urban streets. In spite of its attractive prospects however, none of the above authors has suggested how this specular-diffuse decomposition should be performed in practice, or what function of wavelength, or what magnitude of the roughness and its distribution, and angle of sound incidence, the breakdown between specular and diffuse terms should be. Investigation of the extensive literature published on rough surface scattering however reveals that there are a number of methods that allow the details of such reflection decomposition models to be evaluated. The main techniques applicable to the realisation of this goal are discussed below, and the typical features of the solutions indicated.

In the assessment of which model to use it is necessary to ascertain whether the surface irregularities are random or periodic in their distribution. The latter case can permit the exact evaluation of a solution, whilst with the former one has to rely on statistical information about the scattering surface's structure. There are a number of techniques that can be applied to either of these distribution types: one of the most widely used of these is based upon the Kirchhoff approximation, and will be studied here in some detail in order to illustrate some of the general features of rough surface scattering. In this particular technique, the scattered field ψ_S at a reciever point $\underline{r}$, for the general surface geometry of Figure 4.3, can be written in terms of the Helmholtz integral as:

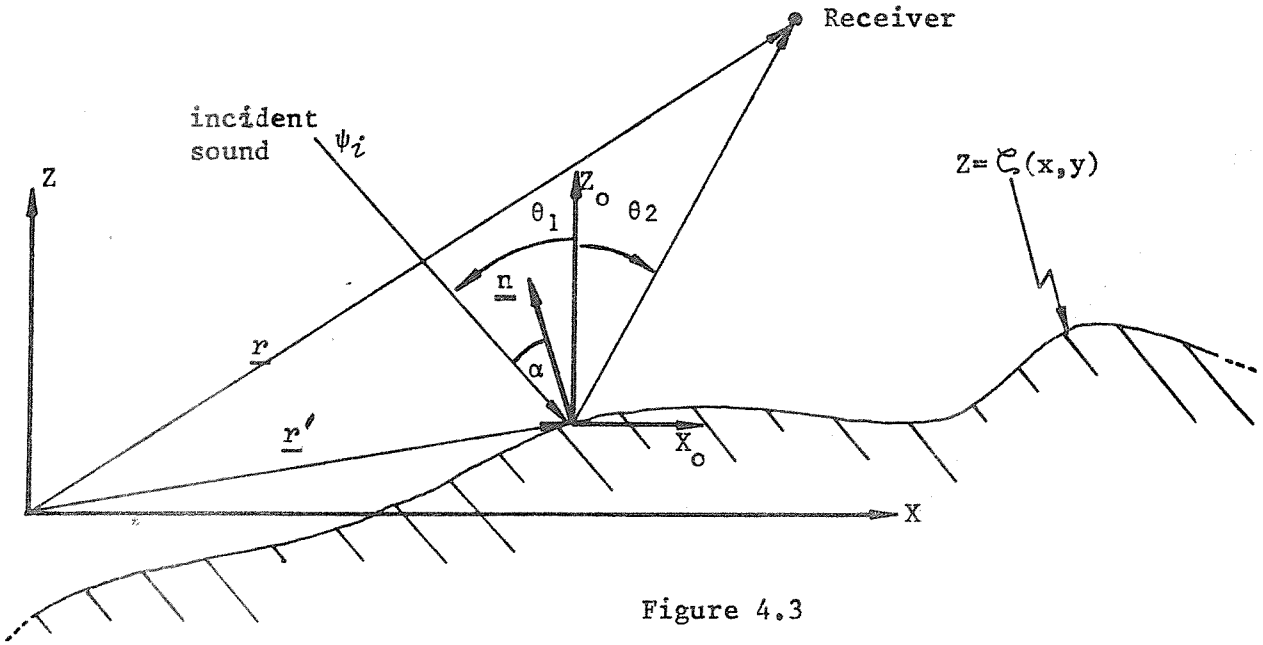

Figure 4.3

Figure 4.3 The General Geometry Considered in the Derivation of the Kirchoff-based Rough Surface Model.

$$\psi_S(\underline{r}) = \int_S \left\{ \psi(\underline{r}')\,\partial G(\underline{r}/\underline{r}')/\partial n - G(\underline{r}/\underline{r}')\,\partial\psi(\underline{r}')/\partial n \right\} dS \ , \tag{4.8}$$

where the integral S is over the entire rough surface, $\psi(\underline{r}')$ is the total field at a point $\underline{r}'$ on the surface, and $G(\underline{r}/\underline{r}')$ is the free field Green function. The Kirchhoff approximation arises from assumptions made about the form of $\psi(\underline{r}')$ and its normal derivative $\partial\psi(\underline{r}')/\partial n$. For example Beckmann [4.30] approximated $\psi(\underline{r}')$ by $(1+R)\psi_i(\underline{r}')$, and $\partial\psi(\underline{r}')/\partial n$ by $(1-R)\psi_i(\underline{r}')\underline{k}_1\cdot\underline{n}$, where $\psi_i(\underline{r}')$ is the incident field at $\underline{r}'$, $\underline{k}_1$ its wavenumber (vector), and R the reflection coefficient for sound incident at an angle α to the local normal (see Figure 4.3) to the plane tangent to the surface at $\underline{r}'$.

For a one-dimensionally rough surface, the z coordinate of a surface point may be written $\zeta(x)$, and its normal, $\underline{n}$, is always in the x-z plane of incidence. If the receiver is moved to the extreme far field, (i.e. into the Fraunhofer zone of diffraction, where the scattered waves are essentially plane), it is possible to represent (as shown in Reference [4.30]) the field scattered by an arbitrary perfectly reflecting one-dimensionally rough surface of length, 2L as

$$\rho = \psi_S/\psi_{spec} = \left(F_S(\theta_1,\theta_2)/2L\right) \int_{-L}^{L} e^{-i\underline{v}\cdot\underline{r}}\, dx \ , \tag{4.9}$$

where ψ_{spec} is the field that would be reflected in the specular direction by an equivalent flat surface (i.e. $\psi_{spec} = -ike^{-ikr}L\cos\theta_1/\pi r$), and $F_S(\theta_1,\theta_2)$ and $\underline{v}\cdot\underline{r}$ are given by the expressions,

$$F_S(\theta_1,\theta_2) = \sec\theta_1 \left(\frac{1+\cos(\theta_1+\theta_2)}{\cos\theta_1+\cos\theta_2} \right) \tag{4.10}$$

and

$$\underline{v}\cdot\underline{r} = k\left((\sin\theta_1-\sin\theta_2)x - (\cos\theta_1+\cos\theta_2)\zeta(x)\right) \ . \tag{4.11}$$

Equation (4.9) is in fact only 'exact' for surfaces where $L>>\lambda$; otherwise there is an 'edge effect' term to be considered as well. Equation (4.9) therefore represents a solution to the problem of far field scattering by a hard, one-dimensionally rough surface, which only requires the form of $\zeta(x)$ to be specified so that integration may be performed. It is easily extendable to two-dimensionally rough surfaces as is indicated in Reference [4.30]. Before specific forms are considered for $\zeta(x)$, corresponding to random and periodic surfaces, the general assumptions behind, and properties exhibited by equation (4.9) will be noted.

The major assumption behind the derivation outlined is that the surface pressure field can be determined solely in terms of the incident field and reflection coefficients. This means that shadowing and multiple scattering effects are neglected in this simple method, and implies that it should only be used to model surfaces devoid of sharp edges, or whose characteristic radius of curvature at any point should be large compared to the wavelength. The point of observation has also been removed to the extreme far field, which may not be strictly applicable in the majority of room acoustics situations. However, the basic formulation of the problem would still hold for points closer to the surface, although the resultant expression would undoubtedly be more complicated than equation (4.9). For these reasons, the simple expression derived will be used for the current discussion of the major features of rough surface scattering.

It will be observed that the actual scattered pressure field is proportional to $\rho\cos\theta_1$; thus equation (4.9) can be seen to obey reciprocity since the expression for ψ_S will be symmetric in θ_1 and θ_2 . When the incident sound arrives at grazing incidence ($\theta_1 = 90^{\circ}$) it can be proved that ρ in the direction $\theta_2 = \theta_1$ goes to unity. This implies that for any hard rough surface, with grazing incident sound, all the incident energy is specularly reflected. It should be noted however that this is for a receiver position at infinity, and therefore does not preclude the existence of evanescent waves near to the surface.

In order to apply the general method described above to a randomly rough surface, $\zeta(x)$ can be assumed to represent a random process with a probability density function $\omega(z)$. If the mean value of $\zeta(x)$, namely $<\zeta(x)>$, is zero, then the mean value of the integral in equation (4.9) may be written as

$$< \int_{-L}^{L} e^{-i\underline{v}\cdot\underline{r}} dx> = \chi(\nu_z) \int_{-L}^{L} e^{-i\nu_x x} dx ,$$

where ν_x and ν_z are the x_o and z_o Cartesian components of the vector $\underline{v}$ (i.e. $\nu_x = k(\sin\theta_1 - \sin\theta_2)$, and $\nu_z = -k(\cos\theta_1 + \cos\theta_2)$ and $\chi(\nu_z)$ is the characteristic function of $\omega(z)$, given by $\sqrt{2\pi}$ times its Fourier transform. This means that $<\rho>$ can be expressed as:

$$<\rho> = \chi(\nu_z)\rho_o ,$$

where ρ_o is the field reflected from an equivalent flat surface (i.e. $\rho_o = \sin(\nu_x L)/\nu_x L$). Unfortunately the mean value of ρ is of little use since ρ is a complex quantity. The more informative measure is the average of its modulus squared, $<\rho\rho^*>$, since this is proportional to the mean scattered power. In order to evaluate this quantity, the correlation function for $\zeta(x)$ must also be specified. Once explicit forms for the distribution of $\zeta(x)$ and its correlation function are known, an expression for $<\rho\rho^*>$ can easily be formulated from the earlier equations, since it can be shown to equal the sum of the variance of ρ, with $<\rho><\rho^*>$. For the case of a normally distributed one-dimensionally rough rigid surface, with a standard deviation σ, and zero mean it can be shown (subject to the conditions outlined in the derivation of equation (4.9)) that the 'specular' part of $<\rho\rho^*>$ namely $<\rho><\rho^*>$, is equal to $e^{-g}\rho_o^2$, where g equals $k^2\sigma^2(\cos\theta_1+\cos\theta_2)^2$. Thus it can be seen that the specular component decreases with increased g. This implies that the specular component is determined by the ratio σ/λ, and is not affected by the 'correlation length', T (defined as the distance for the autocorrelation coefficient to drop to e^{-1}), of the distribution. For the Kirchhoff approximation to be valid, T must be much greater than λ, and for the model used here T must be much less than the length of the surface considered.

The 'diffusely' reflected term, represented by the variance of ρ, is affected by the values of both g and T. Its angular spread increases with roughness (g), but for surfaces of equal roughness, those with smaller T values (which generally correspond to more 'jagged' surfaces) scatter more diffusely than those with larger T values. This behaviour will only be discernible for $g>>1$, as otherwise the specular $\langle\rho\rangle\langle\rho^*\rangle$ term will dominate. Thus for a normally distributed one-dimensionally rough surface it appears that the roughness parameter g determines what proportion of the incident energy is specularly reflected, whilst the correlation function of the surface determines (for $g>>1$) the angular spread of the diffuse term.

A periodic surface is merely a random surface with a periodic correlation function. This class of surface can thus be easily treated by use of this Kirchhoff-approximation-based technique, by substitution of $\zeta(x+\Lambda)$ for $\zeta(x)$ in equations (4.9) and (4.11). In these equations Λ represents the 'wavelength' of the surface distribution's repetition. If the surface is an integral number, n, of periods long (i.e. $n\Lambda = L$) then equation (4.9) ultimately becomes (see Reference [4.30] for details),

$$\rho = \left(\frac{\sin(2np\pi)e^{+ip\pi}}{2n\sin p\pi}\right)\frac{F_s(\theta_1,\theta_2)}{\Lambda}\int_0^{\Lambda} e^{-i\underline{v}\cdot\underline{r}}\,dx \qquad (4.12)$$

where $F_s(\theta_1,\theta_2)$ and $\underline{v}\cdot\underline{r}$ are as given by equations (4.10) and (4.11) respectively, and p equals $(\sin\theta_1-\sin\theta_2)\Lambda/\lambda$. This solution represents a directivity pattern with a number of lobes, their directions coinciding with integral avlues of p. Thus the direction of the m^{th} lobe is given by $\theta_{2m} = \sin^{-1}(\sin\theta_1+m\lambda/\Lambda)$, $m = 0, \pm1, \pm2\ldots$. The lobe for $m = 0$ therefore corresponds to the specular reflection direction, and $m = \pm 1$ to the two adjacent lobes. The limit on the number of lobes possible is imposed by the condition $|\sin\theta_{2m}| << 1$, since $|\sin\theta_{2m}| = 1$ corresponds to propagation along the surface. For small values of λ/Λ, the value of p can go through many integer values, m, before this condition is broken. Thus the scattered field will be very diffuse under these circumstances, independent of the actual form of $\zeta(x)$ inside each period. This also suggests that for $\lambda/\Lambda>> 1$ a surface of any roughness will still tend to reflect

specularly; but, although true, this cannot be concluded from these results since they were derived under the inherent Kirchhoff assumption that the wavelength is less than the period of the disturbance.

The above examples, although clearly demonstrating some of the principle features of rough surface scattering, were derived under some assumptions which make them both approximate and potentially strictly inapplicable to room acoustics, since the observer is near infinity. It is possible to gauge their degree of accuracy either by comparison with experiments (see, for example, Reference [4.31]), or exact theories. The latter only exist in forms capable of direct implementation for periodic surfaces. The most studied of these periodic surfaces is the sinusoidally corrugated one. Probably the earliest solution to this problem was that due to Rayleigh [4.32]. Debate still persists as to how accurate this solution is (see References [4.33] and [4.34] for a detailed discussion). Essentially the Rayleigh method consists of postulating that the scattered field at all points above a corrugated surface can be represented in terms of an infinite series of outgoing plane waves. The boundary conditions are then applied, so that, for example, for a pressure release surface, the incident pressure field is set equal to minus the scattered field at all boundary points. Both the incident and scattered components are then expanded in terms of Fourier series. This allows the unknown terms in the infinite series for the scattered field to be expressed in terms of the known Fourier coefficients for the incident field, which results in an infinite series of linear equations. These can be solved by methods such as successive approximation, to give the coefficients in the series for the scattered waves up to some desired order.

The form of the final solution due to Rayleigh is similar to that of equation (4.12) except that, since the surface considered by Rayleigh was infinite, the scattered field consists only of plane waves which propagate in the directions of the lobes seen in the earlier, finite surface Kirchhoff method expression. From the Rayleigh solution it also becomes apparent that for $|\sin\theta_{2m}|>1$ the wavenumber of the scattered mode becomes complex, which corresponds to waves which propagate along the surface but decay exponentially away from it.

Unfortunately, Rayleigh's solution for reflection from a corrugated surface is not exact, since he assumed that the field can be represented at all points above the surface solely in terms of outgoing plane waves. This assumption breaks down in the 'valleys' between the 'peaks' because upward and downward travelling waves will exist. Uretsky [4.35] observed this fact and constructed an alternative solution based on Green's theorem. He concluded that the Rayleigh equations are useful when the magnitude of the undulations is small. Many other improvements to the Rayleigh theory, or alternative formulations of the problem, have since been used; a comprehensive review of these techniques has been given by Wirgin [4.34], who finally concluded that the Rayleigh theory is adequately accurate over a wider range than previously thought, and possibly more useful than the other solutions since it is generally much simpler to compute.

Another type of periodic surface for which exact solutions exist, but for which the Kirchhoff method cannot be assumed to work, is one with rectangular corrugations. Such surface models have been used by de Bruijn [4.36, 4.37] to study anomalous absorption effects caused by diffraction for periodic surfaces of rectangular profile. The method adopted is again one of mode-matching, where the field above the top of the grooves is expanded in terms of outgoing plane waves, whilst that in the grooves is expressed in terms of a spectrum of positive and negative travelling waves. The boundary conditions at the mouth of the grooves, and the top of the corrugations, must next be applied. Subsequent expression of incident, reflected, and duct fields in terms of Fourier series allows the construction of an infinite series of linear equations, which can again be solved by some method such as successive approximations. In this manner any desired degree of accuracy can be obtained.

The mode-matching approach, although much more time-consuming to compute, does permit the evaluation of exact solutions to specific problems. It can also be used for some surfaces where sharp edges exist and thus the Kirchhoff solution should not be used. The general use of these mode-matching approaches would seem fairly limited however from a practical point of view.

The major alternative method, which can be used for either periodic or random rough surfaces, is that due to Twersky (see References [4.8, 4.38, 4.39]). This model is based upon representation of surface roughness in terms of a distribution of cylinders or bosses, for the cases of one- or two- dimensionally rough surfaces respectively. Use is then made of the fact, as originally suggested by Rayleigh [4.40], that the field scattered by an arbitrary object protruding from a hard plane is the same as that for the object and its reflection in the plane, when illuminated in free space by the incident wave and its image in the plane. This is shown diagrammatically in Figure 4.4.

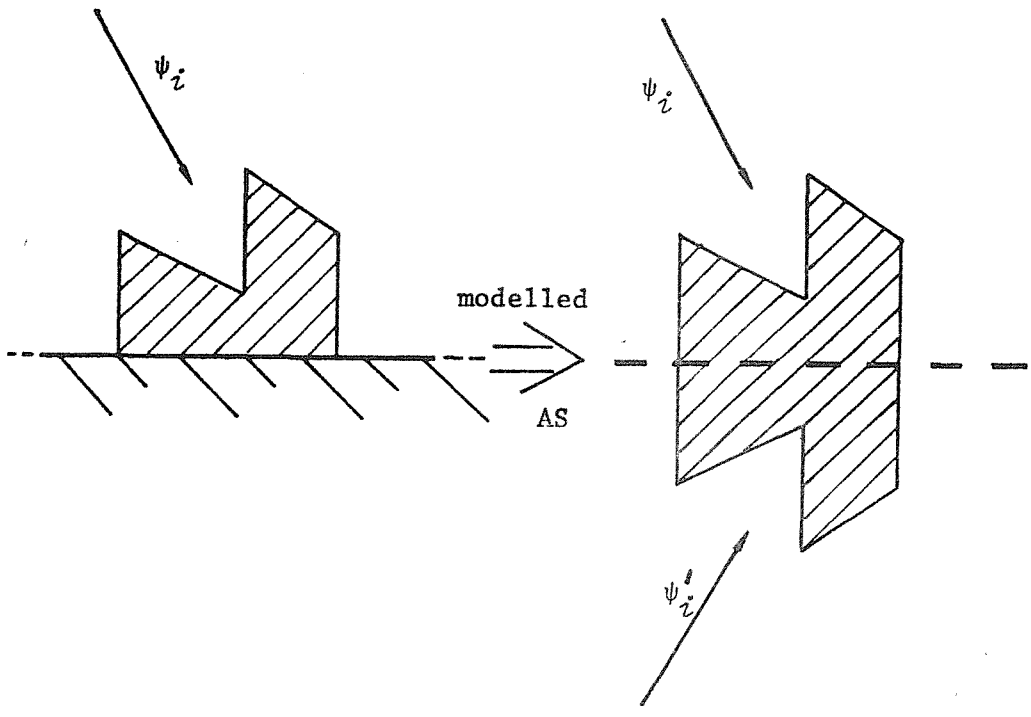

Figure 4.4 Diagram representing the basis of the image model used by Twersky.

Thus once the general form of the field scattered by a single body, as composed of the real object and its image in the plane is determined the problem is in princple solved (as indicated by the general formulation of the multiple scattering problem at the start of section 4.1.3). This scattering behaviour due to the individual objects can either be determined from experimental measurements or

analytic methods. Twersky considered both randomly [4.38] and regularly [4.8] spaced objects. For spacings between objects that are large compared to the object size he used the bodies' scattering coefficients (i.e., the angular weighting that must be applied to a simple source in order to give the correct form of the scattered far field) to derive comparatively simple formulae for the values of specular and diffuse reflection components. These formulae take into account shadowing and certain multiple scattering effects and are therefore superior to simple Kirchhoff methods. Twersky presented results for distributions of hemispheres and semicylinders based on exact solutions (see for example Reference [4.38]) and also the case of elliptically striated surfaces, based on approximate scattering coefficients [4.39]. Consideration was also given to single scattering approximations by Twersky, from which it is seen that the effect of neglecting multiple scattering is in general only slight, since Twersky's results are derived for comparatively large inter-object spacings. However, the use of a single order of scattering model does lead to anomalous behaviour at grazing incidence, since under these conditions only the multiple scattering model predicts perfect reflection, which was noted above to be the correct result.

The major rough surface models can therefore be seen to be of Kirchhoff, mode-matching, or imaging types. (Further models are described in References [4.30], [4.33] and [4.38], Appendix (A)). Of the three, the mode-matching method is probably the easiest to use to get exact results, but is still very difficult to compute, and can only simply be applied to comparatively few cases. The Kirchhoff method outlined is conceptually easy to understand and generally requires only the evaluation of a surface integral. However this method involves a number of approximations, and is hence unable to accurately model surfaces with sharp edges, or to account for multiple scattering behaviour. The image model derived by Twersky does permit the inclusion of such effects but generally requires a spacing between objects that is large compared with their size. Under such conditions however, simple expressions exist for the specular and diffuse reflection components, provided that the composite object's scattering coefficient can be found, and of course that the surface in question can be adequately represented as an ensemble of bosses. The Twersky approach can even be extended to

cases where the bosses are of more than one type (see Reference [4.38]), and can therefore be used to represent an extensive range of real situations where more than one type of scatterer is present.

4.1.5 The implications of the literature survey of multiple scattering techniques for the prediction of sound levels in 'non-Sabine' spaces.

The initial, 'diffuse-field', technique described in section 4.1.2, is only really applicable to situations where single scatterers are situated in well defined wave fields, and therefore is only of passing interest in the study of non-Sabine room behaviour. The other two prediction methods, of 'volume' and 'surface' scattering have great potential for studies of the effects due to the presence of many scatterers in highly disproportionate rooms. Statistical treatments of volume scattering have already been used in this context (see, for example, References [4.13] and [4.14]) and found to give results which indicate that the scatterers increase the levels near the source, and decrease them further away. However these models rely on an omnidirectional scattering assumption, and it is also hard to know what to use for a complicated object's scattering cross-section. Furthermore for the class of buildings typified by the factory shown in the frontispiece, the scattering objects are almost all situated on the floor and have a typical height very much less than that of the room itself. This makes the volume scattering model appear rather inappropriate, since the objects could hardly be said to be uniformly distributed across the room's vertical cross-section. Also if the roof of such a building is acoustically absorbent to any degree, the imaging process required to exactly treat volume scattering becomes inexact.

The apparent solution for cases where the above points are problems is to treat the floor as a 'rough surface'. The rough surface reflection models have not been previously applied to the study of the acoustics of highly disproportionate rooms, and even where they have been used for proportionate rooms (see for example References [4.24] and [4.25]), a totally diffuse, Lambert's Law reflection model has been adopted. It is however unlikely that, for all the possible reflection situations of interest in the study of a typical disproportionate room,

the floor will behave as a perfectly rough surface. Inspection of the structure of the floor surface of this type of building indicates that it will often take the form of virtually identical machine lines, or rows of shelves, etc., repeated at intervals down the length of the room. This type of surface typifies the type of structure for which the Twersky rough surface reflection model is ideally suited. Since there is little by way of comprehensive published results for such scattering configurations, the rest of this Chapter will be devoted to a study of a structure chosen to model an idealised scattering floor. In the next section, therefore, the major steps in the derivation of the Twersky model are outlined, and in the subsequent section i.e. results for one particular configuration of scatterers are evaluated.

4.2 Investigation of the Twersky Rough Surface Model.

4.2.1 Introduction:

This section contains brief details of the derivation of the model proposed by Twersky for reflection from a surface, composed of identical protruberances, spaced at distances large compared to their individual sizes. The derivation follows that given in Reference [4.38], with particular attention paid to the two-dimensional case of reflection from a surface composed of rigid parallel infinitely long hemicylinders (initially of arbitrary cross-section) on a hard plane, with a plane wave incident normal to their length.

4.2.2 General formulation of scattering by a single cylinder on a hard plane:

For any scattering body in free space, as has been seen earlier, the scattered field at any point $\underline{r}$, external to the object, can be expressed in terms of the field on the body's surface $\psi(\underline{r}')$, and the free field Green function, $G(\underline{r}/\underline{r}')$:

$$\psi_s(\underline{r}) = \int_S \left(\psi(\underline{r}')\,\partial G(\underline{r}/\underline{r}')/\partial n - G(\underline{r}/\underline{r}')\,\partial\psi(\underline{r}')/\partial n\right) dS \ ,$$

where n is the outward normal to the surface at any point. This form of integral equation will be denoted by curly brackets for the rest of this chapter: i.e.,

$$\psi_s(\underline{r}) = \{G(\underline{r}/\underline{r}'), \psi(\underline{r}')\} \quad . \tag{4.13}$$

For two-dimensional problems, with an assumed $e^{i\omega t}$ time factor, the Green function which ensures outgoing waves at infinity is $H_o^{(2)}(k|\underline{r}-\underline{r}'|)/4i$. For $kr>>1$ and $r>>r'$, this approximates to $(2i/\pi kr)^{\frac{1}{2}}e^{-ikr+ikr'\cos(\phi'-\phi)}$, where $\underline{r}$ and $\underline{r}'$ have been expressed in polar co-ordinates as (r,ϕ) and (r',ϕ') respectively (see Figure 4.5). Hence, under these conditions, the value of $\psi_s(\underline{r})$ from equation (4.13) approaches

$$\psi_s(\underline{r}) \simeq H(kr)g(\phi,\alpha) \quad , \tag{4.14}$$

where $H(kr)$ and $g(\phi,\alpha)$ are defined as

$$H(kr) = (2i/\pi kr)^{\frac{1}{2}}e^{-ikr} \quad , \tag{4.15}$$

and,

$$g(\phi,\alpha) = \{e^{ikr'\cos(\phi'-\phi)}, \psi(\underline{r}',\alpha)\} \quad , \tag{4.16}$$

where $\psi(\underline{r}',\alpha)$ is the total field at a point $\underline{r}'$ on the scatterer's surface for a plane wave incident at an angle α, and $g(\phi,\alpha)$ is the free space scattering amplitude for the single object, and indicates the scattered far field in a direction ϕ, for a plane wave incident at α (see Figure 4.5).

Now if the scatterer is symmetric about the $x = 0$ plane, it can be used to model a hemicylinder in the half space $x \geq 0$, sitting on the rigid plane $x = 0$. For the case of a real plane wave incident at $\pi-\alpha$, it can be seen (from the discussion of Section 4.1.4) that the scattering amplitude for the scattered field in the half-space $x \geq 0$ can be written as

$$f(\phi, \pi-\alpha) = g(\phi,\alpha) + g(\phi,\pi-\alpha) \quad . \tag{4.17}$$

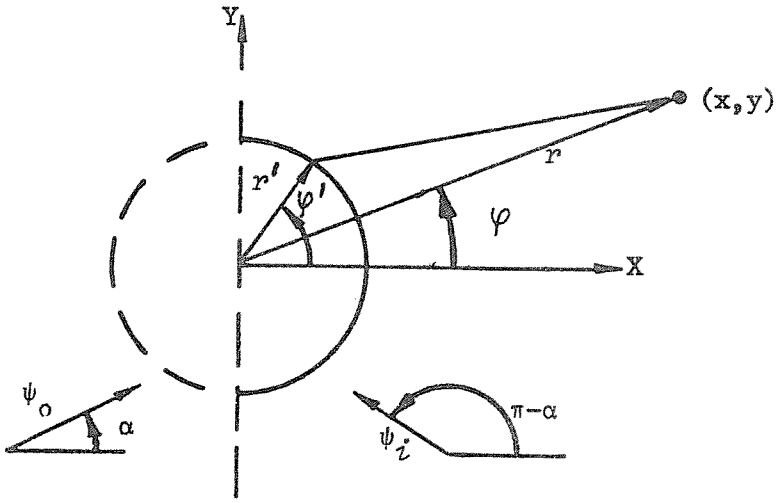

Figure 4.5

Figure 4.5 Single Scattering Object Geometry.

The total field at any point $x \geq 0$ is therefore given by,

$$\psi(\underline{r}) = \psi_o(\underline{r}) + \psi_i(\underline{r}) + \psi_s(r) \quad , \tag{4.18}$$

where

$$\psi_o(\underline{r}) = e^{-ikx\cos\alpha - iky\sin\alpha} = e^{-ikr\cos(\phi-\alpha)} \quad , \tag{4.19}$$

$$\psi_i(\underline{r}) = e^{ikx\cos\alpha - iky\sin\alpha} = e^{-ikr\cos(\phi-\pi+\alpha)} \quad , \tag{4.20}$$

and

$$\psi_s(\underline{r}) \quad H(kr)f(\phi,\pi-\alpha) \quad . \tag{4.21}$$

One thus has a very generalised far field prediction scheme for scattering by any single object on a rigid surface, which can be used so long as the far field scattering amplitude of the equivalent object created by reflection in the base plane can be defined. This can normally be done either by experimental or analytic methods. Moreover, since it is asymptotic in form some of the approximate methods discussed in Chpater 2 could well prove useful where exact scattering solutions are not available for the body in question.

4.2.3 Scattering by an ensemble of identical parallel hemicylinders of arbitrary cross-section placed on a rigid plane:

For the case of a planar array of arbitrary parallel hemicylinders on a hard plane, the total field at any point $\underline{r}$, can be written as

$$\Psi(\underline{r}) = \psi_o(\underline{r}) + \psi_i(\underline{r}) + \Psi_s(\underline{r}) \quad , \tag{4.22}$$

where $\Psi_s(\underline{r}) = \Sigma_N \psi_s^n(\underline{r})$, and if an infinite number of cylinders are considered, ψ_s^n, the wave scattered by the n^{th} cylinder, must have an outgoing form for $|\underline{r}-\underline{r}_n| \to \infty$. $\Psi(\underline{r})$ then satisfies the wave equation and all the relevant boundary conditions. The wave scattered by the hemicylinder at the origin (where the phase of both incident and reflected fields are zero) can therefore be approximated as

$$\psi_s^o(\underline{r}) \simeq H(kr)F(\phi,\alpha) \quad , \tag{4.23}$$

where

$$F_o(\psi,\alpha) = G_o(\psi,\alpha) + G_o(\psi,\pi-\alpha) \tag{4.24}$$

and

$$G_o(\psi,\alpha) = \{e^{ikr'\cos(\psi'-\psi)}, \Psi(\underline{r}',\alpha)\} \tag{4.25}$$

G_o is the multiple scattered amplitude of cylinder O of the configuration, and F_o is the multiple scattered amplitude of the equivalent hemicylinder on a rigid plane. Both are functions of $\Psi(\underline{r}',\alpha)$, the total field at $\underline{r}'$ on the surface due to a plane wave incident at an angle α, and hence both F_o and G_o are functions of the positions of all the other cylinders.

In principle, it is possible to solve this problem by the application of suitable boundary conditions in the expressions for the fields scattered by the individual objects in order to reduce equation (4.22) to a set of coupled integral equations which can be solved for Ψ and its normal derivative on the boundary. However, in practice such techniques are almost impossible to apply, and consideration of less arbitrary configurations leads to simpler results. In the rest of this section therefore a random distribution of these parallel, arbitrary cross-section cylinders on a hard plane will be considered.

Rather than exactly duplicate Twersky's derivation of the solution to this problem (see Reference [4.38]), the salient features of his method will be outlined, and the final results stated. The initial aim is to obtain an average for the ensemble scattered wave $\Psi_s(\underline{r})$ of equation 4.22, for a random planar distribution of N cylinders in free space. This is essentially achieved by the summation over all N of the product of the average waves scattered, $\langle\psi_s\rangle_n$, by each cylinder at its position y_n, (where the averaging is performed over all the possible configurations of the other cylinders), with the probability of finding that particular cylinder at y_n, independent of where all the other objects are. This probability is assumed to equal ρ/N, where ρ is the average number of cylinders per unit length of the distribution. If the average field scattered by the cylinder, n, is further assumed to differ only from that scattered by a cylinder at the origin by a phase factor due to the change in the incident field at y_n, the average value of the ensemble scattered wave can be written in terms of an integral over the surface,

$$\langle \psi_s \rangle = \rho \int_{-\infty}^{\infty} \langle \psi_s \rangle_n dy_n \ ,$$

here,

$$\langle \psi_s \rangle_n = e^{-iky_n \sin\alpha} \langle \psi_s \rangle_0 \tag{4.26}$$

is the average wave scattered by a cylinder at y_n expressed in terms of a cylinder at the origin. The explicit form of this latter quantity is,

$$\langle \psi_s \rangle_0 = \{ H_0^{(2)}(k|\underline{r}-\underline{r}'|), \langle \psi(\underline{r}',\alpha) \rangle \} \ .$$

This suggests the asymptotic form,

$$\langle \psi_s \rangle_0 \simeq H(kr)G(\phi,\alpha) \ , \tag{4.27}$$

where

$$G(\phi,\alpha) = \langle G_0(\phi,\alpha) \rangle_0 = \{ e^{ikr'\cos(\phi'-\phi)}, \langle \Psi(\underline{r}',\alpha) \rangle_0 \} \ ,$$

in which $G(\phi,\alpha)$ is the average scattering amplitude of any fixed cylinder, independent of position. Thus the total average field can now be written as

$$\langle \Psi_s(\underline{r},\alpha) \rangle \simeq \{ \rho \int_{-\infty}^{\infty} H_0^{(2)}(k|\underline{r}-\underline{r}_n'|) e^{-iky_n \sin\alpha} dy_n, \langle \Psi(\underline{r}',\alpha) \rangle_0 \} \ , \tag{4.28}$$

where r_n' is as shown in Figure 4.6. The integral term inside the curly brackets of equation (4.28) can then be rewritten in terms of plane waves, to give:

$$\langle \Psi_s(\underline{r},\alpha) \rangle = 2C\{ e^{-ik(y-y')\sin\alpha - ik|x-x'|\cos\alpha}, \langle \Psi(\underline{r}',\alpha) \rangle_0 \} \tag{4.29}$$

where C is the number of scatterers illuminated by a length $1/k$ of the wavefront (i.e, $C = \rho/k \cos\alpha$) . It now remains only to evaluate an explicit form for $\langle \Psi(\underline{r}',\alpha) \rangle_0$: that is, the field on a fixed cylinder at the origin averaged over all the other cylinders' possible positions.

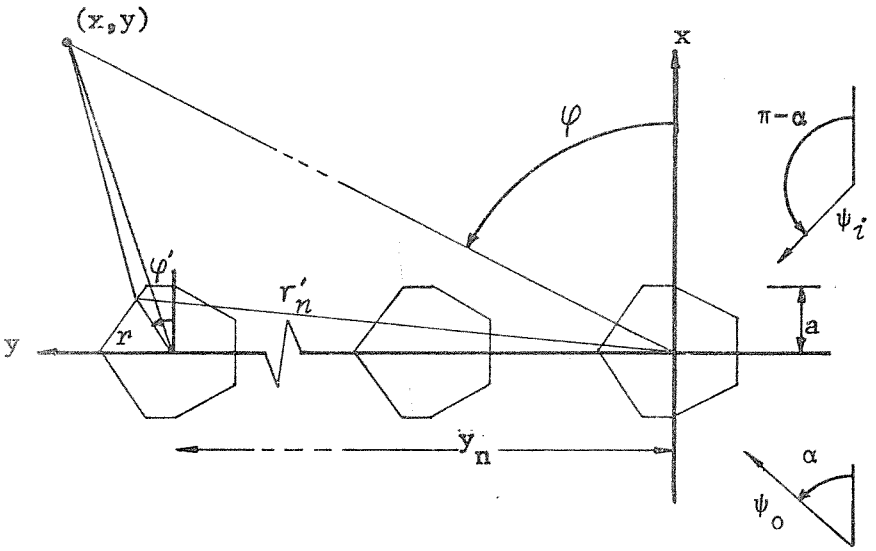

Figure 4.6 The Configuration of Identical Parallel Arbitrary Cross-Section Cylinders Considered in the Derivation of Twersky's Model.

The total average field at the surface of a cylinder fixed at the origin can be expressed in terms of the incident field, and the sum of the average waves scattered by the cylinders, given that the one at the origin is fixed. This latter quantity is equal to the sum of the average wave scattered by all N cylinders at their individual positions y_n. Now, since the cylinder at the origin is fixed, its contribution is definitely $\langle\psi_s\rangle_o$, and the remaining sum is the product over $N-1$ cylinders of the conditional probability that they are each at y_n given that the cylinder at the origin is fixed, with the value of the average field scattered by the cylinder at y_n, when only it and the cylinder at the origin are assumed fixed. For simplicity the conditional probability will be assumed to still equal ρ/N. The average field scattered by a cylinder when two cylinders' positions are fixed will be approximated by that when only the one at y_n is fixed. This approximation is the same as starting a successive scattering process with the average single scattered wave. With these two approximations, and an infinite N, the total averaged field on the central cylinder, held fixed at the origin is

$$\langle\Psi(\underline{r}')\rangle_o = \psi_o(\underline{r}') + \langle\Psi_s(\underline{r}')\rangle + \langle\psi_s(\underline{r}')\rangle_o , \qquad (4.30)$$

where $\langle\Psi_s(\underline{r}')\rangle$ can be obtained from equation (4.29). It is apparent from equations (4.27) and (4.29) that for $x > a$ (see Figure 4.6), it is possible to represent $\langle\Psi_s(\underline{r},\alpha)\rangle$ for a planar configuration of parallel identical cylinders in space, as $2C\psi_o G(\alpha,\alpha)$, whilst for $x < -a$, this becomes $2C\psi_i G(\pi-\alpha,\alpha)$. Twersky has demonstrated that for $|x| < a$, it is possible to represent the field as the mean of these two forms, thus resembling an interference field due to two plane waves. Substitution of this average form into equation (4.30), renders it apparent that the total field on the surface of the central scatterer has the form of the sum of two incident plane waves, and the average wave scattered by the cylinder itself. The asymptotic form of this latter quantity is given by equation (4.27), where $G(\psi,\alpha)$ can be deduced from the superposition of the single cylinder scattering amplitude $g(\psi,\alpha)$ in response to the positive and negative travelling plane waves at the cylinder. This results in the following form for the multiple scattering coefficient of any cylinder:

$$G(\psi,\alpha) = g(\psi,\alpha) + g(\psi,\alpha)CG(\alpha,\alpha) + g(\psi,\pi-\alpha)CG(\pi-\alpha,\alpha).$$

The first term in this expression equates to single scattering, the others to multiple scattering. From this result it can be seen that $G(\psi,\alpha)$ equals the response of the scatterer to the incident wave, and the mean of the waves coherently scattered by the other scatterers.

The equivalent problem of a planar array of indentical hemicylinders on a rigid base plane can now be considered. The scattering amplitude $F(\psi, \pi-\alpha)$ for this problem can be deduced in terms of the multiple scattering amplitude G, and subsequently re-expressed in terms of the single hemicylinder scattering amplitude as

$$F(\psi, \pi-\alpha) = f(\psi, \pi-\alpha)/(1-Cf) \tag{4.31}$$

where

$$f = f(\alpha,\pi-\alpha) .$$

From this form, the total reflected field can be shown to have the form,

$$\langle\psi_r\rangle = \psi_o(1+z)/(1-z) , \tag{4.32}$$

where z is defined as $Cf(\alpha, \pi-\alpha)$. Thus this equation can be seen to equate to an average coherently reflected wave, which will exist only at the specular reflection angle. A specular, coherent, energy reflection coefficient R, may therefore be defined such that,

$$R = \left|\frac{1+z}{1-z}\right|^2 . \tag{4.33}$$

In order to obtain an expression for the energy that is reflected in non-specular directions, Twersky considered the average intensity flow. By neglect of the effects that fluctuations in the average field scattered by all the other scatterers have on that scattered by the one under consideration, he showed this intensity flow to be composed of coherent ('specular') and incoherent ('diffuse') terms. Integration over a control surface above the plane then shows that (for non-absorbent semi cylinders),

$$1 = R + \rho P \sec\alpha \ , \tag{4.35}$$

where

$$\rho P = \int_{-\pi/2}^{\pi/2} \sigma(\psi, \pi-\alpha)\, d\psi \ , \tag{4.36}$$

and

$$\sigma = \frac{2\rho}{\pi k} \left| \frac{f(\psi, \pi-\alpha)}{1-z} \right|^2 \ . \tag{4.37}$$

Equation (4.35) therefore demonstrates that the assumptions used in the derivation are self-consistent, since it implies that the total incident power per unit area equals the sum of that coherently reflected and that incoherently scattered by the area illuminated by a unit area of the incident wave, where $\rho P \sec\alpha$ gives the magnitude of the incoherently scattered part, and σ denotes the distribution of this term with angle of observation (i.e. the power scattered into a wedge of unit angle and height by unit area). Twersky showed that for grazing incidence, for this multiple scattering model, the specularly reflected term tends to unity, whereas the diffusely reflected term goes towards zero. He also compared these results with a single order of scattering approximate model, where this behaviour was not seen.

Thus, the multiple scattering model described, although approximate, is self-consistent, and apparently realistic. Moreover, it can be used for any planar array of randomly spaced identical cylinders, and can thus be more easily applied to practical situations than some other techniques. Twersky [4.38] also extended his model to the 3-dimensional problem of a random array of regular bosses on a plane, and also considered arrays with more than one type of scatterer present. Unfortunately, he did not illustrate his results particularly well with computed examples, so a few representative cases are examined in the next section.

4.2.4 *Computation of the reflection characteristics of a random array of parallel circular hemicylinders on a rigid base*

As very little illustrative information is available on typical results predicted by Twersky's method, it was decided to compute some values of practical interest. Since the form of far field scattering by cylinders can be deduced from the well known exact solution (see, for example, Reference [4.6]) , and as computer programs to generate integer order Hankel functions had already been written in connection with the work reported in Chapter 2, it was decided to study the case of parallel circular hemicylinders on a rigid base plane. Under such conditions, the equation for the single body scattering amplitude (see equation (4.17)) is:

$$f(\phi,\pi-\alpha) = 2\sum_{n=0}^{\infty} A_n\left\{\cos\left(n(\phi-\alpha)\right)+(-1)^n\cos\left(n(\phi+\alpha)\right)\right\} \quad , \quad (4.38)$$

where the A_n's are given by minus $J_n'(ka)/H_n^{(2)'}(ka)$. Thus substitution of values of f from equation (4.38) into equations (4.33) and (4.37) permits inspection of the parametric variation of the 'specular' (R) and 'diffuse' (σ) terms. This has been performed and the results of such calculations are shown in Figures 4.7 and 4.8. The convergence of the series was checked by computation of the energy sum of equation (4.35), and by comparison with the few comparable results of Reference [4.39]. The energy check was found to lie within 0.1% of unity for all the results checked. The trends observed in the results and their practical implications are discussed in the next section.

4.2.5 *Discussion of the computed results:*

It is obvious from the results shown in Figure 4.7 that the specular (coherent) reflection coefficient, R ,is a relatively strong function of the angle of incidence. For the parameter values of Figures 4.7(a) and (b) the only difference is the spacing between the hemicylinders. These results are at the limit of the region where the Twersky approach might be expected to work. They do however indicate that in this regime

Figure 4.7(a) ka = 5
k = 5
ρ = 0.1

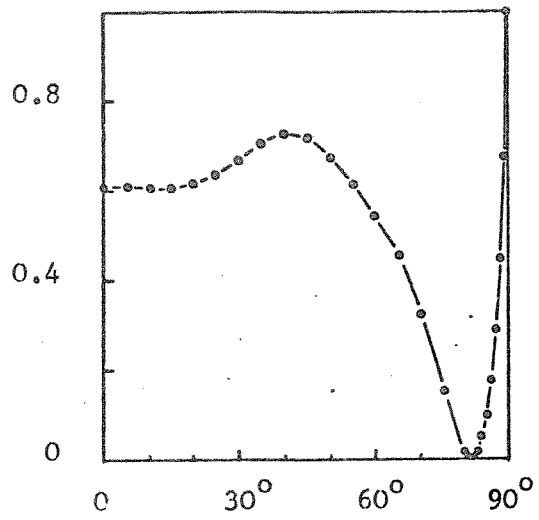

Figure 4.7(b) ka = 5
k = 5
ρ = 0.2

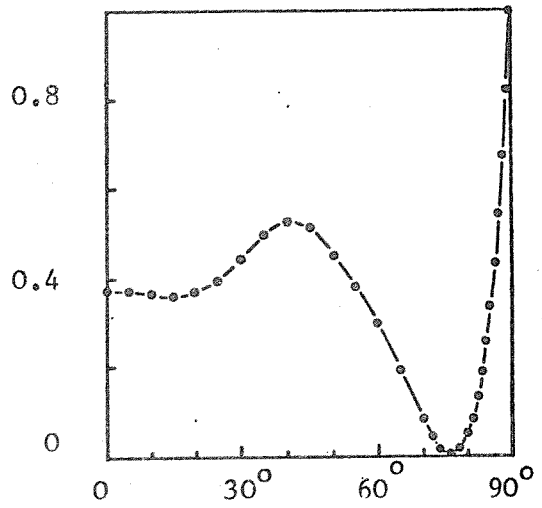

Figure 4.7(c) ka = 10
k = 10
ρ = 0.1

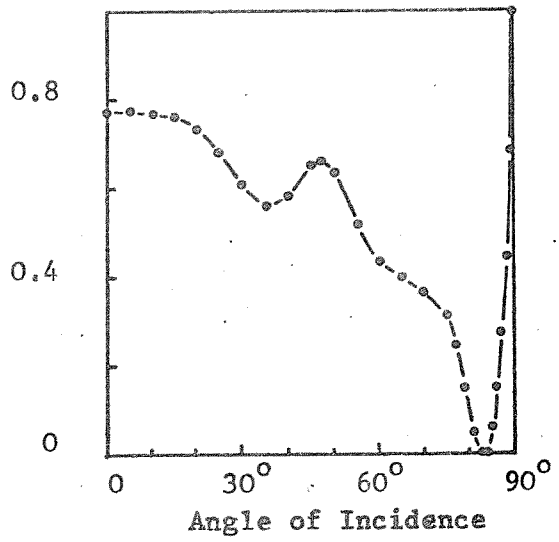

Figure 4.7. Plot of the coherent (specular) reflection coefficient R for a planar array of randomly-spaced parallel circular hemicylinders on a hard base plane. Parameter values as indicated.

the ka value determines the shape of the curve, whilst the density of the array governs the overall magnitude. The change when the density is reduced by 50% is not to double the R value, but to increase it by about 50%. Increasing the ka value (see Figure 4.7(c)) increases the number of fluctuations seen in the curve. At grazing incidence (i.e. an angle of incidence of 90° to the normal) the value of R goes to unity as predicted by the other analytic model discussed in Section 4.1.4. Although of passing interest this feature is of comparatively little practical significance since relatively few of the sound 'rays' that determine the overall level at any point will have undergone reflections with a rough surface at angles sufficiently close to grazing for this effect to be important for practical purposes. As a first approximation to the behaviour observed, therefore, some sort of weighted sine curve could well prove an acceptable estimate for the trends in the behaviour of R in the range of frequency, object size and array density studied.

Investigation of the results shown in Figure 4.8 reveals that Twersky's model predicts that a comparatively large proportion of the incoherent energy is scattered in a narrow angular range about the specular angle (in this case being, for all practical purposes, indistinguishable from the coherent and properly specular faction R). This can be seen from the existence of a 'ridge' which follows the line for which the angle of incidence equals that of observation. The angular width of the spread around the specular angle appears to be determined by the ka value, whilst the array density governs the overall magnitude. There are further small peaks in the plots of Figure 4.8 to either side of this main 'ridge', the numbers of which increase with frequency These features are in contrast to the behaviour predicted by the much simpler Lambert's law. Indeed if a fraction $(1-R)$ of the energy of a plane wave, of intensity I, incident at an angle α to the normal is assumed to be reflected according to Lambert's law, then the intensity at any observation angle θ to the normal is $I(1-R)\cos\alpha\cos\theta/\pi r^2$, where r is the distance of the observer point from the element of the surface under consideration. (Here of course θ is the polar angle of a spherical co-ordinate system, but the scattered intensity is independent of the azimuthal angle ϕ). This reflection model can be shown to satisfy the requirement for conservation of energy that,

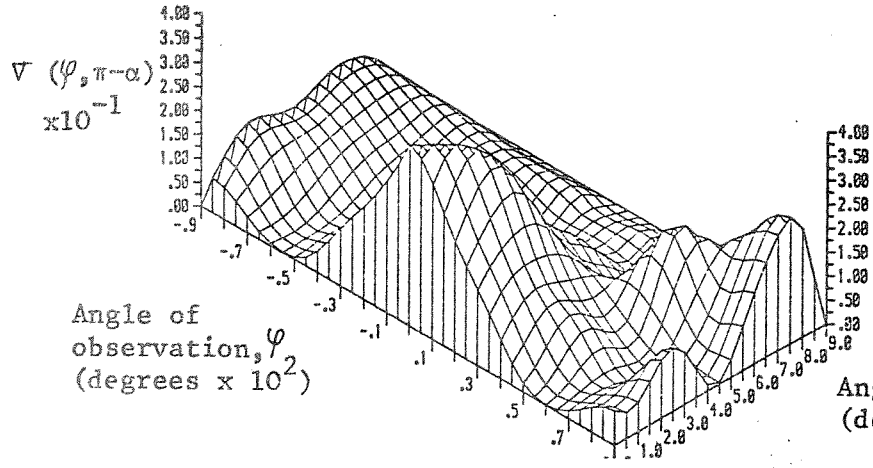

Figure 4.8(a)

ka = 5
k = 5
ρ = 0.1

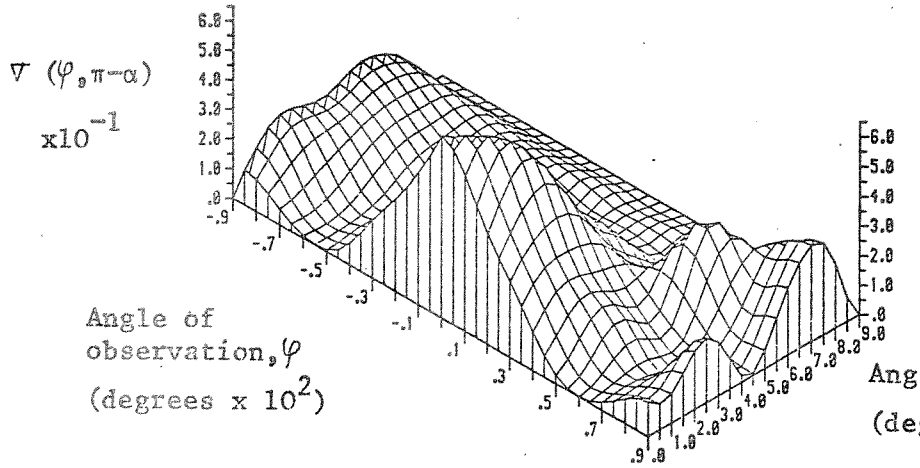

Figure 4.8(b)

ka = 5
k = 5
ρ= 0.2

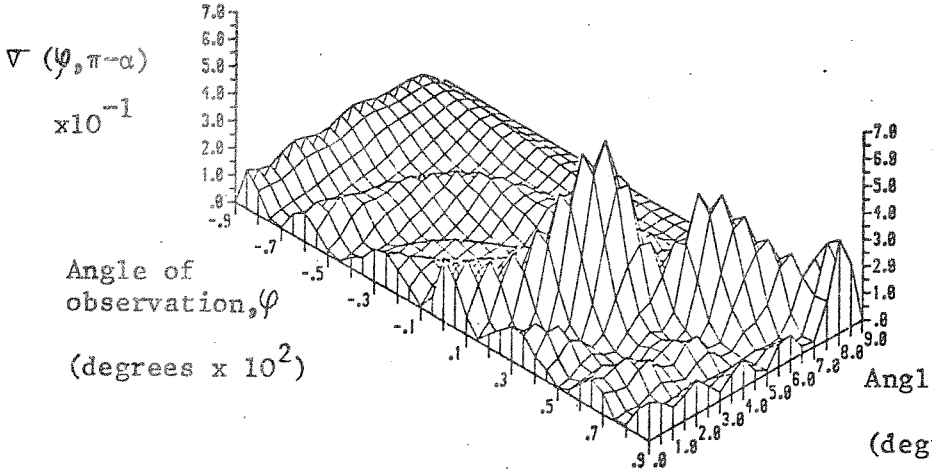

Figure 4.8(c)

ka = 10
k = 10
ρ = 0.1

Figure 4.8. Isometric plots of the distribution of the incoherently scattered energy term $\nabla(\varphi,\pi-\alpha)$ for a randomly spaced array of parallel circular hemicylinders on a hard base plane. Parameter values are as shown.

$$I\cos\alpha = IR\cos\alpha + \int_0^{\pi/2} I(1-R)\cos\alpha\sin 2\theta d\theta \quad ,$$

which can be rewritten as:

$$1 = R + \sec\alpha \int_0^{\pi/2} (1-R)\cos\alpha\sin 2\theta d\theta \quad . \qquad (4.39)$$

(This expression is valid in particular in the plane of the incident and specularly reflected wave directions, in which θ here coincides with the cylindrical polar co-ordinate systems θ used previously in the Twersky theory). Comparison of equation (4.39) with equations (4.35) and (4.36) reveals that the angular variation implicit in the analogous form of σ derived from Lambert's law is $\cos\alpha\sin 2\theta$. Thus the analogous Lambert's law σ would be largest for small α values, and values of θ close to $\pi/4$. There would also be equal amounts scattered in forwards and backwards directions. This is in marked contrast to the Twersky model, where a large amount of the incoherently scattered energy is still contained in an angular region close to the specular direction, and noticeably more energy is scattered forwards than back towards the source. Part of the difference between the results of Lambert's law and those of the Twersky model can be attributed to the fact that whilst Lambert's law produces a three-dimensional scattered field, the incoherent scattering in the Twersky model is strictly a two-dimensional phenomenon when the axes of the infinitely long cylinders are perpendicular to the plane in which θ is measured and in which the sound is incident. For cases where the incident plane wave is not perpendicular to the cylinders' axes, a three-dimensional σ would be required to take into account scattering in directions parallel to the axes as well. This would produce a σ value indicative of the energy scattered per unit solid angle. Under such circumstances the three-dimensional form of σ for the hemicylinder problem would depend upon both the directions of incidence and observation (i.e. both polar and aximuthal angular components in each case). Thus it could not be expected to resemble the rotationally symmetric three-dimensional form of σ for Lambert's law which has a $\cos\alpha\cos\theta$ form. In fact the normal incidence situation studied for the hemicylinder problem probably gives rise to the strongest

scattering effects. These can be expected to decrease as the angle of incidence becomes tangential. Thus waves at grazing incidence to the cylinders' length will hardly be scattered at all. What is possibly surprising however is the magnitude of the incoherently scattered energy in the situations studied, which correspond to comparatively sparse distributions of scatterers.

For hemicylinders of 1m radius, the ka values of 5 and 10 used to produce the results of Figure 4.8 equate to frequencies of 270 Hz and 540 Hz respectively; such frequencies are typical of those which can be reproduced in a 1/50 scale model. The array density values of 0.2 and 0.1 similarly correspond to one row on average every 5 m or 10 m respectively. Under these conditions, which may be thought of as being very broadly typical of situations such as that illustrated by the factory in the frontispiece, it would therefore appear that use of a Lambert's (or cosine) law reflection model to describe the angular distribution of reflected energy would prove inaccurate. Use of some more appropriate reflection model, such as that described here would therefore produce more accurate results at the expense of mathematical simplicity.

4.3 Conclusions

This chapter contains a relatively comprehensive survey of techniques for the inclusion of scattering effects in room acoustics models. Only two significantly different approaches were discovered that seemed applicable to the prediction of the acoustics of disproportionate or non-Sabine spaces containing scatterers. One of these models, volume scattering, has already been used in a many current room acoustics models. Its application normally suffers from a number of approximations and problems, however, such as assuming a random distribution of isotropic point scatterers throughout the entire room volume, and becoming theoretically inaccurate when the room has partially absorbent wall surfaces. The alternative approach to multiple scattering problems is to represent the scatterers attached to a surface as perturbations of that surface. There are various rough surface scattering models possible,

which involve varying degrees of complexity and related accuracy. These models would seem better suited to situations such as, for example, when the scatterers on the floor only occupy a small proportion of the total room height. Under such conditions the volume scattering approach is least appropriate. These rough surface scattering models have not been used previously to study the acoustics of disproportionate enclosed spaces.

The particular rough surface reflection model developed by Twersky has been studied. This at least partly includes multiple scattering effects and is physically realistic as the angle of incidence tends to grazing. Results, broadly illustrative of some real situations, were numerically computed. These results indicate that the coherent specular reflection coefficient can be strongly angularly dependent. However there is still a large proportion of the incoherently scattered energy contained within a comparatively narrow angular range about the specular direction in the cases studied. The angular width of this range is largely determined by the ka value whilst the ρ value governs the overall magnitude. In the cases studied it did not appear that Lambert's law was a good approximation to the behaviour predicted by the model of Twersky.

CHAPTER 4 - REFERENCES

4.1 R.K. COOK and P. CHRZANOWSKI, 1946. J. Acoust. Soc. Amer. 17, 315-325. Absorption and scattering by sound absorbent cylinders.

4.2 R.K. COOK, and P. CHRZANOWSKI, 1949. J. Acoust Soc. Amer. 21, 167-170. Absorption by sound absorbent spheres.

4.3 R.V. WATERHOUSE, 1963. J. Acoust. Soc. Amer. 35, 1610-1620. Diffraction effects in a random sound field.

4.4 J.W.M. BAARS, 1964. Acustica 14, 289-300. On the diffraction of sound waves by a circular disc.

4.5 V. TWERSKY, 1952. J. Acoust. Soc. Amer. 24, 42-46. Multiple scattering of radiation by an arbitrary configuration of parallel scatterers.

4.6 P.M. MORSE and K.U. INGARD, 1968. Theoretical Acoustics. New York : McGraw-Hill Book Company.

4.7 V. TWERSKY, 1962. J. Math. Phys. 3, 700-715. On scattering of waves by random distributions: I. Free-space scatterer formalism.

4.8 V. TWERSKY, 1973. J. Acoust. Soc. Amer. 53, 96-112. Multiple scattering of sound by a periodic line of obstacles.

4.9 T.F.W. EMBLETON, 1966. J. Acoust. Soc. Amer. 40, 667-670. Scattering by an array of cylinders as a function of surface impedance.

4.10 S. CHANDRASEKHAR, 1954.Stochastic problems in physics and astonomy in N.WAX (Editor). Selected papers on noise and stochastic processes. New York : Dover Publications.

4.11 H. KUTTRUFF, 1967. Acustica, 18, 131-143. Über Nachhall in Medien mit unregelmässig verteilten Streuzentren, inbesondere in Hallräumen unit angehängten Streuelementen.

4.12 H. KUTTRUFF, 1981. J. Acoust. Soc. Amer. 69, 1716-1723. Sound decay in reverberation chambers with diffusing elements.

4.13 S. JOVICIC, 1971. Untersuchungen zur Vorausbestimmung des Schall spegels in Betriebsgebäuden. Bericht Nr. 2151, Müller-BBN GmbH; München.

4.14 E.A. LINDQVIST, 1982. Acustica 50, 313-328. Sound attenuation in factory spaces.

4.15 R. BULLEN, 1979. J. Sound Vib. 65, 11-28. Statistical evaluation of the accuracy of predictions arising from models.

4.16 O. BSCHORR, 1977. VDI-Berichte 219, 31-37. Berechnung der Lärmverteilung in Arbeitsräumen.

4.17 C.J. HURST and L.D. MITCHELL, 1978. Computer-aided noise prediction: Final report on an investigation into the prediction of noise levels in manufacturing areas. Dept. of Mech. Eng., Virginia Polytechnic Institute and State University.

4.18 S. CZARNECKI and E. KOTARBINSKA, 1977. Archives of Acoustics 1, 269-298. Properties of acoustic barriers in a field of reflected waves.

4.19 R.J. BERACHA, 1980. Acustica 44, 330 - 332. Sound reduction by barriers in rooms.

4.20 R. POMPOLI, 1977. Internoise 77 Conference Proceedings (Zurich, Switzerland) B97-B103. Noise reduction by barriers in rooms.

4.21. H. KUTTRUFF, 1976. Room Acoustics. London : Applied Science Publishers Ltd.

4.22 W.B. JOYCE, 1975. J. Acoust. Soc. Amer. 58, 643-655. Sabine's reverberation time and ergodic auditoriums.

4.23 M.M. CARROLL and C.F. CHIEN, 1977. J. Acoust. Soc. Amer. 62, 1442-1446. Decay of reverberant sound in a speherical enclosure.

4.24 M.M. CARROLL and R.N. MILES, 1978. J. Acoust. Soc. Amer. 64, 1424-1428. Steady-state sound in an enclosure with diffusely reflecting boundaries.

4.25 R. GERLACH, 1975. The reverberation process as Markhoff Chain : Theory and initial model experiments, in R. MACKENZIE (Editor) Auditorium Acoustics. London : Applied Science Publishers.

4.26 E. KRUZINS and F. FRICKE, 1982. J. Sound Vib. 81, 549-564. The prediction of sound fields in spaces by a 'random-walk' approach.

4.27 W.B. JOYCE, 1978. J. Acoust. Soc. Amer. 64, 1429-1436. Exact effect of surface roughness on the reverberation time of a uniformly absorbing spherical enclosure .

4.28 C.F. CHIEN and M.M. CARROLL, 1980. J. Acoust. Soc. Amer. 67, 827-829. Sound source above a rough absorbent plane.

4.29 H.G. DAVIES, 1978. J. Acoust. Soc. Amer. 64, 517-521. Multiple reflection diffuse-scattering model for noise propagation in streets.

4.30 P. BECKMANN and A. SPIZZICHINO 1963. The Scattering of Electromagnetic Waves from Rough Surfaces. Oxford : Pergammon Press.

4.31 E.O. LACASCE and P. TAMARKIN, 1956. J. Appl. Phys. 27, 138-148. Underwater sound reflection from a corrugated surface.

4.32 LORD RAYLEIGH, 1896. The Theory of Sound. London : MacMillan and Company.

4.33 L. FORTUIN, 1970. J. Acoust. Soc. Amer. 47, 1209-1228. Survey of the literature on reflection and scattering of sound waves at the sea surface.

4.34 A. WIRGIN, 1980. J. Acoust. Soc. Amer. 68, 692-699. Reflection from a corrugated surface.

4.35 J.L. URETSKY, 1963. J. Acoust. Soc. Amer. 35, 1293-1294. Reflection of a plane sound wave from a sinusoidal surface.

4.36 A. DE BRUIN, 1971. Acustica 24, 75-84. Anomalous effects in sound absorption of periodically uneven surfaces.

4.37 A. DE BRUIJN, 1967. Acustica 18, 123-131. The sound absorption of an absorbing periodic surface of rectangular profile.

4.38 V. TWERSKY, 1957. J. Acoust. Soc. Amer. 29, 209-225. On Scattering and reflection of sound by rough surfaces.

4.39 J.E. BURKE and V. TWERSKY, 1966. J. Acoust. Soc. Amer. 40, 883-895. Scattering and reflection by elliptically striated surfaces.

4.40 LORD RAYLEIGH, 1907. Phil. Mag. 14, 350-359. On the light dispersed from fine lines ruled upon reflecting surfaces or transmitted by very narrow slits.

CHAPTER 5

THE ACOUSTICAL ABSORPTION CHARACTERISTICS OF MODERN LIGHTWEIGHT BUILDING CONSTRUCTIONS

5.1 Introduction

5.1.1 Background:

Many modern building shells make use of lightweight construction techniques. These structures are normally composed of essentially plane surfaces which consist of arrays of rectangular panels. These are generally supported along their edges, where they meet adjacent panels. Such arrays may consist of either single or double layers of panels. When the double thickness construction is used, the space between the inner and outer surfaces may either contain air or some lining material, which is normally chosen for its thermal insulation properties. Typical of single layer panel arrays are the glass walls often found for example in public buildings, swimming pools or offices, whilst the double panel arrangement is more usual for the construction of factory or warehouse roofs and walls. In these cases the panels are typically made from either asbestos, or more recently P.V.C.-clad steel. For these double panel arrays, the outer surface is often corrugated, whilst the inner one is flat.

Consideration of the interiors of the buildings in which these panel structures occur reveals that they may well contain little absorption on any of the other surfaces. Thus if these panel arrays do noticeably absorb sound, their behaviour could well control the acoustics of the building they enclose. Furthermore, since the shape of buildings such as factories is often highly disproportionate, it seems unlikely that a statistically diffuse sound field will exist in their interiors. It is therefore necessary to establish whether the absorption characteristics of these panel array structures are likely to be strongly dependent upon the angle of sound incidence.

In order to establish the degree to which any of the above points are covered in the published literature, a review was performed, the results of which are contained in the next section. The implications of the published results for this research programme are discussed in Section 5.1.3.

5.1.2 *Survey of the literature on the absorption characteristics of lightweight building shell structures*

Little information is available in the standard building acoustics texts on the measured absorption characteristics of lightweight building shell materials, such as surfaces constructed from glass, asbestos, or PVC-clad steel sheets. Of these three materials, glass sheeting is the best documented. However, there is often no indication of either the thickness or size of the panel tested, or how it was mounted. All three of these factors undoubtedly effect the acoustic absorption. Lewis [5.1] has presented diffuse field absorption coefficient results for a glass pane of dimensions 1.25 m × 0.85 m × 0.003 m , although he stated that 0.004 m and 0.006 m thicknesses are standard. Parkin, Humphries and Cowell [5.2] have given values for the diffuse field absorption coefficient for these thicknesses, but do not indicate the size of sheet tested. The results from References [5.1] and [5.2] are plotted in Figure 5.1.

PVC-clad steel is a relatively recent industrial building material Reports of diffuse field tests on an extensive range of configurations of sheets and lining materials have been given by Friberg [5.3 and 5.4]. The magnitude of the possible absorption is great, with absorption coefficients of about unity in certain frequency bands. However, Friberg concluded that there is no simple way of characteristing their performance. Surprisingly, the absorption characteristics of the more 'old-fashioned' asbestos roofing sheets appears much less well documented. Before the start of this research programme no information was readily available. As part of the current SERC-funded research into the scale modelling of factory acoustics it was therefore found necessary to perform absorption measurements for this type of structure (see Reference [5.5]). The tests were performed on a 2.03 m × 2.44 m sample which consisted of two panels, one corrugated, the other essentially flat. The sample was placed in the opening between reverberant and anechoic chambers, with the flat (inner) panel facing into the reverberant environment. Standard absorption coefficient tests were then performed in the reverberation chamber and the results are presented in Figure 5.2, for two configurations, one with 0.019 m spacers between the panels, the other without such spacers.

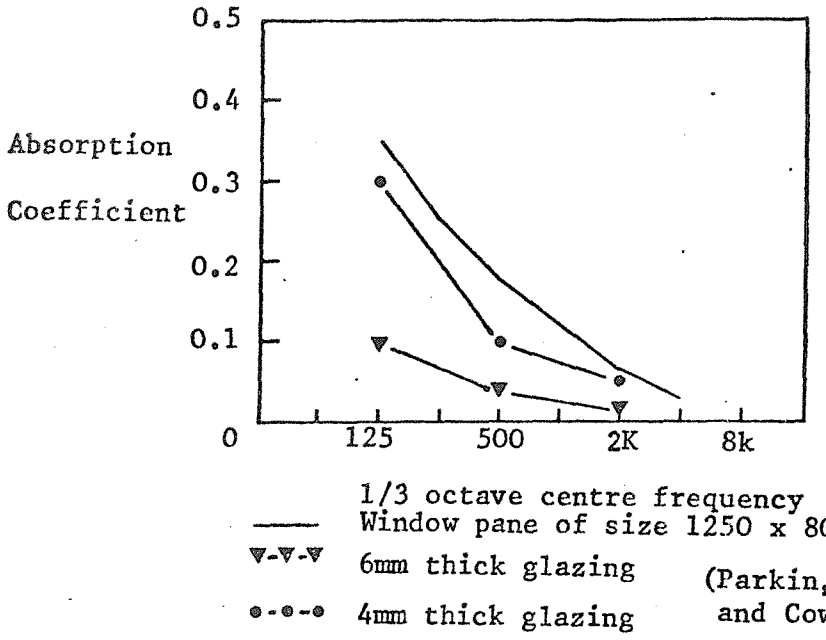

Figure 5.1 Variation of the absorption coefficient of glazing with frequency.

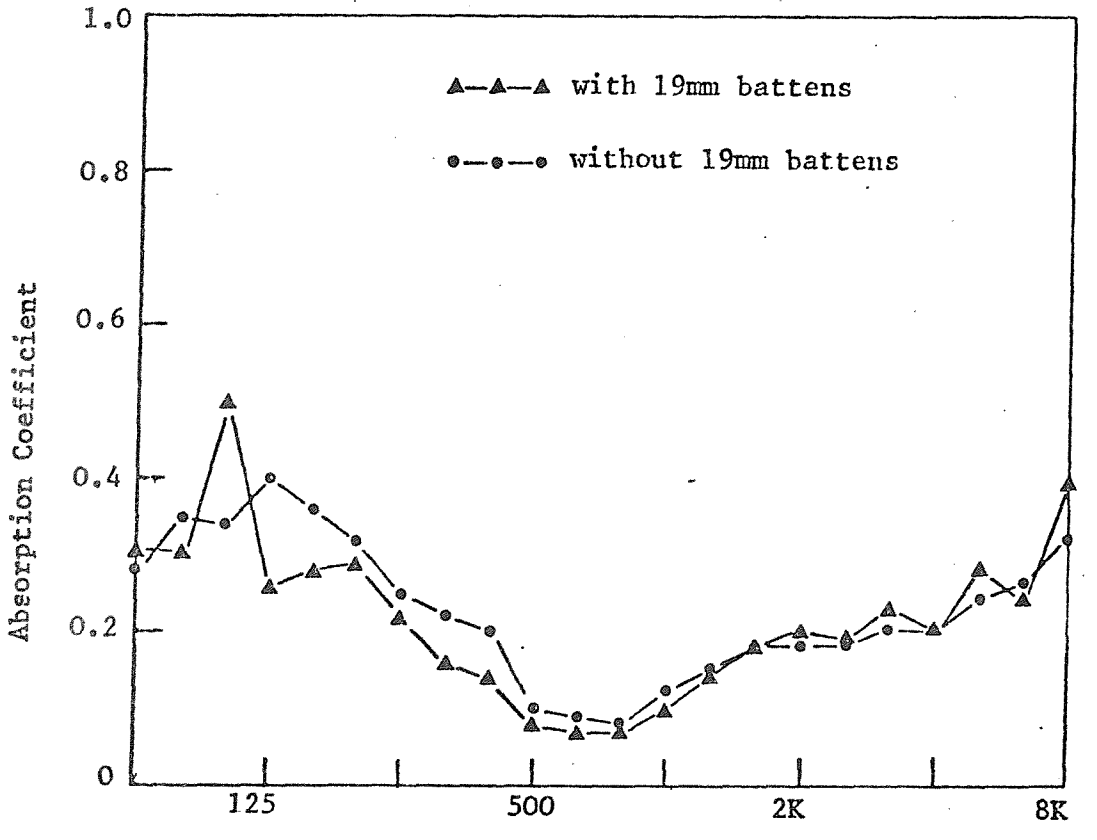

Figure 5.2 The experimentally measured absorption coefficient of asbestos roofing (from Reference [5.5]). With and without spacing battens between the outer, (corrugated) and inner (lining) panels.

It is apparent from the published results [5.3, 5.4, 5.5] that the acoustical absorption of these double panel constructions can be very significant.

The survey of the literature on experimental results indicated that there is a large body of work on the transmission loss of panels, such as glass. Unfortunately, these cannot be converted directly into absorption values, since the absorption coefficient applicable to room acoustics predictions represents the sum of the energy both transmitted and dissipated by the panel structure. A review of the published theoretical work on the acoustics of panel structures revealed a similar preponderance of papers concerned with transmission loss. However, it is often possible to use the analytic techniques described to evaluate a structure's absorption coefficient. Since there appear to be experimental values for diffuse field conditions, but not for the variation with plane wave angle of incidence, it is this latter case which will be one of the prime concerns in assessment of the theories. This is because the buildings where these panel structures occur are often not statistically acoustically diffuse. Once the variation of the plane wave absorption coefficient with angle of incidence has been established, it is comparatively easy to ascertain the diffuse field value. The literature reviewed below therefore does not cover all the theoretical methods used to model sound transmission, or absorption, by multiple panel constructions. Any specific areas omitted will be indicated in the text.

The earliest papers on sound transmission by double panel constructions cover only infinite panels. The two original solution methods appear to be those due to Beranek and Work [5.6] and London [5.7]. Beranck and Wak considered the case of two or more infinite plates separated by one of more spaces, which may contain either air, or some 'flexible blanket',for the case of a normally incident plane wave. The solution method is based upon an 'impedance transfer' technique. This method shows that pressures either side of a partition are related by the ratios of the two impedances there; whilst pressures across an air space or porous blanket can be determined from a transfer of impedance derived from one dimensional wave theory. Thus Beranek and Work were able to evaluate the transmitted wave in terms of that incident. They could have equally well progressed from the expression for the normal

impedance of the front surface to a value for the reflection coefficient for the whole system, and hence obtained an 'absorption' coefficient (which includes both the transmitted and dissipated energy). Apparently the only report of application of this technique to the prediction of absorption coefficients is due to Tseo [5.8], who estimated the transmission, reflection and absorption of sample structures for a normally incident plane wave.

London [5.7] used a different approach to estimate the diffuse field transmission loss of two infinite plates, separated by an air space, although in principle this method can be extended to any number of panels. The method essentially consists of expressing the wave field in each air-filled section in terms of plane waves of unknown amplitudes, for a given incident plane wave. Application of velocity continuity across the partitions, and the known impedance conditions there, allows the $2N$ simultaneous equations that are set up to be solved (N equals the number of partitions in the system). Once the transmission loss, $\tau(\theta,\omega)$, for a particular angle of incidence θ has been calculated, it is then simply a matter of integrating over angle to obtain the diffuse field value, according to the expression:

$$\bar{\tau}_{diff}(\omega) = \frac{\int_0^{\theta_2} \tau(\theta,\omega)\cos\theta\sin\theta d\theta}{\int_0^{\theta_2} \cos\theta\sin\theta \ d\theta} \ , \qquad (5.1)$$

where θ_2 is the limiting angle beyond which no sound can arrive. London used 90^o for θ_2 but some other authors (see for example References [5.9] and [5.10]) have preferred to use a value between 75^o and 85^o. Using this technique London obtained good agreement with experimental results. However, Mulholland, Parbrook and Cummings [5.9] have indicated that London's impedance term contains a resistance factor, R, which they disputed, alleging that "he introduced this term to align the theoretical values of transmission loss with the measured values. There appears to be no other reason for the introduction of the R term, nor any physical process that would necessitate its introduction". They presented an alternative model based upon ray theory. In this model, an incident ray at a panel is partly specularly reflected and partly transmitted, the amount transmitted being deduced from mass law.

The sum of the transmitted rays' amplitudes follows a geometric progression which can be summed to obtain a value in agreement with Beranek and Work's results. This method was extended to finite panels in Reference [5.10]. In the extended model, rays which pass through a panel are still attenuated by a mass law determined factor, but any arriving at the partitioning between two panels at their edges are assumed to be absorbed by a certain amount.

The final addition to the published multiple infinite panel transmission loss theory came from Mulholland, Price and Parbrook [5.11], who modified the Beranek Work method to cover non-normal angles of incidence, and then performed a numerical integration of equation (5.1) to obtain a diffuse field value.

In the consideration of the behaviour of finite panels statistical energy analysis (SEA) is commonly used. A description of the application of this method to the prediction of transmission loss of multiple panel systems is contained in Reference [5.12]. This technique requires a high modal density in each portion of the system and is hence really only suited to the prediction of high frequency transmission loss measurements, especially in transmission suites. It is thus inappropriate to the case considered here as, amongst other problems, it cannot provide predictions of the plane wave angle of incidence absorption characteristics.

There are a number of multi-mode matching approaches to the problem of a cavity-backed single or double panel structure, which typifies the case of a room behind a window (see, for example Reference [5.13]). These will not be explicitly considered as a modal model for a large room is out of the question at realistic frequencies, and only one panel can be considered. The cases of sound transmission through both single and double finite panels in infinite surrounds have been considered by Sewell [5.14, 5.15]. Unfortunately, the presence of an infinite surround makes the models rather more appropriate for the prediction of laboratory tests than for the field behaviour of the type of structures considered here, where a whole surface is composed of these finite panels.

The only other type of model possible relies on the surface being adequately large, and possessing a regularly repeated panel structure, in order that one can use the simplifying assumption of infinite periodicity. An example of the use of this assumption is the paper by Lin and Garrelick [5.16]. They solved the problem of two infinite plates connected by identical periodically spaced frames, and thus compared the strengths of the two transmission paths (i.e. the structural path through the studding, and the airborne one through the cavity space). Their model is somewhat restricted however since they only considered infinite plate behaviour, and only allowed standing waves between the front and back panels. However the idea of using the infinite periodicity of the structure to simplify the problem is otherwise very attractive.

5.1.3 Implications of the literature review.

Although there does not appear to be much experimental data available on the absorption characteristics of arrays of glass, PVC-clad steel, or asbestos sheets, that which is, although only measured on comparatively small samples indicates that the diffuse field absorption coefficient can be fairly high. This is particularly significant at low frequencies where the panel surfaces are likely to be the major absorbers in the buildings where they occur. The insertion of insulation material raises the level of absorption at the higher frequencies. There do not appear to have been any tests of the variation of this absorption with angle of incidence, since the majority of the tests were designed to measure transmission loss under diffuse field conditions. Unfortunately, experimental transmission loss cannot be converted directly into absorption coefficient values, since the latter also include any energy dissipation effects.

The theoretical models are similarly concentrated on the prediction of transmission loss. However, although virtually no-one has published calculated absorption values, it is in principle possible to obtain these from a number of the theories developed. Of these, that due to Beranek and Work [5.6] is probably the most versatile, especially with the ammendments proposed by Mulholland, Price and Parbrook [5.11]. No-one appears to have used this approach to calculate the diffuse field absorption coefficients of such structures.

An investigation as to whether these simple infinite plate models can match observed diffuse field absorption values would therefore seem to be extremely worthwhile. If such a model can duplicate this diffuse field behaviour, it can then also be used to provide information on the variation of the plane wave absorption coefficient with angle of incidence. However, if this simple model proves unrealistic, it may than be necessary to proceed to a more advanced model. In this case, one possibly is to use the regularly repeated arrangement of the panels in the real structure to simplify the problem.

In the next section, the development of the infinite plate absorption models, based on the 'impedance transfer' technique is described. Values typical of some of the materials under consideration will then be inserted in the derived expression in order to calculate the diffuse field behaviour. These results are then compared with the published data.

5.2 *Theoretical Model for the Absorption of Sound by Multiple Infinite Panel Structures*

5.2.1 *Determination of the acoustic impedance of an infinite panel for an incident plane wave*

Before any theoretical model of a composite structure can be considered, the behaviour of the fundamental components must be well understood. In this case the impedance of a single infinite plate is therefore studied. The geometry to be investigated is shown in Figure 5.3.

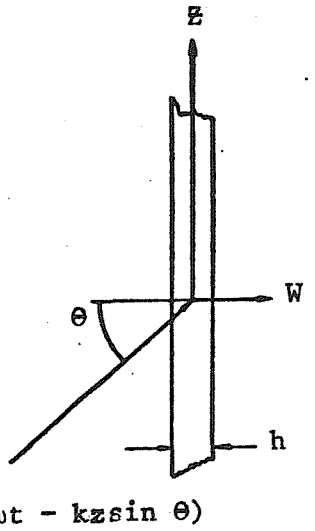

Figure 5.3 The Infinite Plate Geometry.

For any point on the plate shown in Figure 5.3, for plane wave incidence, the equation of motion is:

$$\left(D(1+i\eta)\partial^4/\partial z^4 + M_s\partial^2/\partial t^2\right)\underline{W} = \underline{P}oe^{i(\omega t - kz\sin\theta)} \qquad (5.2)$$

where $\underline{W}$ is the plate displacement, M_s is the plate's mass per unit area, η the loss factor for the material (i.e. the fraction of the total energy of vibration dissipated per radian) and D is the bending stiffness. For a flat isotropic plate, this last term is given by the expression $Eh^3/12(1-\nu^2)$, where E and ν are the material Young's modulus and Poission ratio values respectively and h the plate's thickness.

The surface velocity of the plate must follow the incident field in time and space; therefore the plate's normal velocity can be assumed to have a form $\dot{\underline{W}}_o e^{i(\omega t - kz\sin\theta)}$. Thus equation (5.2) may be rewritten as

$$\dot{\underline{W}}_o\left(D(1+i\eta)k^4\sin^4\theta - M_s\omega^2\right) = i\omega\underline{P}_o \quad . \qquad (5.3)$$

The plate's impedance is simply the complex ratio of pressure to normal velocity at its surface. From equation (5.3) it is obvious that this can be written as

$$Z_W(\theta) = \eta A + j(\omega M_s - A) \quad , \qquad (5.4)$$

where

$$A = Dk^4\sin^4\theta/\omega \quad .$$

Equation (5.4) gives the (*in vacuo*) normal acoustic impedance of an infinite flexible partition for a plane wave pressure distribution on it, incident at an angle θ to the normal. It can be seen to have a minimum value when ωM_s equals A. Under these conditions the impedance is entirely resistive and its value is determined by the loss factor term, ηA. The lowest incident frequency at which this resonant behaviour can occur is given by $\omega = 2\pi f_c = c^2\sqrt{M_s/D}$. This happens when θ equals 90^o, and f_c is termed the panel's critical frequency. For frequencies well below this value the impedance will be mass-controlled. However, for frequencies greater than critical there will always be some angle of incidence for which ωM_s can equal A; this condition occurs at the so-called 'coincidence' frequency. Thus in a diffuse field,

both stiffness and mass terms must be retained. The expression for $Z_W(\theta)$ will be used as a basic component for the construction of a multiple infinite panel absorption model in the next section.

5.2.2 *Details of the double infinite plate absorption model.*

The aim of this section is to establish the absorption coefficient 'seen' by an incident wave at an angle θ to the normal at interface 1 in Figure 5.4, and hence evaluate the diffuse field value.

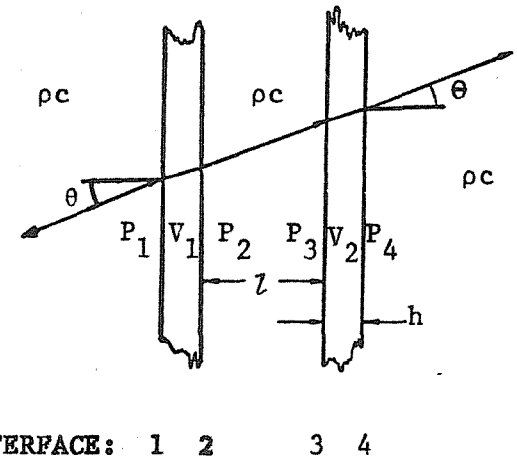

Figure 5.4 Double Infinite Plate Absorption Model Geometry

In order to predict the absorption values, the surface normal impedance at interface 1 must first be established. This can be done by use of an 'impedance transfer' technique similar to that of Beranek and Work [5.6]. For any generalised multi-panel system of the kind shown in Figure 5.4, the impedance must be transferred either across partitions or air-spaces. To obtain the impedance on one side of a component panel given a value for the other side, it is simply a matter of adding the **normal** impedance of the panel (in vacuo) to that on the other side (taking care to ensure that 'normal' velocities are always taken in the same direction). This can be seen from consideration of the force balance across panel 2 in Figure 5.4, whence at any point

$$P_3 = P_4 + Z_{W2}(\theta)\, V_{2n} \qquad (5.5)$$

where V_{2n} is the normal particle (and hence plate velocity at interfaces 3 and 4) and $Z_{W2}(\theta)$ is the normal impedance of plate 2 as defined by equation (5.4) . Since there is continuity of velocity across the panel,

division of equation (5.5) by V_{2n} results in

$$Z_3 = Z_4 + Z_{W2}(\theta) = \rho c/\cos\theta + Z_{W2}(\theta) \quad . \qquad (5.6)$$

In order to transfer impedances across an airspace, one dimensional standing wave theory can be used. For instance, to evaluate the impedance at interface 2 ('looking right') of Figure 5.4, given the value at interface 3, one may write (see Reference [5.19])

$$Z_2(\theta) = (\rho c/\cos\theta)\left[\coth(jk\ell\cos\theta+\psi_2)\right], \qquad (5.7)$$

where ψ_2 equals $\coth^{-1}(Z_3\cos\theta/\rho c)$. In order to now calculate the normal impedance at the front surface for the whole structure it only remains to add the (in vacuo) normal impedance of panel 1 (from equation (5.4)) to the value of $Z_2(\theta)$ (from equation (5.7)).

The general method can be applied to sequentially transfer acoustic impedance across any combination of infinite panels separated by air spaces. The method can be extended to cover situations where there are 'flexible blankets' (i.e. porous materials) in between the panels, the major changes being to alter the values of ρc and k in the cavity. This also causes the angle at which the sound leaves the first panel and enters the next panel to differ from the angle of incidence, θ , for angles other than normal. These effects have been considered by Beranek and Work [5.8] for normal incidence, and Mulholland, Parbrook and Price [5.11] for oblique incidence.

Now that the front surface impedance of the complete structure has been formulated, the next step is to use this to evaluate an equivalent reflection coefficient. It can be shown (see for example Reference [5.17]) that for any impedance surface with a plane wave incident at an angle θ, the pressure reflection coefficient $R(\theta)$, may be written as

$$R(\theta) = (\zeta_n(\theta)\cos\theta-1)/(\zeta_n(\theta)\cos\theta+1),$$

where $\zeta_n(\theta)$ is the specific normal acoustic impedance of the surface (here equal to $Z_1(\theta)/\rho c$). It is now possible to obtain the plane wave

absorption coefficient for the whole structure from the expression

$$\alpha(\theta) = 1 - |R(\theta)|^2 \quad . \tag{5.8}$$

The method outlined above enables the calculation of the absorption coefficient to be made, for any combination of infinite panels and airspaces for a given plane wave angle of incidence. However, to permit comparison with laboratory-measured results, a diffuse field value is required. This can be calculated by use of Paris' formula, which states (see for example Reference 5.18):

$$\alpha_{diff} = 2 \int_0^{\pi/2} \alpha(\theta) \cos\theta \sin\theta d\theta \quad . \tag{5.9}$$

where the integration is generally most easily performed numerically. Further integration of equation (5.9) over a frequency band, and subsequent normalisation by the bandwidth, allows the final evaluation of theoretical 1/3 octave (or octave) diffuse field absorption coefficients for any multiple infinite panel - air cavity structure. The only requirements for the implementation of this model are the panels' physical constants (i.e., Young's modulus, surface density, and loss factor) and the geometry of the situation (i.e. inter-panel spacing, and panel thicknesses). The determination of these constants and some resultant computations are described in the next section.

5.2.3 Use of the infinite panel - airspace model to predict the absorption of an asbestos roof construction

In order to use the simple model of section 5.2.2 to predict the absorption of a double panel asbestos roof, it is necessary to know the mass per unit area, bending stiffness and loss factor typical of the materials. Since the back panel is corrugated, whilst the model can only accommodate plane surfaces, it will be modelled as being flat, but with altered mass per unit area and bending stiffness. Little published information was available for asbestos sheeting, so measurements were performed on samples similar to the material of the sheets used to obtain the experimental absorption values of Figure 5.2.

The ratio of the measured mass to surface area for the flat panels gave a mass per unit area of 12.09 kg/m^2 . The effective increase in mass for the corrugated panel was estimated from the increase in surface area due to the corrugations, which were assumed sinusoidal, of period 0.145 m and amplitude 0.027 m. This produced an effective surface density (i.e. mass/projected area normal to surface) of 15.72 kg/m^2. The thickness of the material used to make both sheets was measured as 0.006 m , which was in agreement with the manufacturer's data.

In order to measure the Young's modulus (which is necessary in order to calculate the bending stiffness), and the loss factor, a 0.67 m × 0.027 m × 0.006 m sample of asbestos material was suspended horizontally from a rig in the laboratory, by two thin nylon lines. An accelerometer (Brüel and Kjaer type 4344) was attached to this beam by means of beeswax, and the output fed via a charge amplifier (Brüel and Kjaer Type 2635), into a Hewlett Packard Digital Signal Analyser (Type 5420). The beam was then excited impulsively with a small hammer, and the accelerometer's output stored in the signal analyser. Subsequent analysis of the results in the frequency domain revealed at which frequencies the beam's first few resonant modes occurred. The first beam mode was found to be at 46.9 Hz, the second at 125 Hz, and the third at 250 Hz. Insertion of these frequencies and the other relevant parameter values into equation (5.1.20) of Reference [5.19] permitted evaluation of the Youngs modulus. The first three modes resulted in Young's modulus values of 5.23×10^7 kN/m^2; 4.89×10^7 kN/m^2; and 5.09×10^7 kN/m^2 respectively. Thus a value of 5×10^7 kN/m^2 will be used in the results presented.

In order to determine the loss factor as a function of frequency, measurements of the vibration decay rate were necessary in various frequency bands. The centre frequencies of these bands were chosen to coincide with where the vibration response had been seen to be a maximum in the earlier inspection of the frequency domain results. This choice ensured the existence of a good signal to noise ratio for all the tests performed. The bandwidth of the filter used in each case was designed to be narrow enough to pick out a single peak in the frequency domain, but not so narrow as to 'ring' and obscure the decay of the beam's vibration after impulsive excitation. With the chosen filter ready, the beam was again impusively excited and the transient decay

in this frequency band recorded. Measurement of the decay rate of the vibration record, and substitution in the equation $\eta = 2.2/f_n T_{60}$, where f_n is the band's centre frequency, and T_{60} is the time taken for the vibration level to decay by 60 dB (see Reference [5.20] for more details), enabled an evaluation of the loss factor, η, to be made in the chosen frequency band. This sequence was repeated for ten more frequencies below 2.5 kHz, and the calculated results for the loss factor of the asbestos specimen are shown in Figure 5.5 as a function of frequency.

The general form for the bending stiffness of any isotropic flat plate is $D = EI/(1-\nu^2)$, where E and ν are the plate material's Young's modulus and Poisson ratio respectively, and I is the second moment of area about the neutral axis, (for a thin isotropic plate, this is given by $d^3/12$ per metre length). The value of Poisson's ratio remains to be found for the material. An investigation of the literature revealed no published data on this value, and the manufacturers were similarly unable to help. It was not felt to justify measurement, since all materials must possess values between 0.0 and 0.5, and most structural engineering materials' ν values are in the close proximity of 0.3. Also, compared to some of the other assumptions contained in the derivation of this model, a small discrepancy in the value of ν will be insignificant since it occurs in the bending stiffness expression as a factor $(1-\nu^2)$. A value of ν equal to 0.3 was therefore used in all the results presented.

In order to implement the model, it only remains to estimate the bending stiffness of the corrugated backplate. For this type of structure, the bending stiffness is obviously dependent upon the direction in which bending occurs. Such plates are termed 'orthotropic', and the mathematical description of their vibrational behaviour is complicated (see for example Reference [5.21]). For simplicity in this model, the backplate was modelled as a flat plate, but with its bending stiffness altered to account for the corrugations. A number of cases were considered with different values of bending stiffness for the backplate. Two of the values used are 0.75 and 31 times the front plate's bending stiffness; these values are bending stiffnesses for a sinusoidally corrugated plate, of 'period' 0.146 m and amplitude 0.027 m, bent across

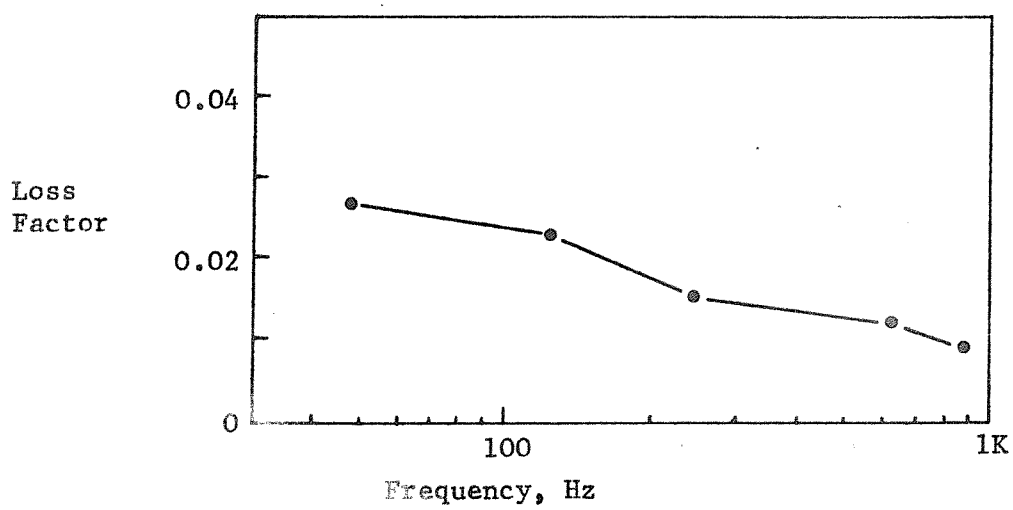

Figure 5.5 The loss factor η for asbestos sheeting, measured from beam tests in the laboratory, as a function of frequency.

the corrugations and along the corrugations respectively. These values were obtained from the equations of Article 86 in Reference [5.21]. Originally it was intended to model the increase in the backplate's bending stiffness as due to the change in its second moment of area about the neutral axis for bending along the corrugations. Unfortunately the original calculations of this factor were incorrect, and estimated a multiplication factor of 140 to be applied to the front plate's bending stiffness value. Subsequent examination of the manufacturer's data revealed the error and produced a multiplication factor of 96. Results based on all of these multiplication factors are presented.

Physical considerations indicate that the bending stiffness 'seen' by a wave incident at a corrugated plate will be markedly larger than that for a flat plate, except for polar angles of incidence lying close to the plane crossing the corrugations at right angles, since it is only for these angles that there is not even one complete corrugation cycle included in the calculation of the relevant moment of area per metre length. Thus as a first order model, the results with any of the stiffer backplates will probably provide a better indication of the adequacy of the approach, but results for all the stiffness parameters indicated above for the back panel are included to illustrate the physics of the situation.

All the parameter values necessary to use the double infinite panel - airspace model of section 5.2.2 to estimate the absorption of asbestos roof constructions have thus been determined. A computer program was written to evaluate the diffuse field absorption coefficient according to equation (5.9). Two different numerical integration schemes were used to evaluate the integral in this equation; the first employed a Simpson's rule formulation, the second a 10 point Gaussian integration scheme in which the integration interval was split in two and the integration performed, each component interval was then split into two and the integration performed once more, this process was repeated until the results of two successive calculations of the complete integral were found to be within 0.1% of each other. In order to estimate an effective 1/3 octave diffuse field absorption coefficient a single 10 point Gaussian integration scheme was then used to integrate the results obtained by the second angular integration method over a 1/3 octave band and the results of the integration over frequency were then normalised by the 1/3 octave bandwidth.

The variation of the 1/3 octave diffuse field absorption coefficients with frequency is shown in Figure 5.6. The single frequency absorption coefficient's variation with angle of incidence is shown in Figure 5.7. Discussion of the main features of these plots is contained in the next section.

5.2.4 Discussion of the infinite plate absorption model results

The results shown in Figure 5.6 illustrate the effects of changes in the back panel's bending stiffness, both panels' loss factors, and the inter-panel spacing. From the results it is evident that for the range of material properties and geometry parameters investigated, over the frequency range 40 Hz to 4 kHz there are three major causes of absorption. At very low frequencies (less than 100 Hz for the results shown) there is a general decrease in absorption with increased frequency. It is assumed that at these low frequencies the two panels' vibration is roughly in phase, and they behave rather like a single panel. Thus in this regime the main 'absorption' phenomenon will be due to transmission through the structure, which will be mass controlled (see Reference [5.20], Section 11.2). From the 'mass' law', the transmission loss is predicted to decrease by 6 dB per doubling of frequency. This would equate to a factor of four decrease in the absorption coefficient, whereas the results of Figure 5.6 indicate a decrease between the 50 Hz and 100 Hz 1/3 octaves by a factor of between 2.5 and 3.0. This suggests that either the panels do not behave exactly like a single unit or that the stiffness term in the impedance does have a noticeable effect even at frequencies below the plate's critical frequency.

The next feature evident in all the plots of Figure 5.6 is the absorption peak in the 160 Hz 1/3 octave band for the results with 0.03 m inter-panel spacing (see Figure 5.6, except 5.6(f)) and the 125 Hz band for configurations with 0.05 m interpanel spacing (see Figure 5.6(f)). This absorption peak is attributable to the fundamental mass-air-mass resonance of the systems invstigated, which occurs at a frequency which can be predicted by modelling the system as two masses connected by a spring. For a structure composed of two identical

Figure 5.6 Plots of the diffuse field 1/3 octave absorption coefficients, estimated from the double infinite plate model. Parameter values: M_{s1} = 12.09 kg/m^2; M_{s2} = 15.72 kg/m^2; D_1 = 989 kg/m^2 (the inter-panel spacing (RL), loss factor (LF) and back panels bending stiffness (D_2) are indicated on the individual figures).

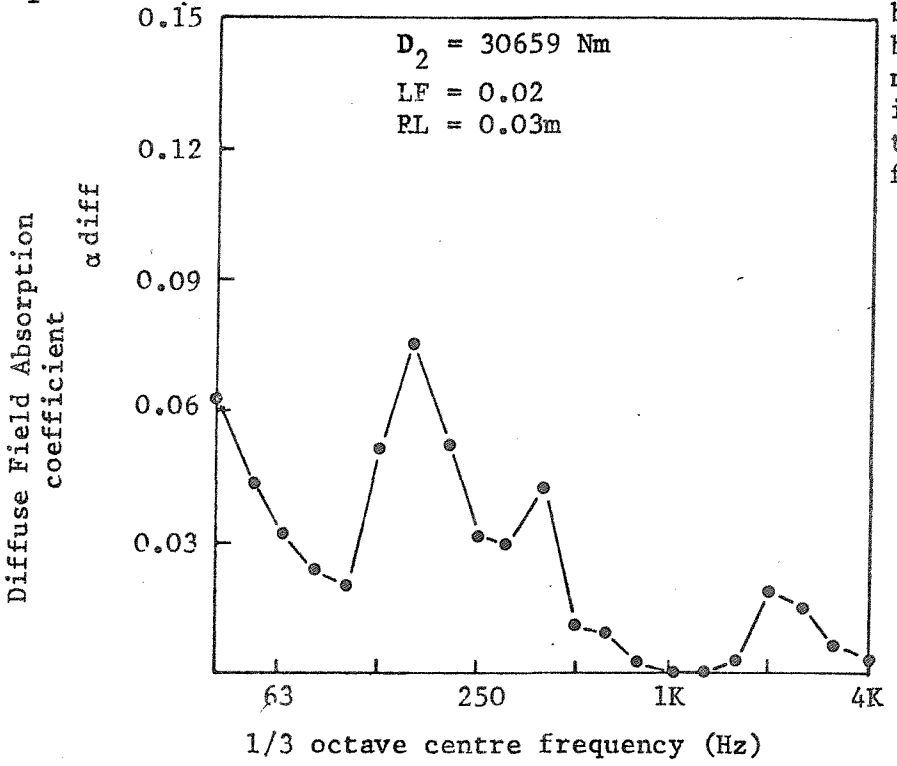

Figure 5.6(a)

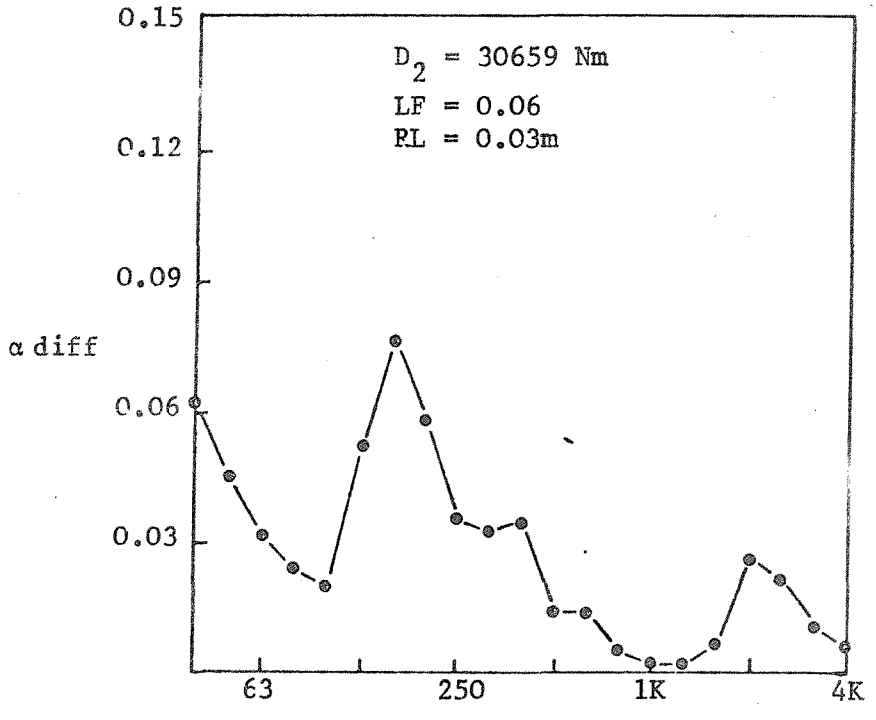

Figure 5.6(b)

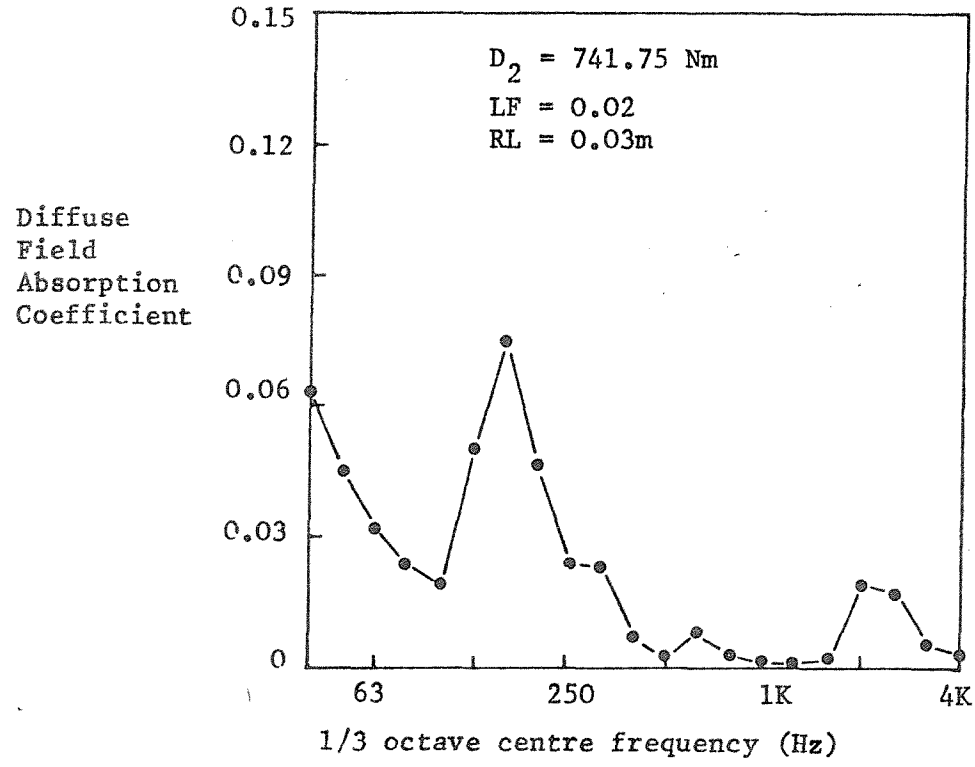

Figure 5.6(c)

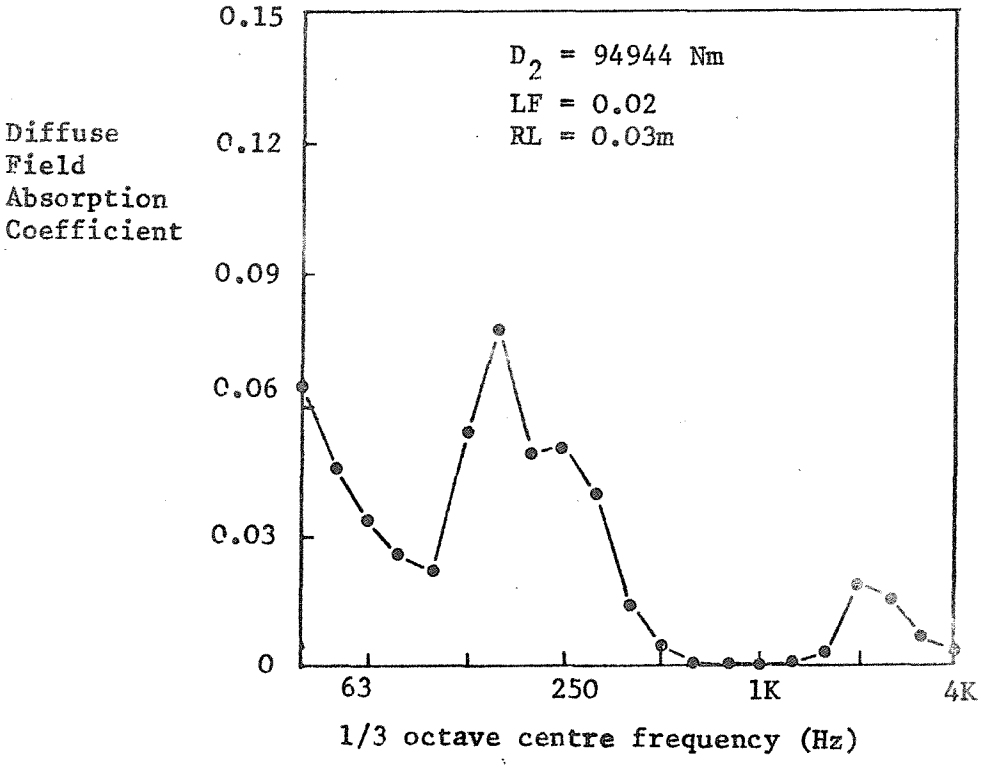

Figure 5.6(d)

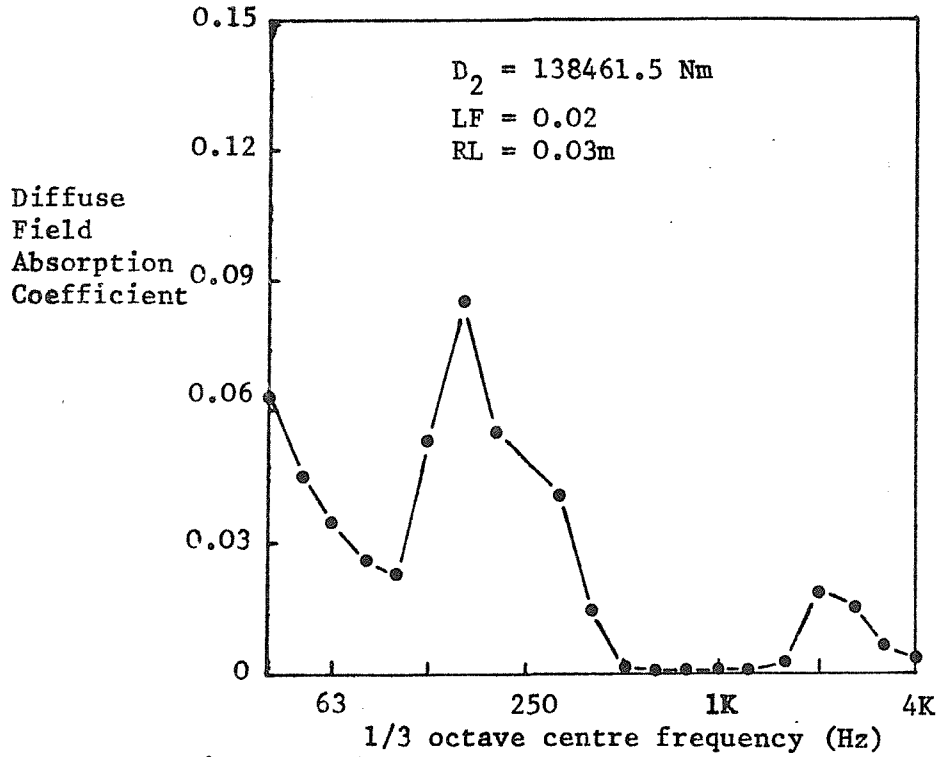

Figure 5.6(e)

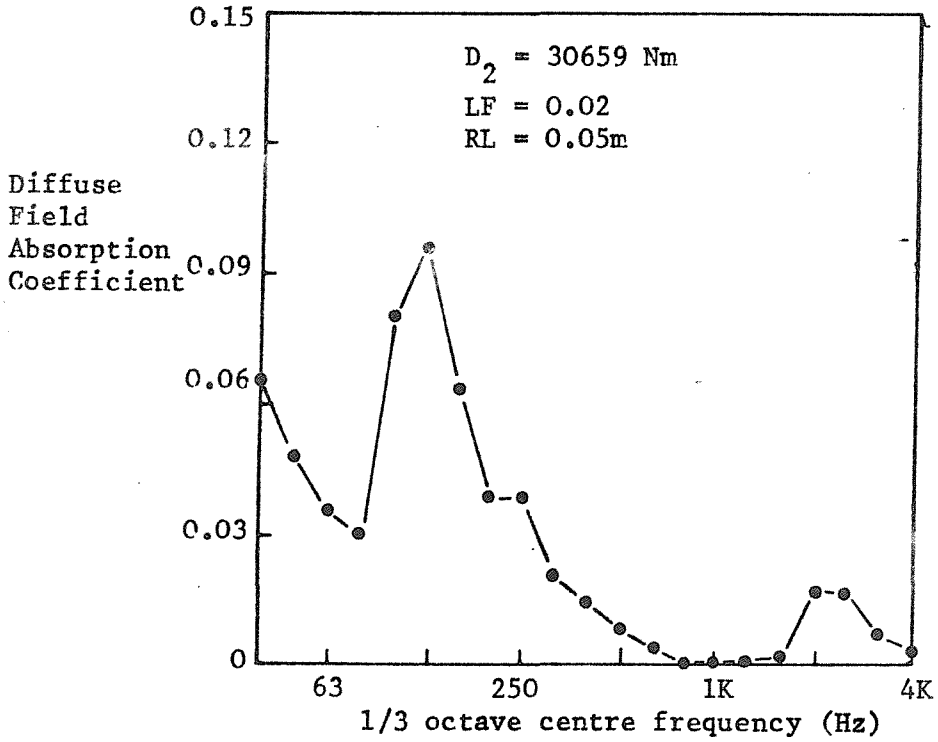

Figure 5.6(f)

panels similar to the front panel here, it is easy to calculate the frequencies at which this behaviour would occur for normally incident sound (see Reference [5.20], equation 11.72); they are 140 Hz for the 0.03 m interpanel spacing and 109 Hz for the 0.05 m spacing. These estimated frequencies tally reasonably closely with the results in Figure 5.6. The fact that the shape of this absorption peak is virtually unchanged by alteration of the back plate's stiffness or loss factor substantiates the hypothesis that this absorption maximum is due to the mass controlled, mass-air-mass resonance.

The third predictable 'absorption' mechanism is that due to 'coincidence' effects (see Section 5.2.2). These occur when the incident field's projected wavelength onto the surface equals the wavelength of the free bending waves in the panel. Under such conditions the plate's impedance is purely resistive, and its *in vacuo* response is only limited by its loss factor. Since the frequency for which a plate's behaviour becomes critical is inversely related to its bending stiffness, in all the plots of Figure 5.6, except for Figure 5.6(e), absorption effects due to coincidence at the backplate will occur at lower frequencies than those due to the frontplate. For a backplate 31 times stiffer than the frontplate (i.e. the backplate's bending stiffness per metre, D_2 = 30659 Nm) the critical frequency f_c = 417 Hz; for the 0.75 times stiffer case (D_2 = 741.75 Nm), f_c = 2.68 kHz; for the 96 times stiffer case (D_2 = 94944 Nm), f_c = 237 Hz; and for the 140 times stiffness increase (D_2 = 138461 Nm), f_c = 196 Hz. The critical frequency of the frontplate (D_1 = 989 Nm) occurs at 2.03 kHz.

Inspection of Figures 5.6(a) and (b) reveals that there are small absorption peaks in the 400 Hz and 2 kHz 1/3 octave bands, and that their levels are slightly altered by a change in loss factor, unlike the other two absorption phenomena discussed. These values agree well with the predicted critical frequencies of the back and front plates respectively. In all the plots of Figure 5.6 an absorption peak, presumably due to coincidence effects at the front plate, can clearly be seen in the 2 kHz 1/3 octave. Absorption peaks due to concidence effects at the backplate are not so evident in all cases; there are various possible reasons for this. For example, it may well be obscured

by some more pronounced absoprtion effect since its behaviour is inter-linked with that of the mass-controlled front plate under most of the cases shown in Figure 5.6(d). Thus, although there is a small peak in the 250 Hz 1/3 octave band of Figure 5.6(d), care should be taken before automatically assuming that this is due to the backplate's critical frequency (f_c = 237 Hz), since there are also slight peaks in the 315 Hz and 630 Hz bands of Figure 5.6(c), where no coincidence effects could exist. Thus there are obviously other interaction effects between the two panels which do give rise to absorption, albeit in comparatively small quantities.

The effect of an increase in the interpanel spacing (compare Figures 5.6(a) and (f)), is to decrease the frequency of the mass-air-mass resonance, and to apparently reduce to insignificance the effect of any absorption peak due to coincidence at the backplate. The peak in the 250 Hz band cannot be due to coincidence, since it is below the backplate's critical frequency. Since this peak occurs at about twice the fundamental mass-air-mass resonance frequency, it was hypothesised to be a 'second harmonic' of the fundamental. Unfortunately however, inspection of its angular variation (see below for general discussion on absorption variation with angle of incidence) revealed no peak at normal incidence where such an effect would have been visible. Thus this 250 Hz peak must be assumed to be due in some more complicated manner to the interaction between the two panels.

The results so far discussed have indicated that in the frequency range of interest, and for the parameter values chosen, three distinct causes of absoprtion can be observed. Unfortunately, however, the absorption levels predicted are far too small when compared to the experimental results of Figure 5.2, even though a range of 'physically realistic' parameter values has been investigated. Some other explanation of the acoustic absorption mechanism of real asbestos roof structures must therefore be sought, but before the model is abandoned, its predictions for the variation of absorption coefficient with angle of incidence will be studied. These are shown in Figure 5.7.

It is immediately obvious from inspection of the plots of the absorption coefficient's angular variation that the absorption mechanism of this model is very 'highly tuned', with very high levels of absorption possible over very limited angular ranges for a given frequency. At frequencies below the major mass-air-mass resonance, the only significant absorption occurs for angles of incidence close to grazing (i.e. near 90^{o}, as in Figure 5.7(a)), when it approaches unity. This behaviour is inherent to this model, since at grazing incidence there is no incident velocity, but there is an incident pressure. Since normal velocities are matched at the surfaces of the panels, there cannot be any plate motion or particle velocity normal to the plate's rear surface. The only way in which this can be achieved is to balance the pressure across the panel, which can be realised by the presence of an identical wave to that incident travelling behind the plate. This therefore appears as perfect transmission and hence the model predicts an absorption coefficient of unity. Whether or not the model is 'correct' in this limit is immaterial to the present discussion for two reasons: Firstly, it is physically impossible to exactly reproduce these conditions in real life, and secondly, because one is at present interested primarily in the calculation of diffuse field absorption coefficient values, the importance of any contributions from near 90^{o} is severely reduced in such calculations by the presence of a $\sin 2\theta$ weighting term in the integral to be performed (see equation (5.9)).

The mass-air-mass resonance discussed in connection with the 1/3 octave diffuse field results above, appears first at normal incidence (see Figure 5.7(b)). Since it is primarily the ratio of the projected wavelength (normal to the surface) to the inter-panel spacing which governs this behaviour, the absorption peak therefore moves towards grazing angles of incidence as the incident frequency is increased. This behaviour can be seen from comparison of Figures 5.7(b) and 5.7(c). As might be expected from the above argument, an increase in the inter-panel spacing has the effect of increasing the angle at which the mass-air-mass resonance is observed for a given frequency, as is seen from comparison of Figures 5.7(c) and (d).

Figure 5.7 The variation of the absorption coefficient with angle of incidence for the double infinite plate model. Parameter values: M_{s1} = 12.09 kg/m^2; M_{s2} = 15.72 kg/m^2; D_1 = 989Nm. (The inter-panel spacing (RL) loss factor (LF), back-plate bending stiffness (D_2) and frequency (F) are indicated on the individual figures).

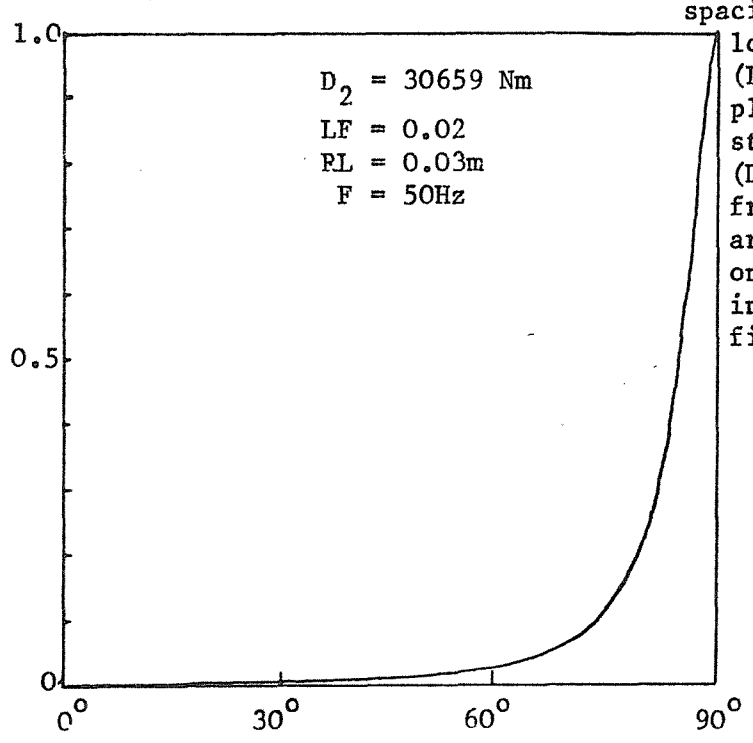

Figure 5.7(a)

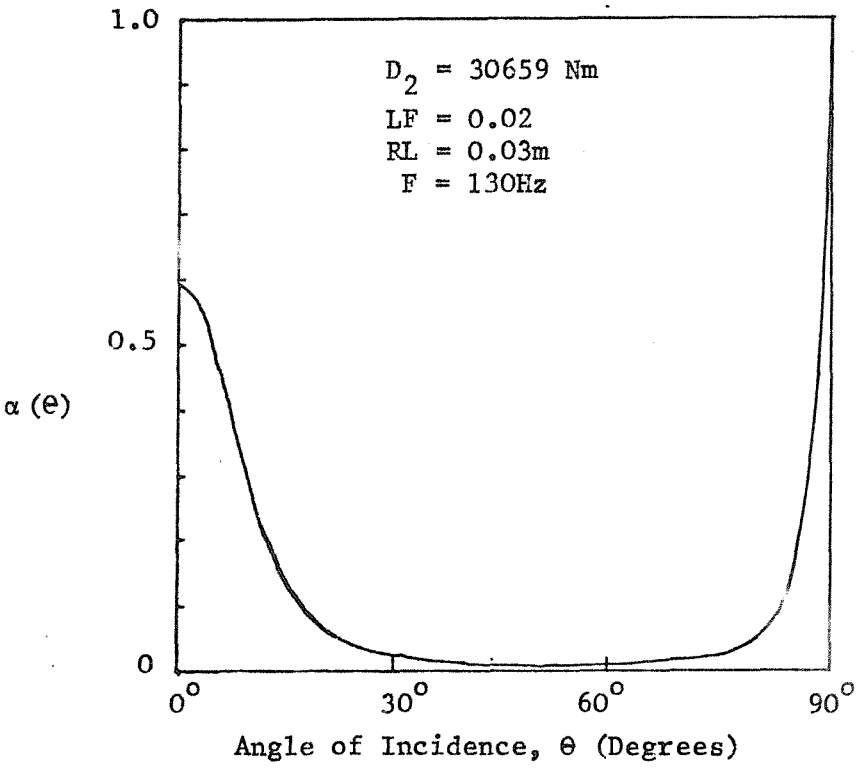

Figure 5.7(b)

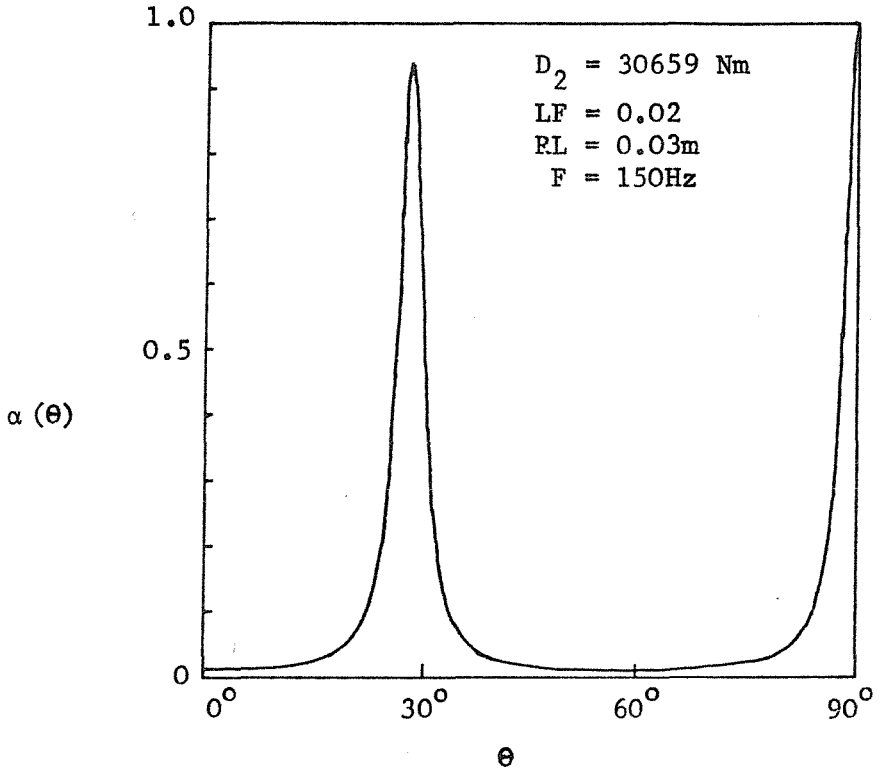

Figure 5.7(c)

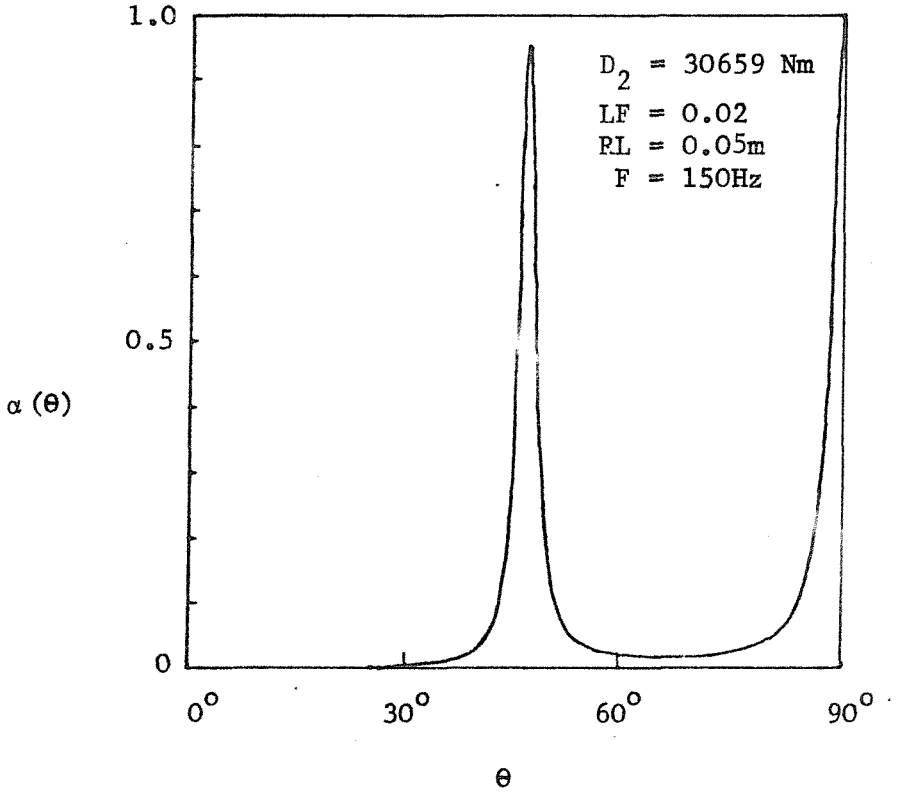

Figure 5.7(d)

In contrast to the mass-air-mass resonance, the absorption due to coincidence behaviour should appear initially at grazing incidence and move towards normal incidence with increased frequency. This is because 'coincidence' occurs when the incident wavelength projected onto the surface equals the wavelength of a free bending wave travelling in the infinite panel. Unfortunately, it is relatively hard to see the detailed characteristics of any absorption peak caused by coincidence effects at the backplate since it is at a comparatively low level and tends to be obscured, if not even actually altered, by the behaviour of the still mass-controlled front panel. However its presence is discernible in the results shown in Figure 5.7(e) since the peak at around 65° moves towards normal incidence with increased frequency, as was predicted for absorption characteristics governed by coincidence effects. Although this absorption maximum is smaller than those which occur at other frequencies for angles nearer to normal or grazing incidence, this peak will be comparatively strongly weighted in the computation of diffuse field values due to the effective $\sin 2\theta$ factor in equation (5.9).

At slightly higher frequencies the main absorption peak continues to move towards grazing. This is shown for 600 Hz in Figure 5.7(f), where a further small absorption peak (probably due to coincidence type behaviour at the backplate) can still be seen at around 55°. The main absorption peak then remains at about 80°, but diminishes in magnitude with increased frequency until the critical frequency of the front plate is reached. At this point the major absorption peak then starts to move towards normal incidence as was predicted above. Results for two frequencies above the critical frequency of the frontplate are shown in Figure 5.7(g). For very high frequencies this simple model would appear to be unable to predict any absorption, and surface absorption effects would need to be considered. However, at present one is primarily interested with low frequency absorption characteristics, that is, for frequencies less than 1 or 2 kHz. From the results discussed it would appear that the angular dependence of the absorption coefficient of a structure that did absorb sound in the manner predicted by this model could be very pronounced in this frequency range. Thus its overall behaviour might well be different in statistically diffuse (Sabine) and 'non-Sabine' spaces, and a knowledge of its angular

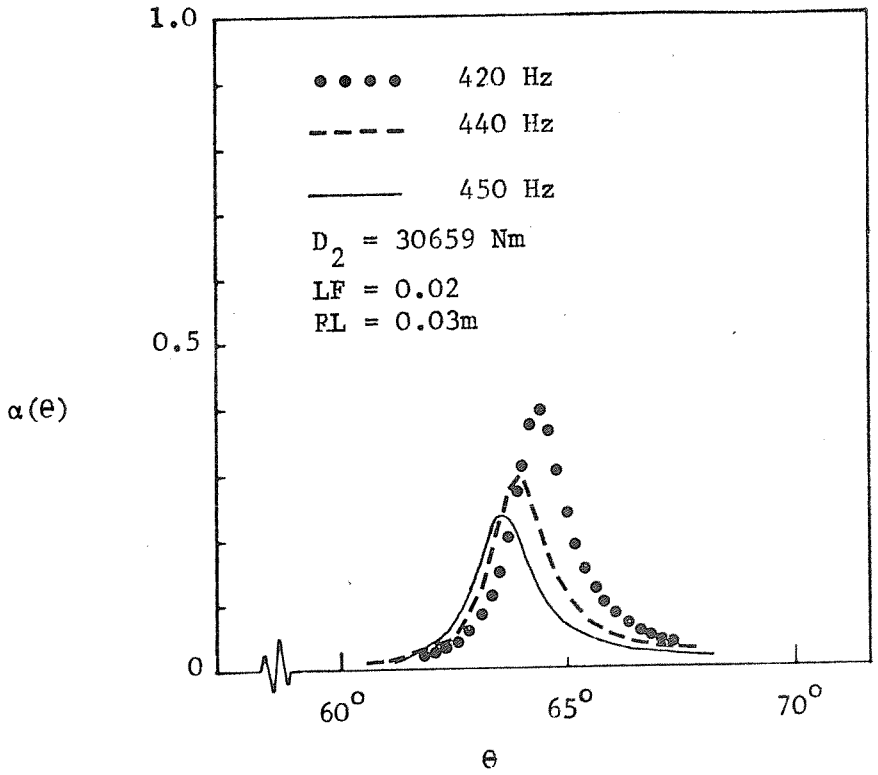

Figure 5.7(e)

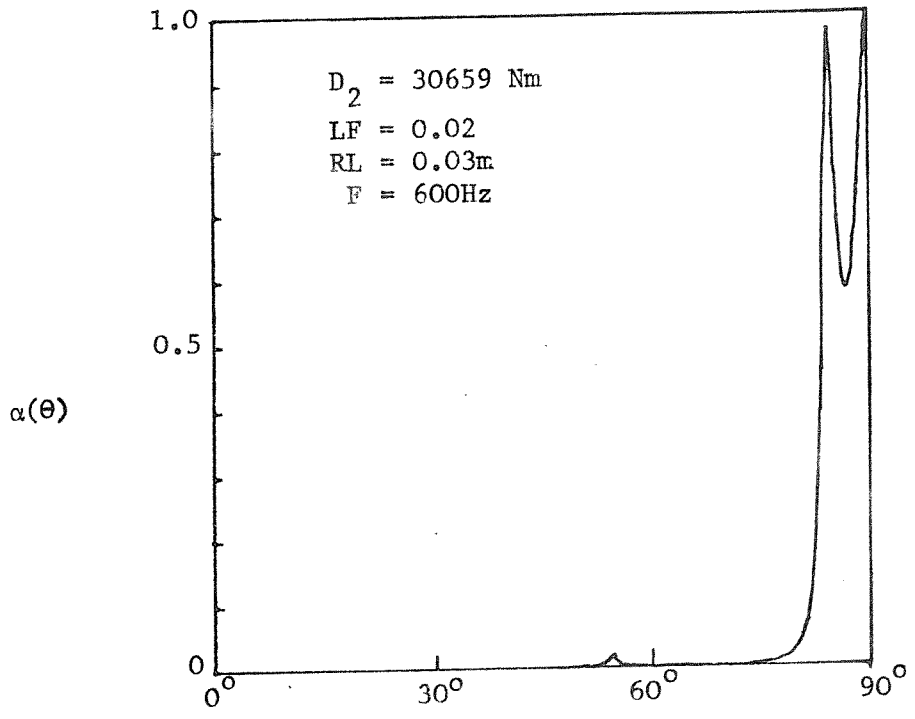

Figure 5.7(f)

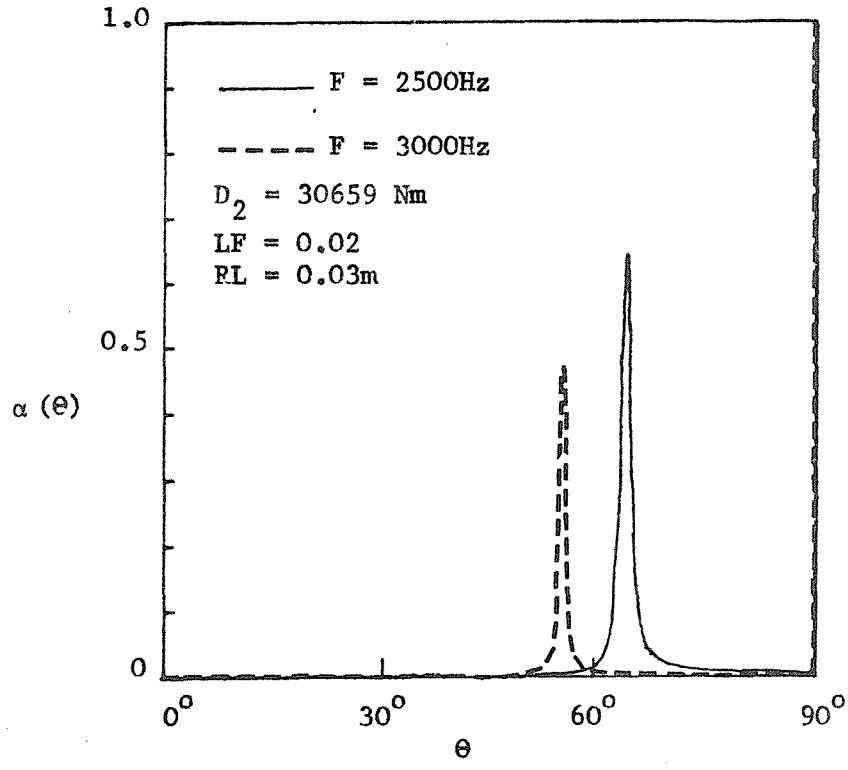

Figure 5.7(g)

dependence could therefore be very important in any predictions made. Unfortunately however this model does not appear to be an adequate representation of the absorption mechanism of a double panel asbestos roof structure, since the 1/3 octave diffuse field predicted absorption values are far too small. Thus an alternative model is considered in the next section.

5.3 Theoretical Model for the Absorption of Sound by Arrays of Finite-Sized Panels.

5.3.1 Introduction:

The results of the previous section indicated that the simple model derived was unable to reproduce the magnitude of the published experimentally measured absorption values when physically realistic values were used for the material's physical constants and geometry in the equations developed. Some alternative explanation of the major absorption mechanism must therefore be sought. One of the principle defects of this model lies in the fact that it is assumed that the plates behave as if infinite. Now, since the component panels in the real structure are typically 1.5 m × 1 m in size, it is unlikely at these low frequencies of interest that the individual panels will appear infinite to the incident sound field. In this section, therefore, a model is developed for the absorption behaviour of plane surfaces which are constructed of finite-sized panels, in single or double layer arrays. Some of the results have already been described in Reference [5.22].

5.3.2 The acoustic impedance of a single finite plate:

In a similar manner to that in which the impedance of a single infinite plate was studied in section 5.2.1 prior to its use in the development of the absorption model, the acoustic impedance of a single finite plate will now be examined. Although the new expression will not be of such direct use in construction of an expression for the absorption behaviour, it will nevertheless demonstrate some of the characteristic differences between the two cases, and prove to be of general service in the formulation of the problem.

For a thin rectangular plate of lengths a and b in the x and y directions respectively, the equation of free vibration is basically the same as for the infinite plate case, except that x and y 'gradients' must be considered since the problem is now essentially two-dimensional. This gives

$$D(1+i\eta)\left(\partial^4 W/\partial x^4+\partial^4 W/(\partial x^2\cdot\partial y^2)+\partial^4 W/\partial y^4\right) + M_s \partial^2 W/\partial t^2 = 0 \ , \tag{5.10}$$

where the symbols have the same meanings as previously. The major difference for the case of a finite plate is that equation (5.10) must now satisfy a series of boundary conditions along the edges at $x = 0, a,$ and $y = 0, b$. These boundary conditions determine the form of the characteristic functions $\psi_\mu(x)$ and $\psi_\nu(y)$ in the generalised expression for the displacement,

$$W(x,y) = \sum_\mu \sum_\nu W_{\mu\nu}\psi_\mu(x)\psi_\nu(y) \quad . \tag{5.11}$$

For a plate that is simply supported along all its boundaries, the required boundary conditions are that the bending moment and displacements should be zero at all its edges. It is well known (see for example References [5.23] and [5.24]) that in this case the problem can be solved exactly, to give,

$$W(x,y) = \sum_{\mu=1}^{\infty} \sum_{\nu=1}^{\infty} W_{\mu\nu}\sin(\mu\pi x/a)\cdot\sin(\nu\pi y/b) \quad . \tag{5.12}$$

Each term in this infinite series will satisfy equation (5.10), provided that its component frequency, $\omega_{\mu\nu}$, is given by

$$\omega_{\mu\nu} = \sqrt{D/M_s}\ \left((\mu\pi/a)^2 + (\nu\pi/b)^2\right) \quad . \tag{5.13}$$

Thus, one has an expression for the displacement of a finite plate that is simply supported at all its edges, in free vibration, and has also discovered the resonant frequencies of its modes. Warburton [5.24] has further demonstrated that it is possible to derive approximate expressions of the form of equation (5.11) for any mixed combination of boundary conditions, composed of any one or two of simply supported, free,

or clamped types of edge condition, although the forms of the functions ψ_μ and ψ_ν will not generally be as simple as in equation (5.12). Thus, although only the case of a simply supported plate is considered explicitly in this section, there is no limitation of the general method developed to these simple boundary conditions alone.

The case of forced vibration of a simply supported finite plate by an incident sound field will be considered next. In this case, the pressure distribution at the surface can be represented in terms of orthogonal functions across the plate. If the orthogonal functions chosen are the same as the plate's x and y eigenfunctions, then any unknown surface pressure distribution, $P(x,y)$, can be written as:

$$P(x,y) = \sum_{\mu} \sum_{\nu} P_{\mu\nu} \psi_\mu(x) \cdot \psi_\nu(y) \qquad (5.14)$$

multiplication of both sides of this equation by the orthogonal functions ψ_μ, and ψ_ν, and integration with respect to x and y over the intervals 0 to a, and 0 to b, respectively results in the following form for each of the $P_{\mu\nu}$ coefficients:

$$P_{\mu\nu} = \frac{\int_0^a \int_0^b P(x,y)\psi_\mu(x)\psi_\nu(y)\,dxdy}{\int_0^a \psi_\mu^2(x)\,dx \int_0^b \psi_\nu^2(y)\,dy} .$$

Thus it is possible to write the equation of forced vibration of any thin flat finite plate, in terms of orthogonal functions ψ_μ and ψ_ν as

$$\left\{D(1+i\eta)\nabla^4 + M_s \partial^2/\partial t^2\right\} \sum_{\mu} \sum_{\nu} W_{\mu\nu}\psi_\mu\psi_\nu = \sum_{\mu} \sum_{\nu} P_{\mu\nu}\psi_\mu\psi_\nu , \qquad (5.16)$$

From which, upon substitution of the relevant forms of ψ_μ and ψ_ν, it is possible to evaluate a plate 'modal impedance' (i.e. the ratio of pressure to velocity for one specific μ,ν combination). To demonstrate this for the case of a simply supported plate, one can rewrite equation (5.16) as

$$\sum_{\mu}\sum_{\nu}\left\{D(1+i\eta)\nabla^4-M_s\omega^2\right\}W_{\mu\nu}\sin k_\mu x\sin k_\nu y = \sum_{\mu}\sum_{\nu}P_{\mu\nu}\sin k_\mu x\sin k_\nu y \quad ,(5.17)$$

where $k_\mu = \mu\pi/a$ and $k_\nu = \nu\pi/b$. Thus, with an assumed $e^{i\omega t}$ time factor, the modal impedance for a simply supported finite plate with an arbitrary surface pressure distribution can be defined as:

$$\begin{aligned} Z_{\mu\nu} &= P_{\mu\nu}/i\omega W_{\mu\nu} \\ &= \left(D(1+i\eta)(k_\mu^2+k_\nu^2)^2-M_s\omega^2\right)/i\omega \end{aligned} \qquad (5.18)$$

where the $P_{\mu\nu}$ terms are obtained from equation (5.15) upon substitution of $\sin k_\mu x$ and $\sin k_\nu y$ for ψ_μ and ψ_ν respectively. Although the form of this impedance is broadly similar to that of the infinite plate seen in Section 5.2.1, it is quite different in detail. For example, the frequency at which a given modal impedance term becomes purely resisitive is given by $\omega = (k_\mu^2+k_\nu^2)(D/M_s)^{\frac{1}{2}}$; furthermore, below this frequency the individual modal impedance terms will be stiffness controlled, whilst above it, the behaviour is determined by the mass. This is the reverse of the infinite plate's impedance behaviour. It will also be observed that there can be an infinite number of these impedance minima, each one corresponding to a particular μ,ν plate mode. This becomes more obvious when the overall response of the simply supported plate at any point $W(x,y)$ is considered. This gives:

$$\begin{aligned} W(x,y) &= \sum_{\mu=1}^{\infty}\sum_{\nu=1}^{\infty}\frac{P_{\mu\nu}\sin k_\mu x\sin k_\nu y}{\{D(1+\eta)(k_\mu^2+k_\nu^2)^2-M_s\omega^2\}} \\ &= \sum_{\mu=1}^{\infty}\sum_{\nu=1}^{\infty}P_{\mu\nu}\sin k_\mu x\sin k_\nu y/i\omega Z_{\mu\nu} \quad , \end{aligned} \qquad (5.19)$$

whence the maximum plate response is seen to occur for minimum plate modal impedance, but also to be a function of $P_{\mu\nu}$, which indicates how closely matched to a given plate mode shape the surface pressure field is. For the case of an extremely large plate the modal impedance term approximates to $i\omega M_s$, and the behaviour is once more mass-controlled as was observed at low frequencies for the infinite plate model. However, for most real finite-sized plates a number of damping-controlled plate resonances may occur at various frequencies below the critical frequency of the infinite plate, and there will usually be some stiffness controlled and some mass controlled plate modes in any situation.

Now that the acoustical behaviour of simply supported isotropic finite plates has been studied, a model can be constructed to predict their absorption characteristics when combined in either single or multiple layer arrays and exposed to an incident wave field. Here only the case of a double layer array exposed to incident plane waves will be specifically considered.

5.3.3 *Model for the absorption of sound by an infinite array of regularly repeated, double layer of simply supported finite panels.*

In this section, sound absorption by an array composed of finite sized panels that extends to infinity in all directions will be considered. The justification for the treatment of such a structure is that the surfaces which are constructed in this manner often are extremely large (see for example the roof in the frontispiece illustration); allied to this is the fact that the side walls of a room will often be hard, which allows the roof structure to be imaged in these walls, and thus appear infinite, although in such cases the image source waves must also be considered. The advantages of consideration of such a structure are great, since because of the periodic nature of the surface, the acoustic field can be assumed to be similarly periodic. Thus in the method described here the field in each region under consideration is expanded in terms of infinite series of orthogonal functions, and then both velocity boundary conditions and the equations of motion at the front and backplates are applied, in order to obtain expressions for the coefficients in the series expansions in terms of the incident field.

The basic geometry considered is illustrated in Figure 5.8.

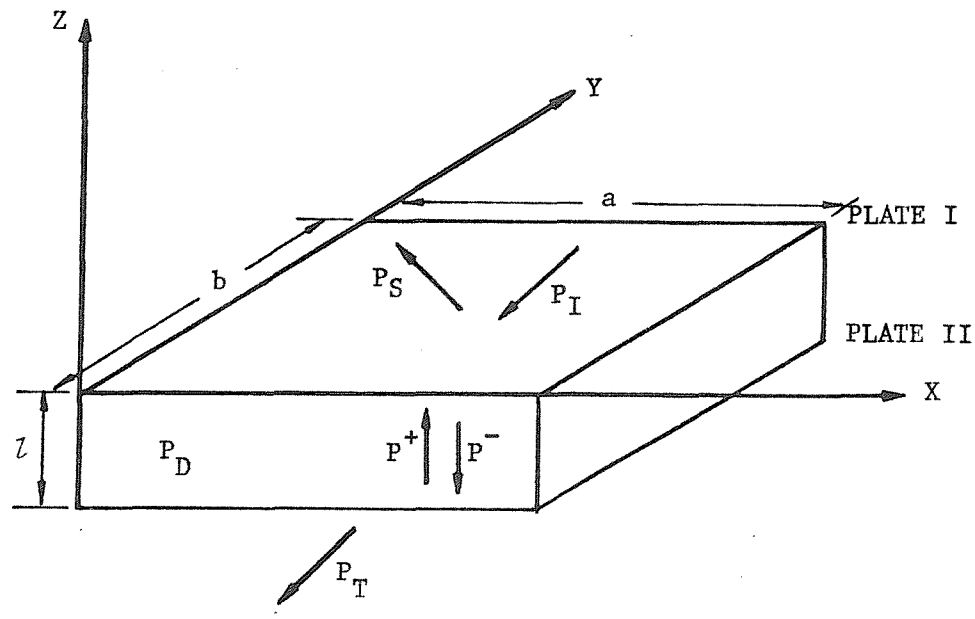

Figure 5.8 The geometry of the basic unit from which the array considered in section 5.3 is constructed.

The incident pressure field, P_I is represented by the form (with an implicit $e^{i\omega t}$ time factor),

$$P_I = Ae^{ik_x X + ik_y y + ik_z z} \quad , \tag{5.20}$$

where $k_x = k\sin\theta\cos\phi$, $k_y = k\sin\theta\sin\phi$, and $k_z = k\cos\theta$. This incident pressure causes transverse vibration of the thin isotropic plate 1, and a scattered pressure field P_S , reflected back into the region $z \geq 0$. The vibration of the front plate will also cause waves to propagate in the negative z direction, between the two plates. These waves will arrive at plate 2 and again give rise to both panel vibration and reflected waves. Thus there will be a standing wave system between the two vibrating plates, denoted by the pressure field P_D , and composed of positive and negative travelling pressure fields (P^+ and P^- respectively). Finally, the vibration of the second plate will give rise to a transmitted pressure field, P_T , in the region $Z \leq -\ell$.

Now, due to the periodicity of the structure considered, the scattered field will itself be periodic. Thus, if all the pressure fields in front of and behind the structure are expressed in terms of similar series of functions which are orthogonal over the plate dimensions, a and b, and also periodic in a and b, then determination of the relationship between say the terms in the series for the scattered and incident fields for one specific plate in the array, implies their values for any other plate.

The pressure field in the region $z \geq 0$ can thus be represented (cf. Reference [5.25]) as:

$$P_I + P_S = A \sum_{u=-\infty}^{\infty} \sum_{v=-\infty}^{\infty} (\beta_{uv} e^{ik_{uv}z} + R_{uv} e^{-ik_{uv}z}) e^{ik_u x} e^{ik_v y}$$

$$= A \sum_{u=-\infty}^{\infty} \sum_{v=-\infty}^{\infty} (\beta_{uv} e^{ik_{uv}z} + R_{uv} e^{-k_{uv}z}) \psi_u \psi_v \quad , \qquad (5.21)$$

whilst in the region $z \leq -\ell$, it has the general form,

$$P_T = A \sum_{u=-\infty}^{\infty} \sum_{v=-\infty}^{\infty} T_{uv} e^{ik_u x + ik_v y + ik_{uv} z}$$

$$= A \sum_{n=-\infty}^{\infty} \sum_{v=-\infty}^{\infty} T_{uv} \psi_u \psi_v e^{ik_{uv}z} \quad , \qquad (5.22)$$

where T_{uv} and R_{uv} are the transmitted and scattered modes transmission and reflection coefficients respectively, and $k_u = k_x + 2\pi u/a$, $k_v = k_y + 2\pi v/b$, and $k_{uv} = \sqrt{k^2 - k_u^2 - k_v^2}$. It can be seen therefore that above a certain 'order' of scattered or transmitted mode, the value of k_{uv} becomes purely imaginary, which corresponds to a wave which travels along the surface of the structure and decays with distance away from it. The order of the mode for which this occurs is determined by the incident wavelength and plate dimensions. The number of modes which do propagate away from the surface also determines how accurate the assumption of propagation only at the specular reflection angle is in the far field.

The β_{uv} term in equation (5.21) is the coupling term between the incident field and the modes ψ_u , ψ_v . It has the general form

$$\beta_{uv} = \frac{\int_0^a e^{ik_x x} \psi_u^* dx}{\int_0^a \psi_u \psi_u^* \, dx} \cdot \frac{\int_0^b e^{ik_v y} \psi_v^* dy}{\int_0^b \psi_v \psi_v^* dy} ,$$

which, since ψ_u and ψ_v equal $e^{ik_u x}$ and $e^{ik_v y}$ respectively (and ψ_a^* and ψ_v^* are their complex conjugates), can be shown to equal unity for both u and v equal to zero, but to be zero otherwise.

In order to couple the sound fields to the vibratory motion of the plates, it is necessary to express this motion similarly in terms of a set of functions which are orthogonal, and periodic in the plate dimensions. For the case of a simply supported plate (as considered in section 5.3.2) it has been seen that its motion can be represented as a series of sine terms as in equation (5.12). This series must now be expressed in terms of the functions ψ_u and ψ_v in order to equate specific terms in the pressure field and plate motion series. The general form for the displacement at the point (x,y) on a finite simply supported plate can now therefore be rewritten as

$$W(x,y) = (A/k\rho c^2) \sum_{u=-\infty}^{\infty} \sum_{v=-\infty}^{\infty} \psi_u \psi_v \sum_{\mu=1}^{\infty} \sum_{\nu=1}^{\infty} W_{\mu\nu} \chi_{\mu\nu uv} , \qquad (5.23)$$

where the factor $A/k\rho c^2$ has been introduced in order to make the plate modal displacement coefficient $W_{\mu\nu}$ non-dimensional, and $\chi_{\mu\nu uv}$ is the 'coupling term' between any μ,ν plate mode and a u,v pressure mode. Its form for any given mode combination is

$$\chi_{\mu\nu uv} = \frac{\int_0^a \sin k_\mu x \, e^{-ik_u x} dx}{\int_0^a e^{ik_u x} e^{-ik_u x} dx} \cdot \frac{\int_0^b \sin k_\nu y \, e^{-ik_v y} dy}{\int_0^b e^{ik_v y} e^{-ik_v y} dy}$$

$$= \frac{k_\mu \left(1 - e^{-ik_u a}(-1)^\mu\right)}{k_\mu^2 - k_u^2} \cdot \frac{k_\nu \left(1 - e^{-ik_v b}(-1)^\nu\right)}{k_\nu^2 - k_v^2} \cdot \frac{1}{ab}$$

$$= I_{\mu u} I_{\nu v} / ab \quad . \qquad (5.24)$$

For the explicit cases when $k_\mu = k_u$, and/or $k_\nu = k_v$, $I_{\mu u}$ and $I_{\nu v}$ both can be shown by use of L'Hospital's rule to equal -i/2.

For the case of a single layer plate array, the plate motion, and incident, scattered and transmitted pressure field have all now been expanded in terms of the same orthogonal functions. It would only remain to use the velocity boundary conditions at the plate,and the plate's equation of motion to reduce the problem to an infinite set of simultaneous linear equations containing infinite series of μ, ν terms. These could then be used to solve for the scattered presssure field in terms of that incident. However in this chapter we will continue to concentrate on a model for a double layer of panels. It is now therefore necessary to consider the form of the pressure field between the two layers of plates. This pressure field will be composed of positive and negative travelling waves, and must again be expressed in terms of a set of orthogonal functions. Thus, generally,

$$P_D = A \sum_m \sum_n (P^+_{mn} e^{ik_{mn}z} + P^-_{mn} e^{-ik_{mn}z}) \psi_m \psi_n \quad . \qquad (5.25)$$

The form of the orthogonal functions ψ_m and ψ_n is determined by the boundary conditions at $x = 0,a$; and $y = 0,b$; for $0 \geq z \geq -\ell$. Two particular forms for these boundary conditions can be easily accommodated in the model developed: they correspond to the cases where either there are acoustically hard immovable walls between the two layers at the edges of every panel, or there is only air between the panel layers and hence there is no lateral containment of fluid in between the two arrays. In the first case the ψ_m and ψ_n terms in equation (5.25) are the rigid walled rectangular duct modes (e.g. $\cos(m\pi x/a)$), which are actually periodic in 2a. In the second case a similar expansion to that already used for P_I , P_S and P_T can be adopted. In this chapter it is this latter model which will be adopted. There are a number of reasons for this. Firstly, since it is primarily the effect of the finite component panel's size that is to be studied, we do not wish to introduce the possibility of transverse cavity resonances to confuse the issue. Secondly, the duct mode model would require another set of orthogonal functions, and thus introduces a new set of coupling coefficients; this would make

the ultimate computation of the solution an order of magnitude lengthier. Thirdly, if there are inter-connections between the two layers of panels, the back panels will almost always be excited not solely by the airborne sound, but also by structural excitation transmitted from the front panel to the back panel via the inter-connections. Although a model which contains such structural transmission paths will in many cases be more physically realistic, it will generally introduce coupling and/or loss factors which are almost impossible to accurately quantify. Finally it should be noted that in most real cases, the situation will probably lie somewhere between these two extremes, but the evaluation of such a model would prove exceedingly difficult.

With the assumption that air alone fills the space between the two panel layers, equation (5.25) can be rewritten as

$$P_D = A \sum_{u=-\infty}^{\infty} \sum_{v=-\infty}^{\infty} (P^+_{uv} e^{ik_{uv}z} + P^-_{uv} e^{-ik_{uv}z}) \psi_u \psi_v \ , \qquad (5.26)$$

where k_{uv}, ψ_u and ψ_v are as used in equation (5.21).

The motion of all the component parts of the double panel model has now been formulated in terms of the same sets of orthogonal functions, ψ_u and ψ_v. It now only remains to apply the equations of motion and velocity boundary conditions at the two plates in order to evaluate the scattered field in terms of that incident.

Application of velocity continuity across plate 1, gives

$$\partial(P_I+P_S)/\partial z\Big|_{z=0} = -i\omega\rho\dot{W}_1 = \partial P_D/\partial z\Big|_{z=0} \ , \qquad (5.27)$$

where $\dot{W}_1$ is the front plate's normal velocity. Similarly, at the backplate:

$$\partial P_D/\partial z\Big|_{z=-\ell} = -i\omega\rho\dot{W}_2 = \partial P_T/\partial z\Big|_{z=-\ell} \ , \qquad (5.28)$$

where $\dot{W}_2$ is the normal velocity of a point on plate 2. Substitution of the forms of P_I, P_S, P_D, P_T, $W_{1\mu\nu}$ and $W_{2\mu\nu}$, from equations (5.21, (5.22), (5.26) and (5.23) into equations (5.27) and (5.28) results in the following identities for any u,v mode:

$$(k_{uv}/k)R_{uv} - i\sum_{\mu=1}^{\infty}\sum_{\nu=1}^{\infty}\chi_{\mu\nu uv}W_{1\mu\nu} = (k_{uv}/k)\beta_{uv} \quad , \tag{5.29}$$

$$P^+_{uv} - P^-_{uv} + R_{uv} = \beta_{uv} \quad , \tag{5.30}$$

$$(k_{uv}/k)(P^+_{uv}e^{-ik_{uv}\ell} - P^-_{uv}e^{ik_{uv}\ell}) + i\sum_{\mu=1}^{\infty}\sum_{\nu=1}^{\infty}\chi_{\mu\nu uv}W_{2\mu\nu} = 0 \quad , \tag{5.31}$$

and

$$(P^+_{uv}e^{-ik_{uv}\ell} - P^-_{uv}e^{ik_{uv}\ell}) + T_{uv}e^{-ik_{uv}\ell} = 0 \quad . \tag{5.32}$$

It can thus be seen that equations (5.27) and (5.28) provide four equalities that link the six unknowns R_{uv}, P^+_{uv}, P^-_{uv}, T_{uv}, W_{1uv} and W_{2uv} (where $W_{uv} = \sum_{\mu}\sum_{\nu}\chi_{\mu\nu uv}W_{\mu\nu}$) in terms of the assumed known incident field. Two further equations are therefore required in order to solve the problem. These can be obtained by application of the equation of motion for a finite simply supported plate (as discussed in Section 5.3.2 to component plates of the front and back layers of panels. Thus, with the non-dimensional modal plate displacement coefficients $W_{1\mu\nu}$ and $W_{2\mu\nu}$ (as defined in equation (5.23)) and a forcing term defined as the net pressure across the plate in the positive z direction, the equation of plate motion (equation (5.16)) can be employed to give the following expressions for any u,v mode:

$$(P^+_{uv}+P^-_{uv}) - (\beta_{uv}+R_{uv}) = \sum_{\mu=1}^{\infty}\sum_{\nu=1}^{\infty} i\zeta_{1\mu\nu}W_{1\mu\nu}\chi_{\mu\nu uv} \quad , \tag{5.33}$$

for the front plate, and

$$T_{uv}e^{-ik_{uv}\ell} - (P^+_{uv}e^{-ik_{uv}\ell} + P^-_{uv}e^{ik_{uv}\ell}) = \sum_{\mu=1}^{\infty}\sum_{\nu=1}^{\infty} i\zeta_{2\mu\nu}W_{2\mu\nu}\chi_{\mu\nu uv} \quad , \tag{5.34}$$

for the back plate. In equations (5.33) and (5.34), $\zeta_{1\mu\nu}$ and $\zeta_{2\mu\nu}$ are the specific normal modal impedances of individual plates in the front and back panel layers, as given by equation (5.18).

Equations (5.29) to (5.34) now give 6 linear relations between the 6 unknowns, and thus the problem is in principle solved. If this set of equations is arranged in matrix form, a Gaussian elimination procedure can be used to reduce the problem to a system of two coupled equations which involve infinite sums over the plate modes, for any particular u-v mode combination. One possible set of equations resultant from such a process is:

$$e^{ik_{uv}\ell}\sum_{\mu=1}^{\infty}\sum_{\nu=1}^{\infty}\left\{\zeta_{1\mu\nu}+2k/k_{uv}\right\}\chi_{\mu\nu uv}W_{1\mu\nu}+\sum_{\mu=1}^{\infty}\sum_{\nu=1}^{\infty}\zeta_{2\mu\nu}\chi_{\mu\nu uv}W_{2\mu\nu}=2ie^{ik_{uv}\ell}\beta_{\mu\nu}, \tag{5.35}$$

$$\sum_{\mu=1}^{\infty}\sum_{\nu=1}^{\infty}\left\{ie^{ik_{uv}\ell}-(k_{uv}/k)\sin k_{uv}\ell\zeta_{1\mu\nu}\right\}\chi_{\mu\nu uv}W_{1\mu\nu}-i\sum_{\mu=1}^{\infty}\sum_{\nu=1}^{\infty}\chi_{\mu\nu uv}W_{2\mu\nu}$$
$$=-2i(k_{uv}/k)\sin(k_{uv}\ell)\beta_{uv}\ . \tag{5.36}$$

These equations can be solved for $W_{1\mu\nu}$ and $W_{2\mu\nu}$ since there are an infinite number of u,v combinations for which these equations must hold true. In practice the series will obviously have to be truncated in order to permit numerical evaluation of the solution. Such practicalities will be covered in Section 5.3.5. The next section will be concerned with the evaluation of an absorption coefficient, given that the scattered pressure field P_S can be determined in terms of the known incident field P_I ; this is obviously possible, since once equations (5.35) and (5.36) have been solved for the $W_{1\mu\nu}$ and $W_{2\mu\nu}$ series terms, they can be substituted back into equations (5.29) to (5.34) to yield any of the acoustic field coefficients desired.

5.3.4 Energy absorption considerations for the finite plate model

If the model of Section 5.3.3 has been correctly constructed, it should be possible to at least partly check the accuracy of any numerical computations by means of an energy balance. Specifically,

the energy incident upon the structure should equal the sum of that reflected, transmitted or dissipated by the two plates' motion (in the present model there are assumed to be no absorption processes present in the space between the plates). Furthermore, from the expression for the reflected energy an 'absorption' coefficient can be deduced; this term includes both transmitted and dissipated energies. To consider first the evaluation of such an absorption coefficient, which is the ratio of the acoustic power going into the front surface to that incident, its general form may be written as

$$\alpha = \frac{\frac{1}{2}\,\mathrm{Re}\left\{\int_0^a\int_0^b (P_I+P_S)(V^*_{nI}+V^*_{nS})\,dydx\right\}}{\frac{1}{2}\,\mathrm{Re}\left\{\int_0^a\int_0^b P_I V^*_{nI}\,dydx\right\}}\,, \qquad (5.37)$$

where an asterisk indicates a conjugate quantity, and V_{nI} and V_{nS} are the normal incident and scattered velocities into the surface respectively. Thus by use of equation (5.21) in conjunction with the linearised momentum equation, the expression for the power entering the front surface of the structure (i.e. the numerator of equation (5.37)) becomes

$$W_{in} = \frac{1}{2}\,\mathrm{Re}\left\{\frac{|A|^2}{\omega\rho}\sum_{u'}\sum_{v'}\sum_{u}\sum_{v}\int_0^a\int_0^b (\beta_{uv}+R_{uv})\psi_u\psi_v\cdot(\beta^*_{u'v'},k_z-k^*_{u'v'},R_{u'v'})\,\psi^*_{u'},\psi^*_{v'},dxdy\right\}. \qquad (5.38)$$

Due to the orthogonal properties of ψ_u and ψ_v, equation (5.38) can be rewritten as

$$W_{in} = \frac{A^2ab}{2\omega\rho}\,\mathrm{Re}\left\{\sum_u\sum_v\left[k_z(|\beta_{uv}|^2+R_{uv}\beta^*_{uv})+k^*_{uv}|R_{uv}|^2-\beta_{uv}k^*_{uv}R^*_{uv}\right]\right\}. \qquad (5.39)$$

It should be remembered (as stated after equation (5.22)) that β_{uv} is a 'dummy variable' and equals zero unless both u and v equal zero, in which case it equals unity. Hence,

$$k_z R_{uv} \beta^*_{uv} - \beta_{uv} k^*_{uv} R_{uv} = 2k_z \mathrm{Im}(R_{oo}) \quad , \tag{5.40}$$

which can be seen to be completely imaginary. Thus the only real parts of equation (5.39) can be written as:

$$W_{in} = \frac{A^2 ab}{2\omega\rho} \left(k_z - \mathrm{Re} \left\{ \sum_{u=-\infty}^{\infty} \sum_{v=-\infty}^{\infty} k^*_{uv} |R_{uv}|^2 \right\} \right) . \tag{5.41}$$

The first term in equation (5.41) (i.e. $A^2 abk_z/2\omega\rho$) can also be shown to represent the normally incident power. Equation (5.37) for the absorption coefficient therefore becomes:

$$\alpha = 1 - \mathrm{Re} \left\{ \sum_{u=-\infty}^{\infty} \sum_{v=-\infty}^{\infty} k^*_{uv} |R_{uv}|^2 \right\} / k_z \ . \tag{5.42}$$

Only a finite number of modes need to be considered in calculation of an absorption coefficient, since above a certain u,v combination, for an assumed lossless propagation medium, k_{uv} becomes completely imaginary. An imaginary k_{uv} value corresponds to waves which propagate along the boundary surface and decay with distance from it. Equation (5.42) therefore demonstrates that it is only the propagating modes which carry power away from the surface, and furthermore that the interaction of the incident and scattered fields dissipates no overall power. This is true since the second term of equation (5.41) represents the scattered power , W_R , alone. That is,

$$W_R = \frac{A^2 ab}{2\rho c} \mathrm{Re} \left\{ \sum_{u=-\infty}^{\infty} \sum_{v=-\infty}^{\infty} (k^*_{uv}/k) |R_{uv}|^2 \right\} . \tag{5.43}$$

The power transmitted through the two layers of panels can be formulated in a similar manner as

$$W_T = \frac{A^2 ab}{2\rho c} \mathrm{Re} \left\{ \sum_{u=-\infty}^{\infty} \sum_{v=-\infty}^{\infty} (k^*_{uv}/k) |T_{uv}|^2 \right\} .$$

This allows a transmission coefficient, α_t, defined as the ratio of power transmitted through the back surface of the structure to that incident on the front surface, to be expressed as:

$$\alpha_t = \sum_{u=-\infty}^{\infty} \sum_{v=-\infty}^{\infty} |T_{uv}|^2 \, \mathrm{Re}(k^*_{uv}/k) \quad . \tag{5.44}$$

The power dissipated by the motion of a component plate in either the front or back layer of the panels can be found from the difference between the energy in front of it and that behind it. This can be written in general terms as:

$$W_D = \frac{1}{2} \mathrm{Re} \left\{ \iint_S P_f V^*_{nf} dS - \int_S P_b V^*_{nb} dS \right\} , \tag{5.45}$$

where S is the plate area, and the subscripts f and b indicate parameter values in front or behind it respectively. Since there is continuity of velocity across all the plates, V_b equals V_f, and thus the integrand of equation (5.45) becomes the product of a pressure difference with the conjugate of the velocity term. Now, in Section 5.3.2, it was seen that if the net forcing pressure is expanded in terms of orthogonal modes it can be related to the product of the relevant modal impedance with the modal velocity term. This can be written in terms of the now non-dimensional plate modal displacement coefficients $W_{\mu\nu}$ as introduced in equation (5.23), and the plate's specific normal impedance, $\zeta_{\mu\nu}$ (given by the expression $\zeta_{\mu\nu} = Z_{\mu\nu}/\rho c$ and $Z_{\mu\nu}$ is defined by equation (5.18)), as $P_{\mu\nu} = i\omega W_{\mu\nu} \zeta_{\mu\nu}$. Thus equation (5.45) becomes:

$$W_D = \frac{A^2}{2\rho c} \mathrm{Re} \left\{ \iint_S \sum_{\mu'} \sum_{\nu'} \sum_{\mu} \sum_{\nu} \zeta_{\mu\nu} W_{\mu\nu} W^*_{\mu',\nu'} \psi_\mu \psi_\nu \psi_{\mu'} \psi_{\nu'} dS \right\} . \tag{5.46}$$

The orthogonal properties of the orthogonal functions ψ_μ and ψ_ν, which are the simply supported plate's eigenfunctions, over the integration limits can be used to evaluate this integral and yield

$$W_D = \frac{A^2 ab}{8\rho c}\left(\sum_{\mu=1}^{\infty}\sum_{\nu=1}^{\infty} \mathrm{Re}\{\zeta_{\mu\nu}\}|W_{\mu\nu}|^2\right) . \qquad (5.47)$$

From this equation a 'dissipation coefficient' , α_d, defined as the ratio of the power dissipated by a particular plate to that incident at the surface of the front plate, can be written as

$$\alpha_d = \sum_{\mu=1}^{\infty}\sum_{\nu=1}^{\infty} k|W_{\mu\nu}|^2 \mathrm{Re}(\zeta_{\mu\nu})/4k_z \quad , \qquad (5.48)$$

where the real part of $\zeta_{\mu\nu}$ can be seen from equation (5.18) to explicity equal $D\eta(k_\mu^2+k_\nu^2)^2/k\rho c^2$. Thus the amount of energy dissipated by any plate is specifically determined in this model by its bending stiffness and loss factor. There is therefore no 'cut-off' point in the number of modes that need to be computed in order to evaluate the dissipation coefficient of a plate, unlike the cases of the transmission or absorption coefficients. However in practice the energy is dissipated only by those plate modes which are relatively well excited and so long as these are included in any numerical computation the results should be reasonably adequate. A check on the accuracy of any calculated results can be obtained through use of equations (5.4.2), (5.44) and (5.18) and the identity

$$\alpha = \alpha_t + \alpha_{d1} + \alpha_{d2} \quad , \qquad (5.49)$$

where α_{d1} and α_{d2} correspond to the dissipation coefficients of the component front and back plates respectively. Equation (5.49) also provides an indication as to whether any given absorption coefficient peak is due to pronounced absorption or transmission effects or some combination of them under the conditions studied. The energy balance of equation (5.49) therefore is invaluable in the checking and interpretation of the results of the numerical implementation of the finite plate absorption model described in the next section.

5.3.5 Details of the implementation of the finite plate absorption model

In order to calculate the plane wave absorption coefficient for an infinite array composed of a double layer of simply supported finite

plates, equations (5.35) and (5.36) must first of all be solved for $W_{1\mu\nu}$ and $W_{2\mu\nu}$. It is then a comparatively simple matter to use the equations of Section 5.3.4 to evaluate the modal reflection coefficients, R_{uv}, and thus to obtain a value for the absorption coefficient from equation (5.42).

The solution of equations (5.35) and (5.36) is only in theory possible since there are an infinite number of u,v term combinations for which these equations hold true. For an approximate solution to be evaluated numerically however, the μ and ν series must be truncated at some finite μ and ν values. A series of linear simultaneous equations can then be constructed, each equation corresponding to a particular u,v term combination and containing all the appropriate terms in the truncated μ,ν series. If the set of equations thus generated are arranged in standard matrix equation form (i.e. $\hat{A}\cdot\hat{X} = \hat{B}$), they can then be readily solved by use of standard computer matrix equation solution routines. The main requirement of such methods is that the matrix $\hat{A}$ is square, which here requires that the product of the number of u terms considered with the number of v terms equals the equivalent μ-ν term product. The resultant matrix arrangement is shown schematically in Figure 5.9. All the results described in the rest of this chapter were obtained by the implementation of this procedure on the University's ICL 2970 computer. Standard NAG Library routines were used to solve the matrix equations (see Reference [5.26] for further details). Both 'exact' and approximate solution methods were investigated, the former by use of NAG Library Subroutine F04ATF, the latter by use of subroutines F03AHF and F04AKF. There was found to be no difference in the absorption coefficients thus calculated to four decimal places, for the results of the two solution methods that were compared. This suggests that the solution converges relatively quickly. Therefore the results presented in this chapter have been calculated by use of the approximate technique as it is much faster than the exact matrix solution method. A full listing of the program used to produce the results shown is contained in Appendix E.

It was not evident *a priori* exactly how many terms in the various series should be used in the matrix formulation for a given case, in order to achieve a given accuracy. However, obviously all the propagating

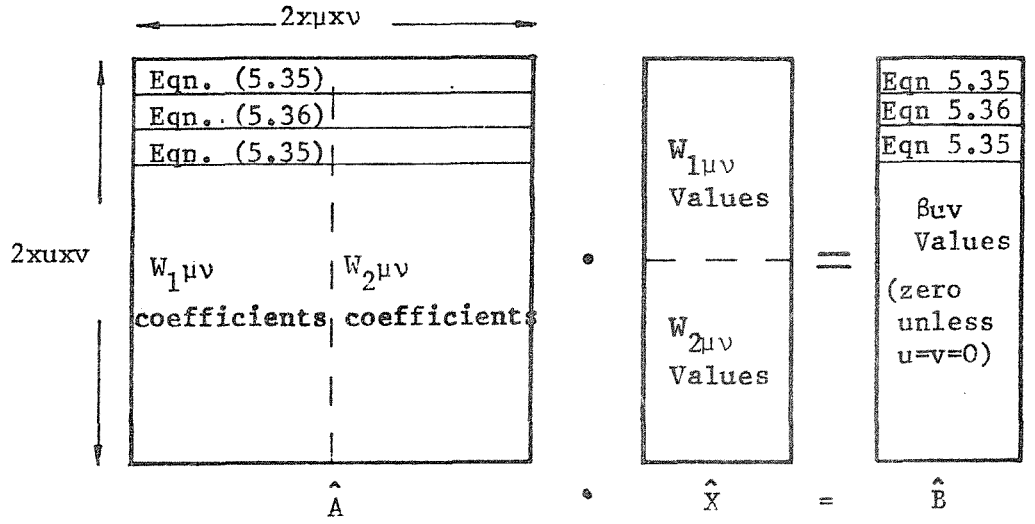

Figure 5.9 Schematic representation of the matrix arrangement used in the solution of the double layer finite panel absorption model. The columns in the A matrix correspond to the specific μν terms in the series of equations (5.35) and (5.36), and each pair of rows corresponds to one particular combination of u,v values in these equations.

u,v modes must be considered, and presumably all μ,ν orders at least up to the plate resonance above the frequency of the incident sound should be included - for the calculation of the simply supported finite plate resonances see Section 5.3.2. In this section use of the model to predict the absorption characteristics of an asbestos roof structure will be considered again. This model consists of two layers of thin isotropic plates, but with the plates of the rear layer modelled as possessing increased mass and stiffness as was described in Section 5.2.3. From equation (5.18), since the backplate's stiffness increase is assumed to be an order of magnitude greater than the mass increase factor, it can be seen that the frequencies at which the frontplate's modal impedance is a minimum will be lower for

specific μ,ν terms taken. Figure 5.10 contains the frequencies for which the front plate's modal impedance is a minimum. From these results the above argument would imply that for frequencies up to, say, 150 Hz the retention of only the first five terms in the μ,ν series would prove reasonably adequate. However, inspection of Figure 5.11 indicates that even for the absorption maximum visible in the region of 100Hz although the solution with 5 terms in both the μ and ν series 'tracks' the behaviour, its magnitude is somewhat in error. The results do indicate a convergence towards some absolute value as the number of terms considered in the series is increased. However, unfortunately the more accurate results take an order of magnitude longer to compute (e.g.,each absorption coefficient took 7 seconds to compute when series with 5μ and 5ν terms were considered, as opposed to 135 seconds for the more accurate 9 term series calculations). An indication of how accurate a particular absorption coefficient estimate is can be gaged from investigation of the energy sum, as discussed in Section 5.3.4. The variation of this quantity near an absorption peak is shown in Figure 5.12 for various sized matrix solutions. It will be seen from these results that the lower order estimates are generally most in error in the vicinity of peaks in the absorption coefficient curve.

The results obtained by use of this model are presented and discussed in the next section. Unless otherwise stated, it should be assumed that all the results shown have an error in their energy sum of less than 10%, when the transmitted, reflected and dissipated energies are summed and expressed as a percentage of the energy incident.

μ ν	1	2	3	4	5
1	44.79	137.81	292.84	509.88	788.94
2	86.13	179.15	334.18	551.22	830.28
3	155.03	248.05	403.08	620.13	899.18
4	251.50	344.51	499.55	716.59	995.65
5	375.52	468.54	623.57	840.61	1119.67

Figure 5.10 Table of the frequencies at which the front plate's modal impedance becomes purely resistive. (All frequencies in Hz).
a = 1.5 m, b = 1 m.
D = 989 Nm; M_S = 12.09 kg/m^2;

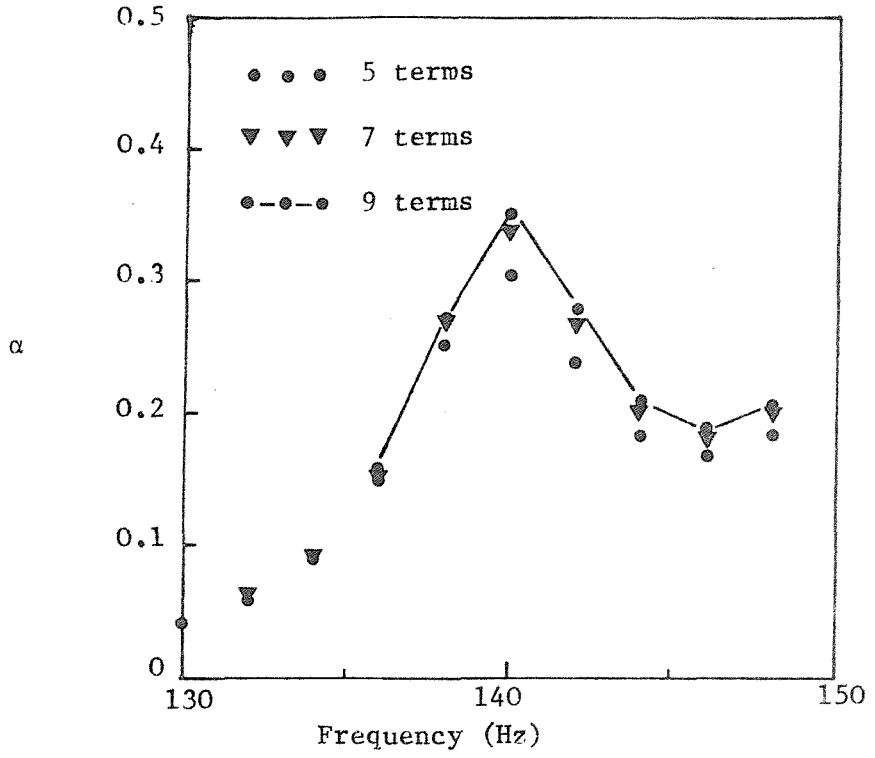

Figure 5.11 Comparison of plate model's predictions for different numbers of terms considered in the plate mode series (in both x and y directions). M_{s1} = 12.09kg/m^2; M_{s2} = 15.72kg/m^2 D_1 = 989Nm, D_2 = 30659Nm, a = 1.5m, b = 1m, d = 0.03m, η = 0.06.

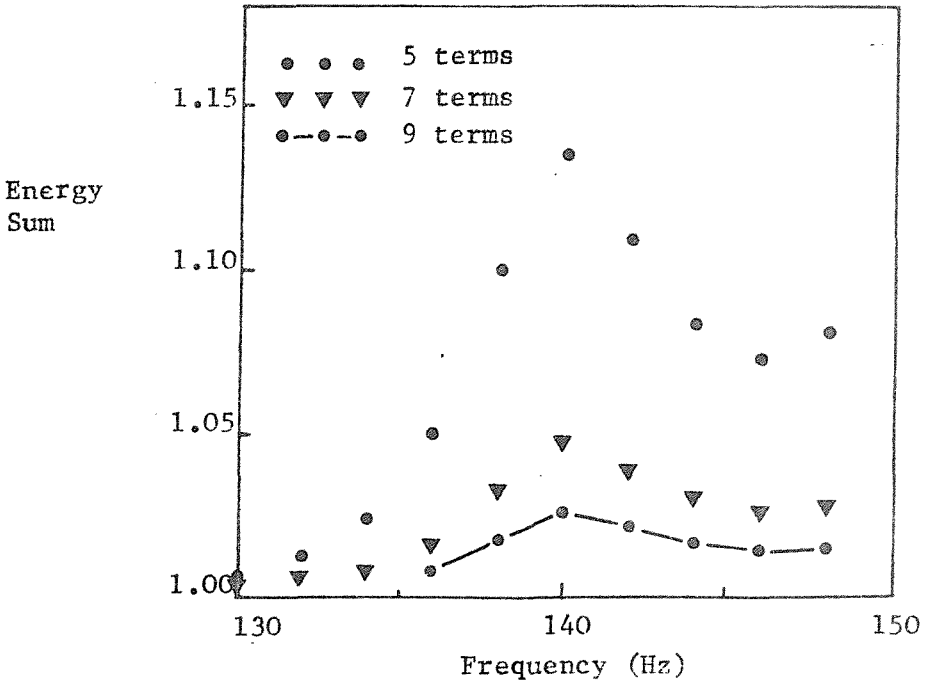

Figure 5.12 Comparison of the energy sum (ie. reflected, transmitted and dissipated energies) as a function of that incident, for different numbers of terms considered in the plate mode series (in both x and y directions). Parameters as for Figure 5.11.

5.3.6 *Presentation and discussion of the finite plate model's results*

In the initial finite plate model results calculated, the effective bending stiffness of the back plate was probably over-estimated as being 140 times greater than that of the front plate. This point has already been mentioned in connection with the infinite plate model in Section 5.2.3. This assumption gives bending stiffnesses per metre length of 138461 Nm and 989 Nm for the back and front plates respectively. When it was appreciated that this increase might be an overestimate, a value of 30659 Nm was used for the back-plate's bending stiffness; this is equivalent to an increase by a factor of 31 compared to a flat plate. The masses per unit area of the front and back plates were again assumed to be 12.09 kg/m^2 and 15.72 kg/m^2. Results for both sets of stiffness values are included in this section as they provide an insight into the physics of the situation. Unfortunately, however, there was not adequate time to repeat all the plots that might have been wished.

It is immediately apparent from inspection of Figure 5.13 that the magnitudes of the absorption coefficient results obtained with the new model are much larger, and many more absorption maxima can be seen to have been stimulated in a comparatively narrow frequency range. The computation method however is so time consuming that evaluation of accurate values at frequencies much above about 200 Hz would not seem to be a practically viable proposition since many terms must then be kept in the μ-ν series. Also the accurate estimation of 1/3 octave diffuse field values would appear impossible unless assumptions about the variation of the absorption coefficient with angle of incidence can be made.

The effects of alteration of the effective bending stiffness of the component plates of the back layer can be seen from comparison of Figures 5.13(a) and 5.13(b), whence it can be noted that for a given angle of incidence, the position of the absorption maxima in the frequency domain has been markedly altered by this change in the backplate's properties. The actual magnitude of the absorption peaks seen in the two cases is about the same however. Thus the back panels' bending stiffness can be seen to have a pronounced effect at these comparatively low frequencies, unlike the results of the earlier infinite plate model results.

Figure 5.13 Variation of absorption coefficient with frequency for two arrays of simply supported finite plates separated by an airspace.

Figure 5.13(a) Parameter Values: M_{s1} = 12.09kg/m^2; M_{s2} = 15.72kg/m^2 D_1 = 989Nm; D_2 = 138461Nm; a = 1.5m; b = 1m; d = 0.03m, θ,ϕ = 45°; η = 0.06 Number of terms in plate series in both x and y directions = 7.

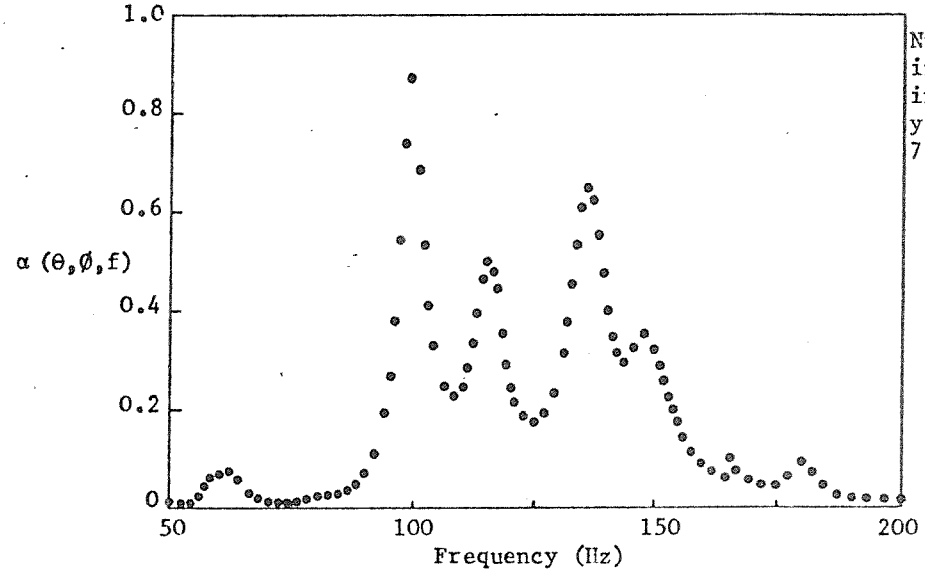

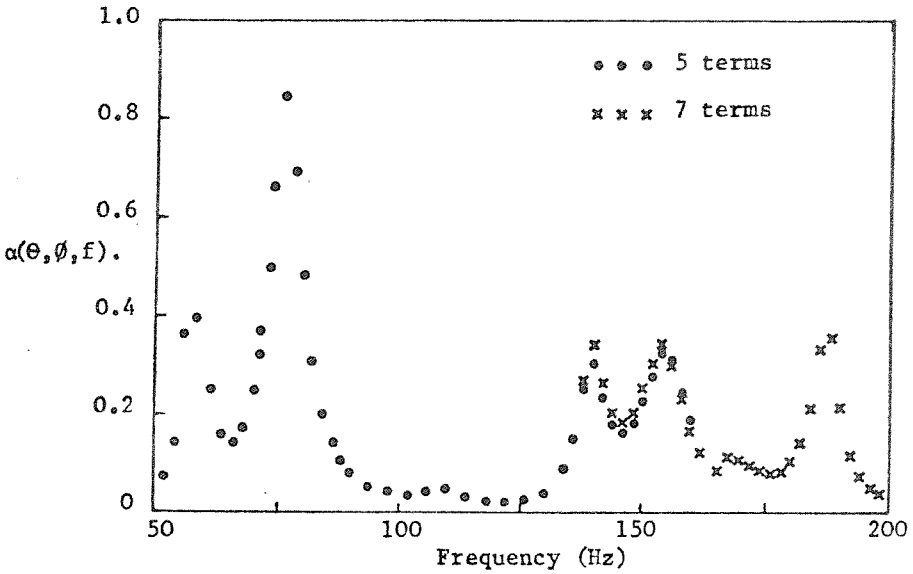

Figure 5.13(b) Parameter Values: As for Figure 5.13(a) except D_2 = 30659Nm. (Number of terms retained in the plate mode series is as indicated on Figure).

These interesting results raise the question as to what the major sound absorption mechanism is in this situation. Two possible methods were investigated to study this problem. In the first method, it is assumed that from the change in the results observed when one parameter is altered it is possible to deduce the major absorption mechanism. The effect of one such parameter change is shown in Figure 5.14, where the inter-panel layer spacing has been increased from 0.03 m to 0.05 m. The resultant marked shift of the major absorption peak in frequency is reminiscent of the mass-air-mass resonant behaviour of the infinite plate model (see section 5.2.4). However, no such specific conclusion can be safely made about the cause of the absorption maximum in this case, since it has already been seen in Figure 5.13 that bending stiffness plays a large part in the determination of the absorption in this region, as might be expected from the finite plate's modal impedance behaviour.

In equation (5.49) however, one has available a second, more precise method by which to discover what the predominant physical absorption processes are in any situation. This is because this equation equates the total power 'absorbed' to the sum of the components which are either dissipated in plate vibration, or transmitted straight through the whole structure. The results of such computations of the breakdown of the absorption coefficient, α , into its components are shown in Figure 5.15 for the variation of α with frequency for a number of different physical configurations. From Figure 5.15(a) it can be seen that almost all the absorption which causes the large absorption peak at around 100 Hz for the stiffer back plates in Figure 5.13(a) is due to the dissipation of energy in the vibration of the front plate (the other two terms α_{d2} and α_t are small and hence not shown). This is unlike the behaviour exhibited by the less stiff back plate configuration in Figure 5.15(b), for the 75 Hz peak of Figure 5.13(b). In this case the amounts of energy dissipated by the two plate layers are almost equal, and the amount transmitted is also not negligible. However for the two absorption maxima observable at 140 Hz and 155 Hz in Figure 5.13(b), the results of Figure 5.15(c) indicate that the behaviour is now more like that of the 140 times stiffer backplate, since most of the 'absorbed' energy is dissipated in plate 1. It thus appears that the majority of the energy absorbed

Figure 5.14. Variation of absorption coefficient with frequency for two planes of simply supported plates separated by an airspace. Parameter values as in Fig 5.13(a) except number of terms in plate mode series = 5.

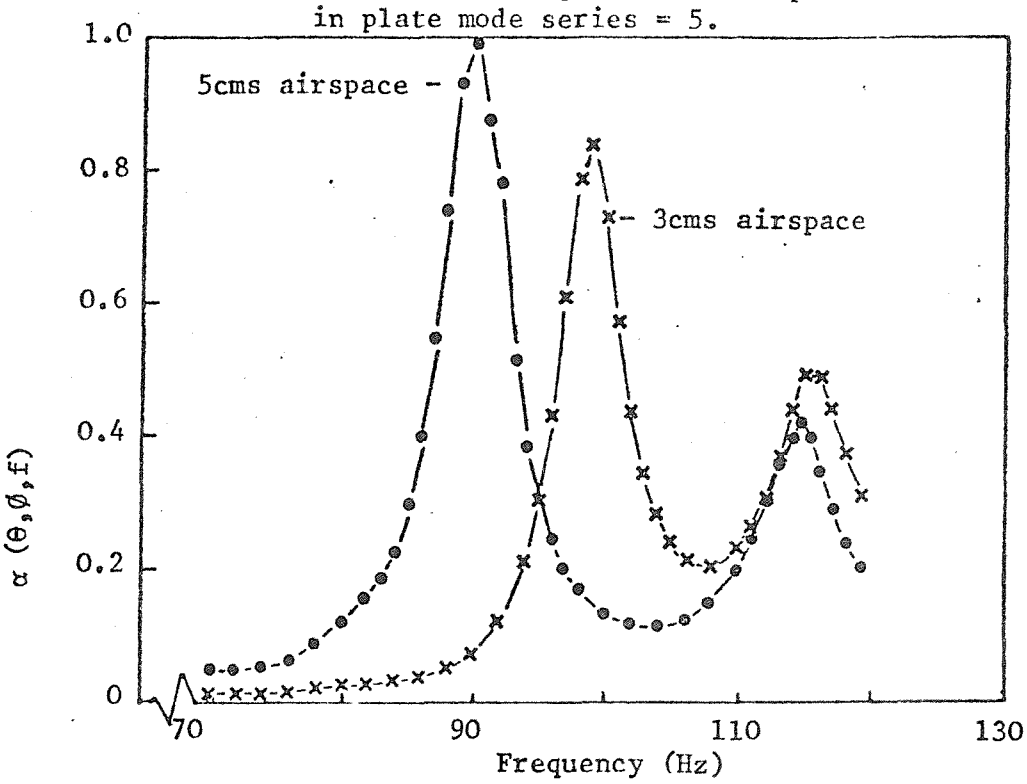

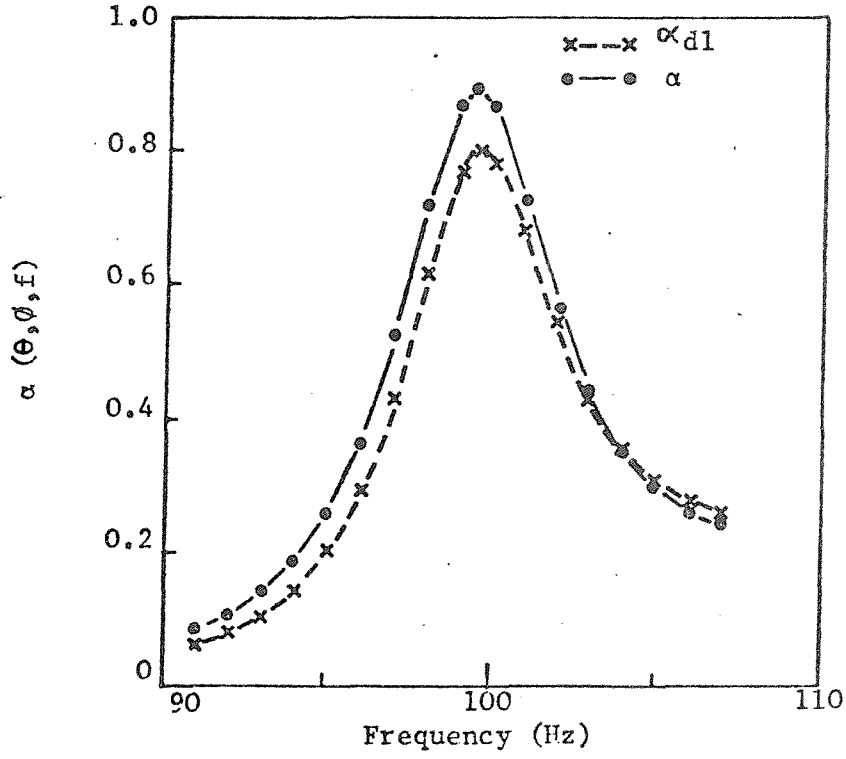

Figure 5.15 Comparison of $\propto$ and $\propto_{d1}$ for two infinite arrays of simply supported finite panels separated by an airspace. Fig 5.15(a) Parameter values: D_1 = 989Nm, D_2 = 138461.5Nm, M_{s1} = 12.09kg/m^2, M_{s2} = 15.72kg/m^2, a = 1.5m, b = 1m, d = 0.03m, θ,ϕ = 45^o, loss factor = 0.06, number of terms in plate mode series = 9.

Figure 5.15(b) Parameter values: As for Figure 5.15(a) except D_2 = 30659Nm, and the maximum number of terms in the plate mode series = 7, (in both x and y directions).

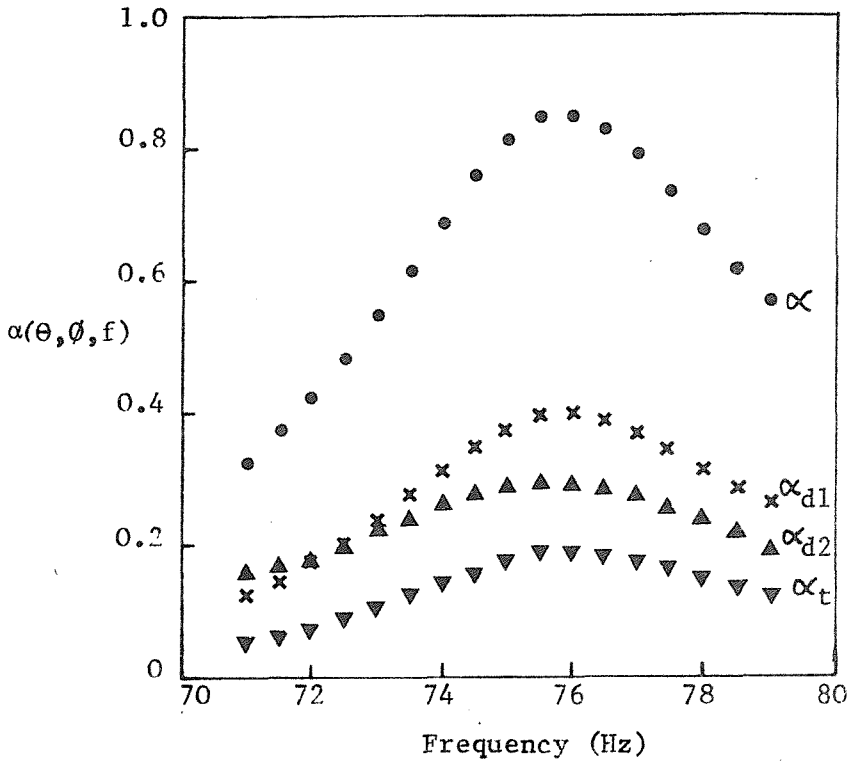

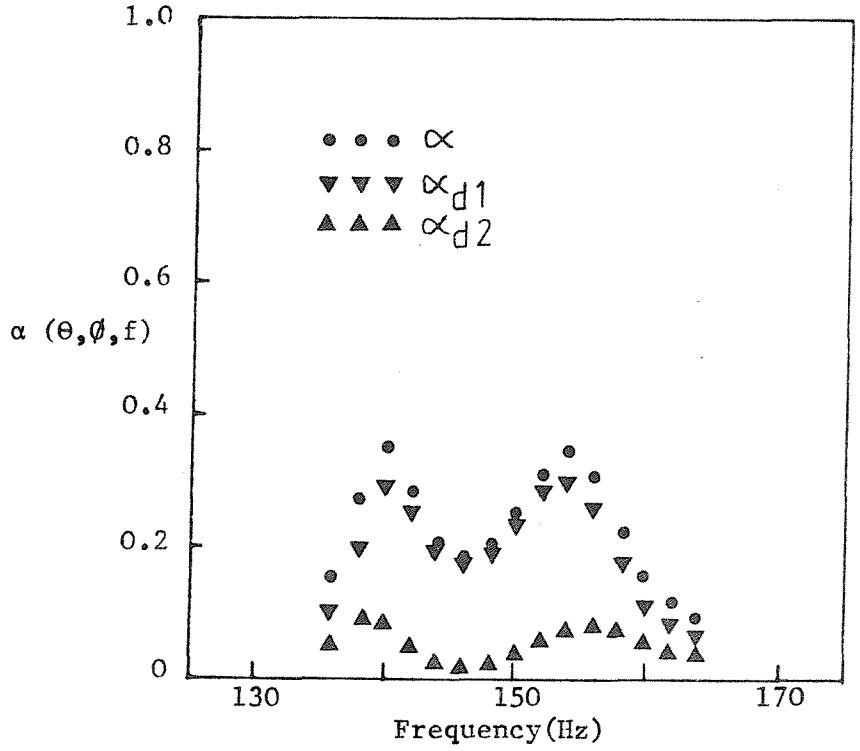

Figure 5.15(c) Parameter values: As for Fig 5.15(a) except D_2 = 989Nm. (αt is too small to plot).

is in fact dissipated in plate motion, with the losses in the front plate probably generally greater than those in the back plate, since it is directly excited by the incident field, and is also effectively less stiff than the corrugated plate.

No consideration has yet been given to the variation of the absorption coefficient with angle of incidence, and whether this is in any way systematic. Figures 5.16 and 5.17 contain the results of calculations of absorption coefficient variation with azimuthal angle θ, and polar angle ϕ respectively. Figure 5.16(a) displays the results for the configuration with the stiffer backplate, from which it can be seen that the absorption coefficient is again a strong function of θ. However, although there are apparent similarities between these results and those of the simple infinite plate model discussed in Section 5.2.4, there are certain differences. These differences include the fact that the major absorption peak (other than that seen at grazing incidence) is now broader, and the overall 'background level' is much higher. The behaviour at grazing incidence is as much as for the infinite plate model, which was hypothesised to be due to the existence of a pressure field behind the plates identical to that incident, so that the plate's normal velocity can be zero, although there is an incident pressure wave. With the current model one can easily test this hypothesis by decomposition of the absorption coefficient into dissipated and transmitted components as discussed above. The results of such a decomposition are presented in Figure 5.16(b) for the less stiff of the two backplates used as a function of θ. From these results it can be seen that the major part of the absorption coefficient is due to energy dissipation at the front plate for all angles up to $\theta \approx 70^{\circ}$. For angles greater than 70° more power is dissipated at the backplate until a θ value of about 89° when a dramatic changeover occurs before 90° is reached (see Figure 5.16(c) for the detailed variation of α for $89^{\circ} \lesssim \theta \lesssim 90^{\circ}$). For these angles very close to grazing, the two dissipation coefficients go to zero, whilst the transmission coefficient approaches unity. Thus the whole absorption coefficient at the limit of grazing incidence is due to apparent perfect transmission in this model. In most situations this behaviour is of little practical significance since it cannot be physically realised (see the previous discussion of this point in connection with the infinite plate model in Section 5.2.4).

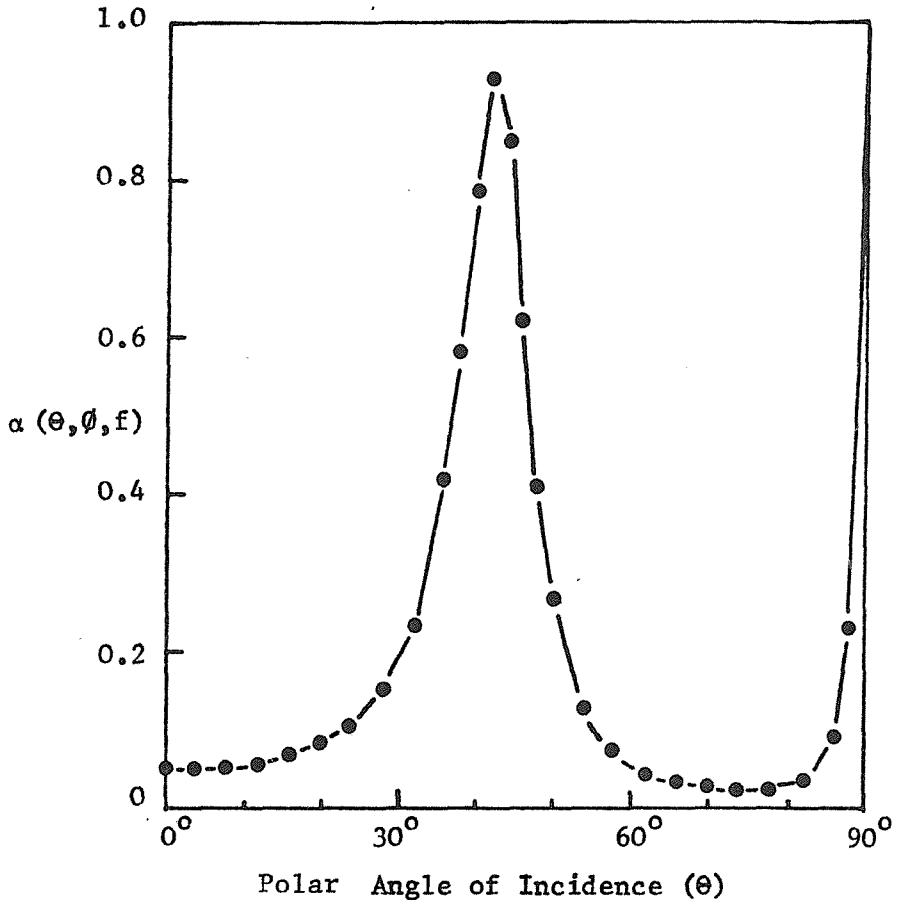

Figure 5.16(a) Variation of plane wave absorption coefficient with polar angle of incidence for two arrays of simply supported finite plates separated by an airspace.

Parameter values: M_{s1} = 12.09 kg/m^2; M_{s2} = 15.72 kg/m^2; D_1 = 989Nm; D_2 = 138461.5 Nm; a = 1.5m; b = 1m; d = 0.03m; loss factor = 0.06; frequency = 98Hz, Ø = 45°. Maximum number of terms in the plate mode series = 7 (in both x and y directions).

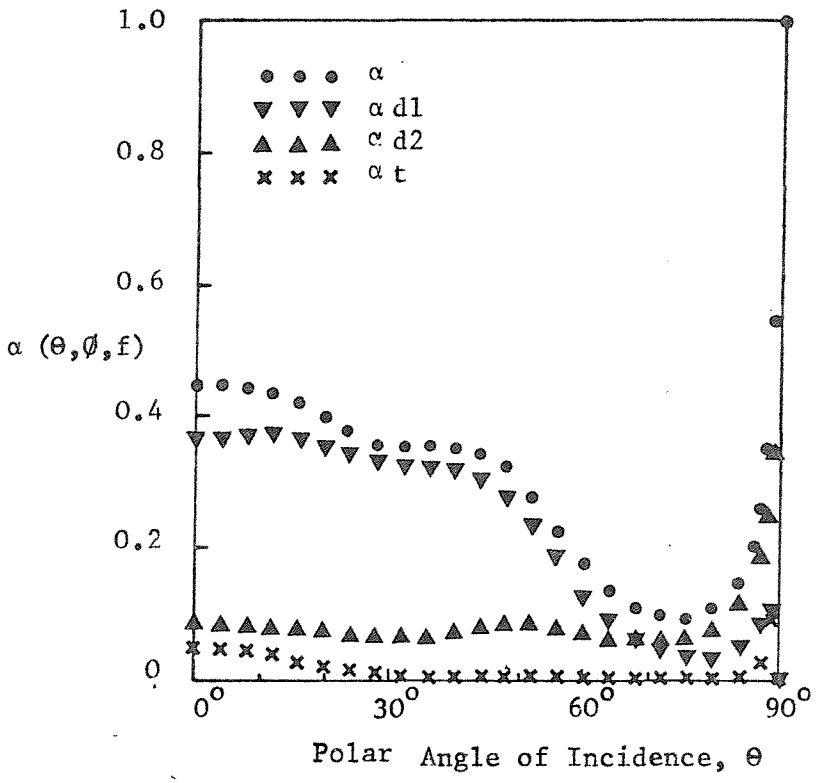

Figure 5.16(b) Parameter values as for Fig 5.16(a) except D_2 = 30659Nm.

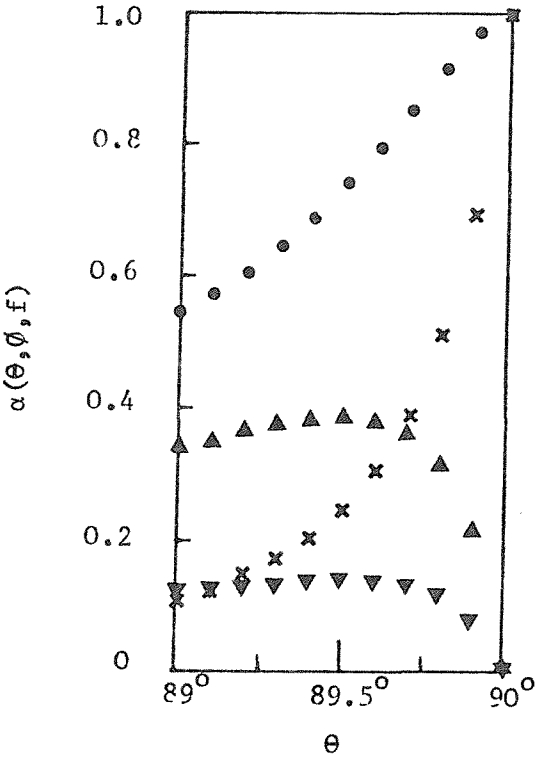

Figure 5.16(c) Magnification of Figure 5.61(b) for grazing incidence conditions.

The results of Figure 5.16(b) again illustrate the fact that the variation of α with θ is a lot less 'highly tuned' in the current model than in the infinite plate model, and thus larger diffuse field absorption values seem likely. However, it does not seem possible to make any simplifying assumptions about the variation of α with θ, and thus evaluation of diffuse field absorption coefficients would appear to require explicit computation of the variation with θ. Unless the variation of α with ϕ can be adequately accurately characterised in some simple manner, the computation of diffuse field 1/3 octave absorption coefficients will therefore prove impossible. The variation of α with ϕ is shown in Figure 5.17 for two specific cases. From these results it would appear that any accurate simplifying assumptions are unlikely since the variation of α is pronounced over the angular range. The behaviour exhibited by the cases shown is probably primarily due to the change in coupling between the incident field and the various plates' vibrational modes that are excited as ϕ is varied. Unfortunately this behaviour implies that the current model's computational requirements prohibit the calculation of 1/3 octave diffuse field results, and so comparison with the experimental results of Figure 5.2 is impossible.

The results of Figure 5.17(b) also illustrate the point that although the results of a solution which uses 7 terms in the μ and ν series appear adequate at 45^{o}, they are obviously in error at 30^{o} since α_{dl} is then marginally greater than α. The graph of Figure 5.17(c) shows that a solution with 9 terms in the μ and ν series alleviates this problem, although the accuracy is still not perfect, even though the sum of the transmitted, reflected,and dissipated energies is well within 10% of the incident energy.

Figure 5.18 is the final absorption coefficient plot to be discussed in this section; it shows an isometric view of α as a function of θ and frequency, for the configuration investigated with the stiffer backplate. Although it cannot be assumed to be very accurate at the highest frequencies depicted (since the results are based on only 5 terms in the μ and ν serires), it does however graphically illustrate the trends in the variation that will exist in practical cases.

Figure 5.17(a). Variation of plane wave absorption coefficient with azimuth angle of incidence for two arrays of simply supported finite plates separated by an airspace. Parameter values: $M_{s1} = 12.09 kg/m^2$; $M_{s2} = 15.72 kg/m^2$; $D_1 = 989 Nm$; $D_2 = 138461.5 Nm$; $a = 1.5m$; $b = 1m$; $d = 0.03m$; loss factor = 0.06; $\theta = 45^o$; Frequency = 100Hz. Maximum number of terms in the plate mode series = 5 (in both x and y directions)

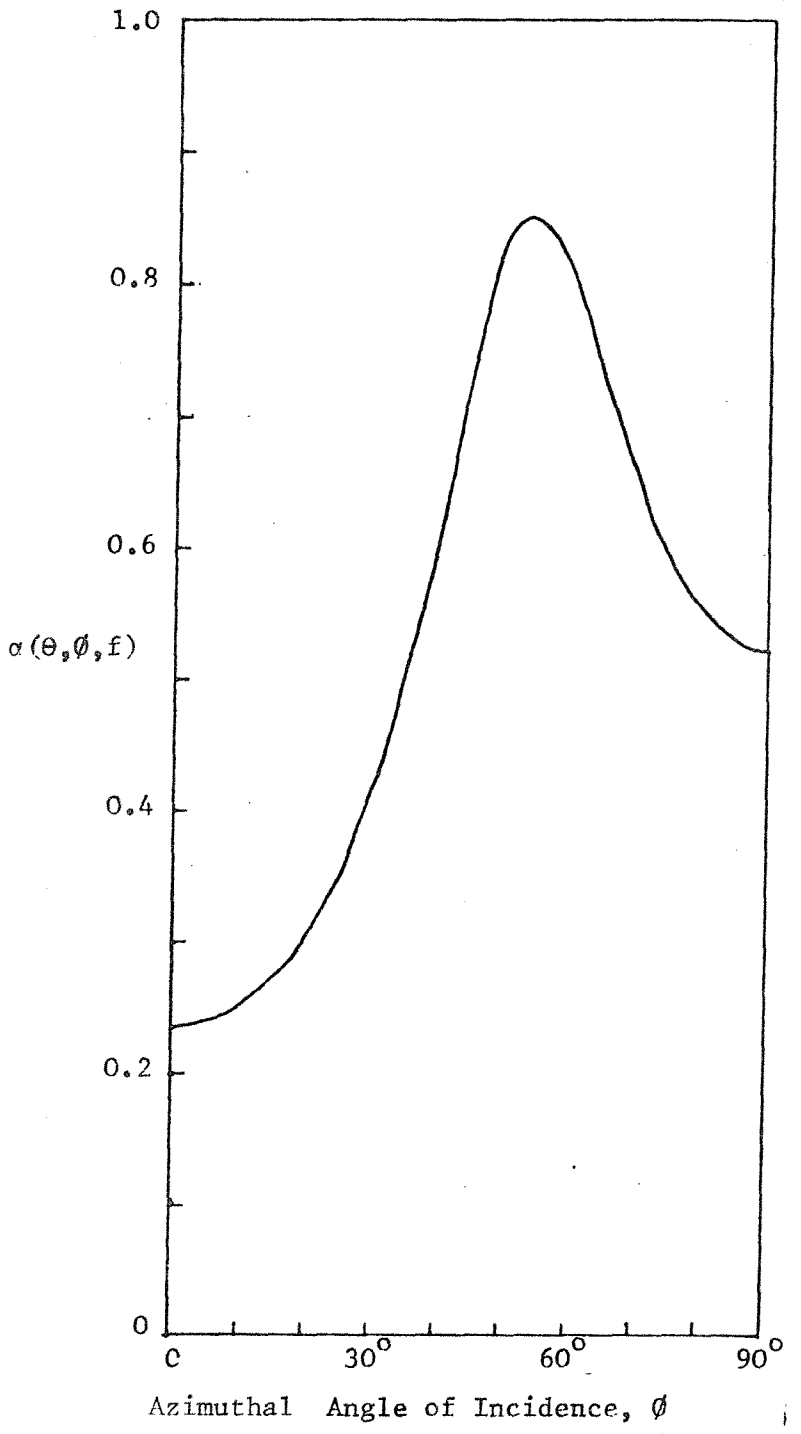

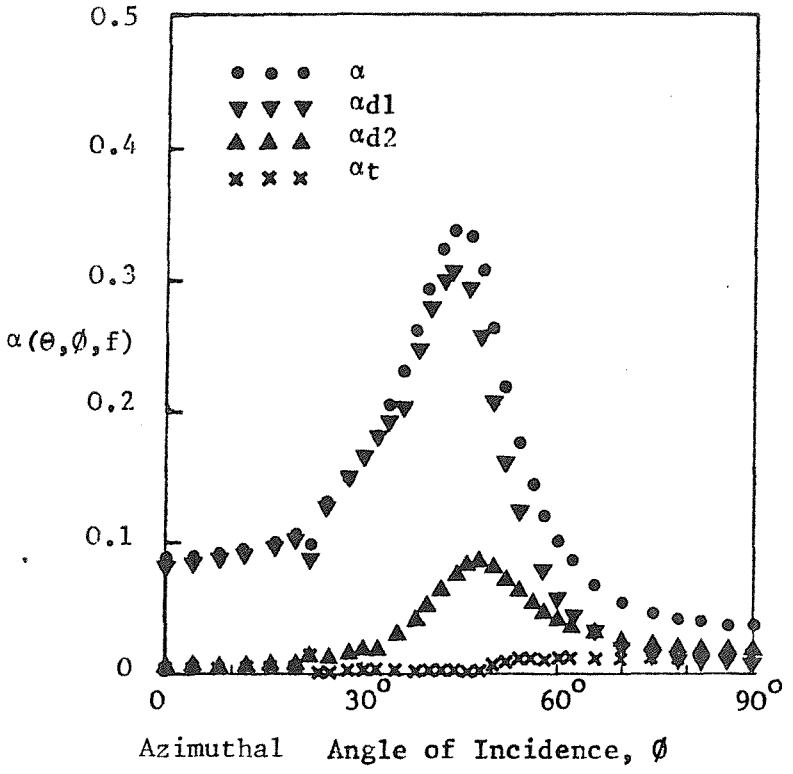

Figure 5.17(b) As for Figure 5.17(a) except D_2 = 30659 Nm, Frequency, f = 140Hz, and the maximum number of terms in the plate mode series = 7 (in both x and y directions).

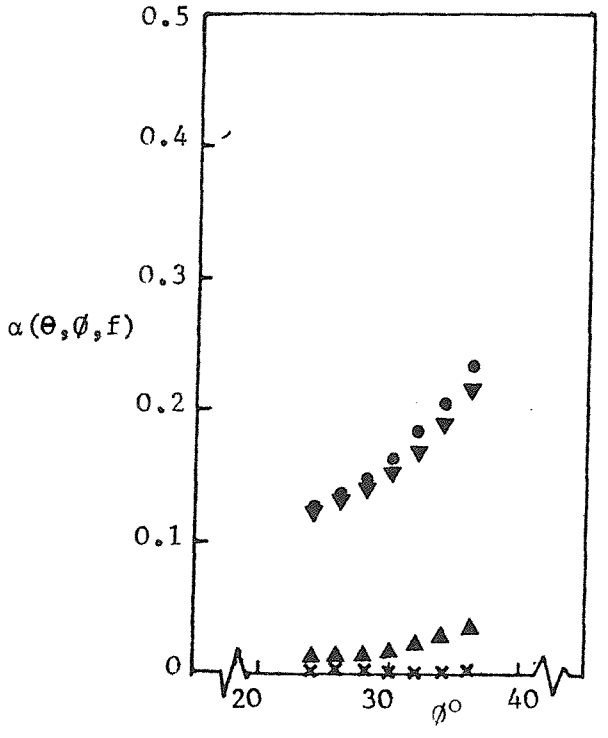

Figure 5.17(c) As for Figure 5.17(b) except the maximum number of terms in the plate mode series = 9.

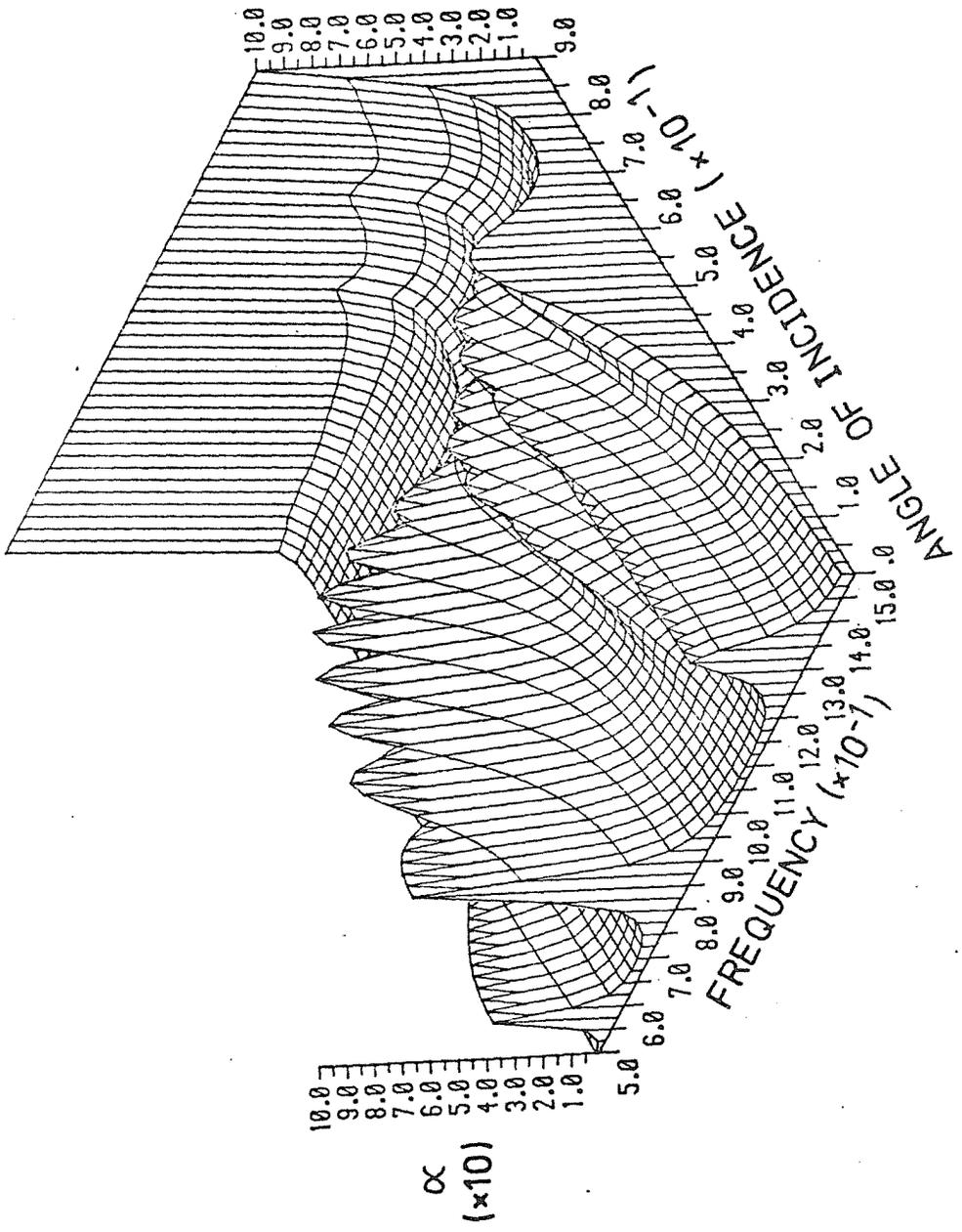

Figure 5.18. Isometric plot of the variation of absorption coefficient with angle θ and frequency f. D_1 = 989Nm, D_2 = 138461.5Nm, M_{s1} = 12.09kg/m^2, M_{s2} = 15.72kg/m^2, η = 0.06, a = 1.5m, b = 1m, d = 0.03.

One other point remains to be considered before the conclusion of this section; this is the fact that only a finite number of the reflected, or scattered, modes actually propagate in the space $z > 0$, under the physical conditions investigated. Thus, although close to the surface there will be non-propagating modes present, at any appreciable distance from the surface only the propagating modes will be in evidence. Thus, the number of these propagating modes that exist in a given situation will indicate how adequate a specular reflection model is. The criterion for whether a specific u,v mode propagates is that the sum of $(\cos\phi\sin\theta \pm 2\pi u/ka)^2$ and $(\sin\phi\sin\theta \pm 2\pi v/kb)^2$ must be less than unity. It can thus be seen that the number of 'cut-on' modes is a function of the angles of incidence, θ and ϕ, and also the non-dimensional parameters ka and kb (where k is the acoustic wavenumber, and a and b are the plates' x and y dimensions respectively). It will thus seen that the larger the values of ka and kb, the greater the number of modes that propagate. However for the majority of the results presented only the specular term (i.e. $u = v = 0$) is cut-on. The first non-specular term to cut on is the $u = -1$, $v = 0$ mode; this occurs in the presented results only for frequencies greater than about 166 Hz for $\theta = \phi = 45^{\circ}$ (see Figure 5.16(b)), and for ϕ values between 0° and about 22° for a frequency of 140 Hz and $\theta = 45^{\circ}$ (see Figure 5.17(b)). (The reasons for the 'blips' on the Figures at these points are not known, but they are small enough to be of little practical significance). In all these cases however the mode propagates very close to the surface and its reflection coefficient is very much less than that of the specular term. Thus for the results presented a specular reflection model would appear to be an adequate far field representation of the field reflected from this type of surface under these conditions.

5.4 Experimental Investigation of the Absorption Mechanism of Asbestos Roof Structures

5.4.1 Introduction

In the last section, a theoretical model was produced for the absorption of sound by double layers composed of simply supported

finite panels. This was then used to try to estimate the absorption characteristics of asbestos roof structures. Unfortunately the model's complexity rendered the computation of 1/3 octave diffuse field values impossible. Nonetheless the model did produce significantly more absorption than the earlier double infinite plate model. It also predicted that the majority of the absorption measured in the results of Figure 5.2 would be due to vibration of the component panels, and furthermore that an array of such panels would exhibit a variation of absorption with azimuthal angle of incidence. Since it appeared impossible to validate the model's predictions in any other way, two experiments were devised to try to verify the two main features of the model's results mentioned above. These tests are briefly described in the following sections, and where possible, results presented.

5.4.2 *Formulation of a procedure to estimate the dissipation coefficient of the front panels of an asbestos roof structure.*

The dissipation coefficient was defined in Section 5.3.4 as the ratio of the energy dissipated by a front panel in vibration to the amount of acoustical energy incident. Thus expressions for each of these energy quantities must first be formulated in order to ascertain which parameter values should be experimentally measured. The total energy per unit area of a plate in vibration is given by (see Reference [5.20])

$$E_p = 2(0.5\ M_s \langle V^2 \rangle) \ , \tag{5.50}$$

where M_s is the front plate's mass per unit area, and $\langle V^2 \rangle$ is a space, and frequency band average of the panel velocity squared. Since the loss factor η represents the fraction of the total vibrational energy dissipated per radian, the energy dissipated per unit area by the surface in one second is (from equation (5.50))

$$W_d = E_p \eta\omega = M\langle V^2 \rangle \eta\omega \ . \tag{5.51}$$

In order to express W_d as a fraction of the acoustic power incident, it will be necessary to make some assumption about the structure of the sound field in front of the panel. If it is assumed

to be 'locally' diffuse (where 'locally' diffuse means that over each panel the incident sound field is comprised of wave incident approximately uniformly over all angles of incidence) it is well known that the energy incident upon a unit area in one second is given by,

$$W_i = \langle p^2 \rangle / 4\rho c \quad ; \tag{5.52}$$

here $\langle p^2 \rangle$ is a local average over space, time and a frequency band of the presssure squared.

Thus from the ratio of equations (5.50) and (5.52) an expression for the dissipation coefficient can be written as

$$\begin{aligned} \alpha_{d_1} &\simeq 4\rho c \eta \omega M_s \langle V^2 \rangle / \langle p^2 \rangle \\ &\simeq 32\pi^3 \rho c \eta f^3 M_s \langle x^2 \rangle / \langle p^2 \rangle \end{aligned} \tag{5.53}$$

where $\langle x^2 \rangle$ is a space, time and frequency band average of the plate displacement squared. It can be seen from equation (5.53) that measurements of $\eta, \langle V^2 \rangle$ and $\langle p^2 \rangle$ are required for a given frequency band in order to estimate the dissipation coefficient in that band, and M_s must also be known.

5.4.3 *Measurement of the parameters required to estimate the dissipation coefficient of the front panels of an asbestos roof structure.*

All the measurements described in this section were performed at the inner roof surface of the factory illustrated in the frontispiece. A scaffolding tower was used to gain access to this surface at positions close to the eaves. For measurements of vibration levels, an accelerometer (Brüel and Kjaer Type 4335) was attached to the panel with beeswax and the output fed into a sound level meter (Brüel and Kjaer Type 2204) with a 1/3 octave filter set attached (Brüel and Kjaer Type 1616). Sound level measurements were performed at about 0.6 m from the surface, with a one inch microphone (Brüel and Kjaer Type 4145) in place of the accelerometer. The system was initially calibrated by use of a pistonphone (Brüel and Kjaer Type 4220) in conjunction with the microphone.

In order to estimate $\langle V^2 \rangle$ and $\langle p^2 \rangle$, vibration and sound pressure level measurements were made at six measurement positions. These are the locations P1.1, P1.2, P1.3, P2.1, P3.1 and P3.2 shown in Figure 5.19. The measurements were performed whilst the whole factory was in operation, in order to try to get as large and diffuse an airborne excitation as possible.

In order to analyse the results,the 1/3 octave vibration levels read from the sound level meter were first converted to absolute values from a knowledge of the accelerometer's sensitivity. Their converstion to displacement values was then approximated by division of the acceleration level in a band by ω^2 , where ω equals $2\pi f_c$ and f_c is the 1/3 octave band's centre frequency. The sound pressure levels were also converted to absolute presssure values, and the ratio $\langle x^2 \rangle / \langle p^2 \rangle$ evaluated for each of the measurement positions. Typical results are presented in Figure 5.20.

Since the front panel's mass per unit area has already been measured as 12.09 kg/m^2, it only remains to evaluate the loss factor η , in order to implement equation (5.53). This was done by recording the accelerometer output (by use of a Nagra IV.2 tape recorder) at each of the four measurement positions of Figure 5.19(a)) in response to the impulsive excitation of the panel by mechanical impact. Since the rate of vibration decay was rapid, the recordings were subsequently transferred onto the I.S.V.R.'s Data Analysis Centre's PDP 11/45 computer via a 1/3 octave analogue filter (Brüel and Kjaer Type 2112). The vibration decay reate was then measured, and the loss factor inferred from the expression (see Reference [5.20]) $\eta = 2.2/f_c T_{60}$, where f_c is the time taken for the vibration level to decay by 60 dB. The resultant loss factor values are shown in Figure 5.21.

All the parameters necessary for the evaluation of equation (5.53) have now been determined. Figure 5.22 shows the variation of the 1/3 octave front panel dissipation coefficient estimated in this manner from the average of all 6 sets of $\langle x^2 \rangle / \langle p^2 \rangle$ results and includes for comparison the previously mentioned experimental absorption coefficient results (from Reference [5.5] , first shown in Figure 5.2) for a $5m^2$ sample of a broadly similar structure to that investigated here.

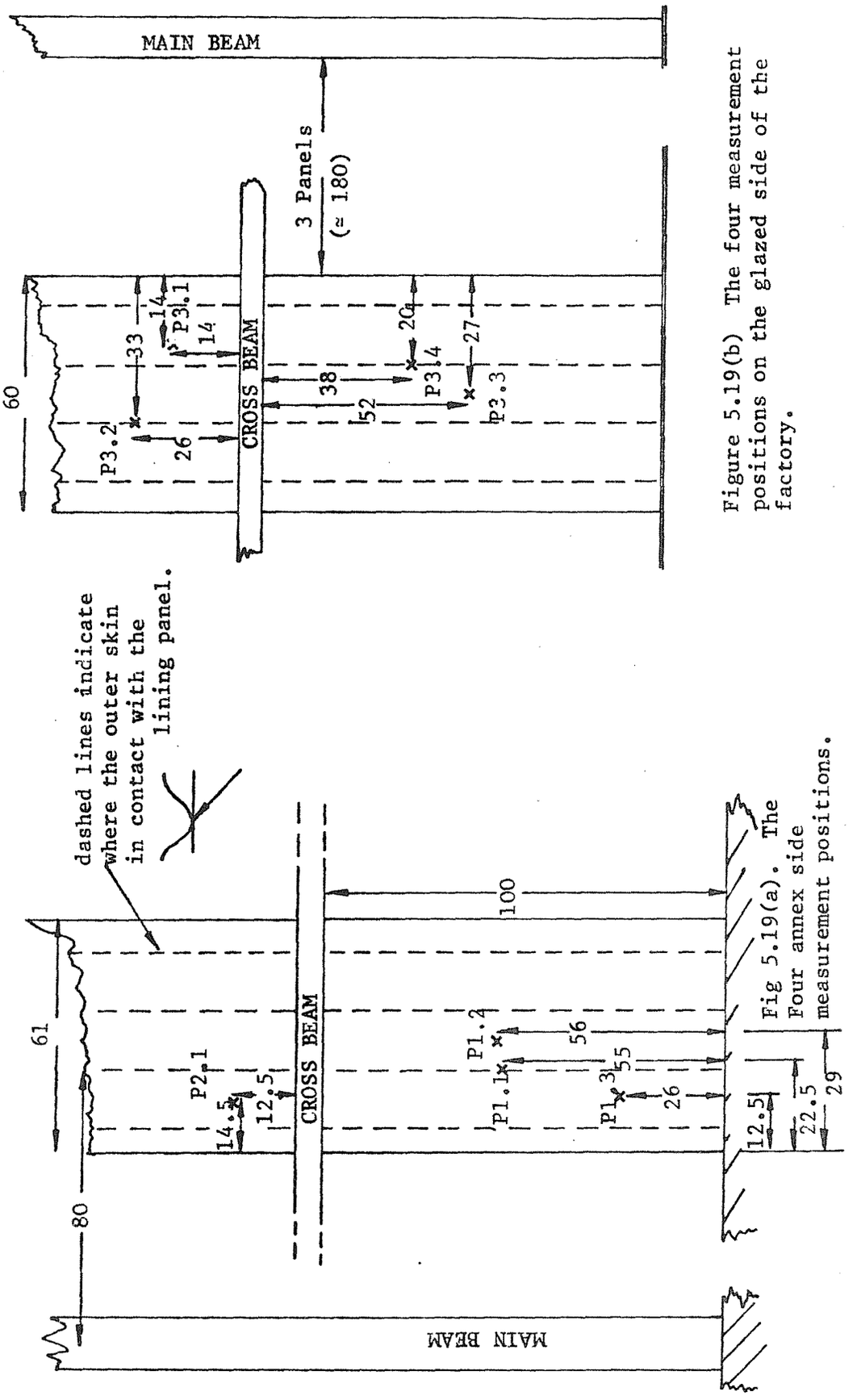

Figure 5.19(b) The four measurement positions on the glazed side of the factory.

Fig 5.19(a). The Four annex side measurement positions.

Figure 5.19. The measurement positions used for the roof vibration measurements in the Hamilton factory. All dimensions are in cms. The geometry is viewed from inside the factory.

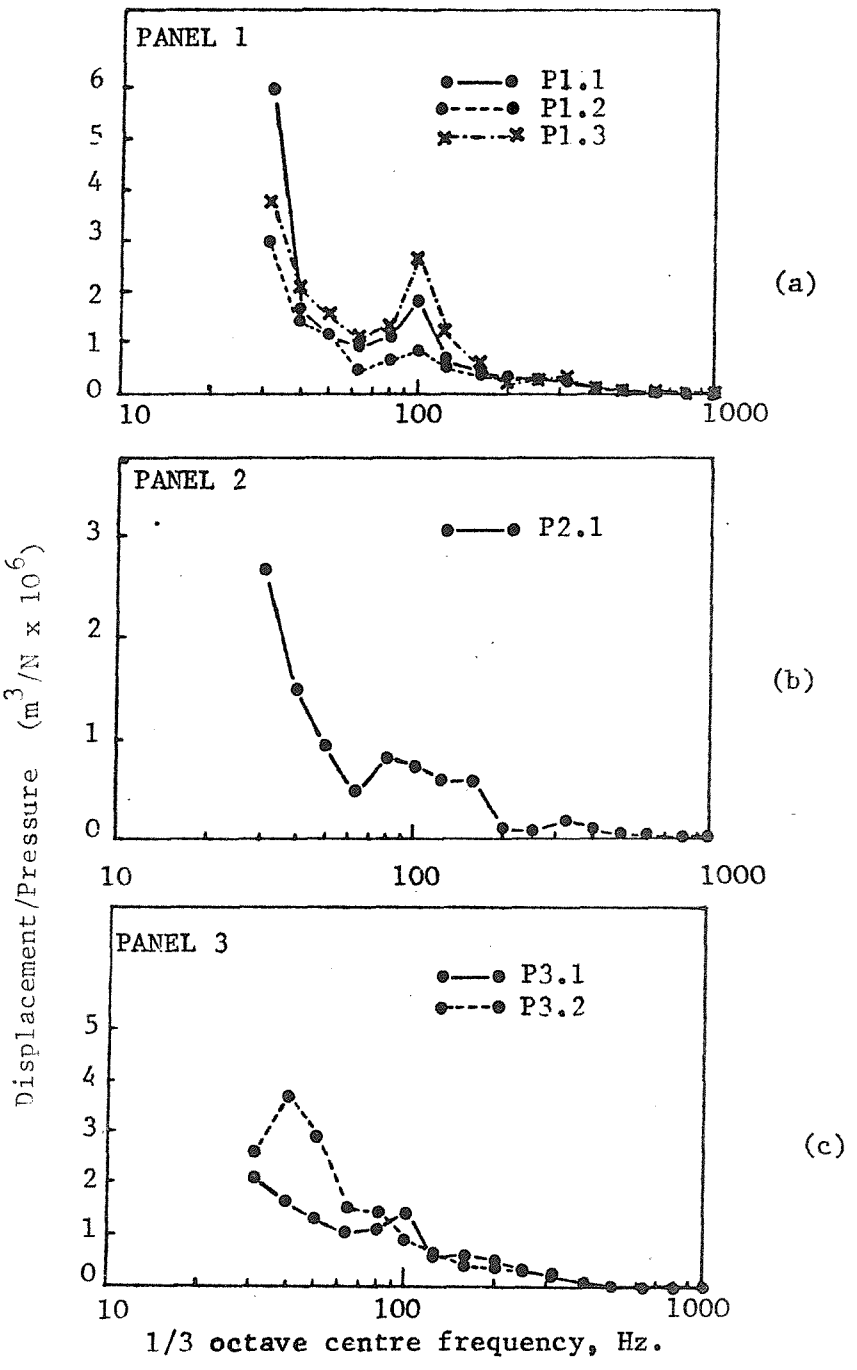

Figure 5.20. Plots of displacement/pressure ($m^3/N \times 10^6$) against 1/3 octave centre frequency for the roof vibration measurements made in the Hamilton factory.

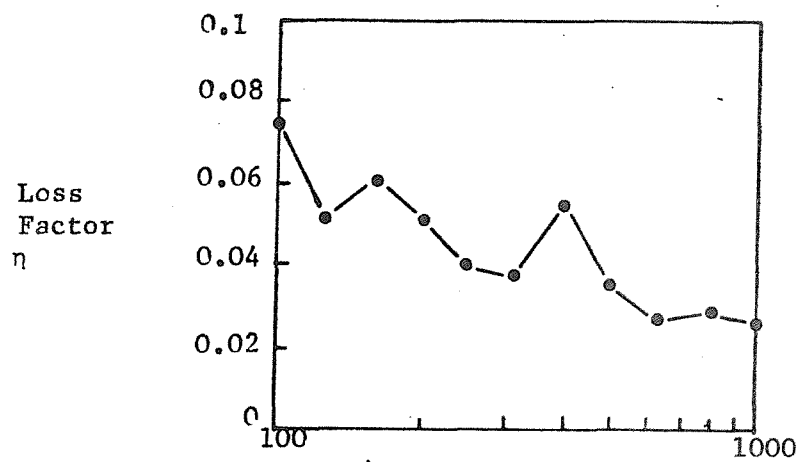

Figure 5.21 Loss factor as a function of frequency from the results for excitation of the Hamilton factory roof structure by mechanical impact.

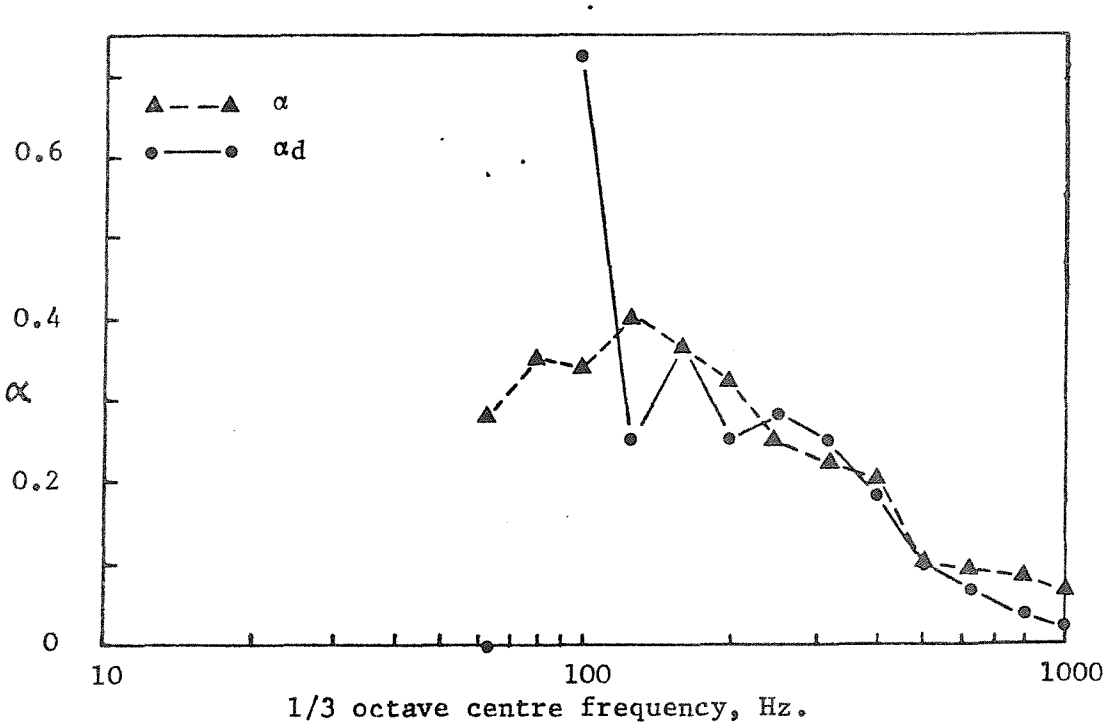

Figure 5.22 Comparison of the experimentally measured diffuse field absorption coefficient (α, from Ref [5.2]) with dissipation coefficient (α_d) estimated from the vibration measurements made in the factory.

5.4.4 *Discussion of the experimental asbestos roof dissipation coefficient results:*

Prior to explicit consideration of the results of Figure 5.21, the major possible sources of error in the measurements and their processing will be discussed. One of the major sources of error is likely to stem from insufficient spatial averaging of the vibration field, since only 6 measurement points were taken. This would be a greater problem at low frequencies, where the modal density is low and hence the variance is high. The sound pressure results may also suffer from inadequate sampling, since at low frequencies reflection interference effects near to a surface in a diffuse field can be pronounced even after 1/3 octave averaging (see Reference [5.26] for a discussion of such effects). Furthermore the assumption of the existence of a statistically diffuse sound field used to calculate the incident acoustic energy will obviously be incorrect near to an absorbent surface.

Further inaccuracies may be caused by the fact that due to equipment constraints it was not possible to measure simultaneously vibration and pressure levels. Thus the estimation procedure contains the inherent assumption of time invariant excitation signal characteristics, which, when the nature of the excitation signal is considered, will be seen to be extremely unlikely.

The above possible error sources indicate that the results presented may not be particularly accurate, but should at least give an indication of the structure's behaviour. This having been said, the dissipation coefficient estimates do seem to be in remarkably good agreement with the conventionally measured diffuse field absorption coefficients. This suggests that the results of the finite plate model, which indicated that the majority of the asbestos roof structure's absorption at low frequencies is due to energy dissipation by panel vibration, are at least qualitatively correct. The experimental results of Figure 5.21 indicate that this phenomenon is evident up to about, say, 1 kHz. Although it must again be stressed that the experimental technique described here is only approximate, and further noted that, since the corrugations of the backplate of the real roof structure in

this case appeared to be in contact with the front panel, the analytic model will not be ideally suited to exact comparisons anyway.

However, the qualitative agreement of the various predicted and measured absorption values was adequately encouraging to stimulate further investigation of ways in which to try to validate the theoretical model's predictions. One such attempt is described in the next section.

5.4.5 *Attempted experimental investigation of the angular variation of the absorption coefficient of an asbestos roof structure:*

(Note: this section contains only brief details of the experimental procedure used, since for a variety of reasons, discussed below, the method produced no valid results).

Since the theoretical finite plate absorption model indicates that there should be a visible variation of the plane wave absorption coefficient with angle of sound incidence for this type of structure, it was decided to investigate this variation for a 'real' roof sample. To this end, a 6 m × 6 m sample of a double layer array of 1.5 m × 1 m asbestos panels was constructed in the large anechoic chamber at the I.S.V.R. It was built in the place of the normal floor grids, about 30 cms above the wedge tips, with its lining panels uppermost, resting on the corrugated panels. Coach bolts were used to secure the panels to a framework of 0.1 m × 0.05 m section timbers positioned below the corrugated panels, with four coach bolts (two at each end) per double panel unit.

A small omnidirectional loudspeaker (a wooden box with one 3.5 cm diameter dome loudspeaker in each face), and a microphone were positioned above the surface so that the path from source to receiver via the surface subtended some desired angle to the normal at the point of specular reflection. Short pulses (5 or 10 ms) were then 'fired' from the source, and the direct and reflected signals picked up by the microphone. The microphone's output was then stored digitally on the I.S.V.R.'s Data Analysis Centre PDP 11/45 computer. The process was then repeated 100 times and the time histories averaged. This was to avoid the need to high pass filter the signal in order to reduce low frequency or random noise, since such filtering appeared to cause a 'ringing' in the results. This process was then repeated for a number of angles over the range 0° to 45°.

The incident and reflected pulses were then extracted from the averaged time history, zeroes added to their tails, and each pulse Fourier transformed. The transforms' moduli were then calculated and then the file containing the reflected values divided by the incident one. The resultant ratio was finally corrected for spherical divergence, since the incident and reflected pulses have travelled different distances. The values arrived at in this way should be the effective spherical wave reflection coefficients of the surface for that particular angle.

Unfortunately the results obtained appeared to be in error, as they were often greater than unity, and possessed a periodic fluctation with frequency. It was finally decided that there were a number of possible causes for this behaviour, some inherent to the technique used, others to the workings of the Data Analysis Centre. Associated with the technique, there is the fact that, as the angle of incidence moved towards grazing, so the incidence pulse's tail tended to overlap the start of the reflected pulse which in turn had its tail apparently contaminated by reflections, possibly from the sample edge. Even where the two pulses did not noticeably interfere, the actual length of data available for the incident pulse was very short and hence the definition in the frequency domain was poor. It was further discovered that due to the nature of the signal used there was very little low frequency energy present, hence the signal to noise ratio in the frequency range of interest was poor.

There were also discovered to be two major problems with the manner in which the computer system was used. First, there was found to be some non-linearity in the acquire circuitry used, whereby signals greater than $\pm$ 1 volt were distorted. Since the values used in this experiment were closer to $\pm$ 10 volts in order to achieve a good signal to noise ratio, some distortion of the results will have occurred. The second problem discovered was that there was not always a constant time interval between the computer's reception of the trigger signal and the start of the data acquisition, since it depended upon what else the computer was doing at the same time. Now, since a time averaging method was used in this experiment, even the slightest misalignment of one data set in time would obviously create problems, possibly similar to the presence of low frequency noise.

Thus unfortunately no conclusive data was obtained from this experiment, although obviously lessons regarding the design of any further experiments can be learnt. No further similar experiments were performed due to lack of time. The technique evidently needs much refinement in order to get accurate results. If further measurements were to be made there are various improvements possible to the technique. For example, assuming that the problems encountered with the computer system could be overcome, one possible method to increase the accuracy would involve the use of a larger test sample. Greater delays between the incident and reflected pulses could then be achieved, along with increased angles of incidence, and any 'edge effects' could be reduced. This increase in the time between the direct and reflected pulses' leading edges would permit a greater frequency definition in the Fourier transforms, and possibly the use of longer pulses with resultant increased low frequency content. Unfortunately the sample used was as large as could be accommodated in the ISVR's anechoic chamber, thus unless some other test site could be found alternative methods for increasing the accuracy would seem to be required. Further improvements might be possible by the use of advanced signal processing techniques such as cepstrum analysis (see Reference [5.28] for a brief description of this technique), for the treatment of the test data. Cepstrum analysis can be used to reconstruct the individual signals in situations where the direct sound and its reflection overlap. This would permit the use of longer signals with both increased low frequency content and spectral definition. The use of such advanced signal processing tecniques would therefore appear to offer the greatest potential for increasing the accuracy of any further experiments of this type.

5.5 Discussion and Conclusions:

It is apparent from the results of both the finite plate theoretical model and the experimental measurements reported in this Chapter that surfaces composed of an array of individual panels can exhibit quite surprisingly large absorption coefficients at low frequencies. For the case of the asbestos sheet roofing investigated, this absorption appears to be due to the dissipation of energy in the vibration of

the component panels for frequencies up to about 1 kHz. This particular case has been studied both theoretically and experimentally, and a general qualitative agreement observed between the results. From these results it appears that most of the energy absorbed is dissipated over the range investigated by the vibration of the front plate. Presumably this is because the back panels are generally stiffer and hence less prone to vibration.

Unfortunately, the evaluation of 1/3 octave diffuse field values from the finite plate theoretical model was not possible due to the complexity of the computations involved. At higher frequencies it might prove possible to speed calculations by use of some mode averaging technique, however, this idea was not pursued here since the model is at best only approximate when applied to the case of asbestos roofing, and also since the experimental evidence seems to indicate that at higher frequencies the level of absorption due to plate vibration decreases. Other possible improvements to the theory in order to model specifically the case of asbestos roofing would include the use of orthotropic plate bending theory to predict the backplate's vibrations more accurately, and a more detailed study of the effects of mounting conditions, or possible structural transmission paths. Alternatively, the current model could be used to study real situations where both the layers are composed of isotropic plates and the mounting conditions are better defined. An investigation of the effects on the low frequency absorption of the inclusion of an absorbent layer between the two plane layers could also easily be performed by modest alterations to the current theoretical model.

The other major feature of the theoretical models' predictions is the marked variation of absorption coefficient with angle of incidence. It proved impossible to accurately validate this point experimentally, but it should be noted that as the major absorption mechanism has been shown to be due to panel vibration, then any variation of the absorption coefficient with angle can be assumed to be broadly similar to that caused by such processes. Thus the angular variation of the absorption as predicted by the theoretical finite plate model may be taken as being at least indicative of that which can be exhibited in the real situation.

Any more definite conclusions about such angular variation would require improved experiments to be performed, drawing from the lessons learnt in the work described in section 5.4.5.

Since surfaces composed of these panel arrays are a relatively common feature in modern lightweight construction techniques, the question arises as to what effect any pronounced angular variation of the absorption coefficient would have on the acoustics of such buildings. Furthermore the validity of tests of the material's properties made under statistically diffuse conditions should be investigated for cases when the material is to be used in a non-Sabine space such as a highly disproportionate room. These points are investigated in the next chapter by incorporation of some of the results of the models presented in this chapter in a computer based, energy-image-sources, room acoustics model.

CHAPTER 5 : REFERENCES

5.1 P.T. LEWIS in T. SMITH, P.E.O'SULLIVAN, B. OAKES and R.B.CONN (Eds) 1971 Building Acoustics. Newcastle Upon Tyne : Oriel Press. See Chapter 7 : "Real Windows".

5.2 P.H. PARKIN, H.R. HUMPHRIES and J.R. COWELL, 1979 Acoustics, Noise and Buildings. London : Faber and Faber.

5.3 R. FRIBERG 1973. Internoise 73 Conference Proceedings (Lyngby, Denmark) 213-217. Transmission loss, and absorption factors for corrugated steel roof, insulated on the outside.

5.4 R. FRIBERG 1975. Swedish Building Research Report R18. The Acoustics of externally insulated sheet metal roofs (in Swedish, English summary).

5.5 R.J. ORLOWSKI, M.R. HODGSON, N.C. BAINES and M.F.E. BARRON, 1980 ISVR Memorandum No.603. Progress report on the acoustic modelling of factories.

5.6 L.L. BERANEK and G.A. WORK 1949. J. Acoust. Soc. Amer. 21, 419-428. Sound transmission through multiple structures containing flexible blankets.

5.7 A. LONDON 1950. J. Acoust. Soc. Amer. 22, 270-279. Transmission of reverberant sound through double walls.

5.8 G.G. TSEO, 1972. J. Acoust. Soc. Amer. 52, 1573-1578. Estimating the noise reduction of wall structures of enclosures.

5.9 K.A. MULHOLLAND, H.D. PARBROOK and A. CUMMINGS. 1967. J. Sound Vib. 6, 324-334. The transmission loss of double panels.

5.10 A. CUMMINGS and K.A. MULHOLLAND 1968. J. Sound Vib. 8, 126-133. The transmission loss of finite-sized double panels in a random incidence sound field.

5.11 K.A. MULHOLLAND, A.J. PRICE,and H.D. PARBROOK, 1968. J. Acoust Soc. Amer. 43, 1432-1435. The transmission loss of multiple panels in a random incidence field.

5.12 A.J. PRICE and M.J. CROCKER, 1970. J. Acoust. Soc. Amer. 47, 683-693. Sound transmission through double panels using SEA.

5.13 R.W. GUY, 1981. Acustica 49, 323-333. The transmission of sound through a finite panel, air gap, panel and cavity configuration - a steady-stage analysis.

5.14 E.C. SEWELL, 1970. J. Sound Vib. 12, 21-32. Transmission of reverberant sound through a single-leaf partition surrounded by an infinite baffle.

5.15 E.C. SEWELL, 1970. J. Sound Vib. 12, 33-57. Two-dimensional solution for transmission of reverberant sound through a double partition.

5.16 G.F. LIN and J.M. GARRELICK, 1977. J. Acoust. Soc. Amer. 61, 1014-1018. Sound transmission through periodically framed parallel plates.

5.17 A.D. PIERCE 1981. Acoustics : An Introduction to its Physical Principles and Applications. New York : McGraw-Hill Book Company.

5.18 H. KUTTRUFF, 1973. Room Acoustics. London : Applied Science Publishers Ltd.

5.19 P.M. MORSE and K.U. INGARD, 1968. Theoretical Acoustics. New York : McGraw-Hill Book Company.

5.20 L.L. BERANEK, 1971. Noise and Vibration Control. New York : McGraw-Hill Book Company.

5.21 S.P. TIMOSHENKO and S. WOINOWSKY-KRIEGER, 1959. Theory of Plates and Shells. New York : Mc Graw-Hill Book Company.

5.22 J.S. BOLTON and N.C. BAINES, 1982. Proceedings Institute of Acoustics Conference on Noise Control in Factory Buildings (Cambridge) 38-41. Sound absorption by double panel factory roof constructions.

5.23 M.C. JUNGER and D. FEIT 1972. Sound, Structures and their interaction Boston : MIT Press.

5.24 G.B. WARBURTON, 1953. Proc. Inst. Mech. Eng., Ser. A, 168, 371-381. The Vibration of rectangular plates.

5.25 A. De BRUIJN, 1967. Acustica, 18, 123-131. The sound absorption of an absorbing periodically uneven surface of rectangular profile.

5.26 NUMERICAL ALGORITHMS GROUP, 1981. Library of Subroutines Mark 8, Oxford.

5.27 R.V. WATERHOUSE, 1955. J. Acoust. Soc. Amer. 27, 247-255. Interference patterns in reverberant sound fields.

5.28 R.B. RANDALL, 1977. Application of B & K Equipment to Frequency Analysis. Naerum : Brüel and Kjaer.

CHAPTER 6

AN INVESTIGATION OF THE EFFECTS OF ANGULARLY VARYING ABSORPTION COEFFICIENTS ON THE ACOUSTICS OF ENCLOSED RECTANGULAR SPACES

6.1 Introduction

6.1.1 Background to the problem

In Chapter 5 the plane wave absorption characteristics of structures which often comprise one or more of the surfaces of a building shell were studied. It was discovered that these may be a relatively strong function of the azimuthal angle of incidence. It is known that many other surfaces often encountered in acoustics also exhibit angularly varying absorption coefficients (see for example Reference [6.1], Section II.3). The question therefore arises as to whether this behaviour must be taken into consideration in predicting sound levels in non-Sabine spaces. Furthermore the adequacy of conventional methods for the assessment of a material's absorption characteristics, when it is to be used in a non-Sabine space, should also be studied.

The major criteria that are normally of fundamental interest in the assessment of a room's acoustics are the overall steady state sound pressure level, at a point a given distance from a continuously steadily operating sound source, and the decay of that level with time when the source is de-activated. In a Sabine or statistically diffuse, sound field, this rate of decay of mean square sound pressure is exponential and can be predicted by a simple formula. The rate of decay is normally quantified as a "reverberation time", T_{60}, which is the time taken for the sound pressure level to decay by 60 dB. This quantity can be related to the absorption potential of the room by the equation, originally derived by Sabine [6.2].

$$T_{60} = 0.161\ V/\sum_i \alpha_i A_i \quad , \tag{6.1}$$

where V is the room volume and α_i and A_i are the absorption coefficient and area of the ith type of material surface (V and A are

in metres). This equation has subsequently been improved to account for factors such as air absorption (see Reference [6.1]) and asymmetric absorption distributions (see Reference [6.3]). In highly disproportionate spaces, these simple laws cannot be expected to be valid since there will not be an equal likelihood of sound arriving from all directions at any point, which is a fundamental requirement for a Sabine type formula to hold. Furthermore since the distribution of sound energy in angle at points on the boundary surfaces of disproportionate rooms may be considerably different to that in a Sabine space, it could prove important to consider the angular variation of the absorption coefficient in predictions of the acoustical qualities of such rooms.

Now, the major experimental method currently used for the assessment of a material's acoustical absorption characteristics is the reverberation chamber method. Essentially this method, which is described in detail in Reference [6.4], consists of averaging the T_{60} values from various measurment positions in a reverberation chamber, with and without the sample of the material to be assessed. Equation (6.1) can then be used to infer the change in the total absorption of the room's surfaces due to the addition of the material sample. From a knowledge of the material's geometric surface area the effective diffuse field absorption coefficient can then be evaluated. The rooms in which such tests are performed are specifically designed to simulate the conditions necessary for equation (6.1) to be valid. This is normally implemented by features such as very hard walls, which are sometimes non-parallel, rotating paddles, and suspended diffusing elements. It will be apparent from the above discussion, that whilst such measurements will provide a good indication of a material's acoustical behaviour under statistically diffuse conditions, it is not evident *a priori* that the same will be true for the prediction of the acoustics of non-Sabine spaces, such as disproportionate rooms. The investigation of such discrepancies could be performed either experimentally or analytically. It was decided to adopt the latter approach here since it would be very difficult to obtain two materials with identical diffuse field absorption coefficients, but radically different absorption mechanisms, as would be required for an experimental investigation. The analytic method used permits the absorption characteristics of a particular wall in a room to be altered at will.

The description of the method used and the results obtained are contained in the rest of this chapter.

6.1.2 *The image source method for the prediction of steady state and transient acoustical characteristics of rectangular enclosed spaces*

The major deterministic method currently in use for the prediction of steady state levels and reverberant decay rates for rectangular rooms is based on the principles of image theory. This is normally implemented numerically on a digital computer (see for example References [6.5, 6.6 and 6.7]). The basis of this model is that the sound field at any point in the enclosure can be represented as arising from a lattice composed of the real source and an infinite array of its images in all the walls. This model is strictly exact only for the case of a perfectly hard walled rectangular room; and for a room with partially absorbent walls some assumption must be incorporated. In such cases the image model is generally only used to represent comparatively high frequency situations, where it can be assumed that the output of the real source propagates according to ray acoustics theory. The ray paths from the real source and each individual image source to the receiver position in the real room are then traced. The energy associated with a particular ray upon its arrival at the receiver can be calculated based on the assumptions of spherical spreading, and absorption at each "image room wall" it has crossed. The energies of all the rays are then summed to obtain the overall sound pressure level at the receiver. The major assumptions involved with this model are that all the image sources are incoherent, and that the absorption characteristics of a wall surface are determined by the surface only in the immediate vicinity of the point of specular reflection. The first of these assumptions is normally adequate where a comparatively broad band noise source operates sufficiently far away from any of the room surfaces (i.e. at a distance of the order of a wavelength), whilst the second assumption is met by most surfaces in their high frequency limit. Even for cases where these assumptions are not satisfied, the image model will generally still indicate the correct temporal spacings of the reflections in the impulse responses of rectangular rooms. Hence, the model may be expected to display the gross effects audible in a room in the majority of practical cases.

If the absorption coefficient of a particular surface is assumed to be a function of the angle of incidence, the plane wave absorption coefficient for that angle may be used, subject again to the inherent assumption that all the reflections occur only at the specular angle (i.e., Snell's Law is obeyed). More often however a constant value is used for the reflection coefficient, β , and no variation with angle of incidence is considered. Generally the value employed in such cases is derived from the type of reverberation chamber tests mentioned briefly in Section 6.1.1. Now, the adoption of this assumption in cases where the absorption coefficient actually is a function of the angle of incidence - as it almost invariably will be to some degree - implies that the angular distribution of the rays' energies at the boundary can be considered to possess a $\sin 2\theta$ distribution. This factor is the effective angular weighting function used in the derivation of Paris' equation (see for example Reference [6.1], Section II.5). This will be restated, for convenience, as

$$\bar{\alpha} = \int_0^{\pi/2} \alpha(\theta) \sin 2\theta \, d\theta \quad , \tag{6.2}$$

where θ is the angle to the normal at the point of specular reflection on the surface (i.e., the usual Snell's Law angle of incidence). Now if the image model used is 'exact', the correct value of $\alpha(\theta)$ would be used in connection with every ray path considered. Each ray would therefore be attenuated by a factor $\left(\beta(\theta)\right)^n$ after n collisions with a set of parallel walls, where $\beta(\theta) = 1 - \alpha(\theta)$. Thus in terms of individual ray calculations the adoption of a diffuse field absorption coefficient in cases where α is a function of θ , is equivalent to the assumption that,

$$\bar{\alpha} \sum_N P_n^2(\theta_i) = \sum_N \alpha(\theta_i) P_n^2(\theta_i) \quad , \tag{6.3}$$

where $P_n^2(\theta_i)$ is the mean square pressure due to the ray from the n^{th} image source, and θ_i is the angle at which the ray due to that image source crosses the boundary under consideration. If the pressure terms are treated as continuous variables over the angular range in question, equation (6.3) can be rewritten as

$$\bar{\alpha} \int_0^{\pi/2} P^2(\theta)d\theta = \int_0^{\pi/2} \alpha(\theta)P^2(\theta)d\theta \quad . \tag{6.3a}$$

If $p^2(\theta)$ is assumed to have the form $A\sin 2\theta$, this equation becomes,

$$\bar{\alpha}A = A \int_0^{\pi/2} \alpha(\theta)\sin 2\theta d\theta \quad . \tag{6.4}$$

This equation, upon division by A , reverts to the form of equation (6.2). Hence it can be seen that a $\sin 2\theta$ distribution of the P^2 terms at a particular boundary will ensure that use of equation (6.3) is justified. Such conditions are to be expected in statistically diffuse fields.

Subject to the above assumptions, the overall intensity at a receiver R at (X_R,Y_R,Z_R) due to a source, S , of power output W situated at (X_s,Y_s,Z_s) in a room of dimensions (a,b,c) with all boundary surfaces possessing a uniform absorption coefficient α , can be written as

$$I(R,t) = \sum_{\ell=-\infty}^{\infty} \sum_{m=-\infty}^{\infty} \sum_{n=-\infty}^{\infty} \frac{W(S,t-d_{\ell,m,n}/c)}{4\pi d_{\ell,m,n}^2} (1-\alpha)^{N_R} \exp(-m_a d_{\ell,m,n}) \quad . \tag{6.5}$$

In this equation m_a is the air attenuation coefficient (in Nepers/metre), and N_R is the number of 'collisions' with imaged walls that a ray has in travelling the distance $d_{\ell,m,n}$ from the image source due to ℓ,m and n reflections in the walls perpendicular to the x,y and z axes respectively. The positions of the various orders of image sources are shown in Figure 6.1 for a section through image space in the plane $n = 0$. It will be seen from this diagram that the image of order $(1,-2,0)$ corresponds to one reflection in the wall $x = a$, one with each of the room's walls perpendicular in the y-axis, and none with any of the surfaces perpendicular to the z axis. A negative sign in the order index expression indicates that the ray arrives at the receiver from the direction of one of the planes with either x or y or z equal to zero. Thus in the example above, the -2 value for the number representing collisions with surfaces perpendicular to the y axis indicates that the ray arrives at the receiver

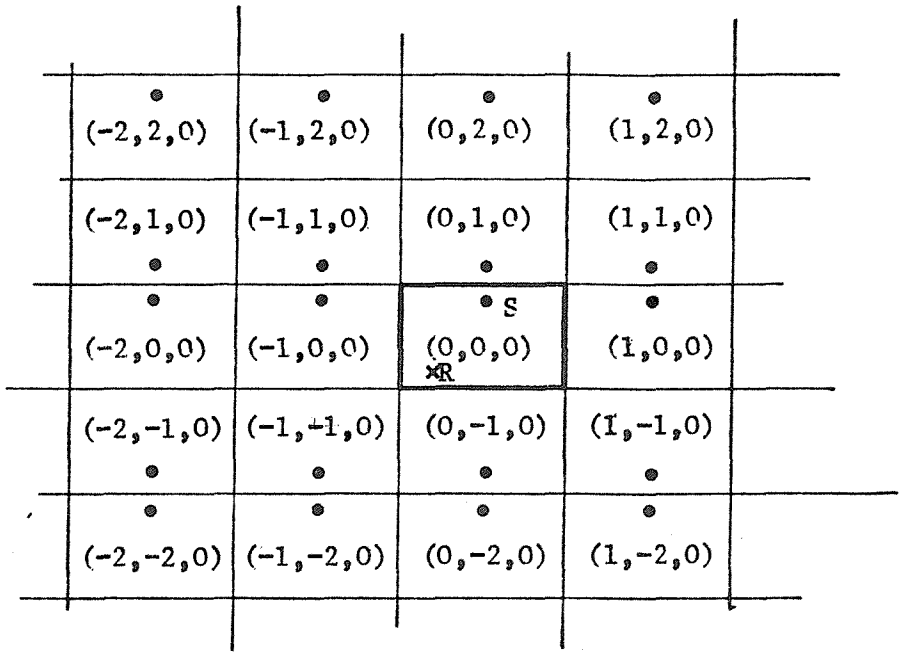

Figure 6.1 The distribution of the image sources in image space for n = 0.

from the direction of the $y = 0$ surface. The total number of reflections N_R, that the contribution from a given image source will have undergone, is given by the expression

$$N_R = |\ell| + |m| + |n| \quad . \tag{6.6}$$

The x,y and z co-ordinates for the position of an image source of order (ℓ,m,n) can now therefore be explicitly written as

$$X_{s\ell} = (\ell+1)a - X_s \quad ,\ell = \text{odd} \quad ,$$

or,

$$X_{s\ell} = \ell a + X_s \quad ,\ell = \text{even} \quad . \tag{6.7}$$

$$Y_{sm} = (m+1)b - Y_s \quad ,m = \text{odd}, \quad ,$$

or

$$Y_{sm} = mb + Y_s \quad ,m = \text{even} \quad . \tag{6.8}$$

$$Z_{sn} = (n+1)c - Z_s \quad ,n = \text{odd} \quad ,$$

or

$$Z_{sn} = nc + Z_s \quad ,n = \text{even} \quad . \tag{6.9}$$

The form for the distance from any image source to the real receiver, can now be written as

$$d_{\ell,m,n} = \left((X_{s\ell}-X_R)^2 + (Y_{sm}-y_R)^2 + (Z_{sn}-Z_R)^2\right)^{\frac{1}{2}} \quad . \tag{6.10}$$

All the parameters necessary for the evaluation of equation (6.5) in a specific geometric configuration have now been evaluated, except for the air attenuation coefficient m_a. This term can be determined, given the temperature and relative humidity for which predictions are required, by use of standard equations or tables (see for example Reference [6.8]).

In order to model a situation where the walls of the enclosure have different absorption coefficients, the factor $(1-\alpha)^{N_R}$ in equation (6.5) must be altered. For example, in the specific case where the two walls of the real room perpendicular to the X axis at X=0 and a have absorption coefficients α_{X1} and α_{X2} respectively, whilst the remaining surfaces have an absorption coefficient α, the attenuation factor becomes

$$(1-\alpha)^{N_R} = (1-\alpha)^{N_R-|\ell|}(1-\alpha_{X1})^{NL1}(1-\alpha_{X2})^{NL2} \quad . \qquad (6.11)$$

Here for ℓ even, NL1 = NL2 = $|\ell|/2$; otherwise NL1 = $|\mathrm{Int}((\ell-1)/2)|$, and NL2 = $|\mathrm{Int}((\ell+1)/2)|$, where 'Int' implies that only the integer part of the argument is considered. This form can obviously be extended to the limit of six different absorbent surfaces.

If, in addition, the absorption coefficient of one particular surface is a function of angle of incidence, it is necessary to calculate the angle to the normal at which each ray meets that surface. Thus if the surface at $y = b$ has a plane wave absorption coefficient $\alpha(\theta)$, the value of θ to be used in the calculation of $\alpha(\theta)$ can easily be determined from the expression

$$\theta = \cos^{-1}(|y_{sm}-y_R|/d_{\ell,m,n}) \quad . \qquad (6.12)$$

All the equations necessary for the numerical implementation of an energy image source room acoustics model have now been described for steady state conditions. In order to actually use the model, only the number of image orders to be considered remains undecided. Consideration of this factor will be left until the numerical implementation of the model is specifically considered in Section 6.2.1. In order to evaluate steady state levels due to a continuous time invariant source, the time dependence of W and I in equation (6.5) can be omitted and the resultant summations performed. However in order to evaluate the rate of sound pressure level decay when such a source is switched off, the level at the receiver at time t is the sum over all the image source contributions that are still 'switched on".

Thus if the direct sound from the source ceases to arrive at the receiver at $t = 0$, the requirement for a source of image order (ℓ,m,n) to be still operative at a time t is that $d_{\ell,m,n} > ct$. Thus at this time t only contributions from outside a sphere 'image space' of radius ct centred at the receiver need to be considered. By calculations in this manner of the level at the receiver at discrete time intervals after the source has been switched off, the decay of the reverberant sound with time can be numerically computed.

One point worthy of mention at this stage concerns the normalisation of any results numerically computed in order to make them more generally applicable. This is possible by division of any values of $I(R,t)$ calculated from equation (6.5) by the value of I that would exist at 1m from the source under free field conditions, denoted I_{1m}. This can be expressed as

$$I_{1m} = (W/4\pi)\exp(-m_a) \quad . \tag{6.13}$$

Now since any results computed will normally be presented in terms of sound pressure levels, in dB, the resultant ratio is equal to the difference between the overall sound pressure level at R and that at 1m from the source under free field conditions. Now, for a simple source this latter value equals the source's sound power level (PWL), thus

$$SPL(R,t) - PWL = 10\log_{10}\left(I(R,t)/I_{1m}\right) \quad . \tag{6.14}$$

Thus one has a more generalised manner for the presentation of any computed results, which indicates how a particular room effects the levels generated by any small omnidirectional source, provided its sound power level is known.

6.1.3 Discussion of the possible incorporation of the panel array absorption models developed in an energy image source room acoustics model.

In the first section of this Chapter it was suggested that measurements made on a sample in a reverberation chamber may not prove

adequate to predict the acoustics of non-statistically diffuse enclosures on occasions when the material's plane wave absorption coefficient is strongly dependent upon the angle of incidence. In section 6.1.2 a method for the evaluation of the acoustics of any rectangular room has been formulated. There is no assumption about the general nature of the field at any point in this model, only that it can be represented as due to the superposition of an array of energy image source contributions, which are estimated from ray acoustics theory. It can also accommodate either uniform, diffuse field absorption coefficients, or ones that vary with angle of incidence. It is thus possible to investigate the differences in predictions which arise between the use of a diffuse field absorption coefficient and one that is a function of angle of incidence. The comparison can be performed both for room geometries that may be expected to be approximately statistically diffuse (e.g., cubic rooms), and those where this will not be the case (e.g., highly disproportionate rooms). It only remains to decide on an absorption characteristic to use in such an investigation.

Since models for the absorption of sound by arrays of panels have been developed in Chapter 5, they would seem ideally suited to incorporation in any proposed investigation. This is especially true since they are representative of a type of surface often found in disproportionate spaces (see Section 5.1.1). However there are a number of points concerning the use of these absorption models which must be noted if they are to be incorporated in an image source room acoustics model in order to represent a real situation. Firstly these plane wave absorption models were only calculable for, and apparently applicable to, comparatively low frequency situations. Under these circumstances, only the specularly reflected mode takes energy away from the surface, and a far field specular reflection approximation will be adequate. Unfortunately, at low frequencies the ray propagation representation of the image model will be inexact. It is theoretically possible to decompose the spherical wave field due to a point source into a superposition of plane waves (as shown in Reference [6.9]). Thus the absorption of each of these component waves by the panel array could be evaluated, and hence the total effect on the spherical field due to a particular image source at a given surface. Such a procedure

although in theory possible, is useless for practical purposes and some simplifying assumptions must be sought. In these cases, since the surface is effectively plane, most of the energy that arrives at the receiver after a single reflection from such a surface arises from the area around the specular reflection point. In order to render the problem tractable, the plane wave absorption coefficient for the specular reflection angle will therefore be assumed to provide an adequate estimate of the surface's effect on a particular source's energy contribution.

One further complication which arises from the use of the panel absorption model developed is due to the presence of surface waves in this model. These waves do not carry any acoustical energy away from the surface, but they do give rise to a pressure field near to the panel array's surface. Thus, since the image source model is based on the summation of P^2 terms, and the presence of any surface waves is neglected, predictions made at points in the vicinity of the panel structure can therefore be expected to possess larger errors than those made for points elsewhere.

Subject to the above qualifications however, the incorporation of the results of the model for absorption of sound by a panel array in an energy image source room acoustics model can be expected to at least indicate the major acoustical trends observable in a real situation. Alternatively, since the main object of this chapter is not to develop a validated prediction method, but rather to study the effect of any angular variation of a surface's absorption coefficient on a room's acoustics, the absorption characteristic can be thought of as being chosen in a purely arbitrary manner. In this case any effects observed can be related to the absorption characteristic chosen, but this need not be thought of as specifically representative of any particular real physical situation. Such an interpretation of the absorption characteristics chosen in this case will still permit greater insight into the fundamental acoustical characteristics of the rectangular rooms investigated.

6.2 Calculation of the Quantitative Effects of Two Particular Angularly Varying Absorption Coefficients on the Acoustics of Two Rectangular Rooms:

6.2.1 The numerical implementation of the energy image source room acoustics model

All of the equations necessary to construct an energy image source room acoustics model have been described in Section 6.1.2. The computer program written to numerically implement such a model in Fortran on the University's ICL 2970 computer is listed in Appendix E. The absorption characteristics to be used are discussed in the next section. It only remains therefore to consider how many image sources to take into account. This is very important since it alters both the accuracy of any results obtained and the computation time necessary to calculate them.

For the steady state case in a rectangular room, Gibbs and Jones [6.5] estimated the difference ΔL (in dB) due to contributions from a sphere of radius a in image space and the complete contribution from an infinitely large sphere. For a room of uniform absorption coefficient α, they related a (in metres) and ΔL by the equation:

$$a \simeq \frac{\bar{\ell}\,(1-10^{-(\Delta L/10)})}{m\bar{\ell}-\ln(1-\alpha)} \qquad (6.15)$$

where $\bar{\ell}$ is the classical mean free path. In the derivation of this expression, Gibbs and Jones calculated the intensities due to both a finite number and an infinite number of sources, in terms of integrals involving the classical mean free pathlength $\bar{\ell}$. For the case of any rectangular room with specularly reflecting surfaces, the mean free pathlength has the classical value of $4V/S$, where V and S are the room's enclosed volume and surface area respectively (see Reference [6.1] Section IV.3). This value can only generally be obtained by averaging over the contributions of many image sources, and is not therefore the average value for any particular ray path. For the ensemble average over many different rays to equal the time average for one random ray propagating in the real room, the field must be statistically

diffuse. This state is normally, at least partially achieved by the presence of features in the room which cause a ray's direction to be changed many times. A roughly proportionate or cubic room with identical almost perfectly reflecting wall surfaces might be expected to exhibit more or less the required conditions for a diffuse field since random rays emitted by a source in any direction will have about the same pathlength collision statistics. Although any rectangular room that possesses diffusely reflecting boundaries can be shown to possess the classical mean free pathlength value as the time average for any particular ray (see Reference [6.1] Section V2), for the case of specularly reflecting walls this value is only true for an ensemble average over all possible ray directions. The difference of individual rays' mean free pathlengths from this ensemble average can obviously be expected to increase as the room's shape become more disproportionate. Thus the integrals performed by Gibbs and Jones will probably be in error to a certain extent for two reasons. Firstly, the finite radius sphere in image space will not contain enough images to have an ensemble average mean free pathlength adequately close to 4V/S; and secondly, the use of the ensemble average mean free pathlength to estimate the contributions of the individual images in the finite radius sphere considered is incorrect in the cases of disproportionate rooms, since it does not equal the average mean free pathlength for any individual ray. Otherwise the equations derived by Sabine would be correct for any enclosure since the field would always be diffuse.

Since the principal interest here is in the acoustical properties of disproportionate rooms, the possible use of equation (6.15) will not be pursued here. Instead the results presented in Section 6.2.3 will be prefaced by an illustration of the effect that the number of image source orders considered has on the calculated steady state levels.

The evaluation of the accuracy of reverberant decay calculations is more complicated. This is because only a finite sphere of image sources is considered in image space; hence at longer times after the source is switched off the spherical shell of image sources that still contribute to the calculations diminishes, and eventially drops to zero. In reality there would still be contributions from all the remaining 'switched on' image sources out to infinity in image space. Thus,

although at short times after the source is switched off the image source contributions considered in the numerical calculations are much greater than those neglected, at times long after the source has been switched off the same will not be true. Hence the rates of decay numerically calculated are more accurate shortly after the source has been switched off than at later times. Although it would be possible to perform an analytic analysis of the errors inherent in the numerical computation of the reverberant decay in a broadly similar manner to that outlined above, it would still be subject to the same assumptions, which are unacceptable here. Therefore it was decided to simply alter the number of images considered in one particular case, and so investigate the change in the rate of sound pressure level decay after the source is deactivated. This will allow the accuracy of the other plots presented to be inferred. The plots computed are presented and discussed in Section 6.2.3.

6.2.2 The absorption characteristics incorporated in the energy image source room acoustics model:

As was discussed earlier in this chapter, the double panel array absorption model of Chapter 5 provides convenient results for incorporation in an energy image source room acoustics model. Great care must be exercised in the interpretation of any results as the predictions for a real situation, however, as was discussed in Section 6.1.3. If so desired, the chosen absorption coefficient characteristics can alternatively be assumed to be purely arbitrary, and the resultant predictions interpreted appropriately.

The two absorption characteristics employed, and the parameter values used in the double layer finite panel array model of Section 5.3, are shown in Figure 6.2. Only variation with the polar angle of incidence is considered. This is partly because many other absorption characteristics are independent of the azimuthal angle ϕ (for example, a normal impedance boundary surface model), and partly because the variation with ϕ in the finite panel array model was not apparently as systematic as the variation with θ. The consideration of variation of the absorption coefficient with θ alone also considerably reduces

the computational requirements. Obviously the fact that any variation with ϕ has been omitted from this model does imply that any results that are to be interpreted as predictions for a real situation will probably only be indicative of broad trends. Therefore the interpretation of the absorption characteristics used as hypothetical results for some unspecified surface is more convenient since the problems inherent in the use of the double panel results are thus avoided (e.g., the presence of non-specular terms or surface waves, and the possible variation of α with ϕ) . The two absorption characteristics chosen display markedly different behaviours (see Figure 6.2). The values shown in Figure 6.2(a) have a steady increase in absorption towards grazing, whereas the trace of Figure 6.2(b) has a distinct absorption peak at a θ value of 45^{o}, in addition to an abrupt increase near to grazing incidence.

The next requirement is for the computation of the equivalent diffuse field absorption coefficients for each of the two plots of Figure 6.2, so that the effect of an angularly varying absorption coefficient can be compared with a uniform one (as might be estimated from reverberation chamber tests) in the image source room acoustics model calculations. In order to estimate the diffuse field value, both sets of results from Figure 6.2 were integrated, according to equation (6.2). The integral was evaluated numerically by use of Simpson's rule with 1^{o} increments uniformly across the integral range. The results of these computations are indicated by the solid lines parallel to the abscissa in Figure 6.2. These results demonstrate that the angular variation of Figure 6.2(b) gives rise to much more absorption in a statistically diffuse field than do those of Figure 6.2(a). This is because of the $\sin 2\theta$ weighting factor in equation (6.2). This favours absorption coefficient values in the region of θ equal to 45^{o}. Since the results of Figure 6.2(b) have a peak in this region, their equivalent diffuse field value is much larger than that for the results of Figure 6.2(b).

The results of Figure 6.2 therefore provide values of either angularly varying or constant absorption coefficients to insert into the energy image source room acoustics model. This will enable the testing of the hypothesis that a knowledge of the angular variation of

Figure 6.2(a)
Absorption
Characteristic 1.

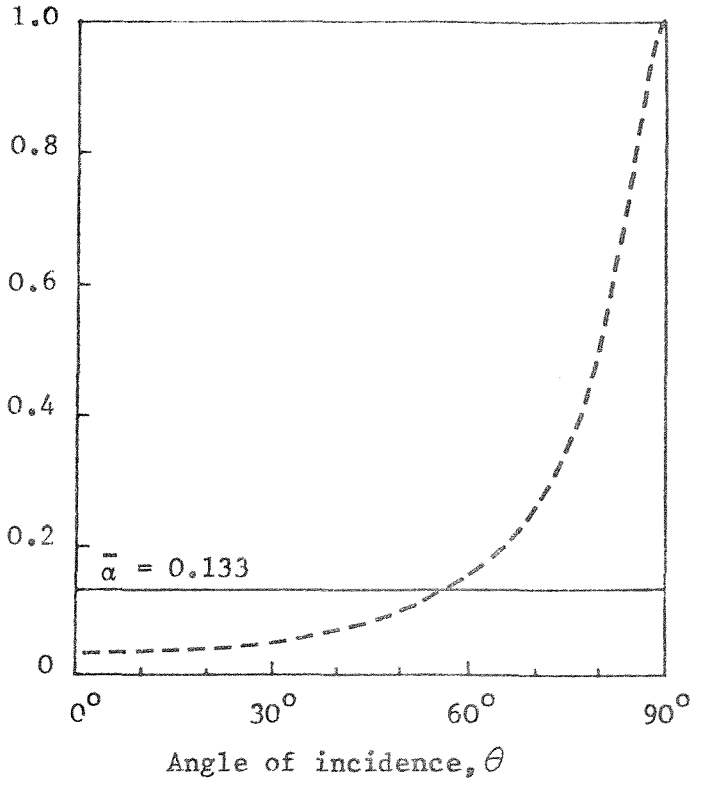

Figure 6.2(b)
Absorption
Characteristic 2.
(cf. Figure 5.16(a))

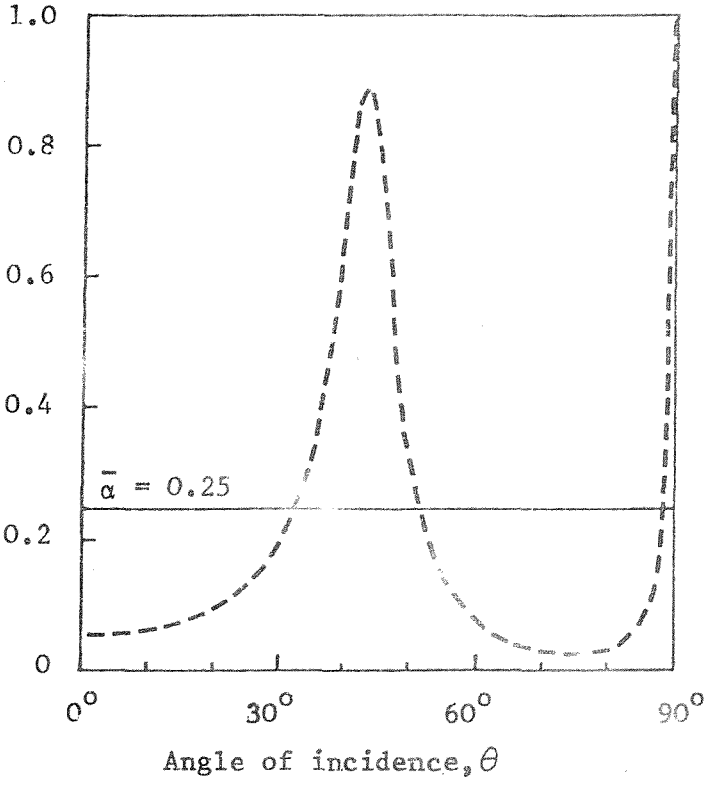

Figure 6.2 The absorption characteristics used in the energy-image-source room acoustics computer program. (Finite plate model parameters for characteristic 1: $D = 989\text{Nm}$; $D_2 = 30659\text{Nm}$; $M_{s1} = 12.09\text{kg/m}^2$; $M_{s2} = 15.72\text{kg/m}^2$; $\eta = 0.06$; $a = 1.5\text{m}$; $b = 1\text{m}$; $d = 0.03\text{m}$; $\phi = 45°$; $f = 90\text{Hz}$).

a material's absorption coefficient may be necessary in order to predict the acoustics of non-Sabine spaces, and hence that reverberation chamber tests may be pointless for the evaluation of materials to be used in such spaces, and conversely that little can be inferred about a material's absorption coefficient from tests performed in non-Sabine spaces. The results of such computations are presented and discussed in the next section.

6.2.3 Presentation and discussion of the results of the energy-image-source room acoustics model.

All the results in this section will be concerned with comparison of the effects of angularly varying absorption coefficients as opposed to uniform ones, for two specific types of room. The two rooms are chosen to be representative of proportionate and disproportionate spaces, and are a cubic room of dimensions 10 m × 10 m × 10 m , and a 'flat' room of dimensions 100 m × 10 m × 50 m. All the surfaces except one possess a uniform absorption coefficient of 0.1 in both cases. It is the absorption coefficient of this last surface (which will be one of the 100 m × 50 m surfaces in the flat room) which will be altered.

However, before any results can be discussed in detail, their likely accuracy must be investigated. This was done by observation of the changes which resulted from alteration of the number of images considered in the calculations. The results are presented in terms of the radius, ct , of the sphere considered in 'image space'. Figure 6.3 contains details of the convergence of the steady state predictions for both the cubic (Figure 6.3(a)) and disproportionate (Figure 6.3(b)) rooms used. In the latter case both a uniform absorption coefficient and an angularly varying one are considered. The levels in all cases appear to be asymptote to some particular value. Unfortunately however, although it is in principle possible to compute predictions to any degree of accuracy desired, in practice increasing the radius of the image source sphere considered leads to dramatic increases in the computation time. For the particular cubic room investigated image source contributions that arrive up to 1.5 seconds after the direct sound will be included in the results presented later in this section.

Figure 6.3 Estimation of truncation error in steady state predictions.

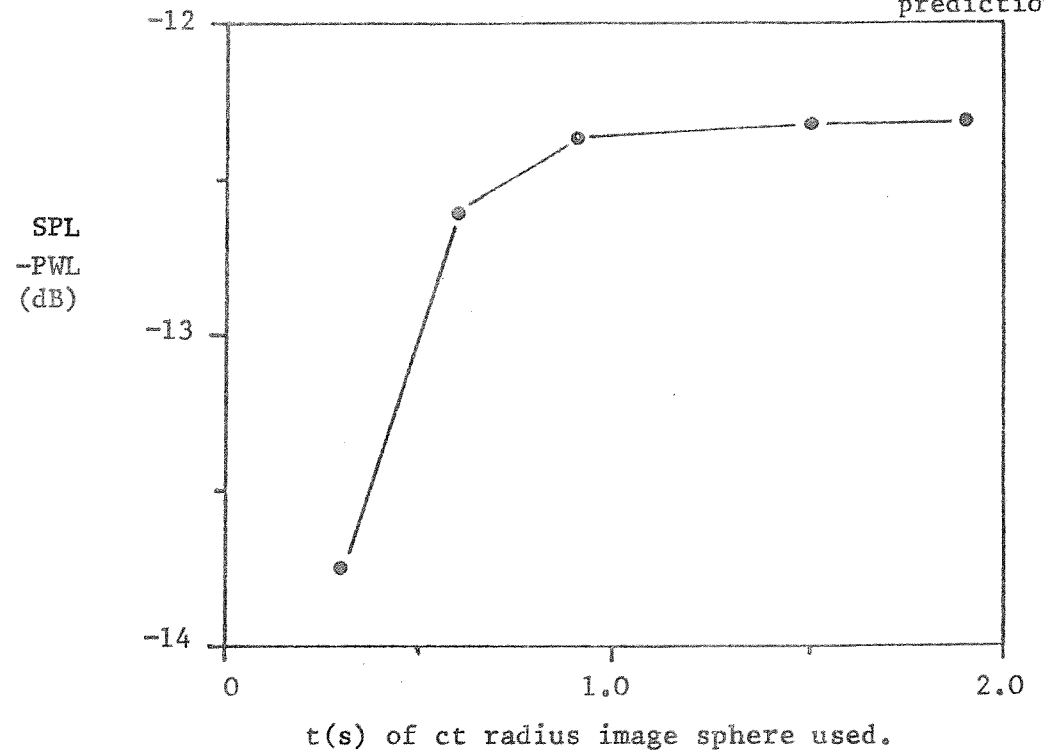

Figure 6.3(a) Room dimensions (10,10,10); Source location (2,3,4); Receiver position (6,7,8); All α's = 0.1; m_a = 0.

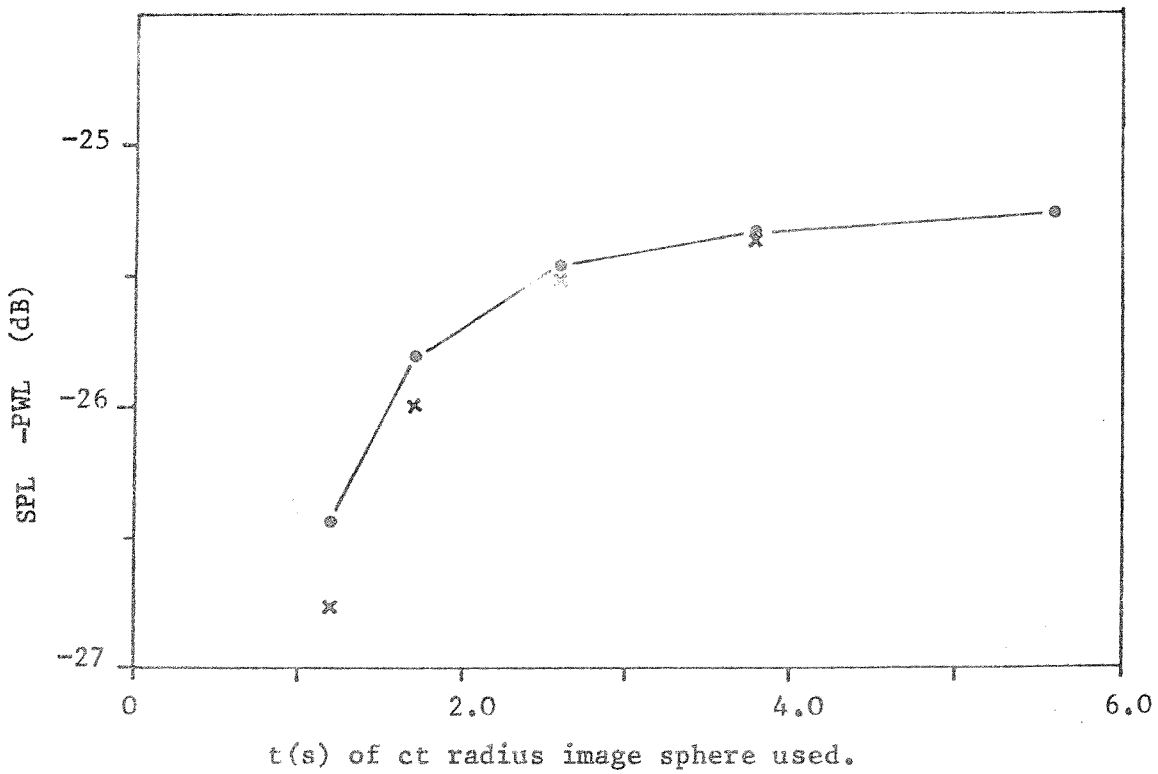

Figure 6.3(b) Room dimensions (100,10,50); Source position (20,1.5,25); Receiver location (60,1.5,25); All α's = 0.1, except surface y = 10m for results given by crosses when $\alpha(\theta)$ is from Figure 6.2(b); m_a = 0.

This gives a predicted level within 0.65 dB of that predictable from diffuse field theory, which might be assumed roughly correct in this situation. For the case of the steady state level predictions in the case of the flat room, there is no equivalent easy estimation method. It appears from the results of Figure 6.3(b) however that consideration of images out to $t = 3.8s$, will prove reasonably adequate (apparently to within about 0.75 dB of the asymptotic level). It can of course be stated that any steady state predictions made in this manner will always be understimates of the "exact" level.

Now that the number of images to be considered in the estimation of steady state levels has been decided, the question remains as to what proportion of the time history of the reverberant decay resultant from these computations will be accurate. Figure 6.4(a) contains the time histories computed for the cubic room case. It is evident from these results that, if the Sabine equation is assumed to be an adequate criterion, then the calculations which consider image source contributions which arrive up to 1.5s after the direct sound will be accurate (to the accuracy representable on the graph) for decay times up to 1 second after the source is switched off. This is borne out by comparison with the computation involving image source contributions out to $t = 1.9s$. The results for the flat room (see Figure 6.4(b)) demonstrate that Sabine's formula is of no use for decay calculations in this type of enclosed space. It is evident however, from comparison of the results for the various sizes of image source spheres considered, that the results of any particular set of calculations are in good agreement with those involving a much larger number of image source contributions, for portions of the time history up to about one second before the image contributions cease. This estimate also appears adequate for the angularly varying absorption coefficient results used (cf. Figure 6.4(c)).

It is interesting to note that the portion of any decay computed for the flat room, between 5 dB and the end of the section considered accurate, appears to possess a roughly uniform decay rate. This part of the time history will therefore be used to characterise the rate of sound decay after the source is switched off, and will be referred to by an equivalent 'T_{60}' value. It should be stressed again however that this has no apparent agreement with the value predicted from equation (6.1).

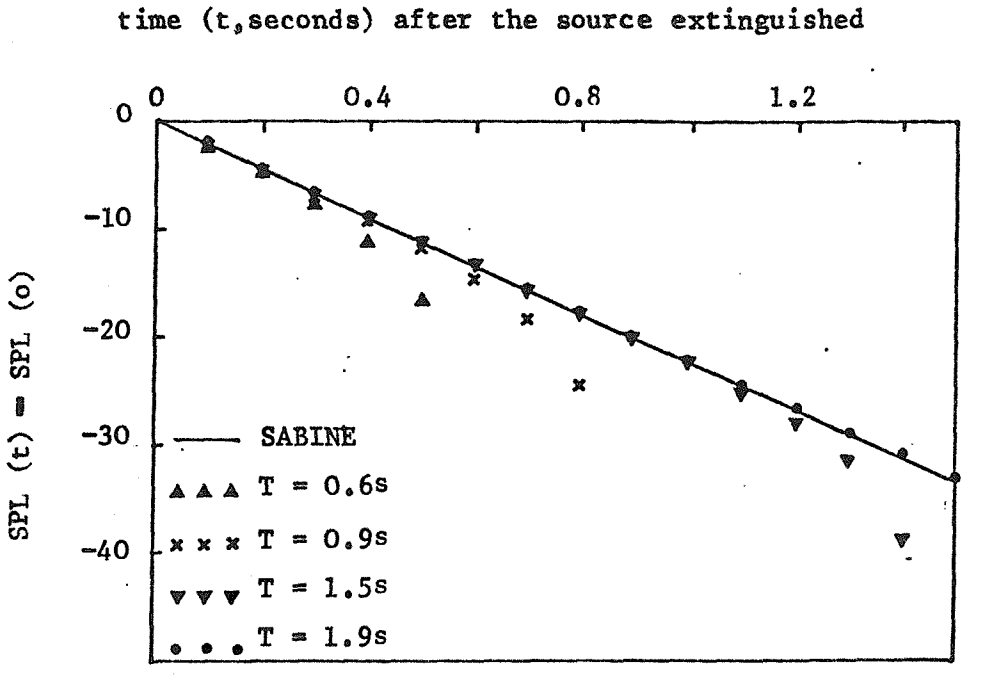

Figure 6.4(a) Truncation effects in the reverberant decay calculations for the cubic room, due to consideration of a finite number of image source contributions. (The T values indicate the maximum delay after the source is extinguished for which image contributions are considered at the receiver).

Room dimensions (10,10,10)
Source position (2,3,4,)
Receiver position (6,7,8,)
All α's = 0.1
m_a = 0.
(All dimensions in metres for room coordinates in figures in this chapter).

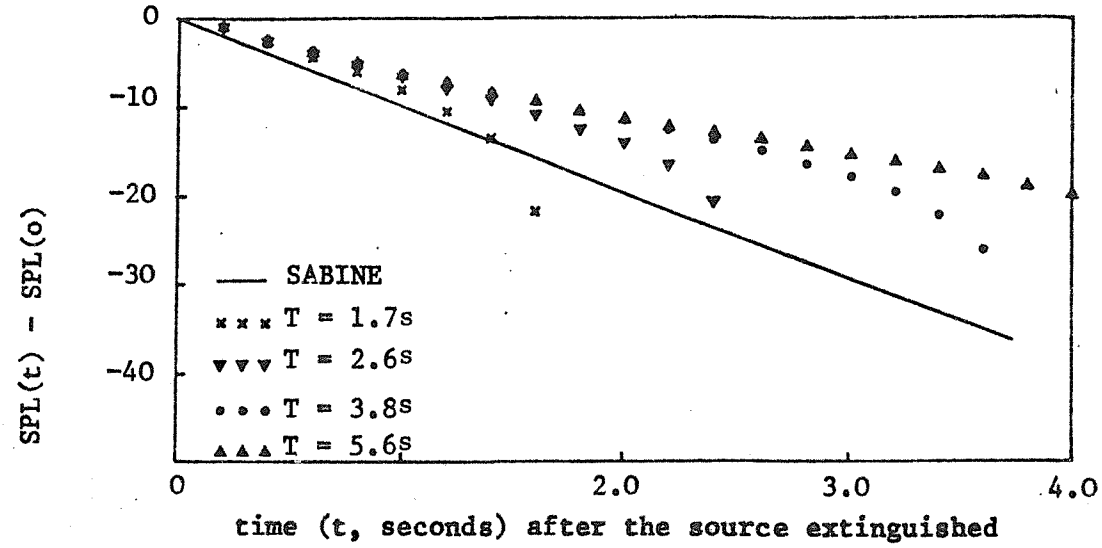

Figure 6.4(b) As for Figure 6.4(a), except Room dimensions (100,10,50), Source position (20,1.5,25) and Receiver position (60,15.,25).

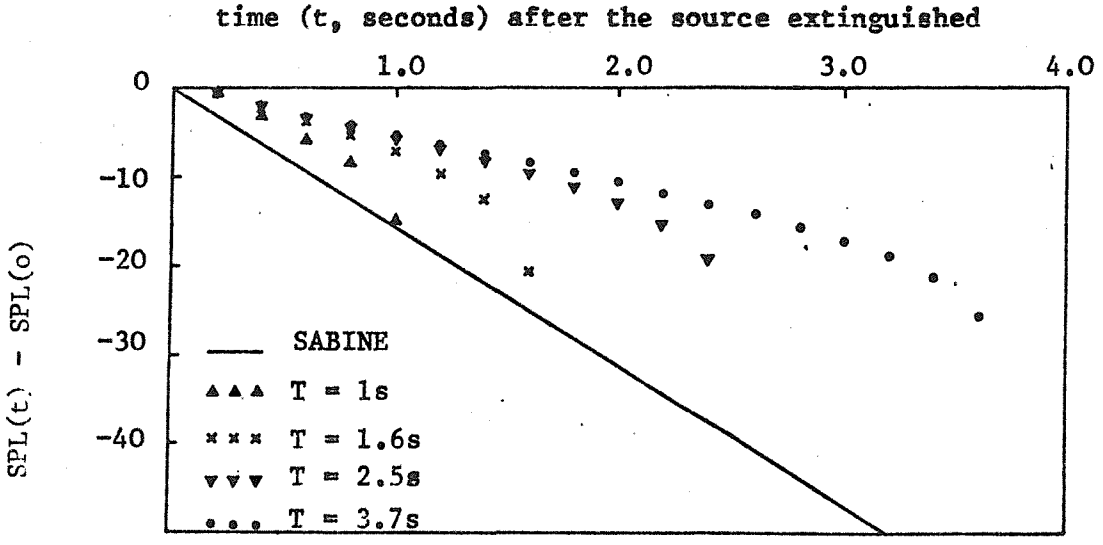

Figure 6.4(c) As for Figure 6.4(b), except that the surface y = 10m has an angularly varying absorption coefficient given by Figure 6.2(b)

The results computed for a particular source-receiver configuration within the cube room are shown in Figure 6.5. Figure 6.5(a) contains a comparison of the predictions which use the angularly varying absorption characteristics of Figure 6.2(a) with those employing the equivalent computed diffuse field value ($\bar{\alpha} = 0.133$). It will be seen that the steady state levels are in agreement with each other to within 0.1 dB, and that the T_{60} values are similarly close. For this case it appears that the Sabine criteria must be approximately satisfied, and a knowledge of the diffuse field absorption coefficient is adequate to accurately estimate the steady state levels and reverberant decay rates within the room. For the case considered in Figure 6.5(b), the agreement between the results for which the angular variation of absorption coefficient shown in Figure 6.2(b) is used with those for which the equivalent diffuse field value ($\bar{\alpha} = 0.25$) is used is not so close. The steady state levels are within 0.6 dB of each other, and the decay rates within 25%. The agreement with Sabine's equations is also poorer than previously. These results suggest that where the absorption of the enclosure surfaces is higher, the requirements for a statistically diffuse field are less closely met (cf. Reference [6.3]). It is also possible that not only the magnitude of the absorption, but also the particular distribution of absorption coefficient with angle of incidence renders a $\sin 2\theta$ distribution of energy at that surface less likely, and thus reduces the agreement between image model calculations for which an angularly varying absorption coefficient is used and those for which the equivalent diffuse field value is used.

The results of calculations of the attenuation of steady state sound pressure levels with distance from a source in the flat room considered are shown in Figure 6.6. This figure contains results for both the angularly varying absorption coefficients and their equivalent diffuse field values. The results indicate that there is no uniform level at some distance from the source. The existence of a diffuse field under these conditions therefore seems unlikely. The differences between the predicted levels for each of the equivalent diffuse field absorption characteristic pairs increase with distance from the source. The magnitude of these differences is larger for those of Figure 6.2(a). However for distances less than 20 m from the source, the difference between levels predicted with a uniform absorption coefficient and those with an angularly varying one is less than 1 dB.

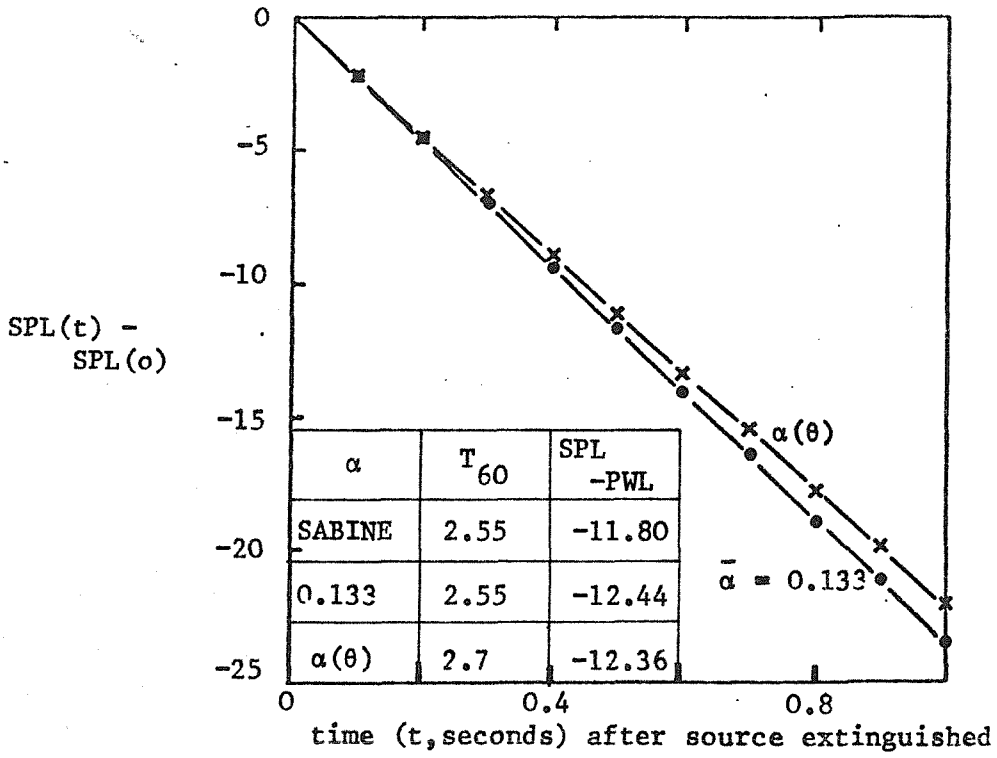

α	T_{60}	SPL -PWL
SABINE	2.55	-11.80
0.133	2.55	-12.44
α(θ)	2.7	-12.36

Figure 6.5(a) Reverberant decay in cubic room when continuous source switched off. Room dimensions (10,10,10), Source position (3,4,5), Receiver location (6,7,8), α's = 0.1 except surface at y = 10m, where α is from Figure 6.2(a), m_a = 0.0.

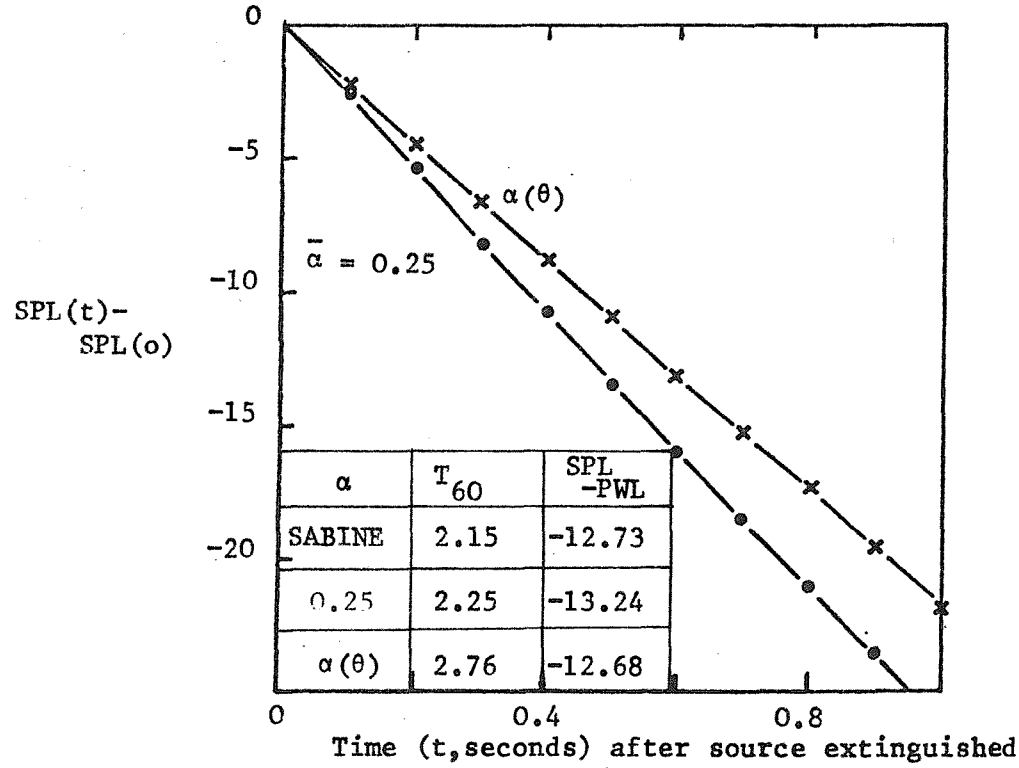

α	T_{60}	SPL -PWL
SABINE	2.15	-12.73
0.25	2.25	-13.24
α(θ)	2.76	-12.68

Figure 6.5(b) As for Figure 6.5(a) except the surface at y = 10m has characteristics given by Figure 6.2(b).

Figure 6.6 Attenuation with distance from source in disproportionate room.

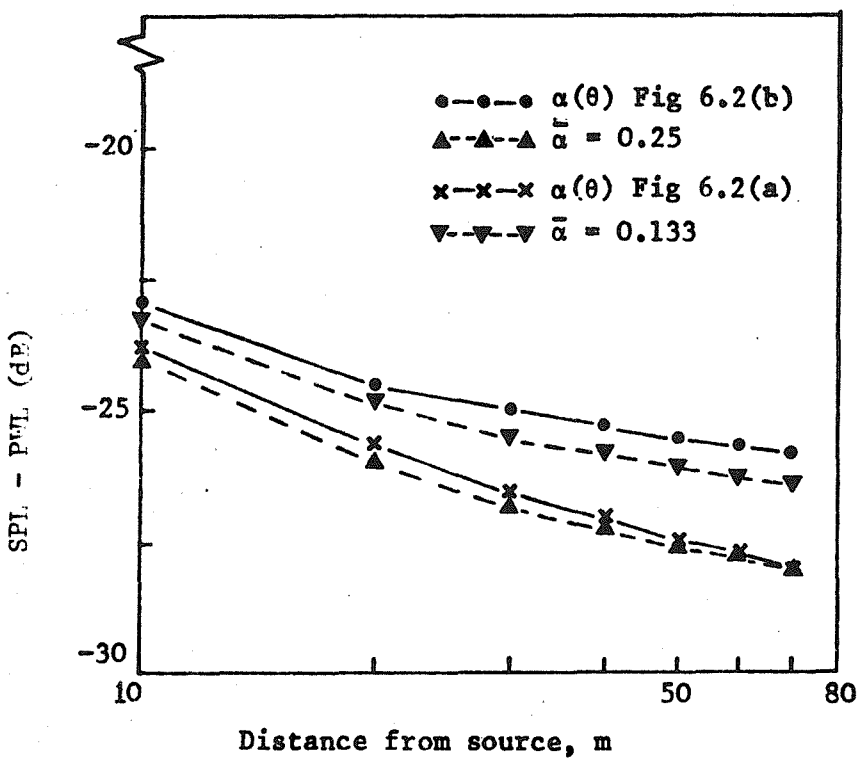

Room dimensions (100,10,50)
Source position(20,1.5,25)
Receiver position (X_R,1.5,25)

All the surfaces' absorption coefficients = 0.1, except for the surface at y = 10m, for which the absorption is as indicated by the key.
Image source contributions considered from a 1500m radius sphere in image space.

It can be seen from the results of Figure 6.7 that there is little change in the rate of sound pressure level decay with distance from the source, except at very early times after the source is switched off. The difference between the predictions which contain an angularly varying absorption coefficient as compared to those with a constant equivalent diffuse field value is only really significant for the absorption characteristics of Figure 6.2(a) (see Figure 6.7(a)). This is in contrast to the steady state predictions, where the absorption characteristics of Figure 6.2(b) produced a larger difference between the calculations which took account of the angular variation and those which did not.

The results of this section have revealed a number of salient points. Firstly, the simple diffuse field, or Sabine, equations cannot be expected to work in highly disproportionate rooms; they also appear to be in greater error in sitations where the room surfaces are more absorbent. Inclusion of the angular variation of a particular surface's plane wave absorption coefficient, as opposed to its equivalent diffuse field value only produced really significant changes in the flat room cases examined. In these cases the two particular absorption characteristics produced different trends. Namely, the absorption characteristic with a larger overall magnitude and most of its absorption around an angle of 45^{o} produced steady state levels which were significantly greater than those predicted by use of an equivalent diffuse field absorption coefficient, whereas the absorption characteristic with most of its absorption near to grazing incidence produced steady state levels which were less than those predicted by use of an equivalent diffuse field absorption coefficient. Use of this latter angularly varying absorption characteristic in the calculation of the reverberant decays also produced a marked change (i.e., about 50%) in "T_{60}", whereas use of the other absorption characteristic produced almost identical rates of decay to those obtained by use of the diffuse field absorption coefficient.

These results suggest that the computed diffuse field absorption coefficient values are inadequate to model the absorption characteristics used,

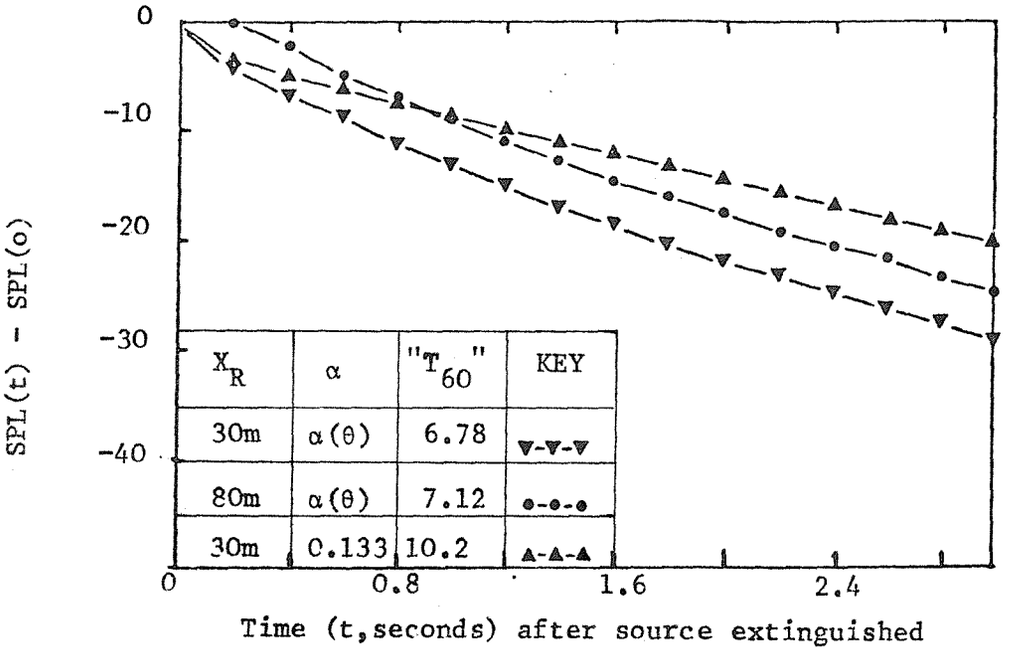

Figure 6.7(a) Reverberant decay in flat room after continuous source switched off. Room dimensions (100,10,50); source position (20,1.5,25); receiver position (X_R,1.5,25). All α's = 0.1 except surface at (x,10,z), which has characteristic given by Fig 6.2(a), m_a = 0.0.

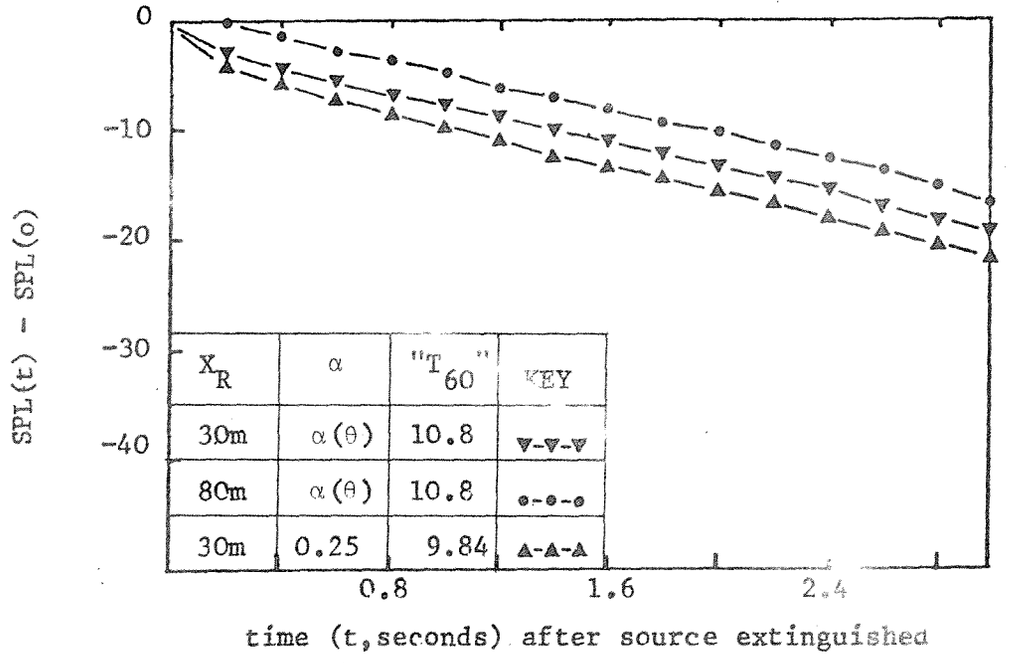

Figure 6.7(b) As for figure 6.7(a), except the absorption characteristics given by Figure 6.7(b).
N.B. In Figs 6.7(a) and (b) images out to 1400m from the receiver considered.

for the purpose of predicting the acoustics of highly disproportionate rooms. The absorption weightings used could apparently make the steady state levels higher or lower in such cases. Their effect on reverberant decay predictions in such spaces was in some cases minimal and in others very marked. Such results suggest that the factors which control the steady state levels and reverberant decay rates are particularly sensitive to image source contributions at different angles at the 'roof'. The remaining sections of this Chapter are therefore devoted to the investigation of the sound energy's distribution at the ceilings of the proportionate and disproportionate room shapes considered in this section. The manner in which a given absorption characteristic will alter either steady state or reverberant decay predictions could then be estimated. Since the angularly varying absorption coefficients used in this section are highly idealised, uniform absorption coefficients (or even perfectly reflecting surfaces) will be used in the remaining sections of this Chapter. In this manner, the effects of altering the room shape alone on the distribution of energy at the roof surface can be investigated.

6.3 Investigation of the Distribution in Angle of Sound Rays at the Surfaces of Rectangular Rooms.

6.3.1 Introduction

The results of section 6.2 indicate that investigation of the distribution of energy at the particular surface altered in the examples presented might well produce some interesting findings. Previous work in this area (e.g. Reference [6.10]) has however produced results which suggest that use of a uniform absorption coefficient is adequate even for highly disproportionate rooms. The method used by Santon and Daumas [6.10] is based on a statistical consideration of all the reflections possible with a given surface. They thus formulated an integral for the average reflection angle $\bar{\theta}$, at that surface. This angle can be represented by the expression

$$\bar{\theta} = \int_{\Omega} \frac{P(\theta_i)\,\theta_i\,d\Omega}{\int_{\Omega} P(\theta_i)\,d\Omega} \quad , \tag{6.16}$$

when $P(\theta_i)$ is the probability of a ray arriving at the angle θ_i to the normal to the surface, and the integral is over all possible directions of arrival. This integral was numerically evaluated and shown to produce $\bar{\theta}$ values which are almost identical for both proportionate and highly disproportionate rooms. Santon and Daumas then used a computer-based ray-tracing technique to study the distribution of the number of reflections in given angular ranges that a ray undergoes. They divided the range of θ_i into 9 separate 10^o intervals (i.e., 0^o-10^o, 10^o-20^o,.....,80^o-90^o), and presented the number of ray reflections that fall within each of these bands as a value associated with the central angle of that particular interval (i.e., 5^o, 15^o,...85^o). The resultant distribution curves agree closely in a number of cases with a $\sin 2\theta_i$ distribution. Santon and Daumas therefore concluded that use of a mean absorption coefficient is valid for ray calculations of both steady state and source switch-on, or switch-off transient behaviour for any rectangular room.

Since the results of section 6.2 appear to be in contradiction to the above hypothesis, there would seem to be a number of points which must be clarified before such broad conclusions can be drawn. Firstly Santon and Daumas only considered the number of rays that arrive in a particular angular range at the surface considered, rather than the energy associated with them when they arrive there. From the discussion of section 6.1.2 it is evident that it is the angular distribution of the incident energy that is actually of prime concern. These two distributions will probably only be identical if spherical spreading can be neglected. The results presented by Santon and Daumas [6.10] are also lacking in two further areas. Firstly they only presented the disproportionate room results for an absorption coefficient of 0.02, which is typical of a very hard surface, and hence many ray contributions will arrive at any receiver position. Secondly there is no indication of the behaviour of these ray distributions under transient conditions. It is therefore impossible to deduce from their results whether the overall shape of the distribution curve is obtained quickly or slowly after a source is switched on in a given situation.

The earlier sections of this chapter contain a description of the development of a deterministic energy-image-source room acoustics computer program. The use of such an approach to study the distribution of image source contributions at the roof surface will be described in the next section of this Chapter. Although the results of such an approach may differ in detail from the probabilistic ray tracing approach of Santon and Daumas [6.10], any broad trends that might exist should be similar, since Santon and Daumas' results are also ensemble averages, but of many random ray paths rather than deterministic image source contributions.

6.3.2 *The method used for the investigation of reflection statistics at one surface of rectangular rooms*

It was decided to investigate a number of features of the reflection statistics at one of the surfaces in three different types of room. The three types of rooms are a cubic room (10 m × 10 m × 10 m), a 'duct' room (10 m × 10 m × 100 m) and a 'flat' room (10 m × 50 m × 100 m); and the surfaces at which the reflection statistics were investigated are of area 10 m × 10 m, 10 m × 100 m, and 50 m × 100 m respectively in these three cases. These surfaces will for convenience be termed the 'roofs' or 'ceilings' of the rooms. In order to reduce computation time it was decided to consider initially only configurations with the source at the centre (a/2, b/2, c/2) of the room (of dimensions a × b × c), and with the receiver on the floor below it (i.e. at (0,b/2, c/2)). With this source-receiver geometry only the positive octant of images (ℓ,m,n $\geq$ 0) will be explicitly considered. Thus images of zero m and/or n order will be effectively over-weighted by a factor of two. This error is less significant at long times after the source is switched on, since then these over-weighted discs of images will be a smaller proportion of the total sphere of contributing image sources. The error as a fraction of the total number of image sources contributing at time t, being roughly 3(b+c)/(ct).

The various reflection parameter statistics will now be discussed. Since Santon and Daumas [6.10] presented the distribution in angle of the number of reflections with a surface, this will be initially computed to provide a comparison of the image method used here with

their ray-tracing calculations. This is easily performed since the angle θ_i at which a particular image source contribution reflects from a given surface has already been formulated (for walls perpendicular to the y-axis) in equation (6.12). It is a simple matter to convert this for collisions with walls perpendicular to the x-axis for this section. The number of reflections that all the image sources of (positive) order (ℓ,m,n) have from the walls perpendicular to the x-axis at $x = a$ (i.e. the 'roof'), is given by $\mathrm{Int}\left((\ell+1)/2\right)$. This is actually equivalent to the treatment of negative image orders as if they were one order less than they actually are. This does not matter in this investigation, since the number of image sources actually considered is not determined by their image order. In fact the use of two criteria for the determination of the number of image sources to be considered was investigated. The first is similar to that used by Santon and Daumas [6.10], who disregarded rays which have lost 10 dB of their energy due to collisions with walls; their criterion does not include spherical spreading, which will obviously effect the energy of ray contributions arriving at the surface considered. Hence the first criterion chosen includes energy losses both due to sphereical divergence and absorption at room boundaries, and requires that any image source contributions considered have energies greater than some set value. The second criterion used involves the consideration of only those image sources which lie within a sphere of given radius in image space. This is similar to the method used in calculating the results of Section 6.2, and should promote a better understanding of them.

The number of reflections that a particular image source contribution has with the surface under consideration is then added to the running total for the particular 10° interval within which its angle of incidence with that surface lies.

Since it was further desired to study the build up of the steady state reflection characteristics with time after the source is switched on, the image source contributions are further categorised by the time, after the source is switched on, at which they arrive at the receiver. In the results presented, the contributions were sorted into time intervals of 0.1 s. Thus for an image source contribution that has had 5 reflections at $\theta_i = 46^{\circ}$ with the surface under consideration, and

arrives at the receiver 0.23 s after the source is switched on, the value 5 will be added to the value for the contributions which arrive between times of 0.2 s and 0.3 s after the source is switched on, and make angles between 40^{o} and 50^{o} with the surface. This process of sorting the total number, N, of contributions that arrive within the time interval t_i, having been reflected in the angular range θ_{in}, can be represented as

$$N(\theta_{in},t_i) = \sum_{\ell=1}^{\infty} \sum_{m=0}^{\infty} \sum_{n=0}^{\infty} N_{\ell,m,n}\, H(\theta_{\ell,m,n})H(t_{\ell,m,n}) \quad , \tag{6.17}$$

where $N_{\ell,m,n}$, $\theta_{\ell,m,n}$ and $t_{\ell,m,n}$ are the number of reflections, their angle of incidence at the surface considered, and their time of arrival at the receiver, respectively, for an image source of order ℓ,m,n. The function $H(\alpha)$ is zero unless α lies with the range of the interval denoted α_n, when it will be unity.

In order to evaluate the angular distribution of the reflection effects observed at the receiver after T time intervals Δt, all the image source contributions which could arrive at the receiver by that time must be summed. This process can be represented as

$$N_t(\theta_{in}) = \sum_{i=1}^{T} N(\theta_{in}, t_i) \quad . \tag{6.18}$$

It is now possible to investigate both the overall angular distribution of the number of wall reflections in the levels observed at a receiver at a given time t after a source is switched on, and also the angular distribution of the reflections due to those images which 'cut-on' during a small interval at that time.

Now that the problem has been formulated for the study of the angular distribution of the number of reflections with a particular surface, it is a comparatively easy matter to extend this to consider the angular distribution of the energies which arrive at that surface. This simply requires the summation of the energies that a particular image source contribution has at each impact with the surface under

consideration. A source of order ℓ,m,n (all positive) will have $\mathrm{Int}\left((\ell+1)/2\right)$ collisions with the surface at $x = a$. Hence the sum $E_{\ell,m,n}$ of the energies which arrive at the various reflections points with that surface can be written as

$$E_{\ell,m,n} = \sum_{i=1}^{\mathrm{INT}\left((\ell+1)/2\right)} \exp(-m_a r_i)\beta^{(i-1)}/r_i^2 \ , \tag{6.19}$$

where the value has been normalised by that at 1m from the source under free field conditions, and r_i is the distance from the image source of order ℓ,m,n to the point of the i^{th} order reflection with the surface $x = a$ (or its image in image space), which has a reflection coefficient of β. By analogy to equation (6.17), the distribution of the energy which is incident upon the surface in the angular range θ_{in} and is received by the receiver in the time interval t_i, can be written as

$$E(\theta_{in},t_i) = \sum_{\ell=1}^{\infty} \sum_{m=0}^{\infty} \sum_{n=0}^{\infty} E_{\ell,m,n} H(\theta_{\ell,m,n}) H(t_{\ell,m,n}) \ . \tag{6.20}$$

Similarly, from comparison with equation (6.18), the overall distribution after T of these Δt time intervals can be written as

$$E_t(\theta_{in}) = \sum_{i=1}^{T} E(\theta_{in},t_i) . \tag{6.21}$$

A method for the investigation of the angular distribution of both the number of reflections and their energies has now been formulated, for the study of reflections at a particular surface. The method described permits investigation of both 'steady state' distributions and their build up with time after a continuous source is switched on. The computer program used in the investigation of these phenomena is listed in Appendix E. The presentation and discussion of the results obtained follows in the next section.

6.3.3 *Presentation and discussion of the results of the investigation of the angular distribution of reflection parameters at one surface in a rectangular room.*

The results of Figure 6.8(a) demonstrate that when a constant radius sphere of image source contributions is considered, the resultant distribution of the number of reflections per angular interval agrees closely with a sin2θ distribution, independent of the room shape. There is a very slight weighting towards normal incidence, but this could be due to the particular source-receiver geometry used. These results therefore appear to be in general agreement with those of Santon and Daumas [6.10]. However use of the criterion where only those image source contributions above a predetermined rejection level are considered produces the results shown in Figures 6.8(b) and (c). Here there is a very marked bias towards grazing angles as the absorption of the surface is increased. This is to be expected since, as all the remaining walls of the room are hard, the rays at grazing incidence to the roof will be attenuated much less than those near normal incidence, for which every other reflection is with the absorbent surface.

As mentioned in Section 6.1.2 it is the angular distribution of incident energy at the surface that is of principle interest in determining whether or not the conditions for the application of Paris' formula are satisfied. The results in Figure 6.9 show the distribution of this parameter from the computations in which a constant radius sphere of images is used, normalised by the maximum value over the angular range. The results normalised in this way were coincident for the absorption coefficients employed (0.002 and 0.25). The shapes of the curves are again almost identical for the cube, duct and flat rooms. The maximum value has moved slightly towards normal incidence however, as compared to the angular distribution of the number of reflections. To test this, another source-receiver configuration was investigated, where the receiver and source are at the centres of the walls perpendicular to the z-axis at $z = 0$ and c, respectively. The results for this configuration are shown in Figure 6.9(d), and can be seen to still be in close agreement with the other plots of Figure 6.9 where the source is in the room's centre with the receiver on the floor directly below it. It therefore appears that, for some reason, the distribution is skewed towards normal incidence when the energies of the reflections, rather than just their numbers are considered.

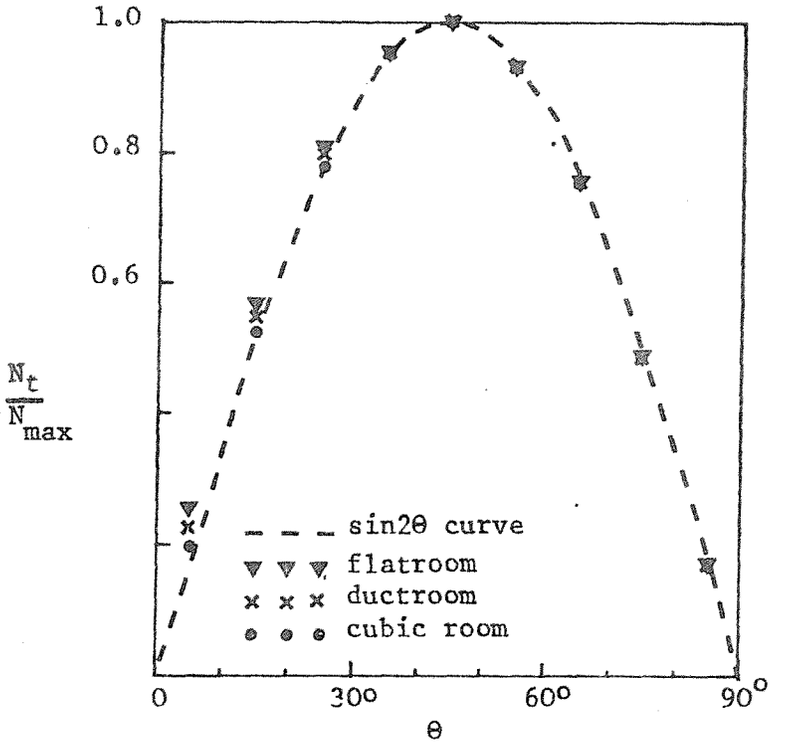

Figure 6.8(a) Plot of the distribution in angle of the number of reflections, N_t, at the roof surface for image sources that lie within 500m of the receiver in image space for the cube room, and 1130m for the disproportionate rooms.

(Normalised by the maximum number which occur in any 10^o interval, N_{max}).

Figure 6.8 (cont'd)

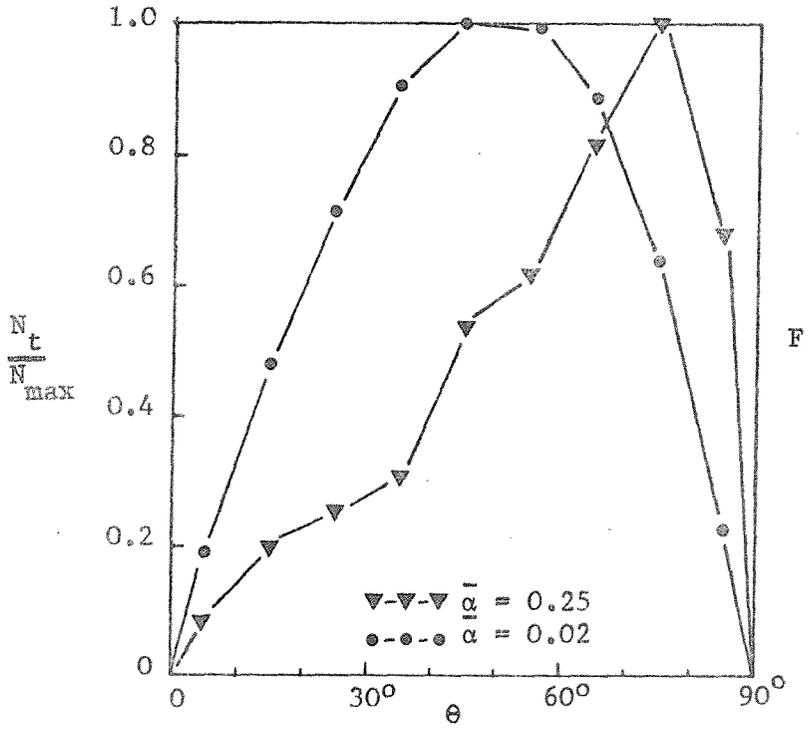

Figure 6.8(b)

As for figure 6.8(a) for the cubic room, except image source contributions more than 50dB below direct level at 1m neglected.

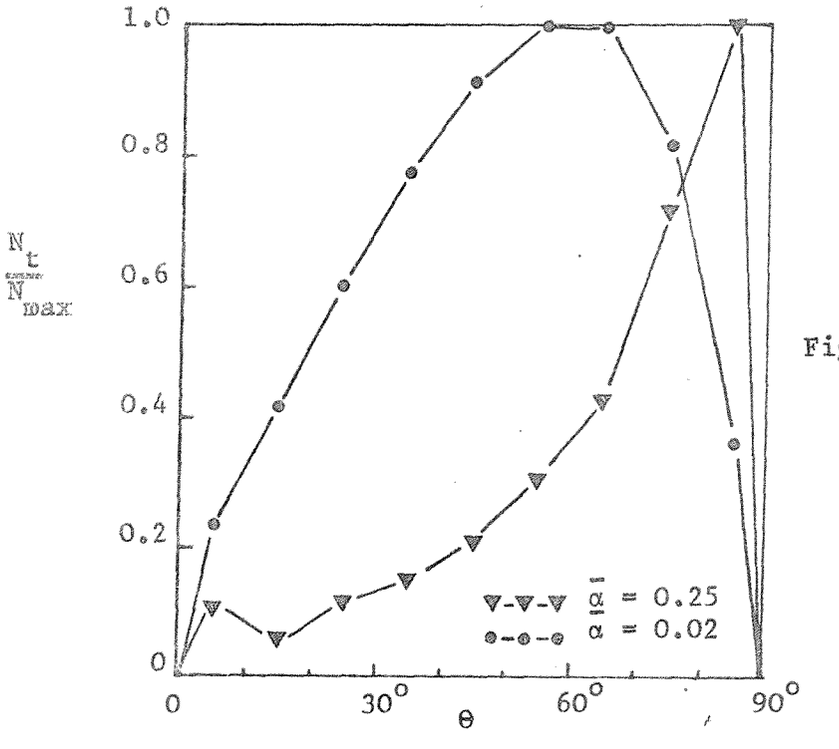

Figure 6.8(c)

Flat room; image source contributions more than 60dB below the direct level at 1m neglected.

Figure 6.9 The angular distribution of energy E_t at the ceiling for contributions from a sphere of energy image sources. (Normalised by the maximum energy in a 10° interval).

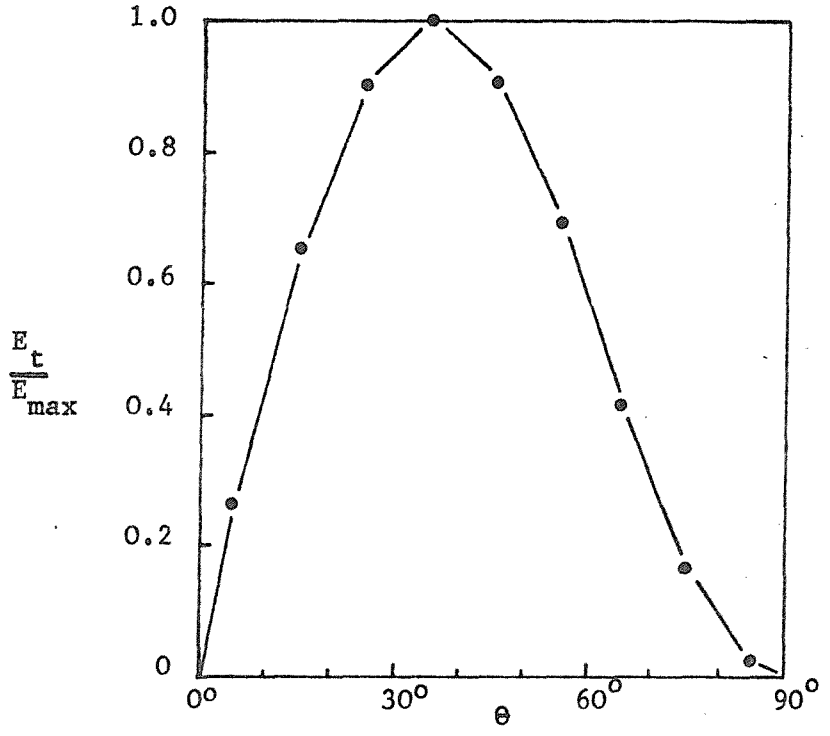

Figure 6.9(a) Cube room, images up to 500m from receiver are considered.

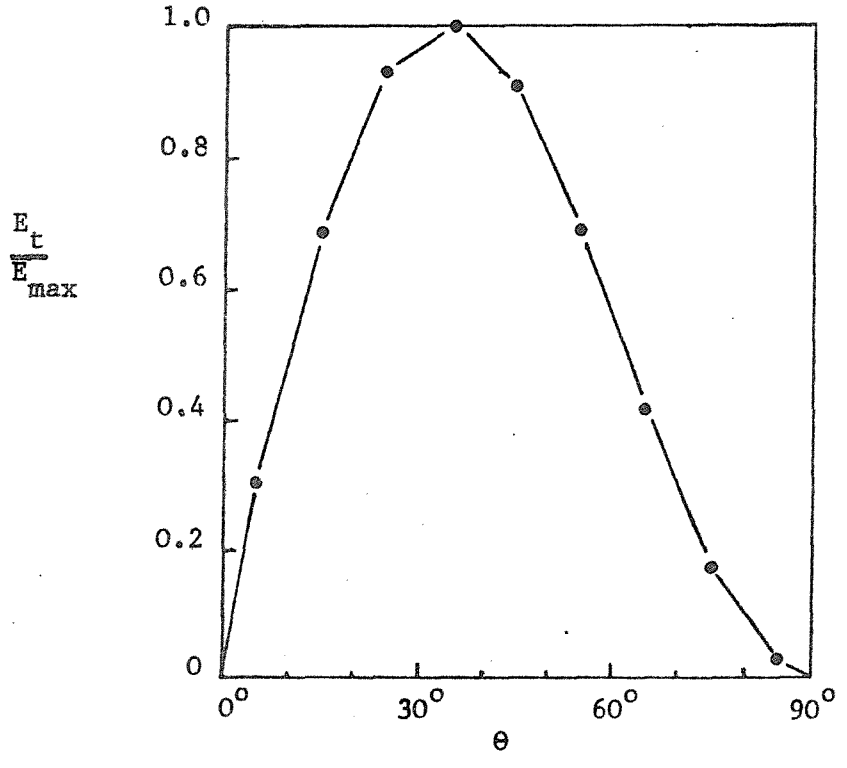

Figure 6.9(b) Duct room, images up to 1130m from the receiver are considered.

Figure 6.9 (cont'td) N.B. Due to the normalisation used the plots for $\alpha = 0.25$ are coincident with those for the $\alpha = 0.02$.

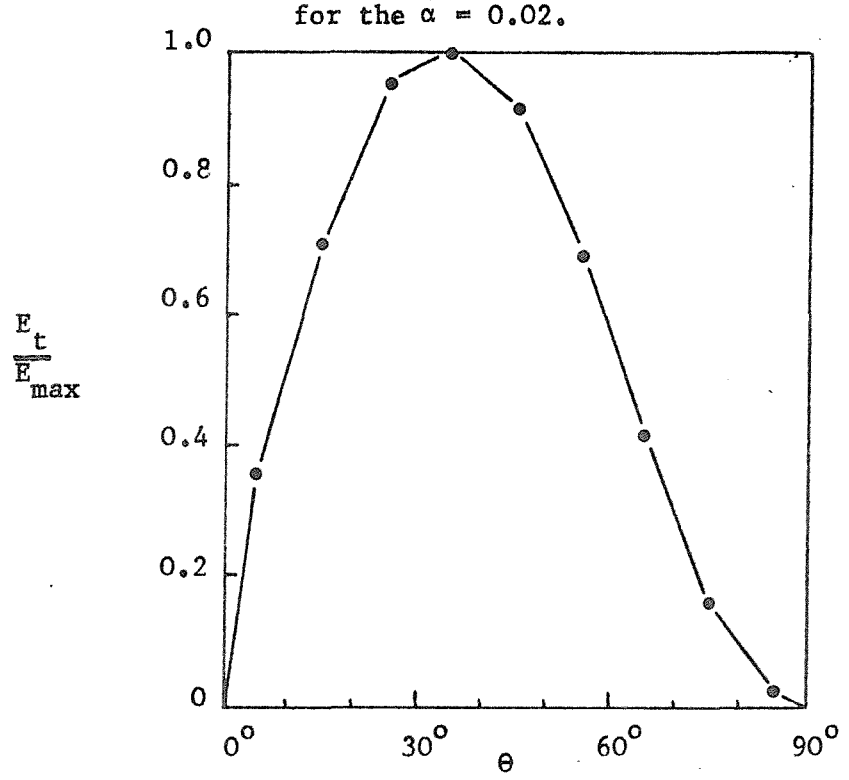

Figure 6.9(c) Flat room, images up to 1130m from the receiver are considered.

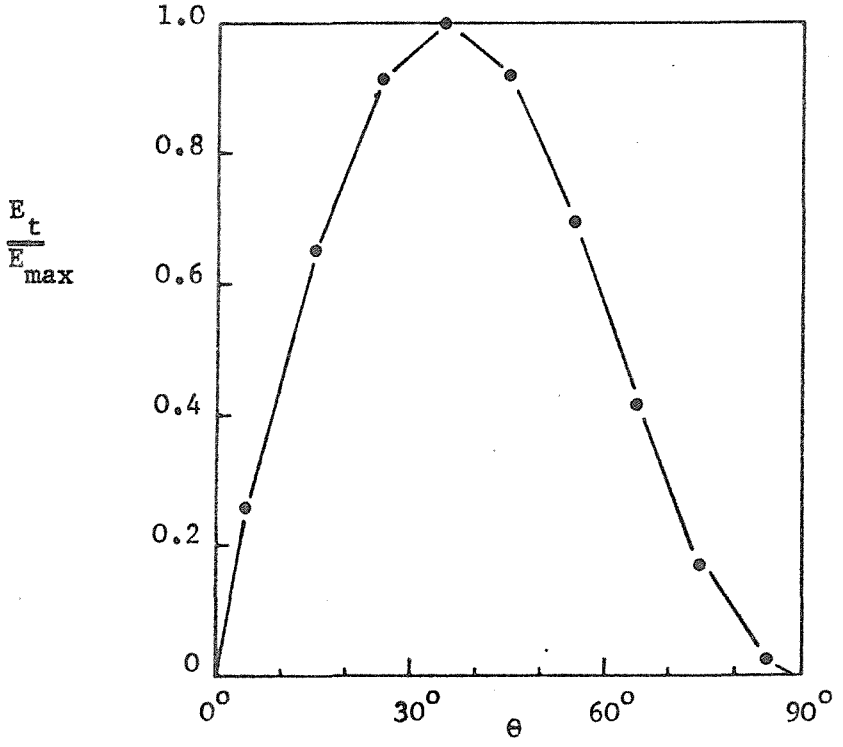

Figure 6.9(d) Flat room, images up to 1130m from the receiver are considered. In this plot receiver at (5.0,25, 0.0), source at (5.0,25,100.0).

If the requirements for equation (6.3) to be true were met, division of any of the plots in Figure 6.9 by those in Figure 6.8(a) should produce a constant value with angle, since there would then be a $\sin 2\theta$ distribution of both the number of reflections and their energies. Figure 6.10 contains the results of such a division for the cubic and flat room results. It will be noted that although the magnitude of the curves is different for the two room cases the shape is not, nor does it appear affected by the absorption coefficient used for the roof. Indeed, when these curves are normalised by their value at 45°, the results for the flat and cube rooms collapse on top of each other. This is shown in Figure 6.11. It will also be seen that both sets of results then have a strong resemblance to the cosine curve plotted (weighted arbitrarily to equal 1 at 45°).

In order to ascertain that this behaviour is not a function of the criterion used to determine which image source contributions are considered, results were obtained by use of the other criterion (i.e. that only contributions above a certain level are considered). The results of such computations for the angular distribution of E_t/N_t are shown in Figure 6.12. The shape of the curve is much the same as that previously observed in Figure 6.10. The main differences between the two figures occur for the higher absorption coefficient, when it is probable that an inadequate number of image source contributions are considered when the -50 dB rejection criterion is applied, since the higher surface absorption quickly reduces a ray's energy below the rejection threshold used. Otherwise these results again seem to indicate the existence of a $\cos\theta$ factor in the angular distribution of E_t/N_t. The shape of this distribution seems to be virtually independent of the room shapes and absorption coefficients used. As the number of images considered is increased, the magnitude of the E_t/N_t distribution decreases, since more low energy reflections are included. This effect is shown in the build up of these distributions with time after the source is switched on, in Figure 6.13. One other point to note about these results is that, although in the case of the cubic room the overall shape of the 'steady state' E_t/N_t distribution is rapidly achieved, for the flat room the distribution takes much longer to stabilise. Thus under the transient conditions shortly after a source is switched on, two angularly varying absorption characteristics could produce similar results in the case of a small

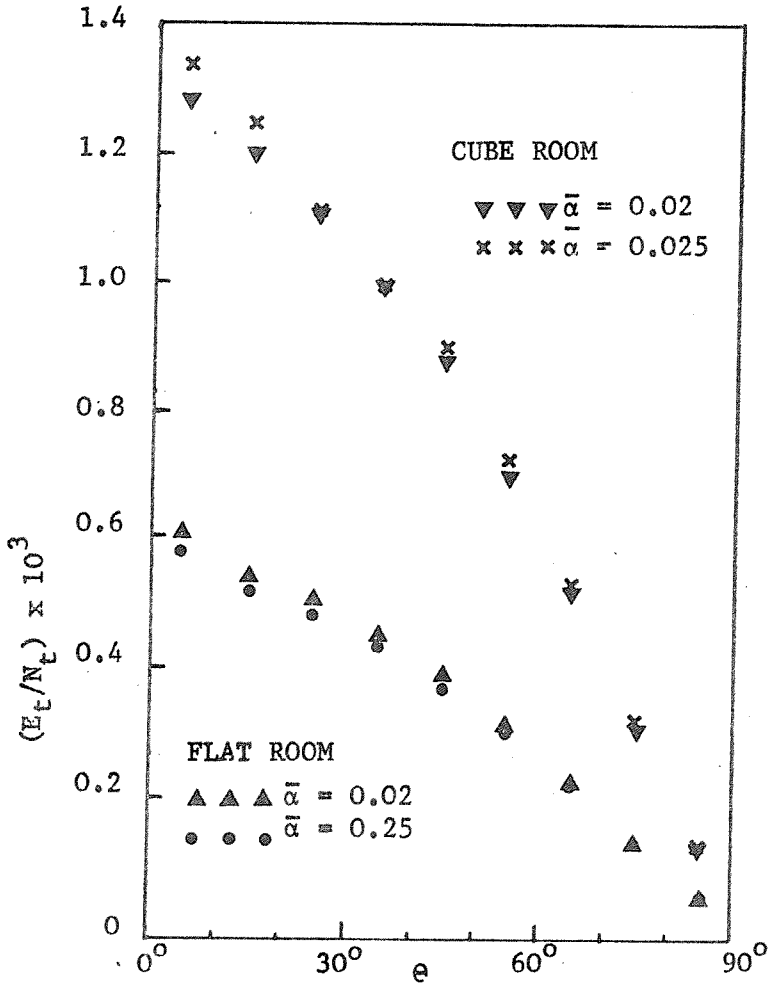

Figure 6.10 Ratio of the angular distribution of energy at the roof surface, E_t, to the angular distribution of the number of reflections, N_t, for image source contributions from images within 500m of the source for the cubic room, and 1130m for the flat room.

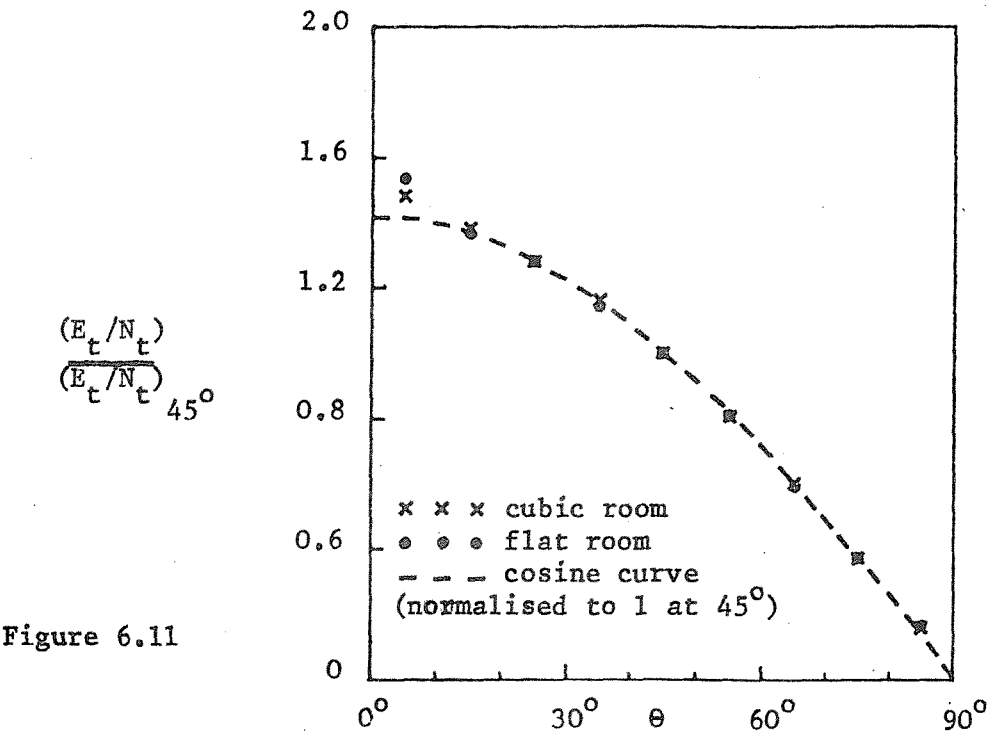

Figure 6.11

Plot of E_t/N_t normalised by the value at 45°. Image contributions from images with 500m of the receiver considered for the cubic room, and 1130m for the flat room.

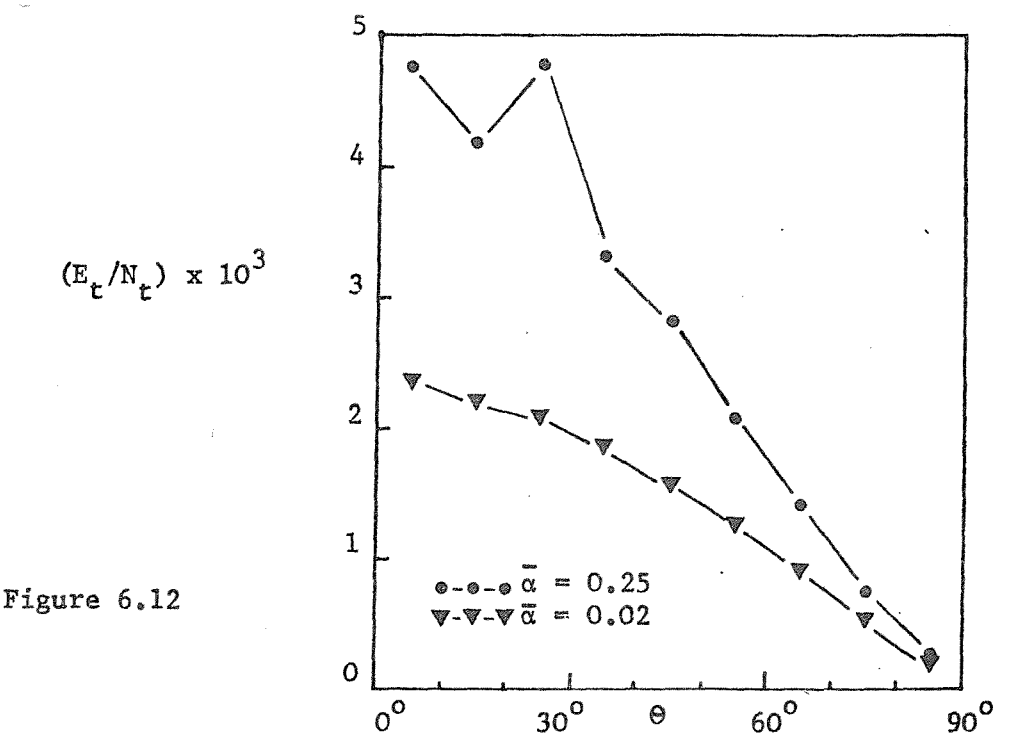

Figure 6.12

Plot of E_t/N_t for the cubic room, ignoring image source contributions which arrive at the receiver more than 50dB below the direct level at 1m from the source.

Figure 6.13 The change in the E_t/N_t curves with time after the source is switched on.

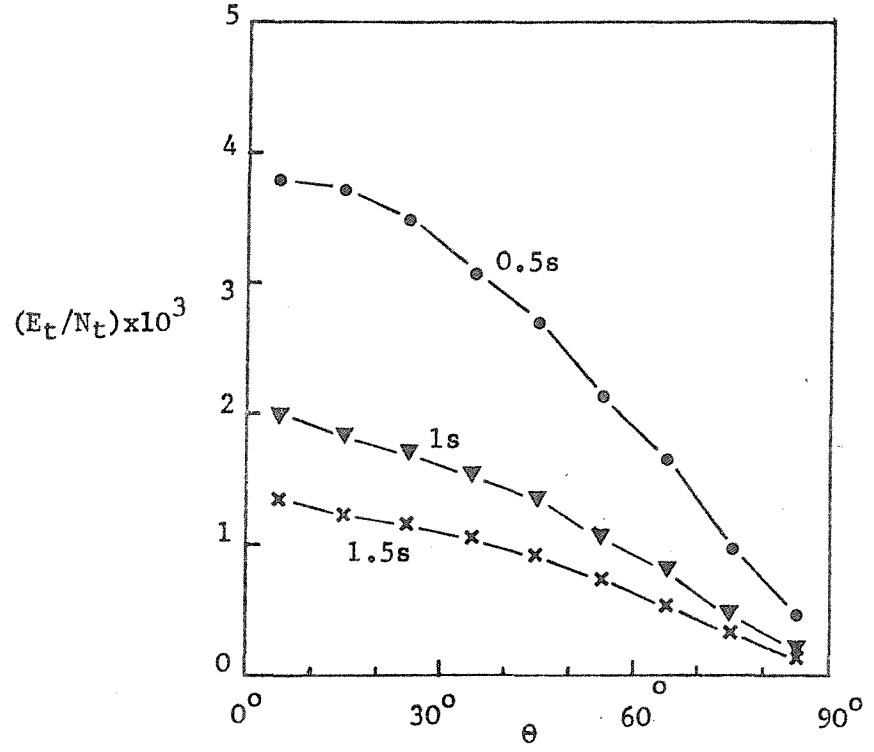

Figure 6.13(a) Cube room, roof absorption coefficient $\bar{\alpha} = 0.02$

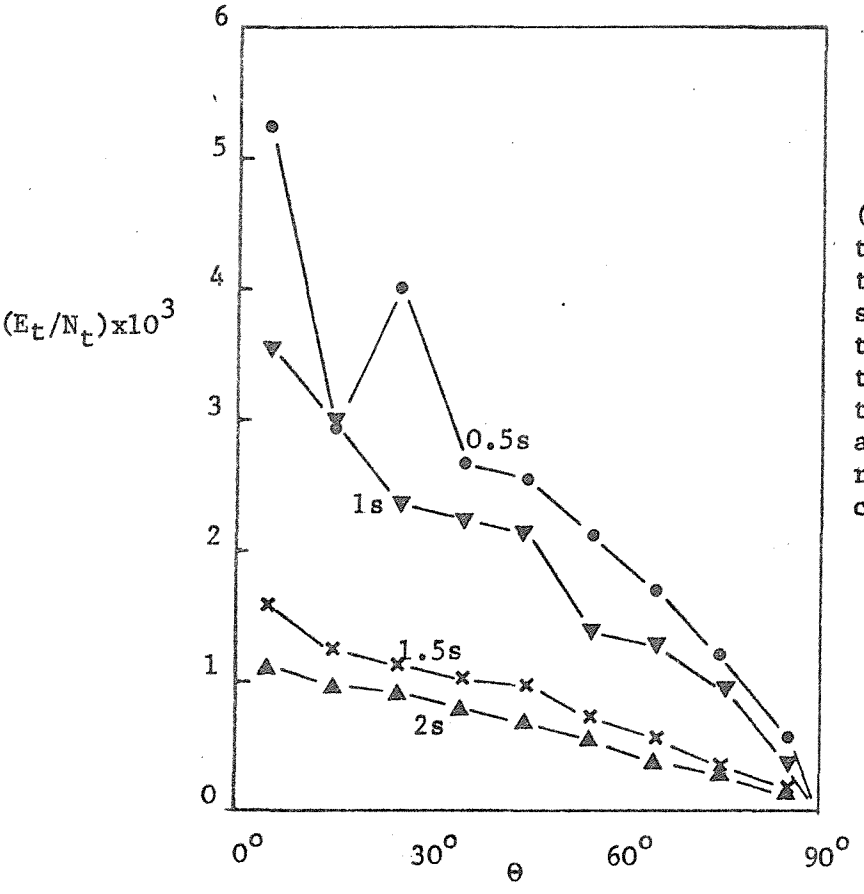

(NB. The times indicate that image source contributions up to that time after the direct sound arrives at the receiver are considered).

Figure 6.13(b) Flat room, roof absorption coefficient $\bar{\alpha} = 0.02$.

cubic room, whilst producing markedly different effects in a larger disproportionate room. Similar behaviour would seem likely under reverberant decay conditions when the source has been switched off. More attention is paid to this last point in Section 6.4.3.

From the results so far discussed it is apparent that there are cosine weightings visible at finite times after a source is switched on in the E_t/N_t distribution at a particular surface in an energy image source room acoustics model. If the sound field were composed of plane, rather than spherically spreading waves, then the only losses in the systems considered would be due to wall reflections. Therefore if all the walls were made perfectly reflecting, the shape of the angular distribution of energy at the surface should be identical to that for the angular distribution of the number of reflections. Thus the E_t/N_t curve for a hard walled room with "plane wave point sources" (i.e. rays emitted from a point that propagate without spherical divergence) should be uniform with angle. If the $1/r_i^2$ spherical divergence term is removed from equation (6.19) the computer program used to study the angular distribution of reflection statistics due to point image sources can be used to investigate how any effects are altered when spherical divergence is omitted. The results of such calculations are shown in Figure 6.14(a), where a uniform value of 1.0 is observable only for the case of a totally hard surface. With any absorption at all the shape of the distribution dramatically changes to resemble a $\sec\theta$ variation. These results produce a test of the hypothesis that it is the spherical spreading which accounts for the distribution shape previously seen. This difference between the two behaviours is graphically illustrated by comparison of Figures 6.14(a) and (b). In the latter case the $\cos\theta$ variation is hardly altered by the alteration of the roof's absorption coefficient from an α value of zero to one of 0.5. This suggests that the variation is due to the magnitude of the spherically spreading wave at its initial point of reflection in any sequence of reflections considered. The existence of this apparent extra $\cos\theta$ from the results may be one reasons why the image model results with a diffuse field absorption coefficient do not equal those with an angularly varying absorption coefficient. It is also possible that for the cases where the absorption characteristic

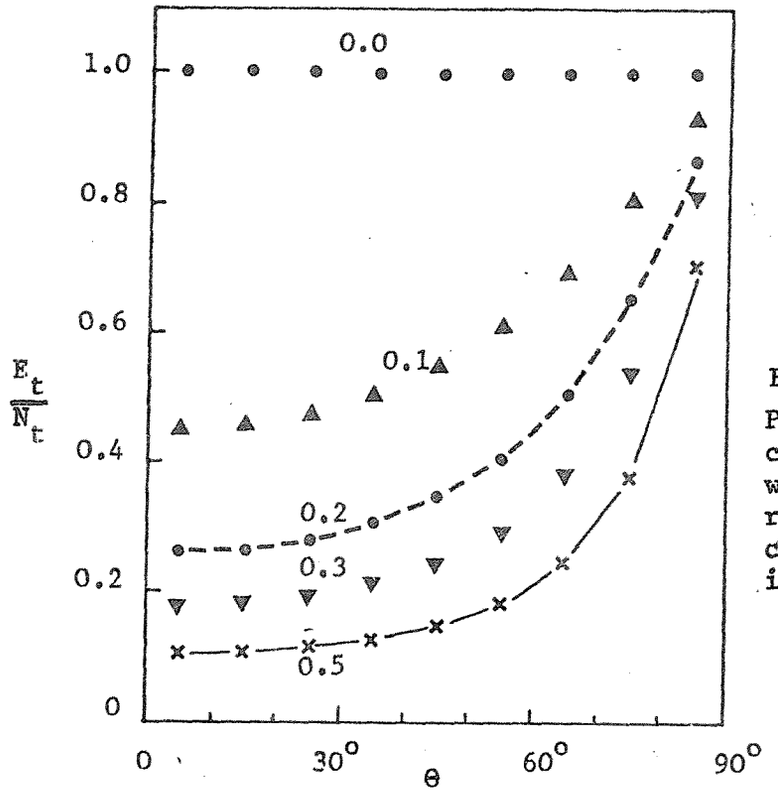

Figure 6.14(a)
Plot of E_t/N_t for cube room with 'plane wave point sources', roof absorption coefficients as indicated.

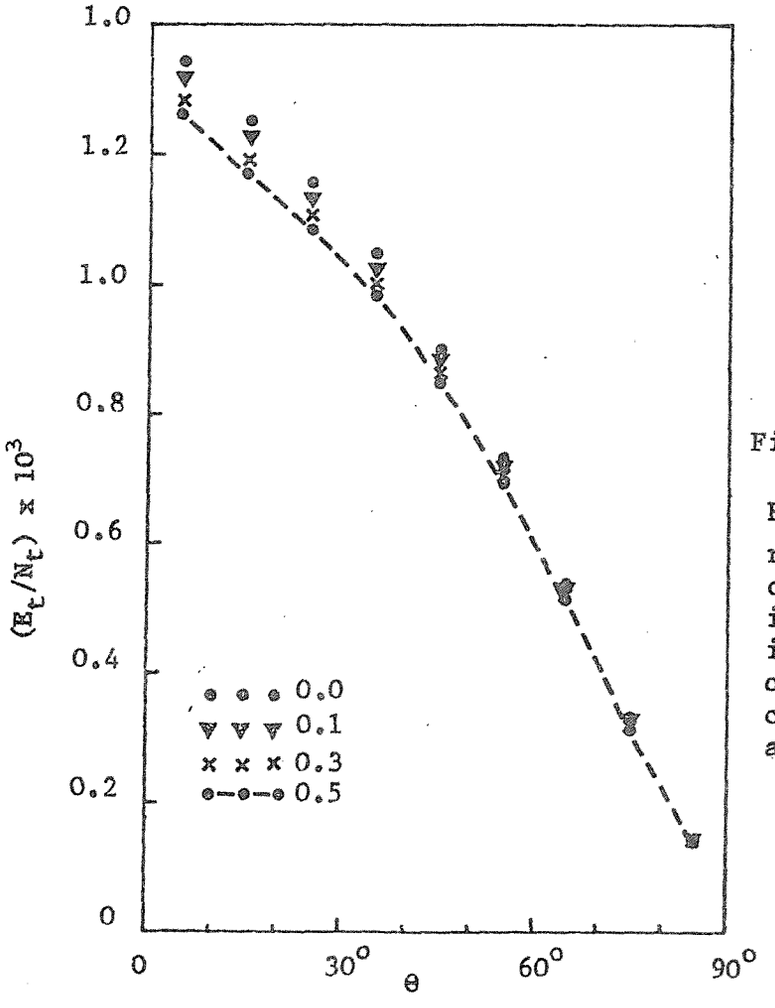

Figure 6.14(b)

E_t/N_t for cube room roof absorption coefficients as indicated. N.F. images within 500m of receiver are considered in (a) and (b).

of one surface has a very large peak at some angle (i.e., $\alpha(\theta) \simeq 1$, for some θ) and the remaining walls are comparatively absorbent, that insufficient energy will arrive at all angles for the reflection statistics observed in this section to be valid at the wall under study. However in other cases the results of this section have produced some very interesting findings. For example, the shape of the distribution of the E_t/N_t curve at long times after the source has been switched on is apparently very insensitive to both room shape, and the value of the (assumed uniform with angle of incidence) absorption coefficient. The only effect not investigated was that of air absorption; this can be expected to reduce, the E_t/N_t values at grazing incidence. This is because image source contributions which arrive at the roof surface at angles close to grazing for a source in the centre of the room must have been reflected many times in the (assumed hard) sidewalls, and so travelled a greater distance than those arriving normal to the roof surface. Since the effect of air absorption is proportional to the distance travelled, obviously any E_t/N_t results will be skewed towards normal incidence by the inclusion of air absorption. This effect will be more noticeable at higher frequencies.

The major difference between the E_t/N_t curves for a large disproportionate room as opposed to a smaller proportionate one is the time taken for the distribution to stabilise after the source is switched on. This implies that any angularly weighted average of an angularly varying absorption characteristic based on steady state reflection statistics will predict the correct acoustical behaviour much sooner after the source is switched on in the proportionate room than in the disproportionate one. Similarly the effects observed when the source is switched off may be expected to differ. This point is considered further in Section 6.4.3.

Estimates of uniform absorption coefficents made from steady state measurements in a reverberation chamber containing an angularly varying absorbent sample would therefore seem to produce adequate results to predict steady state levels in disproportionate rooms containing a similar sample. Since the reflection distribution statistics appear

to be fairly stable under transient conditions in the case of small proportionate rooms, similar estimates of uniform absorption coefficients based on transient tests might also therefore be expected to prove adequate for the prediction of steady state levels in disproportionate rooms with surfaces composed of the same material. The above points obviously rest on the assumption that the image models developed are adequate representations of any real situations considered.

The last major point worthy of mention is that the use of Paris' formula to weight an angularly varying absorption coefficient appears to be inappropriate for the energy-image-source room acoustics models used. This appears, as discussed above, to be due to the fact that spherical divergence effects are incorporated in the image source models. This seems to introduce a $\cos\theta$ factor into the angular distributions of E_t/N_t observed. This point is considered from the standpoint of statistical geometric acoustics in the next section.

6.4 The Use of Statistical Geometric Acoustics Concepts to Study the Effects observed in the Angular Distribution of Image Source Contributions at a Room Boundary Surface.

6.4.1 Introduction

The last section contained an investigation of the average angular distribution of energy at a particular boundary in rectangular rooms. The investigation used an energy image source room acoustics model, numerically implemented on a digital computer. It was found that the angular distribution of energy only appeared to satisfy the conditions necessary for the application of Paris' equation (see Section 6.1.2) in the limit of 'plane wave point sources' and totally hard surfaces. In the case of image point sources a cosine factor appeared to govern the angular distribution of the parameter E_t/N_t. The shape of this distribution appeared relatively insensitive to both the room shape and the absorption coefficient of the roof. In this section some of the techniques of statistical geometric acoustics are used to investigate this phenomenom. The method involves 'smearing out' the positions of the individual image sources in image space,

and replacing them by an equivalent source power per unit volume. Thus it can be expected to work best for small hard walled proportionate rooms at higher frequencies.

It was also observed in the last section that although the 'steady state' angular distributions of reflection energies were roughly independent of the room shapes investigated, the times taken for these characteristics to stabilise after the source is switched on were different in the various rooms studied. This fact suggests that the transient reflection energy distribution characteristics may be more sensitive to room shape and/or volume, and hence the behaviour of an angularly varying absorption coefficient may be different under transient conditions in proportionate and disproportionate rooms. This suggestion is at least partly substantiated by the image model results of Section 6.2.3 where a 50% change in "T_{60}" was observed when one of the angularly varying absorption characteristics was used in the flat room instead of the equivalent diffuse field value, whilst the two absorption characteristics produced almost identical decay rates in the cubic room case studied. A very approximate statistical approach will also therefore be used to study which particular image source contributions govern the reverberant decay characteristics. The findings of this approximate method will be used to qualitatively explain the computed energy-image-source room acoustics results.

6.4.2 Statistical geometric acoustics investigation of the angular distribution of sound energy at one surface in a rectangular room

In this investigation, the discrete energy-image sources that have been used in the previous models of this chapter (see Figure 6.1) will be 'smeared' throughout image space. Thus each volume element dV in image space will have a source strength $\rho W dV$ associated with it, where ρ is the density of the sources and W the strength of the real source(s). For the present investigation, the case of a single source operating in a comparatively small proportionate room of volume V will be implicitly considered; thus ρ equals $1/V$. Given this configuration, expressions for E_t and N_t are required, equivalent to the earlier discrete image source format equations (i.e., equations

(6.21) and (6.18) respectively). In this section both spherical and plane wave propagation characteristics will be investigated.

The geometry to be studied is shown in Figure 6.15. The surface at which the reflection statistics will be investigated is that at $y = h$. All the wall surfaces other than this one will be assumed to be hard. At a time t after the direct sound has reached a point on this surface, contributions will be arriving from all the smeared image sources within sphere of radius ct in image space centred on the surface point. The effective number of sources that contribute to the effects seen at the surface at that time can be written as an integral of the source density ρ over the volume of the sphere. In order to estimate the total number of reflections that occur in the production of any effects seen at time t in the real room, each volume element must be multiplied by a factor to account for the number of reflections with the roof that its contribution will have had. For points on the shaded element in Figure 6.15 (actually a ring in three dimensions), this factor can be seen to be approximately $(r\cos\theta/2h)$. A complete expression for the total number of reflections that occur in the contributions which make up the level seen at a time t after the arrival of the direct sound in the angular range $d\theta$ about θ, can now be formulated as,

$$N_t \simeq \int_0^{ct} 2\pi\rho \sin\theta r^2 d\theta \left(\frac{r\cos\theta}{2h}\right) dr$$

$$= 2\pi\rho \frac{\sin\theta\cos\theta d\theta}{2h} \int_0^{ct} r^3 dr$$

$$= \frac{\pi\rho \sin\theta\cos\theta}{h} \frac{ct^4}{4} d\theta \quad . \qquad (6.22)$$

This can be seen to possess an effective $\sin 2\theta$ angular variation, as was seen in the computed discrete image source model results of Section 6.3.4 (see Figure 6.8(a)). However as stated previously, it is the distribution of energy at the surface that will decide whether or not Paris' equation provides an adequate estimate of the angular weighting to use in the calculation of mean absorption coefficient values for application in image source room acoustics models. A smeared image

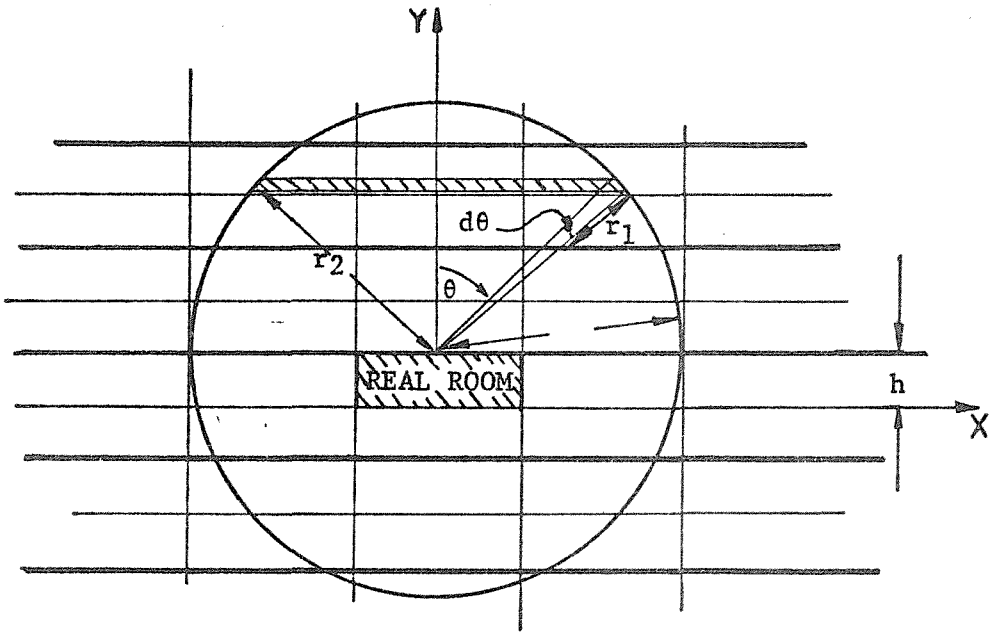

Figure 6.15 The geometry considered in the statistical geometric acoustics investigation of the angular distribution of reflection parameters.

form of equation (6.21) for E_t must therefore be formulated next. Two cases will be considered; the first is that of the physically unrealistic plane wave propagation case, in which the contributions from the image space source sphere do not exhibit spherical divergence. The second covers the case where spherical spreading is present. This second model is that normally used in geometric acoustics, since it preserves energy in a physically realistic manner.

E_t is the sum of all the energies that image source contributions which arrive at the receiver within t seconds of the direct sound, possess on their previous encounters with the roof surface, in the angular interval $d\theta$ about θ. Thus, for the plane wave propagation model,

$$E_t \simeq \int_0^{ct} 2\pi\rho W r^2 \sin\theta d\theta \sum_{i=1}^{n} \beta^{(i-1)} dr \ , \qquad (6.23)$$

where β is the roof's reflection coefficient, and the summation is over all the possible reflections with the roof surface, hence (see Figure 6.15) $n = \text{Int}(r\cos\theta/2h)$. In the limit of no absorption at the roof surface, $\beta = 1.0$, and equation (6.23) becomes

$$E_t \simeq 2\pi\rho W \frac{\sin\theta\cos\theta}{2h} \int_0^{ct} r^3 dr \ ,$$

$$= \pi\rho W \frac{\sin\theta\cos\theta}{h} \frac{ct^4}{4} d\theta \ . \qquad (6.24)$$

Division of this equation by equation (6.22) demonstrates that in this case the ratio E_t/N_t equals a constant value of W , and hence Paris' weighting appears correct. However, when the image source contributions are assumed to exhibit spherical spreading, the equivalent form to that of equation (6.23) is:

$$E_t \simeq \int_0^{ct} 2\pi\rho W r^2 \sin\theta d\theta \sum_{i=1}^{n} \frac{\beta^{(i-1)}}{r_i^2} dr \ , \qquad (6.25)$$

where r_i is the distance from the source volume element under consideration to the i^{th} specular reflection point at angle θ with the roof surface in image space (see Figure 6.15). Since the roof surfaces are a distance $2h$ apart in image space, r_i is roughly equal to $2ih/\cos\theta$. Thus, in the limit of a perfectly reflecting roof, equation (6.25) becomes:

$$E_t \simeq 2\pi\rho W \frac{\sin\theta\cos^2\theta}{4h^2} d\theta \int_0^{ct} r^2 \sum_{i=1}^{n} \frac{1}{i^2} dr \quad . \tag{6.26}$$

The summation over i can be replaced by an equivalent integral, as follows:

$$\sum_{i=1}^{n} \frac{1}{i^2} \simeq \int_0^n i^{-2} di = 1 - \frac{1}{n} \quad . \tag{6.27}$$

As a first order approximation the $\frac{1}{n}$ term will be neglected. This is only important for small ct values, and is therefore equivalent to neglecting the direct field's and first few reflections' effects. With this approximation equation (6.26) can be rewritten as:

$$E_t \simeq 2\pi\rho W \frac{\sin\theta\cos^2\theta}{4h^2} d\theta \int r^2 dr \quad .$$

$$= \pi\rho W \frac{\sin\theta\cos^2\theta}{2h^2} \cdot \frac{ct^3}{3} d\theta \quad . \tag{6.28}$$

Division of this equation by equation (6.22) yields the following form for the E_t/N_t distribution:

$$E_t/N_t \simeq \frac{2W\cos\theta}{3hct} \quad . \tag{6.29}$$

It can thus be seen that the $\cos\theta$ shape of the normalised E_t/N_t curves of Section 6.3.4 can be accounted for by this relatively simple model. Furthermore, it has been demonstrated that the deviation of this distribution from the uniform one necessary for the accurate

application of Paris' formula can be accounted for by the spherical properties of the propagating waves. A more apt weighting function for use in image models might therefore involve a $\cos^2\theta\sin\theta$ factor normalised in some manner.

Thus although Paris' equation is correct for the conditions necessary for a true diffuse field, it appears to be a poor representation of the conditions found to exist in the situations investigated. This might at least partly account for the observed discrepancies between the computed image model steady state results in which a diffuse field absorption coefficient was used and those with an angularly varying characteristic. However the level of absorption can also effect the results, as can be seen from consideration of an angularly varying absorption coefficient which has peak values of unity for some angles. Any energy arriving at these angles will not be reflected and hence the reflection statistics of the adjacent surfaces will be altered. Thus the positions of the images in space and the magnitude of the absorption characteristic are competing effects. However for the room geometries and uniform absorption characteristics used the distribution of E_t/N_t appeared comparatively insensitive to room shape or absorption level as was observed above.

6.4.3 A brief consideration of the image source contributions which govern the rate of reverberant decay in rectangular rooms

The sound pressure level at a point in a room is normally expressed in decibels with reference to some datum. Thus the level L at time t could be written as:

$$L(t) = (10\log_{10}P^2(t) - 10\log_{10}P_o^2)\,dB \ , \qquad (6.30)$$

where $P^2(t)$ is the mean square pressure at that time and P_o is some reference pressure. Reverberant decays are normally characterised by the slope of the decay curve of L after the source has been switched off. Thus it is the quantity $dL(t)/dt$ that is of interest. This can be written as

$$dL(t)/dt = (10/P^2(t))\cdot dP^2(t)/dt \ . \qquad (6.31)$$

It has been seen in Section 6.3.4 that the normalised distribution of incident energy averaged over a room boundary some time after the source has been activated appears relatively insensitive to room shape. Thus since $P^2(t)$ is only contributed to by image sources outside a sphere of radius ct, it is unlikely to be much affected by any change from an angularly varying to an appropriately weighted uniform absorption coefficient. It seems likely therefore that it is the $dP^2(t)/dt$ term that is more sensitive to the use of angularly varying absorption coefficients as opposed to diffuse field ones when the room shape is altered. This will now be statistically considered in terms of image source contributions.

At a time t after the direct source contribution reaches a receiver, the N image sources within the sphere of radius ct can be considered to contribute to the level at the receiver. The rate at which the number of image sources contributing increases with time can be written as dN/dt. Elementary considerations show that this must be equal and opposite to the rate of decrease of the number of image sources that contribute to the level at a time t after the direct sound ceases to arrive at the receiver when the sound source has been switched off. Thus it is possible to estimate the rate of change of the number of image sources that contribute to the level at any time t after the source is switched off.

If it is desired to study how the energy which ceases to arrive in a time interval dt, about t, is partitioned between the various image sources, each individual β^n term must be computed for all the sources that 'cut-off' in the time interval. The β^n term indicates the attenuation of the particular image source contribution due to n reflections with the room surfaces which have a uniform reflection coefficient β. Spherical spreading can be neglected since it is the same for all the image source contributions that cut-off at any instant. It would be possible to compute this numerically by use of an image source room acoustics computer program. However, in this section a very approximate model is used to try to illustrate what is happening physically in a given situation and relate this to previous computed results.

In this model the image sources will be divided into three classes - axial, tangential and oblique. Axial image source contributions will be defined as those which have only been reflected from one set of parallel walls. Thus, for example x-axial images have been reflected in the walls $x = 0$ and/or $x = a$ alone. The tangential source contributions are defined as only reflecting in two sets of parallel walls. Thus the x-y tangential images can be defined as having had at least two reflections, one in a wall perpendicular to the x-axis, the other in one perpendicular to the y-axis, but no reflections in walls perpendicular to the z-axis. The final class of image sources are the oblique ones. These have undergone at least three reflections (i.e. one with a wall perpendicular to each of the x,y and z axes). Having defined these three categories of image source it is an easy matter to formulate the approximate rate at which each of these types of sources cut on. This is because at a time t after the direct sound reaches the receiver, when the source is switched on, all the axial images which contribute lie within the limits $\pm ct$ in each of the rows of image rooms on axis. Similarly, the tangential ones lie within the three discs of rooms of radius ct in the axial planes (although the axial images must be subtracted from the total number of image sources in these discs). Finally the oblique ones lie within the sphere of radius ct, once the numbers of axial and tangential image sources have been subtracted. The average number, N_i, of each class of image source contributing to the level at a time t can thus be found by dividing each of these volumes in image space by the volume of the real room. The rates of change of the numbers of each type of source contributihg can then be found from differentiation of the expressions for N_i with respect to time.

It only remains to estimate the average attenuation that contributions from sources that are being cut-off at a time t in each of these classes exhibit due to wall reflections. Each of these three classes of sources can be shown to possess its own mean free path. This is generally an ensemble average over all the possible image source contributions ofthe distance travelled between reflections from walls. The number of reflections that the source contributions being cut-off at time t have had will therefore be approximated by ct divided by the relevant mean free pathlength (mfp). This will

be an approximation since the time average for one particular ray path only equals the ensemble average over all ray contributions in a perfectly diffuse field. However the results can be expected to be at least indicative of any trends exhibited in real situations.

The product of the rate of change of the number of image sources in a particular class, dN_i/dt , with the relevant attenuation factor for wall absorption effects (i.e. $\beta^{ct/mfp}$) can thus be calculated. The generalised form of these terms for a room of dimensions (L,L,ML) is shown in Figure 6.16. The percentage of the total change in source strength that each of these three classes of image source comprises was calculated for 3 types of image room - namely a cubic room, a duct room and a flat room. The results of such calculations are shown in Figure 6.17.

The results indicate that the decay rate in the three shapes of room is controlled by markedly different proportions of the three classes of images. In the proportionate room case the oblique images dominate the decay rate at all the times investigated. However in the disproportionate rooms investigated, the axial and tangential modes can play a large part in determining the rate of decay. This is because, at a specific time after the real source is deactivated, all of the image sources which are ceasing to contribute to the overall level are attenuated equally due to both spherical spreading and/or air absorption. Thus it is solely the ratio of the rate at which the number of image sources cutting off increases to how rapidly the $\beta^{ct/mfp}$ term changes with time for each class of images that determines their relative importance. The fact that axial and/or tangential images appear to play a significant part in determining the rate of decay in the disproportionate rooms investigated, but not in the proportionate one, is therefore of interest. This is because, although the rate of change of numbers of oblique images is obviously much greater than for axial and/or tangential images, the contributions of these oblique images must be much more severely attenuated than those of the other two image classes in disproportionate rooms but not in proportionate ones. The difference must be due therefore to the relatively few reflections that image sources in the smallest walls of the disproportionate rooms have had compared to the other image sources at a similar radius in

Figure 6.16 The generalised forms for the rates of change of the numbers of each type of source contributing (dN_i/dt), and their relative attenuation due to wall absorption effects. Formulated for a room of dimensions: (L, L, ML).

IMAGE CLASS	dN_i/dt	β^{ct}/mfp
AXIAL:		
X	$2C/L$	$\beta^{ct/L}$
Y	$2C/L$	$\beta^{ct/L}$
Z	$2C/ML$	$\beta^{ct/ML}$
TANGENTIAL:		
XY	$2C/L\ (^{\pi ct}/L - 2)$	$\beta^{\frac{4}{\pi}\frac{ct}{L}}$
YZ	$2C/L\ (^{\pi ct}/ML - (\frac{M+1}{M}))$	$\beta^{\frac{2}{\pi}(\frac{M+1}{M})\frac{ct}{L}}$
XZ	$2C/L\ (^{\pi ct}/ML - (\frac{M+1}{M}))$	$\beta^{\frac{2}{\pi}(\frac{M+1}{M})\frac{ct}{L}}$
OBLIQUE:		
XYZ	$\frac{2C}{L}(\frac{2\pi}{M}(\frac{ct}{L})^2 - \frac{\pi ct}{L}(1+\frac{2}{M}) + (2+\frac{1}{M})$	$\beta^{\frac{ct}{2L}\ (\frac{2M+1}{M})}$

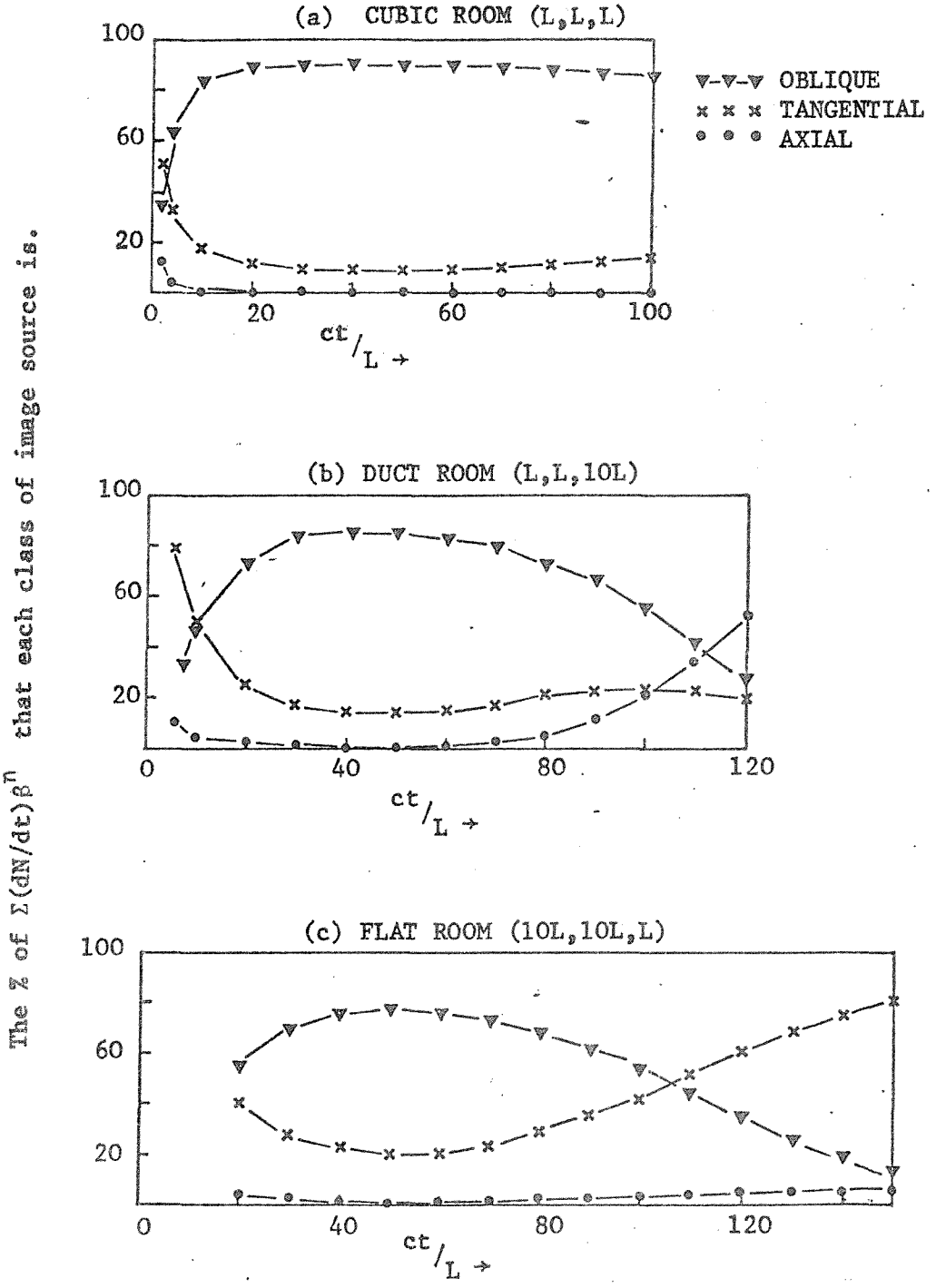

Figure 6.17 Plot of the % contribution to the decay rate from oblique/tangential/axial image sources for three types of room.

$\beta = 0.9$

image space. Thus when these sources cut-off, although they are few in number they represent a comparatively large proportion of the energy contributions being lost at that time. This suggests that absorption placed on these walls in disproportionate rooms should have the largest effect in the reduction of "reverberation times". This agrees with the published results of Schroeder [6.11]. Image sources to either side of the axial image sources in line with the longest room dimension will have suffered only one more reflection than their neighbouring axial image sources. Thus they can be assumed to similarly play a comparatively large role in the determination of reverberant decay rates. The extra reflection undergone by these 'just-off-axis' sources will occur at angles close to grazing with the larger room surfaces. Thus if these surfaces exhibit a strong level of absorption for angles of incidence near grazing the reverberant decay rate will probably increase markedly over that exhibited by a surface with an equivalent diffuse field value. Since in the case of an 'almost diffuse field' (i.e. the cubic room) it appears that different images control the rate of decay. This hypothesis would appear to be borne out by the results of Figure 6.7. Thus although the method used in this section is at best only approximate, it does seem capable of explaining some of the transient decay results in terms of physically plausible reasoning.

6.5 Discussion and Conclusions

This chapter has incorporated some of the absorption characteristics of Chapter 5, in order to study the effects of an angularly varying absorption coefficient on the acoustics of both proportionate and disproportionate rooms, by use of an energy-image-source room acoustics model. This was contrasted to the acoustical behaviour in these rooms when an equivalent diffuse field absorption coefficient, as determined by Paris' formula was used. There were found to be discrepancies in most of the cases considered. This prompted an investigation of the average angular distribution of reflection parameters at one surface in both cubic and flat rooms. There was seen to be a $\sin 2\theta$ factor in the angular distribution of the number of reflections at

the surface under study which contribute to the level at the receiver. However the equivalent normalised energy distribution appeared to exhibit a $\cos^2\theta\sin\theta$ factor when spherical spreading was included in the image model. These normalised distributions were relatively insensitive to changes in room shape or the surface's absorption coefficient (which was assumed uniform with angle).

These findings imply that, in so far as the image source models used are adequately accurate representations of real situations, then Paris' formula is a poor estimate of an average value to be used in practical situations. Also, since these normalised 'steady state' angular distributions of the reflection parameters investigated were almost independent of room shape, and further because these distributions appear more or less the same under 'start up' transient conditions in the cubic room case, there is the suggestion that measurements made in a simple reverberation chamber of the absorption characteristics of an angularly varying sample may prove adequate to predict the same material's behaviour under steady state conditions in a disproportionate space. This assumes that the sample occupies the whole of one surface in both of these rooms, and again that the image models used are adequate representations of real situations.

The chapter concludes with a section devoted to approximate statistical investigations of some of the phenomena noted earlier in the chapter. There was again found to be a $\cos^2\theta\sin\theta$ angular distribution at the surface for the energy contributions which make up the level at a receiver at time t after the direct sound has arrived there. There was also found to be a different dependence upon the groups of images which govern the rate of reverberant decays in disproportionate as opposed to proportionate rooms. This led to suggestions for the placement of absorption or the choice of absorption characteristics in order to reduce 'T_{60}' values. In fact in so far as the absorption models of Chapter 5 are adequate representations of the absorption characteristics of real roof structures, they would appear ideally suited to increasing the reverberant decay rate in disproportionate spaces at low frequencies. This is because under these conditions the majority of the absorption occurs at angles close

to grazing incidence, and it is the image source contributions at these angles to the roof which can govern the reverberant decay rate in disproportionate spaces.

The work of this chapter can therefore be seen to be of a fundamental nature, and suggests that a knowledge of the angular variation of the absorption coefficient may be necessary for accurate reverberant decay rate predictions in disproportionate spaces. However, for steady state level predictions, absorption coefficient measurements made in proportionate rooms may well prove adequate, although use of Paris' equation to estimate a diffuse field value would be inappropriate. All these conclusions are based on the assumption that the image model constructed is an adequate representation of any real situation encountered. These hypotheses could only really be adequately tested by an accurate experimental investigation. In many practical sitautions however there are scattering objects present. The next chapter is therefore concentrated on how, in the case of severely disproportionate rooms, such scattering objects, when placed upon the floor alter the acoustical behaviour typical of the type of disproportionate spaces investigated in this chapter.

CHAPTER 6 : REFERENCES

6.1 H. KUTTRUFF, 1973. Room Acoustics. London : Applied Science Publishers.

6.2 W.C. SABINE, 1964. Collected Papers on Acoustics. New York: Dover (see pages 3 -42).

6.3 A.D. PIERCE, 1981. Acoustics : An Introduction to its Physical Principles and Applications. New York : McGraw-Hill Book Company.

6.4 INTERNATIONAL ORGANISATION FOR STANDARDISATION 1963. Measurement of absorption coefficients in a reverberation room. ISO/R 354.

6.5 B.M. GIBBS and D.K. JONES 1972. Acustica 26, 24-32. A simple image method for calculating the distribution of sound pressure levels within an enclosure.

6.6 A.G. GALAITSIS and W.M. PATTERSON, 1976. J. Acoust. Soc. Amer. 60, 848-856. Prediction of noise distribution in various enclosures from free-field measurements.

6.7 Y. HIRATA, 1979. Acustica 43, 247-252. Geometrical acoustics for rectangular rooms.

6.8 E.M. BAZLEY, 1976. Sound absorption in air at frequencies up to 100 KHz. NPL Acoustics Report Ac74.

6.9 P.M. MORSE and H. FESHBACH, 1953. Methods of Theoretical Physics. New York : McGraw-Hill Book Company.

6.10 F. SANTON and A. DAUMAS, 1982. Acustica, 50, 209-212. Remarques sur l'angle d'incidence des rayons sur les parois d'une salle.

6.11 M.R. SCHROEDER and R. GERLACH, 1974. J. Acoust. Soc. Amer. 56, 1300. Diffusion, room shape and absorbent location - influence on reverberation time.

CHAPTER 7

INVESTIGATION OF THE ACOUSTICAL INTERACTION BETWEEN ABSORBENT AND SCATTERING SURFACES IN DISPROPORTIONATE RECTANGULAR ROOMS

7.1 Introduction

7.1.1 Background:

Idealised surfaces typifying those often found in disproportionate rooms have been studied in Chapters 4 and 5. The former chapter contains details of models for the description of the sound reflection characteristics of rough surfaces with either random or regular roughness distributions. The latter chapter contains analytic models for the absorption of sound by surfaces composed of lightweight panels. The models of Chapter 4 are therefore indicative of the acoustical characteristics of floors with scattering objects on them, whilst those of Chapter 5 are representative of the absorption behaviour of a whole class of lightweight building structures. Such features would seem to be the dominant factors in the determination of the acoustics of an enclosed space, once its overall dimensions have been determined. This point is well illustrated by many factory buildings such as that shown in the frontispiece. The effect of the absorbent surfaces alone on the enclosed space's acoustics can be studied by use of an image source room acoustics model, as in Chapter 6. However the presence of scattering objects renders assumption of a perfectly specular reflection from the floor surface invalid, as was observed from the models of Chapter 4. The degree to which a specular reflection assumption would be incorrect in a given case is a function of the number, size and physical properties of the scattering objects present, and the frequency of the incident sound. However, since in many practical cases such a specular reflection assumption will clearly be inadequate, the aim of this chapter is to study possible methods to model situations where the surfaces of a highly disproportionate enclosure are composed of either rough or absorbent surfaces. However the aim is not to produce a well validated prediction technique but rather to provide a means by which the acoustical interaction of these two types of surface can be studied and results presented for a number of parameter combinations.

7.1.2 Summary of the published work on room acoustics incorporating rough and/or absorbent surfaces:

A survey of the literature on prediction methods for the acoustics of disproportionate non-Sabine spaces, such as factories (see for example Reference [7.1]) reveals that almost all the previously used models have been concerned with volume scattering, as was noted in Chapter 4.

However there is a whole class of rooms - such as that illustrated in the frontispiece - where such a model appears inappropriate, since all the scattering objects are concentrated on one major surface,and do not extend out a significant proportion of the room's smallest dimension from that surface. As outlined in Chapter 4, rough surface scattering models would appear better suited to this type of situation. Unfortunately the complexity of some of these models would appear to prohibit their practical use. The simplest 'realistic' rough surface reflection model is that described by Lambert's Law (see Reference [7.2] Section IV.1). However as was seen from the computed results of Section 4.2.4 the behaviour in the simple cases investigated was unlike that predicted by use of Lambert's Law. This was evident since in the cases investigated a significant proportion of the reflected energy was still contained in the angles close to the specular direction, even if not actually given by the coherent term. This indicates that a mixed specular-diffuse reflection model for the characterisation of the floor's acoustical behaviour might be the best 'first order' model. Such models have been proposed for use in the prediction of rooms' acoustics by Kuttruff [7.2], and Joyce [7.3]. Both writers developed integral equation techniques, but were primarily concerned with proportionate rooms.

An alternative use of a part specular-part diffuse reflection model was developed by Davies [7.4]. He applied it to the problem of noise propagation in urban streets, which are typified by two parallel rough walls, separated at their base by a hard smooth road, and open to free space above. This model contains the assumption that once a component of a specular ray has been diffusely scattered it does not recontribute to the specularly reflected field. Instead this energy joins a field that is diffuse across planes normal to the two rough surfaces. By means of this simplification Davies obtained a comparatively

simple expression for the level as a function of distance down the street, given the situation's geometry, and the (assumed known) breakdown of reflected energy into specular and diffuse terms.

Although this last model was developed for environmental acoustics, it would be a comparatively easy matter to convert it for the study of disproportionate rooms with objects on their floors. This is because the geometry is much the same except that the main scattering surface is now the floor of the room as opposed to the walls of the buildings which line the streets, and there would also generally be no surfaces open to free space.

Sergeev [7.5] briefly considered the effect of scattering objects in disproportionate rooms. He analysed the acoustics of disproportionate rooms by smearing all the image sources in the plane of the real source normal to the room's longest axis. This source plane was then imaged in the room's end walls and approximate expressions derived for both steady state levels and the decay of sound after the source is switched off. In Sergeev analysis these expressions contained two main terms - one for sound propagating mainly in transverse directions, at angles from 30° to 90° with respect to the room's long axis, the other for longitudinally travelling sound which makes angles between 0° and 30°. The first term is controlled mainly by the absorption of the surfaces parallel to the room's long axis, whilst the latter is controlled by the absorptivity of the walls perpendicular to that axis. The relative importance of the two terms in any given situation is therefore determined both by the relative magnitudes of the absorption coefficients and also by the attenuation of the sound in air. In consideration of the effects of scattering bodies in the room, Sergeev proposed that they would tend to transfer energy from longitudinal directions to transverse ones. Sergeev suggested that this might be modelled as a change in the surfaces' absorption coefficients - namely a decrease of the absorption coefficient for those walls parallel to the room's long axis and an increase for those perpendicular to it. However no indication was given for a method of quantifying any such effects in terms of a particular scattering geometry within a given room.

The literature therefore appears to be devoid of models developed to study the acoustics of disproportionate rooms with one or more scattering surface. The development of such a model appears a worthwhile task therefore, and this is considered in the rest of this chapter.

7.1.3 Discussion of the work necessary to develop a model for disproportionate rooms with scattering surfaces

From the discussion of the last section it appears that there is a need to develop a model suitable for the study of the acoustics of disproportionate rooms with comparatively small scatterers situated on the floor. Of the models described, only that proposed by Davies [7.4] for urban noise prediction appears to be in a readily tractable form. Unfortunately it contains inherent assumptions about the nature of the field generated by the scattered energy, and hence it can only be expected to be approximate. However if it could be demonstrated to produce adequately accurate results, its inherent simplicity would make it very attractive for practical purposes. The more accurate integral equation approach (see References [7.2 and 7.3]) is obviously likely to produce more accurate results, but suffers from the drawback of large computational requirements. Consideration of a simplified geometric arrangement, still broadly representative of disproportionate rooms, might however render this approach more tractable.

The next sections of this Chapter will therefore be devoted to the adaptation of the type of model proposed by Davies [7.4] to the prediction of levels in, say, 'duct' rooms (i.e. very long rooms where the two smaller room dimensions are roughly equal). Later sections of the chapter will then briefly consider the possibility of using the integral equation type approach to study a very much simplified room geometry. Scale model test results will then be compared to those of these models, and conclusions drawn.

7.2 Development of a Mixed Image Source - Diffuse Scattering Model for the Acoustics of Disproportionate Rooms

7.2.1 Construction of the basic model:

The model developed in this section is for the geometry shown in Figure 7.1. Initially the case of an infinitely long room, or tunnel,

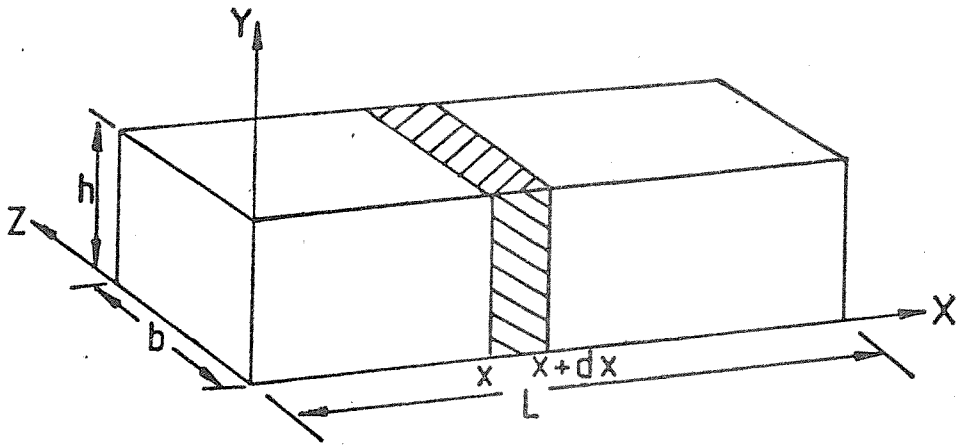

Figure 7.1 The geometry considered in the room acoustics model developed in Section 7.2

will be examined, since this is broadly similar to that considered by Davies [7.4]. Thus L in Figure 7.1 will be considered infinite in this section. In the model developed here, the 'floor' (i.e. the plane for which $y = 0$) will be considered rough and hard. All the other surfaces will be assumed smooth and partially absorbent, the absorption coefficient of the 'roof' (i.e. the surface for which $y = h$) being denoted by α_{rf} whilst that of the two walls at $z = 0$ and h, being α_w.

Since the floor is rough, any rays that strike it will be considered part specularly reflected, and part randomly scattered. The portions of the incident energy that are reflected in these manners being denoted R and β respectively. The specularly reflected portion then continues to propagate according to the laws of geometrical acoustics until it is again decomposed into a further reduced specular term, and another diffuse component. This process is then repeated *ad infinitum* for the remaining specular component at each stage. The portions of the energy that have been scattered are assumed to be scattered in all directions, and to feed a field which is diffuse across the tunnel's cross section. Upon further reflections with the floor, this scattered energy reflects with a reflection coefficient $R + \beta$, which will be taken as equal to unity in any computations performed here since the floor is assumed hard. Thus once energy has been diffusely scattered it is not considered to recontribute to the specularly reflected field component.

The total specularly reflected intensity at a distance x down the tunnel from the source can be formulated according to the principles of image acoustics (as outlined in Chapter 5, except that here all the images lie in one plane). For the case of a source and receiver lying in the centre of the tunnel's cross-section perpendicular to x axis, this can be written as:

$$I_{sp}(x,h/2,b/2) = \frac{W}{4\pi}\left\{\sum_{m=-\infty}^{\infty}\sum_{n=-\infty}^{\infty}\frac{(1-\alpha_w)^{|n|}R^{m_1}(1-\alpha_{rf})^{m_2}}{\left(x^2+(mh)^2+(nb)^2\right)}\right\}, \quad (7.1)$$

where for m even, $m_1 = m_2 = |m|/2$, otherwise $m_1 = |\mathrm{Int}((m-1/2)|$, and $m_2 = |\mathrm{Int}((m+1)/2)|$. Although only uniform reflection and absorption coefficients are explicity considered in this section, it would be a comparatively easy matter to alter equation (7.1) to accommodate their possible angular variation. Similarly air absorption has been omitted from equation (7.1). This could easily be remedied as in equation (6.5), but will be omitted here since the assignment of an air attenuation coefficient makes any results presented directly applicable to a particular frequency, whereas this section is designed to study the interaction of a rough floor with its neighbouring plane surfaces in a generalised manner. Hence, the results will be presented with air absorption absent and its likely effects subsequently discussed.

Thus the specularly reflected intensity at any point down the tunnel can be computed as was performed in Chapter 6. Indeed the series should converge more rapidly here since as well as losses due to absorption at boundary surfaces, energy is also lost to the diffusely reflected field at each reflection with the floor surface. The energy that actually goes from the specular into the diffuse field, at a particular area of the floor, can be determined by the summation of all the specular intensity components incident upon it. (Only the image source contributions above the real floor in image space need to be considered, since those below have already been reflected once). Thus this contribution can be written as:

$$I_{ni}(x) = \frac{W}{4\pi} \sum_{m=0}^{\infty} \sum_{n=-\infty}^{\infty} \frac{(1-\alpha_w)^{|n|} R^{m_1} (1-\alpha_{rf})^{m_2} (m+\frac{1}{2})h}{(x^2+(m+\frac{1}{2})^2h^2+(nb)^2)^{3/2}} \quad . \qquad (7.2)$$

This intensity is considered to contribute to positive and negative travelling fields, which are diffuse across the tunnel's cross-section. Thus a power balance can be written in terms of the energy entering and leaving the room segment between x and x + dx (see Figure 7.1). This can then be expressed in terms of the positively and negatively travelling diffuse field's powers W^+ and W^- , which give rise to diffuse intensities (W^+/bh) and (W^-/bh) respectively. (N.B. There is always an implicit x dependence of W^+ and W^-). These intensities are uniform across the tunnel's cross-section and radiate into a

hemisphere in the direction in which they are travelling. Thus across an elemental tunnel section between x and $x + dx$, it follows that,

$$W^+(x) = W^+(x+dx) + 2\alpha_w(W^+/bh)hdx + \alpha_{rf}(W^+/bh)bdx + \frac{1}{2}(R+\beta)\left((W^+-W^-)/bh\right)bdx - \frac{1}{2}\beta\, I_{ni}(x)bdx \,, \qquad (7.3)$$

for the positively travelling field, whilst for the negatively travelling one:

$$W^-(x+dx) = W^-(x) + 2\alpha_w(W^-/bh)hdx + \alpha_{rf}(W^-/bh)bdx + \frac{1}{2}(R+\beta)\left((W^--W^+)/bh\right)bdx - \frac{1}{2}\beta\, I_{ni}(x)bdx \,. \qquad (7.4)$$

In both of these equations the second and third terms on the right hand side denote the power absorbed at the walls and roof respectively. The fourth term indicates the amount scattered from the positively to the negatively travelling fields, and *vice versa*; and the last terms give the proportion of the normally incident specular intensity that is scattered into the diffuse fields ∿ assumed equally split between the two. Equations (7.3) and (7.4) can be rewritten as

$$-dW^+/dx = AW^+ - BW^- - \frac{1}{2}b\beta I_{ni}(x) \,, \qquad (7.5)$$

$$dW^-/dx = AW^- - BW^+ - \frac{1}{2}b\beta I_{ni}(x) \,, \qquad (7.6)$$

where $A = 2\alpha_w/b + \alpha_{rf}/h + (R+\beta)/2h$, and $B = (R+\beta)/2h$. Differentiation of equations (7.5) and (7.6) with respect to x and the subtraction of one from the other finally leaves

$$d^2(W^++W^-)/dx^2 - (A^2-B^2)(W^++W^-) = -(A+B)b\beta I_{ni}(x) \,. \qquad (7.7)$$

This second order linear inhomogeneous differential equation must now be solved. This will be performed by a Green function method. If the term on the right hand side of equation (7.7) is rewritten as $F(x)$, the equation becomes

$$d^2(W^++W^-)/dx^2 - (A^2-B^2)(W^++W^-) = -F(x) \,. \qquad (7.8)$$

The required Green function equation is

$$d^2g(x,x')dx^2 - (A^2-B^2)g(x,x') = -\delta(x-x') , \qquad (7.9)$$

given that some $g(x,x')$ can be found to satisfy this equation and suitable boundary conditions. Multiplication of equation (7.8) by $g(x,x')$ and similarly equation (7.9) by $(W^+ + W^-)$ and subtraction of the latter from the former leaves

$$g(x,x') \frac{d^2(W^+ + W^-)}{dx^2} - (W^+ + W^-) \frac{d^2g(x,x')}{dx^2} + g(x,x')F(x) = \delta(x-x')(W^+ + W^-) ,$$

or

$$\frac{d}{dx}\left[g(x,x') \frac{d}{dx}(W^+ + W^-) - (W^+ + W^-) \frac{dg(x,x')}{dx}\right] + F(x)g(x,x') = \delta(x-x')(W^+ + W^-) . \qquad (7.10)$$

If x and x' are now interchanged, the functions g and δ being symmetric, then the resultant expression can be integrated over x' to give

$$(W^+ + W^-) = \int_{x_1}^{x_2} F(x')g(x,x')dx' + \left[g(x,x') \frac{d(W^+ + W^-)}{dx'} - (W^+ + W^-) \frac{dg(x,x')}{dx'}\right]_{x_1}^{x_2} \qquad (7.11)$$

For the case of the infinitely long tunnel the integration limits are plus and minus infinity; hence the final expression for the diffuse field intensity at any distance x down the tunnel from the source is

$$I_d(x) = \left(\frac{W^+ + W^-}{bh}\right) = \int_{-\infty}^{\infty} \frac{(A+B)}{h} \beta I_{ni}(x')g(x,x')dx' . \qquad (7.12)$$

It only therefore remains to formulate the correct form for the Green function $g(x,x')$, and then perform the integration in order to estimate the diffusely scattered intensity at any point in an infinitely long rectangular tunnel with a rough floor, and all the other surfaces smooth but absorbent.

The total intensity is then simply the sum of the two components $I_{sp}(x)$ and $I_d(x)$ as given by equations (7.1) and (7.12) respectively. Subsequent normalisation of this sum by the intensity I_o, at 1 m from the source in free space, and presentation in terms of decibels gives

$$SPL(x) - PWL = 10\log_{10}\left\{\frac{I_{sp}(x)+I_d(x)}{I_o}\right\} . \qquad (7.13)$$

The next section details the form of the Green function that is required for both finite length and infinitely long rooms. The subsequent section then covers numerical evaluation of some of the derived expressions.

7.2.2 *The choice of Green functions for the mixed image source - diffuse scattering room acoustics model:*

A function $g(x,x')$ is required which satisfies equation (7.9). The form of this equation indicates that $g(x,x')$ is likely to be an exponential of the general form $\exp\left(-(A^2-B^2)^{\frac{1}{2}}(x-x')\right)$. However care must be taken to ensure that although $g(x,x')$ is continuous at x', $dg(x,x')/dx$ has a unit step discontinuity there. This requirement can be seen since if equation (7.9) is integrated with respect to x, over a small interval around x', this gives

$$\int_{x'-\varepsilon}^{x'+\varepsilon} \frac{d^2g(x,x')}{dx^2}\,dx - \int_{x'-\varepsilon}^{x'+\varepsilon} (A^2-B^2)g(x,x')\,dx = -1 . \qquad (7.14)$$

As ε tends to zero the second integral on the left hand side of this equation vanishes, to leave

$$\left.\frac{dg(x,x')}{dx}\right|_{x'-\varepsilon}^{x'+\varepsilon} = -1$$

Therefore the required form of the free field (i.e. no end walls) Green function is,

$$g_{\infty}(x,x') = \frac{\exp\left(-(A^2-B^2)^{\frac{1}{2}}(x-x')\right)}{2(A^2-B^2)^{\frac{1}{2}}} \quad , \; x > x' \quad ,$$

$$= \frac{\exp\left(-(A^2-B^2)^{\frac{1}{2}}(x'-x)\right)}{2(A^2-B^2)^{\frac{1}{2}}} \quad , \; x' > x \; ,$$

$$= \exp(-\gamma|x-x'|)/2\gamma \quad , \qquad (7.15)$$

where γ equals $(A^2-B^2)^{\frac{1}{2}}$, and the signs of the exponent are chosen to ensure that $g(x,x')$ always decays with distance from x'.

Now that a Green function has been found for the configuration where the room is infinitely long, attention will next be paid to the case of finite length rooms. Under these circumstances the integral in equation (7.11) is only over a finite range and the term in brackets on the right hand side of the equation cannot in general be ignored. If the values of $(W^{+}+W^{-})$ and its normal derivative are known at the end walls this bracketed term may be evaluated, provided that the correct Green function can be found. For the specific case of hard end walls, the derivative of the $(W^{+}+W^{-})$ term will be zero. The derivative of the Green function can similarly be made to equal zero if the free field Green function of equation (7.15) is replaced by an image series (see Reference [7.6] for further detials). For this one-dimensionally propagating field only images in the end walls need to be considered. The configuration considered is shown in Figure 7.2. If the position of the receiver is now defined as being a distance x_o from one end wall of a room of length L, then the x co-ordinates of the imaged receivers can be defined as:

$$X_{even} = x_o + 2mL \; ,$$

and

$$X_{odd} = 2nL - x_o \; . \qquad (7.16)$$

Thus the required Green function for the new problem, valid for observation points x in the range $0 \leq x \leq L$, is given by the expression

$$g_I(x,x') = \frac{1}{2\gamma}\left\{\sum_{m=-\infty}^{\infty} \exp\left(-\gamma|(x_o+2mL)-x'|\right) + \sum_{n=-\infty}^{\infty} \exp\left(-\gamma|(2nL-x_o)-x'|\right)\right\} \quad , \qquad (7.17)$$

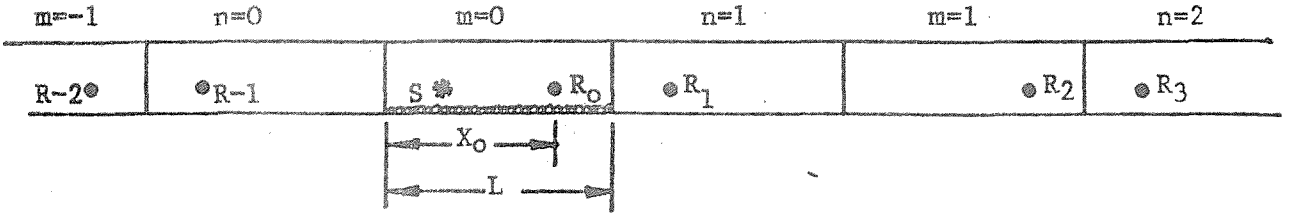

Figure 7.2 The geometry considered in the derivation of the Green function for the duct room with end walls present.

where g_I is the imaged Green function. This can be explicitly evaluated for the two cases of x_o greater, or less than x', to give the following forms:

$$g_I(x,x') = \frac{1}{\gamma}\left\{\frac{2\cosh\gamma x_o}{1-e^{-2\gamma L}} - e^{\gamma x_o}\right\}\cosh\gamma x' \quad , \quad x_o > x' \qquad (7.18)$$

$$g_I(x,x') = \frac{\cosh\gamma x_o}{\gamma(1-e^{-2\gamma L})}\left(e^{-\gamma x'}+e^{\gamma x'}e^{-2\gamma L}\right) \quad , \quad x_o < x' \; . \qquad (7.19)$$

These forms can then be used in place of the free field Green function in equation (7.12) for $I_d(x)$. Care must be taken since x was originally the distance from the source, whereas here x_o is measured from one end wall, and the integration limits are now 0 and L.

7.2.3 Numerical evaluation of the mixed specular-diffuse scattering model for an infinitely long rectangular room

The computation of the specularly reflected field at any point can be accomplished as for the energy image source model of Chapter 6. However, before the diffuse field terms can be explicitly evaluated the integration in equation (7.12) must be carried out. Substitution of equation (7.15) into equation (7.12) yields

$$I_d(x) = \frac{(A+B)}{\sqrt{A^2-B^2}}\,\frac{\beta}{h}\int_{-\infty}^{\infty} I_{ni}(x')\exp\left(-\sqrt{A^2-B^2}\,|x-x'|\right)\,dx', \qquad (7.20)$$

The exact solution of this integral is not possible analytically. The integral can either therefore be evaluated numerically or approximated in some manner. Davies [7.4] provided an approximate form for the solution which is valid for large distances from the source. He commented that it overestimates levels close to the source, but gives results in "surprisingly good agreement with numerical estimates over much of the range of z/ℓ" (i.e., x/b in the notation of this section), provided that $b \simeq h$. Davies' approximate form also contains an integral form for the specular intensity component, whereas in this section the sum of the image contributions is explicitly considered.

Figure 7.3 shows schematically the form of the two functions, $I_{ni}(x')$ and $\exp(-\gamma|x-x'|)$, which occur together as a product in the integral of equation (7.19). When the receiver is far away from the source the contributions to the integral can be considered to be in two parts, as follows. Both the functions are symmetric about some point - the function $I_{ni}(x')$ about the source position (i.e., $x' = 0$), and the function $\exp(-\gamma|x-x'|)$ about the receiver position (i.e., $x' = x$). Since most of the contributions to the integral come from the neighbourhoods of the peaks of these functions, it can be approximated as follows,

$$\int_{-\infty}^{\infty} I_{ni}(x')\exp(-\gamma|x-x'|)dx' \simeq 2\left\{I_{ni}(x)e^{-\gamma x}\int_{x}^{\infty} e^{\gamma x'}dx' + e^{-\gamma x}\int_{-\infty}^{0} e^{\gamma x'}I_{ni}(x')dx'\right\}$$

$$= \frac{2I_{ni}(x)}{\gamma} + \frac{2I_{ni}(0)}{\gamma}e^{-\gamma x} - 2e^{-\gamma x}\int_{-\infty}^{0} \frac{I_{ni}(x')}{\gamma}e^{\gamma x'}dx' .$$

Now since the function $I_{ni}(x')$ is symmetric about the origin, its derivative in the region of $x' = 0$, which gives the main contribution to the remaining integral will be small, whence, as a first approximation, this remaining integral term can be neglected compared to $2I_{ni}(0)e^{-\gamma x}/\gamma$. Hence the approximate far field expression for the diffuse field intensity at a point x is given by

$$I_d(x) \simeq \frac{2\beta}{(A-B)}\left\{I_{ni}(x) + I_{ni}(0)e^{-\gamma|x|}\right\} . \qquad (7.21)$$

Equations (7.1), (7.21) and (7.13) thus provide a simple method for the estimation of the overall sound pressure levels along the length of a very long room with a diffusely scattering non-absorbing floor, and all the other surfaces smooth and partially absorbent. Although it would be a comparatively easy matter to include the effect of end walls (as outlined in Section 7.2.2), it was decided to first compute some results for the very simple model outlined in this section, in order to discover whether the model appears adequate. A Fortran computer program was written in order to implement the model on the University's ICL 2970 computer. A listing is contained in Appendix E (N.B. in the

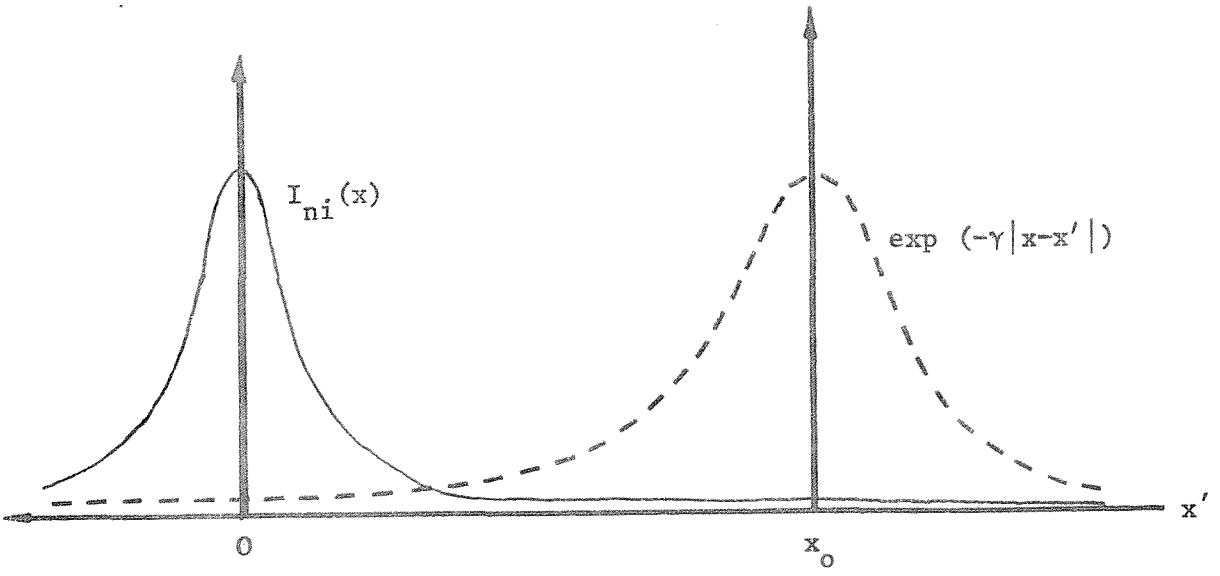

Figure 7.3 The schematic form of the two functions of which the product is integrated in the room acoustics model of section 7.2.2.

computer program, the x axis indicates the room's width, the y axis its height, and the z axis its length). Results obtained from this program are presented and discussed in the next section.

7.2.4 Presentation and discussion of the mixed specular-diffuse scattering room acoustics model's results.

The results of the mixed specular-diffuse scattering model are shown in Figures 7.4 to 7.7. It is immediately obvious from these results that the effect of increasing the floor's roughness (i.e., decreasing its R value), is to increase the levels near to the source and decrease them further away. This is similar to the trends observed in the currently used volume scattering room acoustics models when the scattering cross-section is increased (see for example Reference [7.7]). In the model developed here the behaviour arises because with a rougher surface more of the source's energy is converted into the diffuse field component. The amount of energy entering the diffuse field component per unit distance down the tunnel will be largest close to the source and will diminish with distance from it. This is due both to the increased distance from the source, and to the fact that the angles subtended by the specularly reflected contributions that enter the diffuse field at any point on the floor tend towards grazing incidence as distance from the source increases, and hence their normal intensity component is reduced. The rate of absorption for a sound particle that enters the diffusely scattered field can also be expected to be higher due to the implicit reduction in the ensemble averaged mean free pathlength.

All of the curves for the results with a scattering floor can be seen therefore to cross the equivalent curve for the smooth floor case. Once all the other parameters have been specified, the distance from the source at which this crossover occurs is insensitive to changes in floor roughness. Increasing the absorption of the other plane surfaces moves this crossover point towards the source (cf. Figures 7.4, 7.5 and 7.6). In the extreme far field there is virtually no contribution to the overall level from the diffusely scattered component in this model. This can be seen from the results of Figure 7.6, where the curve for $\alpha = 0.2$, $R = 0.8$ asymptotically approaches the $\alpha = 0.4$, $R = 1.0$ curve.

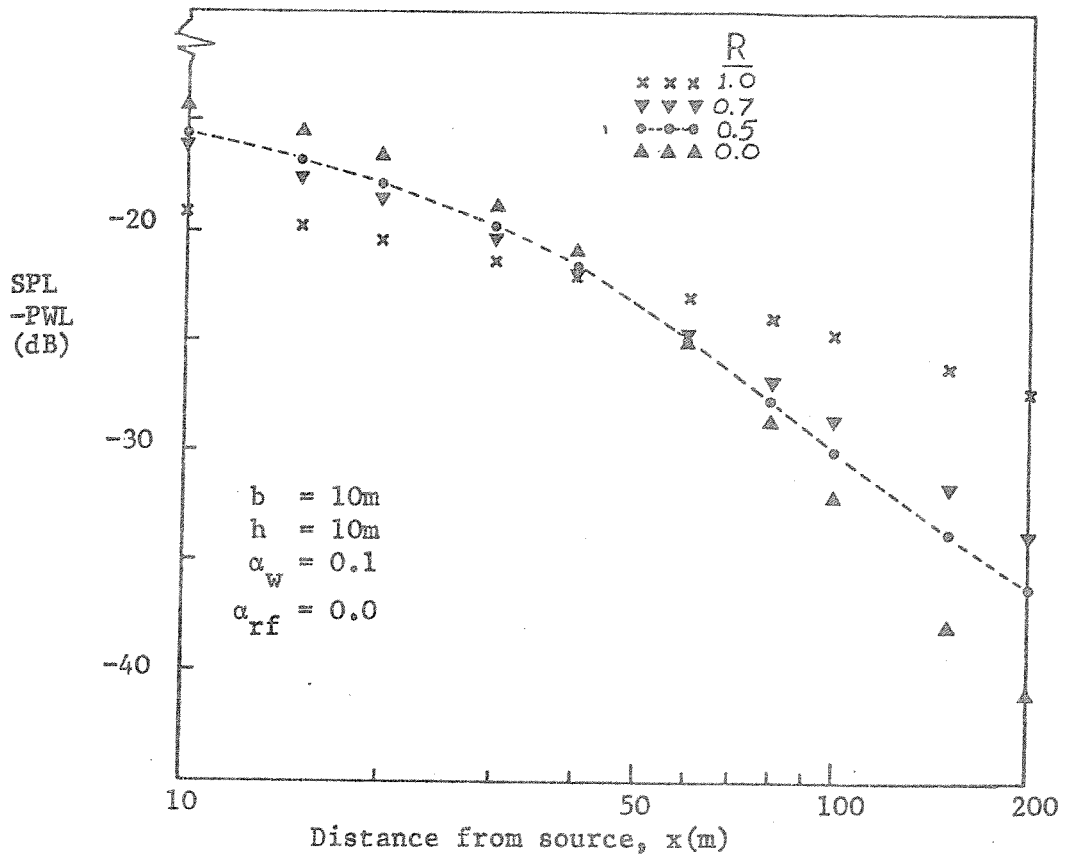

Figure 7.4 Results of the model of section 7.2 for the parameter values indicated. Image sources within 1200m of the source considered.

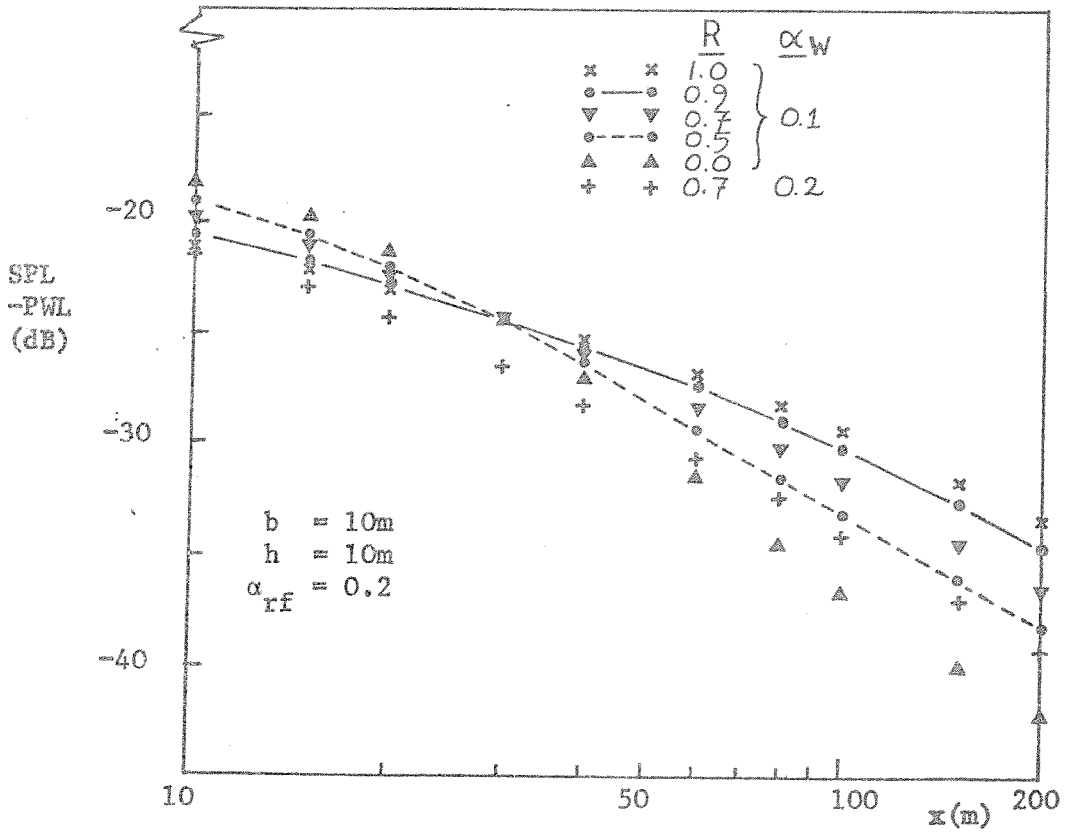

Figure 7.5 As for Figure 7.4, parameters as indicated.

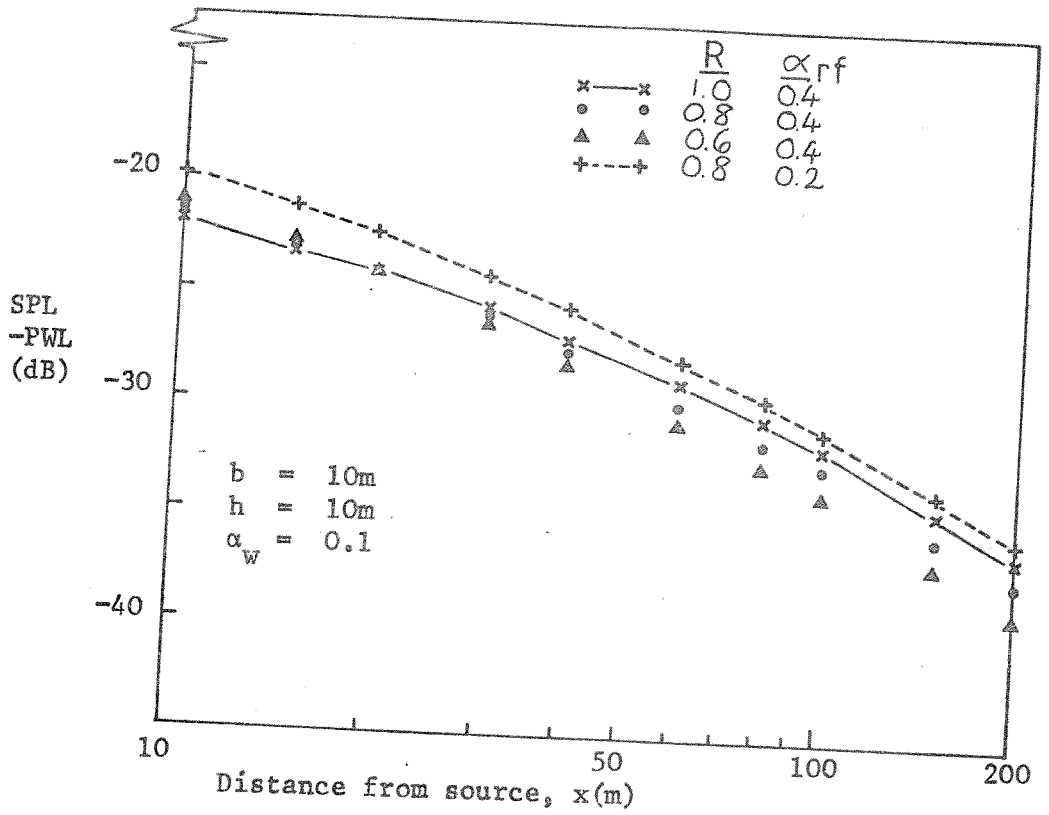

Figure 7.6 As for Figure 7.4 Parameter values as indicated.

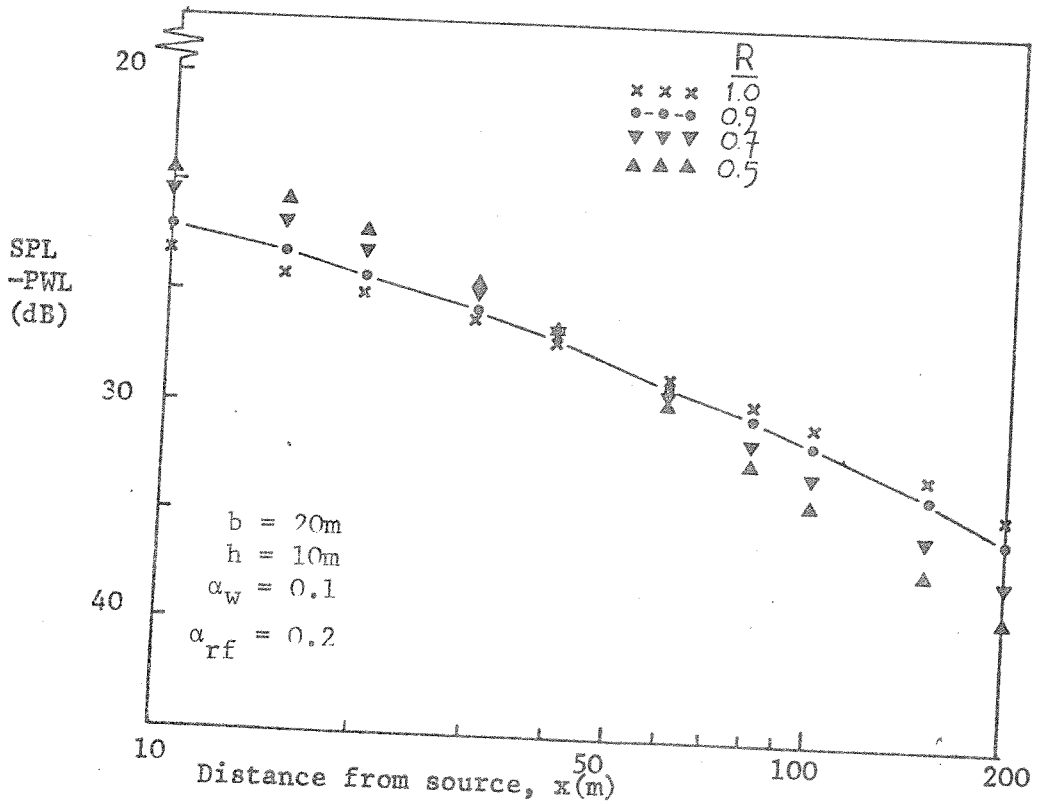

Figure 7.7 As for Fig 7.4. Parameter values as indicated.

Thus at great distances from the source a roughened floor has a similar effect to an equivalent increase in absorption, although close to the source it leads to increased levels. The magnitude of the increase in the levels when the floor is roughened is greatest when the overall absorption level is lowest. Such configurations also lead to the greatest decrease in levels far from the source. This behaviour can be explained as follows. Most of the energy entering the diffuse field does so close to the source; hence under conditions where the flat surfaces are not very absorbent there will be a greater increase in level than under conditions where they are significantly absorbent. As the diffuse field propagates down the tunnel, so energy is lost at the flat absorbent surfaces. Therefore increasing the absorption of these surfaces leads to a decrease in the distance from the source to the point where the curves for rough floors cross the equivalent curve for a specularly reflecting floor. Ultimately in the extreme far field the curves for cases with rough floors will asymptotically approach the equivalent curve for a floor (or ceiling) which reflects specularly but has an absorption coefficient increased by $d\alpha$ where $d\alpha$ equals $1-R$. This is both because the scattered field's energy is more rapidly attenuated with distance from the source, and since there is very little specular intensity entering the diffuse field far from the source plane.

The effect of changes in the cross-sectional area of the tunnel in this model can be seen from comparison of Figures 7.5 and 7.7. There are two basic effects incurred by such a change. One is the redistribution of the specular image sources in image space, the other is the increased absorption and scattering potential per unit length of the tunnel. The change between Figures 7.5 and 7.7 is a doubling of the tunnel's width. In this particular case this doubles the scattering potential per unit length, but only increases the absorption by 50% over the same distance. The density of the specular image sources in image space is also halved. The net results of these changes are to lower the absolute levels and move the point at which the results with a rough floor cross those with a flat floor away from the source. This behaviour ties in with the facts that the relative magnitude of the specular contribution drops when the width is doubled, whilst the proportional increase in the area in which energy is scattered into the diffuse field is bigger than the proportional increase in absorption

per unit length. These changes also result in a greater increase in the levels close to the source when the floor is roughened, but have minimal effect upon the similar changes observed at great distances, since under these conditions the specularly reflected field dominates (including of course, an increasing proportion of near grazing incidence components). It is thus the ratio of scattering to absorption per unit length that controls the behaviour of the scattered field, whilst the overall levels and extreme far field trends are influenced by the specular image source distribution.

The results for a finite length room with hard end walls and a scattering floor can also be predicted from results such as those presented in Figures 7.4 to 7.7. This is possible by imaging the source plane in the end walls (rather than the receiver as in Section 7.2.2). Thus the level at the receiver will be equivalent to that due to an infinite number of regularly spaced sources in an infinitely long tunnel. Hence the level can be estimated from the superposition of the levels due to each of these sources, where each individual level is calculated as above. The addition of end walls will probably therefore serve to reduce the increase in levels close to the source when the floor is roughened, since the levels due to the source planes that are imaged in the end walls will be less reduced with a smooth floor than with a rough floor. Similarly, at greater distances from the source in very long rooms the levels could be decreased even further by the introduction of a rough floor.

Although not specifically considered, the likely effect of air absorption can be deduced from a knowledge of the field's constitution at any point. Air absorption will only significantly affect levels where major contributions to the overall level have travelled a long way with few reflections or where the surfaces' absorption coefficients are very small. Thus, its main effects will tend to be at great distances from the source (and of course at higher frequencies). Under these conditions the scattered field does not contribute much to the overall level, and hence air absorption's effects on it will be unimportant. At great distances from the source the effects of air absorption should be roughly equal on the levels with and without a rough floor. It may however affect the smooth floor results to a slightly greater

extent since reflections from the floor in this case are assumed perfect, whereas in the extreme far field with a rough floor, the results observed were similar to those for a floor of absorption coefficient (1-R) . Thus air absorption may be expected to have a slightly smaller effect, leading to reduction in the spread of the results with increased floor roughness at great distances from the source.

The effects predicted by the model of this section are generally quite physically plausible. Only direct comparison with experimental measurements will allow any more definite statements, given the approximate nature of the model due to assumptions contained in its construction (e.g., diffuse scattering and the existence of a diffuse field across the room's cross-section) and subsequent numerical evaluation (e.g., the consideration of a finite number of image contributions, and the approximation of the integral in equation (7.20)). Nevertheless, the effects observed certainly correlate, at least qualitatively, with previously published results (e.g., those, for example, of Reference [7.7]).

In order to investigate further the accuracy of the type of approach adopted in this model, the results of a series of scale model tests will be described later in this chapter (see Section 7.4). Before that, however, an alternative more rigorous (and hence less easily evaluated!) model will be described. It will be considered in particular for a type of room for which the model developed in this section would not seem ideally suited. The type of room to be considered will be termed a 'flat room'. This room type will be characterised by the existence of one room dimension very much smaller than the other two. This dimension will be termed the 'room height'. It is therefore unlikely that a diffuse field will exist across the entire cross-section of such a room when only one source is in operation, and whilst an analogous approach to that used in this section could be developed it was felt better to develop a somewhat more rigorous formulation for this problem - especially since 'flat rooms' are typical of a whole class of industrial workspaces. The details of such a model are therefore contained in Section 7.3.

7.3 A Model for the Acoustics of 'Flat' Rooms with Absorbent Roofs and Scattering Floors.

7.3.1 Introduction:

It is well known that the steady state sound pressure levels in many industrial workspaces are controlled by the presence of two parallel planes, separated by an airspace. Such a configuration is representative of situations where a rectangular room has a large volume, but its height is appreciably smaller than the other two characteristic dimensions. This geometry has been studied for the case where the two surfaces are smooth partially absorbent planes by Hurst [7.8]. However the situation where one of these planes has scatterers on its surface does not appear to have been explicitly considered in the literature. In such a configuration the plane upon which the scatterers stand could easily be modelled as a 'rough surface', by using for example one of the techniques outlined in Chapter 4. This simplified arrangement would then be ideally suited to modelling by integral equation methods, as proposed by Kuttruff [7.2], since only two surfaces need to be explicitly considered and both are infinite.

A model based on energy principles will therefore be formulated for this geometry by an integral equation approach, and possible solution methods considered. In this manner a different class of rooms to those studied in the last section will be examined and some findings about the controlling parameters presented for discussion.

7.3.2 A model for the propagation of sound between absorbent and rough infinite planes.

The geometry considered in this section is illustrated in Figure 7.8(a). The upper surface at $z = h$, is smooth and possesses a uniform absorption coefficient α. The lower plane surface at $z = 0$ is assumed to be non-absorbing but 'rough'; that is, it will be modelled as a flat plane which does not reflect energy totally according to Snell's law: a proportion s of any energy incident upon this surface is assumed to be specularly reflected. The remaining energy (i.e. a portion (1-s) of that originally incident) is assumed to be reflected according

Figure 7.8 The geometry considered in the flat room model of Section 7.3.

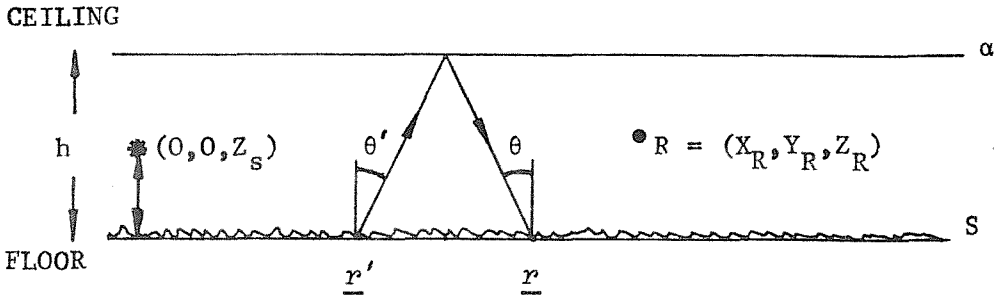

Figure 7.8(a) The actual geometry considered in the model.

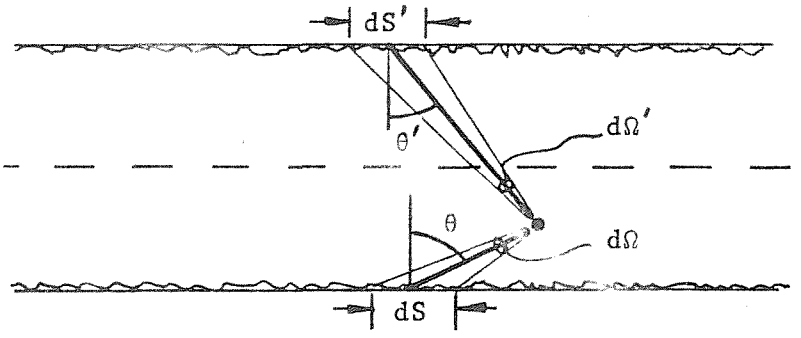

Figure 7.8(b) The image of the floor surface in the ceiling necessary to include the scattered field which is specularly reflected from the ceiling.

to some scattering law determined by the actual geometry of the objects situated on the floor.

The intensity I_{sp} at a receiver point R due to the specularly reflected portions of the energy from the source can be written as a sum of the energy contributions from the images of the real source in the two parallel surfaces. Hence for a source at $(0, 0, z_s)$ the level at the point (x_R, y_R, z_R) can be written as

$$I_{sp}(R,t) = \sum_{n=-\infty}^{\infty} \frac{W(t-r_n/c)}{4\pi r_n^2} (1-\alpha)^{N1_s N2} \qquad (7.22)$$

where

$$r_n = \left(x_R^2+y_R^2+(z_{sn}-z_R)^2\right)^{\frac{1}{2}} ,$$

$$z_{sn} = (n+1)h-z_s , \qquad n = \text{odd.}$$

$$z_{sn} = nh + z_s , \qquad n = \text{even.}$$

$$N1 = N2 = n/2 , \qquad n = \text{even.}$$

$$N1 = \left|\text{Int}(n+1)/2\right| , \qquad n = \text{odd.}$$

$$N2 = \left|\text{Int}(n-1)/2\right| , \qquad n = \text{odd.}$$

It only therefore remains to formulate an expression for the level at R due to all the scattered energies which arrive there. This will be expressed initially in a completely general manner and then the case of a specific reflection law considered. The integral equation approach used relies upon establishing the intensity incident at any surface point in terms of the energy scattered from all the other surface points and the component of the specular field which is converted into the diffuse field there. This results in the formation of an integral equation for the scattered intensity at the floor surface, which must then be solved. The scattered field at any point off the surface can finally be formulated in terms of an integral of the contributions of scattered intensity from the whole floor surface.

The scattered energy which arrives at a floor surface point $\underline{r}$ from any other surface point $\underline{r}'$, is determined by the reflection matrix $K(\underline{r}\,\underline{r}')$. Scattered energy can only get from one point on the floor to another by specular reflection from the roof surface. Thus for the geometry considered, the total intensity contributing to the scattered field at any floor surface point $\underline{r}$ at a time t can be written as

$$I(\underline{r},t) = \int_{S'} K(\underline{r},\underline{r}')I(\underline{r}',t-R'/c)(1-\alpha)dS' + (1-s)I_{spi}(\underline{r},t), \qquad (7.23)$$

where R' is the shortest distance from $\underline{r}'$ to $\underline{r}$ via the ceiling, I_{spi} indicates the contribution to the scattered field from the specularly reflected components, and hence is a sum only over the images for which $n \geq 0$ in equation (7.22), with each image contribution weighted by a $\cos(\theta_i)$ term, where θ_i is the angle to the normal at $\underline{r}$ for the i^{th} image source contribution. The integral in equation (7.23) is over the whole floor surface. From conservation of energy requirements it is apparent that $K(\underline{r},\underline{r}')$ can be any function of angle of sound incidence or position on the floor that satisfies the equation

$$\int_{S'} K(\underline{r},\underline{r}')dS' = 1 \; . \qquad (7.24)$$

If it is now assumed that the scattered portion of the energy reflects according to Lambert's Law (see Reference [7.2]), then $K(\underline{r},\underline{r}')$ takes the explicit form,

$$K(\underline{r},\underline{r}') = \frac{\cos\theta\cos\theta'}{\pi R'^2} \qquad (7.25)$$

where θ' and θ are the angles to the normal subtended by the sound leaving $\underline{r}'$ for $\underline{r}$ and that at which it arrives at $\underline{r}$ respectively. (See Figure 7.8(a)). Since the two planes are parallel in the geometry considered here, θ' equals θ. Hence if $\underline{r}$ and $\underline{r}'$ have co-ordinates $(x,y,0)$ and $(x',y',0)$ respectively, $K(\underline{r},\underline{r}')$ becomes:

$$K(\underline{r},\underline{r}') = \frac{4h^2}{\pi\left((x-x')^2+(y-y')^2+4h^2\right)^2} \quad , \tag{7.26}$$

It should be stressed that this reflection law is chosen primarily for mathematical convenience rather than from any directly physical considerations. Hence although the form chosen for $K(\underline{r},\underline{r}')$ here does not contravene any energy requirements, it is probable that a more realistic form could be devised from a knowledge of the scattering geometry in any given situation. This might well involve use of one of the surface scattering models of Chapter 4. It would also be possible to make α and/or s dependent upon the angle of sound incidence and/or the position on the surface, in search of greater agreement with any set of experimental measurements. However, as the principle aim of this section is to formulate a possible model, α and s will be treated as constants in order to reduce the complexity of the problem's formulation and solution.

It now remains to evaluate an expression for the intensity, I_d, (i.e., the product of the speed of sound, c, and the acoustical energy density) at any point R off the surface due to the scattered field at the surface. This can be obtained by integrating over all the points on the floor, the expression (see Reference [7.2]).

$$I_d(R,t) = \frac{1}{\pi}\left\{\int_S I(\underline{r},t-d/c)\,d\Omega + \int_{S'} I(\underline{r}',t-d'/c)\,(1-\alpha)\,d\Omega'\right\} \tag{7.27}$$

where $d\Omega$ and $d\Omega'$ equal $(\cos\theta/d^2)dS$ and $(\cos\theta'/d'^2)dS'$ respectively. The geometrical parameters θ, d, θ' and d' are identified in Figure 7.8(b). The first term in the brackets of equation (7.27) represents the scattered sound component which travels directly from the floor to the receiver, whilst the second term denotes that which arrives at the receiver after specular reflection from the roof surface. The total intensity I_t at the point R can now be obtained from the expression:

$$I_t(R,t) = I_{sp}(R,t) + I_d(R,t) \quad , \tag{7.28}$$

where I_{sp} and I_d are the specularly reflected and scattered intensities obtainable from equations (7.22) and (7.27) respectively.

A complete system of equations has now been constructed for the evaluation of total intensity levels at any point between two infinite planes, one non-absorbent but able to partly scatter the sound incident upon it, the other specularly reflecting and partly absorbent. If the system is assumed to be operating under steady state conditions with a continuous time invariant source operating between the planes, these equations may be rewritten without time dependence as

$$I_{sp}(R) = \sum_{n=-\infty}^{\infty} \frac{W}{4\pi r_n^2} (1-\alpha)^{N1_s N2} \tag{7.22a}$$

$$I(\underline{r}) = \int_{S'} K(\underline{r},\underline{r}')I(\underline{r}')(1-\alpha)dS' + (1-s)I_{spi}(\underline{r}) \tag{7.23a}$$

$$I_d(R) = \frac{1}{\pi}\left\{ \int_S I(\underline{r})d\Omega + \int_{S'} I(\underline{r}')(1-\alpha)d\Omega' \right\} \tag{7.27a}$$

$$I_t(R) = I_d(R) + I_{sp}(R) \ . \tag{7.28a}$$

It is these steady state equations that will be explicitly considered in the subsequent sections. The specularly reflected contribution can easily be calculated from image theory as in the models used in Chapter 6. The scattered component requires the solution of the integral equation of equation (7.23a), and then integration of this result according to equation (7.27a). The solution for this scattered field will be studied in the next section.

7.3.3 Solution of the integral equation for the diffusely reflected field component:

The solution method discussed in this section is similar to that used by Carroll and Miles [7.9], the basis of which is to write

equation (7.23a) in operator form. That is,

$$(J-L)I(\underline{r}) = (1-s)I_{spi}(\underline{r}) \quad , \tag{7.29}$$

where J is the identity operator, and L is a linear operator such that

$$Lf(\underline{r}) = \int_{S'} (1-\alpha)K(\underline{r},\underline{r}')f(\underline{r}')dS' \tag{7.30}$$

The solution to equation (7.29) has the form

$$\begin{aligned} I(\underline{r}) &= (J-L)^{-1}(1-s)I_{spi}(\underline{r}) \quad , \\ &= \sum_{n=0}^{\infty} L^n(1-s)I_{spi}(r) \quad . \end{aligned} \tag{7.31}$$

This equation is only valid provided that $J-L$ is non-singular. This condition is shown by Carroll and Miles [7.9] always to be met, and hence the solution of equation (7.31) applies. This solution represents a sum over the number of times n that the field has been diffusely reflected. Thus the $n = 0$ term is the specularly reflected. field's contribution to the scattered field, whilst the $n = 1$ term is the field that has been scattered once already. The problem could now therefore be solved to any degree of accuracy required by use of numerical methods. However such techniques can be extremely intensive in their use of computer time, and so the rate of convergence of the series in equation (7.31) will next be studied.

7.3.4 Investigation of the error involved when only a finite number of diffuse reflections are considered.

Any term in the series in equation (7.31) can be expressed as an integral of the term one order of n lower than it as follows:

$$I_n(\underline{r}) = \int_{S'} K(\underline{r},\underline{r}')I_{n-1}(\underline{r}')(1-\alpha)dS' \quad . \tag{7.32}$$

If a factor $\max(I_{n-1})$ is defined such that it is greater than or equal to $I_{n-1}(\underline{r})$ for all $\underline{r}$, it then follows that since $I_n(\underline{r})$ and $K(\underline{r},\underline{r}')$ are always positive the following inequality is valid (as can be derived from the first mean value theorem, see Reference [7.10], Chapter 1):

$$I_n(\underline{r}) \leq \int_{S'} K(\underline{r},\underline{r}')\max(I_{n-1})(1-\alpha)dS' \quad . \tag{7.33}$$

Since α and $\max(I_{n-1})$ are assumed independent of position, this becomes

$$I_n(\underline{r}) \leq (1-\alpha)\max(I_{n-1}) \int_{S'} K(\underline{r},\underline{r}')dS' \quad . \tag{7.34}$$

From energy conservation requirements the integral must equal unity (see equation 7.24). Thus equation (7.34) becomes

$$I_n(\underline{r}) \leq (1-\alpha)\ \max(I_{n-1}) \quad , \tag{7.35}$$

and this inequality is valid for all $\underline{r}$. The total of the scattered field at a point on the surface can be explicitly written as a series of scattering orders:

$$I(\underline{r}) = I_o(\underline{r}) + I_1(\underline{r}) + I_2(\underline{r})+\ldots,$$

hence

$$I(\underline{r}) \leq \max(I_o) + \max(I_1) + \max(I_2)+\ldots \quad . \tag{7.36}$$

By application of the inequality in equation (7.35), equation (7.36) can be rewritten as

$$I(\underline{r}) \leq \max(I_o)(1+\beta+\beta^2+\ldots) \quad , \tag{7.37}$$

where β equals $(1-\alpha)$. Evaluation of the geometric progression in equation (7.37) yields

$$I(r) \leq \max(I_o)/\alpha \quad .$$

This must be true for all $\underline{r}$, and hence

$$\max(I) \leq \max(I_o)/\alpha \quad . \tag{7.38}$$

Now, I_o is in fact given by the component of the specular intensity that is scattered at the floor. Thus equation (7.38) becomes,

$$\max(I) \leq \frac{(1-S)}{\alpha} \max(I_{spi}) \quad , \tag{7.39}$$

where the maximum value of I_{spi} will occur on the floor directly below the source.

The above inequalities can be used to estimate the error involved in only taking a finite number of terms in the series of equation (7.31). For example, if only the $n = 0$ term is computed, equation (7.38) yields

$$\frac{\max(I)}{\max(I_o)} \leq \frac{1}{\alpha} \quad . \tag{7.40}$$

This obviously produces the correct trends since the error will be zero for a perfectly absorbent ceiling, since then only the direct intensity enters the scattered field. The error can also be related to the total specularly reflected intensity. This is because the maximum value of I_{spi} occurs directly under the source, where the specular intensity component arrives normal to the surface. This means that the value of I_{spi} is equal to half the total specular component there, I_{sp} . This gives:

$$\frac{\max(I)}{\max(I_{sp})} \leq \frac{(1-S)}{2\alpha} \tag{7.41}$$

The scattered component is therefore less significant for floors with a low value of S , and highly absorbent ceilings.

This error estimation method could obviously be extended to any calculations involving only a finite number of terms in the series of

equation (7.31). It can thus be used to provide error bars in specific situations, although it only relates the maximum values of the terms, and does not give an error estimate for individual points. It should be noted however that the derivation is completely general and without any assumptions about the form of the reflection matrix $K(\underline{r},\underline{r}')$.

In the next section the form of the field due to I_o term will be evaluated for receiver points above a surface which reflects according to Lambert's Law, and the significance of the results discussed.

7.3.5 Estimation of the field due to the I_o scattering term:

In this section the findings of Chien and Carroll [7.11] are briefly restated and their implications for the model of this section are discussed. Chien and Carroll formulated an expression for the field above a rough absorbent plane which stretches to infinity in all directions. The model they used is broadly similar to that used for the floor in the model of section 7.3.2, except that the floor was assumed non-absorbing. They assumed that the plane is flat but that only a proportion s of the incident energy is reflected specularly (i.e. according to Snell's Law), and that the remainder reflects diffusely (i.e., according to Lambert's Law).

By integrating the diffusely reflected energy contributions from the whole of the rough surface, Chien and Carroll demonstrated that it is possible to represent the intensity at any receiver point above the plane as follows:

$$I(R) = \frac{W}{4\pi}\left(\frac{1}{r_1^2} + \frac{\beta s}{r_2^2} + \frac{2\beta(1-s)\cos\phi}{r_2^2}\right) \qquad (7.42)$$

where r_1 and r_2 are the distances from the source to receiver directly and via the specular reflection point respectively, β is the surface's (uniform) reflection coefficient, and ϕ is the angle to the normal subtended by a ray at the point of specular reflection.

The first term in the brackets on the right hand side of equation (7.42) is therefore the direct sound, and the second term is the conventional specularly reflected component attenuated by a factor s . The last term in the brackets is however the most interesting since it indicates that the diffusely reflected field can be modelled as originating from an energy image source at the same location in image space as a conventional image source, but directionally weighted by a factor $\cos\phi$. This term will therefore tend to increase levels close to the source and decrease them further away, as compared to the equivalent specularly reflecting surface. Such findings correlate with the results of the model of Section 7.2.

Unfortunately attempts at similar analytic evaluation of the next terms in the series of equation (7.31) for I proved unsuccessful The computation of the estimated total diffusely scattered field due to the I_o term was not felt to be justifiable. However it should be noted that equation (7.42) does allow the level directly above or below the source due to the first order scattered field (i.e., the I_o term) to be estimated along with an error term in a given situation. This is because at these positions the $\cos\phi$ term equals unity for all the specularly reflected image source contributions. Thus the increase due to first order scattered reflections alone from the floor as compared to the equivalent smooth surface is proportional to

$$\frac{S/r_2^2+2(1-S)/r_2^2}{1/r_2^2} = 2 - S \ ,$$

for each image source contribution (from $z > 0$) . Thus for a perfectly specularly reflecting floor, there is no increase, whereas for a perfectly rough floor the component of the mean square pressure due to reflections from the floor will be doubled. For example, in a case where the reflections from the floor account for half the overall level, then this would lead to a 50% increase in the total mean square pressure. Obviously the degree to which this first order approximation is adequate is governed by the ceiling as outlined in Section 7.3.4. In all cases (with the exception of a perfectly absorbing ceiling) the actual level will always be higher than that predicted by this first order estimate, provided that the model is a good representation of a given physical situation. The results of the analytic rough

surface scattering models of Chapter 4 demonstrate that a Lambert's Law reflection model will overestimate the scattering of most typical floor surfaces. To investigate the adequacy of the trends predicted by the two analytic room acoustics models developed so far in this chapter, a few selected scale model tests, chosen to be broadly representative of typical full size geometries, were carried out and these are described in the next section.

7.4 Scale Model Investigation of the Acoustics of Disproportionate Enclosures with Scattering Floors

7.4.1 Introduction:

In Sections 7.2 and 7.3 two different approaches were used to formulate prediction techniques for the acoustics of two different classes of disproportionate spaces with boundary surfaces which may not reflect sound in a totally specular manner. In the former of the two sections, sample results were presented for an idealised 'tunnel' configuration, and a brief parameter study performed. The results presented provide indications of how the observed behaviour is likely to change with alteration of the various parameters, but no attempt was made to duplicate a real situation in any detail. Thus the accuracy of the models remains questionable especially as the computed results presented were only expected to be approximate.

In the method of scale modelling it is again possible to fairly easily change parameters in any given situation. It would also appear to be somewhat easier to reproduce a real situation. This would require the scaling down of the full scale geometry whilst retaining the correct absorption behaviour at the scale model frequencies. This makes it a very attractive method by which to substantiate the trends observed in the results of the analytic model of Section 7.2. It was therefore decided to perform a further brief parameter study of the factors affecting the acoustics of disproportionate rooms with scattering objects on their floors - this time by use of scale model techniques. The aim of this study is to investigate the trends in the attenuation of steady state levels with distance from the source as the various parameters are altered. These results can then be compared to those

of Section 7.2. If a qualitative comparison appears encouraging, a brief quantitative comparison should prove adequate to illustrate whether the parameter values required in the analytic model for close agreement with the experimental results appear physically realistic. Thus the results of this scale model investigation will both shed further light on the physics of the situation and also indicate whether the assumptions and approximations contained in the model of Section 7.2 are adequate.

7.4.2 The equipment and method used.

All the tests reported in this section were performed by using the facilities of the Acoustical Modelling Group in Cambridge University's Architectural Department. The measurements were made inside the large 'tent' there, which is dried continuously from a drying plant which re-cycles automatically. The equipment set-up used is shown schematically in Figure 7.9. The source used was a crossed air jet type developed by Hodgson [7.12 and 7.13]. This had a tetrahedral arrangement of crossing nozzles, each of 1.5 mm internal diameter. Hodgson [7.12] estimated that such a source was directionally uniform to within 5 dB in all directions. The one used was fitted with an open-celled foam ball over the nozzles which reduces the effect of air currents and may be expected to further improve directivity although reducing the output, particularly at higher frequencies. The regulator and solenoid in the line to the air jet were set to 40 p.s.i.. This arrangement has been calibrated in terms of sound power by Hodgson [7.13].

The sound from the source was received by a microphone and cathode follower fitted to a boom which could be traversed down the length of the model as desired. The microphone's output was filtered by using an octave band filter, and the resultant signal was then equalised to account for the air jet source's frequency characteristics (see References [7.12 and 7.13] for more details of this procedure). Prior to commencement of each test the equipment was calibrated by application of a pistonphone (Brüel and Kjaer Type 4220) to the microphone. In this way the levels recorded can be interpreted in terms of the difference

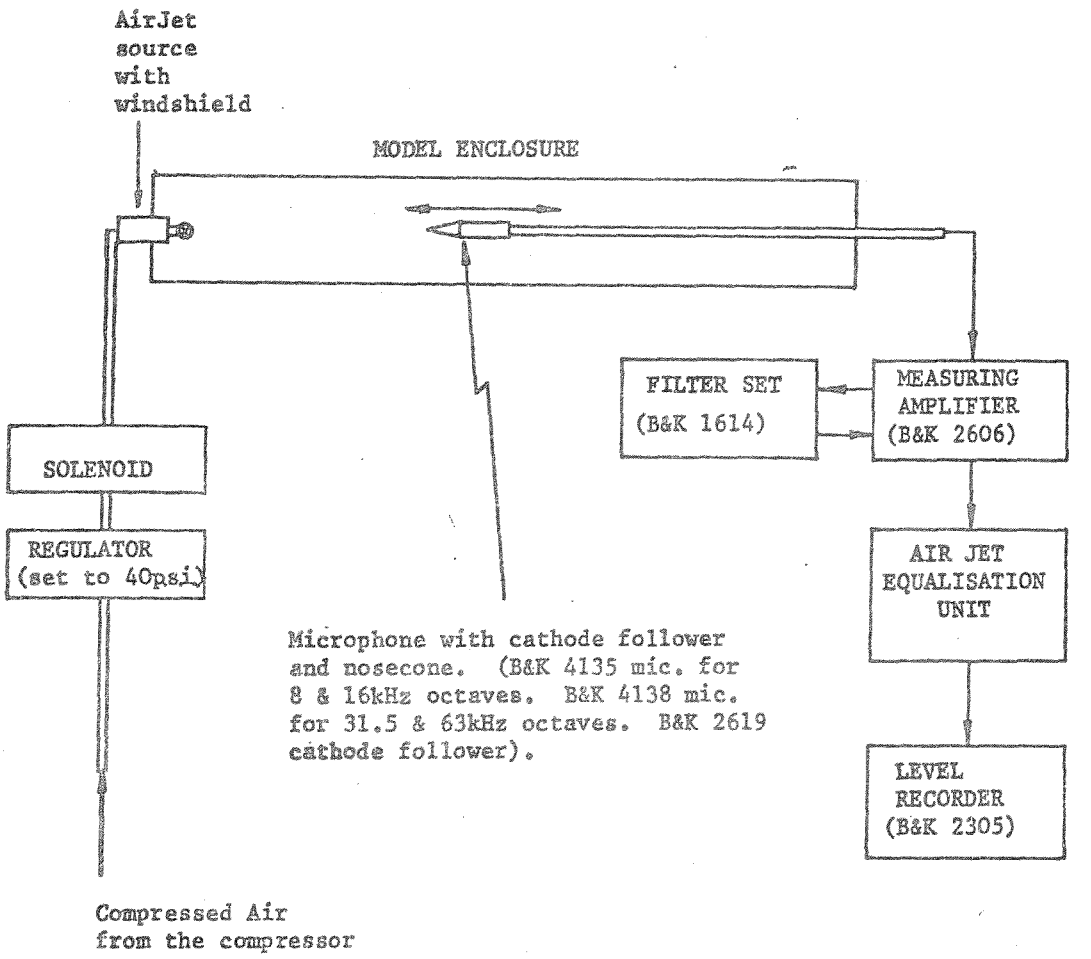

Figure 7.9 Schematic representation of the equipment set up used in the scale model investigation.

between the overall sound pressure level at any point and the source's free field sound power level in the particular octave band studied. This enables easy comparison to be made with the analytic model's predictions.

Three different model enclosures, each constructed from well varnished 9 mm plywood, were investigated. Their dimensions, along with the corresponding full scale values (for a 1:50 scale factor) are as follows:

MODEL	MODEL DIMENSIONS	EQUIVALENT FULL SIZE DIMENSIONS
A	2.2m×0.28m×0.28m	110m×13.75m×13.75m
B	2.2m×1.1m ×0.11m	110m×55m × 5.5m
C	2.2m×1.1m × 0.28m	110m×55m × 13.75m

Models A and B are broadly representative of 'duct' and 'flat' rooms respectively (and thus may be expected to exhibit similar trends to the analytic models of Sections 7.2 and 7.3 respectively), whilst model C is somewhere in between these two rather more extreme cases.

The air jet source was positioned in the centre of one of the smallest walls in each case, so that its centre(i.e. where the air jets cross) was about 5m full-scale from the end wall. The microphone was then moved down the longitudinal axis through the centre of the box's cross-section, and the level recorded in the 8,16,31.5, and 63kHz octave bands, which equate to octaves centred at 160 Hz, 320 Hz, 630 Hz, and 1260 Hz if a 1:50 scale reduction is assumed. The relative humidity and temperature were also monitored inside the 'tent' during the course of the measurements.

One side of the enclosure was then removed so that scattering objects could be introduced into the enclosed space. Since all the theoretical models developed have been concerned with situations where all the scatterers are concentrated on one surface it was decided to adopt this type of configuration in the scale model investigation.

To this end a number of hemicyclindrical rods were constructed from well varnished dowel of diameter 0.04 m (which equates to 2 m full scale diameter if a 1:50 scale factor is assumed). The rods were designed to fit across the width of the floor of each of the room models so that they just touched the side walls of the room, and their long axes were normal to these walls, whilst their flat bases were flush on the floor. Different arrangements of the hemicylinders were used with either 10 or 20 parallel rows either regularly or randomly spaced down the length of the enclosure.

Once the scatterers were in position the roof of the enclosure was reinstated and the measurement process repeated. This was performed for each of the room models with various different arrangements of the scatterers present. Representative results of the attenuation of sound pressure level with distance from the source are shown in Figures 7.10, 7.11 and 7.12 for room models A,B and C respectively. These results are discussed in the next section.

7.4.3 Discussion of the scale model sound propagation results

The first point to consider is the overall magnitudes of the levels in the three rooms investigated. Upon casual observation there does not appear to be much difference between them. Closer scrutiny of the results however reveals that over most of the microphone traverse the duct room levels are greatest and those in model C lowest. The rate of decay with distance is greatest in the flat room, and thus at the furthest distances from the source the levels in the flat room tend to overlap those of model C. It should of course be remembered that the climatic conditions (i.e. temperature and relative humidity) will fluctuate from test to test. The relevant values are indicated in the captions to Figures 7.10, 7.11 and 7.12. Unfortunately since Sabine's equations are not valid in the room types investigated, there is no simple method of compensating for any such climatic changes. In the results presented, the changes should be comparatively small however,due to the relatively small range of conditions encountered.

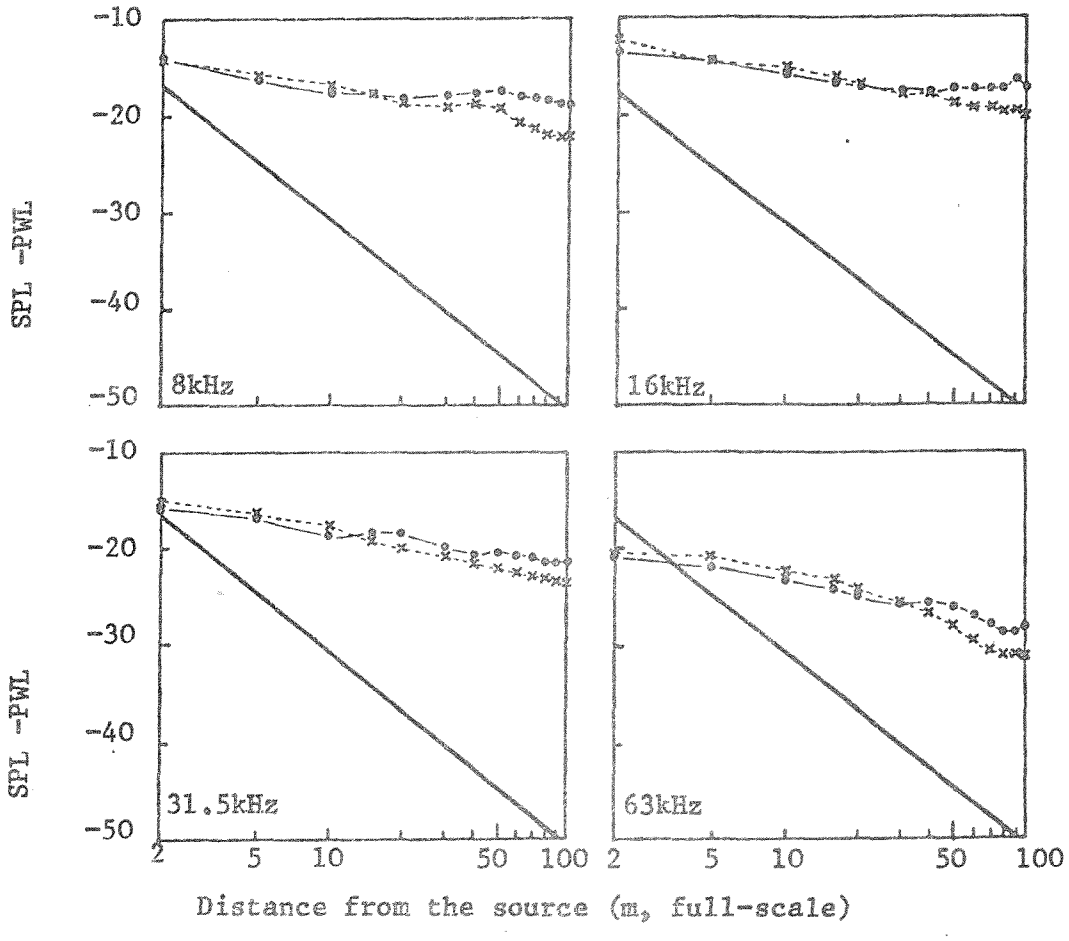

Figure 7.10 Scale model results for attenuation with distance from the source in the duct room (equivalent full-scale dimensions 110m x 13.75m x 13.75m). Model scale octave band centre frequencies are as indicated (divide by 50 to get the full scale equivalent).

KEY (climatic conditions during test as indicated, r.h. = relative humidity).

o——o——o Empty (r.h. = 6%; temperature = 18.7°C)

x----x----x 20 regularly spaced hemicylinders (r.h. = 6%; temperature = 20.2°C).

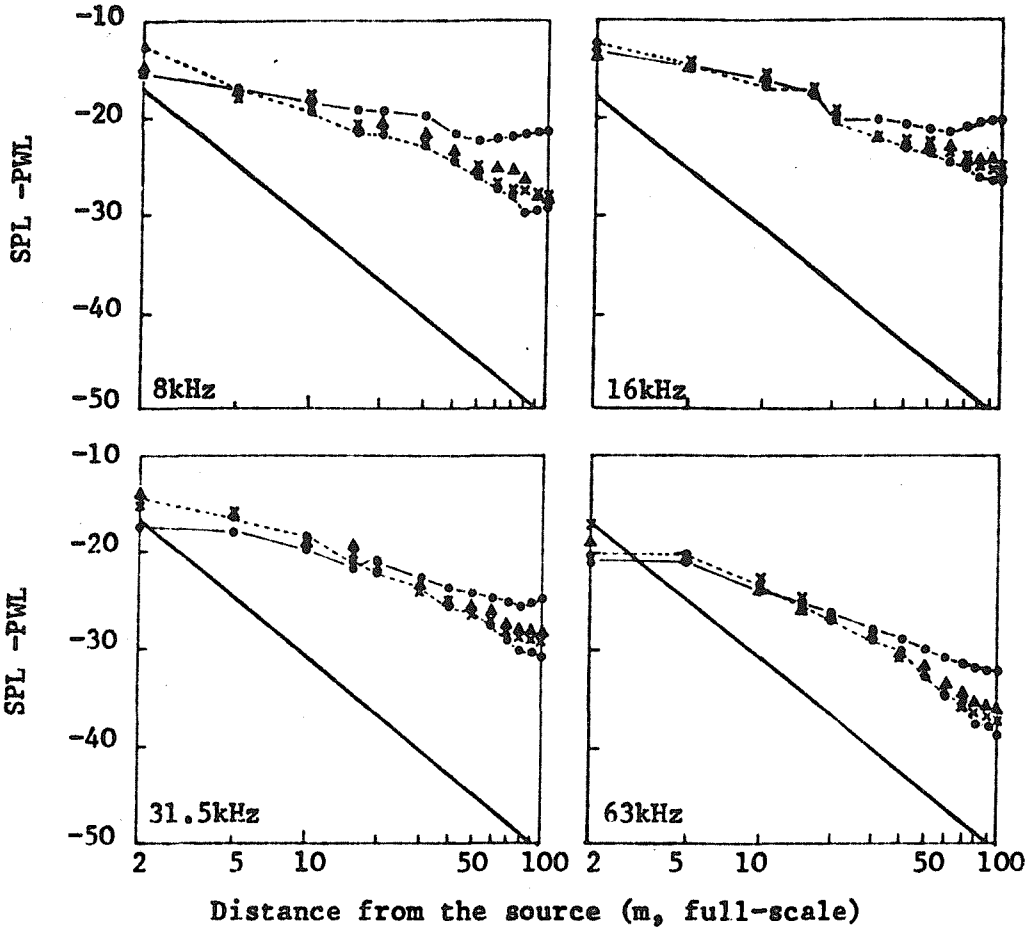

Figure 7.11 Scale model results for attenuation with distance from the source in the flat room (equivalent full-scale dimensions: 110 m x 55m x 5.5m). Model scale octave centre frequencies are indicated (divide by 50 to get full scale equivalent).

KEY

●——●——● Empty (6% r.h.; 28.5°C)

▲ ▲ ▲ 10 regularly spaced cylinders (6.5%; 24.5°C)

x x x 20 regularly spaced cylinders (4%rh; 24°C)

●---●---● 20 randomly spaced cylinders (5% rh; 28°C)

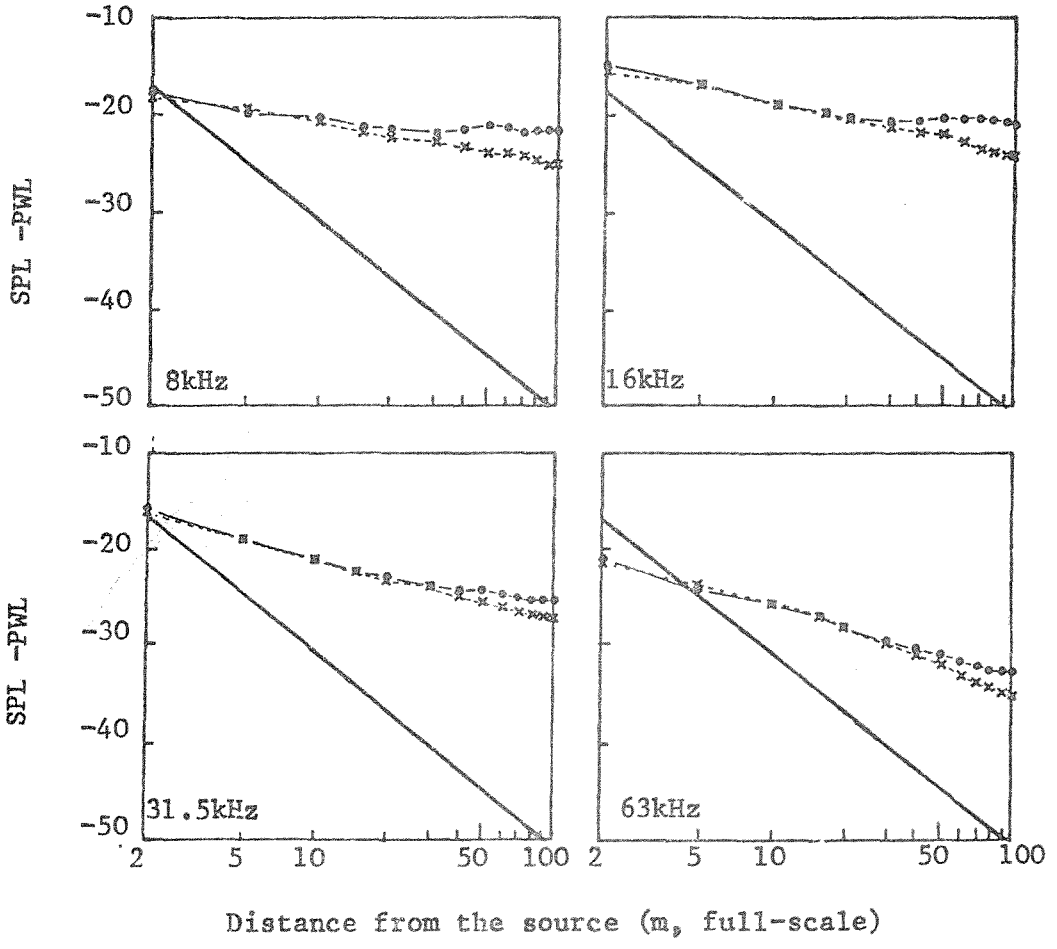

Figure 7.12 Scale model results for attenuation with distance from the source in Model C (110m x 55m x 13.75m full-scale). Model scale octave frequency bands are indicated.

KEY

•—•—• Empty (8% r.h.; 26°C)

×---×---× 20 regularly spaced parallel hemicylinders on the floor (8% rh; 26°C).

In almost all of the results for the empty enclosures there is a slight increase in the level as the end wall farthest from the source is approached. This is due to the relatively strong reflections from the end wall under such circumstances. This behaviour will obviously not be reproduced in the infinite room models of Section 7.2 and 7.3 as they stand, unless they are altered to include end walls.

The insertion of the scatterers does raise the levels close to the source whilst reducing them further away from it. This is in agreement with the trends of results of the theoretical model of Section 7.2. However the magnitude of the changes observed experimentally close to the source is not generally as significant as the analytic model suggests. This is particularly evident when the diffuse field absorption coefficient of well varnished plywood is considered. Typical values for the type of plywood used are listed below (these values are by courtesy of the Cambridge University Acoustical Modelling Group):

Octave Band	α
8 kHz	0.037
16 kHz	0.043
32 kHz	0.054
63 kHz	0.07

Possible reasons for the discrepancies between the theoretical and experimental results must therefore be considered next. One possibility is that the scatterers are partly absorbent, and thus when they are inserted the overall level of absorption within the enclosure rises. This is unlikely to be the complete cause of the discrepancies observed, however, since the absorption coefficient for the hemicylinders is probably of the same order of magnitude as the floor which they are covering up. Although some absorption could occur due to poor fitting of the scatterers' bases to the floor, this is also unlikely to be the major cause as there is little difference in the results of Figure 7.11 when 10 hemicylinder rows are used as opposed to 20. Observation of the results of Figure 7.11 with the

different scatterer configurations reveals another interesting feature, however: namely that there is almost as much difference between the far field results for 10 rows as opposed to 20 as there is between the results for the two configurations involving 20 rows. Although the difference is very small, it does seem consistent and does not appear to correlate to changes in the relative humidity. These results indicate that the randomly spaced arrangement scatters sound more effectively than the regularly spaced one and hence reduces the extreme far field levels as would be predicted by the analytic model of section 7.2. This scattering behaviour was also indicated by the analytic rough surface reflection models investigated in Chapter 4. Further consideration of the models described in Chapter 4 reveals that although the coherent reflection coefficient can be small for some angles of incidence, the incoherently scattered power often remains concentrated around the specular angle. Thus there would appear to be two possible problems associated with the current use of the analytic model developed in section 7.2. These are firstly that most of the specular reflection coefficients used in the parameter study may be too small for direct comparison with the experimental results, and secondly that the diffuse scattering assumption may prove unjustified thus rendering the existence of a diffuse field across the room's cross-section unlikely. Development of a more sophisticated model, along the lines of that in section 7.3, and incorporation of a more physically realistic reflection process would help to illuminate the above points.

Another reason why the results of the analytic model are in comparatively poor quantitative agreement with the experimentally measured values is the fact that the theoretical results are for an infinitely long room. As discussed in Section 7.2.4 the effect of hard end walls would be to reduce the increase in levels close to the source when scatterers are introduced and increase the reduction in levels further away. This indicates that choice of an R value between about 0.05 and 0.2 for insertion in the model of Section 7.2 could yield reasonably realistic results. Before any more detailed comparisons are performed a numerical investigation of the accuracy of the approximation used in the evaluation of the integral in

equation (7.20) would be desireable. Consideration should also be given to the possible effects of the source directivity. Insertion of some more physically realistic scattering model could then prove most interesting.

Because the increase in measured levels close to the source when scatterers are introduced is so small, it is very hard to establish whether the trends with change in room width in the scale tests (cf. Figures 7.10 and 7.11) agree with those predicted by the analytic model (cf. Figures 7.5 and 7.7). The major criterion is the change in the distance from the source at which the curve with scatterers present crosses that for the empty room. If anything it appears that the trends in most of the frequency bands are reversed between the experimental and theoretical results, but their magnitude is so small that no definite conclusions can be drawn on this point. It should furthermore be noted that the wider room (model C) will also differ most from the conditions required for the application of the analytic model of Section 7.2. This is both because the 4:1 width-to-height ratio is unlikely to provide suitable conditions to approximate a diffuse field across the room's cross section, and also since the scatterers employed are more likely to scatter sound which is incident normal to their long axis than that which arrives from directions near to the longitudinal axes of the hemicylinders. Sound from these latter directions will be more significant in the case of the wider room because the specular images in the side walls are further away than those for the same number of side wall reflections in the narrower room.

When the approximations involved in the development of the model in Section 7.2 are considered, the trends are in sufficiently close agreement with the experimental results to recommend its further development.

7.4.4 Recommendations for further work:

The scope for further work is vast and could follow any one of a number of lines. For example, no real use of the roof absorption model results has been made in this chapter. Their incorporation would bring the investigation one step closer to an accurate representation

of real situations. It is suspected that the accuracy of the model of Section 7.2 only warrants the inclusion of diffuse field absorption coefficient values, whereas use of an 'exact' model such as that outlined in Section 7.3 could well justify the accurate modelling of the roof. The big advantage of the model of Section 7.3 is that it can be used to study situations where conventional models, such as those currently used to predict factory acoustics (see Reference [7.1] for a detailed survey) cannot generally be expected to work accurately. Direct comparison of both of these types of model with experimental (full- or model-scale) measurements will indicate the errors involved in the conventional and new models in a given situation. The further development of the type of model described in Section 7.3. is particularly appealing for a number of reasons. Firstly it can incorporate a distribution of scatterers on the floor for which a reflection matrix can be evaluated by a method such as those outlined in Chapter 4. This removes some of the approximations and uncertainties associated with the scattering assumptions contained in, say, the currently developed factory acoustics prediction schemes. One avenue of further work in connection with this point concerns the investigation of the possibility of specifying the objects on the floor in terms of a mean height and variance. This would allow the construction of a simplified computer-based technique or even a series of design tables. Other advantages of the integral equation formulation are that it can be used to accurately study the reverberant decay of sound after a steady source is switched off, and can also easily incorporate the effects of air absorption. Both of these points are research areas worth pursuing.

The further development of the diffuse scattering model of Section 7.2 would also be useful. Probably the most rewarding line of further research would be first to include the effect of end walls and then to carry out an extensive comparison between experimental and theoretical results. This would establish R values to be used in the theoretical model to achieve optimum correlation with the experimental results. This would permit the development of a simplified estimation technique which could still be related to practical situations.

7.5 Conclusions:

This chapter contains the formulation of two different analytic models forthe prediction of steady state levels in two classes of extremely disproportionate spaces, with hard floors that do not reflect sound in a totally specular manner and all other surfaces smooth but possibly absorbent. One approach is approximate and best suited to duct rooms where a uniform diffusely scattered field is assumed to exist across the duct cross-section. The other approach is exact, more readily applicable to flat rooms, and its numerical implementation would involve the solution of an integral equation.

The approximate model was used to carry out a brief parameter study of the behaviour in an infinitely long duct room, which produced the following results.

(i) The levels near to the source are increased in any situation when the floor is 'roughened' (i.e., its R value decreases).

(ii) The levels far from the source are decreased when the floor is roughened.

(iii) The extreme far field levels for a hard rough floor asymptote to those for a smooth absorbent floor, of absorption coefficient α, where $\alpha = 1 - R$.

(iv) The magnitude of the increase in the 'near field' and decrease in the 'far field' are governed by the relative proportions of absorption and scattering potential per unit length down the duct.

(v) For a given geometry and absorption per unit duct length, alteration of the floor's R value does not significantly affect the distance from the source where the results curve with a scattering floor crosses that for the smooth floor case. This implies that this cross-over point is largely controlled by the absorption per unit length.

(vi) The level at the point where the results curves for situations with a scattering floor cross the curve for a smooth floor is governed by the distribution of the specular image sources.

In conjunction with the development of these analytic models, 1/50 scale model tests were performed. The trends observed in the approximate analytic model's results were generally preserved in those of the scale model measurements, although their magnitudes appeared to be slightly in error. The results are sufficiently encouraging to recommend further lines of research. The most promising of these lies in the use of the integral equation model to study the accuracy of existing prediction methods, with the aim of producing a new one for use in situations where the scatterers are situated on the floor, and there is a significant distance between the top of the scatterers and the ceiling, which can be modelled in detail if it is of a panel array type.

CHAPTER 7 : REFERENCES

7.1 M.R. HODGSON, 1980. Review of Published Literature Relevant to Sound Fields in Factories. ISVR Memo No. 604.

7.2 H. KUTTRUFF, 1973. Room Acoustics. London : Applied Science Publishers Ltd.

7.3 W.B. JOYCE, 1978. J. Acoust. Soc. Amer. 64, 1429-1436. Exact effect of surface roughness on the reverberation time of a uniformly absorbing spherical enclosure.

7.4 H.G. DAVIES, 1978. J. Acoust. Soc. Amer. 64, 517-521. Multiple-reflection diffuse-scattering model for noise propagation in streets.

7.5 M.V. SERGEEV, 1979. Sov.Phys. Acoust. 25, 335-338. Acoustical properties of rectangular rooms of various proportions.

7.6 P.M. MORSE and H. FESHBACH, 1953. Methods of Theoretical Physics. New York : McGraw-Hill Book Company.

7.7 E.A. LINDQVIST, 1982. Proc. Inst. of Acoustics Conf. Noise Control in Factory Buildings 20-23. Sound Propagation in Large Factories : a Mathematical Model.

7.8 C.J. HURST, 1980. J. Acoust. Soc. Amer. 67, 206-213. Sound transmission between parallel absorbing planes.

7.9 M.M. CARROL and R.N. MILES, 1978. J. Acoust. Soc. Amer. 64, 1424-1428. Steady-state sound in an enclosure with diffusely reflecting boundary.

7.10 H. JEFFREYS and B. JEFFREYS, 1972. Methods of Mathematical Physics, Cambrdige University Press.

7.11 C.F. CHIEN and M.M. CARROLL, 1980. J. Acoust. Soc. Amer. 67, 827-829. Sound source above a rough absorbent plane.

7.12 R.J. ORLOWSKI, M.R. HODGSON, N.C. BAINES, and M.F.E. BARRON, 1980. ISVR, Memorandum No. 603. Progress Report on Acoustic Modelling of Factories. (see Part 2).

7.13 R.J. ORLOWSKI, M.R. HODGSON, N.C. BAINES and M.F.E. BARRON, 1981. ISVR Memorandum No. 614. Final Report on Acoustic Modelling of Factories and Aduitoria (see Part 2).

CHAPTER 8

SUMMARY AND CONCLUSIONS

It appeared at the start of the research programme that there is a whole range of room types in which statistically diffuse fields do not exist (e.g. factories, open-plan offices, living rooms etc.). Due to the lack of diffusion in such rooms the simple equations derived by Sabine cannot be expected to produce adequately accurate predictions of the room's acoustical performance. Consideration of this class of 'non-Sabine' rooms revealed a number of features which could be responsible for their acoustical characteristics. These features can be broadly divided into three categories, as summarised below.

(i) Room Shape : In extreme cases, such as tunnels, it is obvious that diffuse field requirements cannot be satisfied. Alternative prediction methods to those of Sabine are therefore necessary in disproportionate rooms. Subsidiary questions arise when the sound field is non-diffuse, such as to whether or not the angular distribution of incident energy averaged over a surface is dependent on room shape, and hence if measurements of a material's statistical absorption coefficient made, say, in a proportionate room are applicable to prediction of the same material's statistical performance in a highly disproportionate room.

(ii) Surface Absorption Characteristics : It is evident that high levels of absorptivity and/or non-uniform distributions of absorption in a room can lead to non-diffuse conditions. Again prediction techniques other than those of Sabine are needed. Furthermore, since under non-diffuse conditions there is not an equal likelihood of sound arriving from all directions a knowledge of the variation of a material's absorption coefficient with angle of incidence may prove necessary, rather than just a diffuse field value (see also the discussion under (i) above).

(iii) Scattering Objects : Although the presence of scattering objects can sometimes make a sound field globally more diffuse (as when suspended diffusers are used in reverberation chambers), it is apparent that the sound field near to a scatterer may well be less diffuse. Hence methods for the accurate inclusion of scattering effects in room acoustics prediction techniques seem essential.

Although prediction techniques exist for various classes of non-Sabine spaces, some contain rather *ad hoc* assumptions, with little investigation of the underlying physical phenomena in each case. The work described in this report therefore has initially covered the investigation of certain aspects of the three features listed above. Finally their combined interaction has been studied for a number of typical non-Sabine conditions. The major aspects and conclusions of the entire research programme are summarised below.

(i) Scattering : Since little information was available on scattering in a form readily applicable to room acoustics, a theoretical investigation of single body free field scattering was performed. Approximate methods were compared to more accurate solutions for the cases of a rigid sphere, disc and half-plane. The following major conclusions were reached.

(a) In all cases high frequency approximations were found to be sufficiently accurate down to comparatively low ka values ($ka \sim 4$), to satisfy energy requirements down to even lower ka values ($ka \sim 2$), and to agree even more closely with exact results further away from the object.

(b) In the high frequency approximation used, the field scattered by thin rigid objects was satisfactorily modelled as being due to a uniform dipole layer.

(c) In the far scattered field ($kr >> ka >> 1$) the 'near field' optical shadow zone disappears, being replaced by a conically spreading diffraction pattern.

(d) The far scattered field of any finite sized thin object can be represented accurately in terms of a superposition of directionally weighted point sources.

The implications of these conclusions are that imaging techniques can be used in a wide range of circumstances to include scatterers in room acoustics models by means of high frequency and/or far field approximations. To confirm the theoretical results and extend them, if possible, from single frequency to wider frequency bands, from simple geometries to more complicated ones, and in some cases from far field to near field regions, an experimental research programme was initiated for the ka range 3 to 30. The major findings of this programme are summarised as follows:

(e) The 1/3 octave averaged mean square pressure shadow zone behaviour is determined by the object's silhouette. The type of edge does not matter (see, for example the sphere and disc results), but its position in space does (see, for example, the results for the various orientations of the cylinder).

(f) On occasions where all the points on the perimeter of the object's silhouette are roughly equidistant from points near the shadow zone centre, a characteristic diffraction pattern (e.g., a Poisson bright spot) is seen in the shadow zone centre. This diffraction pattern for 1/3 octave bandlimited noise is only slightly different from that for a single frequency. In the centre of the shadow zone the level under such circumstances may be comparable to the direct level alone.

(g) The characteristic behaviour in the bright region to the front of the scatterer is governed by reflection. Hence there is a marked difference between the behaviour for 1/3 octave bandlimited noise and that for a single frequency (i.e., the variations observed in the single frequency pressure level with observation angle appear to be averaged out).

(h) The magnitude of the sound pressure level increase and reduction in the bright and shadow zones in the cases investigated was not very great.

These findings imply that the overall effect of any one individual scatterer in a large room is small. For this reason multiple scattering prediction methods were investigated, and the model due to Twersky numerically implemented. This investigation of multiple scattering produced the following findings.

(i) In previous studies of non-Sabine spaces a volume distribution of randomly spaced point isotropic scatterers usually has been used. The only other method used for the inclusion of scattering effects in room acoustics predictions has been to model the surface as scattering omnidirectionally. The former of these two models appears from the single scatterer results to be grossly idealised for the case of real scatterers, especially when the sort of real room geometries commonly encountered are considered.

(j) The results obtained from Twersky's rough surface model demonstrate that the amount of energy coherently reflected in the specular direction by a geometry which is representative of many real situations is strongly angularly dependent.

(k) The energy incoherently scattered by the geometry considered in the numerical evaluation of the Twersky model had a large proportion of its energy concentrated near the specular direction. Hence agreement with the mathematically simpler Lambert's Law is poor.

In the context of statistical room acoustics it appears, as an overall conclusion for the work on scattering, that the presence of scatterers can significantly affect the mean free pathlength value in a room, and thus must in general be taken into account. Secondarily, scattering can result in significant localised sound energy redistribution effects in the close vicinity of objects.

(ii) Non-Uniform Absorption Characteristics : There is not much published information on the absorption characteristics of some of the most typical surfaces from which the shells which enclose many non-Sabine spaces are constructed - namely lightweight panel arrays. Theoretical models were developed to investigate the acoustical behaviour of such surfaces with the following conclusions.

(a) Infinite plate models are unable to produce adequately large absorption levels when physically realistic parameters are used.

(b) Modelling the roof surface as an array of finite plates can produce adequate levels of absorption, but computation is very time-consuming.

(c) Finite plate models indicate that at low frequencies the majority of the absorption observed is due to the dissipation of energy in component panel vibration - this was confirmed experimentally for a surface composed of asbestos panels for frequencies up to 1 kHz.

(d) Finite and infinite plate absorption models indicate that the absorption coefficient will depend strongly on the angle of incidence, and exhibits large amounts of absorption at angles close to grazing at low frequencies.

In order to investigate the importance of the last point above for the acoustics of a space enclosed by such surfaces, sample roof absorption model results were incorporated in an energy image source room acoustics computer program. From comparison of the results when either an angularly varying or its equivalent constant value were used to characterise one wall in a cubic ($1000m^3$) room the following conclusions were drawn:

(e) Sabine theory agreed with the image theory for low absorption walls, and discrepancies between Sabine theory and the image calculations increased with a larger absorption coefficient.

(f) There was little apparent difference either in steady state SPL or reverberant decay calculations in which, respectively, an angularly varying and an equivalent diffuse field absorption coefficient were used, although the slight differences that existed were larger for the greater magnitude absorption coefficient used.

These findings suggest that use of Sabine's equations to deduce overall absorption levels or to predict overall noise levels will not be grossly in error in geometrically proportionate rooms, even with a non-uniformly distributed absorption, provided the absorption magnitude is not too great.

iii) Room Proportionality Effects : A similar investigation to that reported above for the cubic room was carried out for disproportionate rectangular rooms. The major findings are as follows:

(a) There was little change in the predicted steady state levels when an angularly varying as opposed to diffuse field absorption coefficient was used. The change in levels could be either positive or negative, and its magnitude increased with distance from the source.

(b) There was virtually no change in the reverberant decay rate with distance from the source in any of the cases investigated.

(c) The reverberant decay rate could be drastically altered by the use of some angularly varying absorption characteristics as opposed to the equivalent diffuse field value.

These findings imply that although experimentally measured diffuse field absorption coefficients may be adequate to estimate the overall sound level in disproportionate spaces, they can be totally inappropriate for the estimation of reverberant decays. Similarly little can be safely inferred about the overall absorption in a disproportionate room from reverberant decay rate measurements. This has implications for estimating such quantities as speech intelligibility and levels due to impact sources in disproportionate spaces such as factories.

An energy image source model was also used to study the average distribution of incident sound at a surface in rectangular rooms with the following conclusions:

(d) At long times after the source is switched on, the angular distribution of the number of reflections undergone by contributions from the 'switched on' image sources closely approximates a $\sin 2\theta$ curve for the proportionate and disproportionate rooms studied.

(e) In all the rooms studied, division of the steady state incident energy angular distribution (E_t) by the angular distribution of the number of reflections (N_t) produced a $\cos\theta$ curve.

(f) The findings (d) and (e) above mean that a $\cos^2\theta\sin\theta$ weighting (normalised in some manner) would provide a better weighting function for the evaluation of averaged absorption coefficients for use in image theory room acoustics predictions.- This was confirmed by a statistical geometric acoustics approach, and the difference between this weighting and that which exists in Paris' equation shown to be due to the fact that the field is composed of spherical rather than plane waves.

(g) The (E_t/N_t) distribution takes longer to stabilise in large disproportionate rooms than in smaller proportionate ones.

(h) A statistical geometric acoustics approach indicated that in a disproportionate room it is the 'axial images' in the walls perpendicular to the longest room axis which control the rate of reverberant decay beyond a certain time after the source is switched off. Thus absorption characteristics which absorb sound at incidence angles close to grazing will increase the reverberant decay rate significantly (except during the very first part of the decay) when applied to surfaces parallel to the room's long axis.

To conclude the research programme, the various component features which had been examined individually were drawn together to study their interaction under non-Sabine conditions. The following were concluded from the results of an approximate analytic model for an infinitely long room with a rough floor:

(a) The steady state levels close to the source are increased when the floor is roughened.

(b) The steady state levels far from the source decrease when the floor is roughened.

(c) The magnitude of the increase and decrease in (a) and (b) above was inversely related to the absorption per unit length down the room.

(d) The results for a given geometry with any rough floor all intersect the results for the same geometry with a smooth floor at the same distance from the source. This distance is largely determined by the absorption per unit length, whilst the level at the 'cross-over' point is determined by the distribution of the specular image sources.

(e) The far field levels for a hard floor which specularly reflects a portion R of the incident energy asymptote to those for a smooth floor with an absorption coefficient α, equal to $1 - R$.

The above behaviour was in close agreement with the results of scale model tests. This agreement prompted recommendations for further work. The major such recommendation is for the further development of the more accurate analytic model formulated in the text, since this would allow the accurate inclusion of both the roof and floor models developed. This development would both allow the fundamental study of the interaction of scattering and absorbent surfaces (which can both have reflective properties which depend upon the angle of sound incidence), and the development of prediction techniques for practical purposes that could be used with confidence under conditions where current methods fail.

APPENDIX E

LISTINGS OF THE MAJOR FORTRAN COMPUTER PROGRAMS USED IN THE RESEARCH REPORTED

(i) PROGRAM SPHERE - this computes the classical (series) solution to the problem of diffraction by a rigid sphere. It uses standard recurrence relationships to generate spherical Hankel and Legendre functions.

(ii) PROGRAM TWRCYL - this numerically implements Twersky's solution for the problem of reflection of an incident plane wave by a randomly spaced array of parallel circular hemicylinders.

(iii) PROGRAM DPFAST - this evaluates the plane wave absorption coefficient of two parallel infinite arrays of finite simply supported plates, where the two arrays are separated by an air space.

(iv) PROGRAM IMAGES - this uses an energy image source approach to predict both the steady state levels and reverberant decays in rectangular rooms. It is possible to have one surface with an absorption coefficient that depends on the angle of sound incidence.

(v) PROGRAM ANGENXMOD - this studies the distribution in angle of both the number and incident energy of reflections undergone by image source contributions that arrive within a given time after the direct sound.

(vi) PROGRAM INFRM - this implements the room acoustics model of Section 7.2. That is, an infinitely long tunnel with a rough but non-absorbent floor, and all other surfaces smooth but partly absorbent.

```
      PROGRAM SPHERE
C
C     THIS PROGRAM EVALUATES THE EXACT SOLUTION TO THE PROBLEM OF
C     DIFFRACTION BY A RIGID SPHERE BY THE CLASSICAL METHOD
C
C     IT PRESENTS THE RESULTS AS A POLAR CALCOMP GRAPH PLOT
C
      COMMON A
      DIMENSION IO(183),R(183),RAD(183),ANG(183)
      INTEGER XTITL(6),YTITL(2),GTITL(9)
       DIMENSION DIRPHA(183),TOTPHA(183),PHADIF(183)
      DATA XTITL/23HSPL DB(REL TO INCIDENT)/
      DATA YTITL/1H /
       PI=3.14159
      CALL PLOTS(0,0,7)
C
C     INPUT DATA
C     AK=K*SPHERE RADIUS(=A),ROK=K*SOURCE-TO-SPHERE DISTANCE(=RO)
C     RK=K*SPHERE-TO-RECEIVER DISTANCE(=R),K=OMEGA/C
C
      READ(5,2) AK,ROK,RK
2     FORMAT(3F8.3)
      READ(5,110) GTITL
110   FORMAT(9A4)
C
C     THE DO-LOOP FOR THE VARIATION WITH ANGLE
C
      DO 1 I=1,181
1     IO(I)=I-1
       O=0.
      DO 3 I=1,181
      COSO=COS(O)
      A=SQRT((RK-ROK*COSO*2.)*RK+ROK*ROK)
      CALL PS(AK,ROK,RK,COSO,PSR,PSI)
      DIRPHA(I)=ATAN(-SIN(A)/COS(A))
      B=PSI-SIN(A)
      A=PSR+COS(A)
       TOTPHA(I)=ATAN(B/A)
       PHADIF(I)=TOTPHA(I)-DIRPHA(I)
      DIRPHA(I)=DIRPHA(I)*180.0/PI
      TOTPHA(I)=TOTPHA(I)*180.0/PI
      PHADIF(I)=PHADIF(I)*180.0/PI
      R(I)=ALOG10(A*A+B*B)*10.
      K=30
      RAD(I)=R(I)+K
      ANG(I)=O
3     O=O+0.01745329252
      DO 15 I=1,181
      IF(I.GT.1) GOTO 10
      WRITE(6,100) AK,ROK,RK
100   FORMAT(1H ,'KA=',F8.3,5X,'KRO=',F8.3,5X,'KR=',F8.3)
10    WRITE(6,200) IO(I),R(I)
200   FORMAT(I5,5X,E15.5)
15    CONTINUE
300   FORMAT(///,' ANGLE INC.PHASE',5X,'TOTAL PHASE',3X,' PHASE DIFF
     1')
      DO 4 I=1,181
310   FORMAT(I4,2X,F10.4,3X,F10.5,5X,F10.5)
4     CONTINUE
C
C     CALLING THE CALCOMP GRAPH PLOTTING ROUTINES FOR POLAR PLOT
C
      CALL PLOT(15.0,4.0,-3)
      CALL AXIS(-10.0,0.0,XTITL,-6,10.0,0.0,20.0,-5.0)
      CALL AXIS(0.0,0.0,XTITL,-6,10.0,0.0,-30.0,5.0)
      CALL AXIS(0.0,0.0,YTITL,-1,10.0,45.0,-30.0,5.0)
      CALL AXIS(0.0,0.0,YTITL,-1,10.0,90.0,-30.0,5.0)
      CALL AXIS(0.0,0.0,YTITL,+1,10.0,135.0,-30.0,5.0)
      CALL CIRCL(10.0,0.0,0.0,180.0,10.0,10.0,0.0)
      CALL CIRCL(8.0,0.0,0.0,180.0,8.0,8.0,0.0)
      CALL CIRCL(6.0,0.0,0.0,180.0,6.0,6.0,0.0)
```

```
      CALL CIRCL(4.0,0.0,0.0,180.0,4.0,4.0,0.0)
      CALL SYMBOL(2.5,10.0,0.3,TITL,0.0,36)
      CALL CIRCL(2.0,0.0,0.0,180.0,2.0,2.0,0.0)
      CALL POLAR(RAD,ANG,181,1,0,1,-10.0,5.0)
      CALL PLOT(20.0,0.0,999)
      STOP
      END
C
C
C
      SUBROUTINE PS(AK,ROK,RK,COSO,PSR,PSI)
C
C     THIS SUBROUTINE RETURNS THE REAL & IMAGINARY SCATTERED PRESSURE
C     COMPONENTS (PSR & PSI) FOR A RIGID SPHERE WITH SPHERICAL WAVE
C     INCIDENT
C
      COMMON D
C
C     BJ & BY =SPHERICAL BESSEL FNS.;A 'D' AFTER THEM INDICATES DERIVATIVE
C     PN=LEGENDRE FUNCTION
C
      AKI=1./AK
      BJA=SIN(AK)*AKI
      BYA=-COS(AK)*AKI
      BJDA=-BJA*AKI-BYA
       BYDA=BJA-BYA*AKI
      ROKI=1./ROK
      BJRO=SIN(ROK)*ROKI
      BYRO=-COS(ROK)*ROKI
      BJ1RO=BJRO*ROKI+BYRO
      BY1RO=BYRO*ROKI-BJRO
      RKI=1./RK
      BJR=SIN(RK)*RKI
      BYR=-COS(RK)*RKI
      BJ1R=BJR*RKI+BYR
      BY1R=BYR*RKI-BJR
      A=BJDA*D/(BJDA*BJDA+BYDA*BYDA)
      B=(BJRO*BYDA-BYRO*BJDA)*A
      A=(BJRO*BJDA+BYRO*BYDA)*A
      PSR=BYR*A-BJR*B
      PSI=BYR*B+BJR*A
      AN2P1=3.
      PN=COSO
      AN=0.
      P=1.
      N=1
      NF=0
C
C     RECURRENCE RELATIONSHIPS USED FOR BESSEL & LEGENDRE FUNCTION GENERATION
C
1     A=BJA
      BJA=BJA*AN*AKI-BJDA
      BJDA=A-(AN+2.)*AKI*BJA
      A=BYA
      BYA=BYA*AN*AKI-BYDA
      BYDA=A-(AN+2.)*AKI*BYA
      A=BJ1RO
      BJ1RO=AN2P1*BJ1RO*ROKI-BJRO
      BJRO=A
      A=BY1RO
      BY1RO=AN2P1*BY1RO*ROKI-BYRO
      BYRO=A
      A=BJ1R
      BJ1R=AN2P1*BJ1R*RKI-BJR
      BJR=A
      A=BY1R
      BY1R=AN2P1*BY1R*RKI-BYR
      BYR=A
      A=AN2P1*BJDA*PN*D/(BJDA*BJDA+BYDA*BYDA)
      B=(BJRO*BYDA-BYRO*BJDA)*A
      A=(BJRO*BJDA+BYRO*BYDA)*A
      PSR=BYR*A-BJR*B
```

```
144         PSII=BYR*B+BJR*A
145         PSR=PSRI+PSR
146         PSI=PSII+PSI
147   C
148   C     CHECKING THE CONVERGENCE OF THE SERIES
149   C
150         IF(1.0E-12-PSRI*PSRI-PSII*PSII) 2,2,3
151   2     AN=AN+1.
152         A=PN
153         PN=(AN2P1*PN*COSO-AN*P)/(AN+1.)
154         P=A
155         AN2P1=AN2P1+2.
156         N=N+1
157         GOTO 1
158   3     IF(NF-N) 4,5,4
159   4     NF=N+1
160         GOTO 2
161   5     RETURN
162         END
```

```
      PROGRAM TWRCYL
C
C     THIS PROGRAM EVALUATES THE COHERENT POWER REFLECTION COEFFICIENT
C     FOR A RANDOMLY ROUGH 2-D ARRAY OF RIGID CYLINDERS ON A HARD PLANE
C     USING AMETHOD PROPOSED BY TWERSKY
C     RHO=NO. OF CYLINDER CENTRES/UNIT LENGTH, INPUT ANGLES IN DEGREES
      COMPLEX AN(31),FI,AHK,AHKP1,AHKD,F,FL,Z,Z1,FB,FLB,ZB,Z2
      COMPLEX ZSPEC
      D=1.E-12
      FI=(0.0,1.0)
      PI=3.141592654
      READ(5,100) AK,RK,RHO
      WRITE(6,120) AK,RK,RHO
C
C     INPUT FLAG:VARIATION WITH OBS. & ENERGY SUM=K=1,VARIATION OF R
C     WITH ANGLE K=0
C
      READ(5,105) K
105   FORMAT(I4)
      IF(K.EQ.1) I3=181
      IF(K.EQ.0) I3=91
      IF(K.EQ.0) GOTO 10
      READ(5,110) IALF
      WRITE(6,130) IALF
      ALFA=IALF*PI/180.
100   FORMAT(3F10.3)
110   FORMAT(I4)
120   FORMAT(' AK=',F10.3,5X,'RK=',F10.3,5X,'RHO=',F10.3)
130   FORMAT(' ALFA=',I4)
C
C     STORING THE AN COEFFICIENTS
C
10    CALL BESJ(AK,0,BJ,D,IER)
      CALL BESY(AK,0,BY,IER)
      AHK=BJ+FI*BY
      DO 1 I1=1,30
      I=I1-1
      CALL BESJ(AK,I1,BJP1,D,IER)
      CALL BESY(AK,I1,BYP1,IER)
      AHKP1=BJP1+FI*BYP1
      BJD=-BJP1+FLOAT(I)/AK*BJ
      AHKD=-AHKP1+FLOAT(I)/AK*AHK
C
C     AN IS STORED IN THE (N+1)TH POSITION
C
      AN(I1)=-BJD/AHKD
125   FORMAT(' I=',I4,5X,'AN=',2(E15.5,5X))
      BJ=BJP1
      AHK=AHKP1
1     CONTINUE
C
C     THE PRESENT FORMAT OF THE PROGRAM IS DESIGNED TO EITHER LOOK AT
C     THE DISTRIBUTION OF R (& SURFACE IMPEDANCE) WITH ANGLE OF INCIDENCE
C     (K=0) OR TO STUDY VARIATION OF SIGMA WITH ANGLE OF OBSERVATION
C     AND TO PERFORM AN ENERGY CHECK (K=1)
C
      IF(K.EQ.1) GOTO 36
      IALF=0
C
C      CALCULATING F (ONLY FOR SPECULAR DIRECTION)
C
30     IALF=IALF+1
      ALFA=IALF*PI/180.0
36    FL=AN(1)
      N=2
      FLB=AN(1)
2      F=FL+AN(N)*(1.+(-1)**(N-1)*COS((N-1)*2.*ALFA))
      FB=FLB+AN(N)*(COS((N-1)*2.*ALFA)+(-1)**(N-1))
      IF(N.LT.5) GOTO 3
      IF(ABS(ABS(F/FL)-1.).GT.0.00001) GOTO 3
      IF(IC.EQ.2) GOTO 5
```

```
      IC=2
      GOTO 4
3     IC=1
4     FL=F
      FLB=FB
      N=N+1
      IF(N.EQ.30) GOTO 14
      GOTO 2
14    WRITE(6,180)
180   FORMAT(' THIS HAS NOT CONVERGED BY N=31!!!!!!')
5     F=2.*F
      FB=2.*FB
C
C     CALCULATING Z (ONLY FOR SPECULAR DIRECTION!!)
C
      Z=F*RHO/(RK*ABS(COS(ALFA)))
      ZB=FB*RHO/(RK*ABS(COS(ALFA)))
      Z1=(1+Z)/(1-Z)
      RSPEC=REAL(Z1*CONJG(Z1))
      Z1=F/(1.-Z)
      Z2=F/(1.-ZB)
      SIGMA=2.*RHO/(RK*PI)*REAL(Z1*CONJG(Z1))
      SIGMAB=2.*RHO/(RK*PI)*REAL(Z2*CONJG(Z2))
       IF(K.EQ.1) ZSPEC=Z
      IF(K.EQ.1) GOTO 31
      WRITE(6,200) IALF,RSPEC,SIGMA,SIGMAB
200   FORMAT(' ALFA=',I4,4X,'R=',F10.5,'   SIGMAS=',2(F10.5,2X))
      IF(IALF.LT.90) GOTO 30
      GOTO 13
C
C     CALCULATING THE DIFFUSE COMPONENTS
C
31    SUM=0.0
      DO 6 I2=1,181,5
      I=-91+I2
      PHI=I*PI/180.
C
C     CALCULATING  F(KO,KI)
C
      IC=1
      FL=AN(1)
      N=2
       ARG1=PHI-ALFA
       ARG2=PHI+ALFA
32     F=FL+AN(N)*(COS((N-1)*ARG1)+(-1)**(N-1)*COS((N-1)*ARG2))
      IF(N.LT.5) GOTO 34
      IF(ABS(ABS(F/FL)-1.0).GT.0.00001) GOTO 33
       IF(IC.EQ.2) GOTO 35
      IC=2
      GOTO 34
33    IC=1
34    FL=F
      N=N+1
      IF(N.EQ.30) GOTO 44
      GOTO 32
44    WRITE(6,180)
35    F=2.*F
      Z=F*RHO/(RK*ABS(COS(ALFA)))
      Z1=F/(1.-ZSPEC)
      SIGMA=2.*RHO/(PI*RK)*REAL(Z1*CONJG(Z1))
      IF(K.EQ.0) GOTO 15
C
C     PERFORMING INTEGRATION OF DIFFUSE TERMS BY SIMPSONS RULE
C
      IF(I2.EQ.1.OR.I2.EQ.181) SUM=SUM+SIGMA
      IF(I2.EQ.1.OR.I2.EQ.181) GOTO 12
      IF(FLOAT(I2)/2.-(I2/2)-0.05) 7,7,8
7     SUM=SUM+4.*SIGMA
      GOTO 12
8     SUM=SUM+2.*SIGMA
      GOTO 12
12    WRITE(6,140) I,SIGMA
```

```
      GOTO 6
6     CONTINUE
15    IF(K.EQ.0) GOTO 13
      SUM=SUM*PI/(180.*3.)
      WRITE(6,150) SUM
       WRITE(6,153) RSPEC
153    FORMAT(' RSPEC=',F10.5)
      TOTAL=RSPEC+SUM/COS(ALFA)
      WRITE(6,155) TOTAL
140   FORMAT(' THETA=',I4,5X,'SIGMA=',E15.5)
141   FORMAT(2I4,E15.5)
145   FORMAT(' ANGLE=',I4,5X,'R=',E15.6,5X,' SPEC.ACOUSTIC IMPEDANCE=',2
     1(E15.6,5X))
150   FORMAT(' THE DIFFUSELY REFLECTED POWER SUM=',E15.5)
155   FORMAT(' THE TOTAL ENERGY REFLECTED(NORMALISED)=',E15.5)
13    STOP
      END
      SUBROUTINE BESJ(X,N,BJ,D,IER)

C
C     THIS SUBROUTINE CALCULATES ABESSEL FN OF ARGUMENT X, ORDER
C     =N,D=ACCURACY
C
      BJ=0.
      IF(N) 10,20,20
   10 IER=1
      RETURN
   20 IF(X) 30,30,31
   30 IER=2
      RETURN
   31 IF(X-15.) 32,32,34
   32 NTEST=20.+10.*X-X*X/3
      GO TO 36
   34 NTEST=90.+X/2.
   36 IF(N-NTEST) 40,38,38
   38 IER=4
      RETURN
   40 IER=0
      N1=N+1
      BPREV=0.
C
C   COMPUTE STARTING VALUE OF M
C
      IF(X-5.) 50,60,60
   50 MA=X+6.
      GO TO 70
   60 MA=1.4*X+60./X
70     MB=N+X/4+2
      MZERO=MAX0(MA,MB)
C
C  SET UP LIMIT OF M
C
      MMAX=NTEST
  101 DO 190 M=MZERO,MMAX,3
C
C    SET F(M),F(M-1)
C
      FM1=1.0E-28
      FM=0
      ALPHA=0.
      IF(M-(M/2)*2) 120,110,120
  110 JT=-1
      GO TO 130
  120 JT=1
  130 M2=M-2
      DO 160 K=1,M2
      MK=M-K
      BMK=2.*FLOAT(MK)*FM1/X-FM
      FM=FM1
      FM1=BMK
      IF(MK-N-1) 150,140,150
  140 BJ=BMK
```

```
  150 JT=-JT
      S=1+JT
  160 ALPHA=ALPHA+BMK*S
      BMK=2.*FM1/X-FM
      IF(N) 180,170,180
  170 BJ=BMK
  180 ALPHA=ALPHA+BMK
      BJ=BJ/ALPHA
      IF(ABS(BJ-BPREV)-ABS(D*BJ)) 200,200,190
  190 BPREV=BJ
      IER=3
  200 RETURN
      END
      SUBROUTINE BESY(X,N,BY,IER)
C     THIS SUBROUTINE CALCULATES A NEUMANN FN. OF ARGUMENT X,
C     ORDER = N
C
C  CHECK FOR ERRORS IN N AND X
C
      BJ=0.
      D=1.E-08
      IF(N) 180,10,10
   10 IER=0
      IF(X) 190,190,20
C
C  BRANCH IF X LESS THAN OR EQUAL TO 3
C
   20 IF(X-3.) 40,40,30
C
C   COMPUTE Y0 AND Y1 FOR X GREATER THAN 3
C
   30 TT=3./X
      TT2=TT*TT
      TT3=TT*TT2
      TT4=TT*TT3
      TT5=TT*TT4
      TT6=TT*TT5
      FF=0.79788456-0.00000077*TT-0.00552740*TT2-0.00009512*TT3+0.00137237*TT4
     137*TT4-0.00072805*TT5+0.00014476*TT6
      FEE=X-0.78539816-0.04166397*TT-0.00003954*TT2+0.00262573*TT3
     1-0.00054125*TT4-0.00029333*TT5+0.00013558*TT6
      Y0=FF*SIN(FEE)/SQRT(X)
      FF=0.79788456+0.00000156*TT+0.01659667*TT2+0.00017105*TT3-0.00249511*
     111*TT4+0.00113653*TT5-0.00020033*TT6
      FEE=X-2.35619449+0.12499612*TT+0.0000565*TT2-0.00637879*TT3+.00074348
     174348*TT4+0.00079824*TT5-0.00029166*TT6
      Y1=FF*SIN(FEE)/SQRT(X)
      GO TO 90
C
C    COMPUTE Y0 AND Y1 FOR X LESS THAN OR EQUAL TO 3
C
   40 XX=X/3.
      XX2=XX*XX
      XX4=XX2*XX2
      XX6=XX2*XX4
      XX8=XX2*XX6
      XX10=XX2*XX8
      XX12=XX2*XX10
      AX=0.36746691+0.60559366*XX2-0.74350384*XX4+0.25300117*XX6
     1-0.04261214*XX8+0.00427916*XX10-0.00024846*XX12
      M=0
      CALL BESJ(X,M,BJ,D,IER)
      Y0=BJ*ALOG(.5*X)/1.570796327+AX
      AX=-0.6366198+0.2212091*XX2+2.1682709*XX4-1.3164827*XX6
     1+0.3123951*XX8-0.0400976*XX10+0.0027873*XX12
      M=1
      CALL BESJ(X,M,BJ,D,IER)
      Y1=BJ*ALOG(X*.5)/1.570796327+AX/X
C
C CHECK IF ONLY Y0 AND Y1 IS DESIRED
C
   90 IF(N-1) 100,100,130
```

```
C
C RETURN EITHER Y0 OR Y1 AS REQUIRED
C
  100 IF(N) 110,120,110
  110 BY=Y1
      GO TO 170
  120 BY=Y0
      GO TO 170
C
C  PERFORM RECURRENCE OPERATIONS TO FIND YN(X)
  130 YA=Y0
      YB=Y1
      K=1
  140 T=FLOAT(2*K)/X
      YC=T*YB-YA
      IF(ABS(YC)-1.0E70) 145,145,141
  141 IER=3
      RETURN
  145 K=K+1
      IF(K-N) 150,160,150
  150 YA=YB
       YB=YC
      GO TO 140
  160 BY=YC
  170 RETURN
  180 IER=1
      RETURN
  190 IER=2
      RETURN
      END
```

```
      PROGRAM DPFAST
C     THE PROGRAM EVALUATES THE ACOUSTIC ABSORPTION COEFFICIENT FOR TWO
C     ARRAYS OF REGULARLY REPEATED SIMPLY-SUPPORTED PANELS SEPARATED BY
C     AN AIRSPACE
C
      DIMENSION AKXU(125),AKYV(125),P(250)
      COMPLEX FI,Z1(125),Z2(125),B1(250),A(250,250),AKUV(125),XMNUV(125,
     1125),XUI,YVI,Z1MN,Z2MN,ARG,CUV,XMN,RUV(125),TUV(125)
      COMMON/BLK1/A
C
C     INPUT DATA IN S.I. UNITS,DEGREES,& HZ.
C     CHOOSE IUMAX*IVMAX=MUMAX*NUMAX
C     RHO1,RHO2 ARE THE FRONT & BACK PANEL SURFACE DENSITIES
C
C     INPUT SECTION
C
      READ(1,100) DS1,DS2,RHO1,RHO2,ETA1,ETA2
      READ(1,110) B,D,RL
C
C     INPUT KF;IF KF=1 FREQ. VARIATION,2 FOR THETA ,3 FOR PHI VARIATION
C
      READ(1,115) KF
      IF(KF.EQ.1) READ(1,120) IN,FL,DF,THETA,PHI
      IF(KF.EQ.2) READ(1,120) IN,THETL,DTHETA,PHI,F
      IF(KF.EQ.3) READ(1,120) IN,PHIL,DPHI,THETA,F
      READ(1,130) MUMAX,NUMAX,IUMAX,IVMAX
      WRITE(6,200) DS1,DS2,RHO1,RHO2,ETA1,ETA2
      WRITE(6,210) B,D,RL
      WRITE(6,230) MUMAX,NUMAX,IUMAX,IVMAX
100   FORMAT(6F10.3)
110   FORMAT(3F10.3)
115   FORMAT(I4)
120   FORMAT(I4,4F10.3)
130   FORMAT(4I4)
200   FORMAT(' DS1=',F10.3,2X,'DS2=',F10.3,4X,'RHO1=',F10.3,2X,'RHO2=',F
     110.3,2X,'ETA1=',F10.3,2X,'ETA2=',F10.3)
210   FORMAT(' PLATE X-DIMENSION=',F10.3,2X,'Y=',F10.3,2X,'BACKING DEPTH
     1=',F10.3)
230   FORMAT(' MUMAX,NUMAX=',2(I4,4X),'IUMAX,IVMAX=',2(I4,4X))
C
C     SETTING UP CONSTANTS,ETC,
C
      IA=250
      IR=1
      IB=250
      IADD=IUMAX*IVMAX
      IFAIL=0
      PI=3.141593
      RHOC=415.0
      C=340.0
      FI=(0.0,1.0)
      IF(KF.EQ.1.OR.KF.EQ.2) PHI=PHI*PI/180.
      IF(KF.EQ.1.OR.KF.EQ.3) THETA=THETA*PI/180.
      DO 15 I1=1,IN
      IF(KF.EQ.1) F=FL+(I1-1)*DF
      IF(KF.EQ.2) THETA=(THETL+(I1-1)*DTHETA)*PI/180.0
       IF(KF.EQ.3) PHI=(PHIL+(I1-1)*DPHI)*PI/180.
      ALFA=0.0
      TRANS=0.0
      ELOSS1=0.0
      ELOSS2=0.0
      OHM=2.*PI*F
      AK=OHM/C
      XK=AK*SIN(THETA)*COS(PHI)
      YK=AK*SIN(THETA)*SIN(PHI)
      ZK=AK*COS(THETA)
C
C     PRE-STORING THE BETA AND KUV COEFFICIENTS FOR THE EQUATIONS
C
      IROW1=0
      IUV=0
```

```
      DO 4 IU2=1,IUMAX
      IU=-(IUMAX/2)+IU2-1
      AKXU(IU2)=XK+2.*IU*PI/B
      DO 3 IV2=1,IVMAX
      IV=-(IVMAX/2)+IV2-1
      AKYV(IV2)=YK+2.*IV*PI/D
      IUV=IUV+1
      IROW=IROW1+1
      IROW1=IROW+1
      B1(IROW)=0.0
      B1(IROW1)=0.0
      AKUV(IUV)=SQRT(ABS(AK*AK-AKXU(IU2)**2-AKYV(IV2)**2))
      IF((AK*AK-AKXU(IU2)**2-AKYV(IV2)**2).LT.0.0) AKUV(IUV)=-FI*AKUV(IU
     1V)
C
C     STORING BETA(0,0) COEFFICIENTS IN ARRAY B1
C
      IF(IU.EQ.0.AND.IV.EQ.0) GOTO 2
       GOTO 3
2     B1(IROW)=2.*CEXP(FI*ZK*RL)
      B1(IROW1)=-2.*FI*COS(THETA)*SIN(ZK*RL)
3     CONTINUE
4     CONTINUE
      ICOL=0
       DO 8 MU=1,MUMAX
      AKMU=MU*PI/B
      DO 7 NU=1,NUMAX
      AKNU=NU*PI/D
      ICOL=ICOL+1
      ICOL1=ICOL+IADD
C
C      CALCULATING THE PLATES' MODAL IMPEDANCE
C
      AK4=(AKMU*AKMU+AKNU*AKNU)**2
      Z1MN=-FI*(DS1*(1.+FI*ETA1)*AK4-RHO1*OHM*OHM)/(AK*RHOC*C)
      Z2MN=-FI*(DS2*(1.+FI*ETA2)*AK4-RHO2*OHM*OHM)/(AK*RHOC*C)
      Z1(ICOL)=Z1MN
      Z2(ICOL)=Z2MN
      IUV=0
      IROW1=0
      DO 6 IU=1,IUMAX
      IF(ABS(AKMU).EQ.ABS(AKXU(IU))) XUI=-FI*B/2.
      IF(ABS(AKMU).EQ.ABS(AKXU(IU))) GOTO 21
      XUI=AKMU*(1.-CEXP(-FI*AKXU(IU)*B)*(-1)**MU)/(AKMU*AKMU-AKXU(IU)**2
     1)
21    DO 5 IV=1,IVMAX
      IROW=IROW1+1
      IROW1=IROW+1
      IUV=IUV+1
      IF(ABS(AKNU).EQ.ABS(AKYV(IV))) YVI=-FI*D/2.
      IF(ABS(AKNU).EQ.ABS(AKYV(IV))) GOTO 22
      YVI=AKNU*(1.-CEXP(-FI*AKYV(IV)*D)*(-1)**NU)/(AKNU*AKNU-AKYV(IV)**2
     1)
22    XMN=XUI*YVI/(B*D)
      XMNUV(IUV,ICOL)=XMN
C
C     STORING THE PLATE COEFFICIENTS FOR THE TWO EQUATIONS
C
      CUV=AKUV(IUV)/AK
      ARG=FI*AKUV(IUV)*RL
      A(IROW,ICOL)=-FI*CEXP(ARG)*(Z1MN+2./CUV)*XMN
      A(IROW,ICOL1)=-FI*Z2MN*XMN
      A(IROW1,ICOL)=(FI*CEXP(ARG)-CUV*CSIN(AKUV(IUV)*RL)*Z1MN)*XMN
      A(IROW1,ICOL1)=-FI*XMN
5     CONTINUE
6     CONTINUE
7     CONTINUE
8     CONTINUE
      N=2*MUMAX*NUMAX
C
C     SOLVING THE MATRIX EQUATION USING THE APPROX. NAG LIBRARY ROUTINES
C
```

```
      CALL F03AHF(N,A,IA,DETR,DETI,ID,P,IFAIL)
      IF(IFAIL.EQ.0) GOTO 25
      WRITE(6,240) IFAIL
240   FORMAT(' IFAIL=',I4)
25    CALL F04AKF(N,IR,A,IA,P,B1,IB)
C
C     THE MATRIX B1 NOW CONTAINS THE PLATE DISPLACEMENT COEFFICIENTS
C
C     CALCULATING THE REFLECTION COEFFICIENTS AND THUS GETTING ALFA
C
      WRITE(6,301)
301   FORMAT(1H1,' TRANSMISSION & REFLECTION COEFFICIENTS')
      IUV=0
      DO 12 IU2=1,IUMAX
      IU=-(IUMAX/2)+IU2-1
      DO 11 IV2=1,IVMAX
      IV=-(IVMAX/2)+IV2-1
      IUV=IUV+1
      RUV(IUV)=0.0
      TUV(IUV)=0.0
      IMUNU=0
      DO 10 MU=1,MUMAX
      DO 9 NU=1,NUMAX
      IMUNU=IMUNU+1
      RUV(IUV)=XMNUV(IUV,IMUNU)*B1(IMUNU)+RUV(IUV)
      IMUNU2=IMUNU+IADD
      TUV(IUV)=XMNUV(IUV,IMUNU)*B1(IMUNU2)+TUV(IUV)
9     CONTINUE
10     CONTINUE
      RUV(IUV)=RUV(IUV)*FI*AK/AKUV(IUV)
      IF(IU.EQ.0.AND.IV.EQ.0) RUV(IUV)=RUV(IUV)+1
      TUV(IUV)=-TUV(IUV)*FI*AK/AKUV(IUV)*CEXP(FI*AKUV(IUV)*RL)
      WRITE(6,330) IU,IV,RUV(IUV),TUV(IUV)
      AMN=REAL(CONJG(AKUV(IUV)*RUV(IUV))*RUV(IUV))
      TMN=REAL(CONJG(AKUV(IUV)*TUV(IUV))*TUV(IUV))
      ALFA=ALFA+AMN
      TRANS=TRANS+TMN
11    CONTINUE
12    CONTINUE
      REFL=ALFA/ZK
      TRANS=TRANS/ZK
      ALFA=1.-REFL
C
C     CALCULATING THE ENERGY DISSIPATED IN THE TWO PLATES
C
      IMUNU=0
      DO 14 MU=1,MUMAX
      DO 13 NU=1,NUMAX
      IMUNU=IMUNU+1
      IMUNU2=IMUNU+IADD
      ELOSS1=ELOSS1+REAL(B1(IMUNU)*CONJG(B1(IMUNU)))*REAL(Z1(IMUNU))
      ELOSS2=ELOSS2+REAL(B1(IMUNU2)*CONJG(B1(IMUNU2)))*REAL(Z2(IMUNU))
13    CONTINUE
14    CONTINUE
      ELOSS1=ELOSS1*AK/(4.*ZK)
      ELOSS2=ELOSS2*AK/(4.*ZK)
      SUM=TRANS+REFL+ELOSS1+ELOSS2
      ITHET=INT(THETA*180./PI+0.1)
      IPHI=INT(PHI*180./PI+0.1)
      WRITE(6,300) F,ITHET,IPHI,ALFA
      WRITE(6,305)
      WRITE(6,310) REFL,TRANS,ELOSS1,ELOSS2
      WRITE(6,320) SUM
       IF(KF.EQ.2) WRITE(2,340) ALFA
15    CONTINUE
300   FORMAT(//,'FREQ=',F10.3,2X,'THETA=',I4,2X,'PHI=',I4,2X,'ALFA=',F10
     1.5)
305   FORMAT(' THE DIVISION OF THE INCIDENT ENERGY IS AS FOLLOWS-')
310   FORMAT(' REFL=',E15.5,2X,'TRANS=',E15.5,2X,'DISS1=',E15.5,2X,'DASS
     12=',E15.5)
320   FORMAT(' THE TOTAL ENERGY SUM=',E15.5)
330   FORMAT(' IU,IV=',2(I4,2X),'RUV=',2(E15.5,2X),'TUV=',2(E15.5,2X))
```

```
216  340   FORMAT(E15.5)
217        STOP
218        END
```

```
      PROGRAM IMAGES
C
C     THIS PROGRAM EVALUATES THE STEADY STATE LEVEL & REVERBERANT
C     DECAY FOR ANY RECTANGULAR ROOM ,WITH SIX DIFFERENT (OR THE SAME
C     ) ABSORBENT SURFACES.
C
      DIMENSION Q(1,3),R(1,3),D(1,3),ALEV(500)
      COMMON AY(91),QS1(151,3),QS2(151,3)
C
C     INPUT GEOMETRY
C     D=ROOM DIMENSION MATRIX,Q=SOURCE POSITION MATRIX,R=RECEIVER
C     POSITION MATRIX,N=NO. OF RECEIVER POSITIONS TO TAKE
C
      READ(1,200) D(1,1),D(1,2),D(1,3)
      READ(1,210) Q(1,1),Q(1,2),Q(1,3)
      READ(1,220) N
C
C     INPUT ABSORPTION COEFFICIENTS
C     IF ANGULAR VARIATION OF ROOF ALFA WANTED PUT AY2=0.0
C
      READ(1,230) AX1,AX2,AY1,AY2,AZ1,AZ2
C
C      INPUT FREQUENCY & AIR ABSORPTION (NEPER/M)
C
      READ(1,240) FQ,BETA
      READ(1,380) L1,M1,N1
C
C     INPUT THE DESIRED RESOLUTION OF THE DECAY IN MS. (INTEGER)
C
      READ(1,260) IT
      WRITE(6,381) L1,M1,N1
      IF(AY2.GT.0.0) GOTO 2
      DO 1 I=1,91
      READ(7,245) AY(I)
1     CONTINUE
2     WRITE(6,300) D(1,1),D(1,2),D(1,3)
      WRITE(6,310) Q(1,1),Q(1,2),Q(1,3)
      WRITE(6,320) AX1,AX2,AY1,AY2,AZ1,AZ2
      WRITE(6,330) FQ,BETA
      W=10.**(WDB/10.)
      DO 4 I=1,N
C
C     READ IN THE RECEIVER POSITION VECTOR
C
      READ(1,250) R(1,1),R(1,2),R(1,3)
      WRITE(6,340) I
      WRITE(6,350) R(1,1),R(1,2),R(1,3)
      CALL SPLIM2(Q,R,D,AX1,AX2,AY1,AY2,AZ1,AZ2,BETA,SONIN,ALEV,AY,L1,M1
     1,N1,IT,L3)
C
C     CALCULATE THE SPL
C
      SPL=10.*ALOG10(SONIN)
      WRITE(6,360) SPL
      REF=ALEV(1)
      DO 3 J=1,L3
      IF(ALEV(J).EQ.0.0) GOTO 3
      J1=J*IT
C
C      NORMALISE BY THE SOURCE'S P.W.L.
C
      RELEV=ALEV(J)-REF
      WRITE(6,370) J1,RELEV
3     CONTINUE
4     CONTINUE
200   FORMAT(3F10.4)
210   FORMAT(3F10.4)
220   FORMAT(I4)
230   FORMAT(6F10.6)
240   FORMAT(2F10.4)
```

```
  245   FORMAT(E15.5)
  250   FORMAT(3F10.4)
  260   FORMAT(I4)
  300   FORMAT(' ROOM DIMENSIONS:X='F10.4,5X,'Y=',F10.4,5X,'Z=',F10.4)
  310   FORMAT(' SOURCE LOCATION:X=',F10.4,5X,'Y=',F10.4,5X,'Z=',F10.4)
  320   FORMAT(' ALFAS:AX1=',F10.3,'AX2=',F10.3,'AY1=',F10.3,'AY2=',F10.3,
       1'AZ1=',F10.6,'AZ2=',F10.6)
  330   FORMAT(' FREQUENCY=',F10.4,5X,'AIR ATTENUATION=',F10.4,'NEPER/M')
  340   FORMAT(' RECEIVER POSITION NO.=',I4)
  350   FORMAT(' RECEIVER LOCATION:X=',F10.4,5X,'Y=',F10.4,5X,'Z=',F10.4)
  360   FORMAT(' PWL-SPL=',F10.4,'DB')
  370   FORMAT(' LEVEL IN ',I4,'MS. SAMPLE=',F10.6,'DB')
  380   FORMAT(3I4)
  381   FORMAT(' NO. OF IMAGES=,X:',I4,5X,'Y=',I4,5X,'Z=',I4)
        STOP
        END
        SUBROUTINE SPLIM2(Q0,R0,D0,AX1,AX2,AY1,AY2,AZ1,AZ2,BETA0,SITOTAL,A
       1LEV,AY2A,L1,M1,N1,IT,L3)
        DIMENSION QS1(151,3),QS2(151,3),Q0(1,3),R0(1,3),D0(1,3)
         DIMENSION D1(8), ALF(8), E1(8), TIME(8)
        DIMENSION X(2),Y(2),Z(2),THETA(8),AY2I(8),C(8),D(8),ALEV(500)
        DIMENSION AY2A(92),ALEVI(500)
        K=1
        IF(AY2.EQ.0.0) K=0
        DO 201 I=1,8
        AY2I(I)=AY2
  201   CONTINUE
        DO 50 I=1,500
         ALEV(I)=0.
        ALEVI(I)=0.0
  50     CONTINUE
         PI=3.141592654
C
C       FINDING ODD +VE IMAGE LOCATION COMPONENTS
C
       QS2(1,1)=0.0
       QS2(1,2)=0.0
       QS2(1,3)=0.0
       DO 1 I0=1,150,2
        I1=I0-1
        QS1(I0,1)=FLOAT(I1)*D0(1,1)+Q0(1,1)
        QS1(I0,2)=(FLOAT(I1))*D0(1,2)+Q0(1,2)
        QS1(I0,3)=(FLOAT(I1))*D0(1,3)+Q0(1,3)
C
C       FINDING ODD  -VE IMAGE LOCATION COMPONENTS
C
       IP1=I0+1
       QS2(IP1,1)=-QS1(I0,1)
       QS2(IP1,2)=-QS1(I0,2)
       QS2(IP1,3)=-QS1(I0,3)
  1     CONTINUE
C
C       FINDING EVEN +VE IMAGE LOCATION COMPONENTS
C
       DO 2 I0=2,150,2
        QS1(I0,1)=FLOAT(I0)*D0(1,1)-Q0(1,1)
        QS1(I0,2)=FLOAT(I0)*D0(1,2)-Q0(1,2)
        QS1(I0,3)=FLOAT(I0)*D0(1,3)-Q0(1,3)
C
C       FINDING EVEN -VE IMAGE LOCATION COMPONENTS
C
       IP1=I0+1
       QS2(IP1,1)=-QS1(I0,1)
       QS2(IP1,2)=-QS1(I0,2)
       QS2(IP1,3)=-QS1(I0,3)
  2     CONTINUE
C
C      FINDING THE SIZE OF CIRCLE OF IMAGES TO CONSIDER
C
       XPMAX=ABS(QS1(L1,1)-R0(1,1))
       XNMAX=ABS(QS2(L1,1)-R0(1,1))
       YPMAX=ABS(QS1(M1.2)-R0(1.2))
```

```
      YNMAX=ABS(QS2(M1,2)-RO(1,2))
      ZPMAX=ABS(QS1(N1,3)-RO(1,3))
      ZNMAX=ABS(QS2(N1,3)-RO(1,3))
      DMAX=MIN(XPMAX,XNMAX,YPMAX,YNMAX,ZPMAX,ZNMAX)
      L3=1+INT(DMAX/(0.34*IT))
      WRITE(6,500) IT,L3
500   FORMAT(' THE MAX NO OF',I4,'MS. INTERVALS VALID=',I4)
C
C     WILL ONLY CONSIDER R.T. TO THREE SECS. AT PRESENT
C
      IF(L3.GE.500) DMAX=500.0*0.34*IT
      IF(L3.GT.500) L3=500
       SIREF=0.
C
C      DECIDING HOW MANY IMAGES TO CONSIDER
C
       IMO=1
       ILO=1
       INO=1
C
C     IL1,IM1,IN1= NO. OF X,Y,Z, WALL CROSSINGS
C
C      FINDING COMPONENTS OF IMAGE TO RECEIVER DISTANCE
C
3      DO 19 NO=INO,N1
       IN1=NO-1
      Z(1)=QS1(NO,3)-RO(1,3)
      Z(2)=QS2(NO,3)-RO(1,3)
       DO 18 MO=IMO,M1
       IM1=MO-1
      Y(1)=QS1(MO,2)-RO(1,2)
      Y(2)=QS2(MO,2)-RO(1,2)
       DO 17 LO=ILO,L1
       IL1=LO-1
      X(1)=QS1(LO,1)-RO(1,1)
      X(2)=QS2(LO,1)-RO(1,1)
400   FORMAT(' LO=',I3,5X,'MO=',I3,5X,'NO=',I3)
C
C      FINDING MAGNITUDES OF IMAGE-SOURCE TO RECEIVER DISTANCES
C
      IN=1
      DO 33 M=1,2
      DO 32 L=1,2
      DO 31 N=1,2
      D1(IN)=SQRT(X(L)*X(L)+Y(M)*Y(M)+Z(N)*Z(N))
      IF(K.GT.0) GOTO 29
      IF(MO.EQ.1) GOTO 29
C
C     FINDING THE ANGLE OF INTERSECTION WITH THE ROOF (IF NECESSARY)
C
      THETA(IN)=ABS(ATAN(SQRT(X(L)*X(L)+Z(N)*Z(N))/Y(M)))
      IANG=1+INT(THETA(IN)*180./PI+0.5)
      AY2I(IN)=AY2A(IANG)
650   FORMAT(' IN=',I4,5X,'ANGLE=',I4,5X,'ALFA(THETA)=',F10.6)
29    IF(IL1.EQ.0.AND.L.EQ.2) D1(IN)=0.0
      IF(IM1.EQ.0.AND.M.EQ.2) D1(IN)=0.0
      IF(IN1.EQ.0.AND.N.EQ.2) D1(IN)=0.0
      IN=IN+1
31    CONTINUE
32    CONTINUE
33    CONTINUE
C
C       FINDING WALL ALFA COMPONENTS (+VE OR -VE,ODD OR EVEN)
C
25    IF(FLOAT(IL1)/2.-INT(FLOAT(IL1/2)))4,4,5
4     A=((1.-AX1)*(1.-AX2))**(IL1/2)
      B=A
      GOTO 36
5      A=(1.-AX1)**((IL1-1)/2)*(1.-AX2)**((IL1+1)/2)
      B=(1.-AX1)**(LO/2)*(1.-AX2)**((IL1-1)/2)
36    DO 35 I=1,8
6     IF(FLOAT(IM1)/2.-INT(FLOAT(IM1/2))) 7,7,8
```

```
215  7      C(I)=((1.-AY1)*(1.-AY2I(I)))**(IM1/2)
216         D(I)=C(I)
217         GOTO 35
218  8      C(I)=(1.-AY1)**((IM1-1)/2)*(1.-AY2I(I))**(MO/2)
219         D(I)=(1.-AY1)**(MO/2)*(1.-AY2I(I))**((IM1-1)/2)
220  35     CONTINUE
221  9      IF(FLOAT(IN1)/2.-(IN1/2)) 10,10,11
222  10      E=((1.-AZ1)*(1.-AZ2))**(IN1/2)
223         F=E
224          GOTO 12
225  11      E=(1.-AZ1)**((IN1-1)/2)*(1.-AZ2)**((IN1+1)/2)
226         F=(1.-AZ1)**(NO/2)*(1.-AZ2)**((IN1-1)/2)
227  C
228  C       FINDING WALL ABSORPTION OVER SPECIFIC PATHS
229  C
230  12     ALF(1)=A*C(1)*E
231         ALF(2)=A*C(2)*F
232         ALF(3)=B*C(3)*E
233         ALF(4)=B*C(4)*F
234          ALF(5)=A*D(5)*E
235         ALF(6)=A*D(6)*F
236         ALF(7)=B*D(7)*E
237         ALF(8)=B*D(8)*F
238  C
239  C       CALCULATING PULSE ENERGIES &DELAYS
240  C
241          DO 15 N=1,8
242         IF(D1(N).EQ.0.0) GOTO 15
243         IF(D1(N).GT.DMAX) GOTO 15
244         E1(N)=ALF(N)*EXP(-BETA0*D1(N))/(4.*PI*D1(N)*D1(N))
245  105    FORMAT(' N=',I3,5X,'ENERGY=',E15.5)
246         SIREF=SIREF+E1(N)
247          TIME(N)=D1(N)/340.
248  C
249  C      SUMMING THE PULSES OVER 'IT' MSEC. INTERVALS
250  C
251         L2=INT(TIME(N)/(IT*0.001))+1
252         IF(L2.GT.L3) GOTO 15
253         ALEVI(L2)=ALEVI(L2)+E1(N)
254  15      CONTINUE
255  17      CONTINUE
256  18      CONTINUE
257  19      CONTINUE
258         DO 51 I0=1,L3
259         ISLOT=L3-I0+1
260         DO 52 I=1,ISLOT
261  52     ALEV(I)=ALEV(I)+ALEVI(ISLOT)
262  51     CONTINUE
263         DO 54 I0=1,L3
264         IF(ALEV(I0).EQ.0.0) GOTO 54
265         ALEV(I0)=10.0*ALOG10(ALEV(I0))
266  54     CONTINUE
267          SITOTAL=SIREF
268          RETURN
269         END
```

```
      PROGRAM ANGENXMOD
C
C     THIS PROGRAM EVALUATES THE RELATIVE ARRIVAL TIMES AND ENERGY
C     WEIGHTINGS OF THE COLLISIONS WITH 'X-WALLS'.
C     ONLY THE +VE OCTANT OF IMAGE SOURCES IS CONSIDERED
C
C     CONSIDERED. Y AND Z WALLS ARE TAKEN TO BE PERFECTLY REFLECTING,
C
      DIMENSION QS(150,3),D(3),Q(3),R(3),EI(50,9),NANGX(50,9)
      DIMENSION EITOT(50),ENORM(50,9)
C
C     INPUT SECTION
C     DO NOT PUT THE SOURCE TOO NEAR THE ROOM SURFACES!
C
C     QS=IMAGE SOURCE POSITION MATRIX,D=ROOM DIMENSION MATRIX;
C     R=RECEIVER POSITION MATRIX;Q=SOURCE POSITION MATRIX;
C     THX=ANGLE TO NORMAL AT THE 'X-WALLS';NANG=NO. OF REFLECTIONS
C     IN ANGULAR RANGE;EI=THEIR INCIDENT ENERGY THERE
C
      READ(5,100) D(1),D(2),D(3)
      READ(5,100) Q(1),Q(2),Q(3)
      READ(5,100) R(1),R(2),R(3)
      READ(5,110) LMAX,MMAX,NMAX,IT
      READ(5,120) DMAX
      READ(5,130) RC,XDB
  100 FORMAT(3F10.3)
  110 FORMAT(4I4)
  120 FORMAT(F10.3)
  130 FORMAT(2F10.5)
      WRITE(6,200) D(1),D(2),D(3)
      WRITE(6,210) Q(1),Q(2),Q(3)
      WRITE(6,220) R(1),R(2),R(3)
      WRITE(6,230) LMAX,MMAX,NMAX
      WRITE(6,240) DMAX
      WRITE(6,250) RC,XDB
  200 FORMAT(' ROOM DIMENSIONS:X=',F10.3,2X,'Y=',F10.3,2X,'Z=',F10.3)
  210 FORMAT(' SOURCE LOCATION:X=',F10.3,2X,'Y=',F10.3,2X,'Z=',F10.3)
  220 FORMAT(' RECEIVER LOCATION:X=',F10.3,2X,'Y=',F10.3,2X,'Z=',F10.3)
  230 FORMAT(' MAX. NO. OF IMAGES:X=',I4,2X,'Y=',I4,2X,'Z=',I4)
  240 FORMAT(' MAX IMAGE DISTANCE=',F10.3)
  250 FORMAT(' X-WALL REFL. COEFF.=',F10.5,4X,'  REFLECTIONS -'F10.5,'DB
     1DOWN NEGLECTED')
C
C                    CONSTANTS
C
      PI=3.14159265
      R2D=180.0/(PI*10.0)
      XR=10.0**(-XDB/10.0)
      NT=INT(DMAX/(0.34*IT))+1
      WRITE(6,260) IT,NT
  260 FORMAT(' TIME RESOLUTION=',I4,4X,'MAX. NO. OF TIME SLOTS=',I4)
C
C     INITIALISING THE SOURCE IMAGE ARRAY
C
      DO 1 I=1,150,2
      IM1=I-1
      QS(I,1)=IM1*D(1)+Q(1)
      QS(I,2)=IM1*D(2)+Q(2)
      QS(I,3)=IM1*D(3)+Q(3)
    1 CONTINUE
      DO 2 I=2,150,2
      QS(I,1)=I*D(1)-Q(1)
      QS(I,2)=I*D(2)-Q(2)
      QS(I,3)=I*D(3)-Q(3)
    2 CONTINUE
C
C       ZEROING THE ENERGY AND NO.OF IMPACTS ARRAYS
C
      EMEAN=0.0
      DO 4 I=1,NT
      EITOT(I)=0.0
```

```
      DO 3 J=1,9
      EI(I,J)=0.0
      NANGX(I,J)=0
    3 CONTINUE
    4 CONTINUE
      DO 8 L=1,LMAX
      X=QS(L,1)-R(1)
      LHIT=INT(FLOAT(L)/2.0+0.05)
      DO 7 M=1,MMAX
      Y=QS(M,2)-R(2)
      DO 6 N=1,NMAX
      Z=QS(N,3)-R(3)
      D2=X*X+Y*Y+Z*Z
      INTT=INT(SQRT(D2)/(0.34*IT))+1
      IF(INTT.GT.NT) GOTO 6
      IF((RC**LHIT/D2).LT.XR) GOTO 6
      IF(L.EQ.1) GOTO 6
      IF(X.EQ.0.0) THX=PI/2.
      IF(X.EQ.0.0) GOTO 21
      THX=ATAN(SQRT(Y*Y+Z*Z)/ABS(X))
   21 ITHX=INT(THX*R2D)+1
      NANGX(INTT,ITHX)=NANGX(INTT,ITHX)+LHIT
C
C      CALCULATING THE ENERGIES AT THE ROOF REFLECTIONS
C
      IF(FLOAT(L)/2.-L/2-0.05) 26,27,27
C
C      EVEN ORDER IMAGES
C
   26  DO 28 I=1,LHIT
      RH=Q(1)+(I-1)*D(1)*2.
      DI=RH/COS(THX)
      EII=(RC**(I-1))
      EI(INTT,ITHX)=EI(INTT,ITHX)+EII
      EITOT(INTT)=EITOT(INTT)+EII
   28 CONTINUE
      GOTO 6
C
C     ODD ORDER IMAGES
C
   27 DO 29 I=1,LHIT
      RH=Q(1)+(2*I-1)*D(1)
      DI=RH/COS(THX)
      EII=(RC**(I-1))
      EI(INTT,ITHX)=EI(INTT,ITHX)+EII
      EITOT(INTT)=EITOT(INTT)+EII
   29 CONTINUE
    6 CONTINUE
    7 CONTINUE
    8 CONTINUE
C
C     OUTPUTING THE VALUES
C
C
C     EXPRESSING THE ENERGY LOST IN ANGLE A %
C     OF THE TOTAL IN THE TIME-SLOT
C
C
      DO 31 I=1,NT
      IF(EITOT(I).EQ.0.0) GOTO 31
      DO 30 J=1,9
      ENORM(I,J)=EI(I,J)/EITOT(I)
   30 CONTINUE
   31 CONTINUE
      WRITE(6,360)
      WRITE(6,300)
      DO 32 I=1,NT
      WRITE(6,310) I,(ENORM(I,J),J=1,9)
   32 CONTINUE
      WRITE(6,300)
      DO 9 I=1,NT
      WRITE(6,310) I,(EI(I,J),J=1,9)
```

```
144  9      CONTINUE
145  C
146  C      AVERAGING THE ARRAY IN TIME
147  C
148         IF(NT.EQ.1) GOTO 99
149         DO 12 I=2,NT
150         ISLOT=NT-I+1
151          ISLOT1=ISLOT+1
152         DO 11 I1=ISLOT1,NT
153         EITOT(I1)=EITOT(I1)+EITOT(ISLOT)
154         DO 10 J=1,9
155         NANGX(I1,J)=NANGX(I1,J)+NANGX(ISLOT,J)
156         EI(I1,J)=EI(I1,J)+EI(ISLOT,J)
157  10     CONTINUE
158  11     CONTINUE
159  12     CONTINUE
160  C
161  C                    OUTPUTING THE AVERAGES
162  C
163         WRITE(6,320)
164         WRITE(6,300)
165         DO 13 I=1,NT
166         WRITE(6,310) I,(EI(I,J),J=1,9)
167  13     CONTINUE
168         WRITE(6,330)
169         WRITE(6,300)
170         DO 14 I=1,NT
171         WRITE(6,340) I,(NANGX(I,J),J=1,9)
172  14     CONTINUE
173  C
174  C       COMPUTING THE MEAN ANGLE AT WHICH THE AVERAGED ENERGY HITS
175  C
176         WRITE(6,370)
177         WRITE(6,375)
178         DO 34 I=1,NT
179         ESUM=0.0
180         DO 33 J=1,9
181         ESUM=ESUM+EI(I,J)*((J*10.0)-5.0)
182  33     CONTINUE
183         IF(EITOT(I).EQ.0.0) GOTO 34
184         EMEAN=ESUM/EITOT(I)
185         WRITE(6,380) I,EMEAN
186  34     CONTINUE
187  C
188  C                PRESENTING THE AVERAGE ENERGY/ANGLE SLOT/ NO. OF HITS
189  C
190  99     WRITE(6,350)
191         WRITE(6,300)
192         DO 16 I=1,NT
193         DO 15 J=1,9
194         IF(NANGX(I,J).EQ.0) GOTO 15
195         EI(I,J)=EI(I,J)/FLOAT(NANGX(I,J))
196  15     CONTINUE
197         WRITE(6,310) I,(EI(I,J),J=1,9)
198  16     CONTINUE
199  300    FORMAT(' TIME INT.',3X,'5',11X,'15',10X,'25',10X,'35',10X,'45',10X
200        1,'55',10X,'65',10X,'75',10X,'85')
201  310    FORMAT(I4,5X,9(E10.4,2X))
202  320    FORMAT(//,' THE TIME-AVERAGED ENERGY VALUES:')
203  330    FORMAT(//,' THE TIME-AVERAGED ANGLE NOS.')
204  340    FORMAT(I4,5X,9(I8,4X))
205  350    FORMAT(//,' AVERAGE ENERGY/HIT')
206  360    FORMAT(//,' THE NORMALISED TIME SLOT ENERGIES')
207  370    FORMAT(//,' THE ANGLE AT WHICH THE MEAN ENERGY HITS X-WALLS')
208  375    FORMAT(' TIME SLOT   ANGLE')
209  380    FORMAT(2X,I4,8X,F10.5)
210  999    STOP
211         END
```

```
      PROGRAM INFRM
C
C     THIS PROGRAM STUDIES THE SOUND FIELD IN AN INFINITELY LONG ROOM
C     WITH AN ANGULARLY VARYING ROOF ABSORPTION & SCATTERING FLOOR
C
      DIMENSION QS1(150,2),DECAY(300),ARF(91),RFL(91),S(3),RR(3),THETA(4
     1),X(2),Y(2),XD(2),B1(4),B2(4),DS2(4),DD2(2)
      DIMENSION SDECAY(500),DDECAY(500),ITIMED(2),ITIMES(4),ALEVS(500),A
     1LEVD(500),F(4)
C
C     INPUT SECTION
C
C     RH=ROOM HEIGHT;RW=ROOM WIDTH;ALFAW=WALL ABSORPTION
C     S=SOURCE POSITION VECTOR (IN FACT Z COORD.=0.0)
C     NR=NO. OF RECEIVER POSITIONS DESIRED
C     KRF & KFL = FLAGS FOR WHETHER ROOF AND/OR FLOOR CHARACTERISTICS
C     VARY WITH ANGLE (SEE COMMENT BELOW)
C
      READ(5,100) RH,RW,ALFAW
      READ(5,110) S(1),S(2),S(3)
      READ(5,120) NR,KRF,KFL
C
C     READ IN THE MAX NO OF X & Y IMAGES AND THE RESOLUTION OF DECAY(MS)
C
      READ(5,125) LMAX,MMAX,IT
C
C     IF ANGULAR VARIATION OF EITHER ROOF OR FLOOR PROPERTIES WANTED PUT
C     KRF OR KFL EQUAL TO 1 RESPECTIVELY
C
      IF(KRF-1)1,2,1
1     READ(5,130) ALFA
      GOTO 4
2     DO 3 I=1,91
3     READ(7,130) ARF(I)
4     IF(KFL-1) 5,6,5
5     READ(5,130) R
      GOTO 8
6     DO 7 I=1,91
7     READ(8,130) RFL(I)
8     IF(KFL-1) 41,43,41
41    DO 42 I=1,4
42    B2(I)=R
43    IF(KRF-1) 44,46,44
44    DO 45 I=1,4
45    B1(I)=1.-ALFA
46    C=340.
      PI=3.14159265358979
      R2D=180./PI
      WRITE(6,210) RH,RW,ALFAW
      WRITE(6,220) S(1),S(2),S(3)
      WRITE(6,230) LMAX,MMAX
      IF(KRF.EQ.1) GOTO 47
      WRITE(6,240) R
      GOTO 48
47      CALL DIFVAL(RFL,R)
      WRITE(6,245) R
48    IF(KFL.EQ.1) GOTO 49
      WRITE(6,250) ALFA
      GOTO 50
49    CALL DIFVAL(ARF,ALFA)
      WRITE(6,260) ALFA
100   FORMAT(3F10.3)
110   FORMAT(3F10.3)
120   FORMAT(3I4)
125   FORMAT(3I4)
130   FORMAT(F10.5)
140   FORMAT(3F10.3)
C
C     CALCULATING THE RELEVANT DIFFUSE FIELD PARAMETERS
C    (ASSUMING THE FLOOR DOESN'T ABSORB!)
C
```

```
 50     AZ=2.*ALFAW/RW+ALFA/RH+1./(2.*RH)
        BZ=1./(2.*RH)
        RN=C*2.*(RH+RW)/(RH*RW*PI)
        AMB=RN*(2.*RH*ALFAW+RW*ALFA)/(2.*(RH+RW))
        CONST=2.*(AZ+BZ)/(AZ*AZ-BZ*BZ)*(1.-R)/RH
        SPEC=(1.-R)*RW/2.
        RKAPPA=SQRT(AZ*AZ-BZ*BZ)
C
C       CALCULATING THE IMAGE SOURCE COORDINATES & STORING THEM
C
C       ODD +VE IMAGE LOCATIONS
C
        DO 9 I=1,150,2
        I1=I-1
        QS1(I,1)=I1*RW+S(1)
        QS1(I,2)=I1*RH+S(2)
 9      CONTINUE
C
C       EVEN +VE IMAGE LOCATIONS
C
        DO 51 I=2,150,2
        QS1(I,1)=I*RW-S(1)
        QS1(I,2)=I*RH-S(2)
 51     CONTINUE
        DO 26 I=1,NR
        READ(5,140) RR(1),RR(2),RR(3)
C
C       FINDING THE RAIUS OF IMAGE CONTRIBUTIONS TO BE CONSIDERED
C
        XPMAX=ABS(QS1(LMAX,1)-RR(1))
        YPMAX=ABS(QS1(MMAX,2)-RR(2))
        LMM1=LMAX-1
        MMM1=MMAX-1
        XNMAX=ABS(-QS1(LMM1,1)-RR(1))
        YNMAX=ABS(-QS1(MMM1,2)-RR(2))
        DMAX=MIN(XPMAX,XNMAX,YPMAX,YNMAX)
        DIMAX=1./DMAX
        D2MAX=DMAX*DMAX
        L3=1+INT(DMAX/(0.34*IT))
        WRITE(6,270) IT,L3
        DO 91 I0=1,500
        SDECAY(I0)=0.0
        DDECAY(I0)=0.0
        ALEVS(I0)=0.0
 91     ALEVD(I0)=0.0
        IF(I.GT.1) GOTO 69
C
C        CALCULATING THE SPECULAR FIELD'S CONTRIBUTION TO THE DIFFUSE
C        FIELD AT (RW/2.,0,0) I.E. ON FLOOR AT SOURCE LOCATION
C
C
        IF(KRF.EQ.1) ALFA=ARF(1)
        IF(KFL.EQ.1) R=RFL(1)
        EI=0.0
        DO 35 L=1,LMAX
        LM1=L-1
        XP=QS1(L,1)-RW/2.
        IF(L.EQ.1) GOTO 29
        XM=-QS1(LM1,1)-RW/2.
 29     A=(1.-ALFAW)**LM1
        DO 34 M=1,MMAX
        MM1=M-1
        YD=QS1(M,2)
        IF(FLOAT(MM1)/2.-(MM1/2)-0.1) 31,31,32
 31     B=((1.-ALFA)*R)**(MM1/2)
        GOTO 33
 32     B=(1.-ALFA)**(M/2)*R**(MM1/2)
 33     IF(L.EQ.1) EI=EI+A*B/(XP*XP+YD*YD)
        IF(L.EQ.1) GOTO 34
        DIP=1./SQRT(XP*XP+YD*YD)
        DIM=1./SQRT(XM*XM+YD*YD)
        IF(DIP.LT.DIMAX) DIP=0.0
```

```
144         IF(DIM.LT.DIMAX) DIM=0.0
145         EI=EI+A*B*(DIP*DIP+DIM*DIM)
146   400   FORMAT(' LM1=',I4,2X,'MM1=',I4,2X,'EI=',E12.5)
147   34    CONTINUE
148   35    CONTINUE
149         EIZO=EI/(4.*PI)
150   C
151   C     CALCULATING THE VALUE OF I AT Z AND ALSO THE SPECULAR CONTRIBUTION
152   C     THERE AS WELL
153   C
154   69    DO 70 J=1,4
155   70    THETA(J)=1.0
156   C
157   C
158         Z=RR(3)
159         EIS=0.0
160         EID=0.0
161         DO 25 L=1,LMAX
162         LM1=L-1
163         X(1)=QS1(L,1)-RR(1)
164         XD(1)=QS1(L,1)-RW/2.
165         IF(L.EQ.1) GOTO 61
166         X(2)=-QS1(LM1,1)-RR(1)
167         XD(2)=-QS1(LM1,1)-RW/2.
168   61    A=(1.-ALFAW)**LM1
169         DO 24 M=1,MMAX
170         MM1=M-1
171   405   FORMAT(//,' NO OF X CROOSINGS=',I4,2X,'NO. OF Y CROSSINGS=',I4)
172         Y(1)=QS1(M,2)-RR(2)
173         IF(M.EQ.1) GOTO 62
174         Y(2)=-QS1(MM1,2)-RR(2)
175   62    YD=QS1(M,2)
176   C
177   C      FOUR THETAS ARE FOUND  ONLY X+VE,Y+VE AND X-VE,Y+VE ARE NEEDED
178   C     FOR THE DIFFUSE FIELD TERMS
179   C     WILL ASSUME THAT THE THETAS ARE THE SAME FOR DIFFUSE & SPECULAR
180   C
181         IJK=0
182         DO 11 IX=1,2
183         IF(L.EQ.1.AND.IX.EQ.2) GOTO 63
184         DD2(IX)=(XD(IX)*XD(IX)+YD*YD+Z*Z)
185         ITIMED(IX)=INT(SQRT(DD2(IX))/(0.34*IT))
186   410   FORMAT(' IX=',I4,2X,'DIFFUSE FIELD DIST.=',F10.5)
187   63    DO 10 IY=1,2
188         IJK=IJK+1
189         IF(L.EQ.1.AND.IX.EQ.2) GOTO 10
190         IF(M.EQ.1) THETA(IJK)=PI/2.
191         IF(M.EQ.1) GOTO 64
192         THETA(IJK)=ABS(ATAN(SQRT(X(IX)*X(IX)+Z*Z)/Y(IY)))
193   64    IF(M.EQ.1.AND.IY.EQ.2) GOTO 10
194         DS2(IJK)=(X(IX)*X(IX)+Y(IY)*Y(IY)+Z*Z)
195         ITIMES(IJK)=INT(SQRT(DS2(IJK))/(0.34*IT))
196   415   FORMAT(' IX=',I4,2X,'IY=',I4,2X,'THETA=',F10.5,2X,'DS2=',F10.5)
197   10    CONTINUE
198   11    CONTINUE
199   C
200   C     EVALUATING THE ROOF AND FLOOR REFLECTION COEFFICIENTS COMBINATIONS
201   C
202         IF(KRF-1) 15,13,15
203   13    DO 14 J=1,4
204   14    B1(J)=1.-ARF(INT(THETA(J)*R2D+0.5))
205   15    IF(KFL-1) 18,16,18
206   16    DO 17 J=1,4
207   17    B2(J)=RFL(INT(THETA(J)*R2D+0.5))
208   18    IF(FLOAT(MM1)/2.-MM1/2-0.1)19,19,21
209   C
210   C     EVEN NO OF REFLECTIONS IN THE ROOF AND FLOOR
211   C
212   19    DO 20 J=1,4
213   20    F(J)=(B1(J)*B2(J))**(MM1/2)*A
214         GOTO 28
215   C
```

```
      C     ODD NO. OF FLOOR & ROOF REFLECTIONS
      C
   21 DO 23 J=1,4
      C
      C     FINDING IF FLOOR OR ROOF REFLECTION FIRST
      C
      IF(J.EQ.1.OR.J.EQ.3) GOTO 22
      C
      C                  FLOOR REFLECTION FIRST
      C
      F(J)=B2(J)**(M/2)*B1(J)**(MM1/2)*A
      GOTO 23
      C
      C                  ROOF REFLECTION FIRST
      C
   22  F(J)=B1(J)**(M/2)*B2(J)**(MM1/2)*A
   23 CONTINUE
      C
      C     CALCULATING THE ENERGIES FOR STEADY-STATE & TIME DECAY
      C
   28 DO 72 J=1,4
      IF(MM1.EQ.0.AND.(FLOAT(J)/2.-J/2-0.1).LT.0.0) GOTO 72
      IF(LM1.EQ.0.AND.J.GT.2) GOTO 72
      IF(DS2(J).GT.D2MAX) GOTO 71
      EISI=F(J)/DS2(J)
  440 FORMAT(' SPECULAR DIST.=',F10.5,4X,'SPEC. FIELD CONTRIBUTION=',E12
     1.5)
      SDECAY(ITIMES(J))=SDECAY(ITIMES(J))+EISI
      EIS=EIS+EISI
   71 IF(J.EQ.2.OR.J.EQ.4) GOTO 72
      IF(DD2((J+1)/2).GT.D2MAX) GOTO 72
      EIDI=F(J)*COS(THETA(J))/DD2((J+1)/2)
      J2=(J+1)/2
  450 FORMAT(' DIFF.FIELD DIST.=',F10.5,4X,'DIFF. FIELD CONTRIBUTION=',E
     112.5)
      DDECAY(ITIMED((J+1)/2))=DDECAY(ITIMED((J+1)/2))+EIDI
      EID=EID+EIDI
   72 CONTINUE
   24 CONTINUE
   25 CONTINUE
      EIS=EIS/(4.*PI)
      EID=EID/(4.*PI)
      C
      C     CALCULATING THE DIFFUSE FIELD STEADY-STATE LEVEL AT Z
      C
      PD2=CONST*(EID+EIZ0*EXP(-RKAPPA*Z))
      P2=PD2+EIS
      DB=10.*ALOG10(P2)
      WRITE(6,300) I
      WRITE(6,310) RR(1),RR(2),RR(3)
      WRITE(6,320) P2,PD2,EIS
      WRITE(6,350) EID
      WRITE(6,330) DB
      DO 93 I0=1,L3
      ISLOT=L3-I0+1
      DO 92 I1=1,ISLOT
      ALEVS(I1)=ALEVS(I1)+SDECAY(ISLOT)
   92 ALEVD(I1)=ALEVD(I1)+DDECAY(ISLOT)
   93 CONTINUE
      PILOG=10.0*ALOG10(4.*PI)
      DO 94 I0=1,L3
      IF(ALEVS(I0).EQ.0.0) GOTO 94
      ALEVS(I0)=10.0*ALOG10(ALEVS(I0))-PILOG
      IF(ALEVD(I0).EQ.0.0) GOTO 94
      ALEVD(I0)=10.0*ALOG10(ALEVD(I0))-PILOG
      IF(I0.EQ.1) WRITE(6,360) ALEVS(I0),ALEVD(I0)
      RELEVS=ALEVS(I0)-ALEVS(1)
      RELEVD=ALEVD(I0)-ALEVD(1)
      WRITE(6,340)I0,RELEVS,RELEVD
  340 FORMAT(' TIME SLOT=',I4,4X,'SPEC. LEVEL=',F10.5,'DB',4X,'DIFF. CON
     1TRIBUTION=',F10.5)
   94 CONTINUE
```

```
288  26    CONTINUE
289  210   FORMAT(' ROOM HEIGHT=',F10.3,'M WIDTH=',F10.3,'M WALL ALFA=',F10.3
290       1)
291  220   FORMAT(' SOURCE POSITION=',3(F10.3,2X))
292  230   FORMAT(' NO. OF IMAGES:X=',I4,2X,'Y=',I4)
293  240   FORMAT(' UNIFORM FLOOR SPEC. REFL. COEFF.=',F10.3)
294  245   FORMAT(' THE DIFFUSE FIELD VALUE OF R WOULD BE=',F10.5)
295  250   FORMAT(' UNIFORM ROOF ABSORPTION COEFFICIENT=',F10.3)
296  260   FORMAT(' THE DIFFUSE FIELD VALUE OF ALFA WOULD BE=',F10.5)
297  270   FORMAT(' THE MAX NO OF',I4,'MS. INTERVALS VALID=',I4)
298  300   FORMAT(//,' RECEIVER POSITION NO.:',I4)
299  310   FORMAT(' RECEIVER COORDINATES:',3(F10.3,2X))
300  320   FORMAT(' OVERALL LEVEL=',E12.5,2X,'DIFFUSE TERM='E12.5,2X,'SPECULA
301       1R TERM=',E12.5)
302  330   FORMAT(' LEVEL IN DB=',F10.6)
303  350   FORMAT(' THE VALUE OF I(Z)=',E15.7)
304  360   FORMAT(' SPEC. REF.=',E15.7,5X,'DIFF. CONTRIB.=',E15.7)
305        STOP
306        END
307        SUBROUTINE DIFVAL
308  C
309  C     THIS ROUTINE FINDS A DIFFUSE (3-D) FIELD VALUE FOR THE REFLECTION
310
311  C     AND ABSORTION COEFFICIENTS ASSUMING THEY ONLY VARY WITH ANGLE OF
312  C     INCIDENCE
313  C     INPUT ARRAY SHOULD CONTAIN THE VARIATION IN 1 DEGREE SPACINGS
314  C     FROM 0 TO 90 INCLUSIVE
315  C
316        DIMENSION ARRAY(91)
317        PI=3.141593
318        D2R=PI/180.
319        DO 1 I=2,90,2
320  1     AVVAL=2.*ARRAY(I)*SIN(2.*(I-1)*D2R)+AVVAL
321        DO 2 I=3,89,2
322  2     AVVAL=ARRAY(I)*SIN(2.*(I-1)*D2R)+AVVAL
323        AVVAL=2.*D2R/3.*AVVAL
324        RETURN
325        END
```